Spring 4-14-2022

Approaches in Molecular Engineering to Optimize the Desired Properties of Photoactive Molecules

Douglas Joseph Breen
University of New Mexico - Main Campus

Douglas J. Breen
Candidate

Chemistry and Chemical Biology
Department

This dissertation is approved, and it is acceptable in quality and form for publication:

Approved by the Dissertation Committee:

Prof. Jeffrey J. Rack , Chairperson

Prof. Martin L. Kirk

Prof. Alejandro Manjavacas

Prof. Dongchang Chen

APPROACHES IN MOLECULAR ENGINEERING TO OPTIMIZE THE DESIRED PROPERTIES OF PHOTOACTIVE MOLECULES

by

DOUGLAS J. BREEN

B.S., Chemistry, The University of New Mexico 2014
B.S., Biology, The University of New Mexico 2014

DISSERTATION

Submitted in Partial Fulfillment of the
Requirements for the Degree of

Doctor of Philosophy
Chemistry

The University of New Mexico
Albuquerque, New Mexico

May, 2022

DEDICATION

To Iyana,

Who has only ever known me

as a broke graduate student,

and loves me anyways.

I could not ask for a better person

to share my life with.

Here's to our next chapter.

To Mom,

Who has looked after me

and helped me in ways

that I do not yet even comprehend.

.

ACKNOWLEDGEMENTS

To the many hardworking staff members within the chemistry department, you have my sincere thanks for keeping the gears of research turning. Bobby and Teri are absolute rock stars, always going the extra mile for the sake of us graduate students.

To our collaborators from other institutions, I extend my appreciation for your input and contributions to our research. I want to personally recognize Dr. Christopher Ziegler, who produced flawless X-ray crystallography data from my often-second-rate crystal samples, Dr. Edwin Webster, for his insightful DFT calculations, and Dr. Ryan O'Donnell, for our work that is too interesting to put into this dissertation.

To my group members, past and present, you have been my friends in the darkest of places. Literally. The Dr.'s Gilbert, Sebastian, and Ellie (and Brad), I'm as cool as you are now. Emigdio and Rajani, you'll be as cool as me by 2023. Glorianne, keep up the hard work! Pauline, Kaan, Melissa, Sam, and Jake, you have added a wonderful spark to our little research family. Jaclyn, never change. Or do, if you want.

To the esteemed members of my dissertation committee: Professor Dongchang Chen, Professor Martin Kirk, and Professor Alejandro Manjavacas, thank you for putting time aside from your busy schedules to assist me in this endeavor.

To my advisor, Professor Jeff Rack, I cannot begin to express how much of a positive force you have been in my life over the last several years. Your empathy, wisdom, and guidance have helped bring about a better version of myself, both professionally and in personally. I hope that you continue to cultivate success and positivity within your research group for years to come.

To my dear friends and family, you have always been my source of inspiration. I will miss you all like crazy when I move away from Albuquerque for the first time in my life. That said, I'm sure we'll still see each other often. I love you.

APPROACHES IN MOLECULAR ENGINEERING
TO OPTIMIZE THE DESIRED PROPERTIES OF PHOTOACTIVE MOLECULES

by

DOUGLAS J. BREEN

B.S., Chemistry, The University of New Mexico 2014
B.S., Biology, The University of New Mexico 2014
Ph.D., Chemistry, The University of New Mexico 2022

ABSTRACT

Within this dissertation, photochemical systems that bear significance to next-generation photonic materials and devices are explored. Notable advances in the design, synthesis, and characterization of three distinct groups of photoactive molecules are achieved through molecular design and spectroscopic analysis. First, novel ruthenium sulfoxide complexes bearing substituted phosphine ligands are found to provide extraordinary control over photoisomerization quantum yields. A comparison of these complexes reveals ground-state characteristics that are instrumental in this reactivity, while a novel spectroscopic technique provides rare structural evidence for an O-bonded metastable isomer. Ruthenium complexes bearing chelating carbene-sulfoxide ligands rapidly thermally revert from the O-bonded metastable isomer to the S-bonded isomer in the ground state and are resistant to photosubstitution, even in strong donor solvents like acetonitrile. Second, the photophysics of pyrene sulfoxide compounds with substituted alkyl and aryl substituents are investigated. These compounds have been researched for over fifty years due to their interesting pyramidal inversion properties, but in-depth excited state studies have been lacking. An excited state pathway is proposed for these compounds that addresses their photochemical response to both changes in

solvent and changes in substituent. Third, platinum-containing small molecules with roller-wheel type stacking interactions, which are a promising in bulk heterojunction photovoltaic devices, are developed. Time-resolved absorption and emission spectroscopies are employed to reveal the excited state dynamics of these systems, as well as the role of extended pi-bridges and electron acceptor units. In total, the projects that are covered herein address how molecular engineering can be used to both drastically alter the chemical properties of a system and employ those changes as spectroscopic handles to gain insight about excited state dynamics.

DECLARATION

This dissertation is a compilation of several projects that I worked on throughout graduate school. Chapters three, four, and five contain bodies of work that are either published in peer-reviewed scientific journals or have been submitted for publication at the time of this writing. Chapter seven contains the supporting information for these bodies of work. The following citations are for published manuscripts contained within.

Chapter Three:

Journal of the American Chemical Society **2018**, *140*, 9819–9822.
doi: 10.1021/jacs.8b05957

Inorganic Chemistry **2021**, *60*, 16120-16127.
doi: 10.1021/acs.inorgchem.1c01558

My contribution to each body of work is as follows. For sections 3.1 and 3.2, I collected UV-Vis, femtosecond transient absorption, electrochemical, infrared, and emission spectroscopic data. I provided written analyses and figures for these data and the X-ray crystallographic and NMR data. My synthetic contribution was minor. For section 3.3, I collected the femtosecond transient absorption data and prepared the analysis and figures for those measurements. In chapter 4, I collected all of the data and prepared the writen analysis and figures. In chapter 4, I collected femtosecond transient absorption, nanosecond flash photolysis, and emission spectroscopic data. I prepared written analysis and figures of the excited-state dynamics and developed a model to explain my findings. All work was performed in cooperation with Professor Jeffrey Rack at the University of New Mexico.

TABLE OF CONTENTS

LIST OF FIGURES

LIST OF TABLES

LIST OF SCHEMES

LIST OF ABBREVIATIONS

$^1O_2$ ---------- Singlet Oxygen

$^3O_2$ ---------- Triplet Oxygen

ATR-IR ---------- Attenuated Total Reflectance Infrared

BDT ---------- Benzenedithiophene

bpy ----------2,2'-Bipyridine

BTD ---------- Benzothiadiazole

CD----------Circular Dichroism

CT ---------- Charge-Transfer

CV ---------- Cyclic Voltammetry

DCE ---------- 1,2-Dichloroethane

DCM ---------- Dichloromethane

DFT ---------- Density-Functional Theory

DI ---------- Deionized

DMSO ---------- Dimethyl Sulfoxide

ECEC ---------- Electrochemical Chemical Electrochemical Chemical

EG ---------- Ethylene Glycol

ESA ---------- Excited State Absorption

ESI-MS ---------- Electrospray Ionization Mass Spectra

ET ---------- Electron Transfer

EtOH ---------- Ethanol

ES ---------- Excited State

FC ---------- Franck-Condon

FTIR ---------- Fourier Transform Infrared

GS ---------- Ground State

GSB ----------Ground State Bleach

HOMO ---------- Highest Occupied Molecular Orbital

IC ---------- Internal Conversion

ICT ---------- Intramolecular Charge Transfer

IR ---------- Infrared

ISC ---------- Intersystem Crossing

LF ---------- Ligand-Field

LMCT ---------- Ligand-to-Metal Charge-Transfer

LUMO ---------- Lowest Unoccupied Molecular Orbital

mCPBA ---------- Meta-Chloroperoxybenzoic Acid

MC ---------- Metal-Centered

MeCN ---------- Acetonitrile

MLCT ---------- Metal-to-Ligand Charge-Transfer

NIR ---------- Near-Infrared

NMR ---------- Nuclear Magnetic Resonance

NTO ---------- Natural Transition Orbital

OPV ---------- Organic Photovoltaic

PMMA ---------- Polymethyl Methacrylate

RWPt----------Platinum Roller-Wheel

S ---------- Singlet State

T ---------- Triplet State

TA ---------- Transient Absorption

TAS ---------- Transient Absorption Spectrometer

TCSPC---------- Time-Correlated Single-Photon Counting

TD-DFT ---------- Time-Dependent Density-Functional Theory

THF ---------- Tetrahydrofuran

TICT ---------- Twisted Intramolecular Charge Transfer

tpy ---------- 2,2';6',2"-terpyridine

UV-Vis ---------- Ultraviolet-Visible

ΔA ----------Difference in Absorbance

λ_{Abs} ---------- Absorption Wavelength

λ_{Em} ---------- Emission Wavelength

λ_{Ex} ---------- Excitation Wavelength

CHAPTER 1
Introduction

The world of photochemistry is rich with molecular systems capable of utilizing photonic energy for fascinating applications. Photochemical systems are typified by the simplicity of their reaction conditions and the complexity of the generated intermediates. High-energy excited states, formed instantaneously upon absorption of a photon, allow molecules to overcome large energy barriers in short periods of time. These excited states are the cornerstone of photochemistry and serve as the basis for natural functions like vision, photosynthesis, and the production of vitamin D; the mechanisms of which have inspired centuries of study and technological progress. Photochemistry is employed throughout the scientific community today and propels the fields of biology (molecular fluorescent probes and biological sensors), energy harvesting (photovoltaics and water oxidation) computing (optical switches and holographic data storage), physics (the development of non-linear optical materials) and beyond.

Excited State Decay Pathways

Once a molecule is in an excited state, it has a myriad of pathways by which it can return to the ground state. Intermolecular relaxation pathways are available if another molecule can engage in energy or electron transfer with the molecule or cause a chemical reaction. Otherwise, intramolecular decay pathways will dominate. The energy level diagram in Figure 1 depicts typical radiative (solid lines) and nonradiative (dashed lines) relaxation pathways available to an excited-state molecule. Here, the lowest-energy state

(S_0) represents a singlet ground state and its many vibrational modes. Absorption of light (blue line) generates a high-energy, vibrationally "hot" electronic state (S_2). From there, the molecule will undergo vibrational relaxation (k_{VR}) via intramolecular vibrational redistribution (IVR) and vibrational cooling. IVR occurs instantly upon excitation to the Franck-Condon (FC) region and involves the transfer of energy among vibrational energy modes of the excited molecule without a loss of energy. Vibrational cooling proceeds by the loss of excited-state potential energy into the solvent bath. As the molecule settles into lower vibrational energy levels of the S_2 state, it undergoes internal conversion (k_{IC}) to the lowest-energy singlet excited state, S_1, without a change in the molecular spin state. Three relaxation pathways are depicted from S_1, including internal conversion to S_0, fluorescence (k_{FL}) to S_0, or intersystem crossing (k_{ISC}) to a triplet excited-state. Intersystem crossing is a non-radiative process, like internal conversion, though it occurs with a change in the spin state of the molecule. The lowest-energy triplet excited state, T_1, can decay back to the ground state by intersystem crossing or phosphorescence (k_{Ph}). Radiative decay processes are only shown as proceeding from the lowest-energy excited states of a given multiplicity; a phenomenon known as Kasha's rule. While there are exceptions to Kasha's rule, it holds for most photochemical systems. The solid red line in Figure 1, excited state absorption, does not represent relaxation, but rather an excitation event that is employed in transient absorption spectroscopy in order gain insight into the dynamics of excited state molecules.

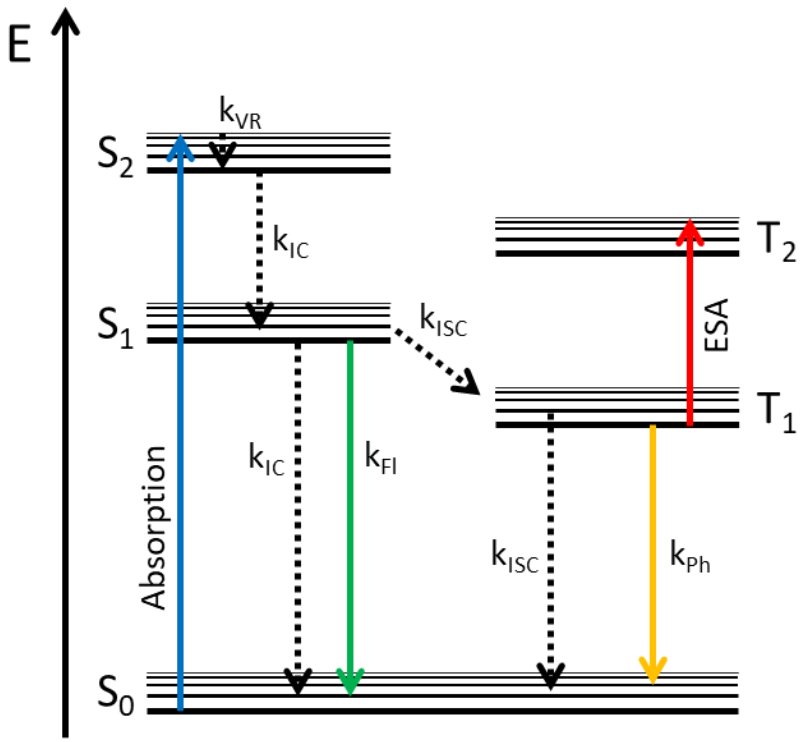

Figure 1. *An energy level diagram depicting intramolecular excited state decay pathways, labeled by their respective rate constants (k). Radiative decay pathways, indicated by solid lines, include fluorescence (k_{FI}) and phosphorescence (k_{Ph}). Non-radiative decay pathways, indicated by dashed lines, include vibrational relaxation (k_{VR}), internal conversion (k_{IC}), and intersystem crossing (k_{ISC}). Also depicted are ground-state absorption (blue line) and excited-state absorption (red line) events.*

Transient Absorption Spectroscopy

The short-lived nature of excited state populations makes them particularly difficult to characterize. While standard experimental techniques like absorption and emission spectroscopy can reveal the relative energy of some excited state, or even provide information about its vibronic structure, they are unable to provide information

as to the evolution of an excited state population over time. The advent of ultrafast lasers in the 1990s revealed a new avenue for studying photochemically interesting molecular systems; especially those with complicated dynamics and short lifetimes. Ultrafast laser systems now routinely provide time resolutions of sub-50 fs, allowing researchers to probe even the fastest excited state relaxation processes. Since the collection and analysis of transient absorption spectra are at the heart of this dissertation, a brief introduction into this technique will be presented below.

A general schematic of an ultrafast pump-probe transient absorption experiment is drawn in Figure 2. Since one cannot promote the entire ground state population to the excited state, this technique measures the difference in absorbance between the two species. When gathering the absorbance of the excited state, two distinct laser pulses are required for data collection. First, a pump pulse is directed onto a sample, generating some excited state molecules. The light from the pump pulse is monochromatic, and its wavelength is tuned to match the energy of a desired optical transition. After some time-delay, τ, a probe pulse is passed through the sample. Some portion of this pulse is absorbed by the sample before it reaches the detector, resulting in the excited-state absorbance measurement. The probe pulse is typically a broad-band (white-light) beam that grants a spectral profile which spans the visible light regime, but monochromatic light is used in some cases. Collecting the ground state absorbance measurement is more straightforward. In this instance no pump pulse is needed, so only the probe pulse passes through the sample. Subtraction of the excited state measurement from the ground state measurement yields a difference spectrum in which ΔOD corresponds to the difference

in absorbance between excited state and ground state species. By incrementally changing the time delay of the probe pulse relative to the pump pulse, a continuum of spectra are collected that reveal the evolution of the excited state with the time resolution of the pulse width. One can study how the transient spectra change as a function of time and how kinetic traces vary as a function of wavelength.

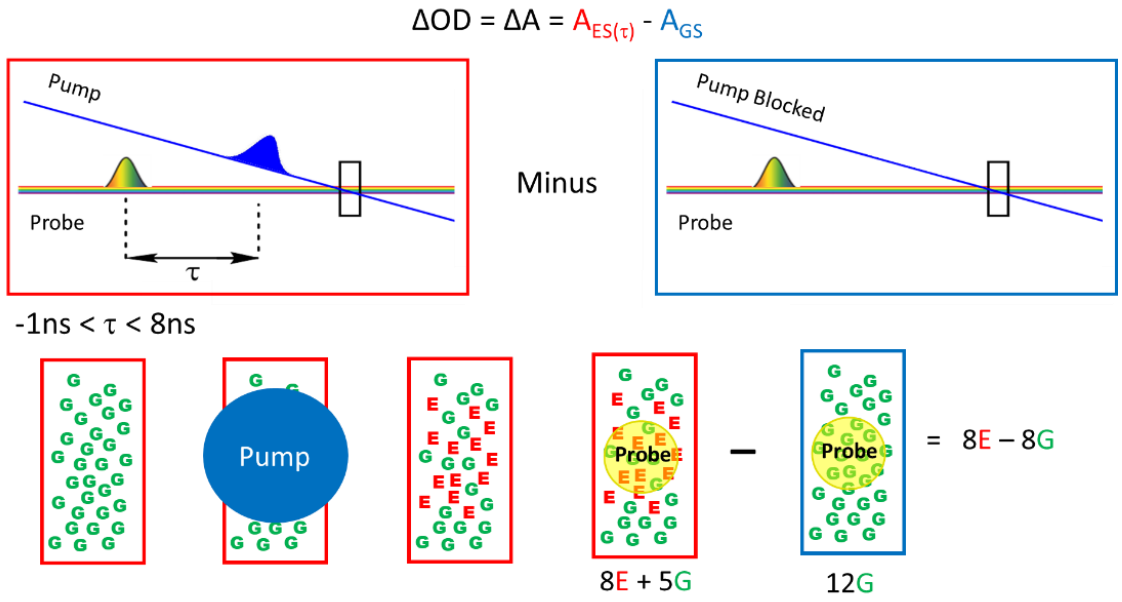

Figure 2. *General schematic for an ultrafast pump-probe transient absorption experiment. The ground state measurement (blue) is subtracted from the excited state measurement (red), yielding a difference spectrum that is representative of the excited state at time* τ.

A diagram of a transient absorption spectrometer (TAS) is shown in Figure 3 and the paths of the pump and probe beams are outlined. Pulses enter the TAS at a frequency of 1 kHz. Due to the nature of a pump-probe experiment outlined above, every other pump pulse needs to be blocked. This is done by passing the pump beam

through a spinning fan, called the chopper, which is tuned to rotate at a frequency 500 Hz. The pump beam also passes through neutral density filters, irises, and lenses, which attenuate the power and size of the pulse before it interacts with the sample. Its energy is then dumped into wall of the TAS.

Shortly after a probe pulse enters the TAS, it encounters an eight pass, mobile delay stage (Figure 3). As the mirrors on the delay stage move away from the corresponding stationary mirrors, the probe pulse is delayed in time relative to the pump pulse. Depending on the position of the delay stage, the probe pulse lags behind the pump pulse between -1 ns and 8 ns. To clarify, between -1 ns to 0 ns, the probe pulse passes through the sample before the pump pulse. After exiting the delay stage, the probe pulse passes through a nonlinear white light generating (WLG) crystal. Passing an ultrashort pulse through this material results in the generation of a supercontinuum that is utilized for broadband detection in pump-probe experiments. Based on the bulk material of the WLG crystal, the generated supercontinuum will span different wavelength regimes. Our lab typically uses CaF_2 crystals, which generate white light between 330 nm – 750 nm, sapphire crystals, which generate light between 450 nm and 750 nm, and YAG crystals, which generate light in the near-IR region of the spectrum.

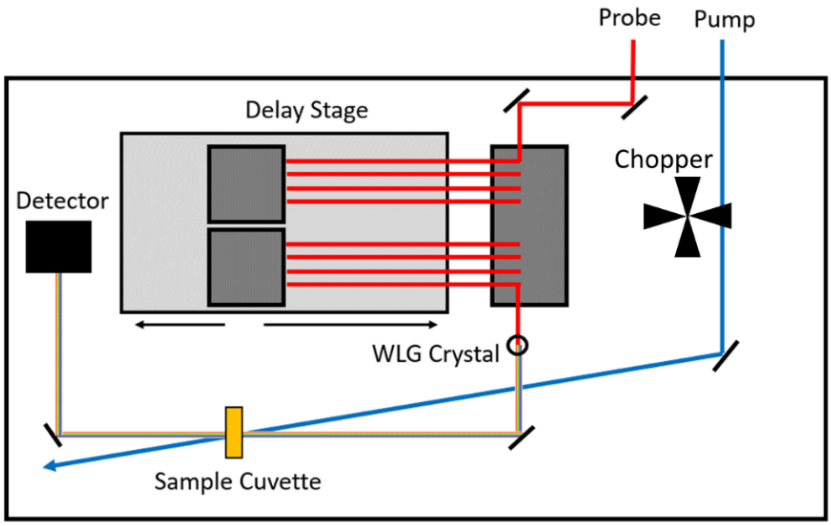

Figure 3. *Diagram of the transient absorption spectrometer used in this dissertation.*

Photochromic Ruthenium Sulfoxide Complexes

Photochromic compounds and complexes comprise a special group of bistable molecules that can interconvert between isomeric forms by the absorption of light. Photonic energy absorbed by the molecule is transformed into potential energy which is used for bond-breaking and bond-forming reactions. The isomers have distinct structural and electronic properties including absorption spectra, refractive indices, molar extinction coefficients, and reactivities. The ability to transform between different chemical properties with light provides photochromic molecules with unique applications. In nature, photochromic compounds are fundamental to visual perception and plant regulation. The *cis-trans* isomerization of rhodopsin, a pigment found within the mammalian eye, is the first event in visual perception. Photoisomerization of rhodopsin occurs in under 50 fs and is facilitated by the vibrational coherence of key

twisting, bending, and stretching modes.[1] Afterwards, a cascade of molecular reactions occur that conclude in an impulse at the optic nerve. Photochromic molecules are also key components in optical data storage, molecular switches, solar energy harvesting devices, transition lenses, and more. Transition metal complexes are particularly well-equipped to perform the functions of photochromic molecules due to their stability, the profound changes in their absorption spectrum upon isomerization, and their well-defined redox couples.

The isomerization of ruthenium polypyridyl complexes bearing sulfoxide moieties was first described electrochemically by Taube in the early 1980's.[2] Cyclic voltammograms of the molecule $[Ru(NH_3)_5(dmso)]^{2+}$, where dmso is dimethyl sulfoxide, showed evidence of electron transfer triggered isomerization. Oxidation of Ru^{2+} yields an S $\rightarrow$ O isomerization, while reduction of Ru^{3+} results in O $\rightarrow$ S isomerization. Photochromic ruthenium sulfoxides were born by a marriage between the electrochemical isomerization of $[Ru(NH_3)_5(dmso)]^{2+}$ and the photochemistry of $[Ru(bpy)_3]^{2+}$.

Polypyridyl ruthenium sulfoxide complexes exhibit photochromic behavior based on ligand isomerization. Generally, these complexes feature a lowest-energy S-bonded isomer and an O-bonded isomer on the ground state potential energy surface. Upon excitation of the MLCT absorption band, ruthenium is formally oxidized as the electron moves onto a bipyridine or terpyridine unit. In the excited state, the O-bonded isomer is energetically favored relative to the S-bonded isomer, and isomerization occurs. Upon relaxation to the ground state, the metastable O-bonded isomer will thermally revert to the S-bonded isomer over time. A four-level diagram, shown in Scheme 1, describes this

process in a simplistic but useful manner. More rigorously, the potential energy surface (PES) is a three-dimensional space, the reaction coordinate exists in the x and y axis for each degree of vibrational motion, and the z-axis represents energy. However, only certain molecular motions are critical for isomerization reactivity, and we can reduce the PES to a two-dimensional model. Manipulation of the ground state and excited PES yields additional functions from these photochromes. For instance, lowering the energy of ground state O-bonded isomer would generate a system in which there is no thermal reversion after isomerization. Further, raising the energy of the excited state O-bonded isomer might induce photoreversibility, in which each isomer could be converted to the other isomer with light.

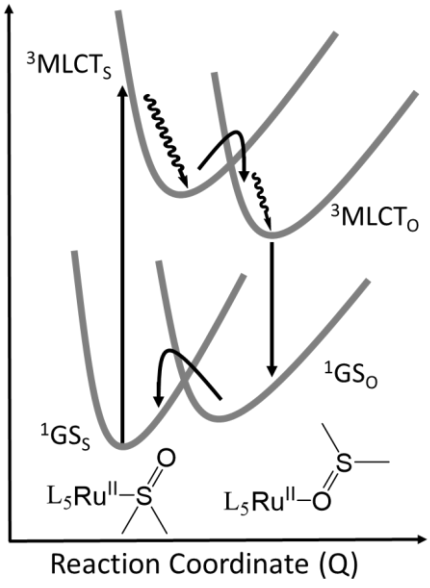

Scheme 1. *A four-level diagram depicting the photoisomerization of S-bonded ruthenium sulfoxide complexes and the thermal reversion of O-bonded ruthenium isomers.*

In this dissertation, phosphine ligands and carbene ligands are explored for their ability to modulate the structural and electronic characteristics of ruthenium sulfoxide complexes. Both types of ligands have been utilized in organometallic chemistry to modulate the electron density of the metal centers to which they are bound, and we wondered if they could be used to yield interesting properties in photochromic ruthenium sulfoxide complexes. The discoveries that we made are highlighted in chapter three.

Inverting Pyrene Sulfoxide compounds

Chirality is a concept bridging all areas of science that distinguish geometric structures that are otherwise identical, but that can have dramatically different applications. A chiral compound is one of a pair of molecules that are non-superimposable mirror images of each other. They have identical physical properties aside from their optical activities, which are equal and opposite. They also react differently to other chiral molecules; a feature which is pervasive in the biochemistry of amino acids, enzymes, and drugs like ibuprofen and thalidomide, among others.

Amines (NR_3), phosphines (PR_3), and sulfoxides ($S(O)R_2$) are chiral so long as their -R groups are unique. In principle, they can change chirality through a mechanism known as pyramidal inversion, depicted in Scheme 2 for a sulfoxide compound. Here, the central sulfur atom passes through the plane formed by oxygen and the two -R substituents and ends up on the other side. Pyramidal inversion rapidly occurs at room temperature for amines because of a low energy-barrier to the planar transition state. Thus, solutions of

amines are typically racemic and contain an equal mixture of both enantiomers. The barrier to pyramidal inversion is much higher in phosphines and sulfoxides, and chiral solutions can be prepared. In the excited state, however, the pyramidal inversion of a sulfoxide can proceed efficiently at room temperature. This photochemical process is known as photostereomutation, or simply photoinversion.

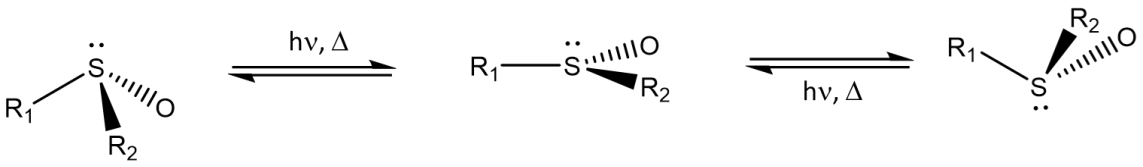

Scheme 2. *The pyramidal inversion of a sulfoxide. The thermal barrier to pyramidal inversion of sulfoxides is too high for the reaction to occur at room temperature, so the application of either light or heat is required.*

The photoinversion of sulfoxide compounds bearing a pyrene substituent has been studied by several researchers. Pyrene is useful as a chromophore in these systems because it absorbs in the UV-Vis region and has well-known excited state dynamics. The nature of the other -R group plays a major role in the photochemistry of pyrene sulfoxide compounds. Pyrene sulfoxides bearing alkyl groups display significantly higher quantum yields of photoinversion than pyrene sulfoxides bearing aryl groups. Additionally, substituting the periphery of aryl groups with electron-donating or electron-withdrawing moieties has a substantial impact on excited state lifetimes. In all, these compounds feature diverse photochemistry that warrants further studies.

To date, no transient absorption measurements have been carried out on pyrene sulfoxide compounds. Inspired by the works of Mislow and Hammond in the 1960's, Tsurutani and Jenks around the turn of the millennium, and most recently Finney in the 2010's, we carried out an extensive spectroscopic investigation on a group of pyrene thioethers and pyrene sulfoxides which shed light on the excited state dynamics of this photochemical system.

Light-Harvesting Platinum Roller Wheel Complexes

The need for sources of renewable energy is only going to increase as the world becomes more populated and the realities of climate change become clearer. According to the EIA, renewable energy sources accounted for only 12% of the primary energy consumption in U.S. in 2020 while natural gas, petroleum, and coal combined to account for 79%. Solar energy, which is one of the main classes of renewable energy along with geothermal, hydroelectric, wind, and biomass, accounted for a mere 11% of all energy consumption from renewable sources. The consistency and abundance of solar radiation incident upon of Earth every day makes it perhaps the best form of renewable energy to harvest.

Solar energy is generally converted into energy by means of photovoltaic (PV) cells, which convert photonic energy into electrical energy. The most common form of PV cells are devices based on silicon, GaAs, and CdTe semiconductors. These devices benefit from relatively high power-conversion efficiencies (PCE), high durability, and well-established supply chains. However, their bulk and hefty installation price drive many people from investing. Since the start of the 21st century, the emergence of organic

photovoltaics (OPVs) as low-cost, light weight, and easily processable alternatives to conventional solar cells has brought significant attention to the field. OPVs come with drawbacks, including lower PCEs and reduced durability compared to conventional solar cells, but they are attractive from a research standpoint because of the extensive tunability of their properties on both molecular and macroscopic scales.

At its core, an OPV is comprised of an electron donor, an electron acceptor, and electrodes (the cathode and the anode). The electron donors and electron acceptors can be either small molecules or polymers, but they require large conjugated systems to promote electron mobility and absorption in the visible light regime. The role of the donor is to absorb light, generate an exciton, and yield an electron to the acceptor. The role of the acceptor is to accept an electron from the donor, further separate the electron-hole pair, and transfer the electron to the electrode before electron-hole recombination occurs. To optimize the efficiency of the donor, high electron-mobility, a broad absorption profile, and a long-excited state lifetime are all necessary. Many strategies have evolved to tune these properties, including the advent of platinum-doped donors.

The incorporation of platinum into the donor of an OPV serves three main purposes: it establishes a square planar geometry useful for ordered stacking, it introduces long lived triplet states through enhanced spin-orbit coupling, and it expands the absorption profile through MLCT transitions. Recently, Qin and coworkers developed platinum roller-wheel complexes which feature the best power conversion efficiencies to date for platinum-doped donor systems.[3,4] They feature Pt-bisacetylides as side chains

that are attached to long, linear, conjugated chromophores. The architecture of these molecules promotes overlap via a slip-stacking mechanism, which increases conductivity and promotes crystallinity. We designed a new series of platinum roller-wheel complexes with the aim of further improving crystallinity and excited-state lifetime. The basic structure and excited state dynamics for these complexes are displayed in Figure 4. By incorporating long alkyl chains near the interface of the Pt-bisacetylide benzenedithiophene unit and the π-bridge, we aimed to prevent twisting of the chromophore and promote π-stacking interactions. We also measured the influence of electron withdrawing substituents near the periphery of the π-bridges on excited state dynamics.

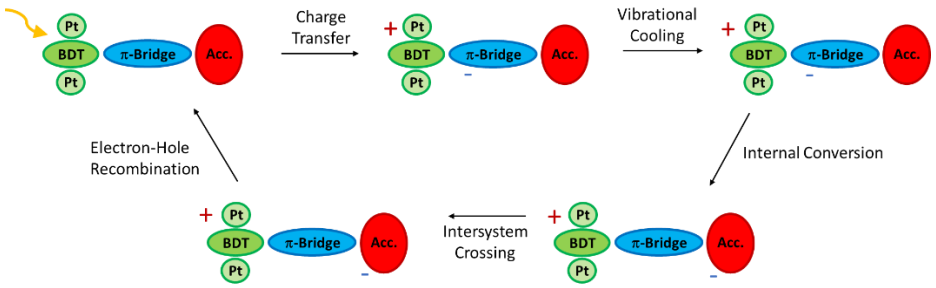

Figure 4. *The basic structure and excited state dynamics of platinum roller-wheel type donor chromophores relevant in organic photovoltaic devices. The donor can be broken into three main sub-structures: the platinum-bisacetylide benzenedithiophene unit (green, labeled as Pt and BDT), the linear conjugated chromophore unit (blue, labeled as π-bridge), and the electron-withdrawing/electron-accepting unit (red, labeled as Acc.).*

CHAPTER 2

Instrumentation and Methodology

Synthesis

All reagents and solvents were obtained commercially and used as received unless stated otherwise. The reactions were performed using standard Schlenk techniques with dry solvents under an inert gas atmosphere. Due to the light-sensitive nature of the ruthenium complexes from chapter three and the pyrene compounds from chapter five, all synthesis was performed under red-light conditions and all samples were stored in the dark.

NMR Spectroscopy

Nuclear magnetic resonance spectroscopy (^{1}H, ^{19}F, ^{31}P) of the synthesized compounds and complexes was performed at room temperature using Bruker Avance III 300 and Bruker Avance 500 spectrometers. NMR data was analyzed and processed using MestReNova (Metrelab Research) data analysis software.

X-Ray Crystallography

Crystals suitable for X-ray crystallography were grown on laboratory benchtops using room-temperature vapor diffusion techniques. X-ray intensity data were measured on a Bruker PHOTON II CPAD-based diffractometer with dual Cu/Mo ImuS microfocus optics (Cu Kα radiation, λ = 1.54178 Å, Mo Kα radiation, λ =0.71073 Å). Crystals were mounted on a cryoloop using Paratone oil and placed under a steam of nitrogen at 100 K (Oxford Cryosystems). The detector was placed at a distance of 5.00 cm from the crystal.

The data were corrected for absorption with the SADABS program. The structures were refined using the Bruker SHELXTL Software Package (Version 6.1) and were solved using direct methods until the final anisotropic full-matrix, least squares refinement of F^2 converged.

UV-Vis Spectroscopy

UV-Vis spectra were recorded on an Agilent Technologies, Agilent 8453 UV-visible Spectroscopy System. Quartz cuvettes with 1 cm pathlengths were used for all standard UV-Vis and bulk photolysis measurements. Olis Inc.'s OlisWorks GUI was used for data collection purposes. Processing and data analysis was performed on OriginPro 8.5 graphing software.

Molar extinction coefficients were determined experimentally by making at least ten dilutions from a stock solution of each compound. The data, plotted in terms of absorbance vs. concentration, are used in conjunction with the Beer-Lambert Law. Since absorbance (A) and concentration (c) are measured and pathlength (l) is known, calculation of molar extinction coefficient, ε, for each sample is straightforward.

Quantum yields were calculated by actinometry in 3 ml solutions of dichloroethane at room temperature. A 405 nm laser diode and a 0-2 OD neutral density were utilized as the light source. The solution was irradiated at a 90° crossbeam geometry using a custom sample holder at a known irradiation power. Incident radiation intensity (moles of photons per second) was calculated by Equation 1 where λ is the irradiation

wavelength, P is the irradiation power, c is the speed of light, h is planks constant and N_A is Avogadro's number.

$$I_0 = \frac{\lambda \times P}{c \times h \times N_A} \qquad \text{Equation 1}$$

The quantum yields of isomerization ($\Phi_{S\rightarrow O}$) were calculated by the absorption changes at 405 nm using Equation 3, where CT is the total concentration in solution, *V* is the volume and A_{irr} is the absorbance of the solution at the irradiation wavelength. Due to fast ground state thermal reversion rates (k_{-1}), the quantum yield was calculated with the 1st order reversible rate law (Equation 2), where $[S]_0$ is the concentration of the S-bonded isomer at the start of the experiment, $[S]_e$ is the concentration of the S-bonded photoproduct at equilibrium between photolysis and reversion.[5]

$$k_1 = \frac{\{ln([S]_0 - [S]_e) - ln([S]_t - [S]_e)\}}{t} - k_{-1} \qquad \text{Equation 2}$$

$$\Phi_{S\rightarrow O} = \frac{C_T \times V \times k_1}{I_0 \times (1 - 10^{A_{irr}})} \qquad \text{Equation 3}$$

Emission Spectroscopy

Emission spectra were collected on an Edinburgh Instruments FLS980 Photoluminescence Spectrometer equipped with a 450W ozone free xenon arc lamp. Light from this lamp is passed through a Czerny-Turner monochromator and an iris with an adjustable opening. The sample is irradiated at a 90° geometry within a 1cm quartz cuvette containing dissolved sample (O.D. is <0.1 at λ_{max}). Adjustable slits at both the excitation and emission arms allow for an appropriate photon count at the detector.

For time-resolved photoluminescence measurements, two techniques are required to span the emission time range from our samples. Time Correlated Single Photon Counting (TCSPC) is used for the acquisition of fluorescent signals in the picosecond to nanosecond time regime. Pulsed lasers with 355 nm and 450 nm emission wavelengths and picosecond pulse widths and attenuated and then reflected onto a sample. For phosphorescent signals in the tens of nanoseconds to seconds time regime, Multi-Channel Scaling is used instead. For singlet oxygen studies, a 1000 nm long pass filter was placed after the sample chamber in order to block second order emission from convoluting the $^1O_2$ emission signal. A lock-in InGaAs detector is used to record emission in the NIR wavelength range.

Electrochemistry

Cyclic voltammetry was conducted in a one-compartment electrochemical cell under inert atmosphere using a platinum wire as the counter electrode, glassy carbon as the working electrode, and Ag^+/Ag as the standard electrode. The sample solution was prepared in 0.1M tetra butyl ammonium hexafluorophosphate in acetonitrile.

The rate constant of electrochemical isomerization was calculated using the equation below. The rate constant, k, was determined using the slope of A against a 1/n plot. $E_{1/2}$ is the average of the cathodic and the anodic peak potential, which can also be obtained from square wave voltammetry. E_p is anodic peak potential. R, T, and F are the universal gas constant, temperature in Kelvin, and Faraday's constant respectively. 1/n is the inverse of the scan rate.

$$A = e^{1.560} e^{(\frac{2nF}{RT})(E½ - Ep)} = \frac{kRT}{nF}\left(\frac{1}{v}\right) \qquad \text{Equation 4}$$

Femtosecond Pump-Probe Spectroscopy

A Spectra Physics Solstice Ace regenerative amplifier containing a Mai Tai femtosecond oscillator and an Ascend pump laser is used to produce 800nm pulses at a repetition rate of 1kHz at 7W average power and a pulse width of 60 fs. Upon leaving the Solstice Ace the beam is split 80:20. One beam (80% intensity) is directed into an optical parametric amplifier (Light Conversion TOPAS) to create the desired pump-beam wavelength before entering a ccutom built Newport TAS (transient absorption spectrometer). The other beam (20% intensity) enters the TAS directly and travels across an adjustable delay stage before passing through a CaF_2 crystal to generate a white light continuum (~330 – 750 nm). The two beams intersect within a 2mm quartz cuvette containing the dissolved sample (O.D. is 0.4 at λ_{max}). The sample is continuously flowed through the cuvette during data collection using a Fluid Metering Inc. Lab Pump Jr (Model RHSY). The signal is filtered to remove excess 800nm light and then coupled into a fiber-coupled Oriel spectrograph. Surface Xplorer Pro v4 (Ultrafast Systems) data analysis software is used for background subtraction and chirp correction, followed by reconvolution fitting of transient lifetimes using a multi-exponential function.

Nanosecond Flash Photolysis Spectroscopy

A Continuum Surelight II Model SLI-10 (Nd:YAG) is used to generate excitation pulses at a repetition rate of 10Hz and a pulse width of 7 ns, with options for SHG and THG in order to produce 532nm and 355nm pulses. A Surelight SSP dichroic filter is placed in the beam path to select for the desired excitation wavelength. An Edinburgh

Instruments XE-900 (450W ozone-free Xenon arc lamp) generates a white light probe beam. The two beams intersect at a 90° geometry within a 1cm quartz cuvette containing dissolved sample (O.D. is 0.4 – 0.6 at λmax). The probe beam then passes through a spectrograph and is coupled into either a Hamamatsu R928 PMT for single wavelength kinetics, or an Andor iStar iCCD camera for transient absorption spectra. Edinburgh Instruments L900 software is used to calculate single wavelength kinetics and plot transient spectra.

IR Spectroscopy

Infrared spectra were collected on a Shimadzu IRAffinity-1 FTIR Spectrometer. Samples for FT-IR were prepared by combining ~ 6 mg of sample with one drop of Nujol mineral oil. The mixture was ground into a paste and sandwiched between two KBr plates. IR spectra for bulk photolysis were recorded after various intervals of irradiation by a Continuum Surelight II Model SLI-10 (Nd:YAG, 10Hz) laser at 355nm with a power of 500mW. ATR spectra were collected by placing powdered sample on a Shimadzu MIRacle 10 Single Reflection ATR Accessory.

Computational Methods

In order to understand the nature of electronic and optical properties of the substituted complexes, a combined density functional theory (DFT) and time-dependent DFT (TD-DFT) study was carried out using Gaussian 09 and Gaussian 16. The PBE0 functional with Grimme's D3 dispersion with Becke-Johnson damping (D3BJ) was used for all computations. All computations utilized default program integration grids: Gaussian 09 defaults to a pruned grid using 75 radial shells with 302 points per shell (75,302) and Gaussian 16 defaults to a pruned grid using 99 radial shells with 590 points per shell (99,590). Basis Set 1 (BS1) is defined as follows: for Ru, the Couty and Hall modification (modLANL2DZ) to the valence basis set of LANL2DZ+ECP combination; for S and P, the LANL2DZ(d,p)+ECP combination; and for H, C, N, O, and F, the 6-31G(d') basis sets (the 6-31G(d') basis sets have the d polarization functions taken from the 6-311G(d) basis sets rather than the default value of 0.8 for C, N, O, and F). BS2 is defined as follows: for Ru, SDD, the triple-zeta quality Stuttgart valence basis set with the quasi-relativistic small core ECP; and, for H, C, N, O, F, S, and P, the jul-cc-pVDZ basis sets. Various gas-phase variational singlet ground-state (^{1}GS) and variational triplet excited-states (^{3}ES) were geometry optimized. TD-DFT single point calculations was performed on the optimized ground-state geometry to simulate the absorption spectra. A total of 50 transitions were considered for single-point TD-DFT computations with BS1 and 10 transitions with BS2. A total of 30 transitions were considered for TD-DFT geometry optimizations. DFT and TD-DFT (10 transitions) single-point energy computations were also performed with BS2 on DFT/BS1 optimized geometries for selected species. The

absorption spectra were simulated with an in-house Fortran program by convoluting the computed excitation energies, oscillator strengths with a Gaussian line shape and applying a broadening of 20 nm. TD-singlet excited states (^{1}TD) were geometry optimized using TD-DFT in Gaussian 09. TD-triplet excited states (^{3}TD) were approximated by a ^{3}TD single-point computation on the optimized ^{1}TD geometries. The nature of each optimized geometry was confirmed as a minimum (zeroth-order saddle point) on the potential energy surface by computing the analytical harmonic vibrational frequencies at the same theoretical level (Gaussian 16 for TD-DFT optimized geometries, and Gaussian 09 for all variational DFT geometries). Images of the natural transition orbitals (NTOs) were generated in Chemcraft with an isosurface value of 0.02.

CHAPTER 3

Light-Driven Molecular Machines:
The Design, Synthesis, and Characterization of
Photoisomerizing Ruthenium Sulfoxide Complexes

3.1 Controlling Photoisomerization Reactivity Through Single Functional Group Substitutions in Ruthenium Phosphine Sulfoxide Complexes

Abstract

We report the crystallography, emission spectra, femtosecond pump−probe spectroscopy, and density functional theory computations for a series of ruthenium complexes that comprise a new class of chelating triphenylphosphine based ligands with an appended sulfoxide moiety. These ligands differ only in the presence of the para-substituent (e.g., H, OCH_3, CF_3). The results show a dramatic range in photoisomerization reactivity that is ascribed to differences in the electron density of the phosphine ligand donated to the ruthenium and the nature of the excited state.

Introduction

An important goal in photoscience is the ability to introduce single atom or simple group changes within a molecule in order to alter the fate of an excited state (ES) reaction. In principle, such advances lead to improvements in photocatalysis schemes, molecular photovoltaic devices, and artificial photosynthetic materials. In practice, most such chemical synthetic changes offer only modest or subtle modification of ES processes, because the relaxation processes do not involve vibrations or other atomic motions responsive to these particular synthetic alterations. Moreover, for transition metal

complexes, the situation is further confounded by the relatively large number of available electronic states (relative to organic systems), which can further mitigate a substituent effect.

Photochromic compounds feature large changes in both electronic and molecular structure following visible light exposure. Thus, these compounds exhibit dramatic changes in the electronic absorption spectra upon irradiation of the ground state (GS) isomer to form a new metastable structure on the GS potential energy surface. We have created and studied a family of photochromic ruthenium and osmium polypyridine based complexes whose photochromic action is based on an ES sulfoxide isomerization reaction.[6-9] In this case, the GS isomer is S-bonded and the metastable isomer is O-bonded. This reaction can be efficient, with quantum yields nearing unity, and rapid, with electronic absorption changes occurring on the picosecond time scale. We report here a ligand design that permits simple group changes on the periphery of the molecule that leads to remarkable control of the ES isomerization reaction. In the series of three complexes reported here, we have found that the quantum yield of isomerization ($\Phi S \rightarrow O$) may vary from 0.8 to 0.0.

Phosphine ligands are well-known to modulate the electron density of the metal through a combination of σ- and π- bonding. Indeed, depending upon the R groups in PR_3 ligands, the ligand may be classified as a σ-only donor (e.g., PMe_3) or as a strong π-acid or acceptor (e.g., PPh_3 or PF_3). Though commonly employed in organometallic chemistry, this ligand class is not widely utilized in the design of photoactive chromophores.[10-22] We

questioned whether a family of chelating phosphine sulfoxide ligands would impart tunable properties in the photochromic behavior of these compounds. The salient connection is that different groups on the phosphine ligand alter the energy of the Ligand Field (LF) or Metal-Centered (MC) states relative to the charge transfer (CT) states during ES evolution, thus modifying reactivity.

Results and Discussion

Shown in Figure 5 are the complexes described in this report. Each molecular structure (determined by single crystal X-ray diffraction) features the identical $[Ru(bpy)_2]^{2+}$ core and a different chelating phosphine sulfoxide ligand that differs only in the substituent in the 4-position on the terminal phenyl rings of the triphenylphosphine moiety. For $RuL1O_H$, this substituent is H, for $RuL2O_{OCH3}$ this substituent is OCH3, and for $RuL3O_{CF3}$ this substituent is CF3. This simple substituent modification results in rather modest GS structural differences, but generates rather dramatic and remarkable distinctions in ES reactivity.

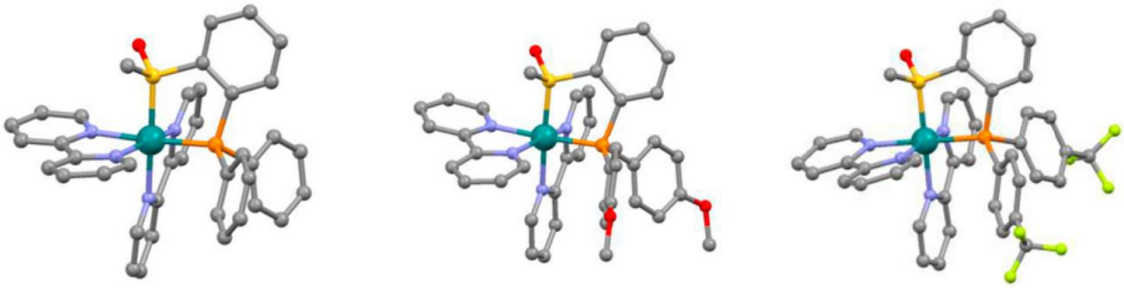

Figure 5. *Molecular structures determined from the X-ray analysis of the S-bonded isomers of $RuL1O_H$ (left), $RuL2O_{OCH3}$ (center), and $RuL3O_{CF3}$ (right). Hydrogen atoms are omitted for clarity.*

The electronic absorption spectra of these three complexes are quite similar revealing absorption maxima of 351, 353, and 348 nm, respectively for S-$[(bpy)_2Ru(L1O_H)]^{2+}$, S-$[(bpy)_2Ru(L2O_{OCH3})]^{2+}$, and S-$[(bpy)_2Ru(L3O_{CF3})]^{2+}$, respectively (Figure 6a). These data demonstrate the effect of the structurally distant substituent group (H vs OCH_3 vs CF_3) on the Ru dπ to bpy π* charge transfer (CT) transition, which is confirmed by TD-DFT (vide inf ra) computations. Irradiation of $RuL3O_{CF3}$ at 355 nm results in striking changes in the electronic absorption spectrum (Figure 6b), with the emergence of a new absorption maximum at 422 nm, and isosbestic points at 332 and 376 nm. Based on literature precedence, we ascribe the newly formed spectrum to the O-bonded isomer of the ruthenium phosphine sulfoxide complex. For example, Wolf has reported the absorption maximum of $[(bpy)_2Ru(PO)]^{2+}$ is 412 nm, where PO is 2-diphenylphosphino-(anisole). This complex features a P and O donor on $[Ru(bpy)_2]^{2+}$.[23,24] The bold red trace displayed in Figure 6b represents pure O-$[(bpy)_2Ru(L3O_{CF3})]^{2+}$ formed from irradiation ($\Phi_{S\rightarrow O}$ = 0.8 ± 0.2) at 355 or 405 nm. Excitation of $RuL1O_H$ at either 355 or 405 nm produces a similar change in the absorption spectrum ($\Phi_{S\rightarrow O}$ = 0.2 ± 0.1). In extraordinary contrast, irradiation of $RuL2O_{OCH3}$ at any wavelength that overlaps with the GS absorption spectrum does not result in any spectral changes, thus providing no indication of isomerization. These observations are supported by computational results and confirmed by time-resolved spectroscopy (vide infra). It is remarkable that such a small structural replacement of either H or CF_3 with OCH_3 alters the photochemical reactivity so dramatically.

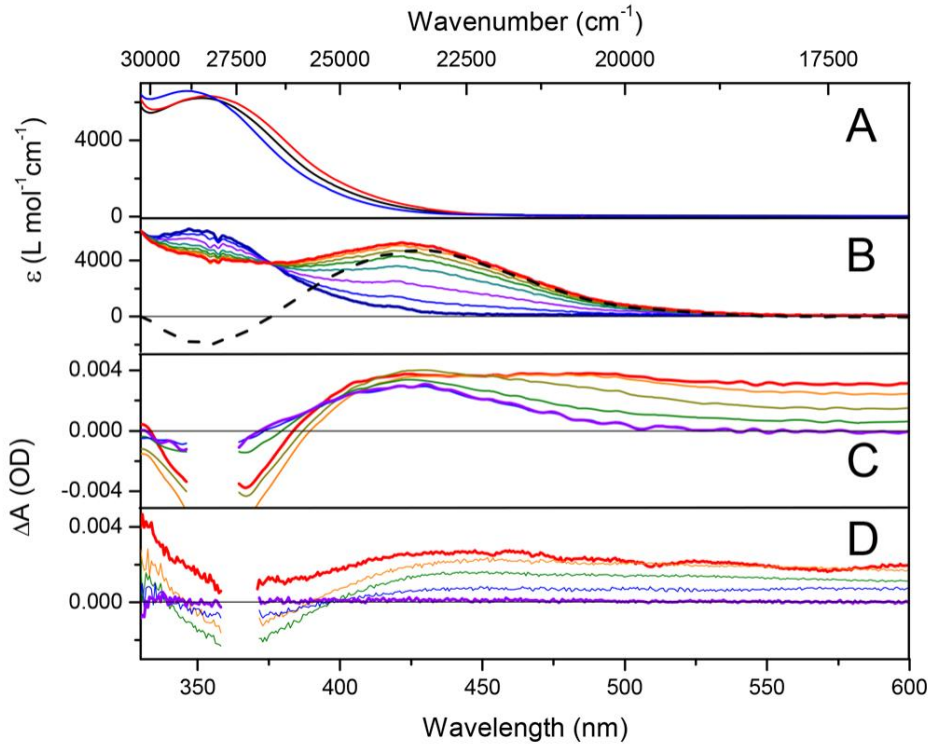

Figure 6. *(A) Absorption spectra for S-$[(bpy)_2Ru(L1O_H)]^{2+}$ (black), S-$[(bpy)_2Ru(L2O_{OCH3})]^{2+}$ (red), and S-$[(bpy)_2Ru(L3O_{CF3})]^{2+}$ (blue). (B) Spectra obtained from bulk photolysis (λexc 355 nm) of $[(bpy)_2Ru(L3O_{CF3})]^{2+}$ in dichloroethane solution. Spectra obtained at 80 s intervals. Black dashed trace is difference spectrum (O isomer − S isomer) extracted from bulk photolysis data. (C) Time resolved spectra of $[(bpy)_2Ru(L3O_{CF3})]^{2+}$ obtained at different pump−probe delays of 2.0 ps (red), 20.1 ps (orange), 202 ps (olive green), 2000 ps (green), and 4990 ps (violet). The new absorption maximum centered at 422 is evidence of a photoproduct, consistent with the bulk photolysis data. (D) Time resolved spectra of $[(bpy)_2Ru(L2O_{OCH3})]^{2+}$ obtained at different pump−probe delays of 0.41 ps (red), 2.51 ps (orange), 199 ps (green), 1000 ps (blue), and 4660 ps (violet). These traces provide no evidence for the formation of a photoproduct (isomerization), consistent with the bulk photolysis data.*

Ultrafast visible pump probe spectroscopy was employed to monitor the spectral changes in these complexes. For $[(bpy)_2Ru(L2O_{OCH3})]^{2+}$, the early time spectra are reminiscent of those obtained for many ruthenium polypyridine complexes (Figure 6d). That is, visible light excitation produces an MLCT with expected features that relax to reform the GS with a lifetime of 790 ± 60 ps. The ES absorption in the red portion of the spectrum is attributed primarily to unreduced bpy → Ru^{III} LMCT transitions, whereas the GS bleach is observed in the blue portion of the spectrum. Although there is typically an ES absorption (reduced bpy, $\pi \rightarrow \pi^*$ ligand centered transition) near 380 nm, its detection is obscured by the coincidence of the MLCT bleach. Evidence of this ES absorption can be seen at $\lambda < 350$ nm.

Representative pump probe data for $RuL3O_{CF3}$ document the absorption changes observed during bulk photolysis (Figure 6c). The early time spectral features are emblematic of an MLCT state, as described above. In contrast to $RuL2O_{OCH3}$, the spectra indicate the formation of a GS photoproduct (isomerization), by the emergence of a new absorption maximum at 422 nm, coincident with loss of absorption in the red portion of the spectrum. The loss of absorption at long wavelengths indicates a transition from the ^{3}MLCT surface to the GS surface. The absorption maximum observed in the bulk photolysis data is nicely reproduced in the pump−probe data, demonstrating formation of the same complex. This is readily observed through visual comparison of the transient spectrum obtained at long pump−probe delays (∼5000 ps, violet trace Figure 6c) with the difference in GS spectra (O-bonded − S-bonded, black dashed trace, Figure 6b) obtained from bulk photolysis. Global fitting analysis and single wavelength kinetics reveal a time

constant for formation of the O-bonded isomer of 630 ± 77 ps. Multiplying by $\Phi_{S\rightarrow O}$ (0.80) yields a time constant for isomerization ($\tau_{S\rightarrow O}$) of 790 ps. The absorption changes in $RuL1O_H$ and $RuL3O_{CF3}$ associated with the picosecond isomerization are completely reversible. Reversion rate constants of $(300\ s)^{-1}$ and $(770\ s)^{-1}$ are found for $RuL1O_H$ and $RuL3O_{CF3}$, respectively (Figure 112). Future studies will reveal the bonding details that are responsible for this unusual reactivity.

We performed DFT and TDDFT computations to determine if there were differences in electronic structure that might explain the observed differences in photochemistry for this family of complexes. Shown in Figure 7 are the NTOs (natural transition orbitals; see Appendix A for full computational details) of the hole (left) and particle (electron, right) that describe the CT excited states for $RuL2O_{OCH3}$ (top) and $RuL3O_{CF3}$ (bottom). While these images show similar bipyridine contributions to the particle orbital, the Ru and sulfoxide contribution to the hole orbital for $RuL3O_{CF3}$ is considerable in comparison to the hole orbital for $RuL2O_{OCH3}$, which exhibits a large contribution from the methoxyphenyl moiety of the phosphine ligand.

The relative energies from triplet single-point computations on time-dependent DFT singlet optimized geometries (^{3}TD/BS2//^{1}TD/BS1) demonstrate that the O-bound isomer in the ES (relative to S-bound in the ES) is disfavored for $RuL2O_{OCH3}$ (ΔG_{rxn} = 2.2 kcal mol^{-1}), competitive for $RuL1O_H$ (ΔGrxn = 0.2 kcal mol^{-1}), and favored for $RuL3O_{CF3}$ (ΔG_{rxn} = −3.5 kcal mol^{-1}). This trend corroborates the experimental observations of isomerization with $RuL1O_H$ and $RuL3O_{CF3}$ and no isomerization with $RuL2O_{OCH3}$. Furthermore, these data show that the isomerization behavior for this class of complexes can be predictably

controlled based on the logic of electron density within the aromatic system of the ligands and, by extension, the degree of electron donation to the metal center. Thus, the computational results provide two insights into the change in reactivity between $RuL3O_{CF3}$ and $RuL2O_{OCH3}$. First, the NTOs identify differences in Ru and sulfoxide character in the hole orbital; second, while calculations do not provide information on the isomerization pathway, at least they indicate that the O-bonded $RuL2O_{OCH3}$ state is thermodynamically uphill.

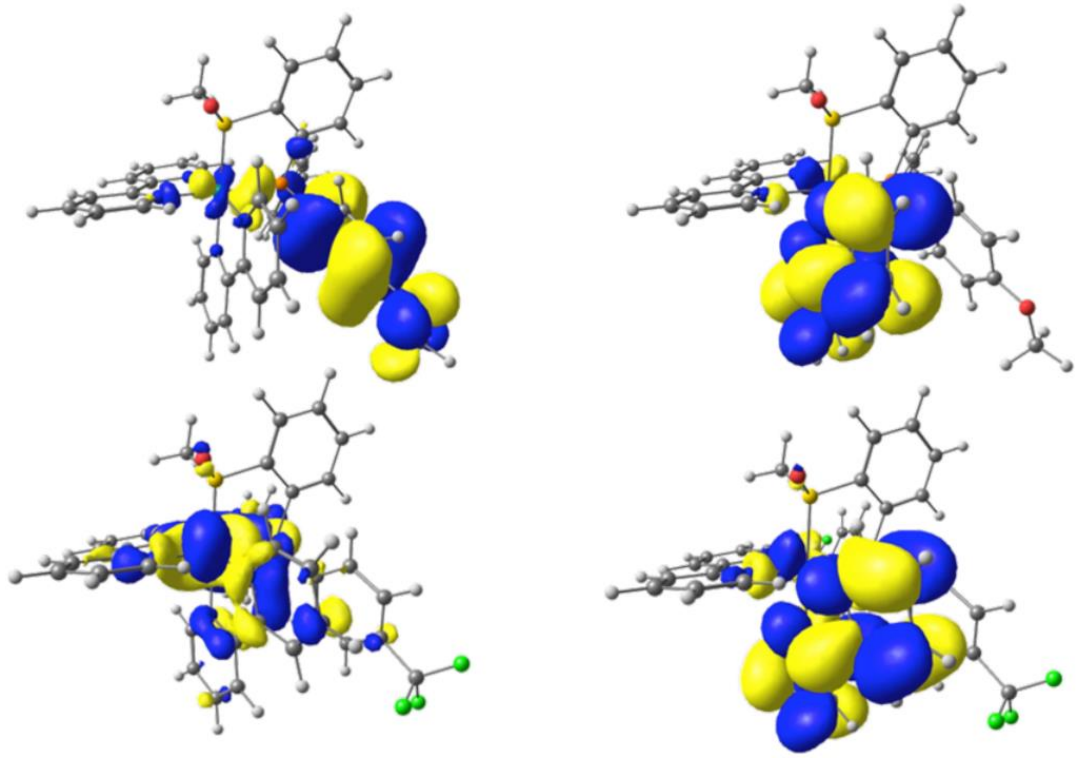

Figure 7. *Natural transition orbitals (NTOs) for the hole (left) and particle (right) for S-$[(bpy)_2Ru(L2O_{OCH3})]^{2+}$ (Top) and S-$[(bpy)_2Ru(L3O_{CF3})]^{2+}$ (Bottom). The NTOs for S-$[(bpy)_2Ru$- $(L1O_H)]^{2+}$ are qualitatively similar to S-$[(bpy)_2Ru(L3O_{CF3})]^{2+}$.*

Structural data obtained from single crystal X-ray diffractometry reveal only subtle differences between the three complexes. The Ru−S bond distances vary only over a small range: 2.2185(6) Å in RuL1O_H, 2.218(1) Å in RuL2O_{OCH3}, and 2.233(2) and 2.235(2) Å in RuL3O_{CF3} (there are two unique molecules in this unit cell). The S−O bond distances display a smaller variation: 1.479(9) Å in RuL1O_H, 1.475(4) Å in RuL2O_{OCH3}, and 1.479(6) and 1.463(5) Å in RuL3O_{CF3}. Interestingly, the Ru−S and S−O bond distances are equivalent in RuL1O_H and RuL2O_{OCH3}, two complexes that display dramatically different photochemical reactivity. The metrical parameters do not reveal any significant differences in the Ru−P distances or in any pertinent angles, thus suggesting that any differences in the photophysical behavior or photochemical reactivity in these complexes is due to an ES phenomenon and not to GS geometric differences.

Emission spectra provide compelling evidence for isomerization at 77 K. Shown in Figure 8 is the 77 K steady state emission spectrum for S-RuL3O_{CF3} in a 4:1 mixture of tetrahydrofuran and propylene carbonate. The emission spectrum reveals two maxima at 525 and 650 nm (340 nm excitation). The lifetimes at these two wavelengths are 33 and 50 μs, respectively indicative of a CT ES. Indeed, these lifetimes are much longer than those observed in $[Ru(bpy)_3]^{2+}$ ($\tau = \sim 5$ μs at 77 K; we obtain 7.7 μs on our instrument).[25] The two different lifetimes indicate two noninteracting emissive populations. Excitation scans at 525 and 650 nm reveal peaks at 340 and 440 nm, respectively corresponding to the absorption maxima of S- and O-RuL3O_{CF3} isomers. The 650 and 525 nm emission bands are assigned to the O- and S- bonded isomers, respectively. We note that the differences in absorption (0.62 V) and emission maxima (0.57 V) are in accord with the difference in

reduction potentials (0.66 V) for the S- and O-bonded isomers. Though we cannot be certain that there is no O-bonded isomer in the original solution, we interpret these results as formation of an O-bonded emissive CT state at 77 K, produced from excitation of an S-bonded GS, which relaxes to both S- and O-bonded GS isomers. The computational data are consistent with these observations. There are weak transitions in these regions for both isomers.

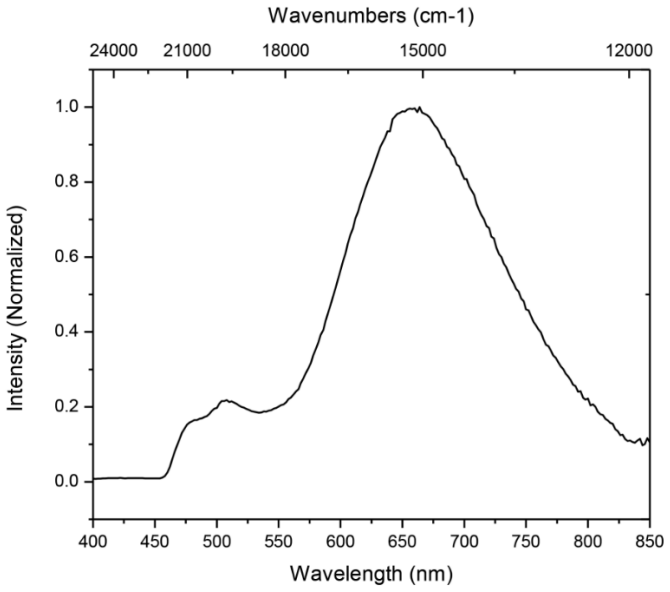

Figure 8. *Corrected steady state emission spectrum of $[(bpy)_2Ru\text{-}(L3O_{CF3})]^{2+}$ at 77 K.*

The 77 K emission data suggest that isomerization occurs adiabatically along the CT surface, whereas the room temperature pump−probe data do not provide evidence for the formation of an O-bonded excited state. We propose that isomerization occurs through nonadiabatic coupling between adiabatic surfaces, which also serve as the basis of the above calculations. Taken together, the temperature dependent data hint at an intricate balance of couplings between surfaces, both excited state and ground state, as well as S- and O-bonded.

Conclusion

In summary, these results indicate that isomerization occurs efficiently in certain of these ruthenium phosphine sulfoxide complexes, and that the phosphine moiety provides remarkable control of the photoisomerization. Moreover, we report the first data that shows evidence of isomerization at 77 K from an unequivocal CT state. Future studies will focus on understanding the unusual reactivity exhibited by these complexes.

3.2 Identifying Structural and Electronic Property Differences between Isomerizing and Non-Isomerizing Ruthenium Sulfoxide Complexes.

Abstract

A group of ruthenium polypyridyl complexes bearing chelating phosphine-sulfoxide or phosphine-thioether ligands were developed and investigated spectroscopically. Previously, we learned that simple substitutions on a triphenylphosphine fragment of these chelating ligands results in dramatic differences in photoisomerization reactivity. To further examine this effect, we carried out additional studies on a larger group of complexes than before. In total, 15 structures are examined (three P,S ligands, five phosphine thioether complexes, and seven phosphine sulfoxide complexes), whereby the P,S ligands differ in the nature of the phosphine substituents, the bridging group, or the R group on sulfur. Femtosecond transient absorption and traditional bulk photolysis studies reveal four photoisomerizing sulfoxides, whose quantum yields of photoisomerization range from 0.2 to 0.9, and three non-photoisomerizing complexes. Kinetic analysis of the transient absorption data reveals that isomerization rates are significantly faster when the P,S ligand has either electron withdrawing groups on phosphine or a flexible bridging ligand. Close inspection of X-ray crystallographic, NMR, electrochemical, and IR data reveal interesting ground state differences between the photoisomerizing and non-photoisomerizing groups of complexes that could account for the differences in excited state reactivity. For the first time, IR spectroscopy provides structural evidence for the formation of an O-bonded metastable isomer upon irradiation of an S-bonded complex.

Introduction

Photochromic compounds and complexes are a special group of bistable molecules that are converted from one isomer or form to another by light.[26] Photonic energy absorbed by the molecule selectively breaks and forms bonds, rendering an isomer with distinct electronic and structural properties. Common mechanisms of photochromism are *cis-trans* isomerization and ring opening/closing which can be found in azobenzenes, stilbenes, diarylethenes, spiro compounds, and Stenhouse adducts, among others.[27-36] In transition metal complexes, the primary mode of photochromism is linkage isomerization in which the coordination mode of a bound ambidentate ligand is changed. Our group is particularly interested in photochromic ruthenium and osmium sulfoxide complexes whereby a thermodynamically favored S-bonded complex undergoes linkage isomerization to a metastable O-bonded isomer upon visible irradiation.[6,7,37-39] A major design challenge for this system is to influence the ground- and excited-state potential energy curves through synthetic modifications, ultimately yielding precise control over the rates and efficiencies (quantum yields) of the forward (S$\rightarrow$O) and reverse (O$\rightarrow$S) isomerization reactions.

Phosphine ligands in organometallic chemistry have long been appreciated for their ability to modify electron density of the metal,[14,15,18,40,41] and yet there are relatively few chelating ligands containing both P and S donor atoms. Notably, the independent work of Darensbourg, Farmer, Grapperhaus and then of Mirkin has established the utility of such ligands for small molecule hydrogenase mimics, among other motivations.[42-49]

Their work, and much of the available literature from other contributors, has focused on phosphine-thiolate ligands on ruthenium. In contrast to their work, our interest is in the development of chelating phosphine thioether ligands, and ultimately phosphine sulfoxide ligands. In a recent study, we described the photochemical reactivity of ruthenium polypyridine complexes containing chelating phosphine sulfoxide ligands.[50] In particular, we found that simple group substitutions on a triphenylphosphine fragment of a chelating phosphine sulfoxide ligand accounts for dramatic differences in photochemical isomerization reactivity. In the case where the *para*-substituent is electron donating (or electron releasing), isomerization is not observed, whereas if the *para*- group is hydrogen or electron withdrawing, then isomerization is efficient and rapid. That photoisomerization can be turned on or off with simple modifications to the molecule's periphery is a unique result, and we were compelled to further investigate this phenomenon.

We report here a continuation of our previous study on phosphine sulfoxides. Four new ruthenium phosphine sulfoxide complexes were synthesized, for a total of seven, in order to further examine our newfound control over photoisomerization. With a substantial library of sulfoxide and thioether complexes at hand, we make extensive comparisons of the electronic and structural properties between the photoisomerizing and non-photoisomerizing groups and shed light on the mechanism by which photoisomerization occurs in this group. Additionally, we provide rare and compelling structural evidence for the formation of an O-bonded photoproduct using IR spectroscopy.

Results and Discussion

The choice to develop chelating phosphine sulfoxide ligands is motivated by the desire to modulate the isomerization quantum yields and isomerization time constants through alteration of the electronic properties of the metal complex. Presented in Table 1 are sulfoxide compounds investigated in this study with their relevant absorption, infrared spectroscopic, and electrochemical data. Molecular structures of these compounds determined from single crystal X-ray diffractometry are shown in Figure 9. The phosphine thioether ligands are typically produced from mixing 2-bromothioanisole with the appropriate phosphoryl chloride. The transition metal compounds displayed in Figure 9 are readily prepared by mixing the phosphine thioether with $[Ru(bpy)_2Cl_2]$, followed by oxidation with *m*-cpba. Attempts to prepare the sulfoxide off the metal result in a mixture of the phosphine oxide and the sulfoxide, which are difficult to separate by chromatography or other methods. Detailed experimental procedures for all ligands and compounds are found in the SI, complete with NMR spectra (^{1}H, ^{31}P, ^{19}F and 2-D COSY NMR; Figures 32 – 99). HRMS and/or elemental analyses (Appendix A) are consistent with the chemical formula, NMR spectra and molecular structure of each compound.

Table 1. *Relevant absorption, IR spectroscopic, and electrochemical data of ruthenium phosphine sulfoxide complexes.*

$[Ru(bpy)_2(LXO)]^{2+}$	L1O	L2O	L3O	L4O	L5O	L6O	L7O
λ_{max} (nm)	351	353	348	359	358	352	358
λ_{max} (nm)	428	N/A	422	N/A	438	N/A	434
$\Phi_{S \rightarrow O}$	0.2	0.0	0.8	0.0	0.9	0.0	0.4
ε ($L/mol^{-1}cm^{-1}$) S-bonded	6230	6330	6580	6930	6110	6520	4230
ν(S=O) (cm^{-1}) S-bonded	1100	1093	1118	1083	1098	1094	1096
ν(S=O) (cm^{-1})	*	N/A	*	N/A	937	N/A	941
E°′ (V) S-bonded	1.64	1.58	1.73	1.59	1.55	1.61	1.58
$S \rightarrow O$ (s^{-1})	0.23	*	0.23	0.04	0.25	0.02	0.24
E°′ (V) O-bonded	0.95	1.13	1.04	0.89	0.92	*	0.97
$O \rightarrow S$ (s^{-1})	0.09	0.07	0.06	0.05	0.05	*	0.07

* Indicates data that is not verified

Structural Characterization

The crystal structures of ruthenium sulfoxides are shown in Figure 9, while some of the ligands (L1, L2, and L3) and ruthenium thioethers (RuL1, RuL2, RuL3, RuL4, and RuL7) are shown in Figures 100 and 101. Relevant NMR shifts and bond distances are summarized in Tables 9 – 12. The bond distances and angles of the $[Ru(bpy)_2]^{2+}$ unit are in accord with previous literature reports.[7,37,51-55] The Ru–N bond distances range from 2.073 Å to 2.125 Å, which are consistent with those found in $[Ru(bpy)_3]^{2+}$. The Ru–P bond distances range from 2.284 to 2.345 Å, and the Ru–S bond distances range from 2.218 to

2.324 Å. These compare well with known ruthenium complexes containing P, S ligands. Wolf has reported the crystal structure of $[Ru(bpy)_2PMe_2T_3\text{-}P,S](PF6)_2$, where PMe_2T_3-P,S is (5,5''-dimethyl-3'-(diphenylphosphino)-2,2':5',2''-terthiophene), featuring a P, S donor chelate. The Ru–S and Ru–P bond distances of this complex are 2.362 Å and 2.340 Å, respectively.[56] Additionally, Grapperhaus reported the crystal structure of $[Ru(DPP\text{-}BT)_3]^-$, [tris-(2-diphenylphosphinothia-phenolato)ruthenium(II)]$^-$, also featuring P, S chelating ligands. The Ru–S bond lengths of this complex range from 2.394Å to 2.445Å and the Ru–P bond lengths range from 2.295Å to 2.353Å.[45]

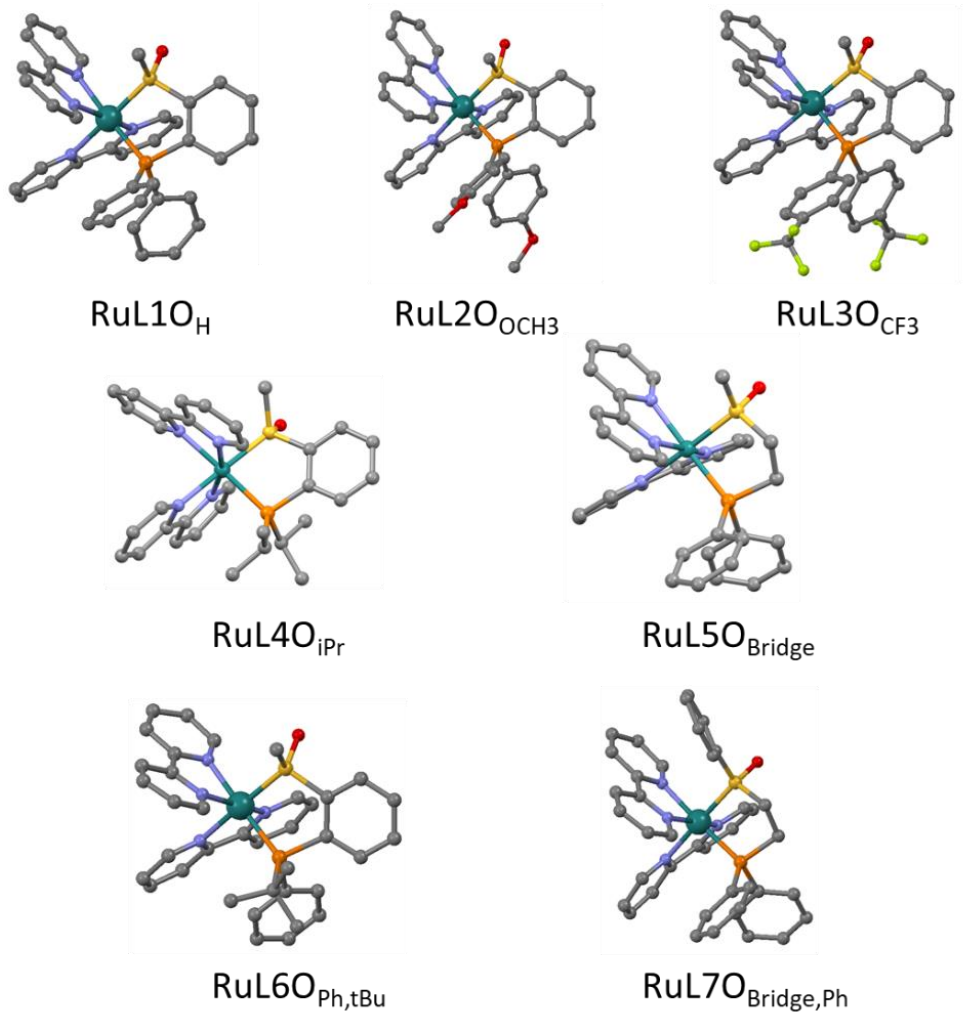

Figure 9. *Molecular structures determined from X-ray diffractometry with the general formula [Ru^{II}(bpy)$_2$(LXO), where LXO is a substituted aryl/alkylphosphine sulfoxide. For RuL5O and RuL7O, the P – S bridge is ethylene instead of phenyl. Molecular structures are depicted as thermal ellipsoid plots at 50% probability, with the Ru atom rendered as a ball. The Ru atom is green, N atoms are blue, C atoms are gray, O atoms are red, the S atom is yellow, and the P atom is orange. Hydrogen atoms and the PF_6^- counterions have been removed for clarity.*

The Ru-S bond length of each thioether complex is shorter than that of the corresponding sulfoxide. For example, the Ru-S bond lengths in $RuL1_H$ and $RuL1O_H$ are 2.318 Å and 2.219 Å, respectively. These results are expected for two reasons. First, the metal-ligand π-stabilizing interaction is stronger in the sulfoxide than in the thioether, as evidenced by a dramatic blue-shift in the absorption spectra of the sulfoxides, as well as their higher oxidation potentials (see below). Second, the sulfur in the sulfoxide is in a higher oxidation state (S^{IV}) and is a smaller atom relative to the thioether (S^{II}). The smaller sulfur atom will form a shorter bond with ruthenium than its thioether counterpart. In accord with these data, the Ru-N bond *trans* to S is longer in the sulfoxide than in the thioether for each pair of complexes that were analyzed. For example, the Ru-$N_{trans\text{-}S}$ bond lengths of $RuL7_{Bridge,Ph}$ and $RuL7O_{Bridge,Ph}$ are 2.066 Å and 2.100 Å, respectively. The sulfur atom accounts for this pattern, imparting a moderate structural *trans*-influence on the Ru-N bond across the metal center.

Crystal structure data for the $L1_H$, $L2_{OCH3}$, and $L3_{CF3}$ group of complexes provide additional insight into the Ru–S and Ru–P bonding interactions. The S–Me bond distances are significantly shorter in the free, uncoordinated ligand than in the thioether complex (Table 11), signifying a weaker S-C bond for the bound thioether. Population of S-C σ^* orbitals through Ru-S π-backbonding could account for this observation. The S–Me bond distances of the ruthenium sulfoxide complexes are shorter than those found in the ruthenium thioether complexes, and even shorter than those found in the free ligand. The smaller S atom in the sulfoxide likely plays a role in this trend reversal. While the

thioether may act in a similar fashion to a phosphine (see below), it is apparent that the bonding between ruthenium and the sulfoxide sulfur is more complicated.

Ru–P and P–R bond distances of the $RuL1_H$, $RuL2_{OCH3}$, and $RuL3_{CF3}$ group behave in accord with a model proposed by Orpen and Connelly,[57-60] which postulates that more electronegative R groups yield shorter Ru–P bonds and longer P–R bonds. These authors examined a large array of crystal structure data, searching for evidence of $d\pi$-stabilization in metal phosphine complexes. Their model explicitly invokes the role of P–R σ^* orbitals in phosphorus π-backbonding with metals. For our complexes, the Ru–P bond distance is shortest in $RuL3_{CF3}$, intermediate in $RuL1_H$, and longest in $RuL2_{OCH3}$, indicating stronger Ru–P bonding with electron-withdrawing substituents. In further support of the Orpen and Connelly model, the P–C bond is longest for $RuL3_{CF3}$, intermediate for $RuL1_H$ and shortest for $RuL2_{OCH3}$. The same trend holds for the corresponding sulfoxide complexes.

All complexes were characterized by ^1H and ^{31}P NMR and are in accord with the mass spectrometric and single crystal X-ray diffraction data. While the large number of aromatic protons defy deep interpretation (e.g., $RuL1O_H$ exhibits 28 protons in the 7–9 ppm range), a few resonances emerge as diagnostic and deserve special mention. Specifically, the singlet arising from the $S–CH_3$ group is particularly sensitive to metal coordination and the oxidation state of the sulfur atom. The chemical shift of this peak first moves upfield as the ligand coordinates to ruthenium, when a strong π-backbonding interaction weakens the $S–CH_3$ bond. For example, this peak moves from 2.10 ppm in $L5_{Bridge}$ to 1.67 ppm in $RuL5_{Bridge}$. Upon oxidation of the thioether to the sulfoxide, the

peak shifts considerably downfield. The high oxidation state of the sulfoxide sulfur removes additional electron density from the methyl hydrogens and deshields them from the field of the NMR spectrometer. This peak shifts from 1.67 ppm in $RuL5_{Bridge}$ to 2.69 in $RuL5O_{Bridge}$. On average, the methyl peak of the sulfoxide is shifted downfield by 0.96 ppm relative to the thioether, similar to the 1.052 ppm shift of the methyl group in DMS (dmethylsulfide) upon oxidation of $[Ru(tpy)(bpy)(dms)]^{2+}$ to form $[Ru(tpy)(bpy)(dmso)]^{2+}$. Here, a correlation is found between the crystal structure and NMR data sets: as sulfur – methyl bond distances shorten, the methyl hydrogen ^{1}H NMR peaks shift downfield.

The ^{31}P NMR is sensitive to metal coordination and the nature of the *p*-substituent. Upon coordination to ruthenium, the P,S ligands shift dramatically downfield. For instance, $L5_{Bridge}$ is -16.79 ppm relative to the H_3PO_4 reference, while $RuL5_{Bridge}$ is 61.61 ppm. In organometallic chemistry, this chemical shift is indicative of successful coordination between the L-type phosphine ligand and the metal center to which it is binding. The ^{31}P NMR chemical shifts of sulfoxide complexes are reasonable based on the phosphine's phenyl substituent; electron withdrawing $RuL3O_{CF3}$ results in a phosphorus peak (67.63 ppm) that is further downfield than that of the electron donating $RuL2O_{OCH3}$ (64.73 ppm), while $RuL1O_{H}$ falls in the middle (65.91 ppm). This follows the bond-length analysis from crystallography, showing that electron-withdrawing groups on phosphine promote π-acidity and shorten metal-phosphorus bond lengths.

UV-Vis and Bulk Photolysis

The ruthenium phosphine sulfoxide complexes feature lowest-energy metal-to-ligand charge-transfer (MLCT) transitions near ~350 nm (Figure 10; Table 1), an assignment based primarily upon the intensity of the transitions (~6000 M^{-1} cm^{-1}) and by comparison to related complexes.[6,37,53,61] The absorption spectra also feature higher-energy electronic absorption peaks that are found in other ruthenium bipyridine complexes and are ascribed to ligand-centered, bipyridine $\pi \rightarrow \pi^*$ transitions.[61] The absorption maxima of the MLCT transitions are sensitive to the chemical substitution on the phosphine ligand. The absorption maxima exhibited by $RuL1O_H$, $RuL2O_{OCH3}$, and $RuL3O_{CF3}$ show predictable shifts based on the electronic properties of the phenyl group substituent on phosphine The *p*-trifluoromethylphenyl derivative ($RuL3O_{CF3}$) features λ_{max} 348 nm, the *p*-methoxyphenyl derivative ($RuL2O_{OCH3}$) features λ_{max} 353 nm, and the phenyl derivative ($RuL1O_H$) absorbs between these two values at λ_{max} 351 nm. In accord with the structural data presented above, these data demonstrate that electron-withdrawing groups on phosphine contribute to dπ-stabilization of the Ru metal center, thus raising the energy of the MLCT band (the bpy π^* orbital exhibits the same energy in all three complexes). Similarly, when comparing the *tert*-butylphenylphosphine complex ($RuL6O_{Ph,tBu}$) and the di-isopropylphosphine complex ($RuL4O_{iPr}$), the more electron-withdrawing alkyl-aryl substituent has a shorter wavelength λ_{max} than the dialkyl substituent (352 nm vs. 359 nm, respectively).

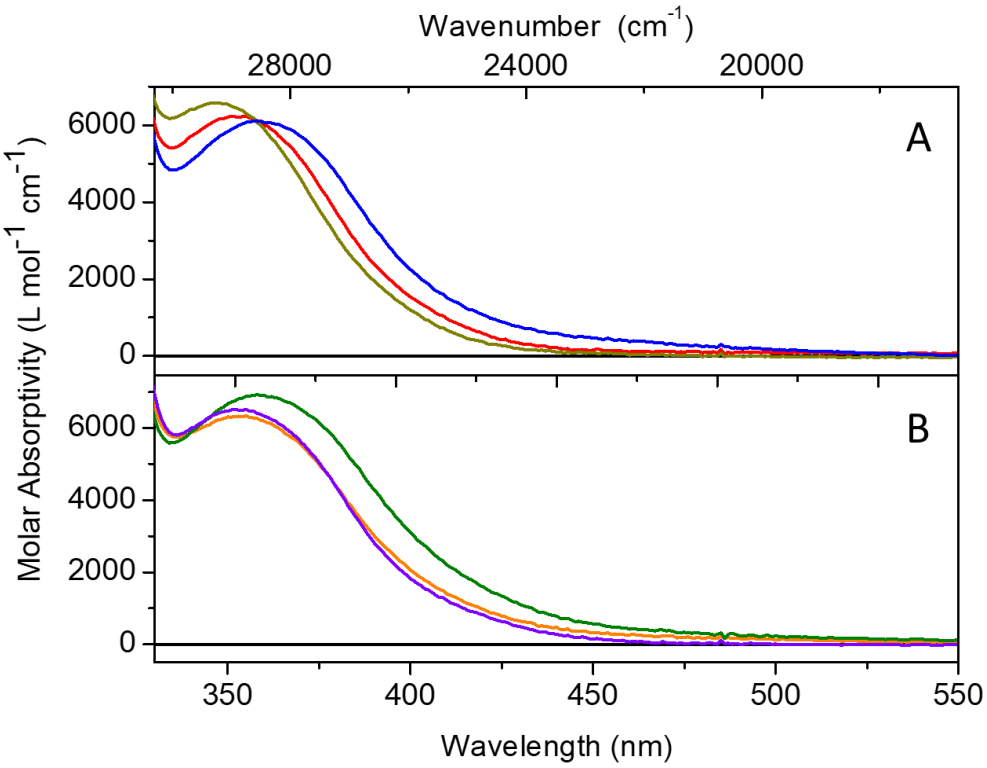

Figure 10. *Absorption spectra of ruthenium sulfoxide complexes in this study. (A) Photoisomerizing complexes: RuL1O$_H$ (red), RuL3O$_{CF3}$ (yellow), RuL5O$_{Bridge}$ (blue) (B) Non-photoisomerizing complexes: RuL2O$_{OCH3}$ (orange), RuL4O$_{iPr}$ (green), and RuL6O$_{Ph,tBu}$ (purple).*

The absorption maxima of the ruthenium phosphine sulfoxides are significantly blue-shifted in energy relative to other ruthenium polypyridyl sulfoxide complexes studied previously.[52,53,62] The parent complex, $[Ru(bpy)_3]^{2+}$, features a lower energy MLCT band (λ_{max} = 452 nm) than any ruthenium polypyridyl complex studied herein. The ruthenium phosphine thioether complexes RuL1$_H$, RuL2$_{OCH3}$, and RuL3$_{CF3}$ feature λ_{max} 382nm, 384nm, and 375nm, respectively (Figure 103). This range of values nearly matches with a set of ruthenium carbene sulfoxide complexes studied previously, despite the

similar binding motifs of phosphines and carbenes to metal coordination compounds.[63] An even greater blue-shift is observed upon converting the phosphine thioether complexes to the phosphine sulfoxide complexes, whose absorption values range from 348 nm to 359 nm (Table 1). The MLCT absorption maxima of the phosphine sulfoxide complexes are higher in energy by ~2000 cm^{-1} compared with their carbene sulfoxide counterparts. These results indicate that chelating phosphine sulfoxide ligands significantly stabilize the Ru dπ (formerly t_{2g}) orbital set, even relative to other chelating sulfoxide ligands. While the orbital interactions between the Ru atom and the sulfoxide that lead to stabilization are not firmly established, it is understood that phosphine P-C σ* orbitals overlap with and stabilize metal dπ orbitals (see above). We presume there are similar interactions between the sulfoxide and Ru that leads to dπ stabilization in these complexes.

Irradiation of $RuL5O_{Bridge}$ (λ_{max} 358 nm) results in dramatic changes in its absorption spectrum (Figure 11). These absorption changes are consistent with those observed in other photoisomerizing ruthenium sulfoxide complexes[6,7,9,63,64] and are representative of the odd-numbered group ($RuL1O_H$, $RuL3O_{CF3}$, $RuL5O_{Bridge}$, and $RuL7O_{Bridge,Ph}$) of complexes investigated here. The spectral changes show the emergence of three isosbestic points (392, 342, and 329 nm) and the appearance of a new absorption maximum at 438 nm. We ascribe this new absorption maximum to the O-bonded isomer of $RuL5O_{Bridge}$. This assignment is based on comparison to relevant literature data. For example, Meyer reports absorption maxima for $[Ru(bpy)_2(PPh_3)X]^{n+}$ (X = Cl^-, NH_3, py, CN^-, and MeCN) complexes, which exhibit absorption maxima of 452, 433, 424, 419, and 418

nm, respectively.[15] The O-bonded sulfoxide features electronic properties similar to a Cl^- ligand, an observation we have made before. Additionally, Wolf describes a ruthenium bipyridine complex bearing a chelating 3'-phosphinoterthiophene ligand whose λ_{max} is 456 nm with a P,C coordination mode.[56]

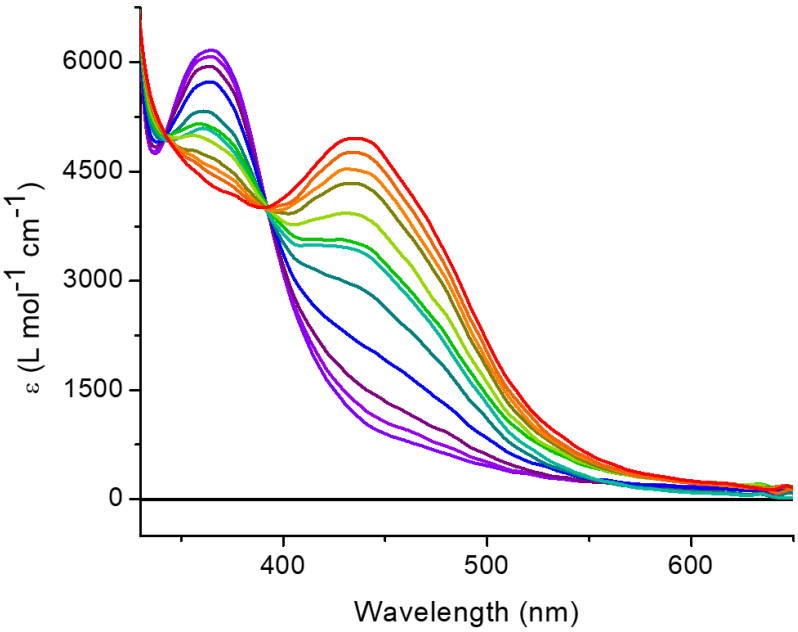

Figure 11. *Bulk photolysis of $RuL5O_{Bridge}$ in DCE irradiated at 405 nm (26 mW) with 2 second intervals between traces: violet trace (0 seconds), green trace (12 seconds), red trace (22 seconds). We assign the purple trace to MLCT absorption from a Ru – S bonded isomer and the red trace to MLCT absorption from a Ru – O bonded isomer.*

The absorption changes leading to the formation of the O-bonded isomer are reversible at room temperature (Figure 112), and the S-bonded isomer is re-formed with a rate constant ($k_{O\rightarrow S}$) of $0.0023 \pm 0.0006\ s^{-1}$. We observe similar changes in the electronic absorption spectrum for $RuL1O_H$, $RuL3O_{CF3}$, and $RuL7O_{Bridge,Ph}$, where the absorption

maxima for S- and O-bonded isomers are 351 nm/421 nm, 348 nm/415 nm, and 358 nm/434 nm, respectively. The corresponding thermal $k_{O\rightarrow S}$ are 0.0029 $\pm$ 0.0004 s^{-1} ($RuL1O_H$) and 0.0013 $\pm$ 0.0001 s^{-1} ($RuL3O_{CF3}$), in accord with that observed for $RuL5O_{Bridge}$.

In contrast, we do not observe any spectral changes upon irradiation of solutions containing $RuL2O_{OCH3}$, $RuL4O_{iPr}$, or $RuL6O_{Ph,tBu}$. This is particularly notable in the case of $RuL2O_{OCH3}$, where the only difference between this complex and $RuL1O_H$ or $RuL3O_{CF3}$ is the *para*-substituent on the phenyl phosphine derivative. Moreover, the MLCT transition (Ru d$\pi \rightarrow$ bpy π*) that triggers the S $\rightarrow$ O isomerization does not formally involve the phosphine ligand. It must be that there is considerable P mixing with the Ru dπ orbitals that alters the fate of isomerization of the sulfoxide.

Femtosecond Transient Absorption

We employed femtosecond pump-probe spectroscopy to elucidate excited-state dynamics that are hidden within the bulk photolysis experiments. In short, the pump-probe data are consistent with bulk photolysis studies; the kinetic rate constants of isomerization are revealed for the photoisomerizing group of complexes and reversion to an S – bonded ground state occurs for the non-photoisomerizing complexes. Shown in Figure 12 is a stack-plot for $RuL5O_{Bridge}$, which is representative of $RuL1O_H$, $RuL3O_{CF3}$, and $RuL7O_{Bridge,Ph}$. The S- and O-bonded spectra obtained from bulk photolysis are represented in Figure 12a, in addition to an “O minus S” spectrum which one observes in a transient absorption experiment when photoisomerization occurs.

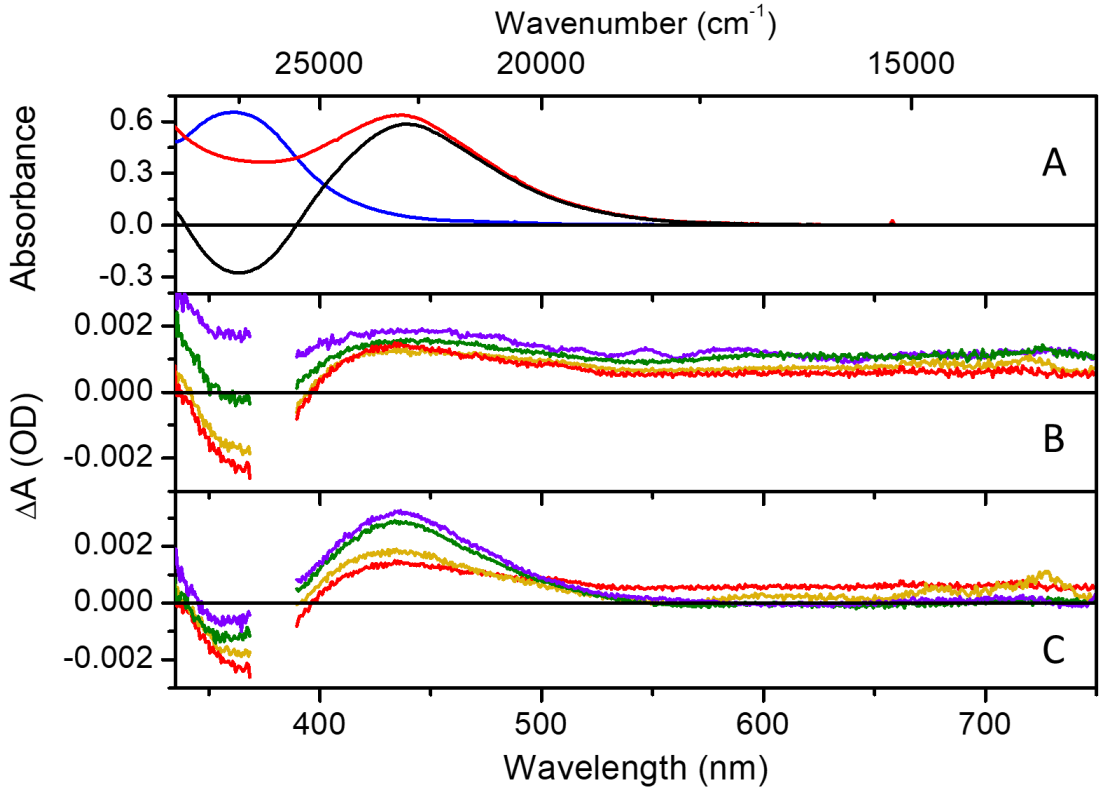

Figure 12. *(A) Steady state spectrum of S-RuL5O$_{Bridge}$ (blue), O-RuL5O$_{Bridge}$ (red), and the difference (black; O-bonded minus S-bonded) in acetonitrile solution. (B) Early transient spectra collected at different pump-probe delays: 1 ps (violet), 2 ps (green), 9 ps (yellow), and 50 ps (red). (C) Late transient spectra collected at different pump-probe delays: 50 ps (red), 100 ps (yellow), 510 ps (green), and 5 ns (violet). Excitation wavelength is 379 nm.*

The transient absorption spectra for RuL5O$_{Bridge}$ are displayed in Figure 12b,c and are grouped according to pump-probe time delay in order to reveal discrete spectral changes as time evolves. At early time delays (Figure 12b; 1 ps – 20 ps), we witness the formation of a thermalized triplet excited state. The first trace (purple, 1 ps) displays a positive, featureless absorption extending throughout the spectral window of the

experiment. Over time, a negative peak forms near ~360 nm that is assigned to a ground-state bleach, as it mirrors the steady-state absorption spectrum. The shape of the transient spectrum by 9 ps (yellow) is emblematic of typical MLCT spectra, with the absorption from 400 nm – 750 nm ascribed to a combination of bpy $\pi \rightarrow Ru^{III}$ LMCT and low-lying bpy $\pi \rightarrow \pi*$ transitions. The positive absorption blue of ~340 nm is due to higher-energy bpy $\pi \rightarrow \pi*$ transitions. Two time-constants are required to fit the early transient absorption data. The first time constant (τ_1 = 110 fs) ^{3}MLCT formation on a sub-picosecond timescale, matching with literature values for ruthenium polypyridyl complexes. The second time constant (τ_1 = 2.85 ps) follows solvent reorganization dynamics. This assignment is best evidenced in the transient absorption spectra of $RuL7O_{Bridge,Ph}$ (Figure 125), which were collected in such a manner as to negate the formation of a laser line. There, we see a clear blue-shift in the ground state bleach at early time delays, which is characteristic of cooling within an excited state. At late time delays (Figure 12c; 50 ps – 5 ns), we observe the emergence of an isosbestic point at 505 nm, situated between the collapse of optical density in the red and the rise in a peak at 438 nm which persists for the remainder of the experiment. We assign this time constant (τ_3 = 204.9 ps) to ground state reversion. The loss in absorbance in the red portion of the spectrum is diagnostic of electron-hole recombination since the bpy $\pi \rightarrow Ru^{III}$ LMCT is no longer operative. Thus, the spectral features in the final TA spectrum (5 ns, purple) are a result of a ground state photoproduct. The similarity between the final time-resolved ΔA spectrum in Figure 12c and the "O minus S" spectrum from Figure 12a allows us to ascribe this photoproduct to an O-bonded ruthenium sulfoxide isomer. Because the loss of

excited state features occurs concomitant with the formation of photoproduct absorption (in the cases of $RuL1O_H$, $RuL3O_{OCH3}$, $RuL5O_{Bridge}$, and $RuL7O_{Bridge,Ph}$), we suggest that isomerization is non-adiabatic and occurs as the molecule transitions from the excited-state to the ground-state potential energy surface.

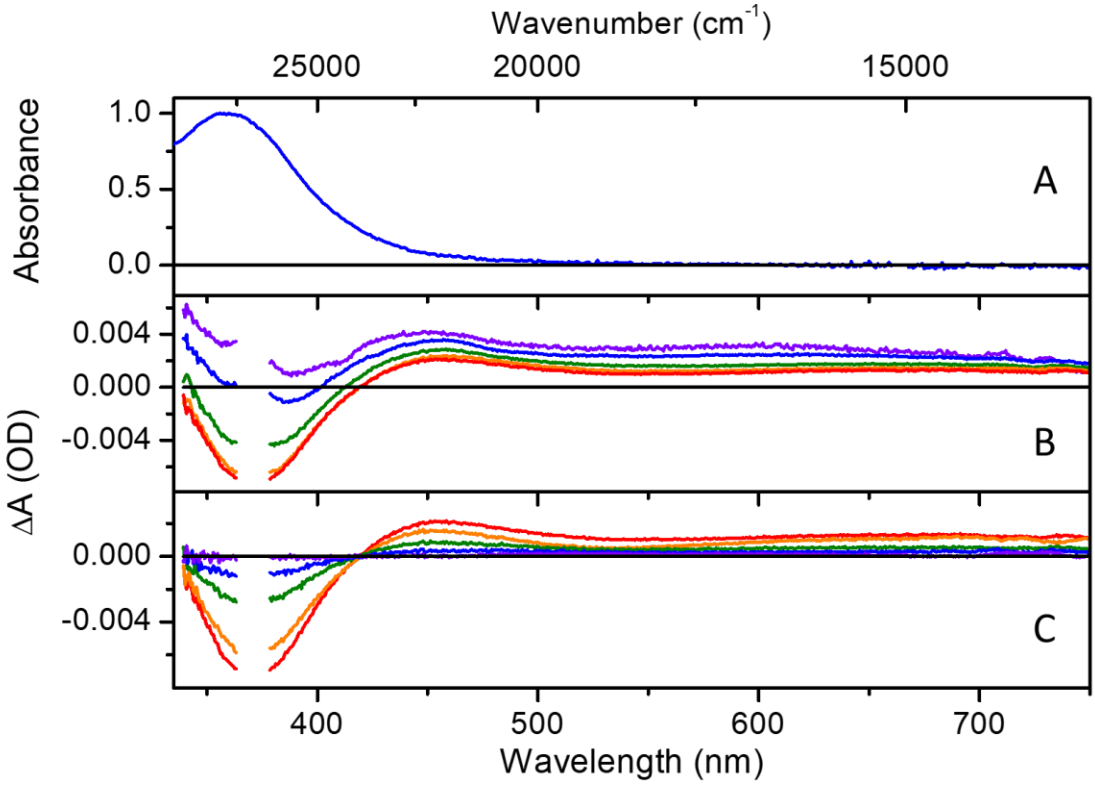

Figure 13. *(A) Steady state spectrum of S-RuL4O$_{iPr}$ in acetonitrile solution. (B) Early transient spectra collected at different pump-probe delays: 0.7 ps (violet), 1 ps (blue), 2 ps (green), 5 ps (orange), and 20 ps (red). (C) Late transient spectra collected at different pump-probe delays: 20 ps (red), 100 ps (orange), 500 ps (green), 1 ns (blue), and 2.5 ns (violet). Excitation wavelength is 370 nm.*

The steady-state and transient absorption spectra of $RuL4O_{iPr}$ (Figure 13) are representative of $RuL2O_{OCH3}$ and $RuL6O_{Ph,tBu}$. At short pump probe time delays (Figure

13b; 0.7 ps – 20 ps), the transient spectra evolve much like they do for RuL5O. The initial trace at 0.7 ps displays a positive absorption that exists throughout the spectral window of the experiment. As it decays, a negative peak forms at ~365 nm, consistent with a ground state bleach. Two time-components are extracted from kinetic analysis, attributed to formation of the ^{3}MLCT state (τ_1 = 0.31 ps) and subsequent solvent reorganization dynamics (τ_2 = 3.67 ps). The latter assignment is bolstered by a lack of any isosbestic points in the early time regime, which would otherwise indicate a transition between two different excited states. Rather, we see a uniform decay of the transient spectra and a slight blue-shift of the MLCT bleach, both indicative of thermalization/vibrational cooling. At long pump probe time delays (Figure 13c; 20 ps – 2.5 ns), an isosbestic point is formed at ~420 nm that persists for the remainder of the experiment. Blue of this point, the bleach feature decays to zero by 2.5 ns. The broad, positive absorption at lower energies decays on the same timescale. This final time component (τ_3 = 529.2 ps), is assigned to electron-hole recombination. In contrast to RuL5O$_{Bridge}$, the collapse of optical density in the red does not coincide with the formation of any long-lived spectral features. Thus, we are watching the return of a ground state, S-bonded isomer. Similar data are obtained for RuL2O$_{OCH3}$ and RuL6O$_{Ph,tBu}$.

Table 2. *Kinetic fits from ultrafast transient absorption spectroscopy. τ_1 is assigned to intersystem crossing from the singlet to triplet manifold, τ_2 is assigned to vibrational cooling and formation of a thermalized ^{3}MLCT excited state, and τ_3 is electron-hole recombination, marking a return to the ground state.*

Complex	τ_1 (ps)	τ_2 (ps)	τ_3 (ps)	$\tau_{(S\rightarrow O)}$ (ps)
$RuL1O_H$	0.27 ± 0.12	2.12 ± 1.04	1156.8 ± 87.3	5784.0
$RuL2O_{OCH3}$	0.23 ± 0.03	4.27 ± 0.83	839.2 ± 92.9	--
$RuL3O_{CF3}$	0.11± 0.04	1.99 ± 0.34	812.4 ± 120.0	1015.5
$RuL4O_{iPr}$	0.31 ± 0.10	3.67 ± 0.74	529.2 ± 31.8	--
$RuL5O_{Bridge}$	0.11 ±0.04	2.85 ± 0.71	204.9 ± 19.9	227.7
$RuL6O_{Ph,tBu}$	0.29 ± 0.04	2.21 ± 1.16	434.2 ± 65.8	--
$RuL7O_{Bridge,Ph}$	0.23 ± 0.14	1.36 ± 0.89	103.7 ± 21.5	259.3

The kinetic fits of each ruthenium phosphine sulfoxide complex are listed in Table 2. While the lifetimes of ^{3}MLCT formation (τ1) and solvation dynamics (τ2) are mostly consistent throughout the complexes, the excited state lifetimes (τ3) vary between 103.7 ps ($RuL7O_{Ph,Bridge}$) and 1156.8 ps ($RuL1O_{Ph}$), and it is this rate that contains isomerization. Notably, τ3 does not show a dependence on photoisomerization quantum yield, as $RuL2O_{OCH3}$ ($\Phi_{S\rightarrow O}$ = 0.0) and $RuL3O_{CF3}$ ($\Phi_{S\rightarrow O}$ = 0.8) have nearly identical excited state lifetimes. Two complexes with notably short excited state lifetimes are $RuL5O_{Bridge}$ and $RuL7O_{Bridge,Ph}$, whose P,S linker is a flexible ethylene bridge instead of a phenyl bridge. Thus, we can directly relate the excited state lifetime with vibrational freedom associated with the P,S ligand. Complexes with alkyl phosphines have shorter lifetimes than those with aryl phosphines, and the unsubstituted $RuL1O_H$ has the longest excited state lifetime. We submit that vibrational motions coupled the υ(S=O) stretching mode are directly

involved in the rate of excited state deactivation and are responsible for photoisomerization reactivity in these complexes.

Calculated isomerization lifetimes are also presented in Table 2. In accord with TD-DFT calculations from our previous report,[50] excited state isomerization is more thermodynamically favored with RuL3O than RuL1O, and RuL3O exhibits a much shorter photoisomerization lifetime than RuL1O. The addition of a flexible P,S bridge yields a roughly 20-fold decrease in this lifetime in RuL5O compared with RuL1O, illustrating how important molecular motions and vibrations are in photoisomerization reactivity.

Transient absorption experiments for each thioether and sulfoxide complex were performed in acetonitrile. Typically, this strong-donor solvent is avoided in spectroscopic studies of ruthenium sulfoxide complexes due to its propensity for solvolysis. However, it seems that the strong bond formed between ruthenium and phosphorous renders these ligands inert to solvent photosubstitution. In fact, these complexes didn't show signs of decomposition in any environment that they were subjected to, including high-power irradiation from a pulsed nanosecond laser.

Electrochemistry

Cyclic voltammograms of the ruthenium phosphine sulfoxide complexes show clear evidence of electron transfer triggered isomerization (Table 1; Figure 106), where oxidation of Ru^{2+} prompts S $\rightarrow$ O isomerization and reduction of Ru^{3+} triggers O $\rightarrow$ S isomerization. These complexes yield voltammograms that are reminiscent of those

obtained by Taube for $[Ru(NH_3)_5(dmso)]^{2+}$.[2] The appearance of the voltammogram is a function of the scan rate, the switching potential, and the rates of isomerization. Shown in Figure 14 are voltammograms of $RuL4O_{iPr}$ and $RuL5O_{Bridge}$ at 0.4 V/s in acetonitrile. Importantly, no current is passed at the less positive, O-bonded couple (+0.89 V) until after oxidation of the more positive, S-bonded couple (+1.59 V). Moreover, if the switching potential occurs at potentials less than +1.59 V, no current is observed at the less positive couple, indicating that the species generating this current is only formed upon oxidation of the more positive couple.

While such voltammograms may be simulated to extract isomerization rate constants, we and others have found analytical equations that provide more accurate isomerization rate constants (see Appendix A).[65] Analysis of these results reveals $Ru^{III}_{S\rightarrow O}$ rate constants ranging from 0.25 s^{-1} ($RuL5O_{Bridge}$) to 0.02 s^{-1} ($RuL6O_{Ph,tBu}$), and $Ru^{II}_{O\rightarrow S}$ rate constants ranging from 0.09 s–1 ($RuL1O_H$) to 0.05 s–1 ($RuL4O_{iPr}$). The $k_{S\rightarrow O}$ values reported here are considerably slower than values reported for sulfoxides of the type [Ru(tpy)(L2)(dmso)] (where L2 is a variable bidentate ligand), which have $k_{S\rightarrow O} \sim 50\ s^{-1}$,[54] but they are similar to other ruthenium complexes bearing chelating sulfoxide ligands.[53,63] The chelate effect must hinder S $\rightarrow$ O isomerization in the ground state after oxidation of Ru^{2+}. Like both the carbene sulfoxides and the photochemical results discussed above, our electrochemical studies in acetonitrile show no evidence of solvolysis of the phosphine sulfoxide ligand. These results further support the choice to pursue this class of ligands in preparing more solvent tolerant ruthenium sulfoxide complexes.

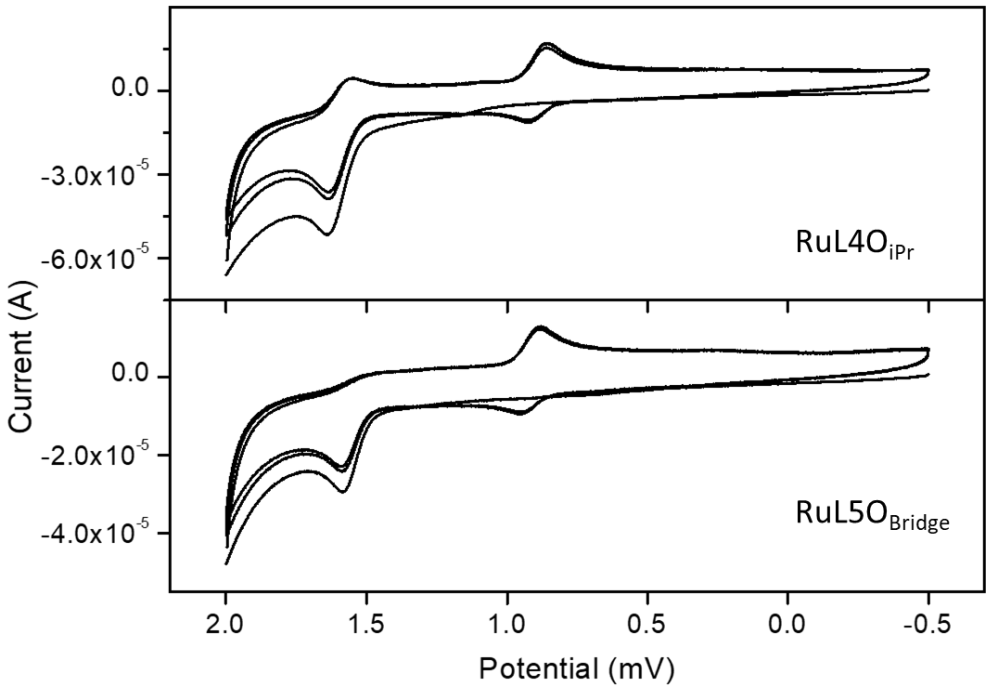

Figure 14. *Cyclic voltammograms of RuL4O$_{iPr}$ and RuL5O$_{Bridge}$ in acetonitrile with a scan speed of 0.4 V/s. RuL4O$_{iPr}$, which does not isomerize photochemically, undergoes electrochemical S $\rightarrow$ O isomerization at a potential of 1.59 V and O $\rightarrow$ S isomerization at a potential of 0.89 V. RuL5O$_{Bridge}$, which photochemically isomerizes on a picosecond timescale, undergoes electrochemical S $\rightarrow$ O isomerization at a potential of 1.55 V and O $\rightarrow$ S isomerization at a potential of 0.92 V. Notably, the rate of S $\rightarrow$ O isomerization is an order of magnitude greater in RuL5O$_{Bridge}$ than in RuL4O$_{iPr}$.*

Infrared Spectroscopy

Attenuated total reflectance infrared (ATR-IR) spectra revealed the emergence of peaks around 1100 cm^{-1} upon oxidation of the ruthenium thioether complexes to form the ruthenium sulfoxide complexes (Figure 15; Figure 143). We attribute these peaks to S – O stretching frequencies of S – bonded metal sulfoxide complexes, in accord with literature values for similar complexes.[66,67] For instance, [*mer*-$RuCl_3$(dmso-S)$_3$]$^-$ and [*fac*-$RuCl_3$(dmso-S)$_3$]$^-$ have S – O stretching frequencies of 1098 cm^{-1} and 1102 cm^{-1}, respectively. Free dmso has a lower-energy S – O stretch at 1043 cm^{-1} while O – bonded metal sulfoxide complexes display even lower S – O stretching frequencies, typically between 900 cm^{-1} and 1000 cm^{-1}. This trend in sulfoxide stretching frequencies based on metal coordination is explained by Calligaris and in Appendix A (Scheme 8).[67-69]

The absorption maximum of the sulfoxide band is blue-shifted in complexes with electron-withdrawing phosphine groups. This is implicative of a cis-effect through ruthenium in which a loss of electron density at the metal destabilizes the sulfoxide ylide resonance condition and promotes greater double-bonding character, and thus a higher-energy sulfoxide vibrational mode. The absorption maximum for the ν(S=O) stretching mode in $RuL3O_{CF3}$ is 1118 cm^{-1} and in $RuL2O_{OCH3}$ is 1093 cm^{-1}. This difference is quite large considering how well-separated phosphine's substituents are from the sulfoxide group, and underscores how effectively phosphine can modulate the complex to which it is bound.

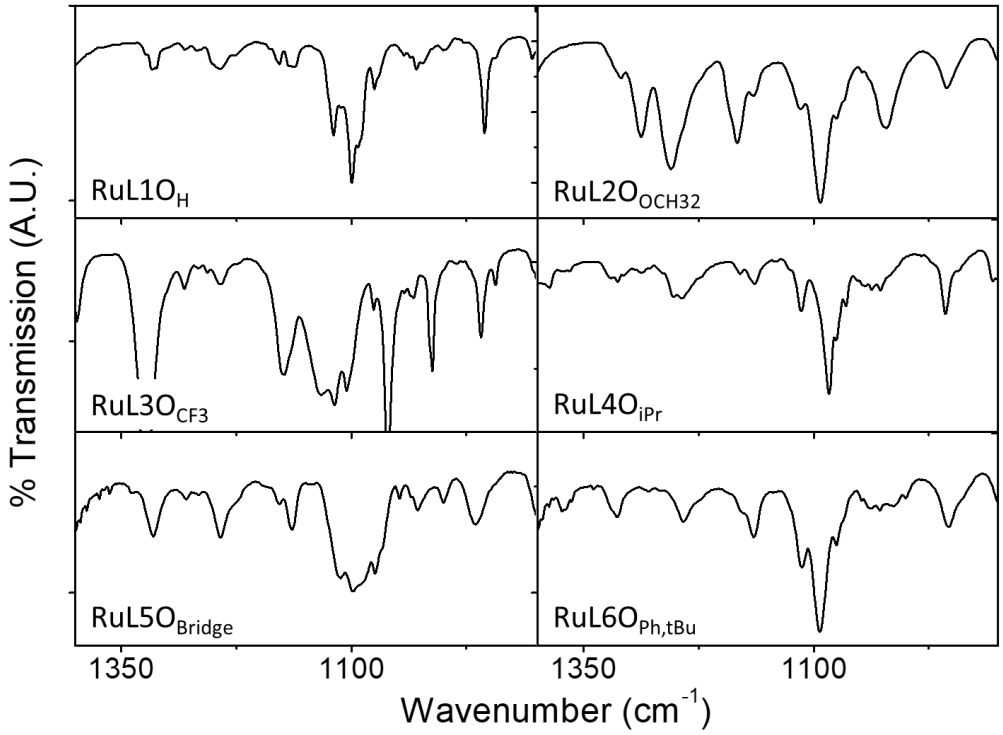

Figure 15. *ATR-IR spectra of ruthenium phosphine sulfoxide complexes. The photoisomerizing complexes (left) exhibit broad peaks in the S – O stretching region (~1100 cm^{-1}) relative to the non-photoisomerizing complexes (right).*

While our group utilizes steady-state and time-resolved UV-Vis absorption techniques to support our notion of S $\rightarrow$ O photoisomerization in ruthenium sulfoxide complexes, these measurements report only on *electronic transitions* and are blind to structural characteristics of molecules. To date, our assignments of the O-bonded sulfoxides have been based on UV-visible data of structurally similar compounds as well as ^{1}H NMR chemical shifts of either a methyl or methylene group *alpha* to the sulfoxide The data in Figure 15 display the strongest ν(S=O) peaks we have observed for any class of sulfoxides. To further our structural characterization of the isomerization reaction, we

performed bulk photolysis on these compounds and investigated the photochemical products by infrared spectroscopy.

Nujol mulls of $RuL4O_{iPr}$ and $RuL5O_{Bridge}$ were irradiated by a 355 nm pulsed YAG laser, with spectral changes recorded using FTIR spectroscopy (Figure 16). For $RuL4O_{iPr}$ (Figure 16a), 25 minutes of irradiation yielded almost no change in the FTIR spectrum between 900 cm^{-1} and 1100 cm^{-1}. This result is expected since traditional bulk photolysis and transient absorption experiments suggest $RuL4O_{iPr}$ does not photochemically isomerize. Instead, the molecule maintains its S-coordination with ruthenium after irradiation, evidenced by the maintenance of the sulfoxide stretching band centered at 1083 cm^{-1} and an unchanged UV-Vis absorption spectrum (Figure 141). For $RuL5O_{Bridge}$, however, 15 minutes of irradiation at 355 nm induced dramatic changes in the FTIR spectrum. The broad absorption band at 1100 cm^{-1} diminished in intensity, concomitant with the growth of an absorption band centered at 937 cm^{-1} and an isosbestic point near 1017 cm^{-1}. These two absorptions are attributed to an S-bonded ν(S=O) and an O-bonded ν(S=O) on the sulfoxide, respectively. Notably, these two absorptions feature similar rates of change (Figure 145). Further evidence for this assignment is shown in the UV-Vis absorption spectra (Figure 141), where loss of the S-bonded MLCT absorption at 360 nm occurs alongside the rise in absorption centered near 440 nm, attributed to an O-bonded MLCT band. It is notable that photoisomerization of $RuL5O_{Bridge}$ caused the entire vibrational band around 1100 cm^{-1} to diminish, not just the absorption of the ν(S=O) stretching mode. We suggest that this is evidence of strong vibrational coupling between the S-bonded sulfoxide stretch and other vibrational modes within the ligand. The data

displayed in Figure 16 provide compelling structural evidence that the UV-visible changes observed in these compounds is due to sulfoxide isomerization.

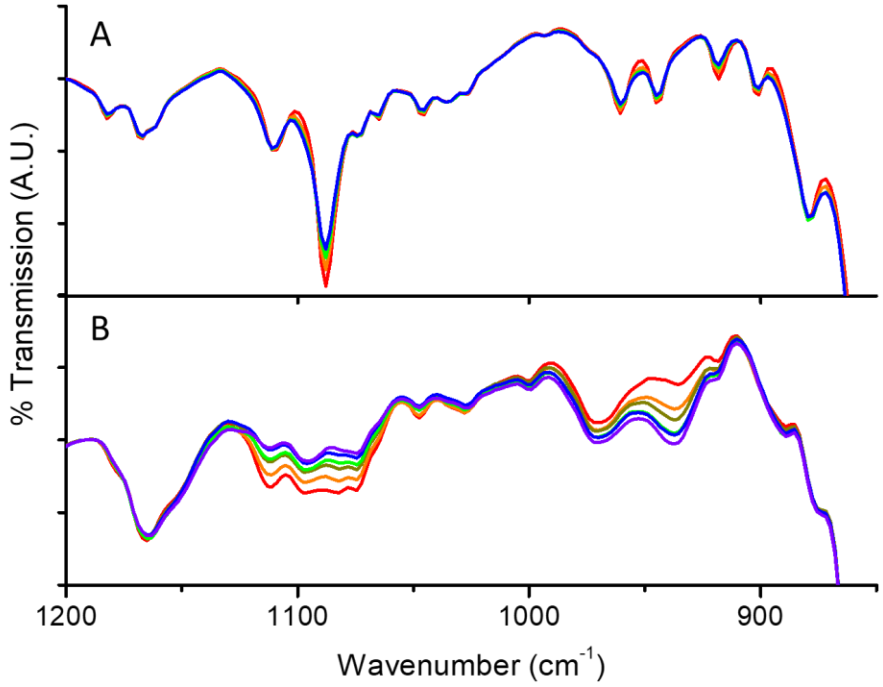

Figure 16. *FT-IR spectra of ruthenium phosphine sulfoxide/Nujol mixtures as they are irradiated by a 355 nm pulsed YAG laser. (A) RuL4O$_{iPr}$ after 0 minutes (red), 10 minutes (orange), 15 minutes (green), and 20 minutes (blue) of irradiation. (B) RuL5O$_{Bridge}$ after 0 minutes (red), 1 minute (orange), 3 minutes (yellow), 6 minutes (green), 10 minutes (blue), and 15 minutes (purple) of irradiation.*

Comparison of Photoisomerizing and Non-photoisomerizing Complexes.

The ruthenium phosphine sulfoxides studied here exhibit the greatest range in quantum yields of photoisomerization we have ever recorded across a group of complexes. That this reactivity can be turned on or off by simple substitutions near the

molecule's periphery is thus far unique and raises the question: are there discernable structural or electronic differences between the photoisomerizing and non-photoisomerizing groups of complexes that might result in their different reactivities? Photoisomerization in a ruthenium sulfoxide complex requires the formation an MLCT excited state and is primarily considered an excited-state process. However, we have unraveled data from electrochemistry, IR spectroscopy, X-ray crystallography, and NMR spectroscopy that not only dichotomize the two groups, but also suggest that the ground state character is integral in the process and that specific ground state properties are predictive of whether a particular complex will photoisomerize.

The results from electrochemistry (see above) are a good starting point for a comparison between photoisomerizing and non-photoisomerizing sulfoxides. Except for $RuL2O_{OCH3}$, every phosphine sulfoxide complex undergoes clear electrochemical S $\rightarrow$ O isomerization. Further, the oxidation potential at which this occurs is similar for every species. This implies that, regardless of photoisomerization reactivity, there lies a ground state O-bonded potential energy surface that is accessible by each S-bonded complex. Upon plotting the relative rates of electrochemical isomerization (Table 1), we note an unexpected trend. The rate of S $\rightarrow$ O isomerization (Figure 109) in the photoisomerizing complexes is an order of magnitude faster than those in the non-photoisomerizing complexes. This is evident in $RuL5O_{Bridge}$ (Figure 14) as there is no observable peak in the cathodic trace of the more positive couple due to rapid S $\rightarrow$ O isomerization after ruthenium oxidation. Since S $\rightarrow$ O isomerization is slower in $RuL4O_{iPr}$, there is still S-bonded ruthenium at the electrode surface during the cathodic scan, owing to the peak

at +1.59 V. The rate of O $\rightarrow$ S isomerization (Figure 110), meanwhile, is roughly equivalent for every complex. Because cyclic voltammetry is carried out on ground state species, we assert that formation of the O-bonded isomer is not only inhibited photochemically for $RuL2O_{OCH3}$, $RuL4O_{iPr}$, and $RuL6O_{Ph,tBu}$. Instead, the barrier that prevents excited state isomerization for the non-photoisomerizing compounds persists in ground state.

Revealing the different electrochemical isomerization rates for the photoisomerizing and non-photoisomerizing complexes motivated further ground-state comparisons. We considered whether vibrational motions involving the sulfoxide moiety were affecting the rates of isomerization, both electrochemically and photochemically, and decided to closely investigate the IR spectra of the two groups of complexes. In doing to, we noticed stark differences in the sulfoxide IR absorption bands between the non-photoisomerizing and photoisomerizing complexes. The non-photoisomerizing complexes feature intense, narrow peaks near 1100 cm^{-1} with low-intensity absorption shoulders and average FWHM values of 23 cm^{-1} (Table 22, Figure 15). The photoisomerizing complexes have broad absorption bands with multiple intense peaks that nearly coalesce into the central peak, resulting in average FWHM values of 52 cm^{-1}. $RuL5O_{Bridge}$ has a particularly broad sulfoxide stretching mode that likely experiences band broadening due to the increased vibrational freedom imparted by the ethylene bridge connecting the phosphine and sulfoxide moieties. Motivated by Kubiak and Keating,[69,70] we performed spectral deconvolution fitting on the sulfoxide stretching bands Crude spectral deconvolution fits for the photoisomerizing complexes indicate significant overlap between the sulfoxide stretch and at least four other vibrational modes, while

the non-photoisomerizing complexes exhibit minimal overlap between the sulfoxide stretch and other modes (Figure 144).

The IR absorption bands of the photoisomerizing complexes report on a sulfoxide stretching mode that is intricately tied to other vibrational modes within the molecule. This notion is strengthened by Figure 16b, as isomerization of $RuL5O_{Bridge}$ causes the entire vibrational band around 1100 cm^{-1} to decay rather than just the S – O stretching mode. This feature, unique to the photoisomerizing complexes, implies that overlap between these vibrational modes might be critical in isomerization reactivity. Because photoisomerization is an excited-state event, the same vibrational coupling would need to be operative upon photoexcitation. Since the ^{3}MLCT state in ruthenium phosphine sulfoxide complexes is formed within a few ps, vibrational modes involved in the initial relaxation of the FC state could profoundly impact the fate of the excited state molecule. The lifetime of the S – O stretching mode in $[Ru(dmb)_2(BzSO)]^+$ is 0.47 ps, so a similar lifetime in a ruthenium phosphine sulfoxide complex might suffice in guiding the molecule along the excited state surface towards an isomerization coordinate. Of course, the IR data presented in this paper pertains to ground state vibrational structure, so additional experiments would be needed to probe the excited state vibrational manifold.

An interesting trend in the ruthenium phosphine sulfoxide bond lengths is extracted when comparing the photoisomerizing and non-photoisomerizing sulfoxide complexes with their respective ruthenium thioether complexes. That is, the Ru–P bond distance is longer in the sulfoxide than in the thioether for the photoisomerizing series of

complexes, while the Ru–P bond is longer in the thioether than in the sulfoxide for the non-photoisomerizing series of complexes. The Ru-$N_{trans\text{-}P}$ bond is sensitive to this as well and simply follows the inverse trend due to the trans-influence being imparted by phosphorus. This disparity is mirrored in the ^{31}P NMR data of these complexes. The phosphorus chemical shift of the photoisomerizing sulfoxides is upfield to their corresponding thioethers, while the chemical shift of non-photoisomerizing sulfoxides is downfield to their corresponding thioethers. It is difficult to determine the reason for this dichotomy, but it stands out as a ground-state effect that might have important implications in the photoisomerization reaction.

The analysis presented in this section portrays the important role of the ground state in photoisomerization. While photoisomerization is typically considered an excited state process, it is clear from electrochemistry, IR spectroscopy, X-ray crystallography, and NMR spectroscopy that the electronic and structural properties of the ground state S- and O- bonded isomers are different between complexes that photoisomerize and those that do not. Notably, the rates of electrochemical S $\rightarrow$ O isomerization are an order of magnitude slower in the non-photoisomerizing group of complexes. We postulate that isomerization in the ground state and excited state is facilitated by a set of distinct vibrational modes that occur in tandem with the sulfoxide stretching mode.

Conclusion

An in-depth spectroscopic analysis was carried out on a novel family of ruthenium phosphine sulfoxide complexes. We found that quantum yields of photoisomerization range from 0.0 to 0.9 and are highly sensitive to simple substitutions on the phosphine moiety; electron withdrawing groups promote photoisomerization and electron donating groups turn off photoisomerization altogether. Additionally, changing the P,S bridge from phenyl to ethylene dramatically increases the quantum yield. Ultrafast pump probe measurements revealed excited state lifetimes, ranging from 104 ps to 1157 ps, that are independent of photoisomerization quantum yield. Instead, shorter lifetimes are associated with molecules whose P,S ligands exhibit vibrational freedom. Except for $RuL2O_{OCH3}$, every sulfoxide complex undergoes clear electrochemical S $\rightarrow$ O isomerization. This rate is an order of magnitude slower in the non-photoisomerizing complexes compared with the photoisomerizing complexes. Because of this, we assert that ground state character is critical in photoisomerization reactivity, despite it being primarily an excited-state event. The IR spectra of the photoisomerizing complexes feature a broad absorption band in the region of the S – O stretching mode with several overlapping transitions, whereas the non-photoisomerizing complexes feature a narrow peak that is primarily attributed to S – O stretching. The additional vibrational modes coupled to the sulfoxide stretch in the photoisomerizing complexes are likely operative during both ground- and excited-state isomerization events. Finally, visible irradiation of photoisomerizing complexes yields dramatic changes in the infrared spectra of these molecules; the Ru-S ν(S=O) diminishes, concomitant with a growth in the Ru-O ν(S=O).

3.3 Slow ^{3}MLCT Formation Prior to Isomerization in Ruthenium Carbene Sulfoxide Complexes

Abstract

A series photochromic complexes of the general formula $[Ru(bpy)_2(NHC\text{-}SR)]^{2+}$ and $[Ru(bpy)_2(NHC\text{-}S(O)R)]^{2+}$ were prepared and investigated by X-ray crystallography, electrochemistry, and ultrafast transient absorption spectroscopy, where bpy is 2,2'-bipyridine and NHC-SR and NHC-S(O)R are chelating thioether (-SR) and chelating sulfoxide (-S(O)R) N-Heterocyclic Carbene (NHC) ligands. The only differences between these complexes are the nature of the R group on the sulfur (Me vs. Ph), the identity of the carbene (imidazole vs benzimidazole) and the number of linker atoms in the chelate (CH_2 vs C_2H_4). A total of 13 total structures are presented (four $[Ru(bpy)_2(NHC\text{-}SR)]^{2+}$ complexes, four $[Ru(bpy)_2(NHC\text{-}S(O)R)]^{2+}$ complexes, and five uncomplexed ligands), and these reveal the expected coordination geometry as predicted from other spectroscopy data. The data do not provide insight into the photochemical reactivity of these compounds. These carbene ligands do impart stability with respect to ground state and excited state ligand substitution reactions. Bulk photolysis reveals that these complexes undergo efficient S→O isomerization, with quantum yields ranging from 0.24 to 0.87. The excited state reaction occurs with a time constant ranging from 570 ps to 1.9 ns. Electrochemical studies reveal an electron transfer triggered isomerization and voltammograms are consistent with an *ECEC* (*E*lectrochemical–*C*hemical *E*lectrochemical–*C*hemical) reaction mechanism. The carbene facilitates an unusually slow S→O isomerization and an unusally fast O→S isomerization. Temperature studies

reveal a small and negative entropy of activation for the O→S isomerization suggesting an associative transition state in which the sulfoxide simply slides along the S–O bond during isomerization. Ultrafast studies provide evidence for an active role of the carbene in the excited state dynamics of these complexes.

Introduction

Photochromic compounds and complexes are examples of molecular machines in which light converts one isomer to another.[26] There are many classes of photochromic compounds such as azobenzenes,[27-29] Stenhouse adducts,[30,31] dithienylethenes,[32-36,72] azoaryltriazoles,[73,74] to name just a few. Our group has focused on ruthenium and osmium sulfoxide compounds,[6,7,39] which comprises a group of transition metal based complexes that show photochromic behavior based on a ligand isomerization.[75-79] Typically, these sulfoxide complexes feature an S-bonded lowest energy isomer, and an O-bonded metastable isomer along the ground state potential energy surface. In an overly simplistic, but useful model, these compounds may be analyzed by a four-energy level diagram (Scheme 3). The synthetic challenge in this field is the manipulation of both ground state and excited state potential energy curves of both S-bonded and O-bonded isomers in order to optimize a specific property. In our study of these complexes, we have identified a few long-standing challenges that include relatively slow ground state reversion rate constants and poor solvent tolerance of the O-bonded isomer. Indeed, for the vast majority of cases that we have investigated, the ground state reversion rate constant (O→S isomerization) is on the order of 10^{-4} s^{-1}, and the O-bonded isomer is unstable with

respect to substitution in aqueous, acetonitrile and even alcohol solvents. We report here a new family of chelating N-Heterocyclic Carbene sulfoxide ligands that addresses these two shortcomings.

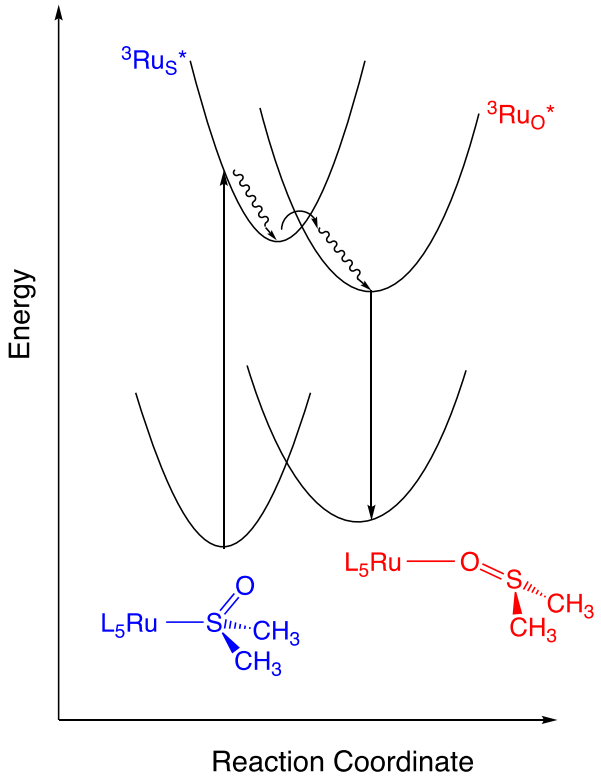

Scheme 3. *Four-level energy diagram describing excited state and ground state isomerization of Ruthenium Sulfoxide complexes.*

Similar to phosphines, N-Heterocyclic Carbene (NHC) ligands are employed in organometallic reaction schemes to modulate the electron density of the metal center.[80-83] They are typically considered to be strong σ-donors and often make strong bonds with most transition metals. They are not commonly used in the formation of photochemically active compounds, though there are a number of existing studies of these ligands on

ruthenium polypyridine complexes.[84-91] In a previous study, we found that chelating phosphine sulfoxide ligands when coordinated to $[Ru(bpy)_2]_{2+}$ centers permitted remarkable control of the quantum yields of isomerization, ranging from 0.8 to 0.0.[50] This was enabled by the σ- and π-bonding capabilities of phosphines. Based on this observation, we questioned if N-Heterocyclic Carbenes (NHCs) might also provide control of the ground- and excited-state properties, as well as impart greater solvent compatibility based on its anionic character and tendency to form strong bonds with metal atoms and ions. Herein, we report efficient quantum yields of isomerization, rapid ground state reversion rates and operation of these photochromic compounds in acetonitrile. These accomplishments represent major advances in the continued development of these compounds.

Result and Discussion

Shown in Figure 17 are the molecular structures of the sulfoxide and thioether complexes investigated in this study (TE ligands in Figure 191). The complexes all feature an identical coordination sphere comprised of two bipyridine ligands in cis geometry and an N-heterocyclic carbene with a chelating sulfoxide or thioether moiety. The only difference in these complexes is the nature of the R-group on the sulfur (Me vs. Ph), the nature of the carbene (imidazole vs. benzimidazole), or the number of atoms in the linker joining these groups (methylene vs ethylene). The Ru–N bond distances are in accordance with other cis-$[Ru(bpy)_2]^{2+}$ centers, and are summarized in Table 3. The Ru–S bond distances for the sulfoxides are 2.2537(10) Å (RuOTE3), 2.2464(11) Å (RuOTE4), 2.2371(5) Å (RuOTE9), and 2.2384(11) Å (RuOTE10), and are shorter than those found in the

thioether complexes, 2.3330(6) Å (RuTE4), 2.3480(14) Å (RuTE7), 2.3437(5) Å (RuTE9), and 2.3179(8) Å (RuTE10). This comparison demonstrates a statistically and significantly shorter Ru–S bond distance for the sulfoxide relative to their corresponding thioether complexes. We also note that both RuOTE9 and RuOTE10 feature Ru–S bond distances that are statistically shorter than that of RuOTE4. The S–O bond distances are 1.489(3) Å (RuOTE3), 1.476(3) Å (RuOTE4), 1.4842(15) Å (RuOTE9), and 1.461(4) Å (RuOTE10). While RuOTE9 and RuOTE10 display statistically distinct S–O bond distances, they both individually overlap with that of RuOTE4. The Ru–CNHC bond distances in the sulfoxide complexes are 2.057(3) Å (RuOTE3), 2.072(5) Å (RuOTE4), 2.061(2) Å (RuOTE9), and 2.043(4) (RuOTE10), whereas they are 2.065(2) Å (RuTE4), 2.046(5) Å (RuTE7), 2.0553(18) Å (RuTE9), and 2.019(3) (RuTE10) for the corresponding thioether complexes. In contrast to the comparison of Ru–S bond distances, the differences in Ru–C bond distances are insignificant, except for RuOTE10 and RuTE10. In aggregate, we note that these differences are the largest structural variations that we have observed within a family of closely related photochromic ruthenium sulfoxide complexes. Lastly, while we were able to serendipitously obtain high quality crystals of RuOTE10, our synthetic procedures of this compound always displayed evidence of an impurity by ^{1}H NMR, and thus we have little other analytical data of this compound.

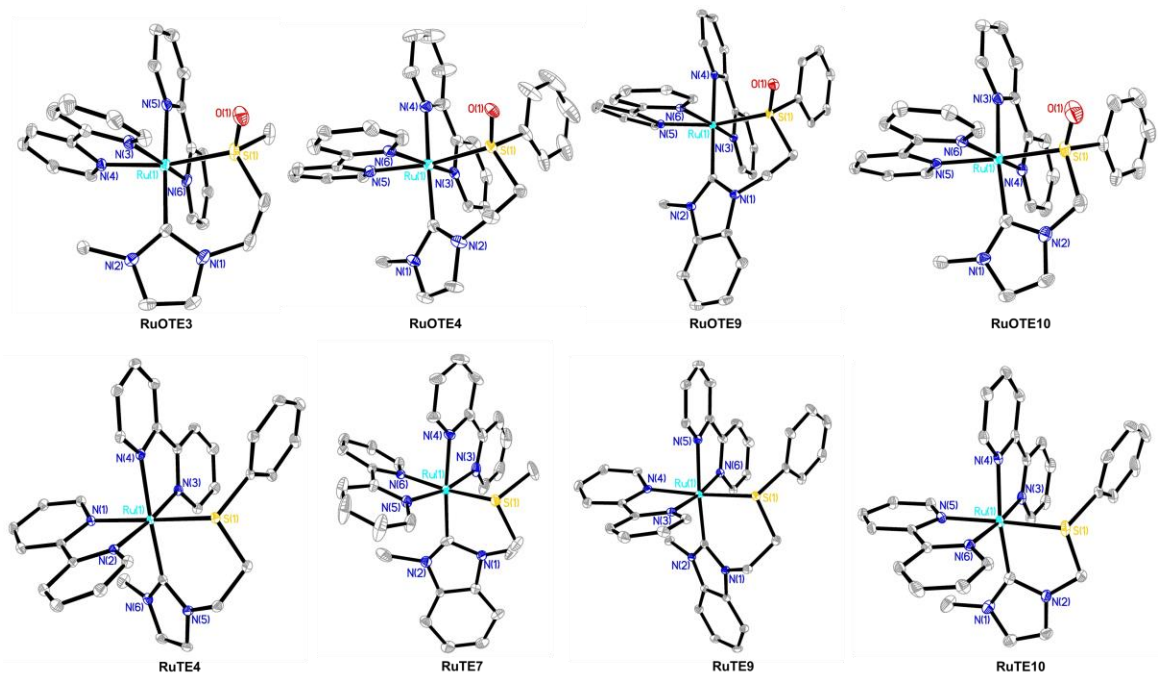

Figure 17. *X-ray crystal structures on the top row, from left to right: RuOTE3, RuOTE4, RuOTE9, RuOTE10, and bottom row, from left to right: RuTE4, RuTE7, RuTE9, and RuTE10 with 35% thermal ellipsoids. Hydrogen atoms and anions have been omitted for clarity.*

Table 3. *Selected bond lengths and angles for compounds: RuOTE3, RuOTE4, RuOTE9, RuOTE10, RuTE4, RuTE7, RuTE9, RuTE10, TE3, TE4, and TE7- TE9.*

	RuOTE3	**RuOTE4**	**RuOTE9**	**RuOTE10**
Ru–C_{NHC}	2.057(3)	2.072(5)	2.061(2)	2.043(4)
Ru–S	2.2537(10)	2.2464(11)	2.2371(5)	2.2384(11)
S=O	1.489(3)	1.476(3)	1.4842(15)	1.461(4)
S-CR R= phenyl, CH_3	1.777(4)	1.783(4)	1.785(2)	1.788(4)
S-$C_{chelate}$	1.787(4)	1.785(5)	1.789(2)	1.832(5)
CR-S-$C_{chelate}$	99.7(2)	100.4(2)	103.00(10)	103.0(2)
	RuTE4	**RuTE7**	**RuTE9**	**RuTE10**
Ru–C_{NHC}	2.065(2)	2.046(5)	2.0553(18)	2.019(3)
Ru–S	2.3330(6)	2.3480(14)	2.3437(5)	2.3179(8)
S-CR R= phenyl, CH_3	1.783(2)	1.803(7)	1.7825(18)	1.780(3)
S-$C_{chelate}$	1.812(2)	1.808(6)	1.8168(19)	1.815(4)
CR-S-$C_{chelate}$	103.46(11)	97.7(4)	103.68(9)	103.84(16)
	TE3	**TE4**	**TE7**	**TE8**
S-CR R= phenyl, CH_3	1.8027(15)	1.762(5)	1.8000(17)	1.810(2)
S-$C_{chelate}$	1.8007(12)	1.803(4)	1.8091(17)	1.802(2)
	TE9			
S-CR R= phenyl, CH_3	1.772(3), 1.779(3)			
S-$C_{chelate}$	1.801(4), 1.806(4)			

The shorter Ru–S bond observed in the sulfoxide complexes relative to the thioether complexes is consistent with the smaller size of the formally S^{IV} in the sulfoxide relative to the larger size of formally S^{II} in the thioether. However, this shorter distance is also consistent with increased π-bonding interaction between Ru and S, which is further supported by the visible spectroscopic and electrochemical data (see below). The precise origin of this stabilization is still an open question, as the structural data provide no definitive answer at this time.

UV-Visible Absorbance, Bulk Photolysis and Thermal Reversion

The electronic absorbance spectra of these complexes all feature lowest energy Ru d$\pi \rightarrow$ bpy π^* Charge Transfer (MLCT) transitions that appear at 378 nm (RuOTE3), 384 nm (RuOTE4), and 372 nm (RuOTE9). This assignment is based primarily on the molar absorptivities (~5000 M^{-1} cm^{-1}) of these complexes, and their similarity to related complexes.[7,64,92-94] These absorption maxima are well-shifted to the blue of many ruthenium polypyridine complexes.[95] We note that these maxima are blue-shifted relative to their respective ruthenium thioether counterparts, thus designating the sulfoxide as the source of dπ stabilization resulting in this shift in the absorption maximum.[64,92-94]

Irradiation of RuOTE3, RuOTE4, or RuOTE9 in acetonitrile, alcohol, halogenated or propylene carbonate solution yields dramatic changes in the absorption spectrum that are consistent with previous reports of sulfoxide isomerization on ruthenium.[6,7,39] Shown in Figure 18a are representative spectra of RuOTE9 of the photochemical transformation from the S-bonded isomer to the proposed O-bonded isomer. We find few complexes in the literature that have a similar coordination sphere for comparison, but we note that Tennyson and coworkers report an absorption maximum of 496 nm for a $[Ru(bpy)_2]^{2+}$ center with a chelating benzimidazolylidene carboxylate (C, O coordination mode).[96] Methylation of this complex yields the ester, and subsequent coordination of the ketone. In that case, the absorption maximum is observed at 454 nm. These absorption maxima are in accord with the photoproduct absorption maxima reported here of 493 nm

(RuOTE3), 490 nm (RuOTE3), and 474 nm (RuOTE9). Based on this report and other examples of sulfoxide isomerization on ruthenium bipyridine centers, we propose that the photoproduct formed upon irradiation is the O-bonded isomer.[6,7,39,64,92-94]

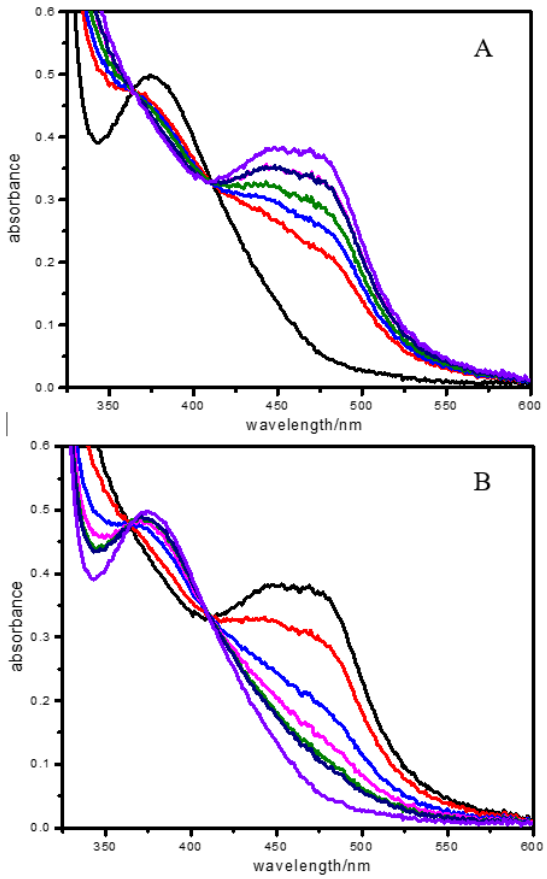

Figure 18. *A) Bulk photolysis of RuOTE9 in propylene carbonate irradiated at 405 nm (26 mW): black trace (0 seconds), red (10 seconds), blue 20 seconds), green (30 seconds), purple (40 seconds) and lilac (50 seconds). B) Thermal reversion of solution in panel A: black trace (O seconds; same as lilac trace from panel A) red trace (10 seconds), blue (12 seconds), pink (15 seconds), green (18 seconds), purple (20 seconds), lilac (25 seconds).*

The spectral changes observed upon MLCT irradiation are fully reversible in propylene carbonate (Figure 18b) and all other solutions investigated, where the original spectrum is recovered after only ~20 seconds of relaxation time at room temperature. The presence of three well-preserved isosbestic points in both sets of data indicates direct conversion between two isomers. These data are notable because they are a rare example of this transformation occurring in acetonitrile, and they show an unusually rapid reversion from the O-bonded photoproduct to the starting S-bonded isomer. Thus, the NHC moiety protects this complex from excited state photosubstitution and ground state solvolysis in acetonitrile, and presumably renders a small activation barrier on the ground state potential energy surface for O $\rightarrow$ S isomerization (Scheme 3). Moreover, the NHC group appears to facilitate the excited state S$\rightarrow$O isomerization as the quantum yields for isomerization for RuOTE3 (ΦS$\rightarrow$O = 0.87 $\pm$ 0.03), RuOTE4 (ΦS$\rightarrow$O = 0.26 $\pm$ 0.02), and RuOTE9 (ΦS$\rightarrow$O = 0.24 $\pm$ 0.02) are all suggestive of efficient transduction of photonic energy to potential energy for excited state bond-breaking and bond-making reactions. In aggregate, these data suggest that the NHC ligand promotes facile conversion between S-bonded and O-bonded potential energy surfaces in both the ground state and the excited state.

In contrast to many other ruthenium and osmium sulfoxide complexes that undergo phototriggered isomerization,[38,54,97] the ground state, thermal O $\rightarrow$ S reversion time constants (typically on the order of 10^3 – 10^5 s) for the NHC complexes here are much more rapid. Kinetic analysis of bulk photolysis data (Figure 18b) yields time constants of O $\rightarrow$ S isomerization of 20 $\pm$ 0.2 s for RuOTE3, 6 $\pm$ 0.07 s for RuOTE4, and 11 $\pm$ 0.2 s for

RuOTE9. We were able to collect the temperature dependence of these isomerization time constants to obtain activation data (Figures 179 – 181; Tables 26 – 27). Over a modest temperature range of –10 °C to 25 °C in propylene carbonate, we extract an enthalpy of activation of ($\Delta H^{\ddagger}$) of 66.0 kJ mol^{-1} K^{-1} for RuOTE3, 61.0 kJ mol^{-1} K^{-1} for RuOTE4, and 57.4 kJ mol^{-1} K^{-1} for RuOTE9. The corresponding entropies of activation ($\Delta S^{\ddagger}$) are –48.3 J mol^{-1} K^{-1} for RuOTE3, –56.3 J mol^{-1} K^{-1} for RuOTE4, and –71.3 J mol^{-1} K^{-1} for RuOTE9. Negative activation entropies indicate a more ordered transition state relative to the starting material. We interpret this to indicate that the isomerization is associative in nature, perhaps proceeding through an η^2-sulfoxide as the ligand translates from O-bonded to S-bonded.

There are a few literature reports that provide activation parameters of photoreactions that are analogous to that discussed here. While not a photoisomerization, the cyclic voltammogram of $[(H_3N)_5Ru(acetone)]^{2+}$ is consistent with an *ECEC* (*Electrochemical–Chemical Electrochemical–Chemical*) mechanism in which the acetone exhibits η^2-bonding (side-on) for Ru^{2+} and η^1-bonding for Ru^{3+}.[98] The activation entropy for the η^2-acetone $\rightarrow$ η^1-acetone isomerization following oxidation of Ru^{2+} to Ru^{3+} is –91 J mol^{-1} K^{-1}, and the activation entropy for η^1-acetone $\rightarrow$ η^2-acetone following reduction of Ru^{3+} to Ru^{2+} is –10 J mol^{-1} K^{-1}. No photochemical study of this system exists, but the values obtained for the formation of the ground state η^2-acetone isomer is analogous to the O$\rightarrow$S isomerization in sulfoxides. Moreover, Schultz has investigated furan and pyran isomerizations (η^1-bonding through oxygen to and from η^2-bonding of

double bond) on $M(CO)_5$ centers (M = Cr, Mo, W). For $Mo(CO)_5$(2,3-dihydrofuran), $\Delta S^{\ddagger}$ = –2.6 J mol^{-1} K^{-1} for the $\eta^1 \rightarrow \eta^2$ isomerization.[99-101] Small negative activation entropies seems to be a general result for these types of reactions, and they suggest that the metal center "walks" around the periphery of the furan to coordinate the double bond following visible excitation. Similarly, Burkey and co-workers interpret the observed activation parameters for an intramolecular pyridine for ketone exchange as evidence that the ligand does not fully dissociate from the metal (a derivatized CpMn center), and that it is loosely bound as it migrates from the nitrogen (pyridine) to oxygen (ketone).[102] In conjunction with our data reported here, we interpret the activation entropy for these thermal isomerization reactions to be consistent with an isomerization pathway in which the sulfoxide simply "slides" from oxygen to sulfur, presumably going through an η^2 sulfoxide as an intermediate or transition state that is effectively 7-coordinate.

Transient Absorption Spectroscopy

We employed ultrafast transient absorption spectroscopy to reveal additional details of the excited state isomerization (See Chapter 2 for instrumental details). Shown in Figure 19 top are the steady state spectra of S- (blue) and O-bonded (red) isomers of RuOTE9 obtained from bulk photolysis (extracted from Figure 18), as well as the O-bonded – S-bonded difference spectrum (black). Shown in Figure 19 middle are the early transient spectra collected at pump-probe time delays ranging from 0.5 ps to 20 ps. The first transient shown at 0.5 ps features a broad excited state absorption assigned to bpy $p\pi \rightarrow$ Ru(III) $d\pi$ charge transfer transition at wavelengths longer than ~425 nm, and an

intense peak near 390 nm ascribed to bpy $\pi^* \rightarrow \pi^*$ interligand transition. These transitions are prototypical for $[Ru(bpy)_3]^{2+}$–type chromophores, and are commonly found in many isomerizable ruthenium sulfoxide complexes. Also present is a shallow bleach feature at ~400 nm. As the pump–probe time delay increases to 20 ps, the 390 nm transition appears to lose intensity and shift to the blue. These dynamics are accompanied by the appearance of an intense ground state bleach feature that shifts to the blue. The ground state bleach feature in the 20 ps transient matches well with the ground state absorption. From 20 ps to 2000 ps, the absorption in the red decreases to zero, a new absorption maximum emerges at 485 nm, and an isosbestic point develops at 505 nm. There is very good agreement between the transient spectrum collected at 500 ps (orange trace, Figure 19 bottom) and 5 ns (red trace) with the difference spectrum obtained from bulk photolysis (black trace, Figure 19 top). These data indicate that the spectral changes observed in the bulk photolysis are accurately captured in the transient spectra, and that these changes are complete on a subnanosecond timescale.

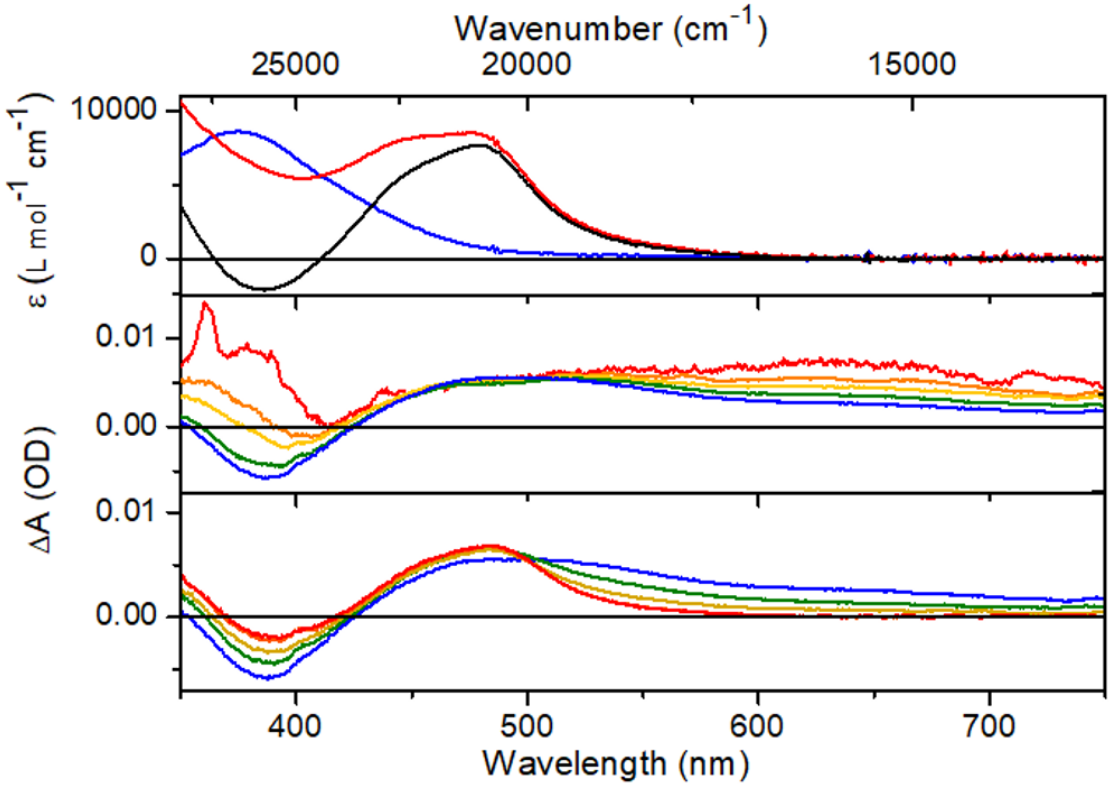

Figure 19.*Top. Steady state spectra of S-RuOTE9 (blue), O-RuOTE9 (red), and the difference (black; O – S; red trace–blue trace) in propylene carbonate solution. Middle. Early transient spectra collected at different pump-probe time delays: red (0.5 ps), orange (1.3 ps), yellow (2.0 ps), green (5.0 ps), and blue (20 ps). Bottom. Late transient spectra collected at different pump-probe time delays: blue (20 ps), green (100 ps), yellow (200 ps), orange (500 ps), and red (2000 ps). Excitation wavelength, 405 nm.*

Close inspection of the 0.5 to 20 ps data (Figure 19 middle) between 350 and 400 nm shows relatively slow formation of ^{3}MLCT state. There are typically two spectroscopic features detected at this wavelength: the bleach associated with loss of the ground state (red trace, Figure 19 top), and the excited state absorption associated with the reduced bipyridine. During this time interval, the traces and bleach minimum shifts to the blue

ultimately yielding a stationary spectrum at 20 ps, with a minimum at 385 nm. While there are (at least) two contributions to the signal in this region, the data strongly indicate slow formation of the excited state in comparison to other ruthenium sulfoxide complexes. The absence of an absorption in this region may suggest that the LF (or Metal-Centered, MC) states are lowest in energy, or that simply the change in absorptivity due to loss of the ground state is greater the absorptivity of the reduced bipyridine. There is yet a third possibility that involves excited state absorptions due to the benzimidazole carbene ligand. We can investigate this third possibility directly by examining the ultrafast spectroscopy of a related compound that does not contain a benzimidazole in the chelating sulfoxide ligand.

Shown in Figure 20 are the ultrafast data for the RuOTE4 compound (structure depicted in Figure 17) in propylene carbonate, which contains an imidazole-based carbene. Similar to Figure 19, Figure 20 top displays the ground state S-bonded (blue), and the O-bonded (red) spectra obtained from the bulk photolysis data, as well as O – S spectrum (black). The first trace obtained with a pump-probe time delay of 0.73 ps (Figure 20 middle) shows the prototypical long wavelength unreduced bpy $\rightarrow$ Ru^{III} LMCT excited state absorption, as well as the bpy $\pi^* \rightarrow \pi^*$ indicative of a ^{3}MLCT excited state. As time evolves from 0.7 ps to 20 ps, the excited state absorption near 375 nm shifts to the blue, loses intensity, and appears to narrow, consistent with vibrational cooling. Isosbestic points emerge at wavelengths of 520 and 450 nm. Also during this same time interval, the MLCT bleach becomes more intense (negative) and shifts to the blue. Similar to RuOTE9, these data again suggest slow formation of a ^{3}MLCT, though the presence of isosbestic

points may suggest an internal conversion process. At longer time delays (20 ps to 3700 ps), the absorption in the red decreases to zero, a new absorption maximum arises near 490 nm, the bleach at 400 nm becomes less intense, and the tail of an absorption peak from 350 to ~380 persists. Importantly, the excited state absorption near 375 nm persists throughout the duration of the experiment, indicating that a ^{3}MLCT is lowest in energy, or at least thermally accessible from a LF state. Recall, the excited state absorption in this region is assigned to a $\pi^* \rightarrow \pi^*$ intraligand bipyridine centered electronic transition. In comparison to RuOTE9, the presence of this excited state may seem puzzling. However, we note that the molar absorptivity (8556 M^{-1} cm^{-1}) at 375 nm (λ_{max}) for RuOTE9 is significantly higher than that of RuOTE4 (molar absorptivity of 5058 M^{-1} cm^{-1} at 384 nm (λ_{max})). Lastly, isosbestic points develop at ~380 nm, ~430 nm, and ~530 nm indicating direct conversion from a ^{3}MLCT excited state to a singlet ground state. Given the similarity between the ground state difference spectrum (green trace, Figure 20 top) and the 3720 ps transient (red trace, Figure 20 bottom), we assign this transient to the O-bonded ground state.

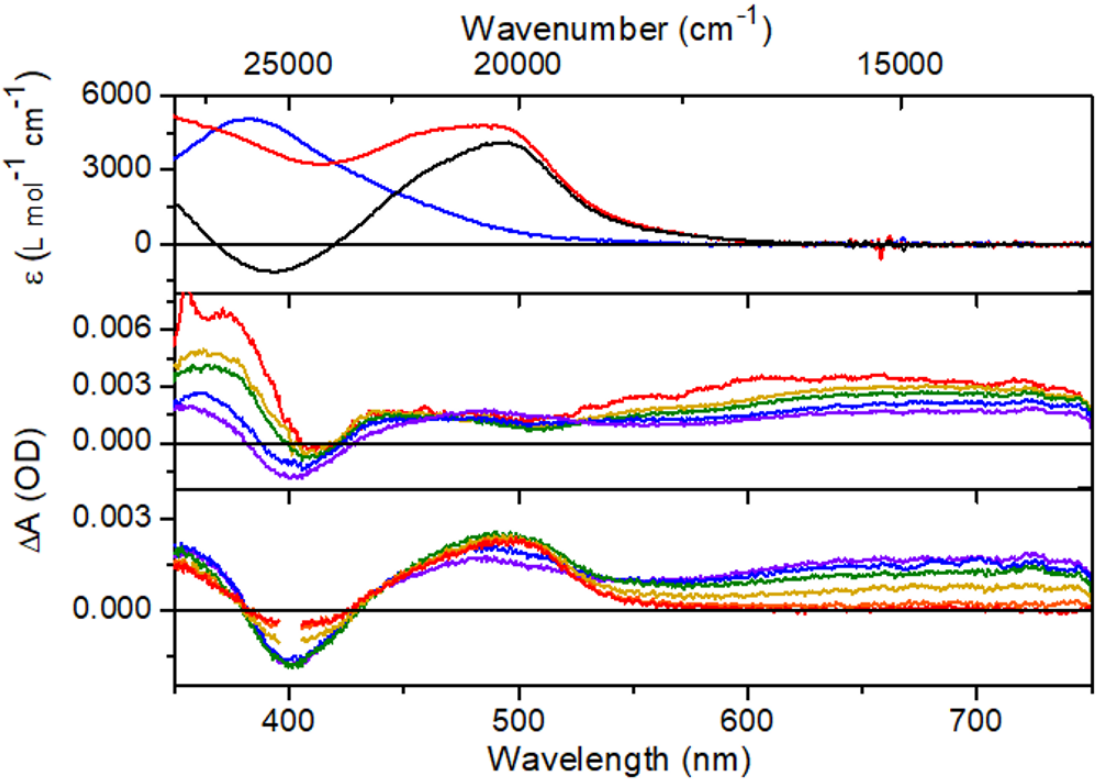

Figure 20. *Top. Steady state spectra of S-RuOTE4 (blue), O-RuOTE4 (red), and the difference spectrum (black; O – S; red trace–blue trace) in propylene carbonate solution. Middle. Early transient spectra collected at different pump-probe time delays: red (0.7 ps), yellow (1.5 ps), green (2.0 ps), blue (6 ps) and purple (20 ps). Bottom. Late transient spectra collected at different pump-probe time delays: purple (20 ps), blue (30 ps), green (100 ps), yellow (501 ps), orange (1790 ps), and red (3720 ps). Excitation wavelength, 405 nm.*

Kinetic analysis of the spectral changes of RuOTE9 and RuOTE4 was achieved by a combination of single wavelength kinetics and global fitting (See Tables 28 and 29) for all complexes in multiple solvents. For RuOTE9, time constants of $\tau_1 = 0.55 \pm 0.1$ ps, $\tau_2 = 3.85 \pm 1.3$ ps, and $\tau_3 = 137 \pm 13$ ps were retrieved from our procedure. We also observe a 16.4

$\pm$ 4.3 ps time constant from wavelengths near the O-bonded maximum and from the S-bonded bleach region. It is not found in the red portion of the spectrum. Importantly, its inclusion in the global fitting is also necessary for a quality fit. For RuOTE4, the time constants are τ_1 = 0.2 $\pm$ 0.1 ps, τ_2 = 5.36 $\pm$ 1.2 ps, and τ_3 = 490 $\pm$ 78 ps, and similar to RuOTE9, we identify a time constant of 25.2 $\pm$ 8.8 ps in the region near the O-bonded maximum.

We assign the longest time constant (τ_3) to excited state relaxation to form both S-bonded and O-bonded ground states. In combination with the quantum yield ($\Phi_{S\rightarrow O}$ = $k_{S\rightarrow O}/(k_{S\rightarrow O} + k_r + k_{nr})$), this yields a time constant of isomerization, $\tau_{S\rightarrow O}$, (= $1/k_{S\rightarrow O}$) of 570 ps for RuOTE9, $\tau_{S\rightarrow O}$ of 1.9 ns for RuOTE4, and $\tau_{S\rightarrow O}$ of 895 ps for RuOTE3 in acetonitrile. We assign the single picosecond time constant (τ_2) to formation of the S-bonded ^{3}MLCT excited state for isomerization, which follows intersystem crossing from the ^{1}MLCT that is known to occur in approximately 40 fs.[103,104] This kinetic phase represents an internal conversion within the ^{3}CT manifold through the emergence of well-formed isosbestic points in the spectra, which are readily observed for RuOTE4 (Figure 20, middle). They are less apparent in the transient spectra of RuOTE9 (Figure 19, middle). This assignment is further supported by the presence of the unreduced bpy $\rightarrow$ Ru^{III} LMCT absorption in the red portion of the spectrum as well as the excited state absorption near 390. Moreover, the blue-shifting of the MLCT bleach and of the excited state absorption support this assignment. Lastly, we propose that the 16.4 ps time constant is attributed to a combination of intramolecular vibrational relaxation and solvent dynamics. We continue

to investigate these dynamics in related complexes and hope to have a more definitive understanding of these dynamics in the future.

Kender and Turro have also observed slow internal conversion kinetics in their study of related ruthenium polypyridine NHC complexes.[86] They proposed the presence of two distinct triplet excited states, the lower energy of which is assigned to metal/ligand-to-ligand charge transfer (ML-LCT). Indeed, for a range of five complexes with different groups located on the chelating NHC ligand, internal conversion from the higher lying triplet to the ^{3}ML-LCT takes place with time constants ranging from 7-22 ps, which are similar in magnitude to our τ_2 values reported here. We see no compelling motivation to assign the 25.2 ps (RuOTE4) or 16.4 ps (RUOTE9) time constants to this internal conversion process. Our chelating sulfoxide NHC ligands imidazole or benzimadizole are unlikely to exhibit electronic transitions at similar energy, and these are both unlikely to occur at similar energies reported by Turro for derivatized phenyl-imidazole. Lastly, we only observe this contribution at wavelengths corresponding to the formation of the ground state isomer, suggesting it does not correspond to an event prior to isomerization.

Electrochemistry

We employed cyclic voltammetry and square wave voltammetry to reveal the S- and O-bonded couples, ligand couples, and rates of isomerization (see Figures 175 – 178, Table 25). The data are found in Table 4, as well as the reduction potentials reported by Tennyson for his benzimidazolylidene carboxylate and benzimidazolylidene ester mentioned above in the absorption discussion. The voltammograms are consistent with an *ECEC* mechanism in which S→O isomerization is prompted by Ru^{2+} oxidation to form

Ru^{3+}, and O→S isomerization follows reduction of Ru^{3+} to yield Ru^{2+}. Accordingly, the appearance of the cyclic voltammogram is dependent upon the scan rate, rates of isomerization and the scan window. Our procedure for precise extraction of the reduction potentials and the isomerization rate constants have been described elsewhere.[65] Following this analysis, the S-bonded couples are 1.2 V (RuOTE3), 1.1 V (RuOTE4), and 1.7 V (RuOTE9), while the O-bonded couples are 0.67 V (RuOTE3), 0.62 V (RuOTE4), and 1.14 V (RuOTE9). For comparison, Tennyson reports reduction potentials of 0.45 V for the benzimidazolylidene carboxylate complex and then 0.82 V for the benzimidazolylidene ester, where the ketone binds directly to ruthenium (both couples are reported vs a silver wire quasi-reference electrode).[96] Lastly, we see two reversible couples representing $bpy^{0/-}$ and $bpy^{-/2-}$ at –1.65 V and ~ –1.8 V in accord with other ruthenium polypyridine complexes,[95] and those comprising an NHC ligand.[86]

Table 4. *Reduction potentials and rate constants of isomerization for RuTE3, RuOTE3, RuTE4, RuOTE4, RuTE9, and RuOTE9.*[a]

	$E^{o'}_{Ru3+/2+}$ (V ± 0.01)			E^{o} (V ± 0.01)		Rate constant(s^{-1})	
Complexes	$E_S^{o'}$	$E_O^{o'}$	$E^{o'}$	$bpy^{0/-1}$	$bpy^{-1/-2}$	$k_{S\rightarrow O}$	$k_{O\rightarrow S}$
RuTE3			+0.84	-1.68	-1.85		
RuOTE3	+1.09	+0.61		-1.60	-1.84	0.18 ± 0.002	1.57 ± 0.02
RuTE4			+0.87	-1.69	-1.94		
RuOTE4	+1.12	+0.65		-1.63	-1.85	0.89 ± 0.01	1.01 ± 0.04
RuTE9			+0.97	-1.65	-1.91		
RuOTE9	+1.24	+0.71		-1.63	-1.85	0.86 ± 0.01	2.97 ± 0.03

a. All data collected in propylene carbonate with 0.1 M n-tetrabutylammonion hexafluorophosphate electrolyte. See SI for experimental details.

Our analysis of the voltammograms reveals the S $\rightarrow$ O isomerization rates constants on Ru^{3+} and O $\rightarrow$ S isomerization rates constants on Ru^{2+}. The S $\rightarrow$ O rate constants of isomerization on Ru^{3+} are $0.18 \pm 0.01\ s^{-1}$ (RuOTE3), $0.89 \pm 0.01\ s^{-1}$ (RuOTE4), and $0.86 \pm 0.01\ s^{-1}$ (RuOTE9). In comparison to other ruthenium polypyridine sulfoxide complexes that feature isomerization following oxidation, these rates are remarkably *slower*, where rate constants on the order of $100\ s^{-1}$ are common.[54,97] In contrast, the O $\rightarrow$ S rate constants of isomerization on Ru^{2+} are $1.57 \pm 0.02\ s^{-1}$ (RuOTE3), $1.01 \pm 0.04\ s^{-1}$ (RuOTE4), and $2.97 \pm 0.01\ s^{-1}$ (RuOTE9), and are among the fastest that we have observed.

Conclusion

We have reported a new class of chelating thioether and sulfoxide ligands comprising an N-Heterocyclic Carbene (NHC) donor. Our results show that these ligands support sulfoxide isomerization on ruthenium polypyridine centers. The ultrafast transient absorption spectroscopy reveals a complicated excited state dynamic behavior and suggests the presence of NHC-based states are involved. Isomerization of the sulfoxide is both rapid, with time constants of isomerization ranging from 570 ps to 1.9 ns, and efficient, with quantum yields of isomerization ranging from 0.24 to 0.87. Activation parameters for the ground state O→S thermal reversion reaction to reform the ground state suggest that the sulfoxide simply "slides" along the S–O bond, in a manner similar to other linkage isomerizations on electron rich metal centers. Lastly, we note that the anionic nature does impart a resistance to photosubstitution in strong donor solvents such as acetonitrile and appears to make fundamental changes to the activation barriers on the Ru^{3+} and Ru^{2+} ground state surfaces. This effect results in unusually fast O→S isomerization on Ru^{2+} and unusually slow S→O isomerization on Ru^{2+}. Our future studies will attempt to reveal and understand the role of the carbene in this isomerization, which may be of importance to others in their preparation of photoactive complexes containing this functional group.

CHAPTER 4

Investigating the Ultrafast Dynamics of Pyrene Sulfoxide and Pyrene Thioether Compounds

Abstract

A group of pyrene thioether and pyrene sulfoxide compounds was synthesized and investigated by UV-Vis, emission, ultrafast transient absorption, and nanosecond flash photolysis spectroscopies. Steady state data reveal characteristic pyrene absorption and emission spectra, though they are broadened and red-shifted. Ultrafast transient absorption spectra of these compounds are similar to pyrene at short pump-probe time delays, with an S_2 ESA in the red portion of the spectrum that rapidly (~100 fs) decays and gives rise to two S_1 absorption bands. From there, however, the compounds feature the formation of a third excited state, attributed to a T_1 state, that grows in over several hundred picoseconds. The rates of formation of the S_1 state and the T_1 state both exhibit a dependence on the dielectric constant of the solvent and the viscosity of the solvent. We propose that T_1 is rapidly formed after S_1 enters a twisted intramolecular charge transfer regime in which a pyrene radical anion and sulfur radical cation are twisted out of conjugation with one-another. Transient absorption data of pyrene sulfoxides bearing *para*-substituted phenyl groups exhibit a 10-fold difference in the lifetime of S_1 that is varies with the electronegativity of the *para*-substituent. In this case, electron-donating groups stabilize the formation of the TICT state while electron withdrawing grounds destabilize the formation of the TICT state.

Introduction

Chirality is a central concept bridging all areas of molecular science that distinguish geometric structures that are otherwise identical, but that can exhibit dramatically different reactivity. This is readily observed for *D*- and *L*-amino acids, where the *L* enantiomers are produced in cells, but the *D* isomers are not.[105,106] Amines, phosphines, and sulfoxides can be chiral, whereby the central atom has three bound atoms and a lone pair of electrons in a trigonal pyramidal molecular geometry. The enantiomers of amines are not isolable, as they rapidly racemize at room temperature through an inversion reaction.[107] Sulfoxide compounds, on the other hand, are stereochemically stable at room temperature due to a high barrier to the ground state inversion reaction of nearly 40 kcal mol^{-1} (1.3 eV).[108] This property makes sulfoxide compounds useful in chiral chemistry, especially as auxiliaries in chiral synthesis.[109,110]

Photostereomutation is a phototriggered molecular rearrangement pathway that converts one stereoisomer to the other. This pathway in sulfoxides was first reported to occur in 1960's through a series of mechanistic studies by Mislow and Hammond.[111-114] They posited a direct inversion pathway is operable in the excited state, but S-C α-cleavage reactions also racemize enantiomerically pure sulfoxide compounds (in addition to producing other photoproducts).[115-119] In 2001, Jenks established the existence of an excited state, non-radical pathway for photostereomutation in alkyl-aryl sulfoxides.[120] His work, along with the work of Tsurutani, has also established that photochemical inversion of sulfoxides occurs from a singlet excited state, has temperature-dependent quantum

yield, and can take place in PMMA films, among other discoveries.[108,121,122] Most recently, Finney noted the prominence of "dark" excited states in the deactivation of a class of pyrenyl-phenyl sulfoxides bearing substitutions at the *para*-position of the phenyl group.[123,124] Using time-resolved emission spectroscopy, he reported that the S_1 excited state decays one order of magnitude faster when the *para*-substituent is electron-donating $–OCH_3$ instead of electron-withdrawing $–CF_3$. He attributed the difference to a lowered energy barrier to pyramidal inversion in the excited state for $–OCH_3$. To date, there have been no transient absorption studies on alkyl-aryl or diaryl sulfoxide compounds, and thus the nature of the dominant, non-emissive relaxation pathway has not been properly addressed.

Herein, we present the first broadband femtosecond pump-probe and nanosecond flash photolysis studies on a group of pyrene sulfoxide and pyrene thioether compounds. Transient absorption spectroscopy provides access to previously hidden, non-emissive excited states that are critical in the photophysical dynamics of this system. The role of solvent is addressed with respect to excited state features of pyrenyl-methyl sulfoxide, including transition energies and lifetimes. Further, we make extensive comparisons between a group of diaryl sulfoxides and diaryl thioethers that ultimately allow us to delineate an excited state potential energy surface for this group of compounds. We suggest that the formation of a twisted intramolecular charge transfer (TICT) state within several hundred picoseconds results in rapid intersystem crossing to a long-lived triplet regime. The energy barrier to the TICT state is regulated by the electron donating or electron withdrawing nature of the substituents on the sulfoxide moiety.

Results and Discussion

As noted above, Finney and coworkers recently reported the results of their study of inversion and emission behavior for a class of pyrenyl-phenyl sulfoxide compounds. We have prepared the same derivatives by a slightly different work-up process, but still in appreciable yield. We also synthesized pyrenyl-methyl sulfoxide. Naturally, we prepared the corresponding thioether (or sulfanyl) derivatives. The thioether compounds were obtained by lithiating 1-bromopyrene with *n*-BuLi and quenching with appropriate *p*-phenyl disulfide or methyl disulfide. Oxidizing thioether compounds with *m*-CPBA afforded the corresponding sulfoxide. Chromatographic purification was obviated when pure compounds were obtained by precipitating and triturating the crude product. Detailed experimental and synthetic steps can be found in Appendix B, complete with ^{1}H NMR spectra (Figures 201-211). Bond-line drawings of the thioether and sulfoxide structures are shown in Figure 21, and the structures will be addressed in this paper by the designations provided there. These structures were chosen because of their disparate excited state behavior. The diaryl sulfoxides have an emissive excited state whose lifetime varies by one order of magnitude between PySOPhOCH$_3$ and PySOPhCF$_3$,[124] while PySOMe is reported to have a quantum yield of photoinversion that is nearly one order of magnitude higher than PySOPhH.[108,121] Additionally, it is useful to compare excited state lifetimes of the thioethers and the corresponding sulfoxides to gauge the impact of pyramidal inversion on excited state deactivation.

Figure 21. *Bond line drawings of the thioether and sulfoxide structures investigated in this study.*

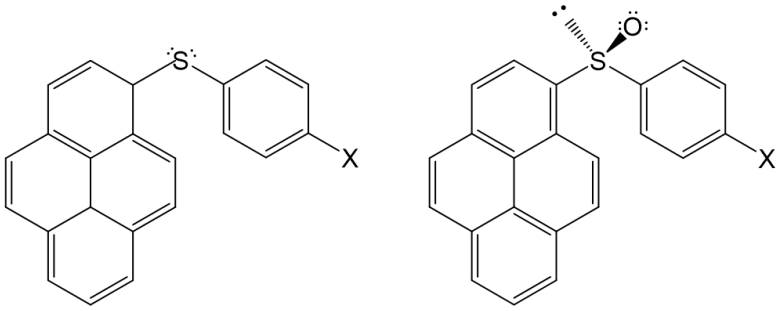

PySPhX PySOPhX

X = H, OCH_3, CF_3

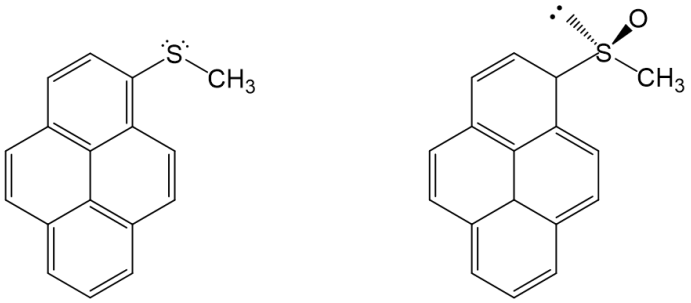

PySMe PySOMe

Steady State Spectra

The UV-Vis spectra for pyrene and the pyrene sulfoxides are shown in Figure 22, while the pyrene thioethers are shown in Figure 212. Relevant steady-state absorption and emission data for each compound are listed in Table 5. Overall, the thioether and sulfoxide compounds feature the characteristic shape and vibronic structure of pyrene absorption. However, the $S_0 \rightarrow S_2$ absorption maxima are significantly red-shifted relative to pyrene (~1,500 cm^{-1}), demonstrating that the presence of a thioether or sulfoxide leads to significant modification of the electronic structure of the compound. Moreover, the

electronic absorption bands of the derivatized compounds, especially the thioethers, are spectrally broadened with respect to the parent pyrene. This is likely due to increased conformational flexibility imparted by the substituents. Similar trends have been noted in other bichromophoric compounds containing pyrene.[125,126]

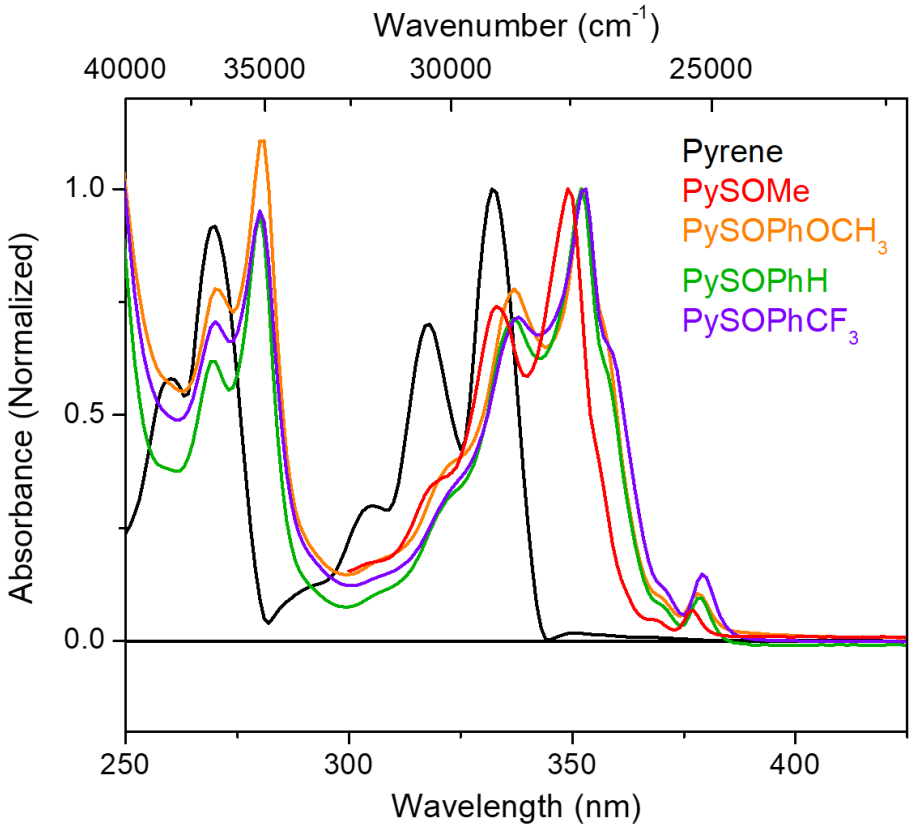

Figure 22. *UV-Vis spectra of pyrene (black), PySOMe (red), PySOPhOCH₃ (orange), PySOPhH (green), and PySOPhCF₃ (violet) in acetonitrile.*

Table 5. *Relevant absorption and emission data of pyrene compounds dissolved in acetonitrile.*

Compound	λ_{Abs} (nm)	λ_{Em} (nm)	Abs – Em (cm^{-1})	Φ_{Em}
Pyrene	333	370	2913	0.72
PySPhH	350	393	3126	0.065
PySOPhH	352	380	2093	0.033
PySPhOCH3	350	398	3445	0.017
PySOPhOCH3	352	380	2039	0.007
PySPhCF3	350	389	2864	0.114
PySOPhCF3	353	381	2082	0.094
PySMe	350	396	3318	0.482
PySOMe	349	377	2128	0.03

The emission spectra are also red-shifted in the derivatized pyrene compounds (Table 5). Analyzing the differences in the absorbance and the emission maxima for these compounds provides an interesting result. The sulfoxides feature an energy difference that is ~1,200 cm^{-1} less than the corresponding thioethers. We interpret that the emissive states of the sulfoxides feature smaller changes to their molecular geometries relative to the ground states than the thioether compounds. This assignment is bolstered by the broadened absorbance spectra of the thioethers relative to the sulfoxides.

The emission quantum yields of the thioether and sulfoxide compounds were obtained experimentally and are listed in Table 5. The sulfoxide quantum yields are similar to those reported by Finney,[124] though ours are slightly higher. Importantly, the same trend emerges from this data; the emission quantum yield of $PySOPhOCH_3$ is 0.68%, roughly an order of magnitude lower than the emission quantum yield of $PySOPhCF_3$,

which is 9.43%. This trend is notable, but we also point out that the thioether compounds exhibit the same trend in emission quantum yield based on the phenyl substituent, where $PySPhOCH_3$ features 1.66% and $PySPhCF_3$ features 11.38%. While electron donating groups account for considerably reduced emission quantum yields compared to electron withdrawing groups, we cannot argue that sulfoxide inversion is the reason. In fact, the reduction in emission quantum yield from a thioether to its corresponding sulfoxide is approximately equal to a compound's pyramidal inversion quantum yield (PySOPhH has Φ_{Inv} ~2% and PySOMe has Φ_{Inv} ~36%).[108,121] Thus, we assert that photoinversion competes with fluorescence in the S_1 state, but that the electronic nature of the thioether or sulfoxide substituent plays a role elsewhere on the excited state potential energy surface.

Transient Absorption of PySOMe and PySMe

The electronic structure and photophysical properties of pyrene are well-documented,[127-134] and it has found many practical uses throughout literature.[124,135-137] Due to similarities in the excited state dynamics of pyrene thioethers, pyrene sulfoxides, and pyrene, we will begin our discussion of transient absorption with pyrene. Our independent studies of pyrene (Figure 23) are in accord with literature precedent. Excitation at 335 nm prompts $S_0 \rightarrow S_2$ formation, followed by rapid internal conversion to S_1 on a sub-picosecond timescale (τ = 75-150 fs).[128] Vibrational cooling within the S_1 state proceeds with a time constant of about 4 ps. The S_1 excited state lifetime of pyrene in solution is 338 ns.[108] In pyrene, S_2 is characterized by an excited state absorption at 581

nm, whereas S_1 features distinct absorptions at 363 nm and at 465 nm. The excited state absorption bands of pyrene in solution are narrow, featuring Lorentzian line shapes for the $S_2 \rightarrow S_n$ transition and for the high-energy $S_1 \rightarrow S_n$ transition. The low-energy S_1 excited state absorption band is a convolution of several transitions.[128]

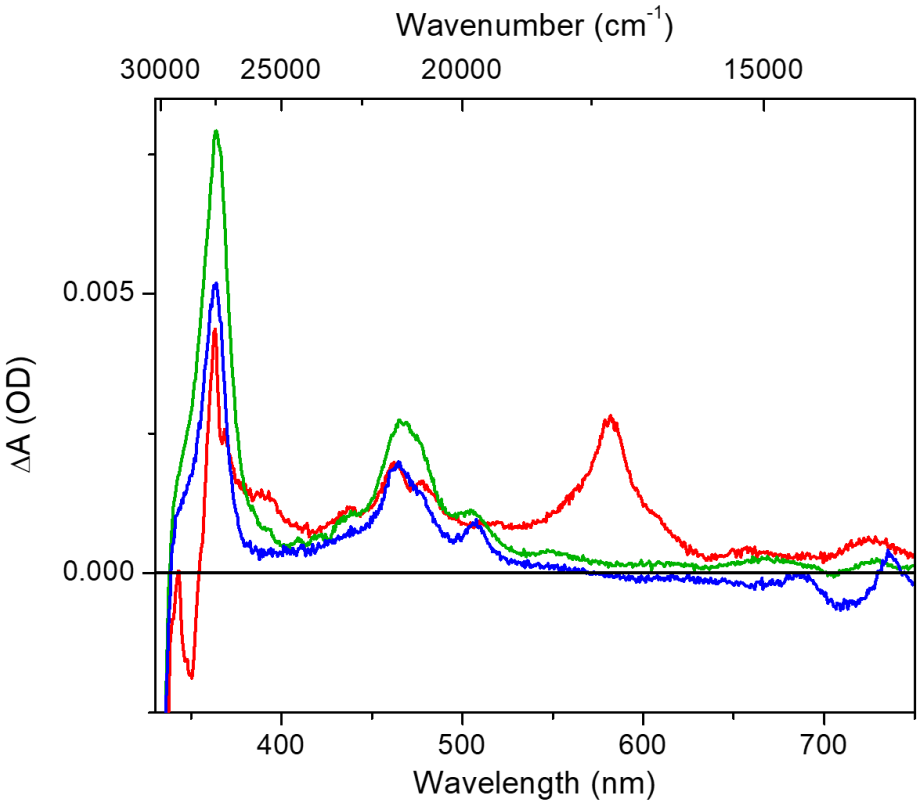

Figure 23. *Pump-probe spectra of pyrene at 225 fs (red), 1.2 ps (green), and 1 ns (blue) time-delays in acetonitrile.*

The transient absorption spectra of the pyrene thioether and pyrene sulfoxide compounds were investigated using ultrafast pump-probe spectroscopy and nanosecond flash photolysis. We will begin our discussion with PySOMe and PySMe below. The spectra of both compounds are depicted as stack-plots, with the ground state absorption and emission spectra presented in the top plot (A). Further down (B-D), the time-resolved

spectra are grouped according to the transient time-delay to show discrete spectral changes as time evolves. In-depth kinetic fitting analysis for every compound can be found in Appendix B.

The transient absorption spectra of PySOMe are displayed in Figure 24b-d. The compound was irradiated at 350 nm to prompt formation of the S_2 excited state. We attribute the negative feature from 330 nm to 355 nm to a ground state bleach since its shape mirrors the ground state absorption spectrum (Figure 24a). At short pump-probe time delays (Figure 24b; 220 fs – 50 ps), a prominent $S_2 \rightarrow S_n$ transition at 575 nm decays on a sub-picosecond timescale. This absorption band is broad, featuring a Gaussian shape as opposed to the Lorentzian shape of the same band in pyrene. Introduction of the methyl sulfoxide unit on pyrene reduces the molecular symmetry from D_{2h} to C_1 and relaxes the selection rules for vibronic coupling. While the S_2 state decays, $S_1 \rightarrow S_n$ transitions grow in at 377 nm and 482 nm. An isosbestic point at 522 nm indicates direct conversion of S_2 to S_1. By 50 ps (green trace), a thermally relaxed S_1 state appears to be formed. Interestingly, there is a low-intensity excited state absorption extending throughout the red portion of the spectrum that persists despite the disappearance of the $S_2 \rightarrow S_n$ transition in that region. Two time-components are required to fit the early transient absorption data. The first time constant (τ_1 = 110 fs) is attributed to rapid internal conversion from S_2 to S_1, matching well with literature values for pyrene and bichromophoric pyrene compounds.[125-128] The second time constant (τ_2 = 4.82 ps) tracks solvent reorganization and vibrational cooling in the S_1 state. Subtle blue-shifts in the S_1 peaks as time evolves support this claim. The formation of intramolecular charge transfer

(ICT) states have been proposed as prerequisites for photoinduced pyramidal inversion in aryl sulfoxide systems, in which electron density at the sulfur is transferred to pyrene in the singlet excited state.[124] We propose that ICT takes place during this second time component since pyramidal inversion is a singlet excited state event. At intermediate pump-probe time delays (Figure 24c; 50 ps – 5 ns), we observe the emergence of isosbestic points at 387 nm, 447 nm, and 517 nm. The S_1 transitions centered at 377 nm and 482 nm decay, concomitant with the rise of a peak at 414 nm. The spectral trace at 5 ns (black) persists for the remainder of the experiment and matches the first spectrum from flash photolysis. The time-component required to fit the intermediate pump-probe data (τ_3 = 1024 ps) represents the S_1 excited state lifetime, which decays to the ground state via fluorescence and pyramidal inversion and converts to T_1 via intersystem crossing. Triplet excited states are not prominent in the transient absorption of pyrene, so efficient intersystem crossing is a result of the appended methyl sulfoxide moiety. In nanosecond flash photolysis (Figure 24d; 30 ns – 50 μs), the excited state absorption collapses to zero along with the ground state bleach. An isosbestic point at 359 nm indicates a direct conversion between two states. We ascribe the final time-component (τ_4 = 18.3 μs) to ground state recovery; $T_1 \rightarrow S_0$.

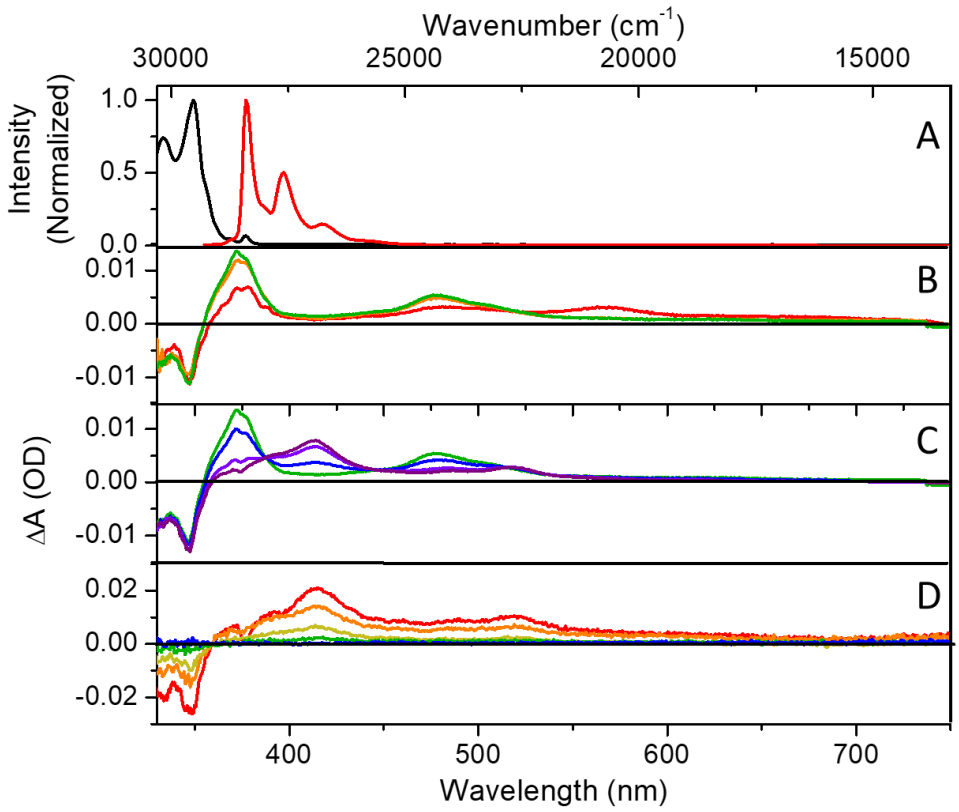

Figure 24. Spectra of PySOMe in Acetonitrile. (A) Absorbance (black) and emission (red) spectra. (B) Pump-probe transients collected at 220 fs (red), 2 ps (orange), and 50 ps (green). (C) Pump-probe transients collected at 50 ps (green), 500 ps (blue), 2 ns (violet), and 5 ns (purple). (D) Flash photolysis transients collected at 30 ns (red), 5 μs (orange), 10 μs (yellow), 20 μs (green), and 50 μs (blue).

Our assignment of the final excited state as a triplet is reasonable based on its long lifetime and is fortified by singlet oxygen emission experiments that we conducted based on previous literature.[138-140] We compared the lifetime of samples that were sparged with N_2 to those that were not. When a sample is not sparged prior to the experiment, dissolved molecular oxygen present in solution can quench triplet excited states through a bimolecular reaction. If this occurs, the measured triplet state lifetime will diminish.

When flash photolysis data is collected on an unsparged solution of PySOMe, the excited state lifetime is shortened to 258 ns. Shortening of the excited state lifetime by oxygen-quenching occurs in every pyrene thioether and sulfoxide compound that we analyzed, with kinetics listed in Appendix B. To confirm that triplet quenching by oxygen is operative in these compounds, we conducted experiments to probe $^1O_2$ emission in irradiated, unsparged samples of pyrene thioether and pyrene sulfoxides (Figure 213). In accord with flash photolysis lifetime experiments, we recorded $^1O_2$ emission resulting from triplet quenching of excited state pyrene compounds.

The transient absorption spectra of PySMe (Figure 25b-d) display similar dynamics to those of PySOMe. For femtosecond pump-probe measurements, the sample was pumped at 350 nm to excite the $S_0 \rightarrow S_2$ transition. At early pump-probe time delays (Figure 25b; 300 fs – 50 ps), we see the decay of the S_2 state and the rise of a thermalized S_1 state. The $S_2 \rightarrow S_n$ excited state absorption is not as prominent in the thioether as it is in the sulfoxide, a trend that holds for every pyrene thioether/sulfoxide pair that we investigated (See Appendix B). The S_2 state decays on a sub-picosecond timescale to reveal an S_1 excited state with absorption peaks centered at 383 nm and 568 nm. Both peaks are broadened relative to the transient absorption of pyrene, and the low energy peak at 568 nm is significantly red-shifted. Two time-components are required to fit the early temporal window. The first time constant (τ_1 = 0.23 ps) tracks internal conversion from S_2 to S_1. The second time constant (τ_2 = 7.56 ps) is attributed to solvent reorganization, vibrational cooling, and ICT from sulfur to pyrene. These assignments are the same as those made for PySOMe. At intermediate pump-probe time delays (Figure

25c; 50 ps – 5 ns), the transient absorption peaks at 383 nm and 568 nm decay and a new transient feature grows in at 419 nm. Isosbestic points at 401 nm and 508 nm signify the direct conversion of one excited state to another. The final transient spectrum (5 ns; purple), closely resembles the first trace retrieved from flash photolysis. The time constant required to fit the intermediate pump-probe regime (τ_3 = 4805 ps) is ascribed to the S_1 excited state lifetime. This state deactivates primarily through fluorescence to the ground state and through intersystem crossing to the triplet excited state. We note that the S_1 lifetime for PySMe is more than four times longer than the S_1 lifetime for PySOMe. The S_1 state in PySOMe has the additional deactivation pathway via pyramidal inversion, which has a quantum yield of 0.36 in acetonitrile and likely accounts for this discrepancy. Flash photolysis (Figure 25d; 30 ns – 20 μs) tracks the evolution of the triplet excited state. Here, an isosbestic point at 374 nm relates the decay of the excited state absorption in the red with the decay of the ground state bleach in the blue. The time-component required to fit this data (τ_4 = 1.75 μs) is attributed to ground state reversion from the triplet excited state. This lifetime is at least an order of magnitude shorter than the triplet lifetime of every other pyrene thioether and pyrene sulfoxide compound studied here. It must be that there is strong coupling of the T_1 and S_0 states in PySMe that is not present in the other compounds.

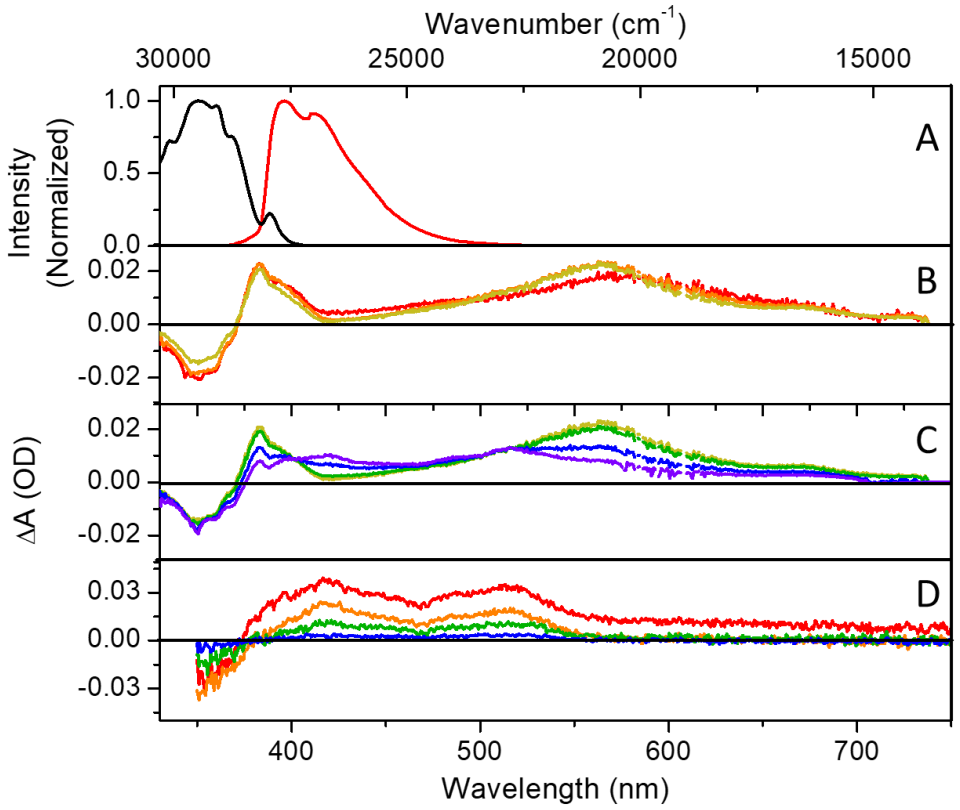

Figure 25. *Spectra of PySMe in Acetonitrile. (A) Absorbance (black) and emission (red) spectra. (B) Pump-probe transients collected at 320 fs (red), 2 ps (orange), and 50 ps (yellow). (C) Pump-probe transients collected at 50 ps (yellow), 500 ps (green), 2.5 ns (blue), and 5 ns (violet). (D) Flash photolysis transients collected at 30 ns (red), 5 μs (orange), 10 μs (green), and 20 μs (blue).*

Transient Absorption of PySOMe in Different Solvents

To further interrogate the excited state dynamics of PySOMe, we analyzed the ultrafast transient absorption spectra of the compound dissolved in a variety of solvents (Figure 26, Table 6). Specifically, we wanted to understand how the dielectric constants and the viscosities of different solvents would impact excited state behavior. Optical

transitions in pyrene are accompanied by changes to the dipole moment of the molecule along specific axes,[128] and the rates of dipole moment-induced solvent reorganization will differ based on the dielectric constant and viscosity of the solvent. Additionally, analyzing the rates of excited state processes as a function of solvent viscosity can provide information on significant molecular rotations and thus allows us to utilize transient absorption to track structural movement that coincide with electronic changes. In Figure 26, hexane and acetonitrile have similar viscosities but dissimilar dielectric constants, whereas acetonitrile and ethylene glycol have similar dielectric constants but dissimilar viscosities.

Starting with the earliest pump-probe time delays, we see that neither the rate of internal conversion from S_2 to S_1 nor the shape of the S_2 excited state absorption changes with solvent. This is reasonable considering the timescale of internal conversion, which occurs before well before any rotational or translational molecular motions are operative. Formation of the S_1 state, however, is greatly impacted by solvent choice. The S_1 state is fully formed in hexane within 500 fs (Figure 26a), as the $S_1 \rightarrow S_n$ and transitions at 379 nm 477 nm feature their maximum ΔA values at this time. We expect that there is almost no solvent reorganization with hexane, so τ_2 only involves processes within PySOMe. From 500 fs onward, S_1 decays and T_1 grows in. This behavior contrasts with the transient absorption behavior in the high-dielectric constant solvents, acetonitrile (Figure 26b) and ethylene glycol (Figure 26c), where the S_1 excited state transitions grow in over a period of several picoseconds. In acetonitrile, τ_2 = 4.82 ps, whereas in ethylene glycol, τ_2 = 248.96 ps. Solvent reorganization occurs in both systems but will take significantly more time in

ethylene glycol due to its high viscosity. We performed polarization anisotropy measurements on PySOMe in acetonitrile and ethylene glycol and arrived at values similar to τ_2 for each solution (Figures 215, 216).

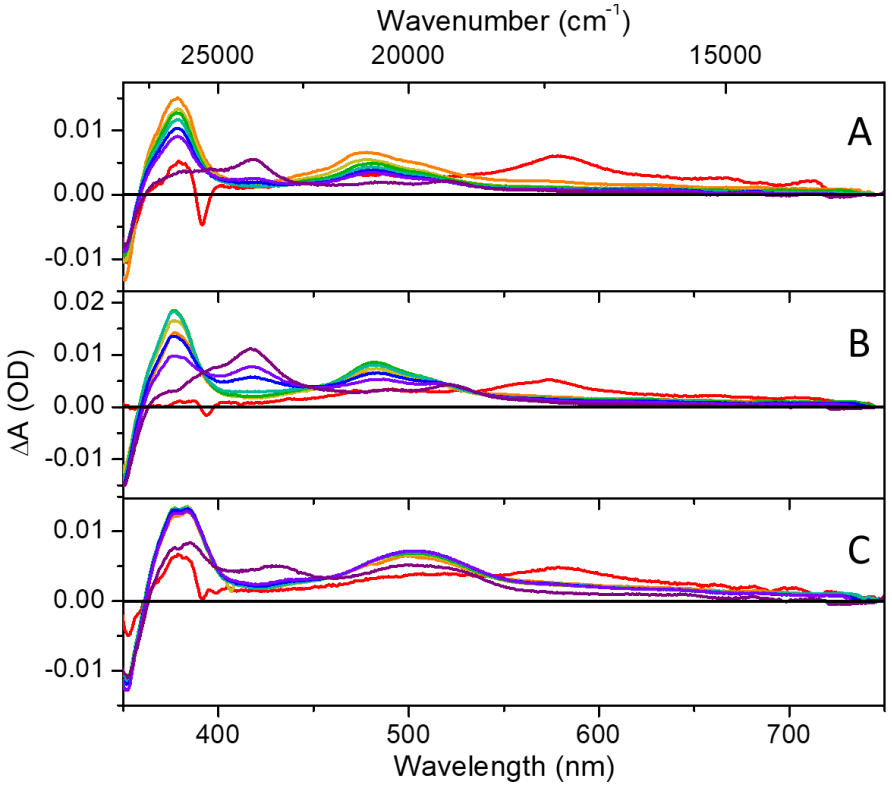

Figure 26*. Pump-probe spectra of PySOMe collected in (A) hexane, (B) acetonitrile, and (C) ethylene glycol. Time delays of individual traces correspond to 200 fs (red), 500 fs (orange), 2 ps (yellow), 20 ps (green), 100 ps (cyan), 500 ps (blue), 1 ns (violet), and 7 ns (purple).*

Interestingly, solvent viscosity plays a significant role in the lifetime of the S_1 state. In acetonitrile, τ_3 = 1024 ps, while in ethylene glycol, τ_3 = 8870 ps. Fluorescence quantum yields of $PySOPhOCH_3$ reflect this solvent-dependent lifetime; The Φ_{Em} in acetonitrile is

0.68% and the Φ_{Em} in ethylene glycol is 3.94% (Table 33). The pyramidal inversion of PySOPhH proceeds with the same quantum yield in PMMA as it does in acetonitrile, benzene, toluene, and chloroform.[121] We propose, then, that a third decay is prevalent in these systems and is responsible for the solvent-dependence of the S_1 lifetime. Through chemical actinometry experiments, Finney deduced that a nonradiative decay pathway other than pyramidal inversion is the dominant mode of relaxation in PySOMe. He invokes the idea of a twisted intramolecular charge transfer (TICT) state in which the pyrene radical anion and the sulfoxide radical cation are twisted out of conjugation.[124] Literature reports on similar systems have also proposed the presence of TICT states.[141-143] The crystal structure of PySOPhH, which features a pyrene/sulfoxide dihedral angle of just 4.5 degrees (Figure 214) indicates a well-conjugated ground state compound that is typical of systems that undergo TICT. The crystal structure of PySOMe features a pyrene/sulfoxide dihedral angle of 0.8 degrees.[124] Our solvent-dependence experiments support TICT formation, though we argue that TICT results in rapid intersystem crossing to T_1 rather than fast internal conversion to S_0. For TICT to proceed, large-scale molecular rotations must take place as the cation/anion pair twist. This process will be considerably slower in ethylene glycol than in acetonitrile due to substantial differences in viscosity. TICT states are stabilized by solvents with large dielectric constants, which also explains why τ_3 is faster in acetonitrile than in hexane, 1,2-dichloroethane, and toluene, even though these solvents have similar viscosities (Table 6).

Table 6. *Transient absorption lifetimes returned from global fitting analysis of PySOMe in different solvents.*

Compound	Solvent	(ε)	(mPa • s)	τ_1 (ps)	τ_2 (ps)	τ_3 (ps)
PySOMe	MeCN	38.8	0.38	0.11 ± 0.06	4.82 ± 0.64	1024 ± 9
	EG	37.0	16.10	0.13 ± 0.02	248.96 ± 81.60	8870 ± 5100
	DCE	10.4	0.84	0.11 ± 0.01	22.47 ± 8.20	2941 ± 86
	Toluene	2.4	0.59	0.10 ± 0.05	3.54 ± 1.50	1846 ± 130
	Hexane	1.9	0.31	0.12 ± 0.01	1.50 ± 0.28	2612 ± 450

ε is a unit of solvent dielectric constant and (mPa •s) is a unit of solvent viscosity.

PySOMe was also incorporated into PMMA thin films and investigated by ultrafast pump-probe spectroscopy (Figure 228). While the characteristic S_2 and S_1 excited state absorptions were operative, absorption from a T_1 state did not occur over the timescale of the experiment. Rather, the S_1 excited state absorption bands decay nearly completely within ~7 ns back to the ground state. While this could simply be quenching due to the high concentration of the sample, it may also be that PMMA hinders rotation to a TICT state, and thus prevents the formation of a triplet state.

Transient Absorption of Diaryl Sulfoxides and Thioethers

The three diaryl sulfoxides and three diaryl thioethers that we chose to examine differ only in the substituent at the *para*-position of the phenyl group, mitigating the role of steric interactions in excited state dynamics. The choice of functional groups provides us with electronic tunability, where $-OCH_3$ is electron-donating, $-CF_3$ is electron

withdrawing, and -H is approximately electron neutral. Finney previously noted that the emission lifetime is dramatically affected by these substituents. We utilized transient absorption spectroscopy to reveal additional details about these compounds.

Transient absorption spectra were collected for each diaryl sulfoxide and diaryl thioether. Ultrafast pump-probe spectra of the sulfoxides are shown in Figure 27, nanosecond flash photolysis spectra of the sulfoxides are shown in Figure 28, and kinetic fits of both sulfoxides and thioethers are displayed in Table 7. Transient spectra and single wavelength kinetic fits for these compounds are detailed in Appendix B. The excited state spectra are similar for each sulfoxide compound. Broad $S_2 \rightarrow S_n$ absorptive features decay on a sub-picosecond timescale and give rise to the characteristic S_1 excited state absorption seen in pyrene and PySOMe. The $S_2 \rightarrow S_n$ absorption maximum shifts to the red as the electronic substituent on the phenyl group is changed from $-OCH_3$ (λ_{max} = 565 nm) to -H (λ_{max} = 568 nm) to $-CF_3$ (λ_{max} = 609 nm), illustrating the impact of these substitutions on pyrene. The S_2 excited state absorptions and the low-energy S_1 absorptions experience inhomogeneous broadening relative to pyrene, again because of symmetry reduction from D_{2h} to C_1.

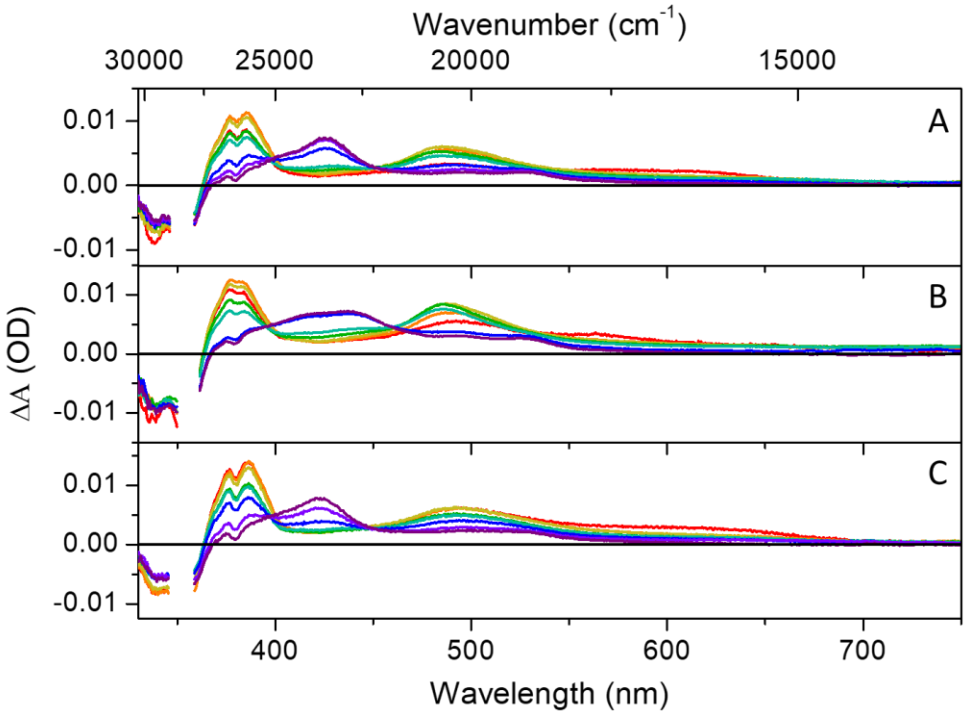

Figure 27. *Pump-probe spectra of diaryl sulfoxides in acetonitrile. (A) PySOPhH 200 fs (red), 2 ps (orange), 10 ps (yellow), 50 ps (green), 100 ps (cyan), 500 ps (blue), 1 ns (violet), and 5 ns (purple) time delays. (B) PySOPhOCH$_3$ at 200 fs (red), 2 ps (orange), 10 ps (yellow), 50 ps (green), 100 ps (cyan), 500 ps (blue), and 5 ns (purple) time delays. (C) PySOPhCF$_3$ at 760 fs (red), 2 ps (orange), 10 ps (yellow), 50 ps (green), 100 ps (cyan), 500 ps (blue), 2 ns (violet), and 5 ns (purple) time delays.*

Table 7. *Transient absorption lifetimes returned from global fitting analysis of diaryl thioethers and diaryl sulfoxides in acetonitrile.*

Compound	τ_1 (ps)	τ_2 (ps)	τ_3 (ps)	τ_4 (μs)
PySPhH	0.18 ± 0.02	23.8 ± 2.8	512.9 ± 32.5	18.64 ± 0.33
PySOPhH	0.25 ± 0.05	28.7 ± 2.6	485.3 ± 27.5	18.29 ± 0.25
PySPhOCH3	0.11 ± 0.04	12.5 ± 6.8	65.1 ± 1.3	24.55 ± 0.42
PySOPhOCH3	0.16 ± 0.08	21.9 ± 3.5	182.9 ± 25.6	37.44 ± 0.54
PySPhCF3	0.17 ± 0.01	14.9 ± 9.6	1485.0 ± 94.2	31.80 ± 0.38
PySOPhCF3	0.20 ± 0.02	25.9 ± 2.9	1590.0 ± 54.7	26.48 ± 0.21

The S_1 excited state lifetimes that we extracted from the transient absorption data match very closely with the emission lifetimes reported by Finney.[124] This lifetime decreases by an order of magnitude as we move from electron withdrawing $PySOPhCF_3$ (τ_3 = 1590.0 ps) to electron donating $PySOPhOCH_3$ (τ_3 = 182.9 ps). Finney had attributed this to differences in the barrier to pyramidal inversion that ultimately results in $S_1 \rightarrow S_0$ internal conversion. We argue that this is not the case. First, the same lifetime reduction is operative with the thioether compounds; the S_1 excited state lifetime changes by more than an order of magnitude as we move from electron withdrawing $PySPhCF_3$ (τ_3 = 1485.0 ps) to electron donating $PySPhOCH_3$ (τ_3 = 65.1 ps). Pyramidal inversion is not available to the thioether compounds, so a different deactivation mechanism must at work. Second, the S_1 lifetimes for thioether/sulfoxide pairs bearing the same *para* substituent match closely with one-another. Thus, excited state pyramidal inversion in these compounds constitutes a relatively minor nonradiative decay pathway. It is likely that the inversion

quantum yield is only modestly affected by the change in the electronic substituent from $-CF_3$ to $-OCH_3$ in these compounds, though CD studies would need to be performed in order to confirm this.

The lowest-energy excited state, T_1, features a uniform decay across the spectral window provided by flash photolysis (Figure 28). There is a fairly large range in the triplet lifetime (τ_4) of the diaryl thioether and diaryl sulfoxide compounds, ranging from 18.28 μs in PySOPhH to 37. 44 μs in $PySOPhOCH_3$. These compounds do not phosphoresce at room temperature, so decay is non-radiative and is likely a function of the energy gap law relating T_1 and S_0. Due to the large spectral window from this experiment, we noticed that there is an additional T_1 excited state absorption for each compound in the red portion of the spectrum that features an absorption maximum at a wavelength greater than 850 nm. A future study on these systems will probe the NIR region on an ultrafast timescale to further investigate this wavelength regime.

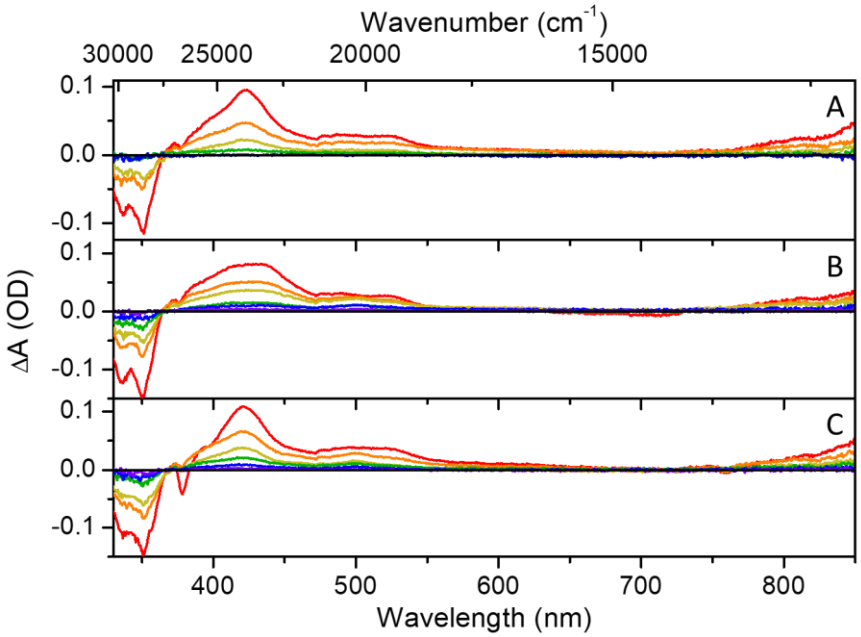

Figure 28. *Flash photolysis spectra of (A) PySOPhH, (B) PySOPhOCH$_3$, and (C) PySOPhCF$_3$ in acetonitrile. Time delays of individual traces correspond to 30 ns (red), 10 μs (orange), 20 μs (yellow), 50 μs (green), 100 μs (blue), 200 μs (violet).*

We propose the potential energy surface in Figure 29 to describe the excited state dynamics of pyrene sulfoxide compounds. The same PES applies to the thioethers, though k_{ISC} is not operable. The compounds featured in this study can be thought of as donor-acceptor systems where pyrene is the acceptor and the alkyl- or aryl- sulfur substituent is the donor. Shortly after photoexcitation, ICT creates a radical cation/anion pair in the S_1 state. While ground state recovery from this state can occur by either fluorescence or inversion, the primary relaxation pathway from S_1 is the formation of a TICT state. Because TICT states rotate the donor and acceptor units out of conjugation with one-another, systems that are better-equipped to handle their radical charges will encounter a lower energy barrier to rotation. In the compounds from this study, electron-donating -

OCH_3 would stabilize the positively charged donor species, while electron-withdrawing -CF_3 would destabilize it. These effects are manifested in k_{TICT}. In the same vein, $PySPhOCH_3$ features a faster k_{TICT} than its sulfoxide analog due to the electronic differences between thioethers and sulfoxides. The ^{1}TICT and ^{3}TICT states have nearly the same energy due to featuring a small exchange integral,[144,145] and the rate of intersystem crossing will be rapid. From there, the ^{3}TICT state quickly reverts to a molecular configuration that resembles the ground state, and ground state reversion occurs on the microsecond timescale.

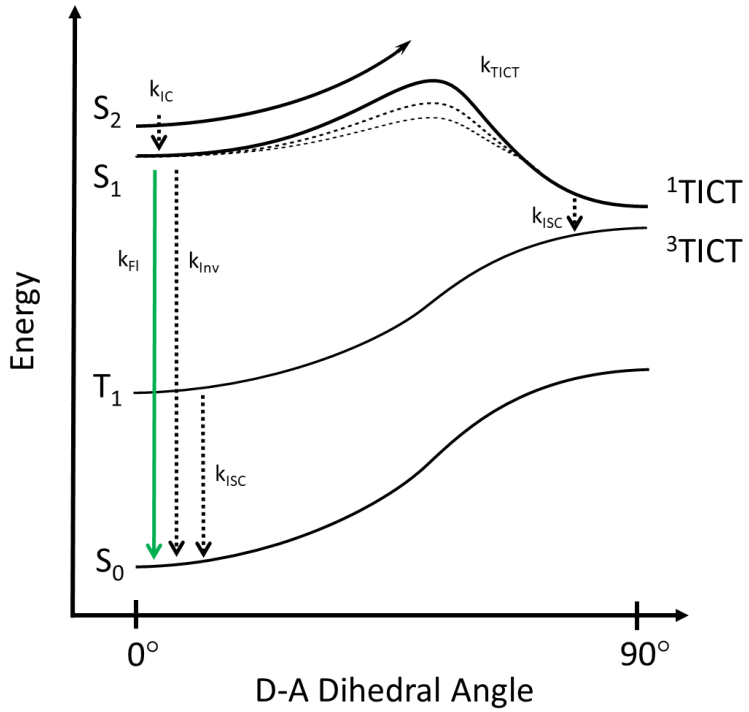

Figure 29. *A potential energy surface that characterizes the excited state dynamics of pyrene sulfoxide systems. The dotted curves represent a decrease in the TICT energy barrier as the substituent on the acceptor becomes more electron-donating.*

Conclusions

Pyrene thioether and pyrene sulfoxide compounds were investigated for the first time by transient absorption spectroscopy. The early excited state dynamics of these compounds match closely with the excited state of pyrene; an initially formed S_2 state undergoes internal conversion within ~150 fs to form an S_1 state which subsequently thermalizes via vibrational cooling and solvent reorganization over several picoseconds. Whereas pyrene primarily relaxes from S_1 to S_0, these compounds exhibit more complex decay dynamics. Ultrafast pump-probe spectroscopy revealed the formation of a long-lived, non-emissive T_1 state and nanosecond flash photolysis allowed us to track its decay. The lifetime of the S_1 state in PySMe and PySOMe is solvent dependent, where viscous solvent drastically increases the excited state lifetime and polar solvent reduces the excited state lifetime. Based on these results, we propose that the formation of a TICT state occurs in S_1 whereby a pyrene radical anion and a sulfur radical cation twist out of conjugation with one-another. Large-scale molecular rotations are slowed in viscous solvent, and TICT states are stabilized in polar solvent. The ^{1}TICT state experiences rapid intersystem crossing to the triplet regime, and from here the molecule relaxes back to the ground state on the microsecond timescale. Transient absorption of substituted pyrenyl-phenyl thioethers and sulfoxides was also carried out. Substitution of an electron withdrawing group at the *para*-position of the phenyl moiety yields an S_1 lifetime that is an order of magnitude longer than substitution with an electron donating group. We propose that the electron withdrawing group destabilizes the formation of a TICT state, while the electron donating group stabilizes its formation.

CHAPTER 5

Pt-Containing Conjugation Polymers and Small Molecules for Bulk-Heterojunction Photovoltaic Devices

Introduction

Organic photovoltaic (OPV) devices exemplify the role of structure-function relationships in chemical systems, as subtle changes in molecular architecture can have profound effects on device efficiency. Because these devices are derived primarily from organic compounds, they typically suffer short exciton lifetimes, narrow absorption windows, and imprecise morphology. However, the accessibility of OPVs to synthetic chemistry has resulted in dramatic improvements to these shortcomings in a relatively short timeframe.[146-148] Among other improvements, researchers have sought to increase exciton lifetimes by accessing long-lived triplet states, which would directly result in better exciton migration and charge separation.[149-151] This is most commonly through the introduction heavy-metal atoms, which impart a large spin-orbit coupling constant and enhance intersystem crossing.[152-155] The donor species, which is responsible for exciton formation and the initial exciton migration, is typically altered in this way.

Donor species doped with platinum-bisacetylide units are a well-studied example of triplet sensitization using heavy-metal atoms. Three main-approaches have been documented previously. The first, and most prominent, systems are Pt-doped conjugated polymers. Unfortunately, these systems feature low performance because of their amorphous nature which results in low conductivity. Additionally, the bulk-

heterojunction of conjugated polymers is not well-defined and favorable interactions cannot be induced. Another approach to Pt-doped donors are "dumbbell" shaped small molecules in which platinum bisacetylide units are bound to either end of a long, linear, aromatic chromophore.[156,157] Utilizing small molecules instead of polymers grants added tunability, though they are arguably more difficult to produce. Studies on these platinum "dumbbells" revealed ways in which the band gaps, triplet yields, triplet lifetimes, morphology, and overall performance could be influenced by synthetic alterations. The placement of the bulky platinum-bisacetylide units proves to be unfavorable, though, as they prevent effective $\pi - \pi$ stacking interactions between the aromatic units and inhibit efficient molecular packing.[158] Recently, platinum "roller-wheel" small molecules were developed to address this problem.[3,4,160] Contrary to the "dumbbell" molecules, the platinum-bisacetylide units are situated in the middle of the aromatic chromophore, serving as side chains. In this new configuration, the bulky platinum substituents do not hinder $\pi - \pi$ stacking, but rather encourage a slip-stacking morphology which improves crystallinity.

Understanding the excited state dynamics of OPV systems is critical in order to develop new architectures which maximize favorable properties. In this report, we developed a group of platinum roller wheel compounds that exhibit distinct features relative to one-another. Specifically, we analyze four platinum roller-wheel donor small molecules that feature a platinum bisacetylide unit, a benzenedithiophene (BDT) unit, and a linear, conjugated chromophore. The chromophores have alterations to long alkyl chains that branch off from aromatic units and different numbers of arene groups.

Three of these compounds also contain fluorinated benzothiadiazole (BTD) units that act as electron acceptors at the periphery of the donor unit. By comparing the transient absorption and emission lifetime behavior of these compounds, we were able to elucidate the effects that those molecular structure play on important photophysical properties like internal conversion, intersystem crossing, emission lifetime and triplet lifetime.

Results and Discussion

Bond line drawings of the compounds investigated in this study are depicted in Figure 266. RWPt-4 and RWPt-4 are structurally identical aside from the identity of the long alkyl chain that branches from the aromatic chain near benzenedithiophene, where RWPt-4 has $C_{10}H_{21}$ and RWPt-5 has C_6H_{13}. Their aromatic chains contain the same number of thiophene units, and they both have an electron-accepting fluorinated benzothiadiazole unit near the periphery of the donor unit. RWPt-6 differs from RWPt-5 in that it bears an extra thiophene unit between BDT and BTD. RWPt-7 lacks BTD altogether. The UV-Vis spectra for these compounds are depicted in Figure 267.

The transient absorption spectra of the platinum roller-wheel complexes were investigated using ultrafast pump-probe spectroscopy and nanosecond flash photolysis. The spectra of each complex are depicted as stack-plots, with the ground-state absorbance spectrum presented in the top plot (A). Further down (B-E), the time-resolved spectra are grouped according to time-delay to show discrete spectral changes

as time evolves. Kinetic fits are mostly reserved for the SI, but the nature of the multi-exponential lifetime for each complex is elaborated herein.

The steady-state and time-resolved spectra of RWPt-6 are presented (Figure 30). The UV-Vis spectrum features a sharp peak at 375 nm and broad peak centered at 496 nm (Figure 30a). Unlike the other complexes studied here, the broad peak lacks a shoulder on the red edge and instead has a small shoulder on the blue edge, at 446 nm. This discrepancy is likely due to the presence of an extra thiophene in the aromatic chain, which increases the conjugation length of the system. The peak at 375 nm is assigned to a benzenedithiophene $\pi \rightarrow \pi^*$ transition based on previous literature reports. [160] The peak at 496 nm is a Pt-bisacetylide benzenedithiophene to terthiophene charge-transfer transition. Exciting this transition at various wavelengths yields no change to transient absorption dynamics (Figure 265), indicating that there are no underlying transitions that can give rise to different photochemical behavior. The same is true for the other complexes involved in this study.

The transient absorption spectra of RWPt-6 are displayed in Figure 30b-e. The negative feature from ~350 nm to ~560 nm is assigned as a ground-state bleach since its shape (especially at early time delays) mirrors the UV-Vis spectrum. The positive portion of the spectrum is due to excited-state absorption, as there is no evidence of photoproduct formation or decomposition. At short pump-probe time delays (Figure 30 b; 500 fs – 7.5 ps), there appear to be isosbestic points at 405 nm and 735 nm, though neither are particularly well-defined. Across the spectral range, there are two main

events of note. In the bleach region, we see a rapid loss in signal over the first picosecond, after which the spectra remain largely the same. The time constant for this process (τ_1 = 120 ± 20 fs) is attributed to relaxation of a vibrationally hot excited state. In the red, a positive absorption grows in over the 7.5 ps window, culminating in a peak near 625 nm. The energy of the peak matches well with the singlet excited states of similar complexes,[153] and we assign this time constant (τ_2 = 2.2 ± 0.5 ps) to formation of the thermalized singlet excited state. During this time window, the spectral peaks shift to higher energies, fortifying our assertions of vibrational cooling and thermalization within the initially formed excited state. At intermediate pump-probe time delays (Figure 30c; 20 ps – 300 ps), an isosbestic point is formed just above zero DA at 569 nm. We note a near-complete loss of the negative peak at 380 nm and loss of the 625 nm peak, which match with the spectra for the remainder of the experiment. We ascribe this time constant (τ_3 = 56 ± 11 ps) as internal conversion to the lowest-energy singlet excited state. At long pump-probe time delays (Figure 30d; 300 ps – 6 ns), the transient spectra form an isosbestic point at 564 nm, where DA is zero. The initial spectra decay slightly until there are no more changes for the duration of the ultrafast experiment. This time constant (τ_4 = 1056 ± 250 ps) matches well with room temperature emission lifetime experiments (Table 38) for RWPt-6 in THF. With the aid of Kasha's rule and the fact that there is a substantial excited state population into the microsecond time-regime, t_4 is ascribed to intersystem crossing from the singlet to the triplet manifold. The nanosecond flash photolysis (Figure 30e; 30 ns – 30 μs) track the complete decay of

signal. An isosbestic point at 564 nm indicates a direct conversion between two states. We assign this final time constant (τ_5 = 8.40 ± 0.25 μs) to electron-hole recombination.

The complexes RWPt-4 and RWPt-5 possess the same excited state spectral evolution as RWPt-6 (Figures 252, 253), which is reasonable considering the structural similarities between these three species. However, the additional thiophene unit in RWPt-6 relative to RWPt-4 and RWPt-5 appears to result in longer lifetimes for τ_3 (internal conversion) and τ_4 (intersystem crossing). Internal conversion in the bithiophene-substituted complexes (RWPt-4 and RWPt-5) is ∼40 ps. In the terthiophene-substituted RWPt-6, this process is ∼60 ps. If the initially-formed excited state involves charge transfer from the central donor to thiophene, perhaps the electron moves along the aromatic side chain towards the acceptor at a rate of one thiophene unit per ∼20 ps. Internal conversion, then, proceeds by electron transfer from thiophene to benzothiadiazole. The larger charge separation in RWPt-6 would also explain the slower rate of the subsequent Pt-assisted intersystem crossing for this complex (1056 ps) compared to RWPt-4 and RWPt-5 (694 ps and 702 ps, respectively).

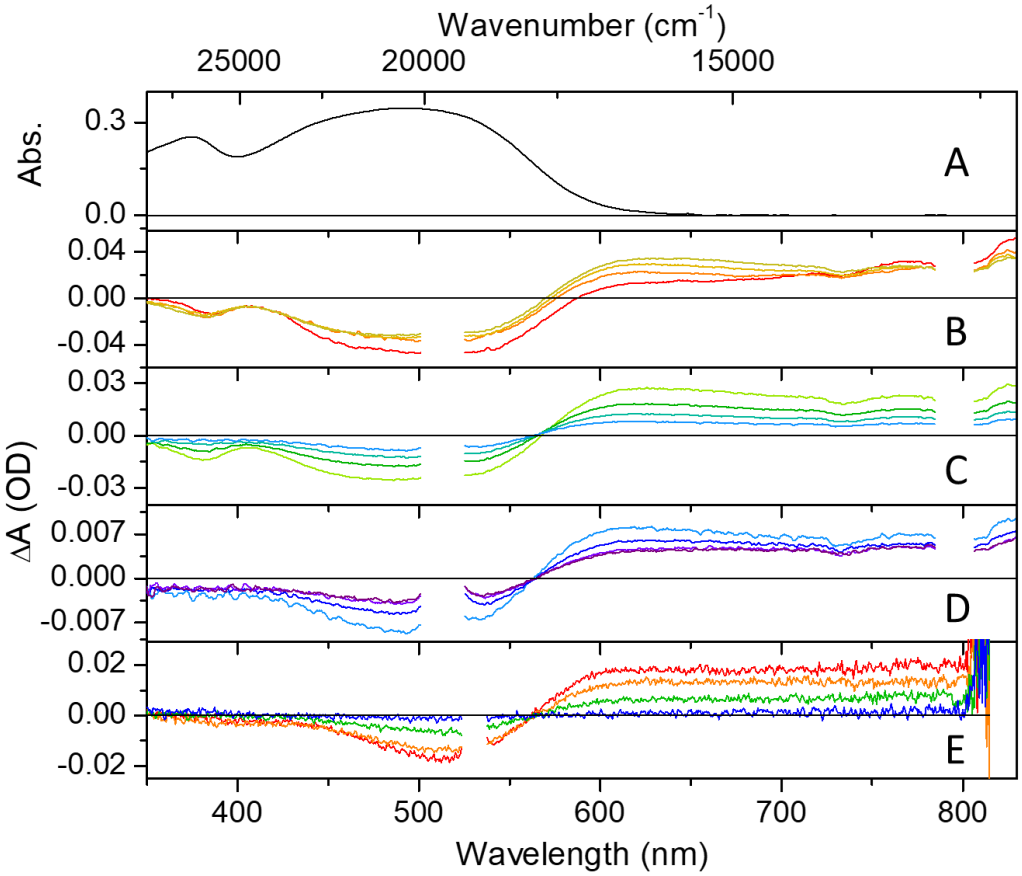

***Figure 30**. (A) Absorbance spectrum of RWPt-6. (B) Pump-probe transients collected at 0.5 ps (red), 1 ps (orange), 2 ps (amber), and 7.5 ps (yellow) time delays. (C) Pump-probe transients collected at 20 ps (yellow-green), 50 ps (green), 100 ps (cyan), and 300 ps (light blue). (D) Pump-probe transients collected at 300 ps (light blue), 1 ns (blue), 2.5 ns (violet), and 6 ns (purple). (E) Flash photolysis transients collected at 30 ns (red), 1 μs (orange), 5 μs (green), and 30 μs (blue).*

The complex RWPt-7 features ultrafast transient spectra that are unlike those of the other complexes in this study while maintaining similar ground state absorption characteristics. The UV-Vis spectrum (Figure 31a) has a sharp peak at 375 nm and a broad transition with a peak at 452 nm and a shoulder at 530 nm. The first peak will

again be ascribed to a benzenedithiophene $\pi \rightarrow \pi^*$ transition, and the broad peak to a Pt-bisacetylide benzenedithiophene to terthiophene charge-transfer transition. The ultrafast pump-probe spectra at early time delays (Figure 31b; 509 fs – 20 ps) have well-defined isosbestic points at 368 nm and 589 nm. The low-energy isosbestic point is blue-shifted by ~3,500 cm^{-1} relative to the same point in RWPt-6, while the high energy isosbestic lies at nearly the same energy. Well-defined negative peaks are present at 378 nm and 450 nm. At the same time, there are also positive peaks at 682 nm, 723 nm, and 768 nm. As the spectra evolve in time, there is a blue-shift in these peaks and a decay of the transient signal except for a positive peak that is formed at 563 nm. Two time-constants are extracted from the kinetic fit (τ_1 = 100 ± 20 fs and τ_2 = 3.7 ± 1.1 ps), which we again attribute to vibrational cooling and formation of a thermalized singlet excited state, respectively. At intermediate time delays (Figure 31c; 20 ps – 1 ns), a new isosbestic point is seen at 729 nm. At higher energies, the spectra move to more positive values and a peak is formed at 690 nm. At lower energies, the spectra decay and blue-shift. This time constant (τ_3 = 324 ± 113 ps) aligns with room temperature emission lifetime experiments of RWPt-7, so we assign t_3 to intersystem crossing from the singlet to the triplet manifold. This species lacks a time component in the 40-60 ps time range that exists in the other three complexes. It could be that this time-component, which is assigned to internal conversion, tracks the movement of the electron onto benzothiadiazole at the periphery of the aromatic chain. Since RWPt-7 lacks benzothiadiazole, the internal conversion process would not be operative. This also explains the shorter ISC time constant in RWPt-7 versus the other complexes. The

electron is confined to thiophene units nearer to the influence of platinum's large spin-orbit coupling. This proximity allows for more facile intersystem crossing to the triplet regime. At long time delays (Figure 31d; 1 ns – 6 ns), an isosbestic point is seen at 527 nm, where DA is zero. The spectra decay slightly as time evolves. The time constant for this process is on the order of 40ns, so it can't be adequately defined by ultrafast pump-probe measurements. When the experiment is repeated at lower pump powers, this time component is not operative. (Figure 264) Thus, we attribute this feature to sample decomposition from pumping at high-intensities. The nanosecond flash photolysis spectra (Figure 31e; 30 ns – 30 us) track the complete decay of signal. An isosbestic point seems to occur where DA is zero near 525 nm, but it is obscured by the laser line. Regardless, we assign this time constant (τ_5 = 16.35 ± 0.18 μs) to electron-hole recombination.

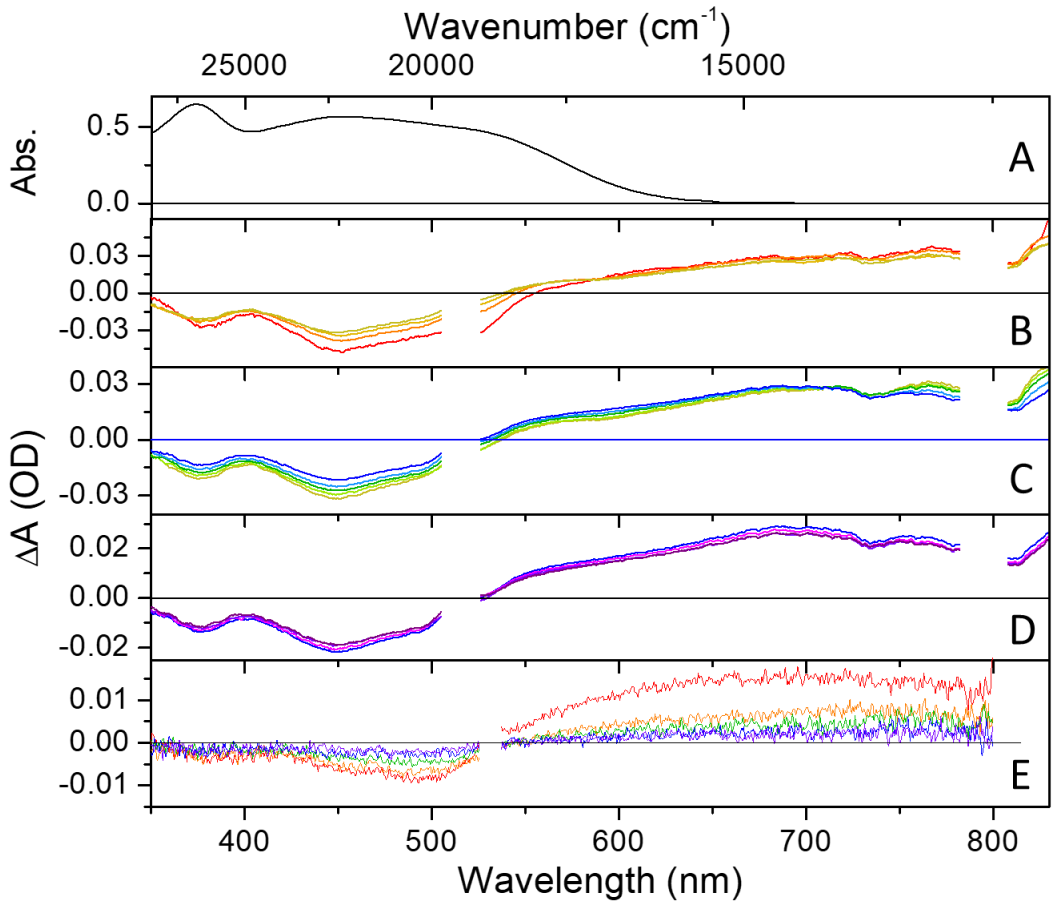

Figure 31. *(A) Absorbance spectrum of RWPt-7. (B) Pump-probe transients collected at 0.5 ps (red), 2 ps (orange), 6 ps (amber), and 20 ps (yellow) time delays. (C) Pump-probe transients collected at 20 ps (yellow), 50 ps (yellow-green), 100 ps (green), 200 ps (light blue), and 1 ns (blue). (D) Pump-probe transients collected at 1 ns (blue), 2 ns (magenta), 3.5 ns (violet), and 6 ns (purple). (E) Flash photolysis transients collected at 30 ns (red), 2 μs (orange), 8 μs (green), 20 μs (blue), and 30 μs (violet).*

Conclusions

We have reported the time-resolved emission and transient absorption data for a novel group of platinum roller-wheel complexes that have implications in next-generation organic photovoltaic devices. Our results show a direct and measurable correlation between the molecular architecture of the molecule and its photophysical properties. Additionally, detailed kinetic and spectroscopic comparisons of the complexes allowed us to create a detailed overview of the excited-state dynamics within this system. Shortly after charge transfer excitation, these complexes undergo vibrational cooling (hundreds of femtoseconds) and relaxation into a thermalized singlet state (several picoseconds). If there is an acceptor moiety at the periphery of the molecule, electron migration to the acceptor will occur over tens of picoseconds. Then, based on the proximity of the electron to platinum, intersystem crossing to a lowest-energy triplet state will take place. Emission lifetime data correlates will with the fourth time-constant extracted from transient absorption, and we assert that ISC occurs in 1056 ps for RWPt-6 and 324 ps for RWPt-7. Using nanosecond flash photolysis, we monitor a long triplet state lifetime that ranges from 7.8 μs to 16.4 μs. The analysis presented here represents the first proposed excited state pathway for platinum roller-wheel complexes.

CHAPTER 6

Conclusions

Within this dissertation, three distinct photochemical systems were developed and characterized using a battery of spectroscopic techniques. By altering functional groups at key points within the molecular architecture, we were able to induce drastic changes in photochemical reactivity. These changes serve two purposes: they allow us spectroscopic handles with which to make assignments about excited state dynamics, and they provide our systems with an array of practical applications based on which photophysical properties these changes affect.

Photochromic ruthenium sulfoxide complexes have been previously studied by our group, resulting in a diverse library of complexes with many unique chemical properties. Still, there are key features that need improving, including photoisomerization reactivity, solvent stability, and ground state reversion rates. By incorporating chelating phosphine sulfoxide ligands into a $[Ru(bpy)_2]^{2+}$ core, we gain unprecedented control over the electronics at the ruthenium center. Photoisomerization quantum yields can be tuned between 0.0 and 0.9 by making relatively simple electronic changes to the periphery of the P,S ligand.

By comparing the photoisomerizing and non-photoisomerizing groups of complexes we learn that photoisomerization reactivity is not entirely an excited state process, as many of the ground state properties are different between the two groups. First, the rates of electrochemical isomerization are an order of magnitude slower in

complexes that do not exhibit photoisomerization reactivity. Second, the ATR-IR spectra display a significantly broadened sulfoxide stretching mode in the photoisomerizing complexes. Third, key NMR and X-ray crystallographic data change in opposite ways upon oxidation of the thioether for photoisomerizing and non-photoisomerizing complexes. Finally, we provide important infrared-spectroscopic evidence for the formation of an O-bonded metastable ruthenium isomer upon visible irradiation.

Pyrene sulfoxides have long been appreciated for their ability to undergo excited state pyramidal inversion while maintaining stereochemistry in the ground state. To date, time-resolved studies on the excited state dynamics of these compounds have been lacking. By performing femtosecond pump probe and nanosecond flash photolysis experiments on a group of pyrene thioether and pyrene sulfoxides, we have uncovered a near-complete excited state pathway for these molecules upon excitation. The role of solvent polarity and viscosity is explored as well, which informs us about rotational motions that occur as the molecule moves across the excited state potential energy surface. We propose that the dominant decay pathway in pyrene thioether and pyrene sulfoxide compounds is through the formation of a TICT state, which then undergoes rapid intersystem crossing to a long-lived triplet state. These studies corroborate with previous research, which asserts that pyramidal inversion brings the molecule from a singlet excited state to the ground state.

The need for efficient forms of renewable energy will only ever increase, especially as the world population continues to grow and the realities of global warming

become clearer. The most ubiquitous form of renewable energy comes from solar energy that bathes our planet every day and can be harnessed by photovoltaic devices. Organic photovoltaics are attractive alternatives to contemporary devices due to their tunability, low cost, light weight, and ability to be processed on a large scale. Within this dissertation, we explore the excited state dynamics of a novel class of platinum roller-wheel compounds, which feature some of the best power conversion efficiencies that organic solar cells have to offer. Because understanding the excited state dynamics of these systems is paramount in making improvements to future generations of devices, we make chemical modifications to key parts of the molecular architecture to gain spectroscopic handles. Transient absorption and time-resolved emission spectroscopies grant us the ability to propose an excited state pathway for these compounds that will be used to make improvements in power conversion efficiency in the future.

CHAPTER 7

Appendices

Appendix A. Chapter 3 Supporting Information

A1. Controlling Photoisomerization Reactivity Through Single Functional Group Substitutions in Ruthenium Phosphine Sulfoxide Complexes

and

A2. Identifying Structural and Electronic Property Differences between Isomerizing and Non-Isomerizing Ruthenium Sulfoxide Complexes.

General Information

2-Bromothioanisole was purchased from TCI Chemicals (America).

Chlorodiphenylphosphine, Chlorodiisopropylphosphine, Diphenylphosphine, 2-Chloroethyl methyl sulfide, 2.5 M *n*-Butyllithium solution in hexanes, and 3-chloroperoxybenzoic acid (*m*-CPBA) 70% were purchased from Sigma Aldrich.

Chlorobis[4-(trifluoromethyl)phenyl]phosphine and chlorobis(4-methoxyphenyl)phosphine were purchased from Alfa Aesar. They were all used as received.

The starting complex, hydrated *cis*-dichlorobis(2,2'bipyridine) ruthenium (*cis*-$[Ru(bpy)_2Cl_2].2H_2O$) and its solvated analogue *cis*-$[Ru(bpy)_2(acetone)_2](PF_6)_2$ were prepared according to literature methods.[161]

All other common reagents and solvents were used as received. The reactions were performed using standard Schlenk techniques with dry solvents under inert gas atmosphere.

Mass Spectrometry (MS) results: Accurate mass analysis of the compounds were run by Electrospray Ionization (ESI) in positive ion mode. Ken Sherrell at the University of New Mexico acquired the data.

Ligand Synthesis

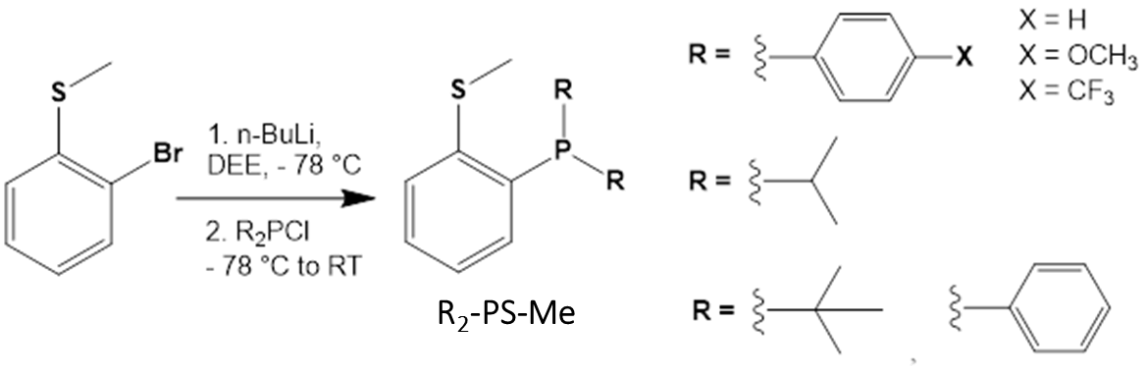

Scheme 4. General synthetic scheme for the phenyl-bridged P,S ligand precursors.

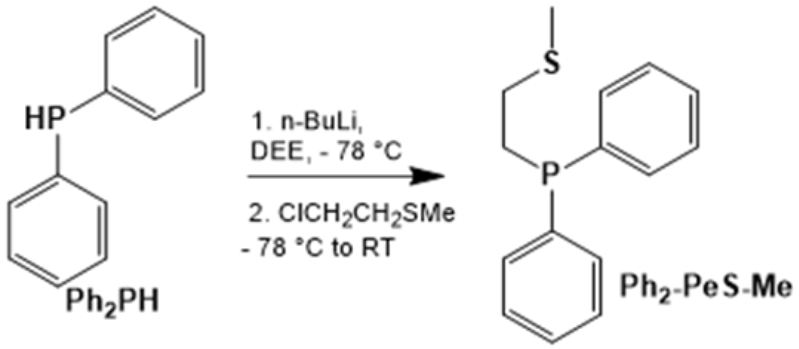

***Scheme 5*.** General synthetic scheme for the ethyl-bridged P,S ligand precursors.

L1) (2-(methylthio)phenyl)diphenylphosphane (Ph_2-PS-Me)

2-Bromothioanisole (1.1 g, 5.42 mmol) in N_2 (g) deaerated anhydrous diethyl ether (DEE) (50 mL) was lithiated dropwise with *n*-butyllithium (2.2 mL, 5.42 mmol of 2.5 M solution in hexanes) at -78 °C. It was stirred for 1 h before adding chlorodiphenylphosphine (1.0 mL, 5.42 mmol) dropwise. It was warmed gradually to RT for 3 h. The solution was hydrolyzed with 50 mL of 5% aqueous NaOH solution. It was extracted with dichloromethane (DCM) (50 mL x 2), dried using anhydrous $MgSO_4$ solid, filtered and concentrated. It was recrystallized using ethanol, filtered using a medium frit and washed with cold (0 °C) EtOH. Yield 1.0 g, 60%. ^{1}H NMR (300MHz, RT, $CDCl_3$): δ (ppm) 7.27 – 7.35 (m, 12H), 7.04 – 7.09 (m, 1H), 6.76 – 6.79 (m, 1H), 2.44 (s, 3H, -CH_3). ^{31}P NMR (δ = -14.09 ppm), relative to 85% H_3PO_4 (δ = 0 ppm) as an external standard. ESI-MS: $[L1+H]^+$, calculated *m/z* = 309.0867, observed *m/z* = 309.0856.

L2) (2-(methylthio)phenyl)bis(4-methoxyphenyl)phosphane (*p*-MeOPh_2-PS-Me)

The ligand was scaled and prepared similarly to **L1**. 2-Bromothioanisole (0.40 g, 1.96 mmol), *n*-butyllithium (0.9 mL, 2.14 mmol of 2.5 M solution) and Chlorobis(4-methoxyphenyl)phosphine (0.5 g, 1.78 mmol). The chloro phosphine was added as a solid via one neck of the three neck round bottom flask while maintaining positive pressure of nitrogen gas in the flask. Yield 0.36 g, 55%. ^{1}H NMR (300MHz, RT, $CDCl_3$): δ (ppm) 7.19 – 7.31 (m, 6H), 7.03 – 7.08 (m, 1H), 6.90 (d, *J* = 8.1 Hz, 4H), 6.75 – 6.79 (m, 1H), 3.81 (s, 6H, -OCH_3), 2.43 (s, 3H, -CH_3). ^{31}P NMR (δ = -17.44 ppm), relative to 85% H_3PO_4 (δ = 0 ppm). ESI-MS: $[L2+H]^+$, calculated *m/z* = 369.1078, observed *m/z* = 369.1084.

L3) (2-(methylthio)phenyl)bis(4-(trifluoromethyl)phenyl)phosphane (*p*-CF_3Ph_2-PS-Me)

The ligand was scaled and prepared similarly to **L1**. 2-Bromothioanisole (0.57 g, 2.80 mmol), *n*-butyllithium (1.3 mL, 3.08 mmol of 2.5 M solution) and Chlorobis[4 (trifluoromethyl)phenyl]phosphine (1.0, 2.08 mmol). The crude product was purified by precipitating and triturating using cold (-78 °C) methanol. The filtrate was concentrated and re-purified three times. Yield 0.432 g, 35%. ^{1}H NMR (300MHz, RT, $CDCl_3$): δ (ppm) 7.62 (d, *J* = 7.5 Hz, 4H), 7.35 – 7.40 (m, 6H), 7.11 (m, 1H), 6.72 – 6.75 (m, 1H), 2.46 (s, 3H, -CH_3). ^{31}P NMR (δ = -14.43 ppm), relative to 85% H_3PO_4 (δ = 0 ppm). ^{19}F NMR (δ = -61.42 ppm), relative to (hexafluorobenzene, C_6F_6) (δ = -164.9 ppm) as an external standard. ESI-MS: $[L3+H]^+$, calculated *m/z* = 445.0615, observed *m/z* = 445.0612.

L4) (2-(methylthio)phenyl)diisopropylphosphane (iPr_2-PS-Me)

The ligand was scaled and prepared similarly to **L1**. 2-Bromothioanisole (1.9 g, 9.50 mmol), *n*-butyllithium (3.8 mL, 9.50 mmol of 2.5 M solution) and chlorodiisopropylphosphine (1.5 mL, 9.50 mmol). The solid product was obtained after dying with $MgSO_4$ and concentrating. It was not recrystallized or washed with ethanol. Yield 1.98 g, 87%. ^{1}H NMR (300MHz, RT, $CDCl_3$): δ (ppm) 7.27 – 7.35 (m, 2H), 7.20 – 7.16 (dd, *J* = 7.5, 3.3 Hz, 1H), 7.11 (t, *J* = 7.2 Hz, 1H), 2.43 (s, 3H, -CH_3), 2.06 – 2.19 (d, sep, 2H, - *i*Pr), 1.18 (d, *J* = 6.9 Hz, 3H, -*i*Pr), 1.13 (d, *J* = 7.2 Hz, 3H, -*i*Pr), 0.98 (d, *J* = 7.2 Hz, 3H, -*i*Pr), 0.94 (d, *J* = 6.9 Hz, 3H, -*i*Pr), ^{31}P NMR (δ = -5.02 ppm), relative to 85% H_3PO_4. ESI-MS: $[L4+H]^+$, calculated *m/z* = 241.1180, observed *m/z* = 241.1177.

L5) (2-(Methylthio)ethyl)diphenylphosphane (Ph_2-PeS-Me)

Diphenylphosphine (1.5 g, 8.06 mmol) in $N_{2(g)}$ deaerated anhydrous DEE (50 mL) was lithiated dropwise with *n*-butyllithium (~3.6 mL, 9.0 mmol of 2.5 M solution in hexanes) at -78 °C. The solution turned gradually to yellow. It was stirred for 1 h before slowly adding 2-Chloroethyl methyl sulfide (1.0 mL, 9.67 mmol). It was warmed gradually to RT and stirred until the yellow color faded away ~3 h. The solution was added water 50 mL and extracted with chloroform (50 mL x 2), dried using anhydrous $MgSO_4$ solid, filtered and concentrated. It was recrystallized, filtered using a medium frit and washed with cold (-78 °C) methanol. Yield 1.83 g, 83%. ^{1}H NMR (300MHz, RT, $CDCl_3$): δ (ppm) 7.38 – 7.46 (m, 4H, Ph), 7.32 – 7.37 (m, 6H, Ph), 2.53 –2.61 (m, 2H, -PCH_2CH_2S-), 2.32 – 2.37 (m, 2H, -PCH_2CH_2S-), 2.10 (s, 3H, -CH_3). ^{31}P NMR (δ = -16.79 ppm), relative to 85% H_3PO_4 (δ = 0 ppm). ESI-MS: $[L5+H]^+$, calculated *m/z* = 261.0867, observed *m/z* = 261.0869.

L6) (2-(Methylthio))phenyl) (*tert*-butyl)phenylphosphane (tBu,Ph-PS-Me)

2-Bromothioanisole (1.1g, 5.42mmol) in N_2(g) deaerated anhydrous diethyl ether (DEE) (50mL) was lithiated dropwise with *n*-butyllithium (2.2mL, 5.42mmol) of 2.5M solution in hexanes at -78 °C. It was stirred for 1 h before adding chloro(tert-butyl)phenylphosphine (1.02mL, 5.42mmol) dropwise. It was warmed gradually to RT for 3 h. The solution was hydrolyzed with 50mL of 5% aqueous NaOH solution. It was extracted with dichloromethane (DCM) (50mL x 2), dried using anhydrous $MgSO_{-4}$ solid, filtered and concentrated. It was recrystallized using ethanol, filtered using a medium frit and washed with cold (0 °C) EtOH.

L7) 2-(Phenylthio)ethyl)diphenylphosphane (Ph_2-PeS-Ph)

To 1 g (5.3 mmol) of diphenyl phosphine in 30 ml of methyl tert butyl ether, 2.6 ml (1.2 eq) of nBuLi in hexane was added dropwise while stirring at -5^oC under nitrogen. After 2 hrs of stirring, 1.2 eq. (1.1 g) of 2-chloro ethyl phenyl sulfide was added to the nBuli and the diphenyl sulfide reaction mixture at -5^oC. The mixture was then stirred for 3 hrs. During this time, it was allowed to warm up to the room temperature. The mixture was extracted using chloroform and 5% aqueous NaOH solution. The organic layer was treated with Na_2SO_4 and filtered. The filtrate was evaporated and the solid was collected. The compound was recrystallized using dichloromethane and hexane. Yield: (1.4 g) 78%. 1H NMR (300 MHz, $CDCl_3$) δ 7.51 – 7.06 (m, 15H), 3.04 – 2.85 (m, 2H), 2.46 – 2.25 (m, 2H). 31PNMR (δ = -15.74 ppm) relative to 85% H_3PO_4 (δ = 0 ppm).

Complex Synthesis:

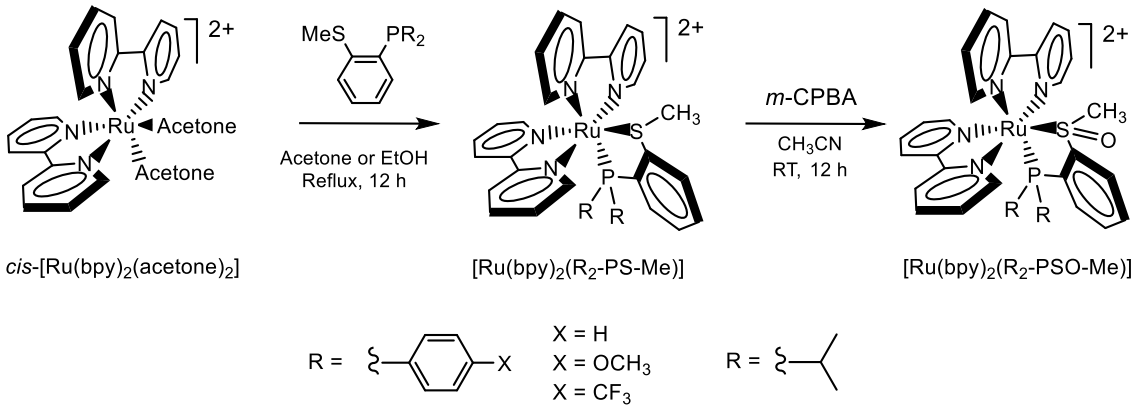

Scheme 6. General synthetic scheme for the ruthenium phosphine-thioether and ruthenium phosphine-sulfoxide complexes bearing phenyl-bridged P,S chelates.

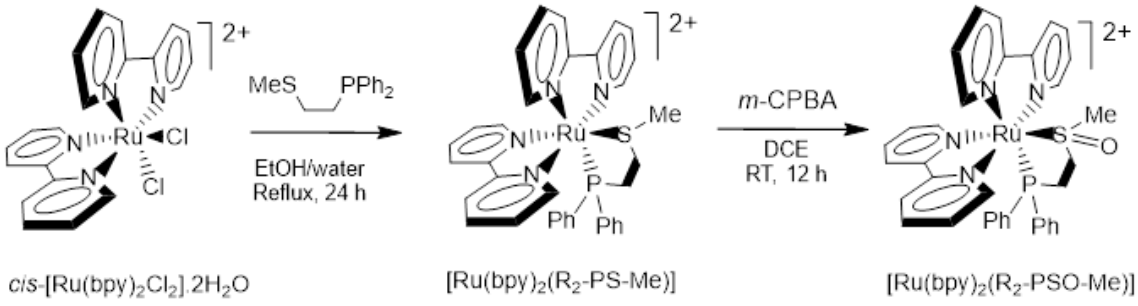

Scheme 7. General synthetic scheme for the ruthenium phosphine-thioether and ruthenium phosphine-sulfoxide complexes bearing ethyl-bridged P,S chelates.

$[Ru(bpy)_2(Ph_2\text{-}PS\text{-}Me)](PF_6)_2$ (RuL1)

The prepared *cis*-$[Ru(bpy)_2(acetone)_2](PF_6)_2$ (0.61 mmol) in $N_{2(g)}$ deaerated acetone (35 mL) was added **L1** (0.19 g, 0.61 mmol) and refluxed for 12 h. The solution was concentrated, dissolved in minimum acetone and precipitated into warm water (50 mL) containing 0.5 g, ammonium hexafluorophosphate (NH_4PF_6). It was filtered, washed with warm water (50 mL) and DEE (20 mL). The solid was dissolved in acetone, filtered and concentrated. It was recrystallized using methanol, filtered using a fine frit and washed with cold methanol. Yield 0.43 g, 70%. Crystals suitable for a single crystal X-ray diffraction were obtained by slow diffusion of DEE into DCM solution of **RuL1**. ^{1}H NMR (300MHz, RT, Acetone-d_6): δ (ppm) 8.89 (d, *J* = 8.1 Hz, 1H, -Ph), 8.84 (d, *J* = 8.1 Hz, 1H, -Ph), 8.75 (d, *J* = 5.7 Hz, 1H, -Bz), 8.57 (d, *J* = 8.1 Hz, 1H, -bpy), 8.47 (d, *J* = 8.1 Hz, 1H, -bpy), 8.40 (d, *J* = 5.4 Hz, 1H, -Bz), 8.16 – 8.35 (m, 2H, -Ph, 3H, -bpy), 8.07 (t, *J* = 7.8 Hz, 1H, -Bz), 7.52 – 7.90 (m, 11H, -bpy), 7.43 (t, *J* = 7.8 Hz, 1H, -Ph), 7.37 (t, *J* = 7.8 Hz, 1H, -Bz), 7.25 (t, *J* = 7.8 Hz, 1H, -Ph), 7.03 (dt, *J* = 7.8 Hz, 2.1 Hz, 2H, -Ph), 6.39 (t, *J* = 7.8 Hz, 2H, -Ph), 2.01 (s, 3H, $-CH_3$). ^{31}P NMR (δ = 67.12 ppm), relative to 85% H_3PO_4. ESI-MS: $[RuL1 - 2PF_6]^{2+}$, calculated *m/z* = 361.0604, observed *m/z* = 361.0588.

$[Ru(bpy)_2(Ph_2\text{-}PSO\text{-}Me)](PF_6)_2$ (RuL1O)

The complex **RuL1** (165 mg, 0.163 mmol) was dissolved in N_2 (g) deaerated acetonitrile (40 mL). In a separate 10 mL of acetonitrile, excess mCPB (183 mg 70% peroxo reagent, 1.06 mmol) was dissolved and added slowly to the **RuL1** solution. The combined solutions were stirred at RT for 12 hours. The solvent was removed by rotary evaporation. The

crude product was purified by precipitating using DEE, filtering and washing with a mixture of MeOH/DEE (1:1, v/v). Yield 160 mg, 96%. Crystals suitable for a single crystal X-ray diffraction were obtained by slow evaporation of mixed solvents; MeOH and CH_3CN or MeOH and DCM or slow diffusion of DEE into CH_3CN solution of **RuL1O**. ^{1}H NMR (300MHz, RT, Acetone-d_6): δ (ppm) 9.25 (d, *J* = 5.4 Hz, 1H), 8.94 (d, *J* = 8.1 Hz, 1H), 8.85 (d, *J* = 7.8 Hz, 1H), 8.76 (d, *J* = 7.8 Hz, 1H), 8.52 (d, *J* = 8.1 Hz, 1H), 8.39 (t, *J* = 7.8 Hz, 1H), 8.21 – 8.33 (m, 4H), 8.05 – 8.15 (m, 3H), 7.99 (d, *J* = 5.7 Hz, 1H), 7.85 (t, *J* = 5.7 Hz, 1H),b7.60 – 7.78 (m, 7H), 7.55 (t, *J* = 6.9 Hz, 1H), 7.35 (t, *J* = 6.6 Hz, 1H), 7.26 (t, *J* = 6.9 Hz, 1H, -Ph), 6.99 (t, *J* = 7.2 Hz, 2H, -Ph), 6.54 (t, *J* = 9.0 Hz, 2H, -Ph), 2.91 (s, 3H, $-CH_3$). ^{31}P NMR (δ = 65.92 ppm), relative to 85% H_3PO_4. ESI-MS: $[RuL1O - 2PF_6]^{2+}$, calculated *m/z* = 369.0578, observed *m/z* = 369.0567.

$[Ru(bpy)_2(Ph_2\text{-}PS^-)]PF_6$ (RuL1D)

The prepared *cis*-$[Ru(bpy)_2Cl_2]2H_2O$ (111 mg, 0.213 mmol) in $N_{2(g)}$ deaerated ethylene glycol (5 mL) was added **L1** (66 mg, 0.213 mmol) and refluxed for 1 h. While still hot, 20 mL of DI water containing 0.2 g of NH_4PF_6 was added to precipitate out the product. It was filtered, washed with warm water (50 mL) and DEE (20 mL). The solid was dissolved in acetone, filtered and concentrated. It was recrystallized using methanol, filtered using a fine frit and washed with cold methanol and DEE. Yield 96 mg, 53%. Green crystals suitable for a single crystal X-ray diffraction were obtained by slow diffusion of DEE into DCM solution of **RuL1**. ^{1}H NMR (300MHz, RT, Acetone-d_6): δ (ppm) 9.04 (d, *J* = 4.9 Hz, 1H), 8.41 (d, *J* = 8.0 Hz, 2H), 8.32 (d, *J* = 5.3 Hz, 1H), 8.13 (t, 2H), 7.86 – 7.99 (m, 4H), 7.71 (t, *J*

= 7.5 Hz, 1H), 7.31 – 7.60 (m, 10H), 6.95 – 7.27 (m, 5H), 6.84 (t, *J* = 8.2 Hz, 2H), 6.30 (t, *J* = 8.6 Hz, 2H). ^{31}P NMR (δ = 70.70 ppm), relative to 85% H_3PO_4.

[Ru(bpy)$_2$(*p*-MeOPh$_2$-PS-Me)](PF$_6$)$_2$ (RuL2)

Method A

The prepared *cis*-[Ru(bpy)$_2$Cl$_2$].2H$_2$O (130 mg, 0.250 mmol) in $N_{2(g)}$ deaerated ethanol/water (40 mL, 4:1, v/v) was added **L2** (93 mg, 0.250 mmol) and refluxed for 24 h. It was concentrated to remove EtOH. DI water (50 mL) was added and filtered using a fine frit. The filtrate was precipitated by adding aqueous solution containing 0.25 g, NH_4PF_6. It was extracted using DCM (50 mL x 2), dried using anhydrous MgSO4 solid, filtered and concentrated. The solid obtained was dissolved in minimum acetone and precipitated in anhydrous DEE and filtered using a fine frit. Yield 0.214 g, 79%.

Method B

The prepared *cis*-[Ru(bpy)$_2$(acetone)$_2$](PF$_6$)$_2$ (0.565 mmol) in $N_{2(g)}$ deaerated acetone (50 mL) was added **L2** (251 mg, 0.565 mmol) and refluxed for 12 h. The solution was concentrated, dissolved in minimum acetone and precipitated into warm water (50 mL) containing 0.5 g, NH_4PF_6. After cooling to RT, it was extracted using dichloromethane (50 mL x 2), dried using anhydrous MgSO4 solid, filtered and concentrated. The solid obtained was dissolved in minimum acetone and precipitated in cold 100 mL absolute ethanol. (It can also be recrystallized using EtOH). It was filtered using a fine frit and washed with cold EtOH followed by anhydrous DEE. Yield 0.317 g, 51%. ^{1}H NMR (300MHz, RT, CH_3CN): δ (ppm) 8.90 (d, *J* = 8.4 Hz, 1H), 8.85 (d, *J* = 8.2 Hz, 1H), 8.76 (d, *J* = 5.6 Hz, 1H), 8.60 (d, *J* =

8.1 Hz, 1H), 8.51 (d, *J* = 8.0 Hz, 1H), 8.11 – 8.39 (m, 7H), 7.80 – 7.87 (m, 3H), 7.52 – 7.76 (m, 5H, (2H, -PhOCH$_3$)), 7.38 – 7.49 (m, 2H), 7.09 (dd, *J* = 8.8 Hz, 1.5 Hz, 2H, -PhOCH$_3$), 6.59 (dd, *J* = 8.8 Hz, 1.8 Hz, 2H, -PhOCH$_3$), 6.24 (td, *J* = 8.8 Hz, 1.6 Hz, 2H, -PhOCH$_3$),3.84 (s, 3H, -OCH$_3$), 3.74 (s, 3H, -OCH$_3$), 1.98 (s, 3H, -CH$_3$). ^{31}P NMR (Acetone-d$_6$, δ = 64.57 ppm), relative to 85% H_3PO_4. ESI-MS: [RuL2 − 2PF$_6$]$^{2+}$, calculated *m/z* = 391.0709, observed *m/z* = 391.0692.

[Ru(bpy)$_2$(*p*-MeOPh$_2$-PSO-Me)](PF$_6$)$_2$ (RuL2O)

The compound was oxidized by following a similar procedure as **RuL1O. RuL2** (120 mg, 0.111 mmol), mCPBA (75 mg, 70% peroxo reagent, 0.437 mmol). Yield 119 mg, 99%. Crystals suitable for a single crystal X-ray diffraction were obtained by slow evaporation of mixed solvents, MeOH and DCM containing **RuL3O**. ^{1}H NMR (300MHz, RT, CH$_3$CN): δ (ppm) 9.28 (d, *J* = 4.9 Hz, 1H), 8.95 (d, *J* = 8.1 Hz, 1H), 8.86 (d, *J* = 7.7 Hz, 1H), 8.71 (d, *J* = 7.2 Hz, 1H), 8.56 (d, *J* = 7.8 Hz, 1H), 7.95 – 8.43 (m, 10H), 7.86 (br, 1H), 7.73 (t, *J* = 5.7 Hz, 1H), 7.52 – 7.64 (m, 4H), 7.43 (t, *J* = 8.7 Hz, 1H), 7.16 (d, *J* = 7.7 Hz, 2H, -PhOCH$_3$), 6.55 (d, *J* = 7.8 Hz, 2H, -PhOCH$_3$), 6.37 (t, *J* = 8.7 Hz, 2H, -PhOCH$_3$), 3.87 (s, 3H, -OCH$_3$), 3.73 (s, 3H, -OCH$_3$), 2.88 (s, 3H, -CH$_3$). ^{31}P NMR (Acetone-d$_6$, δ = 64.73 ppm), relative to 85% H_3PO_4. ESI-MS: [RuL2O − 2PF$_6$]$^{2+}$, calculated *m/z* = 399.0684, observed *m/z* = 399.0673.

[Ru(bpy)$_2$(*p*-CF$_3$Ph$_2$-PS-Me)](PF$_6$)$_2$ (RuL3)

The prepared *cis*-[Ru(bpy)$_2$(acetone)$_2$](PF$_6$)$_2$ (0.565 mmol) in $N_{2(g)}$ deaerated acetone (50 mL) was added **L3** (251 mg, 0.565 mmol) and refluxed for 12 h. The solution was concentrated, dissolved in minimum acetone and precipitated into warm water (50 mL)

containing 0.5 g, NH_4PF_6. After cooling to RT, it was extracted using dichloromethane (50 mL x 2). The DCM layer was washed with DI water (50 mL). The DCM layer concentrated, re-dissolved in acetone, dried using anhydrous $MgSO_4$ solid, filtered and concentrated. It was recrystallized using methanol, filtered using a fine frit and washed with cold MeOH followed by anhydrous DEE. Crystals suitable for a single crystal X-ray diffraction were obtained by slow diffusion of DEE into DCM solution of **RuL3**. A few drops of CH_3CN was added to the DCM layer to ensure complete solubility of the complex. Yield 0.415 g, 64%. ^{1}H NMR (300MHz, RT, CH_3CN): δ (ppm) 8.58 (d, *J* = 8.1 Hz, 1H), 8.53 (d, *J* = 8.4 Hz, 1H), 8.47 (d, *J* = 5.4 Hz, 1H), 8.28 (d, *J* = 7.8 Hz, 1H), 8.01 – 8.21 (m, 6H), 7.98 (d, *J* = 5.7 Hz, 1H), 7.66 – 7.92 (m, 8H), 7.50 (d, *J* = 5.4 Hz, 1H), 7.45 (t, *J* = 6.3 Hz, 1H), 7.37 (t, *J* = 6.6 Hz, 1H), 7.14 – 7.26 (m, 4H, (2H, -Ph)), 6.45 (t, *J* = 9.0 Hz, 2H, -Ph), 1.76 (s, 3H, -CH_3). ^{31}P NMR (Acetone-d_6, δ = 68.57 ppm), relative to 85% H_3PO_4.^{19}F NMR in Acetone-d_6: δ (ppm) PF_6^- (doublet at 61.34 and 61.43) and **RuL3** (68.79 and 71.30) relative to (hexafluorobenzene, C_6F_6). ESI-MS: $[RuL3 - 2PF_6]^{2+}$, calculated *m/z* = 429.0478, observed *m/z* = 429.0489.

$[Ru(bpy)_2(p\text{-}CF_3Ph_2\text{-}PSO\text{-}Me)](PF_6)_2$ (RuL3O)

The compound was oxidized by following a similar procedure as **RuL1O. RuL3** (0.2 g, 0.174 mmol), mCPBA (0.195 g 70% peroxo reagent, 1.13 mmol). Yield 0.196 g, 96%. Crystals suitable for a single crystal X-ray diffraction were obtained by slow evaporation of mixed solvents, MeOH and DCM containing **RuL3O**. ^{1}H NMR (300MHz, RT, Acetone-d_6): δ (ppm) 9.27 (d, *J* = 5.2 Hz, 1H), 8.98 (d, *J* = 7.8 Hz, 1H), 8.88 (d, *J* = 8.1 Hz, 1H), 8.81 (d, *J* = 7.8 Hz, 1H), 8.60 (d, *J* = 8.0 Hz, 1H), 7.94 – 8.45 (m, 14H), 7.88 (br, 1H), 7.77 (t, *J* = 6.4 Hz, 1H), 7.64 (t, *J* = 6.5 Hz, 1H), 7.53 (t, *J* = 6.6 Hz, 1H), 7.41 (t, *J* = 6.3 Hz, 1H), 7.37 (d, *J* = 7.6 Hz, 2H, -

$PhCF_3$), 6.84 (t, *J* = 9.1 Hz, 2H, -$PhCF_3$), 2.96 (s, 3H, -CH_3).^{31}P NMR (Acetone-d_6, δ = 68.57 ppm), relative to 85% H_3PO_4.^{19}F NMR, Acetone-d_6: δ (ppm) PF_6^- (doublet at 61.37 and 61.42), **RuL3O** (68.70, and 71.21) relative to (hexafluorobenzene, C_6F_6). ESI-MS: [RuL3O − $2PF_6$]$^{2+}$, calculated *m/z* = 437.0452, observed *m/z* = 437.0448.

$Ru(bpy)_2(iPr_2$-PS-Me)]$(PF_6)_2$ (RuL4)

The prepared *cis*-[$Ru(bpy)_2(acetone)_2$]$(PF_6)_2$ (0.58 mmol) in $N_{2(g)}$ deaerated acetone (50 mL) was added **L4** (140 mg, 0.58 mmol) and refluxed for 12 h. The solution was concentrated, dissolved in minimum acetone and precipitated into warm water (50 mL) containing 0.5 g, NH_4PF_6. After cooling to RT, it was extracted using dichloromethane (50 mL x 2). The DCM layer was washed with DI water (50 mL). The organic layer was dried using anhydrous $MgSO_4$ solid, filtered and concentrated. It was recrystallized using methanol, filtered using a fine frit and washed with cold DEE. Yield 0.26 g, 47%. Crystals suitable for a single crystal X-ray diffraction were obtained by slow diffusion of DEE into DCE solution of **RuL4** in a freezer. ^{1}H NMR (300MHz, RT, Acetone-d_6): δ (ppm) 9.66 (d, *J* = 6.0 Hz, 1H), 8.86 – 8.74 (m, 4H), 8.46 (t, *J* = 7.5 Hz, 1H), 8.31 (t, *J* = 7.8 Hz, 1H), 8.25 – 8.17 (m, 4H), 8.11 – 7.98 (m, 3H), 7.79 – 7.70 (m, 3H), 7.61 – 7.52 (m, 3H), 3.23 (sep, 1H, *J* = 6.9 Hz, - *i*Pr), 1.92 (s, 3H, -CH_3), 1.55 (sep, 1H, - *i*Pr), 1.36 – 1.29 (m, 3H, -*i*Pr), 0.86 – 0.79 (m, 3H, -*i*Pr), 0.62 – 0.55 (m, 3H, -*i*Pr), 0.50 – 0.42 (m, 3H, -*i*Pr). ^{31}P NMR (δ = 67.23 ppm), relative to 85% H_3PO_4. ESI-MS: [RuL4 − $2PF_6$]$^{2+}$, calculated *m/z* = 327.0760, observed *m/z* = 327.0756.

$[Ru(bpy)_2(iPr_2\text{-}PSO\text{-}Me)](PF_6)_2$ (RuL4O)

The complex was synthesized by following a similar procedure as **RuL1O. RuL4** (117 mg, 0.124 mmol), excess mCPBA (138 mg, 70% peroxo reagent, 0.81 mmol). Yield 108 mg, 91%.

Crystals suitable for a single crystal X-ray diffraction were obtained by slow evaporation of mixed solvents, EtOH and DCM containing **RuL4O**. ^{1}H NMR (300MHz, RT, Acetone-d_6): δ (ppm) 10.12 (d, *J* = 6.0 Hz, 1H), 8.80 – 8.93 (m, 4H), 8.28 – 8.52 (m, 6H), 8.03 – 8.11 (m, 4H), 7.95 (d, *J* = 6.0 Hz, 1H), 7.84 (d, *J* = 6.0 Hz, 1H), 7.65 – 7.69 (m, 3H), 3.30 (sep, 1H, *J* = 6.0 Hz, - *i*Pr), 2.77 (s, 3H, -CH_3), 1.89 (sep, 1H, - *i*Pr), 1.24 – 1.31 (m, 3H, -*i*Pr), 0.71 – 0.80 (m, 6H, -*i*Pr), 0.54 – 0.61 (m, 3H, -*i*Pr). ^{31}P NMR (δ = 71.75 ppm), relative to 85% H_3PO_4. ESI-MS: $[RuL4O - 2PF_6]^{2+}$, calculated *m/z* = 335.0735, observed *m/z* = 335.0734.

$[Ru(bpy)_2(Ph_2\text{-}PeS\text{-}Me)](PF_6)_2$ (RuL5)

The prepared *cis*-$[Ru(bpy)_2Cl_2].2H_2O$ (0.3 g, 0.577 mmol) in N_2(g) deaerated Ethanol/water (50 mL, 4:1, v/v) was added **L5** (150 mg, 0.577 mmol) and refluxed for 24 h. It was concentrated to remove EtOH. DI water added and filtered using a fine frit. The filtrate was precipitated by adding aqueous solution containing 0.5 g, NH_4PF_6. It was filtered, washed with DI water (50 mL) and DEE (20 mL). The solid obtained was dissolved in acetone, dried using anhydrous $MgSO_4$ solid, filtered and concentrated. It was precipitated and washed using anhydrous DEE. Yield 0.456 g, 82%. ^{1}H NMR (300MHz, RT, Acetone-d_6): δ (ppm) 8.97 (d, *J* = 5.4 Hz, 1H), 8.87 (d, *J* = 8.3 Hz, 1H), 8.79 (d, *J* = 8.1 Hz, 1H), 8.72 (d, *J* = 5.5 Hz, 1H), 8.58 (d, *J* = 8.2 Hz, 1H), 8.30 – 8.37 (m, 3H), 8.19 – 8.27 (m,

2H), 8.00 – 8.06 (dt, *J* = 7.8 Hz, 1.2 Hz 1H), 7.76 – 7.89 (m, 3H), 7.66 – 7.71 (dt, *J* = 7.8 Hz, 1.2 Hz 1H), 7.46 – 7.63 (m, 6H), 7.11 – 7.17 (dt, *J* = 7.8 Hz, 1.2 Hz, 1H, -Ph), 6.94 – 7.00 (dt, *J* = 7.8 Hz, 2.2 Hz, 2H, -Ph), 6.62 – 6.69 (t, *J* = 9.0 Hz, 2H, -Ph), 3.56 – 3.65 (m, 2H, -PCH_2CH_2S-), 3.37 (br, 2H, -PCH_2CH_2S-), 1.67 (s, 3H, -CH_3). ^{31}P NMR (δ = 62.09 ppm in Acetone-d_6), relative to 85% H_3PO_4. ESI-MS: $[RuL5 - 2PF_6]^{2+}$, calculated *m/z* = 337.0604, observed *m/z* = 337.0597.

$[Ru(bpy)_2(Ph_2\text{-}PeSO\text{-}Me)](PF_6)_2$ (RuL5O)

The complex was synthesized by following a similar procedure as **RuL1O. RuL5** 252 mg, 0.261 mmol), excess mCPB (120 mg, 70% peroxo reagent, 0.680 mmol). Yield 222 mg, 90%. The major isomer is reported. ^1H NMR (300MHz, RT, Acetone-d_6): δ (ppm 9.48 (d, *J* = 5.7 Hz, 1H), 8.96 (d, *J* = 7.9 Hz, 1H), 8.83 (d, *J* = 8.2 Hz, 1H), 8.64 (d, *J* = 8.1 Hz, 1H), 8.41 – 8.47 (m, 2H), 8.26 – 8.35 (m, 3H), 8.03 – 8.08 (m, 2H), 7.70 – 7.83 (m, 4H), 7.44 – 7.65 (m, 6H), 7.17 – 7.22 (dt, *J* = 7.8 Hz, 1.5 Hz, 1H, -Ph), 7.01 – 7.07 (dt, *J* = 7.8 Hz, 2.2 Hz, 2H, -Ph), 6.78 – 6.84 (t, *J* = 9.0 Hz, 2H, -Ph), 4.33 – 4.51 (m, $1H_b$, -PCH_2CH_2S-), 4.04 – 4.24 (m, $1H_b$, -PCH_2CH_2S-), 3.68 – 3.81 (m, $1H_a$, -PCH_2CH_2S-), 3.26 – 3.41 (m, $1H_a$, -PCH_2CH_2S-), 2.69 (s, 3H, -CH_3). ^{31}P NMR (δ = 58.51 ppm, 87% (major); 57.36 ppm, 13% (minor) in Acetone-d_6), relative to 85% H_3PO_4. ESI-MS: $[RuL5O - 2PF_6]^{2+}$, calculated *m/z* = 345.0578, observed *m/z* = 345.0576.

$[Ru(bpy)_2(tBu,Ph\text{-}PS\text{-}Me)](PF_6)_2$ (RuL6)

The prepared *cis*-$[Ru(bpy)_2(acetone)_2](PF_6)_2$ (0.4 g, 0.488 mmol) in N_2 (g) deaerated acetone (50 mL) was added **L6** (141 mg, 0.488 mmol) and refluxed for 12 h. The solution

was concentrated, dissolved in minimum acetone and precipitated into warm water (50 mL) containing 0.5 g, NH_4PF_6. After cooling to RT, it was extracted using dichloromethane (50 mL x 2). The DCM layer was washed with DI water (50 mL). The organic layer was dried using anhydrous $MgSO_4$ solid, filtered and concentrated. It was recrystallized using methanol, filtered using a fine frit and washed with cold DEE. Yield 0.28 g, 58%. ^{1}H NMR (300MHz, RT, Acetone-d_6): δ (ppm) 8.70 (s, 1H), 8.52 – 8.49 (d, 1H), 8.45 – 8.43 (d, 1H), 8.29 – 8.15 (m, 4H), 8.05 – 7.92 (m, 5H), 7.86 – 7.70 (m, 3H), 7.58 – 7.52 (t, 1H), 7.42 – 7.36 (t, 1H), 7.33 – 7.19 (m, 3H), 7.11 – 7.0 (m, 2H), 6.79 (s, 1H), 6.2 (s, 1H), 1.86 (s, 3H), 1.21 – 1.61 (d, 9H). ^{31}P NMR (δ = 73.866 ppm), relative to 85% H_3PO_4.

$[Ru(bpy)_2(tBu,Ph\text{-}PS\text{-}Me)](PF_6)_2$ (RuL6O)

The complex was synthesized by following a similar procedure as **RuL1O. RuL6** (150 mg, 0.151 mmol), excess mCPBA (165 mg, 70% peroxo reagent, 0.97 mmol). Yield 140 mg, 92%.

Crystals suitable for a single crystal X-ray diffraction were obtained by slow evaporation of mixed solvents, EtOH and DCM containing **RuL6O**. ^{1}H NMR (300MHz, RT, Acetone-d_6): δ (ppm) 9.38 – 9.29 (q, 1H), 9.00 – 8.97 (d, 1H), 8.86 – 8.70 (m, 2H), 8.61 – 8.57 (t, 1H), 8.50 – 8.45 (d, 1H), 8.47 – 8.19 (m, 5H), 8.10 – 7.95 (m, 4H), 7.89 – 7.85 (d, 1H), 7.72 – 7.65 (m, 1H), 7.53 – 7.44 (m, 2H), 7.36 (d, 1H), 7.30 – 7.24 (t, 1H), 6.95 (s, 2H), 6.60 – 6.53 (t, 1H), 6.47 – 6.39 (q, 1H). ^{31}P NMR (δ = 75.070 ppm), relative to 85% H_3PO_4.

$[Ru(bpy)_2(Ph_2\text{-}PeS\text{-}Ph)](PF_6)_2$ (RuL7)

30 mL of DCE (dichloroethane) was set aside sparging with nitrogen. 52 mg (0.1 mmol) of $Ru(bpy)_2Cl_2.2H_2O$ and 1.2 eq (40.3 mg) of L7 and 2.2 equivalent of silver hexafluorophosphate was added to a round bottom flask. To this flask the previously sparged DCE was added and refluxed overnight under nitrogen. The solution was allowed to cool and filtered through fine frit. The residue, silver chloride was discarded, and the filtrate was evaporated. The residue was dissolved in minimum volume of acetonitrile and precipitated in diethyl ether. The precipitate was collected using fine frit and washed with 50 mL of 20% methanol in diethyl ether. The crystals were grown by allowing diethyl ether to slowly diffuse into the acetonitrile solution of RuL7. Yield: 60% (61.8 mg). ^{1}H NMR (300 MHz, Acetone) δ 9.27 (d, *J* = 5.5 Hz, 1H), 8.59 (t, *J* = 7.5 Hz, 2H), 8.50 – 7.78 (m, 11H), 7.58 (dd, *J* = 18.4, 11.5 Hz, 6H), 7.42 – 7.27 (m, 1H), 7.18 (t, *J* = 7.4 Hz, 2H), 7.02 (t, *J* = 7.0 Hz, 2H), 6.90 (t, *J* = 7.6 Hz, 2H), 6.83 – 6.57 (m, 4H), 4.14 – 3.78 (m, 2H), 3.76 – 3.49 (m, 2H). ^{31}PNMR (d = 62.17 ppm) relative to 85% H_3PO_4 (d = 0 ppm). ESI-MS $[M\text{-}PF_6]^+$ Calculated m/z= 881.1005 Observed m/z = 881.1016.

$[Ru(bpy)_2(Ph_2\text{-}PeS\text{-}Ph)](PF_6)_2$ (RuL7O)

50 mg (0.048 mmol) of RuL7 was dissolved in 20 mL of acetonitrile sparged with nitrogen. 2 eq of meta chloro perbenzoic acid dissolved in acetonitrile was added dropwise to the solution and stirred for 3 hours at room temperature. The solvent was then evaporated, and the residue was dissolved in methanol and precipitated in diethyl ether and the precipitate was collected using a fine frit, washed with 50 mL of 20%

methanol in diethyl ether. ^{1}H NMR (300 MHz, Acetone) δ 9.74 (d, *J* = 5.9 Hz, 1H), 8.68 (d, *J* = 8.1 Hz, 1H), 8.43 (d, *J* = 7.4 Hz, 2H), 8.32 (t, *J* = 7.9 Hz, 3H), 8.14 (dt, *J* = 21.3, 7.7 Hz, 3H), 7.91 (d, *J* = 5.4 Hz, 1H), 7.80 (dd, *J* = 16.1, 8.9 Hz, 3H), 7.72 – 7.50 (m, 6H), 7.43 (t, *J* = 6.6 Hz, 1H), 7.35 (t, *J* = 7.4 Hz, 1H), 7.23 (t, *J* = 7.5 Hz, 1H), 7.08 (t, *J* = 8.0 Hz, 4H), 7.00 – 6.84 (m, 4H), 4.77 (d, *J* = 6.0 Hz, 1H), 4.35 (d, *J* = 26.2 Hz, 1H), 3.96 – 3.64 (m, 2H). ^{31}PNMR (d = 60.13 ppm) relative to 85% H_3PO_4 (d = 0 ppm). ESI-MS $[M\text{-}PF_6]^+$ Calculated m/z= 897.0954 Observed m/z = 897.0950.

NMR

Table 8: *Selected chemical shifts of the ligands and ruthenium complexes from this study.*

Molecule	^{31}P NMR Shift (ppm)	^{1}H NMR Shift (S – C<u>H</u>$_3$, ppm)	Solvent
L1	-14.09	2.44	$CDCl_3$
RuL1	67.12	1.94	Acetone-D_6
RuL1O	65.91	2.84	Acetone-D_6
L2	-17.45	2.43	$CDCl_3$
RuL2	64.57	2.05	Acetone-D_6
RuL2O	64.73	2.85	Acetone-D_6
L3	-14.44	2.46	$CDCl_3$
RuL3	68.56	1.76	Acetone-D_6
RuL3O	67.63	2.96	Acetone-D_6
L4	-5.02	2.43	$CDCl_3$
RuL4	67.23	1.92	Acetone-D_6
RuL4O	71.63	2.78	Acetone-D_6
L5	-16.79	2.10	$CDCl_3$
RuL5	61.61	1.67	Acetone-D_6
RuL5O	58.50	2.69	Acetone-D_6
L6	--	2.43	$CDCl_3$
RuL6	74.06	2.06	Acetone-D_6
RuL6O	76.50	3.19	Acetone-D_6
L7	-15.35	NA	$CDCl_3$
RuL7	62.21	NA	Acetone-D_6
RuL7O	60.14	NA	Acetone-D_6

P,S ligand precursors:

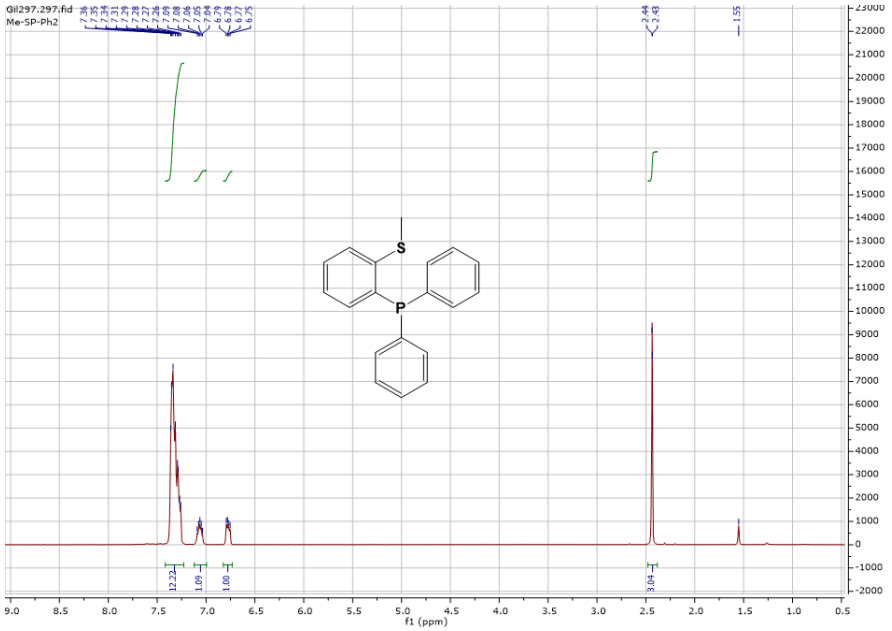

Figure 32: *^{1}H NMR of L1*

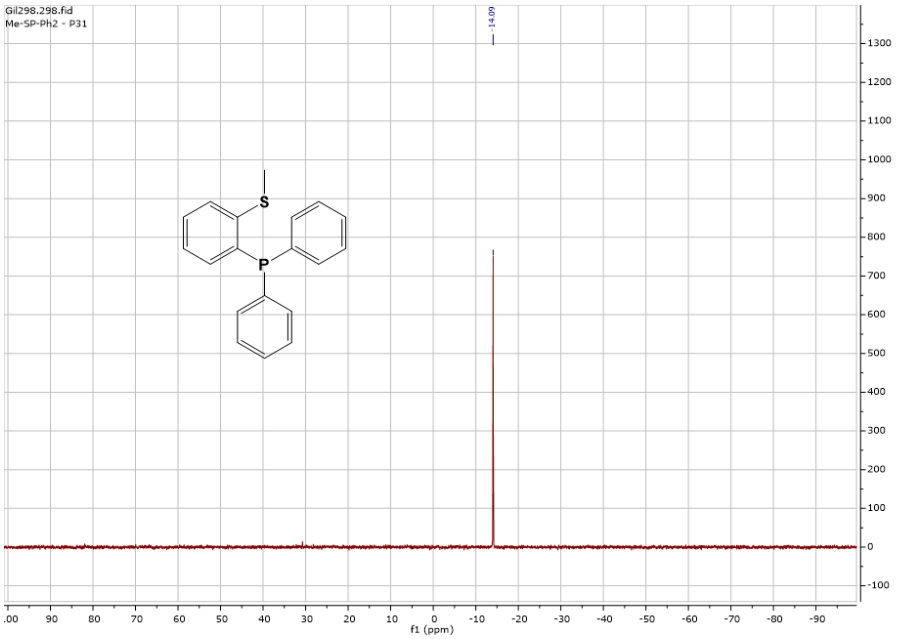

Figure 33: *^{31}P NMR of L1*

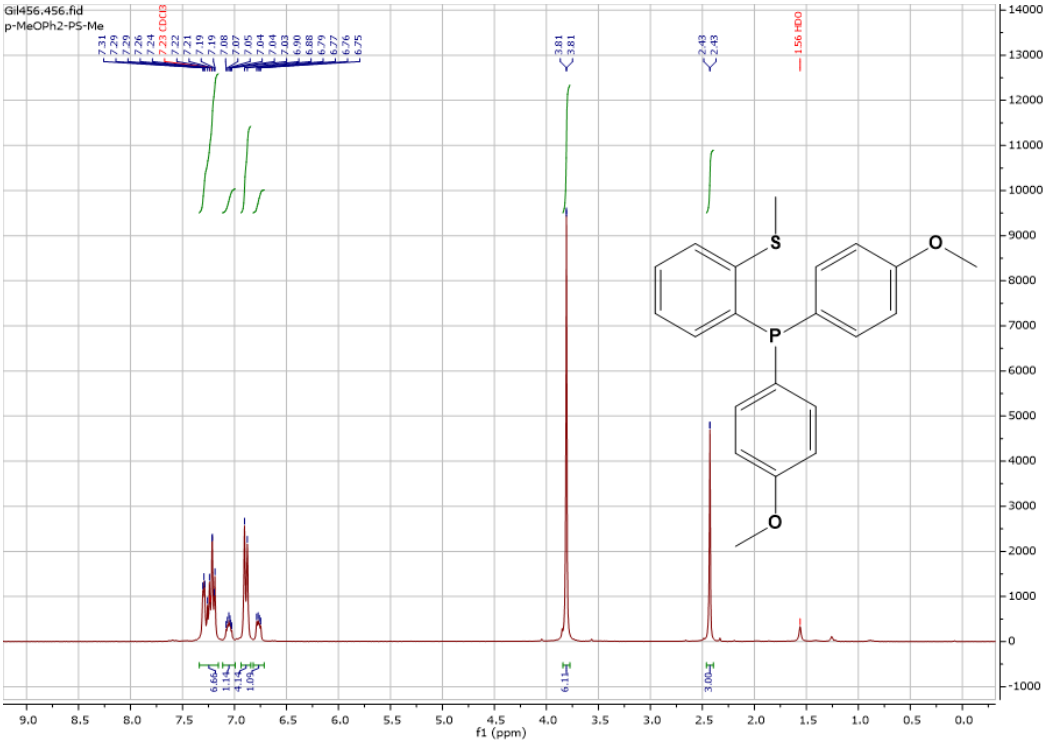

Figure 34: *^{1}H NMR of L2*

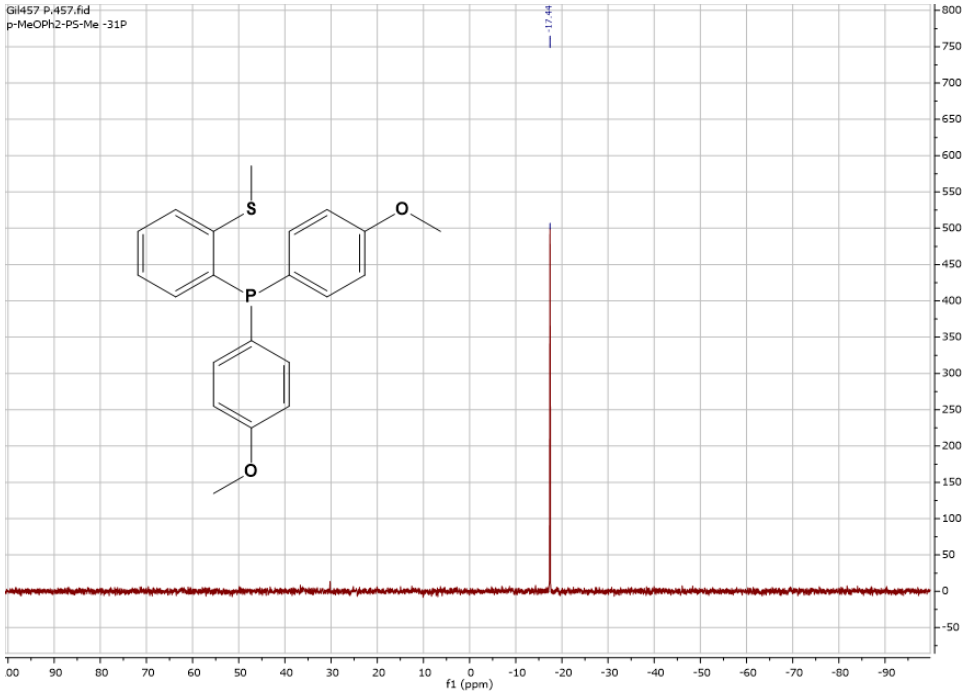

Figure 35: *^{31}P NMR of L2*

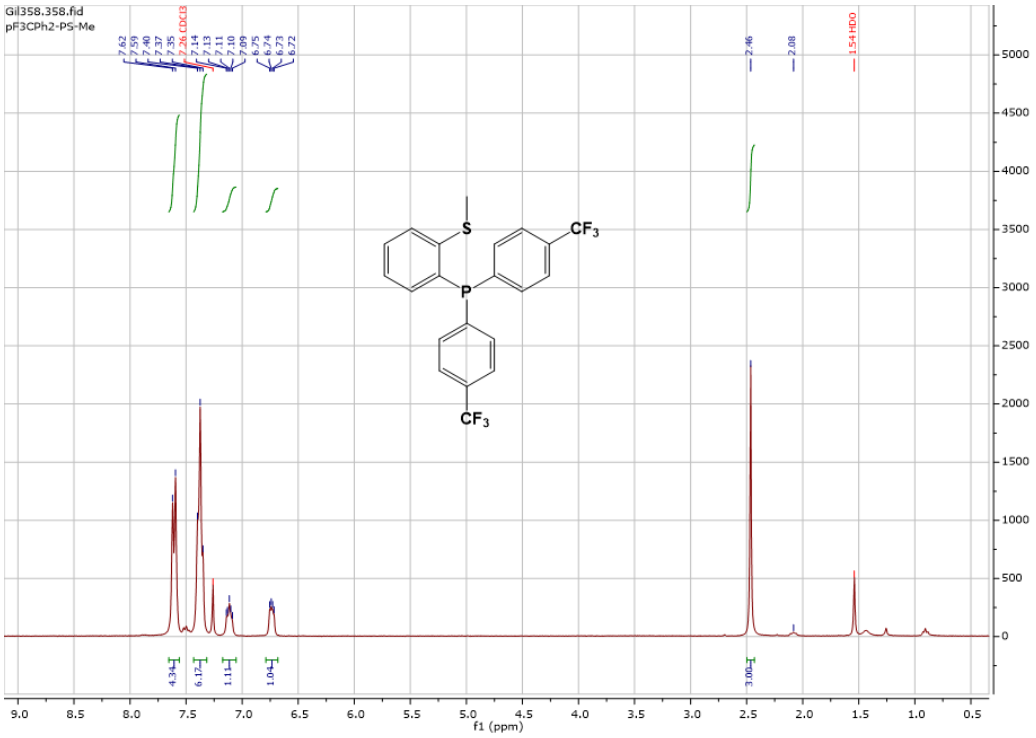

Figure 36: *^{1}H NMR of L3*

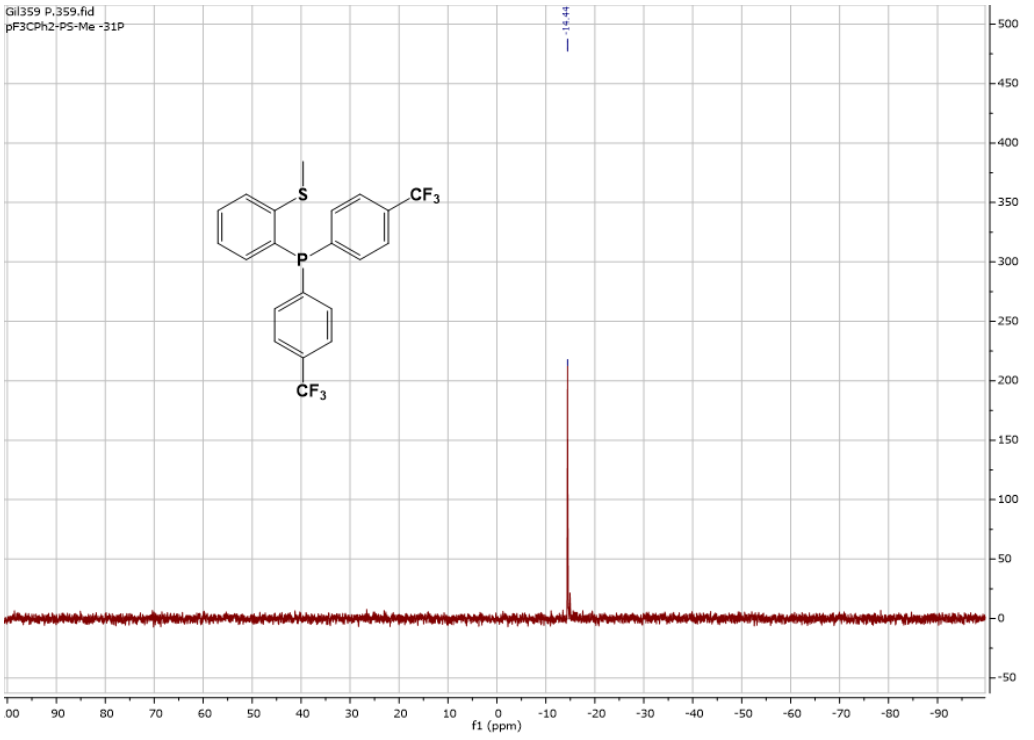

Figure 37: *^{31}P NMR of L3*

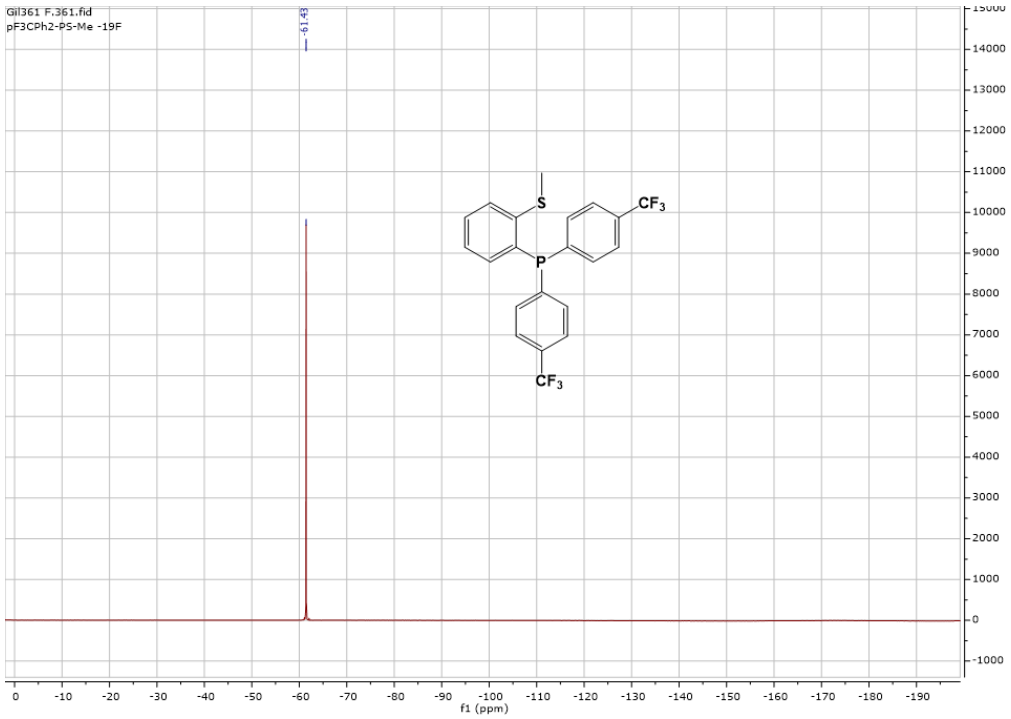

Figure 38: *^{19}F NMR of L3*

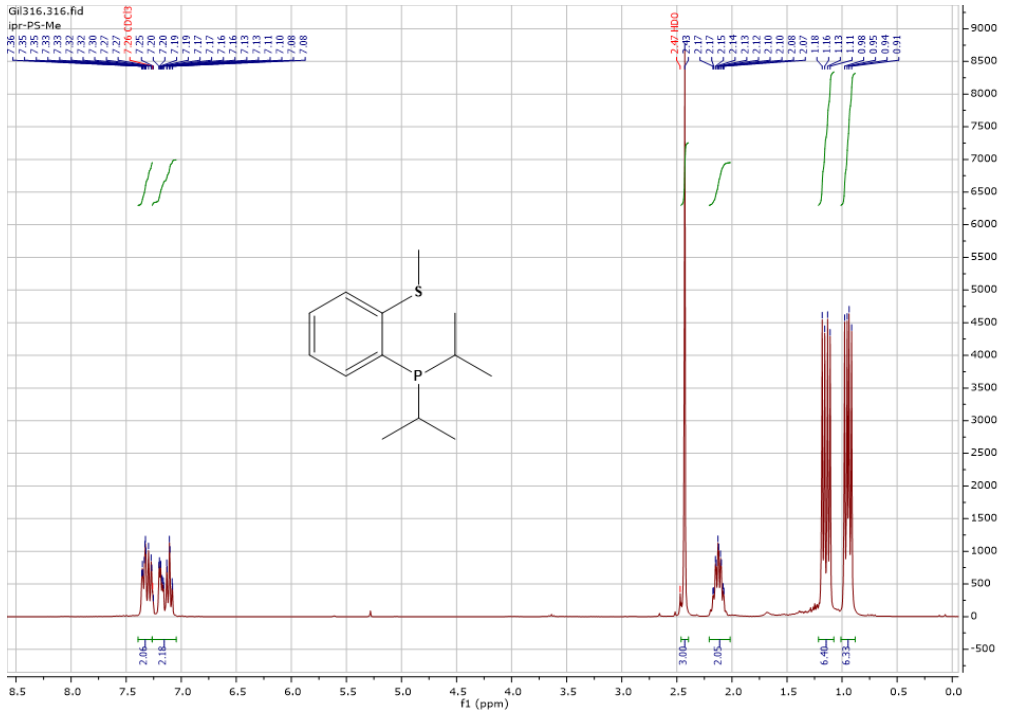

Figure 39: *^{1}H NMR of L4*

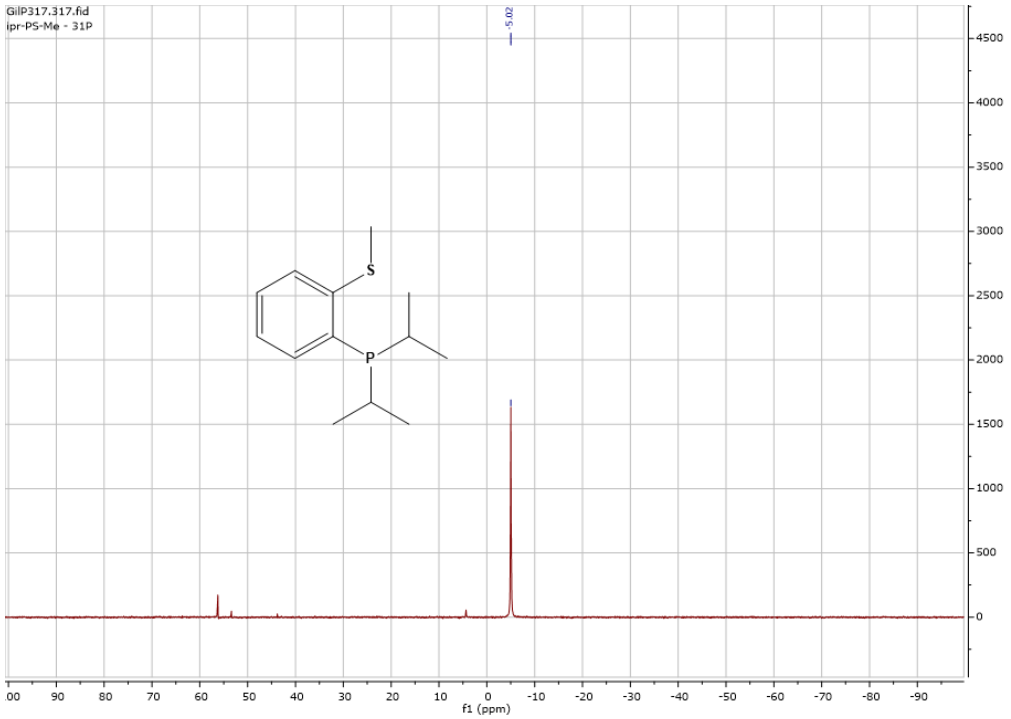

Figure 40: *^{31}P NMR of L4*

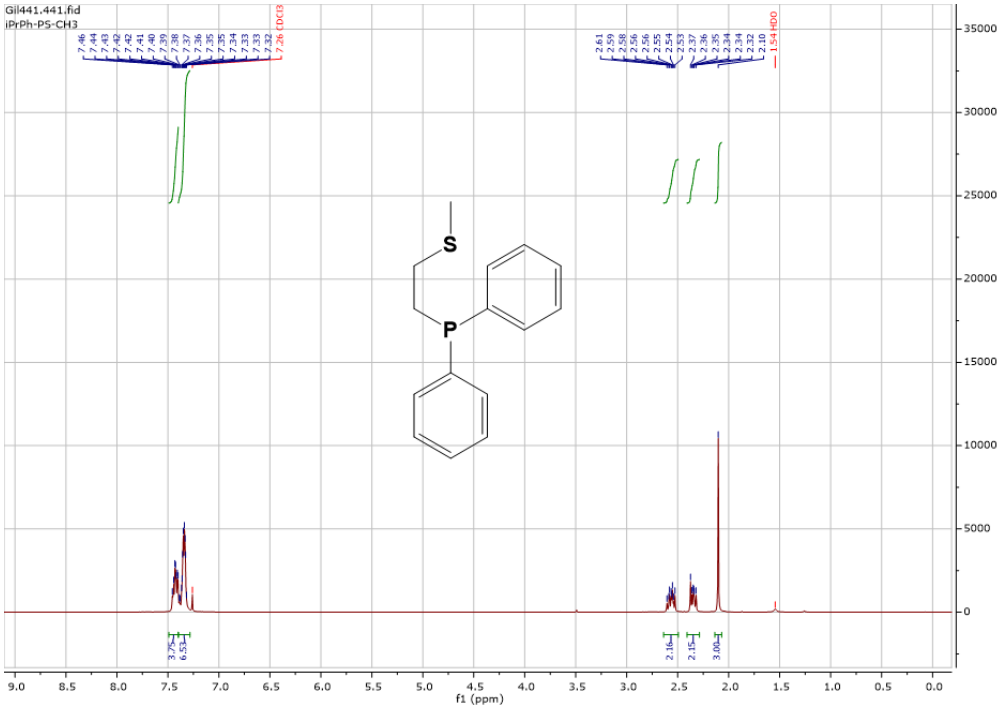

Figure 41: *^{1}H NMR of L5*

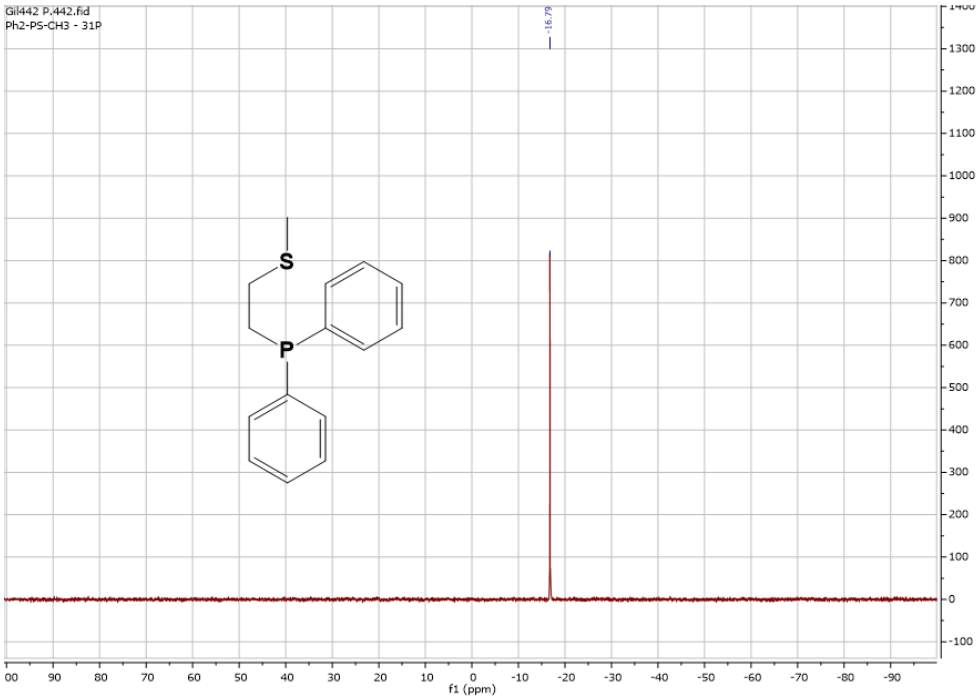

Figure 42: *^{31}P NMR of L5*

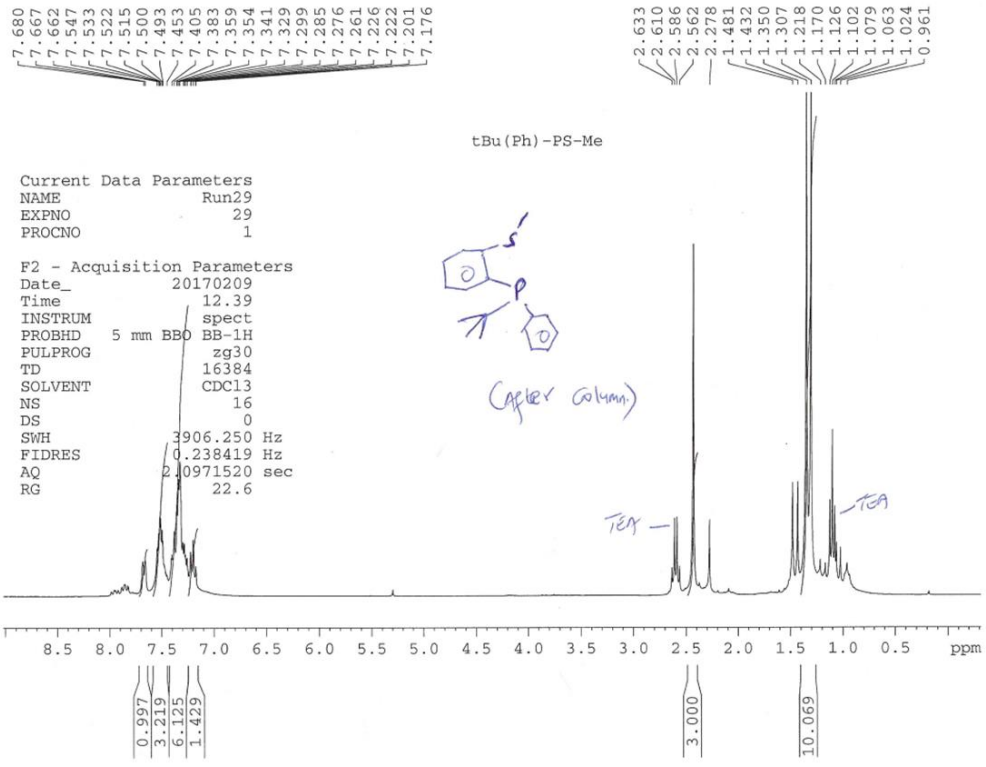

Figure 43: *^{1}H NMR of L6*

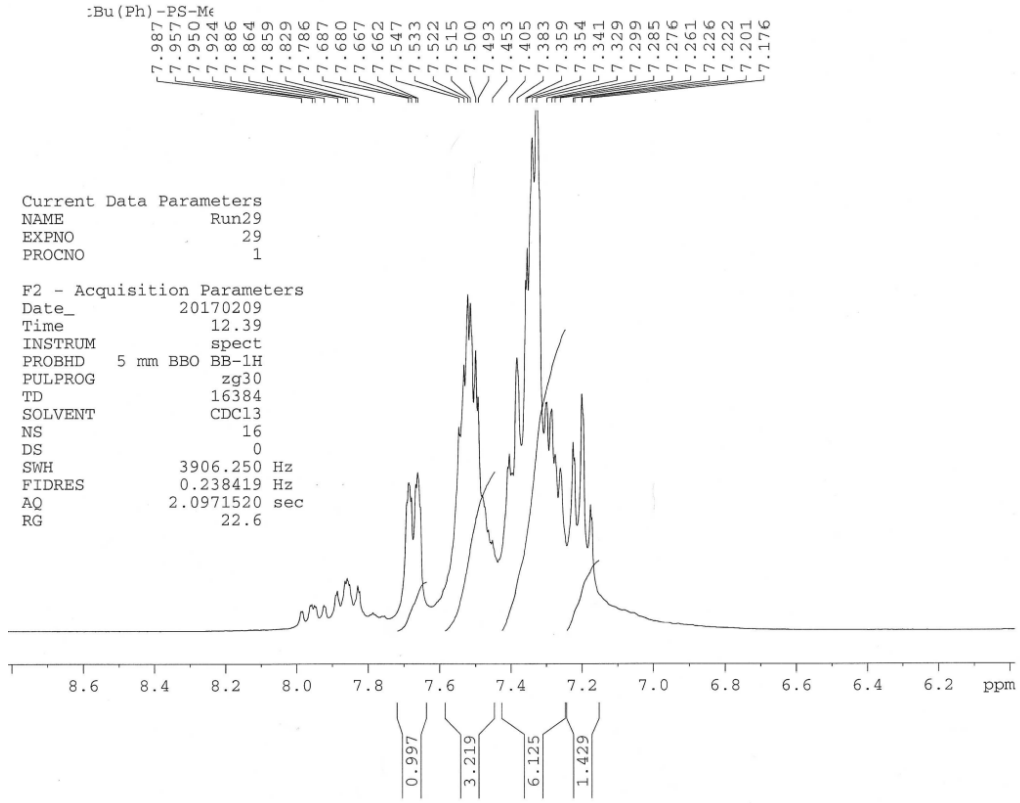

Figure 44: *^{1}H NMR of L6*

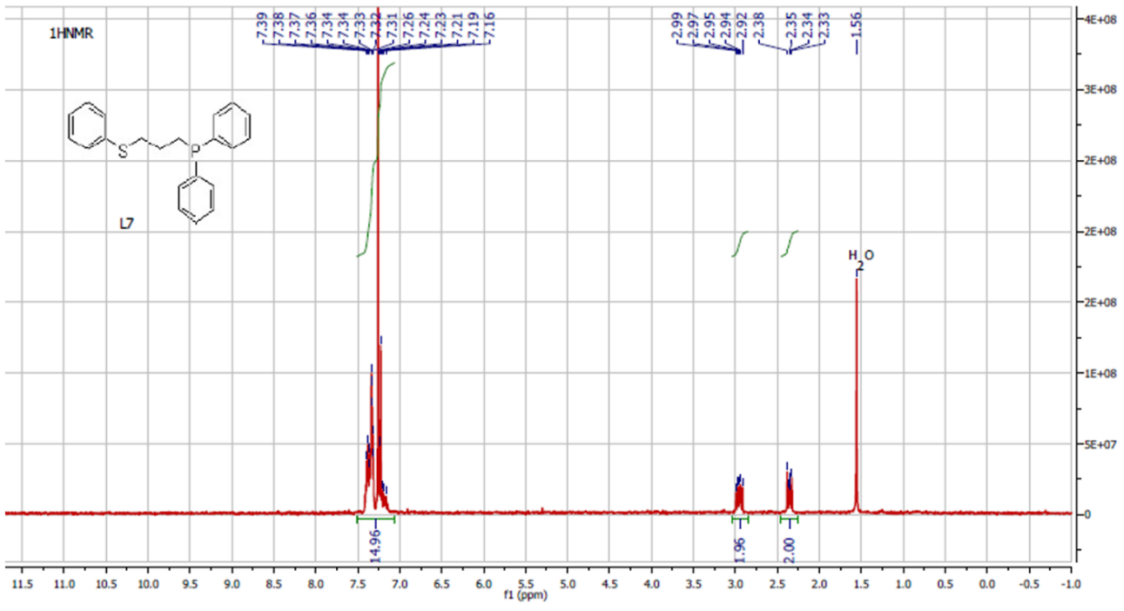

Figure 45: *^{1}H NMR of L7*

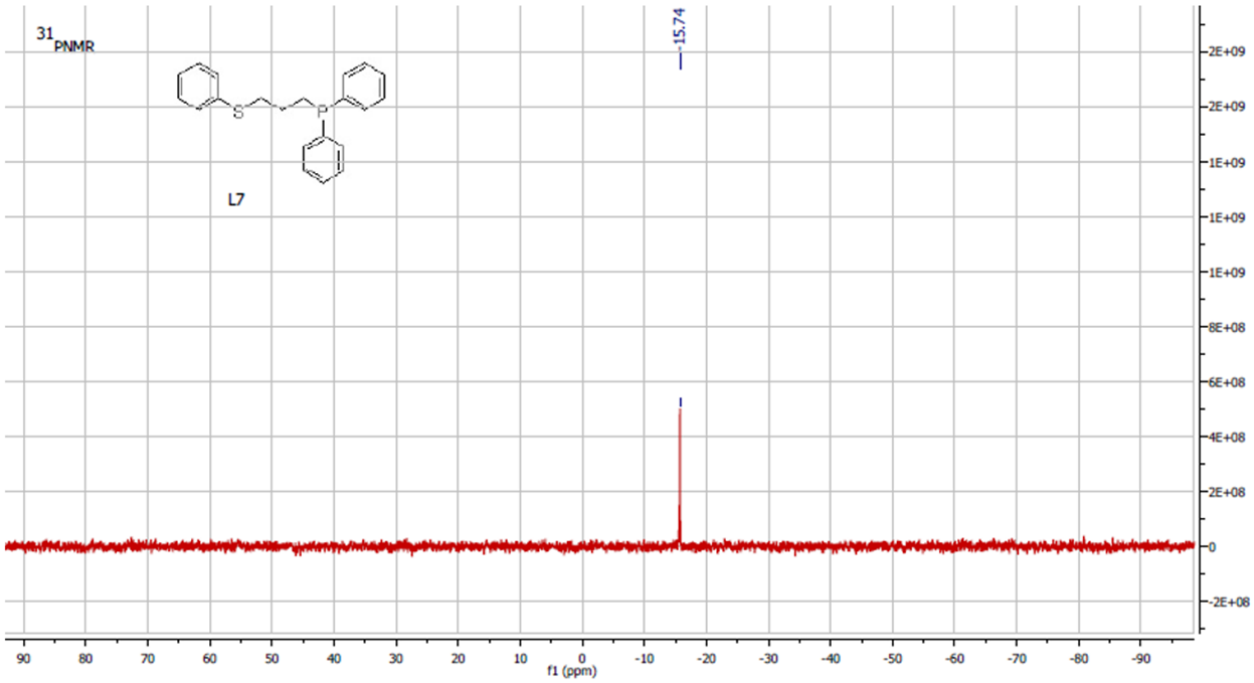

Figure 46: *^{31}P NMR of L7*

Ruthenium P,S Complexes:

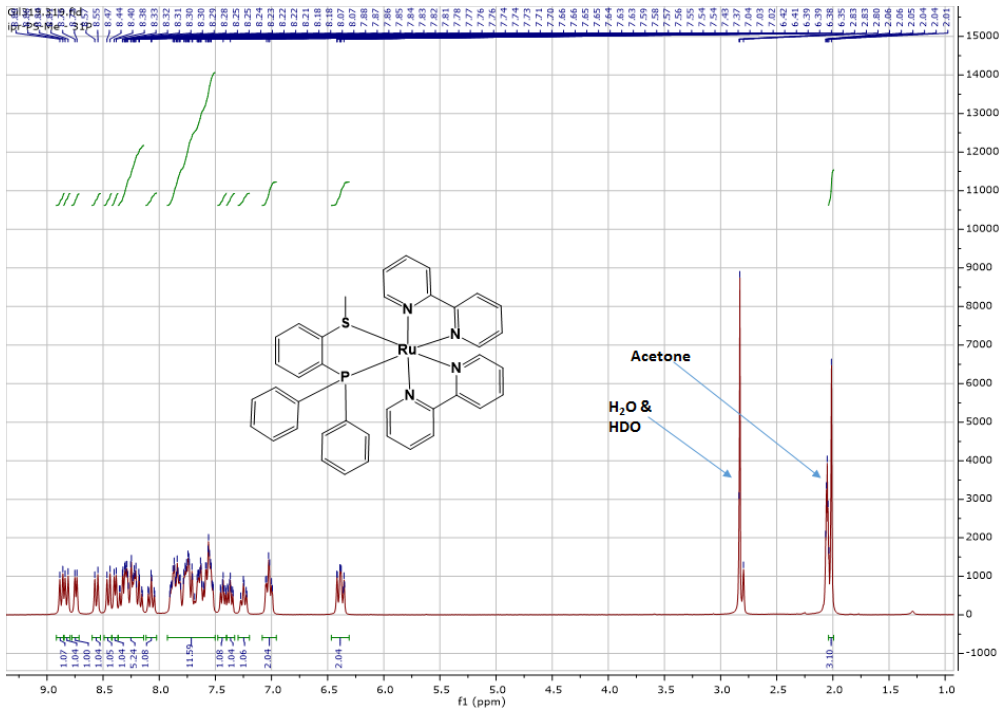

Figure 47: *^{1}H NMR of RuL1*

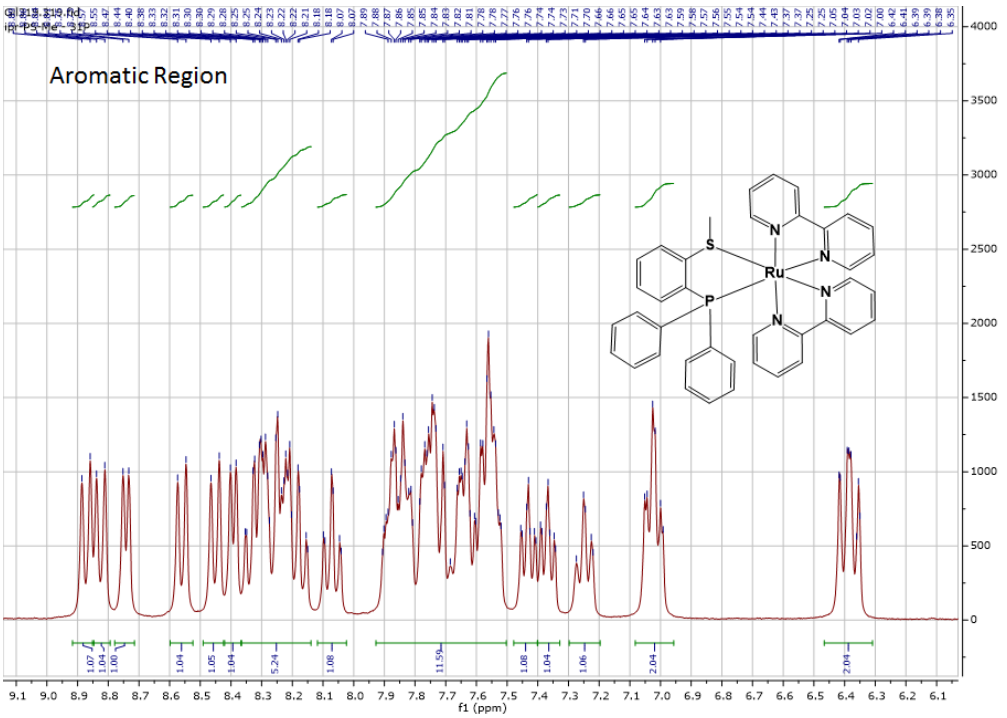

Figure 48: *^{1}H NMR of RuL1 aromatic region*

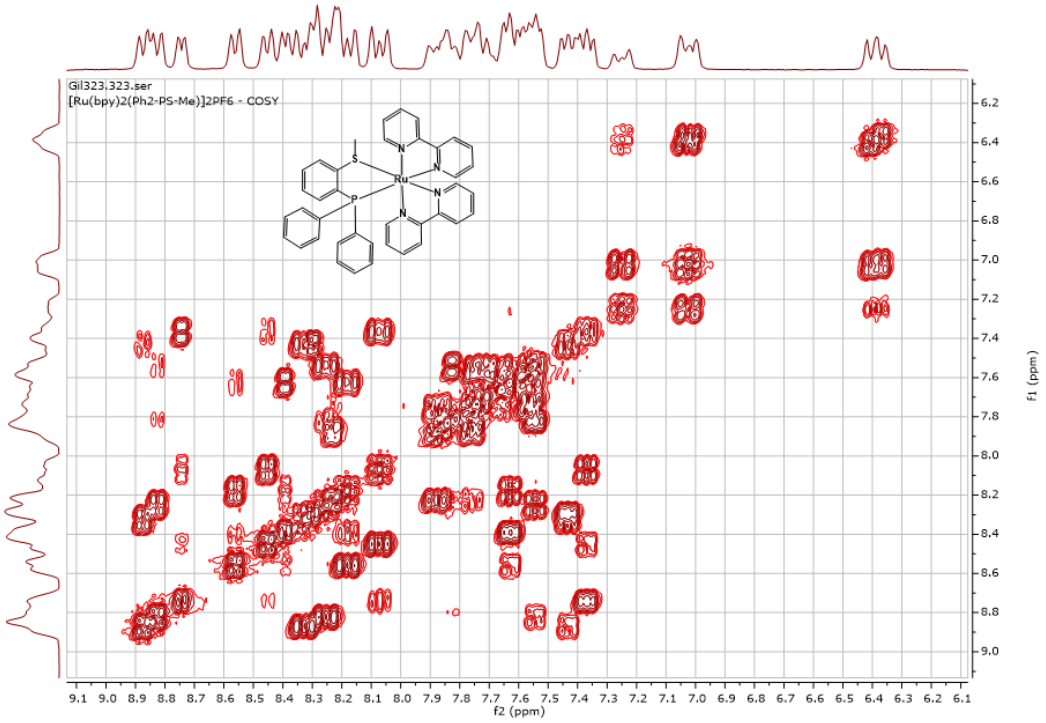

Figure 49: *2D NMR of RuL1*

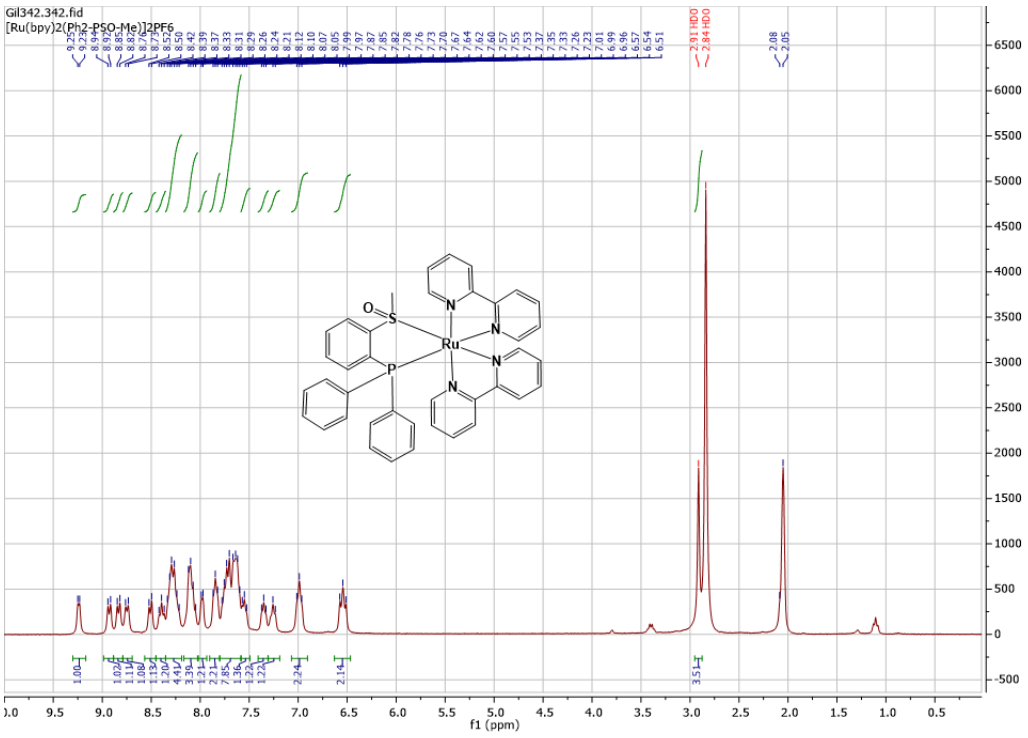

Figure 50: *^{1}H NMR of RuL1O*

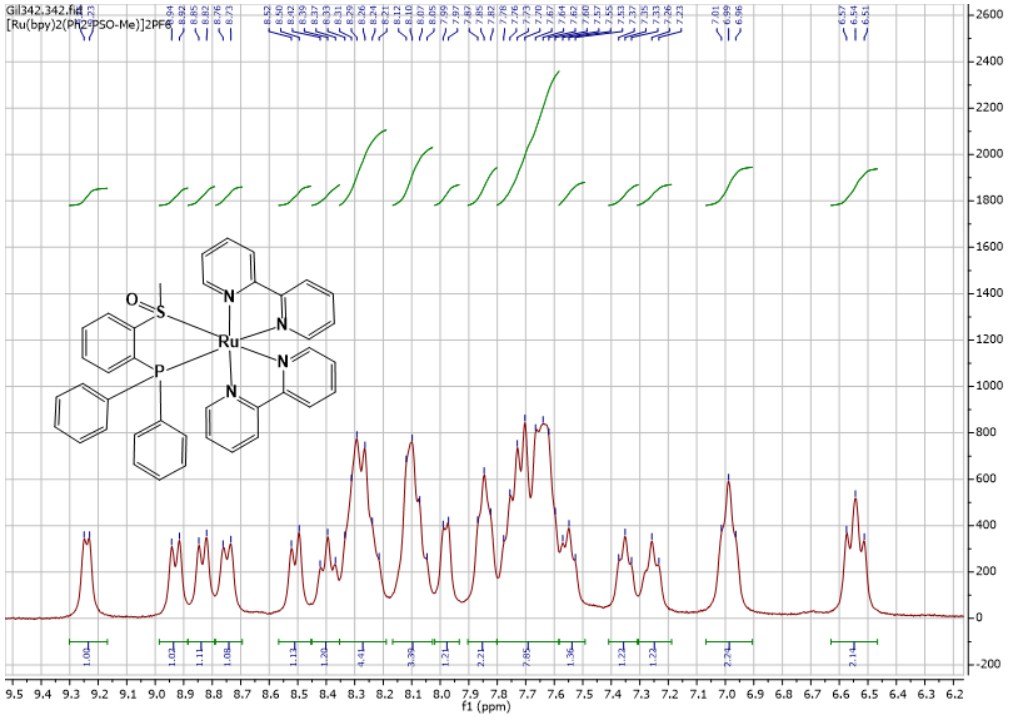

Figure 51: *^{1}H NMR of RuL1O aromatic region*

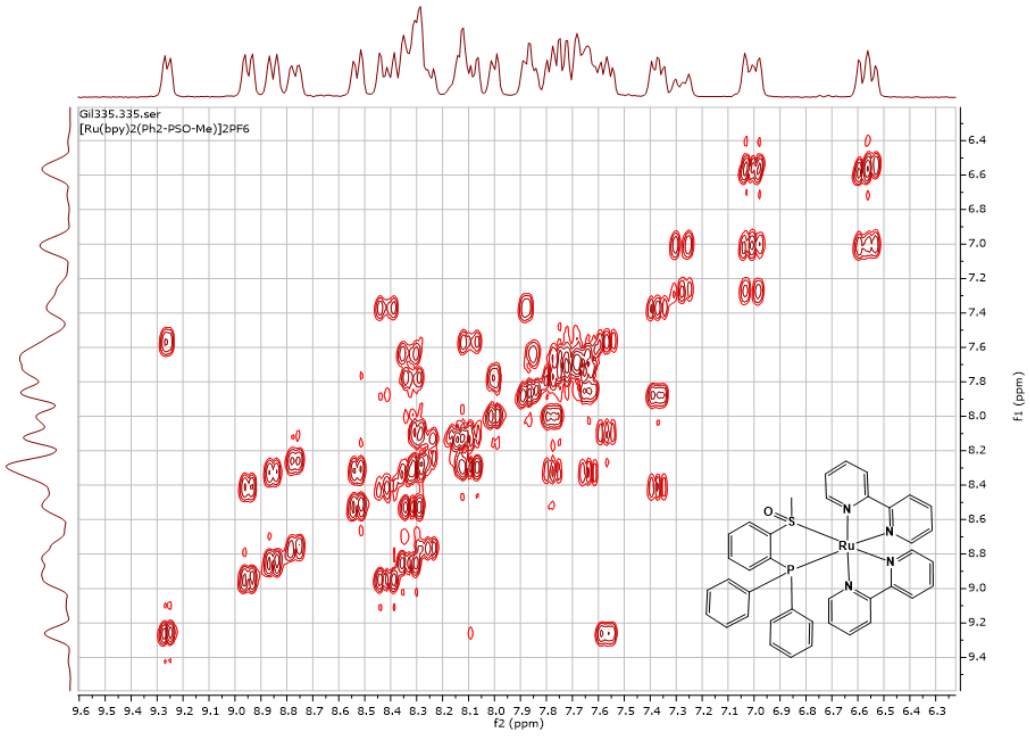

Figure 52: *2D NMR of RuL1O*

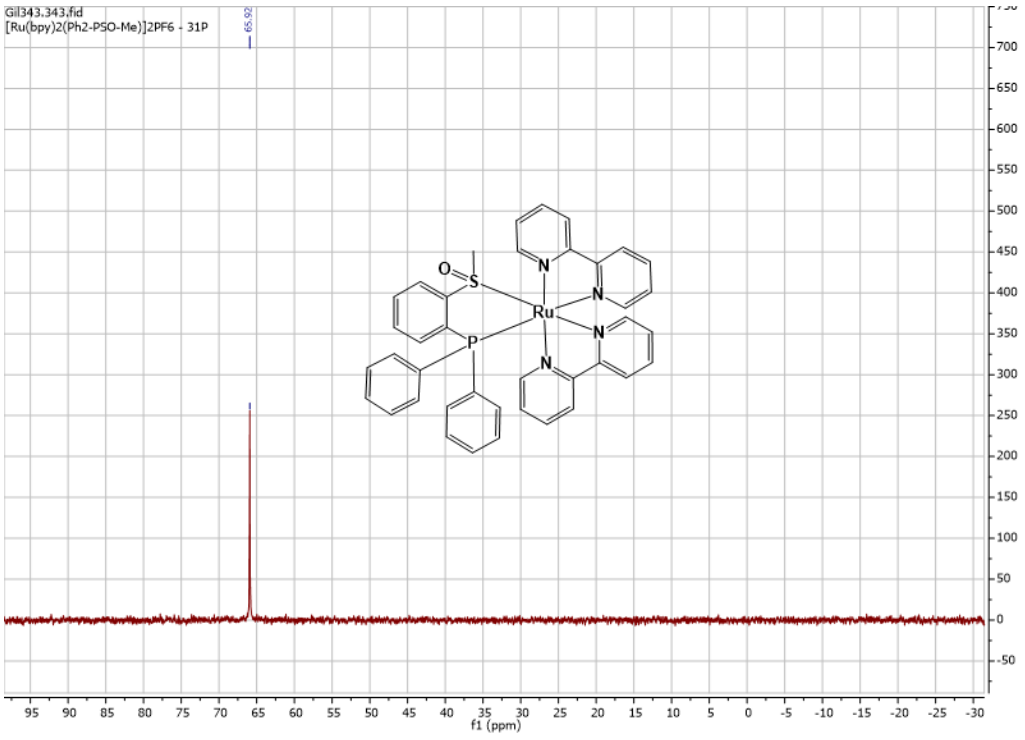

Figure 53: *^{31}P NMR of RuL1O*

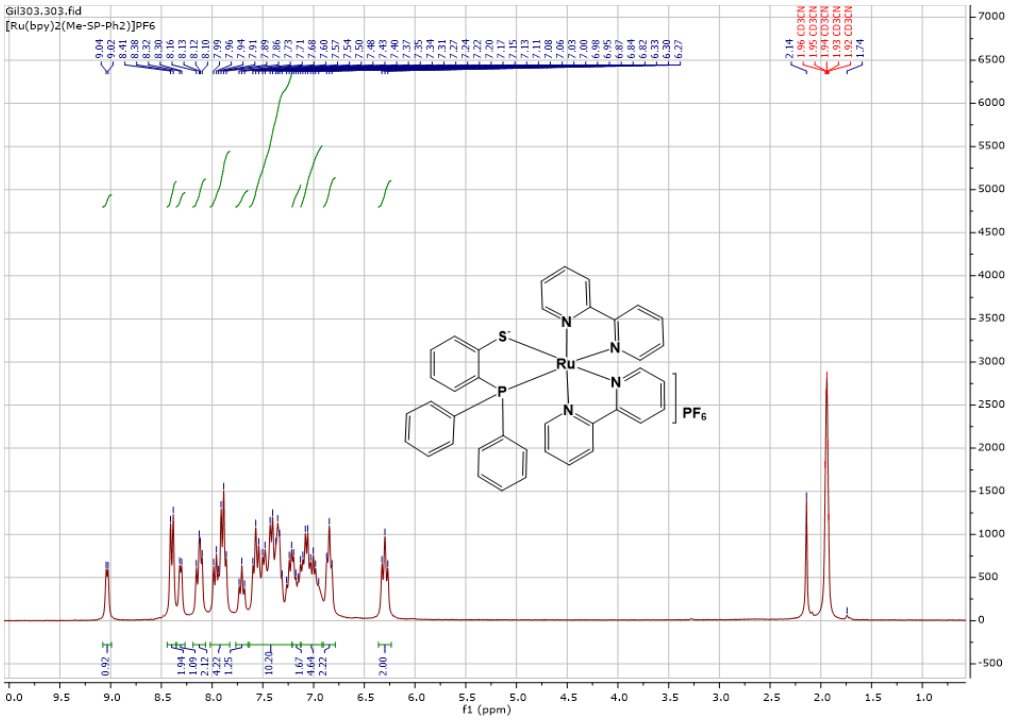

Figure 54: *^{1}H NMR of RuL1D*

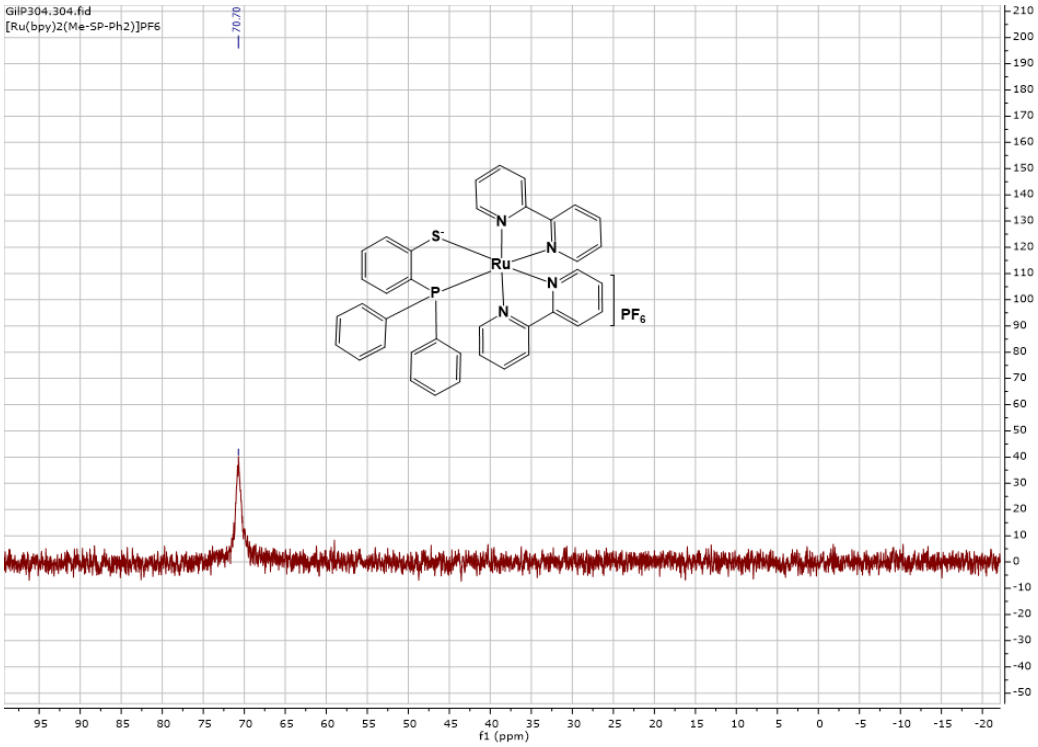

Figure 55: *^{31}P NMR of RuL1D*

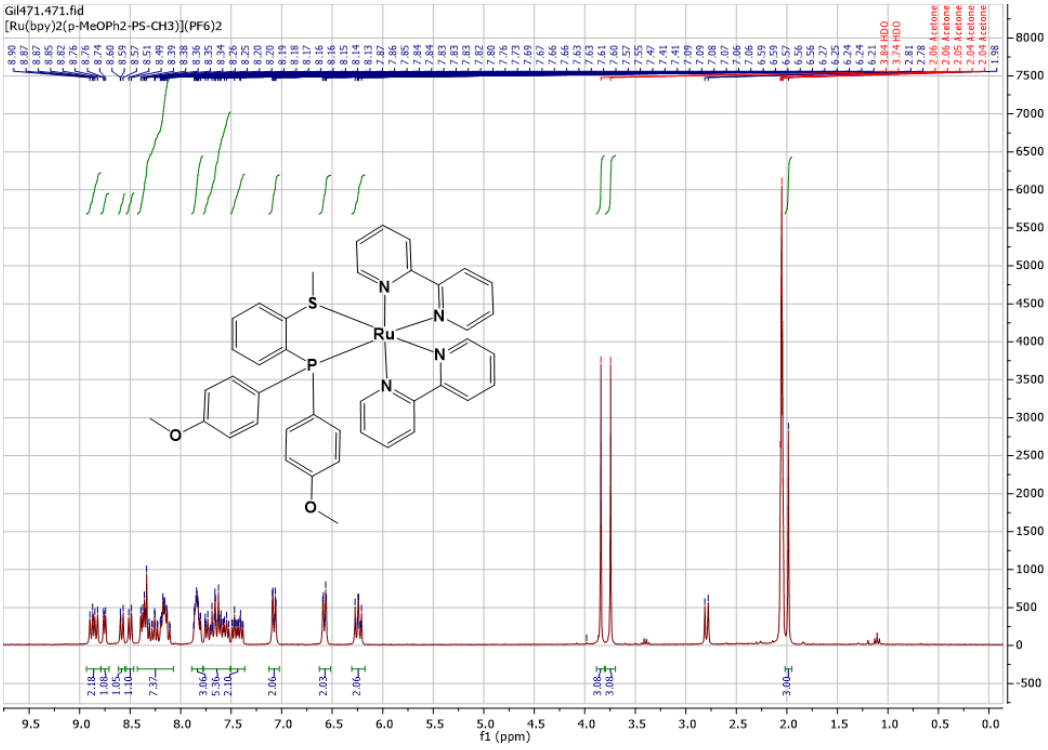

Figure 56*: ^{1}H NMR of RuL2*

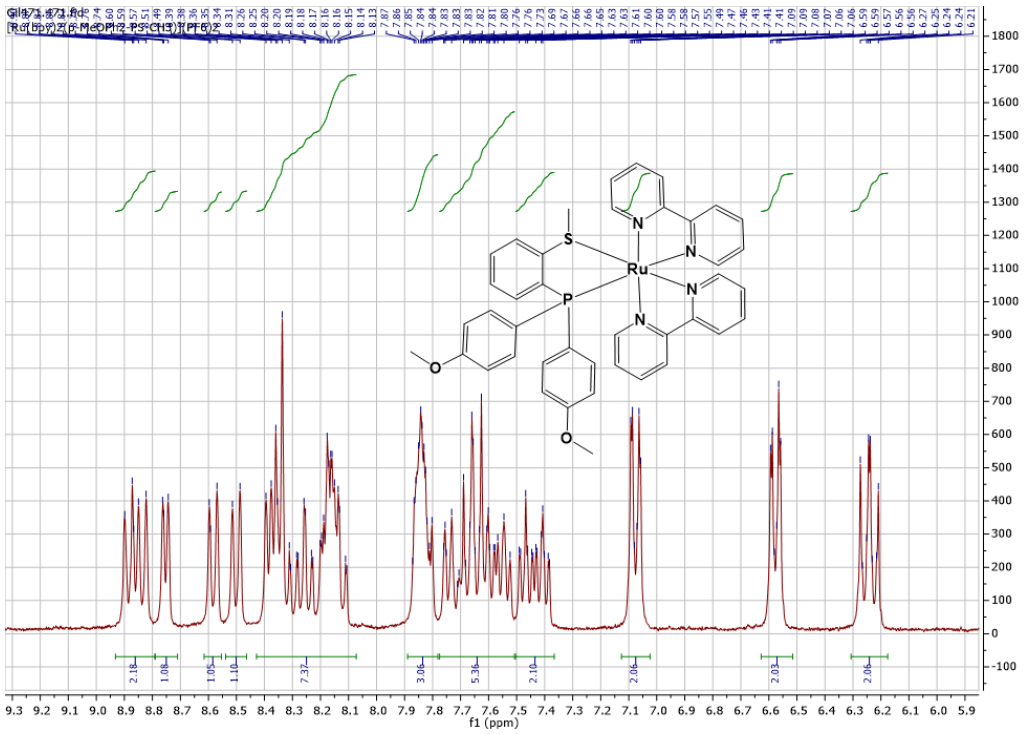

Figure 57: *^{1}H NMR of RuL2 aromatic region*

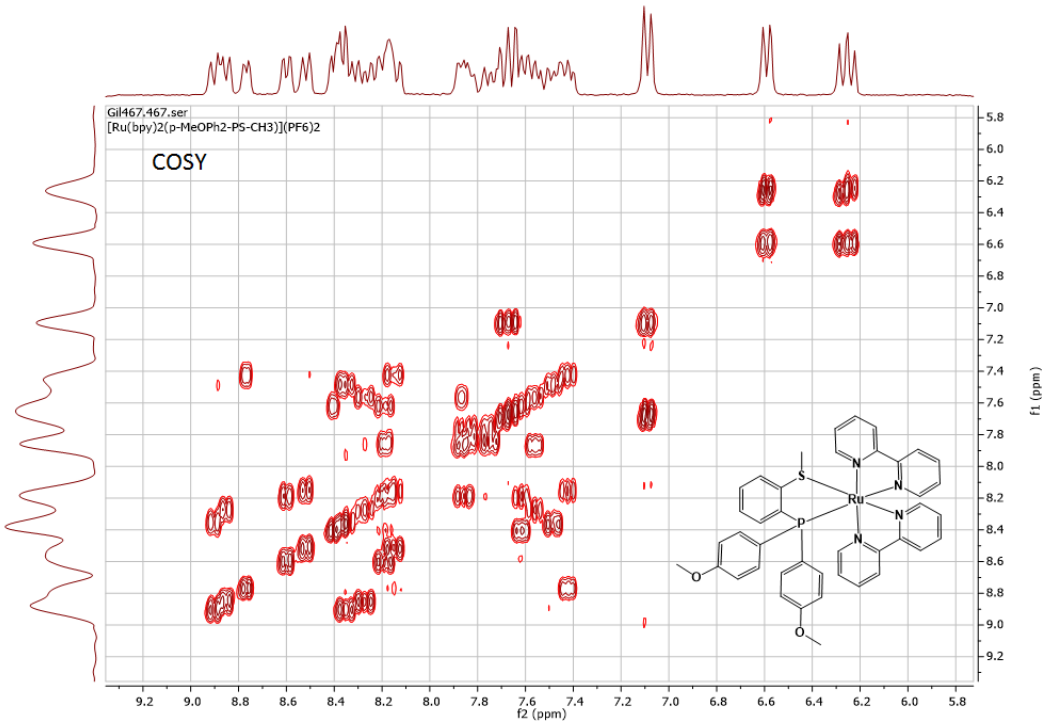

Figure 58: *COSY of RuL2*

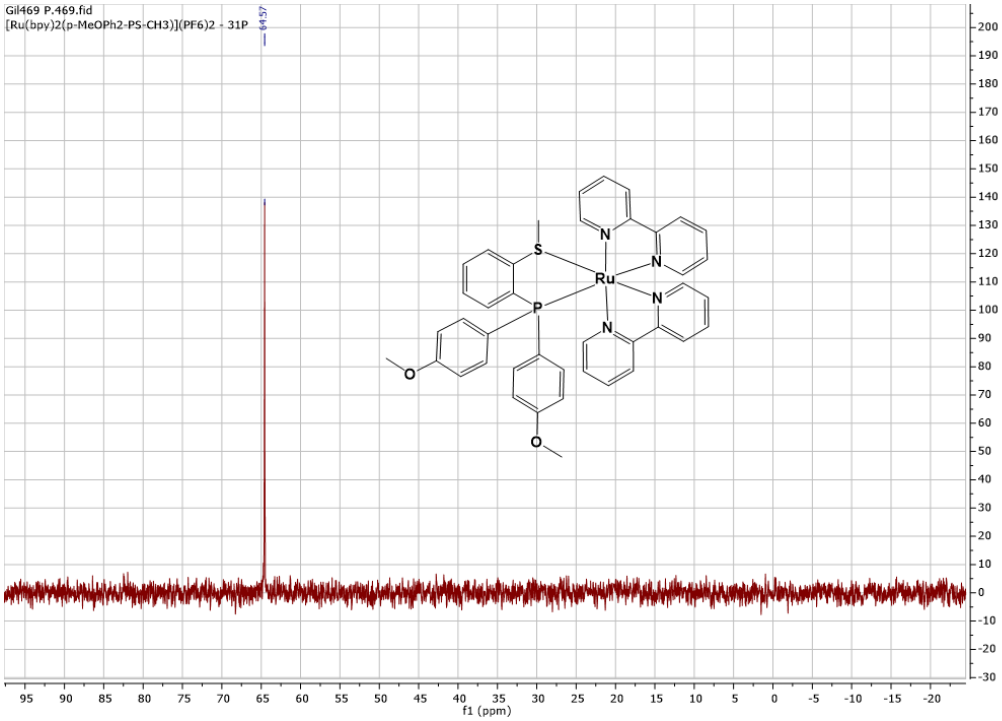

Figure 59: *^{31}P NMR of RuL2*

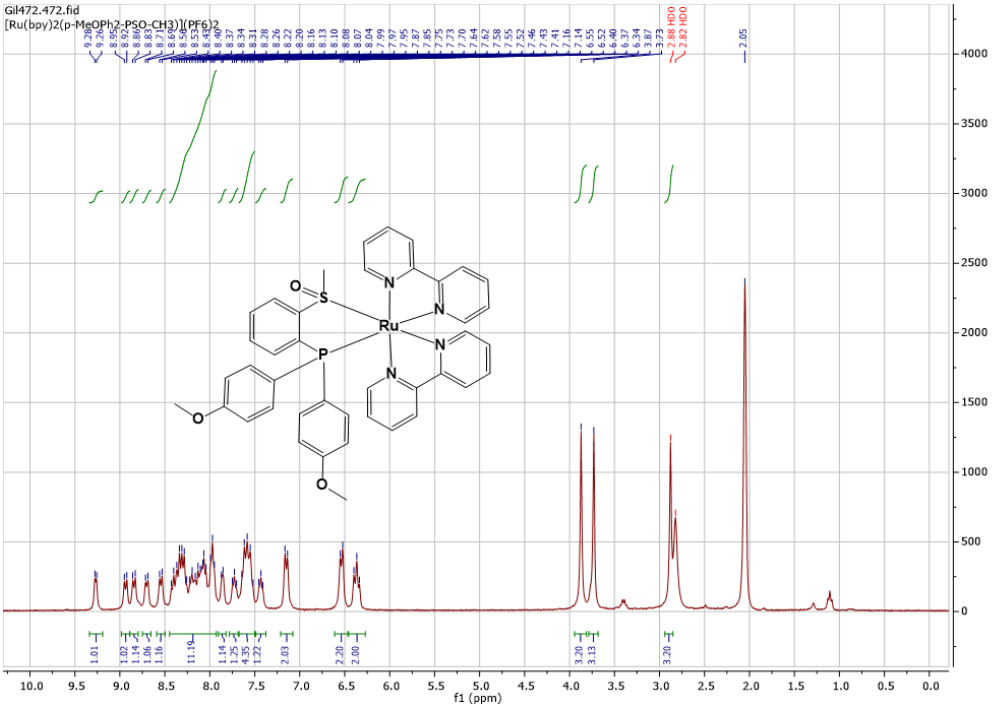

Figure 60: *^{1}H NMR of RuL2O*

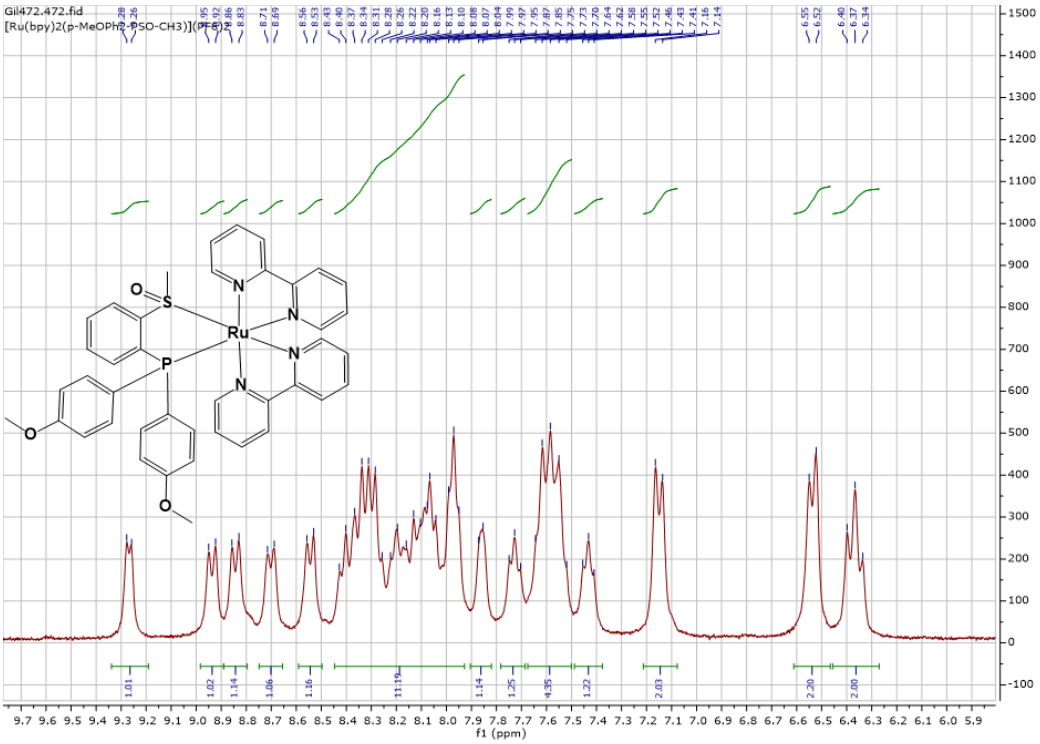

Figure 61: *^{1}H NMR of RuL2O aromatic region*

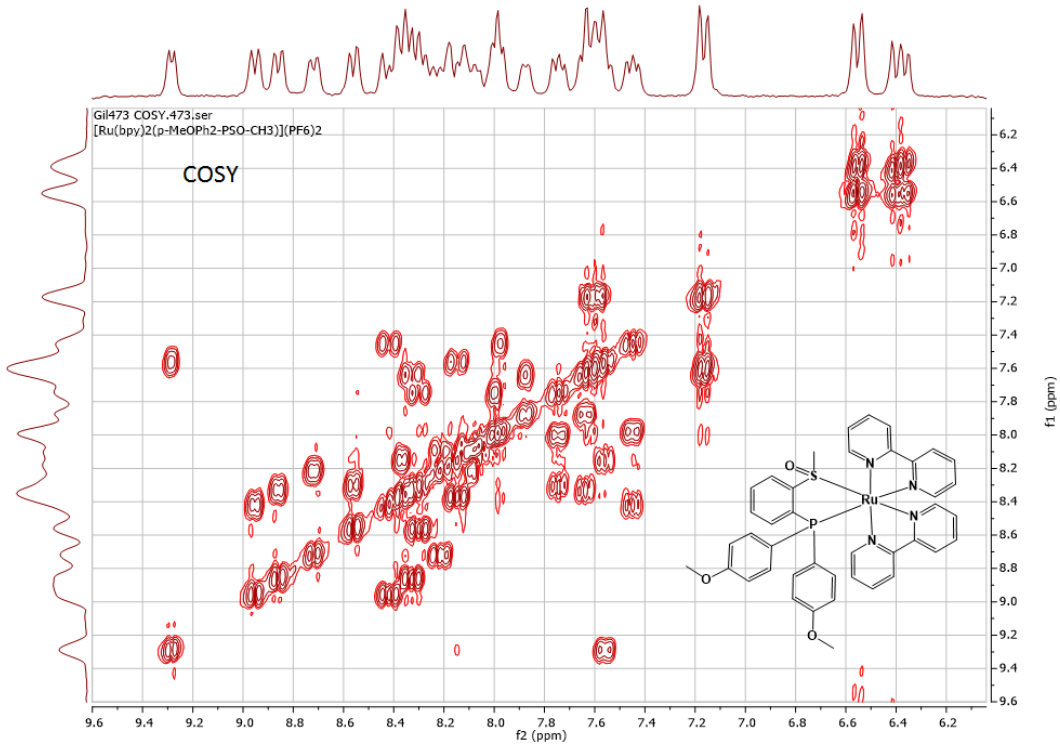

Figure 62: *COSY of RuL2O*

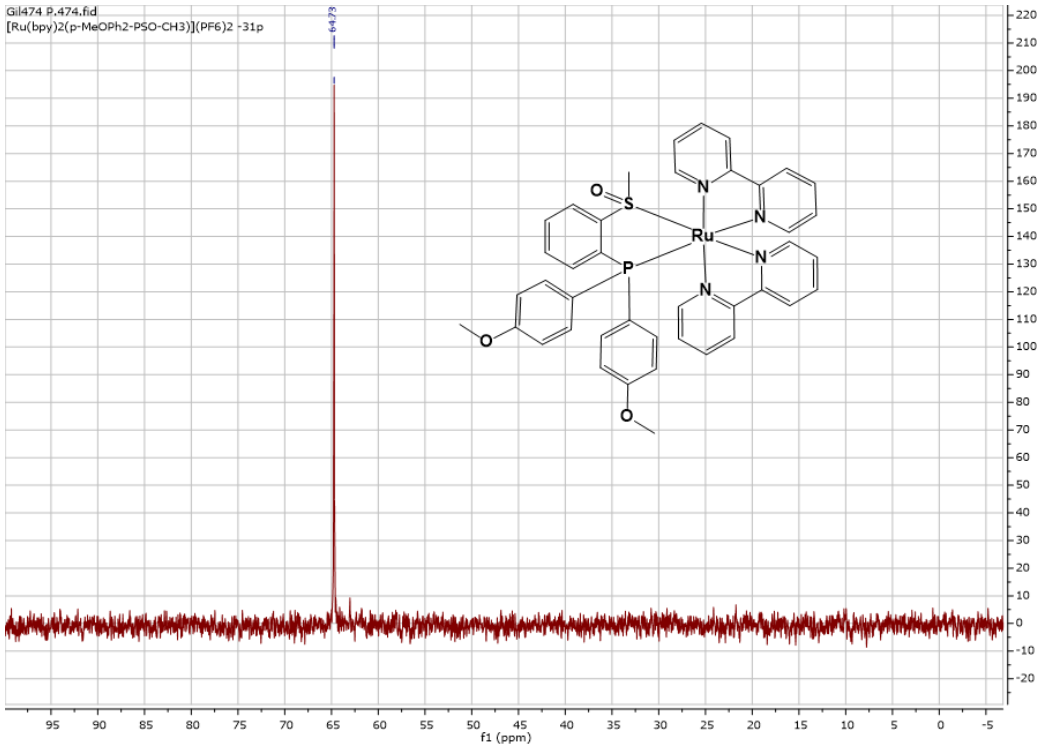

Figure 63: *^{31}P NMR of RuL2O*

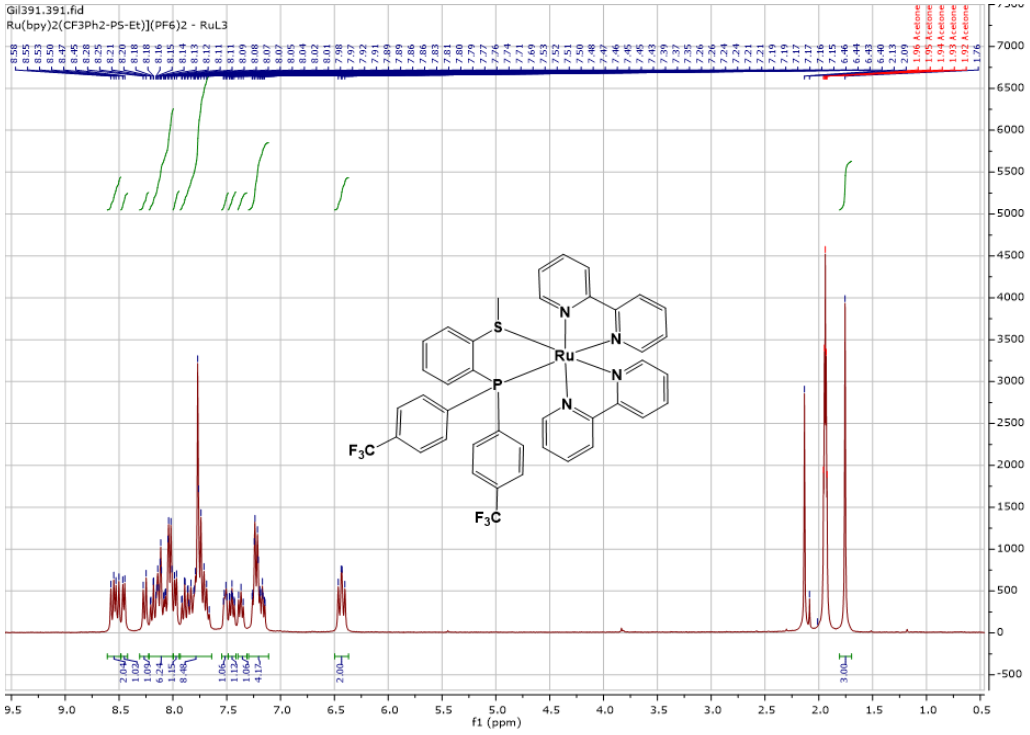

Figure 64: *^{1}H NMR of RuL3*

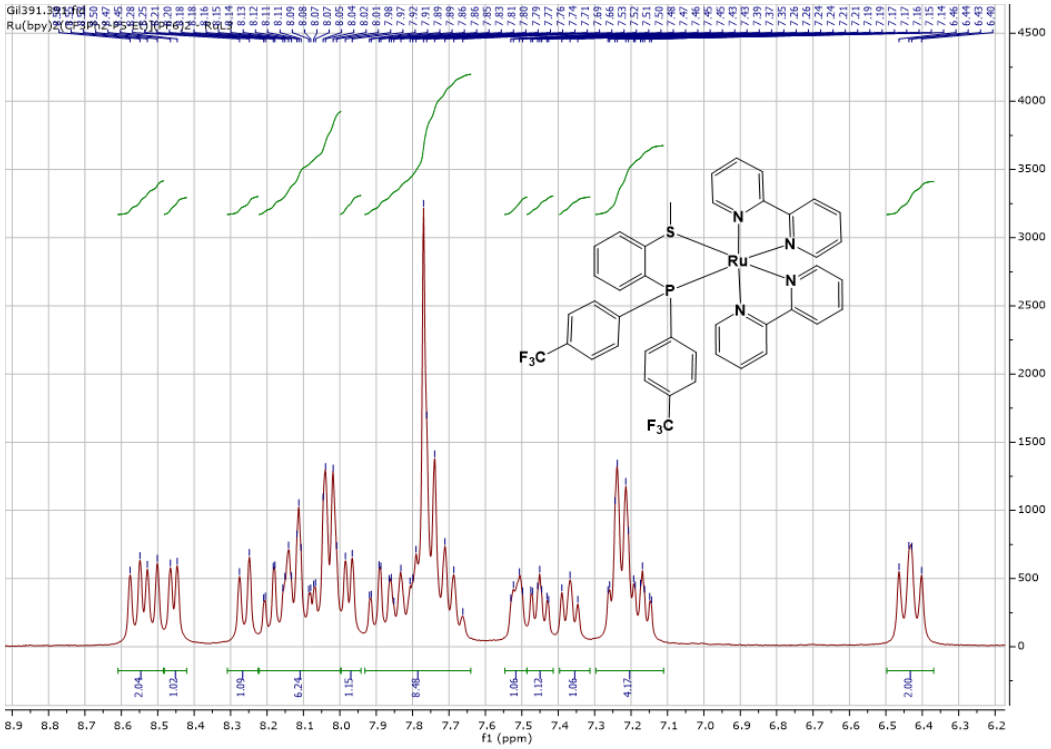

Figure 65: *^{1}H NMR of RuL3 aromatic region*

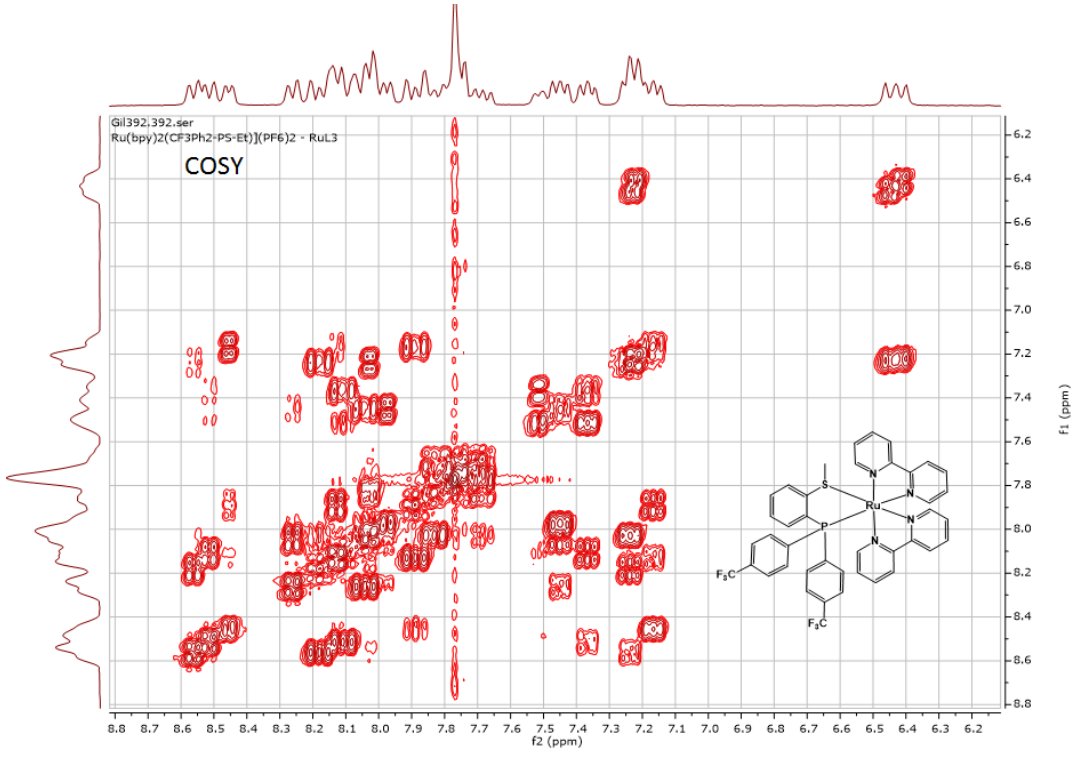

Figure 66: *COSY of RuL3*

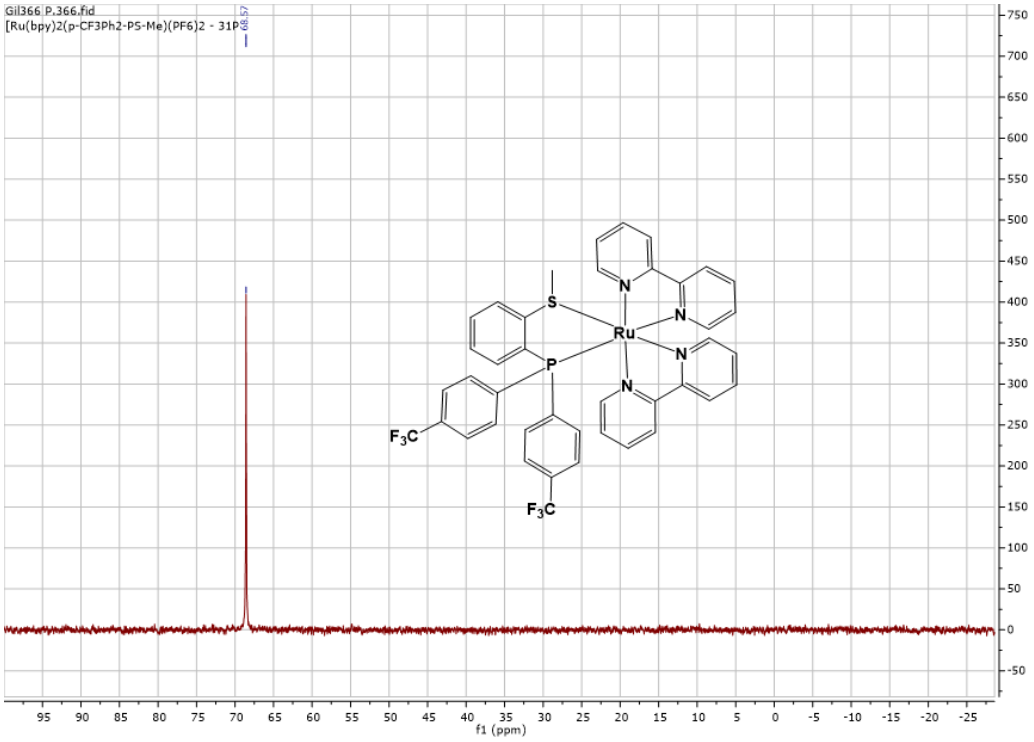

Figure 67: *^{31}P NMR of RuL3*

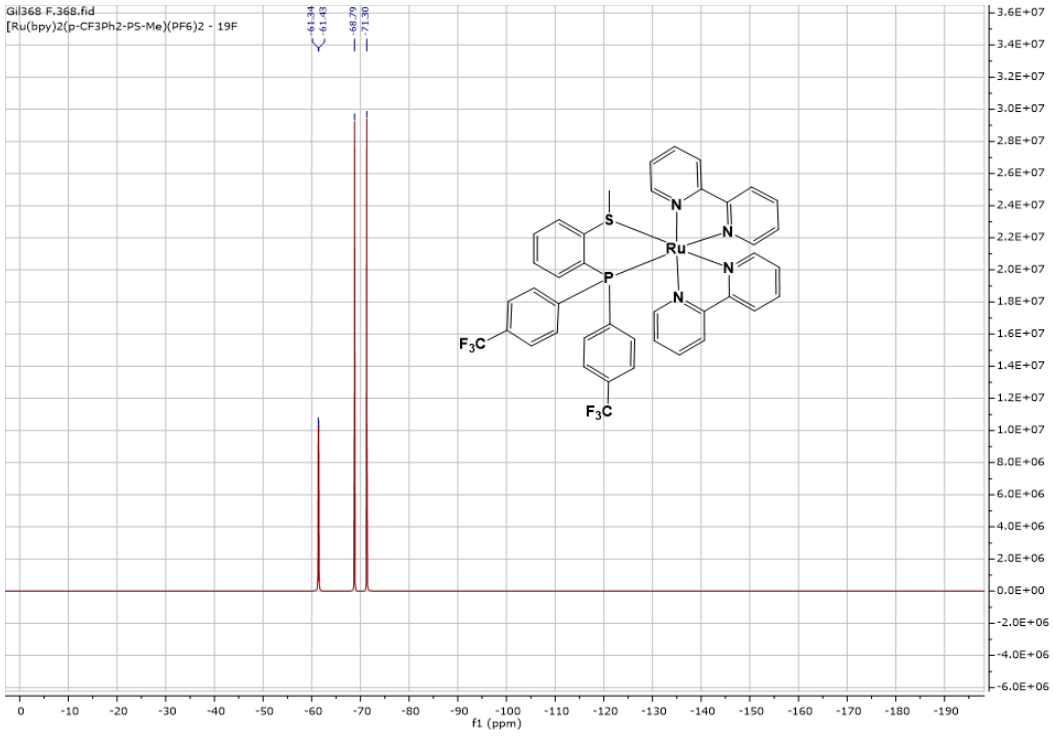

Figure 68: *^{19}F NMR of RuL3*

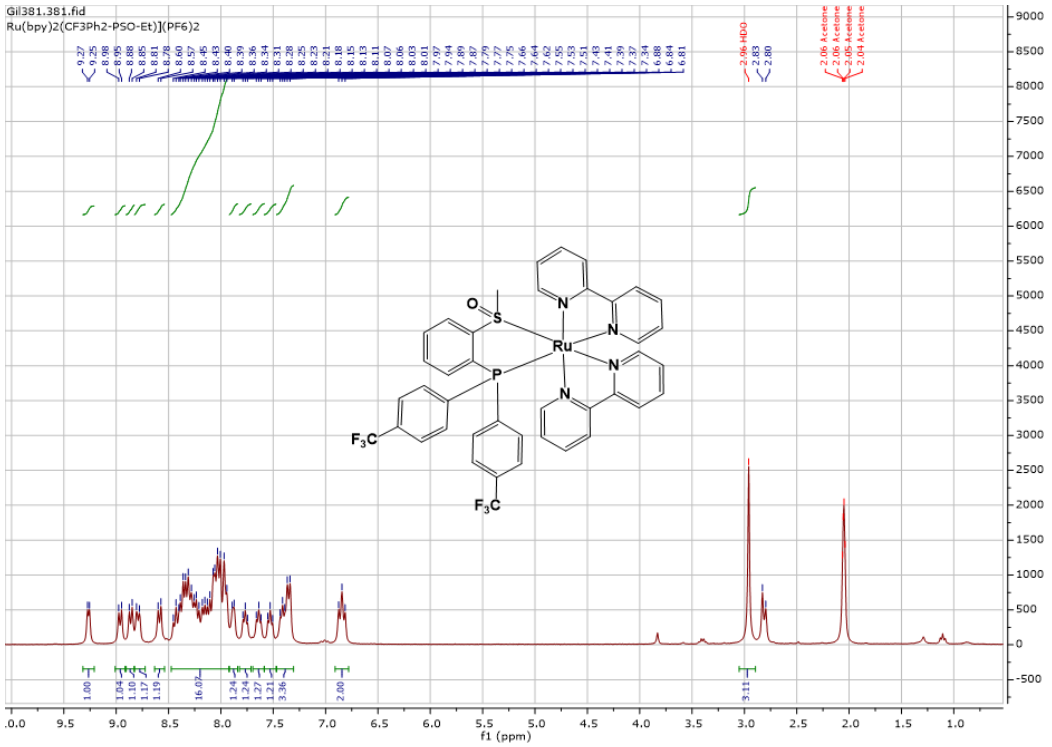

Figure 69: *^{1}H NMR of RuL3O*

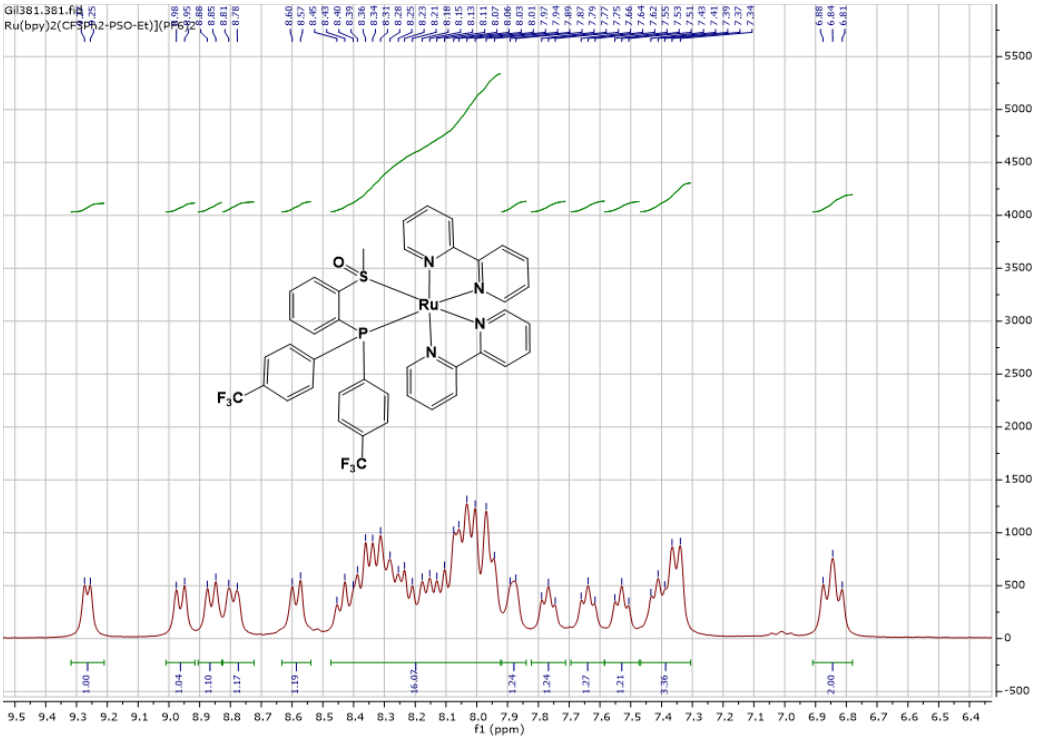

Figure 70: *^{1}H NMR of RuL3O aromatic region*

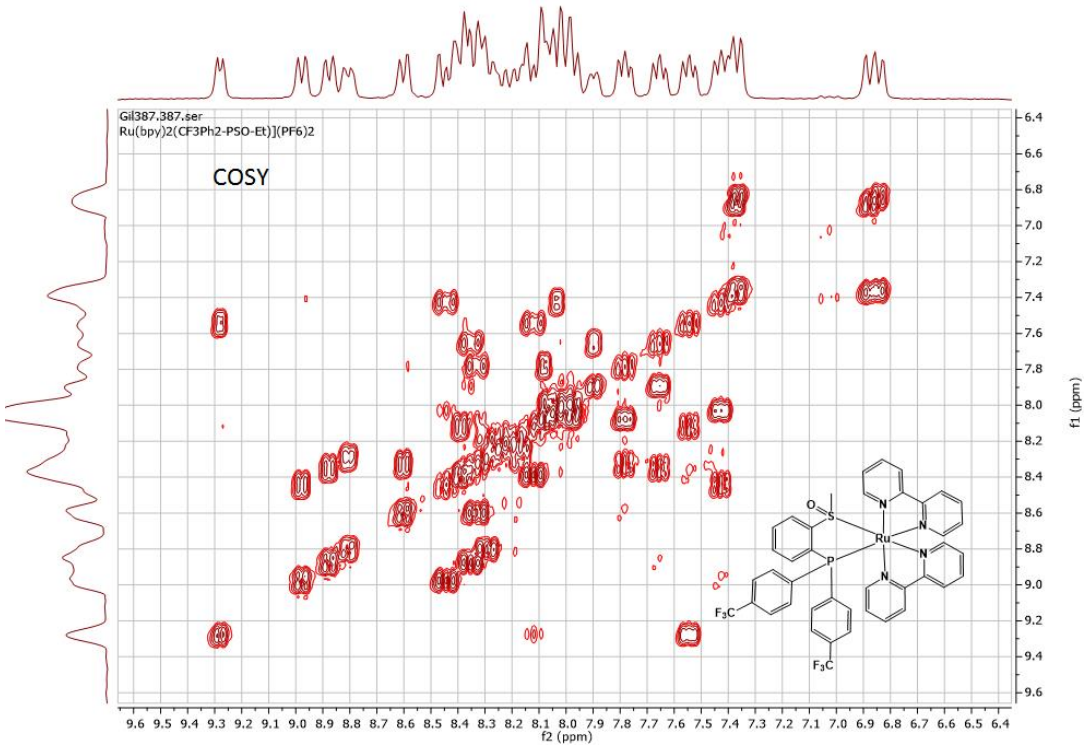

Figure 71: *COSY of RuL3O*

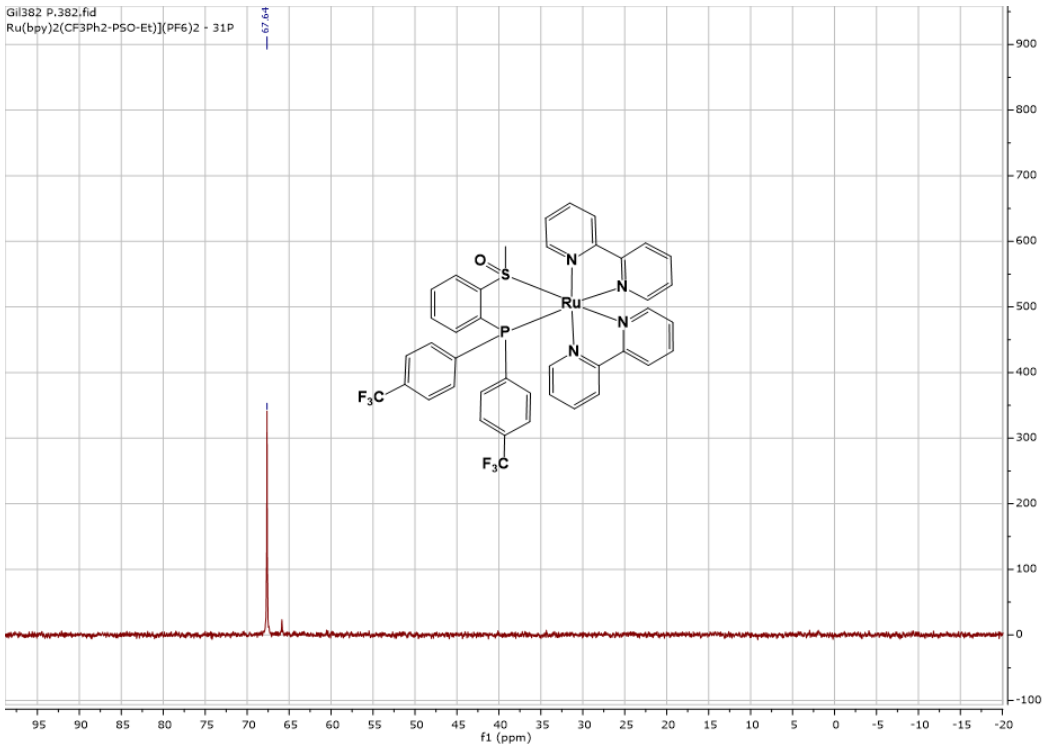

Figure 72: *^{31}P NMR of RuL3O*

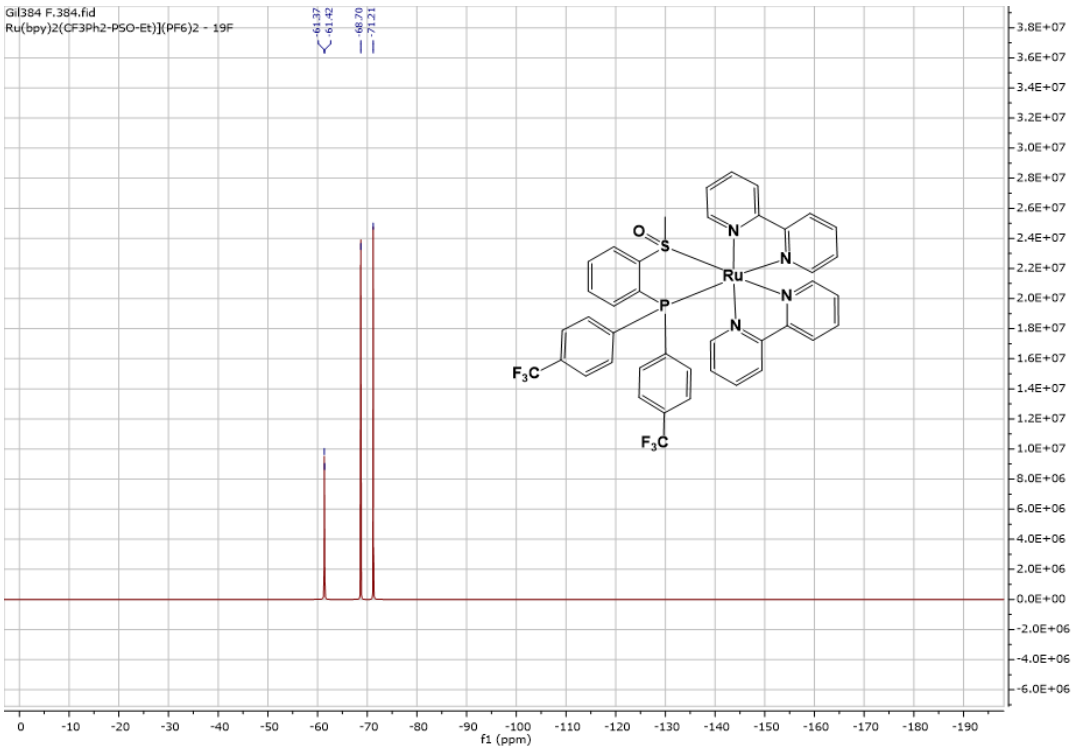

Figure 73: *^{19}F NMR of RuL3O*

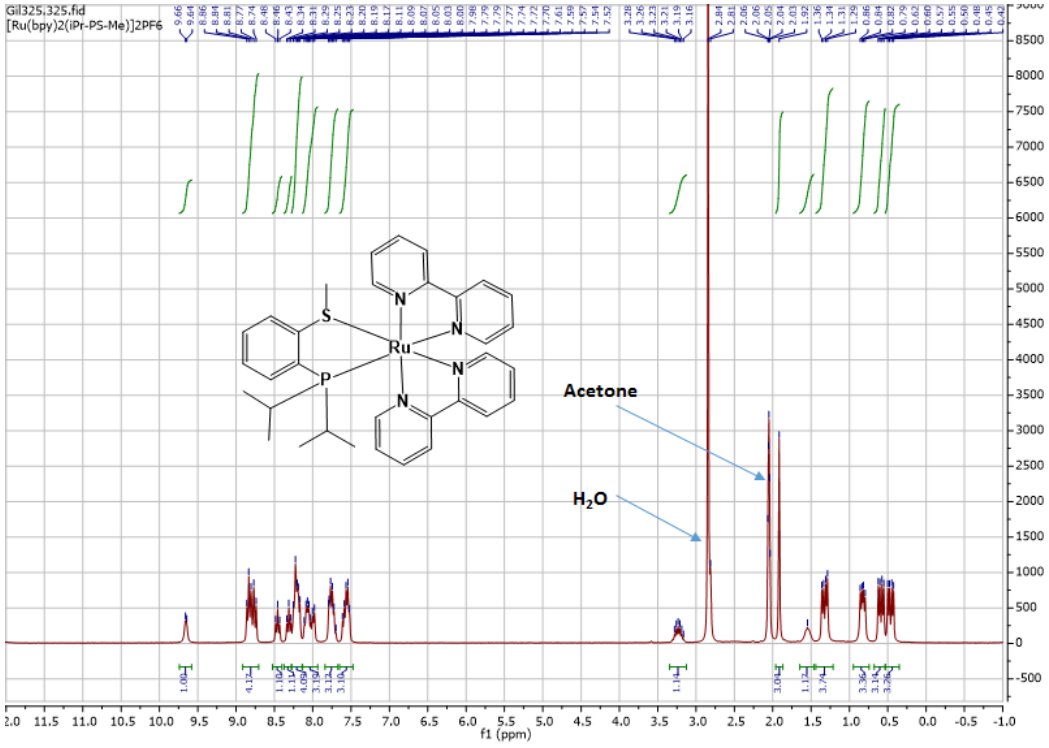

Figure 74: *^{1}H NMR of RuL4*

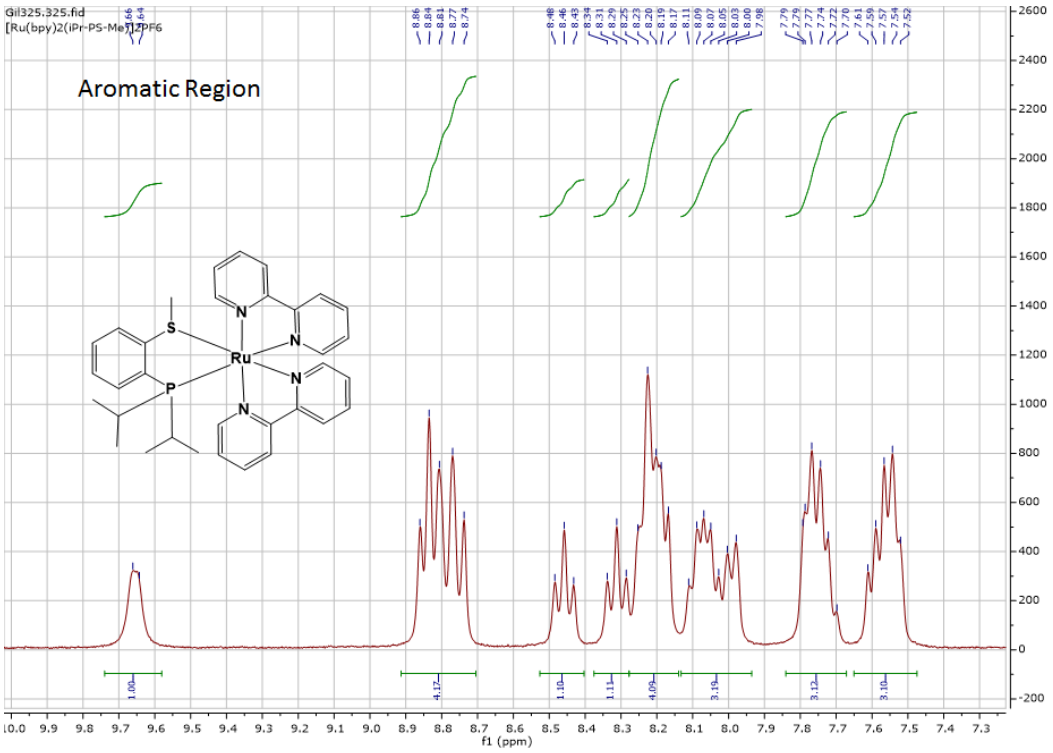

Figure 75: *^{1}H NMR of RuL4 aromatic region*

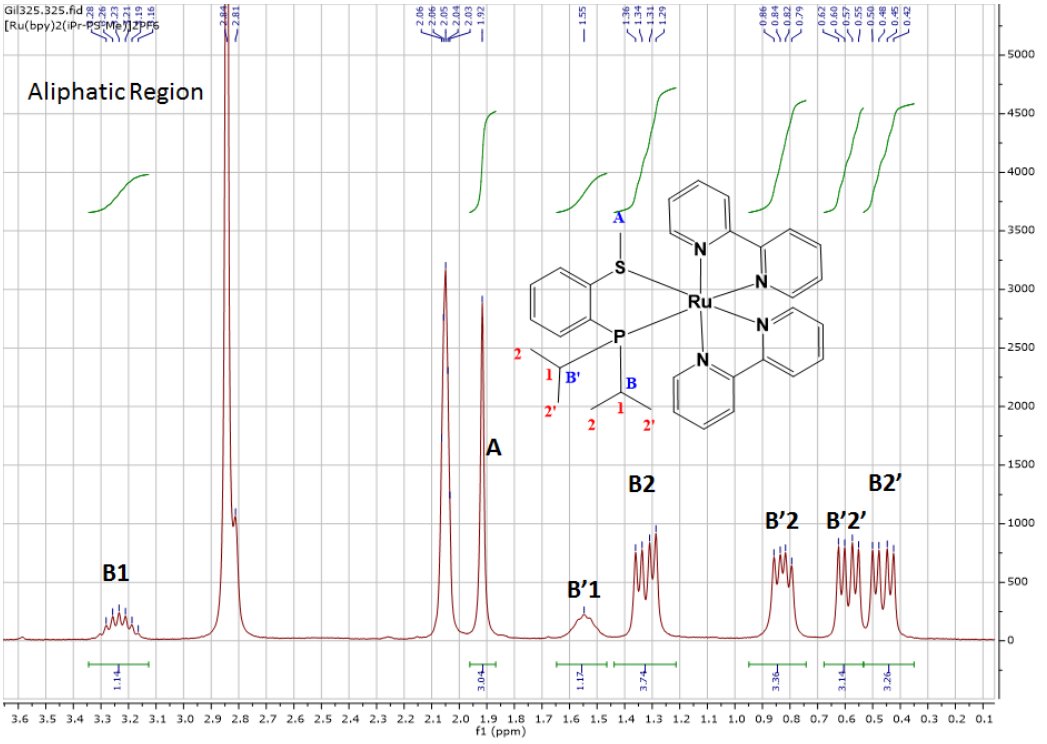

Figure 76: *^{1}H NMR of RuL4 aliphatic region*

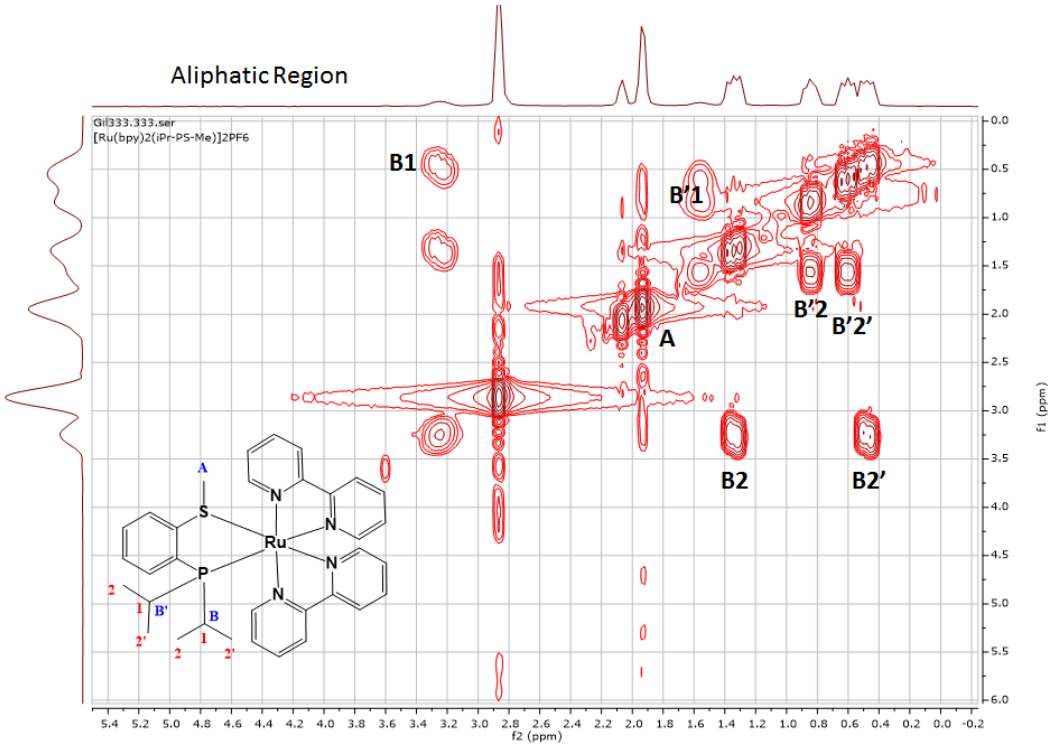

Figure 77: *COSY of RuL4 aliphatic region*

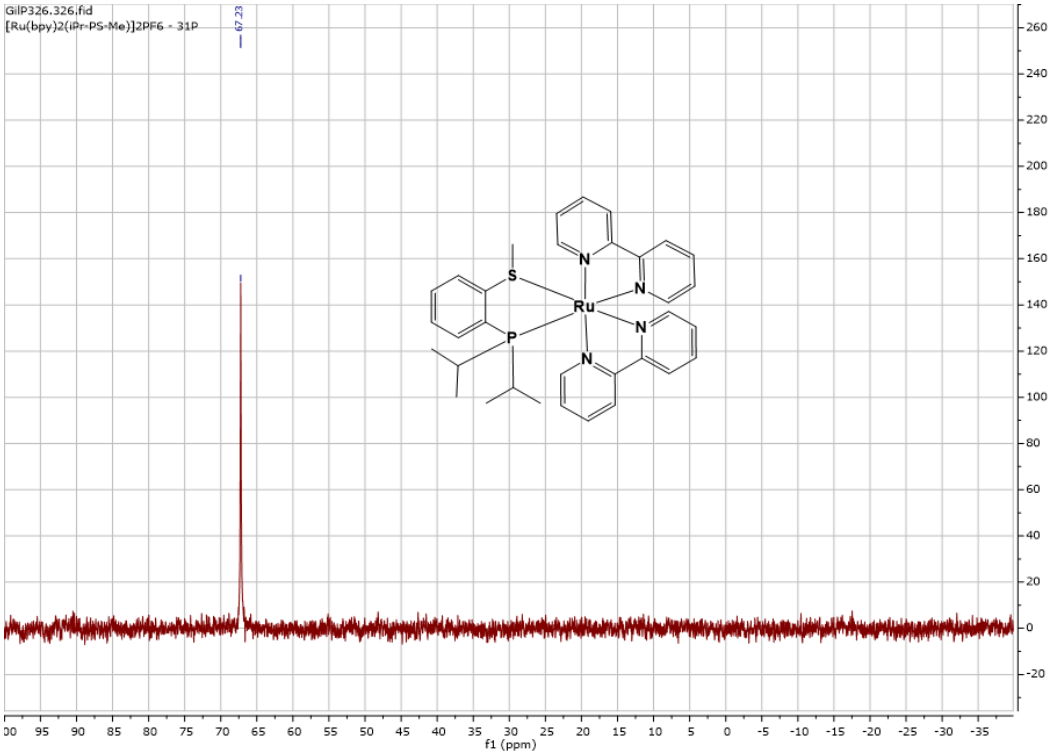

Figure 78: *^{31}P NMR of RuL4*

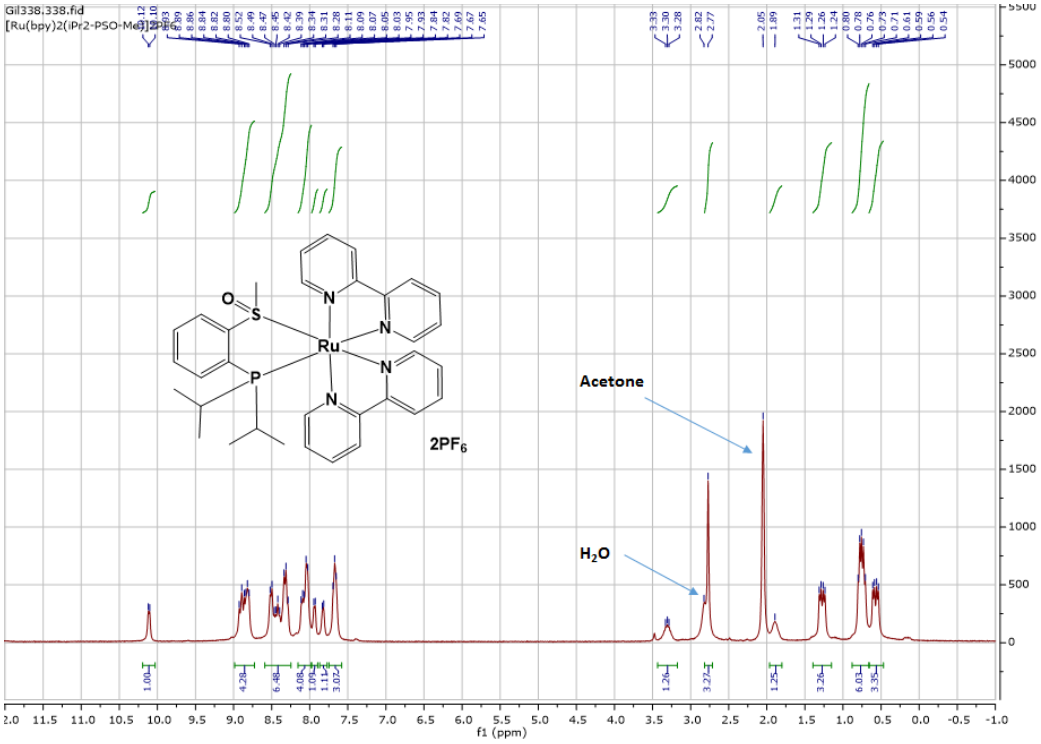

Figure 79: *^{1}H NMR of RuL4O*

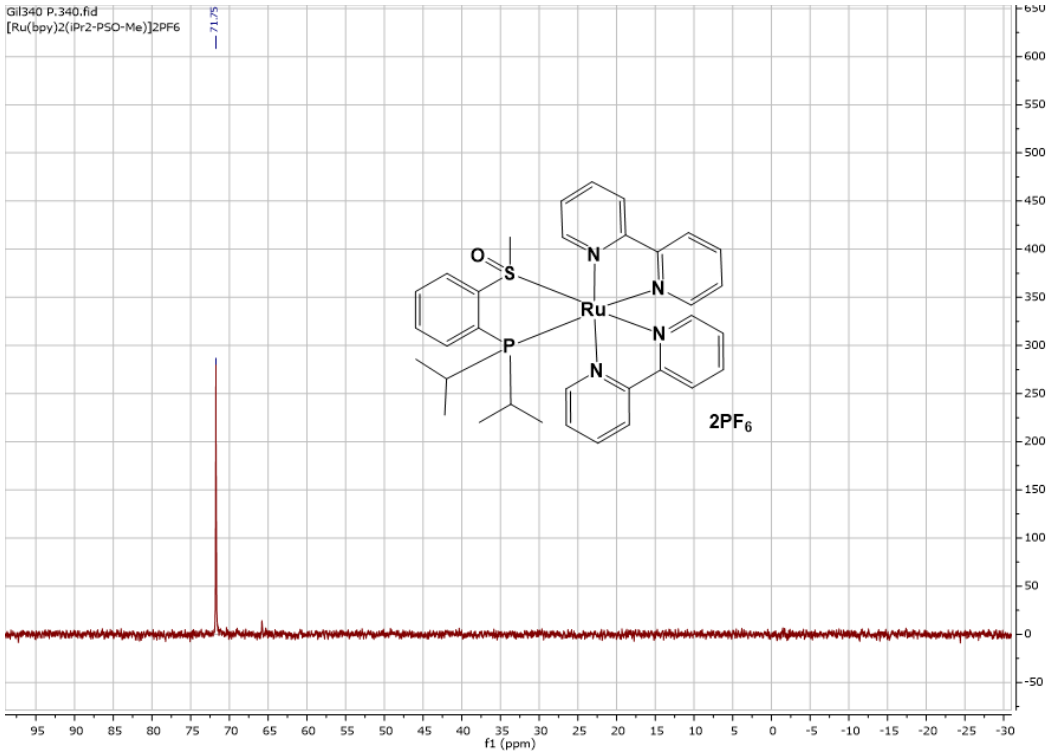

Figure 80: *^{31}P NMR of RuL4O*

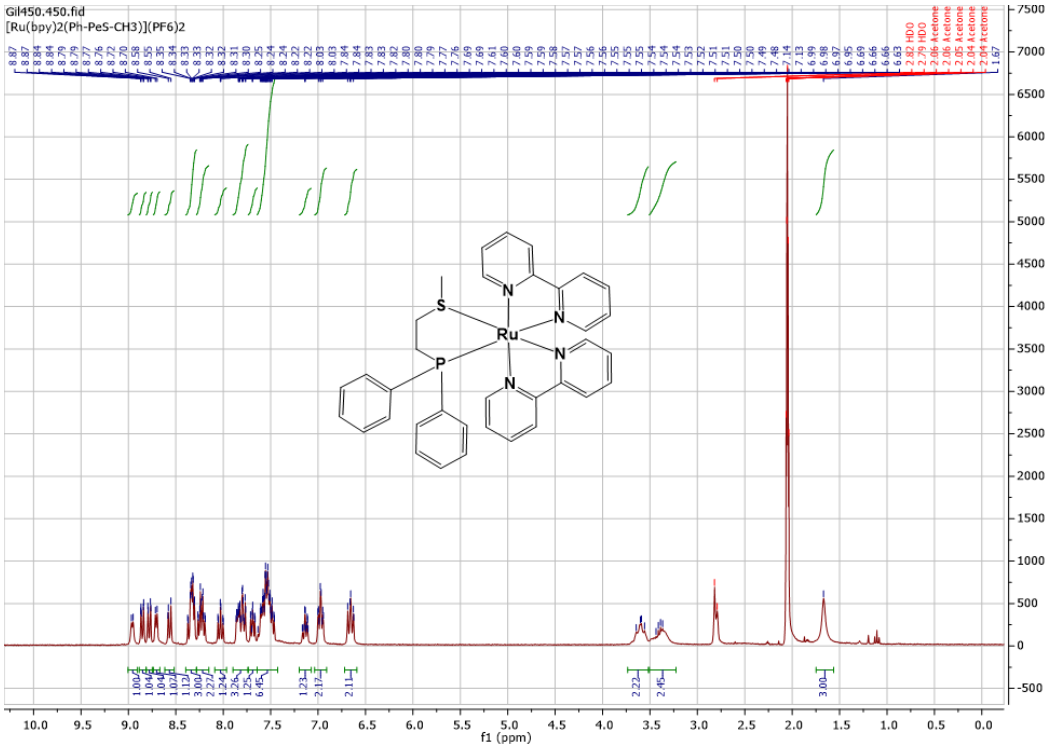

Figure 81: *^{1}H NMR of RuL5*

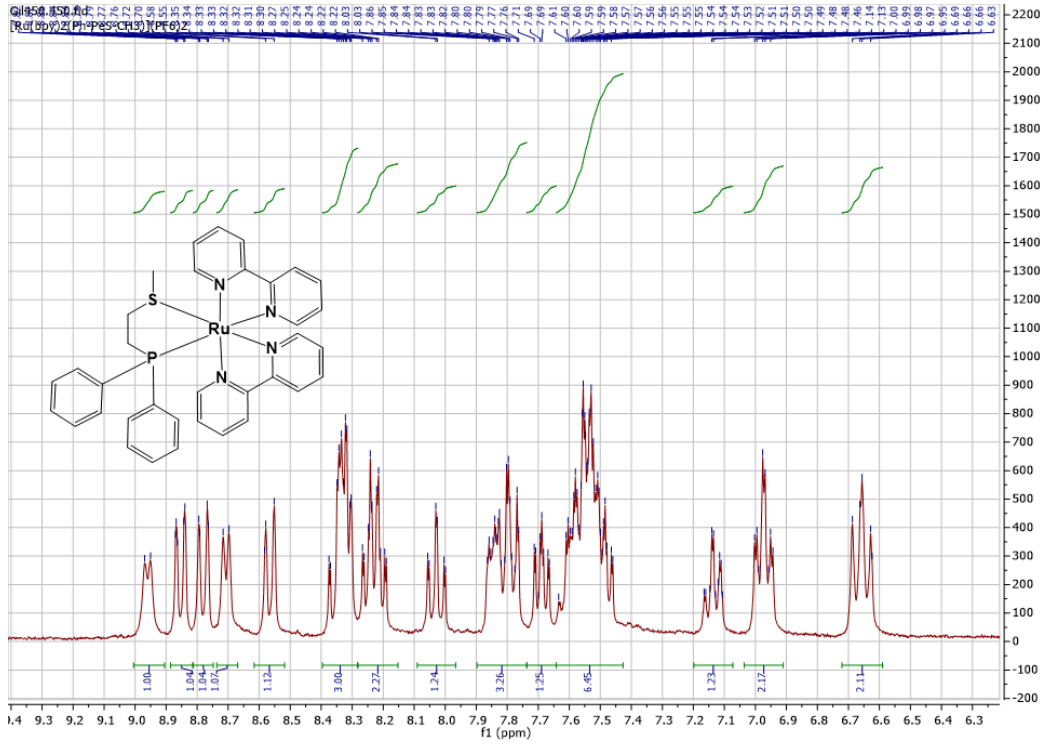

Figure 82: *^{1}H NMR of RuL5 aromatic region*

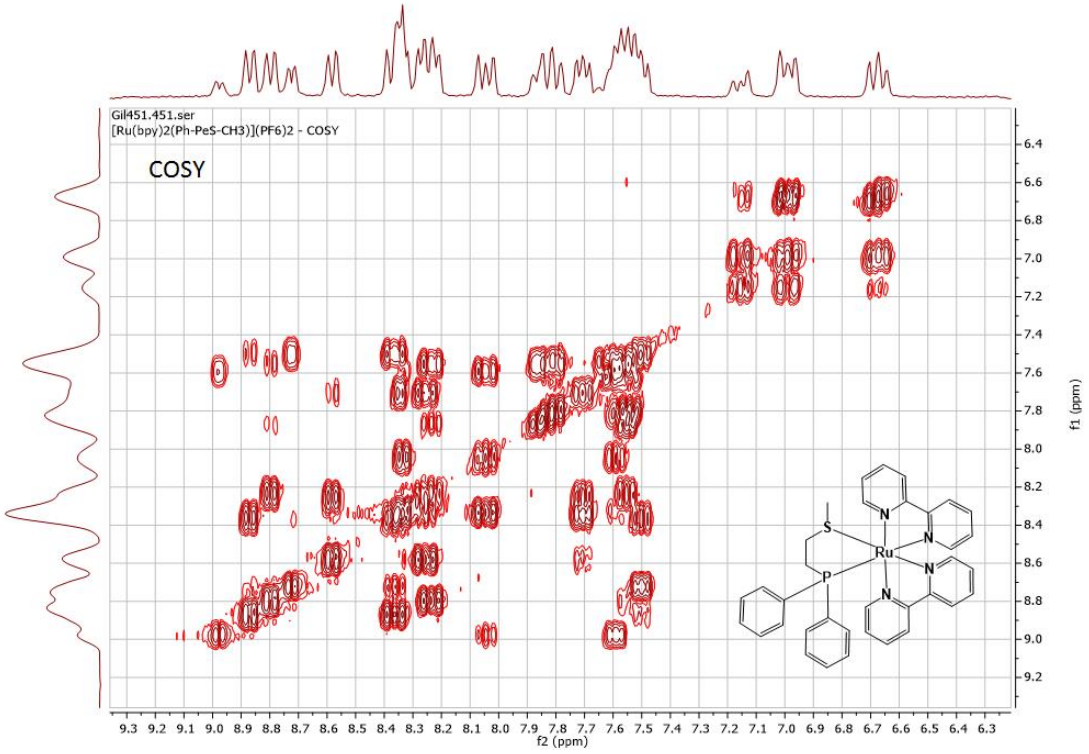

Figure 83: *COSY of RuL5*

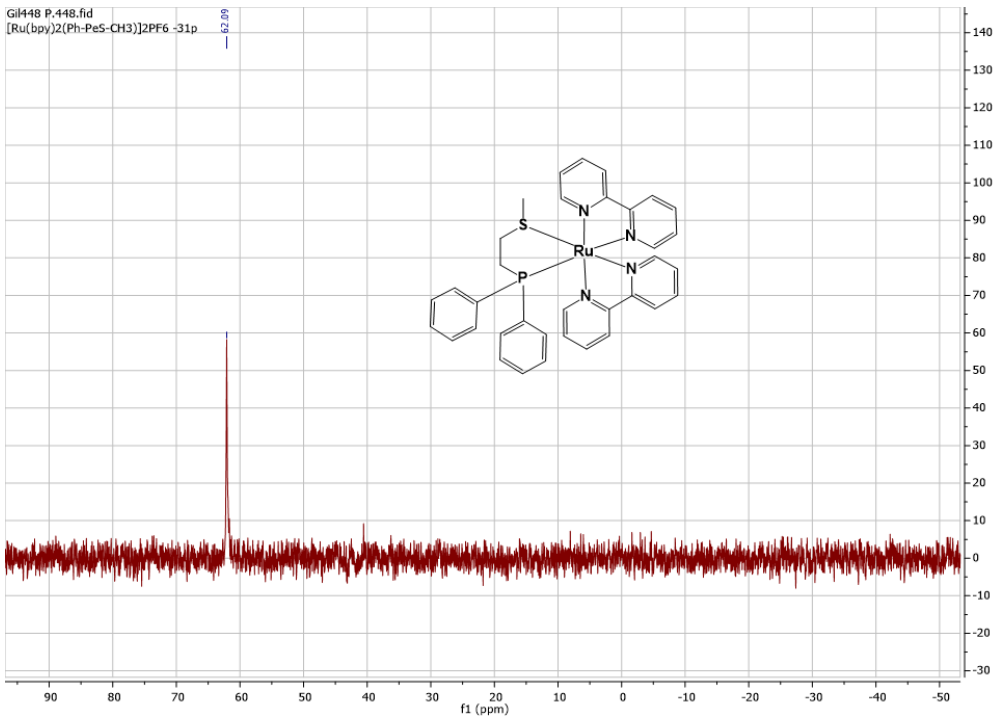

Figure 84: *^{31}P NMR of RuL5*

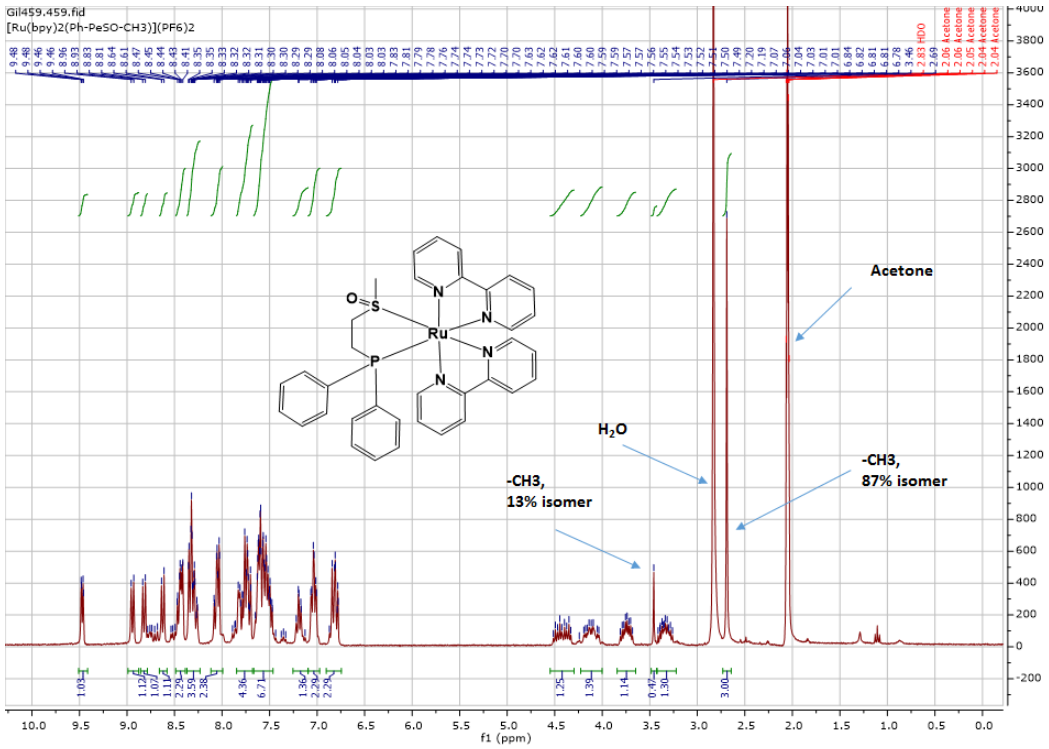

Figure 85: *^{1}H NMR of RuL5O*

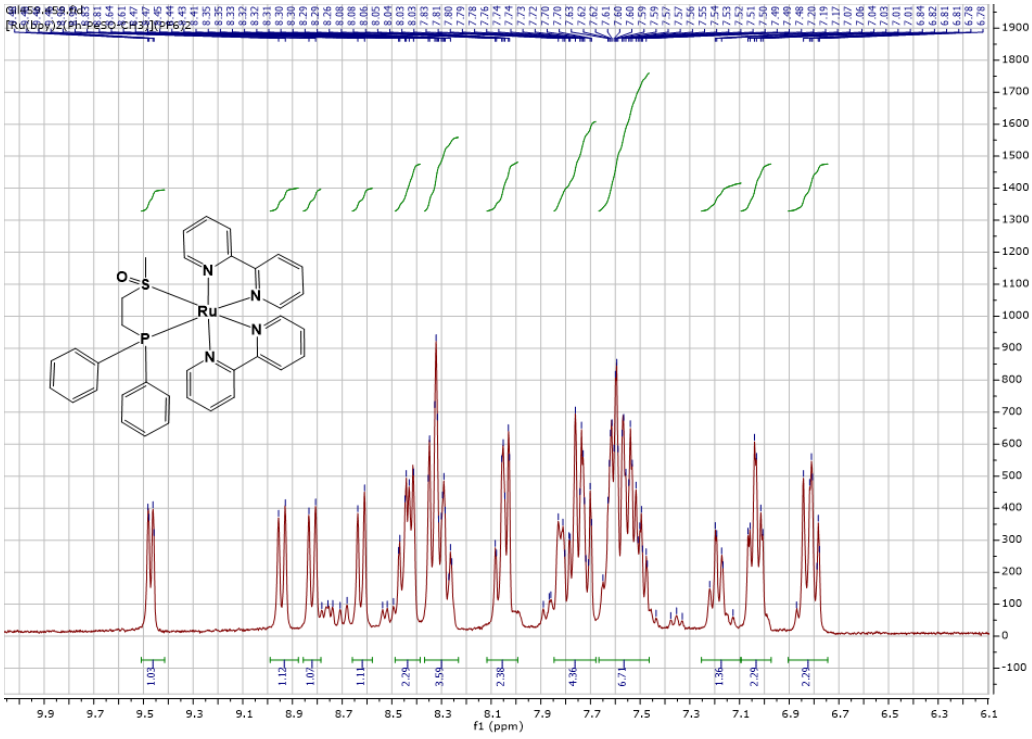

Figure 86: *^{1}H NMR of RuL5O*

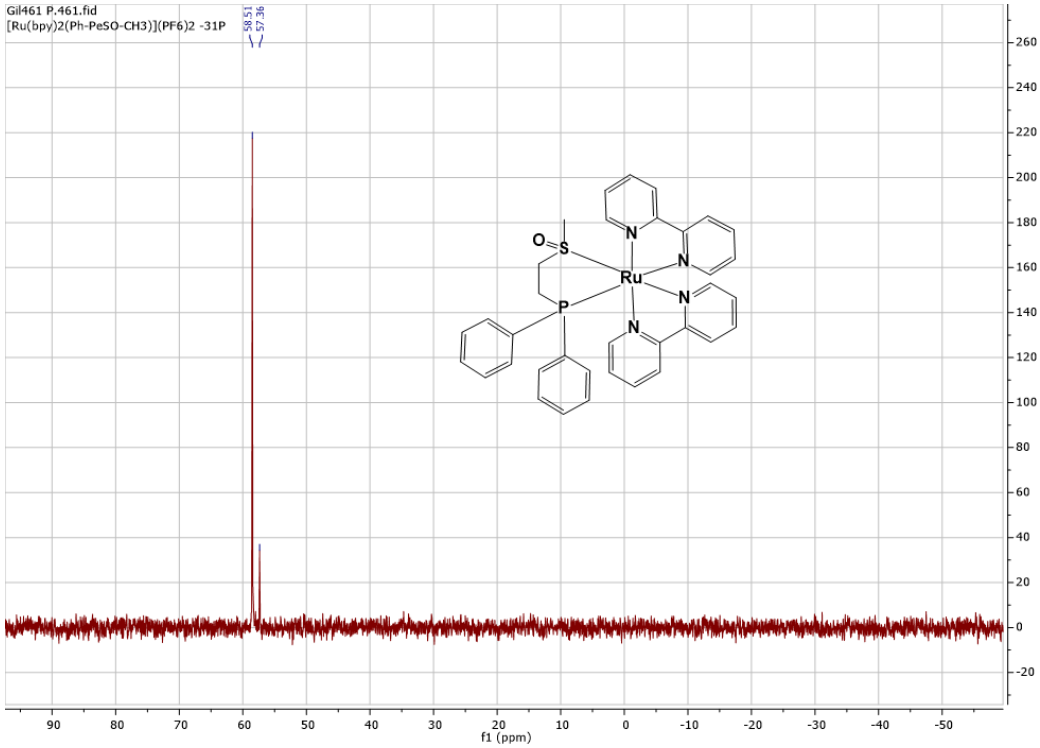

Figure 87: *^{31}P NMR of RuL5O*

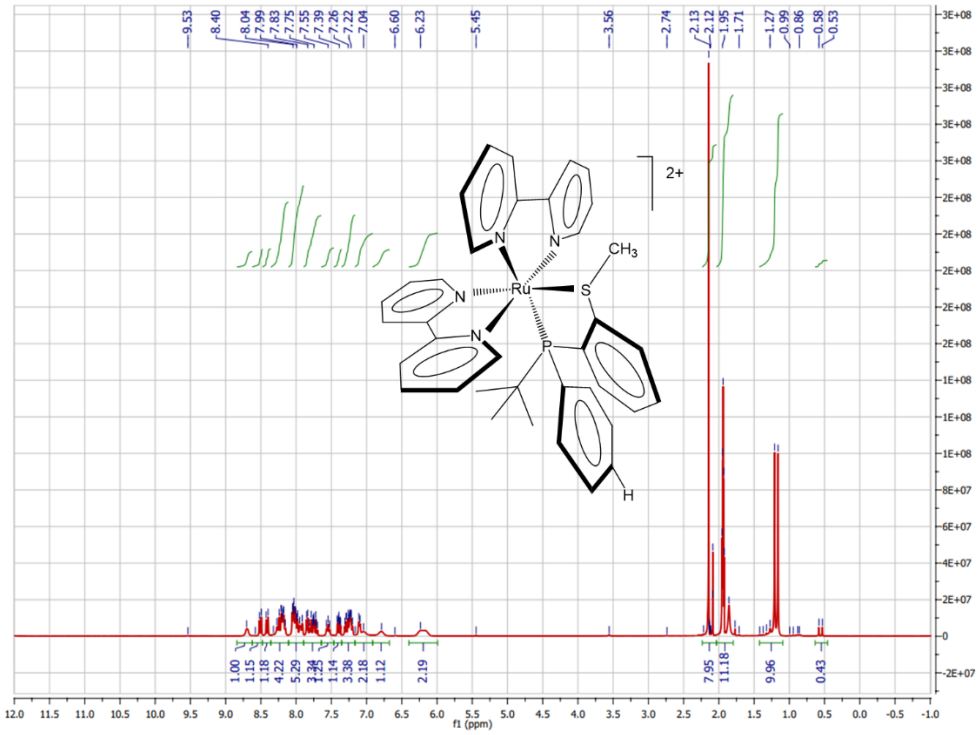

Figure 88: *^{1}H NMR of RuL6*

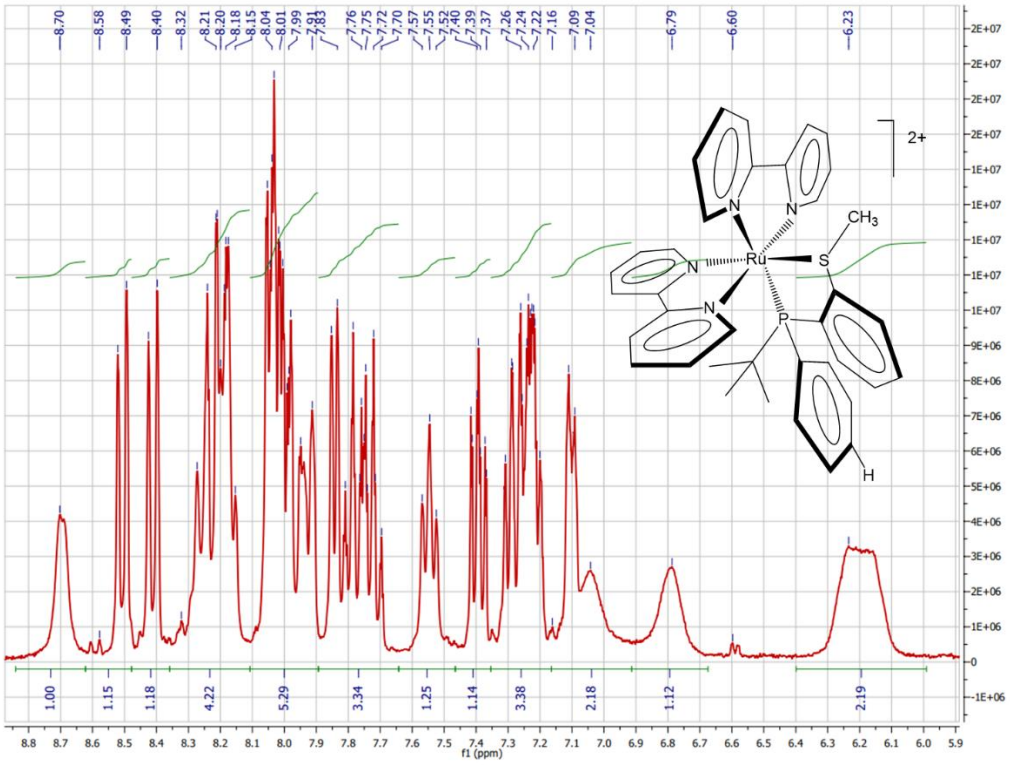

Figure 89: *^{1}H NMR of RuL6*

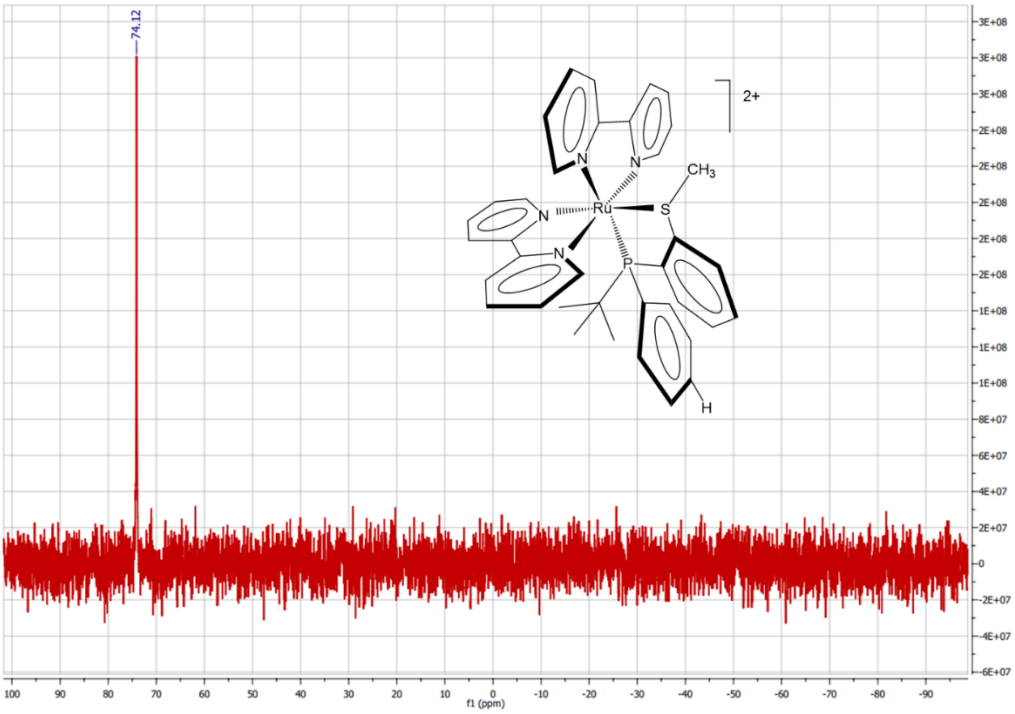

Figure 90: *^{31}P NMR of RuL6*

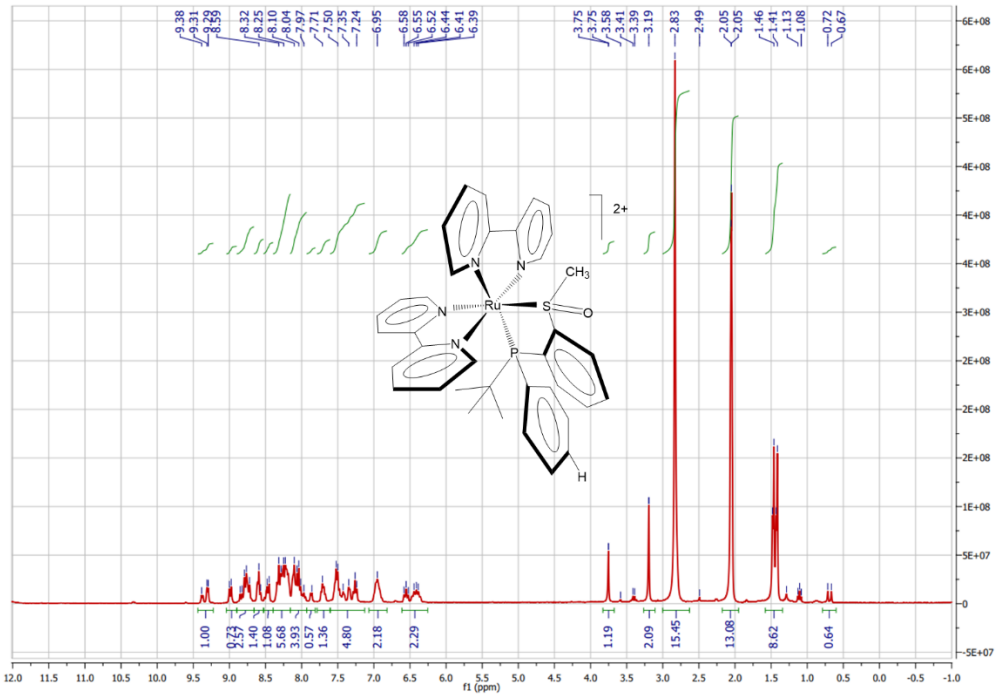

Figure 91: *^{1}H NMR of RuL6O*

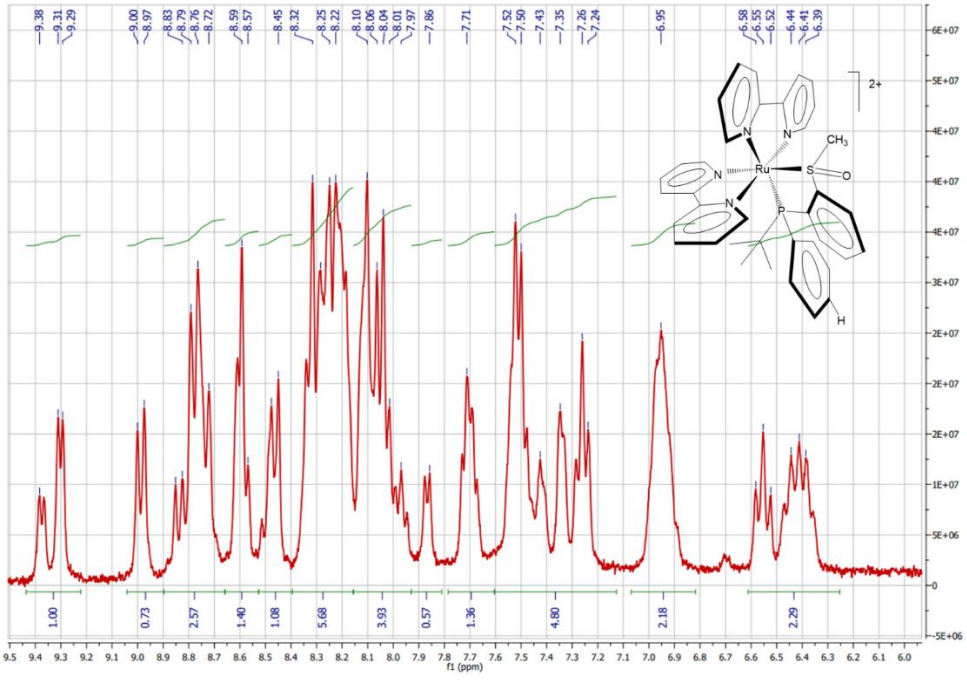

Figure 92: *^{1}H NMR of RuL6O*

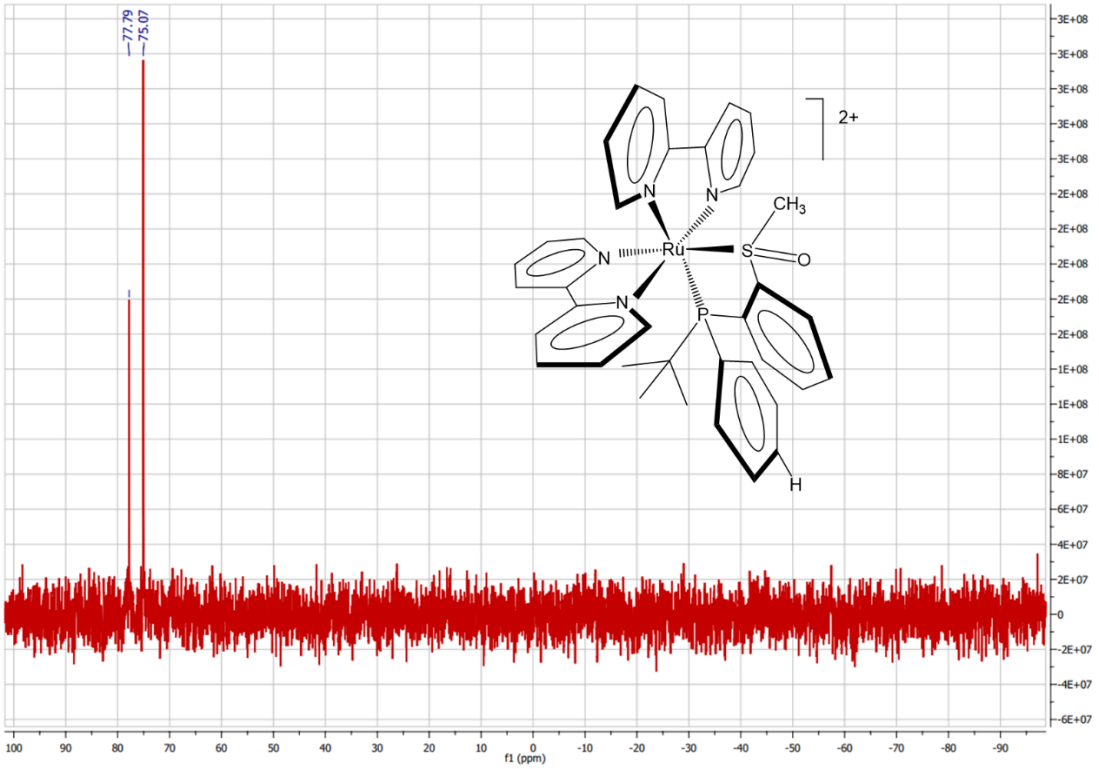

Figure 93: *^{31}P NMR of RuL6O*

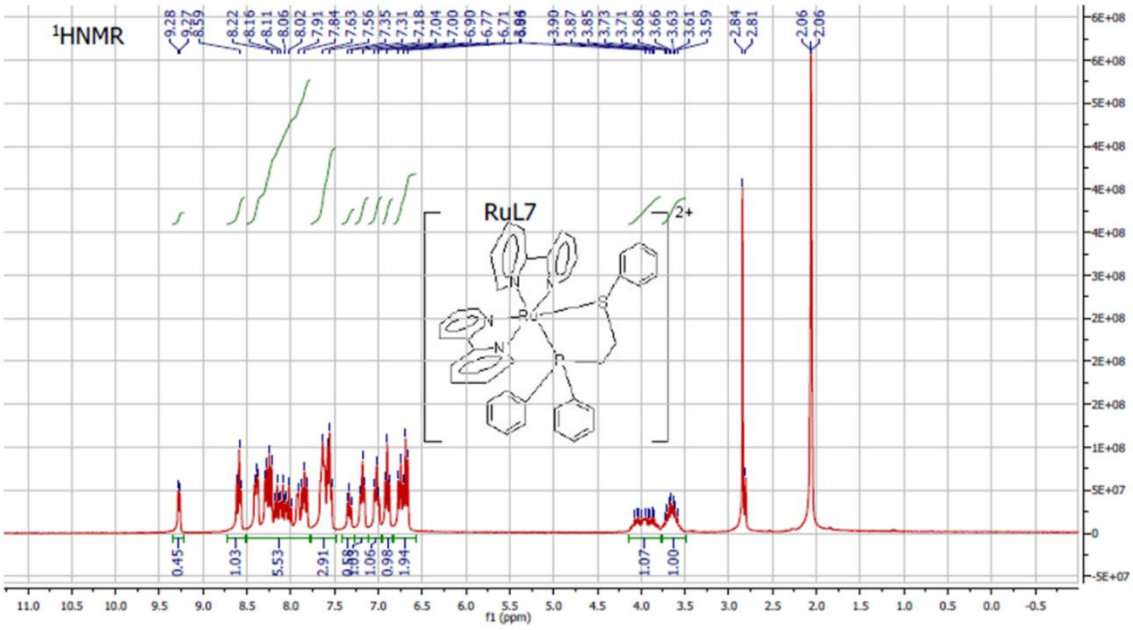

Figure 94: *^{1}H NMR of RuL7*

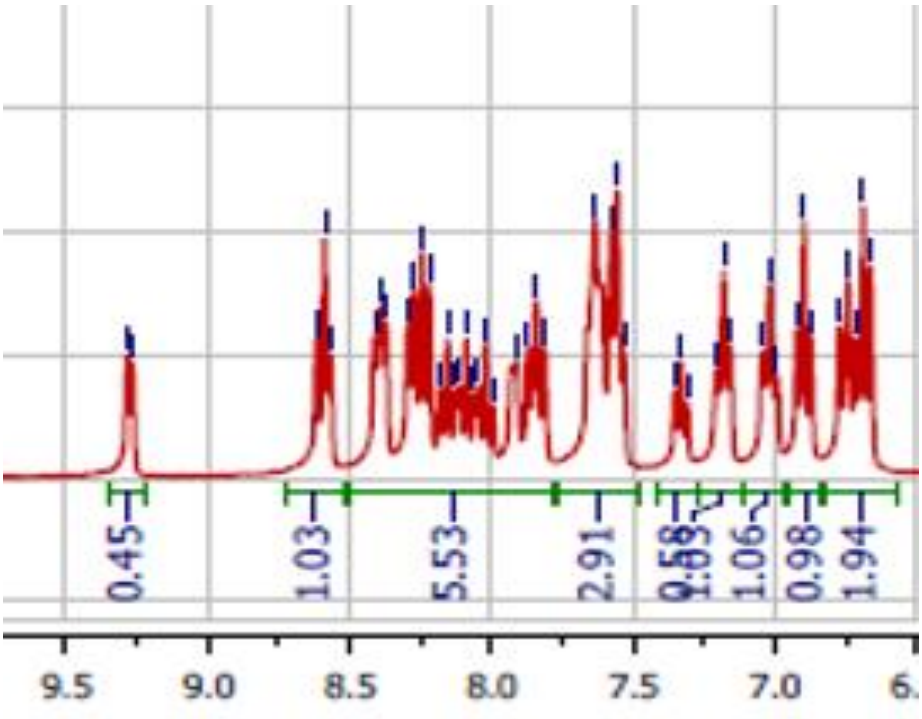

Figure 95: *^{1}H NMR of RuL7*

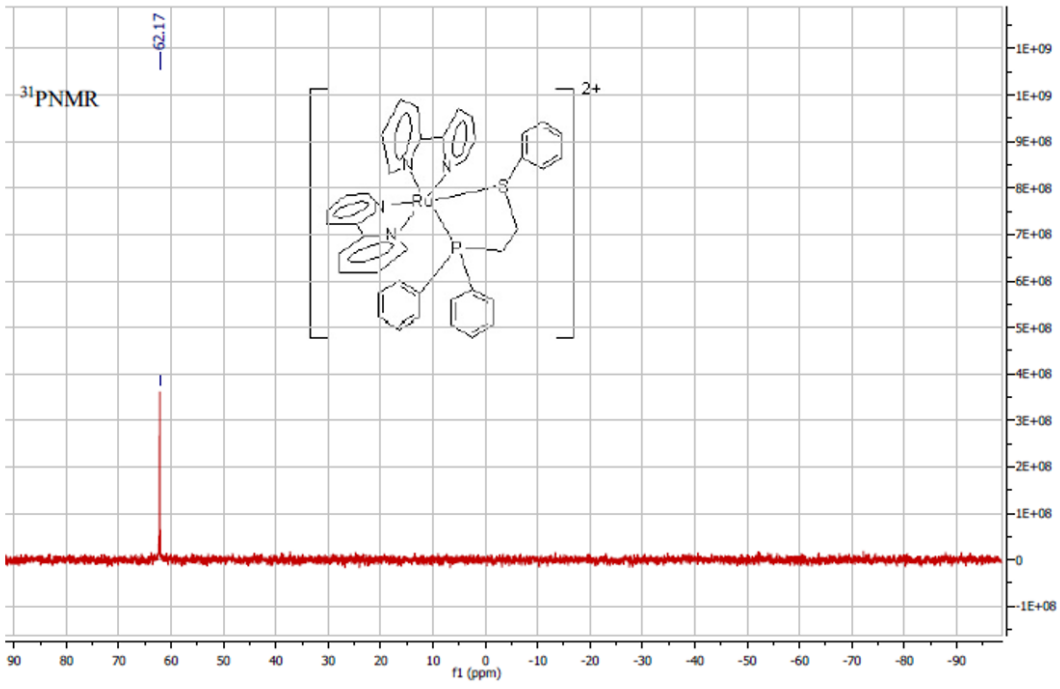

Figure 96: *^{31}P NMR of RuL7*

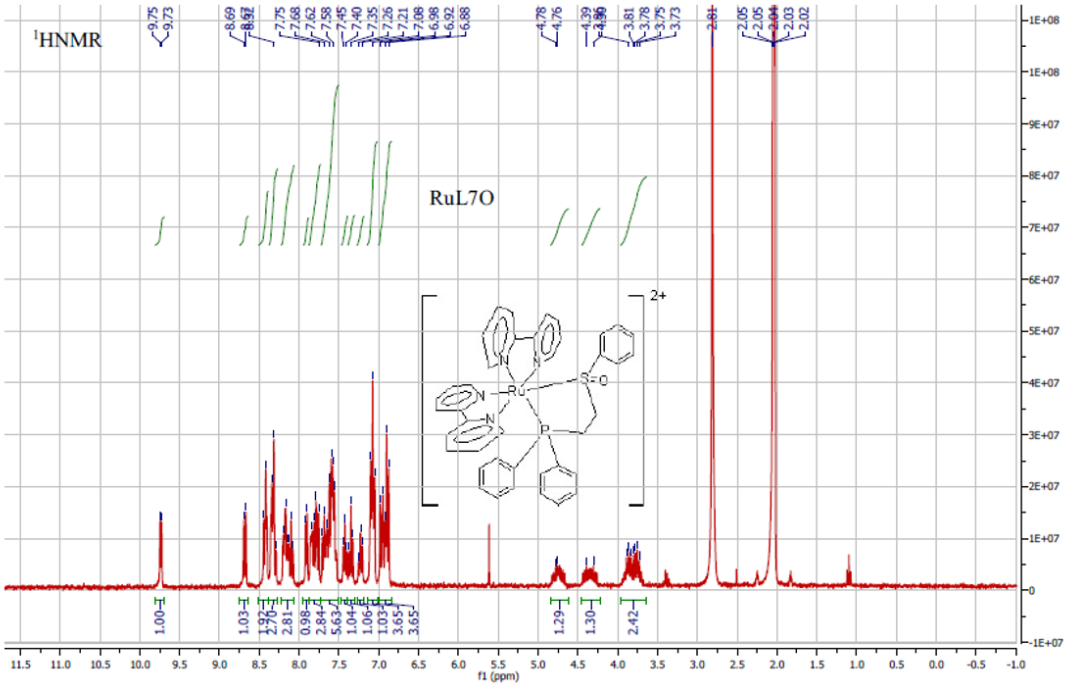

Figure 97: *^{1}H NMR of RuL7O*

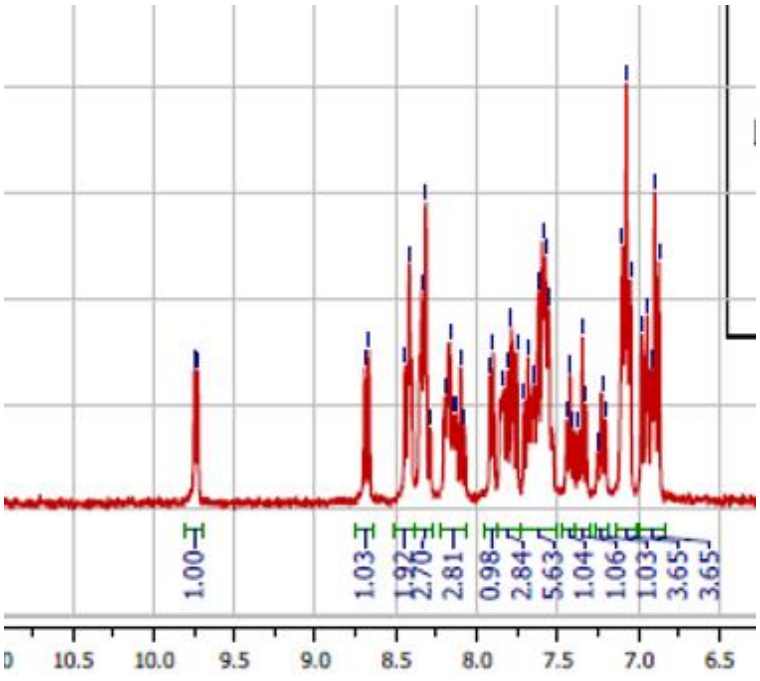

Figure 98: *^{1}H NMR of RuL7O*

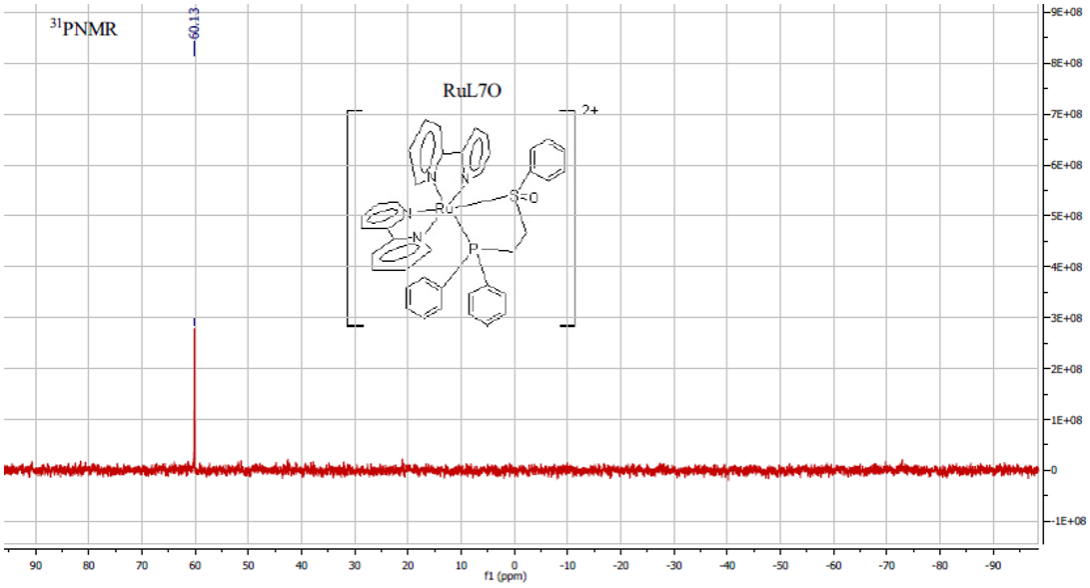

Figure 99: *^{31}P NMR of RuL7O*

X-Ray Crystallography

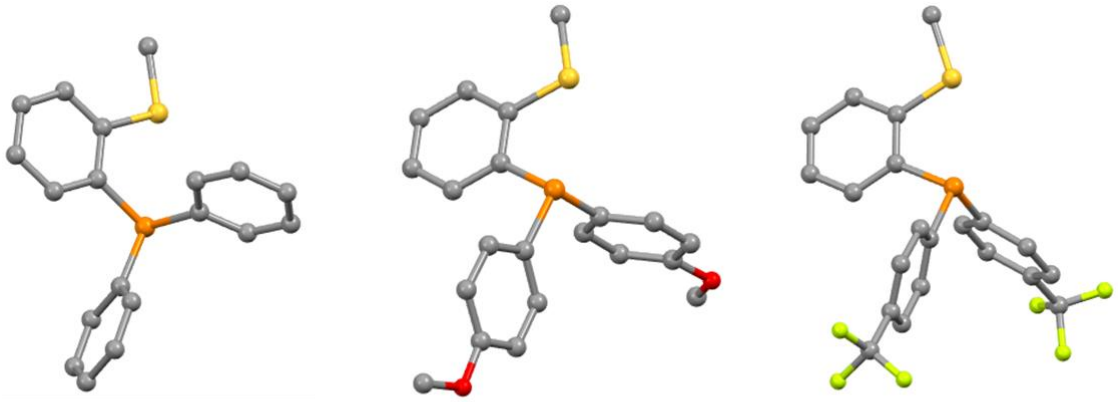

$L1_H$ $L2_{OCH3}$ $L3_{CF3}$

Figure 100: *Molecular structures of $L1_H$, $L2_{OCH3}$, and $L3_{CF3}$ determined from X-ray diffractometry. Molecular structures are depicted as thermal ellipsoid plots at 50% probability. The S atom is yellow, the P atom is orange, C atoms are grey, and O atoms are red.*

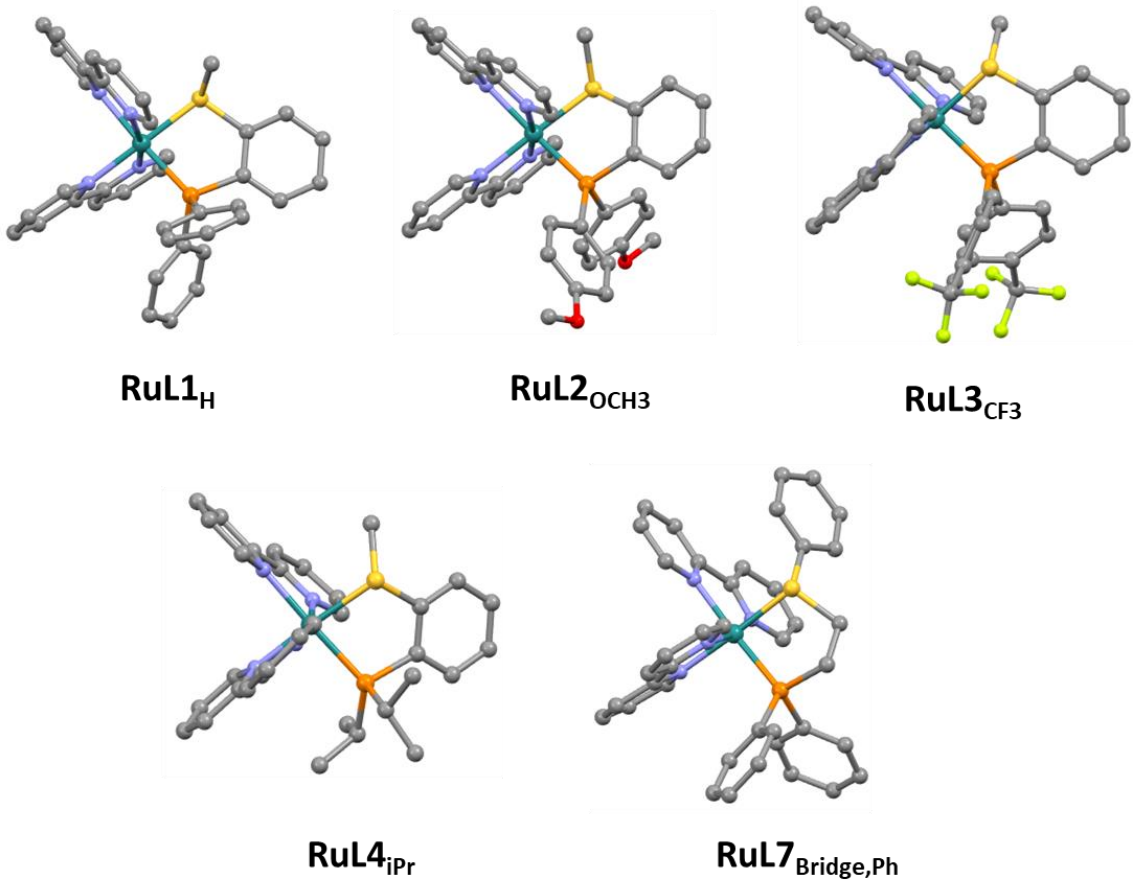

Figure 101: *Molecular structures of RuL1$_H$, RuL2$_{OCH3}$, RuL3$_{CF3}$, RuL4$_{iPr}$, and RuL7$_{Bridge,Ph}$ determined from X-ray diffractometry. Molecular structures are depicted as thermal ellipsoid plots at 50% probability. The Ru atom is green, the S atom is yellow, the P atom is orange, C atoms are grey, N atoms are blue, and O atoms are red.*

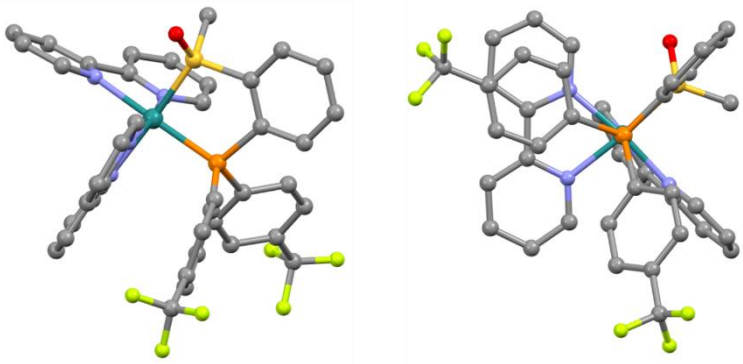

Figure 102: *Two views of a p – stacking interaction found in crystal structures of ruthenium phosphine thioether and ruthenium phosphine sulfoxide complexes. (Left) A side view of the p – stacking interaction in RuL3O$_{CF3}$ between a bipyridine and a phenyl group on phosphine. The distance between these centroids is 3.47 Å. (Right) A front-on view of the p – stacking interaction. The offset geometry between the two phenyl groups means that the p – system of one ring lies over the p – cavity of the neighboring ring, resulting in a p – s attraction that dominates any p – p repulsion of the two rings.*[163]

Table 9: *Centroid – centroid distances between bipyridine and phenyl phosphine moieties for various ruthenium complexes from this study.*

Centroids	Distance
RuL1O	3.96
RuL2O	3.96
RuL3O	3.47
RuL5O	3.74
RuL6O	3.57
RuL7O	4.19
RuL1	4.10
RuL2	3.47
RuL3	3.54

Table 10: *Bond distances for S – O, Ru – S, and Ru – N (trans-S) for the ruthenium thioether and ruthenium sulfoxide complexes. Note that Ru – S bond distances are shorter in the sulfoxide, while Ru – N (trans-S) bond distances are longer in the sulfoxide, for each thioether/sulfoxide pair examined. These data are consistent with a trans influence being imparted across the ruthenium center by sulfur and support the notion the Ru – S p-backbonding is greater in the sulfoxide than it is in the thioether.*

Compound	S-O	Ru-S	Ru-N (t*rans*-S)
RuL1	N/A	2.318(4)	2.073(2)
RuL2	N/A	2.320(2)	2.092(5)
RuL3	N/A	2.319(5)	2.079(2)
RuL4	N/A	2.324(3)	2.074(3)
RuL7	N/A	2.350(1)	2.066(3)
RuL1O	1.479(1)	2.218(5)	2.097(1)
RuL2O	1.475(4)	2.218(1)	2.100(5)
RuL3O	1.479(5)	2.233(2)	2.099(60
RuL4O	1.49 (2)	2.248(4)	2.100(2)
RuL5O	1.479(4)	2.268(3)	2.108(5)
RuL6O	1.487(3)	2.224(1)	2.095(3)
RuL7O	1.476(3)	2.245(9)	2.100(3)

Table 11: *Sulfur – methyl bond lengths for the $L1_H$, $L2_{OCH3}$, and $L3_{CF3}$ group of complexes. These bond distances are longest in the ruthenium thioether, medium in the free ligand, and shortest in the ruthenium sulfoxide.*

Compound	S-Me
L1	1.797(2)
L2	1.794(2)
L3	1.782(7)
RuL1	1.814(3)
RuL2	1.807(8)
RuL3	1.808(2)
RuL1O	1.789(2)
RuL2O	1.783(7)
RuL3O	1.778(9)

Table 12: *Ru – P and Ru – N (trans-P) bond lengths for ruthenium thioether/sulfoxide pairs examined in this study. For the photoisomerizing (odd-numbered) groups, oxidation of the thioether results in longer Ru – P bonds and shorter Ru – N (trans-P) bonds. In contrast, for the non-photoisomerizing (even-numbered) groups, oxidation of the thioether results in shorter Ru – P bonds and longer Ru – N (trans-P) bonds.*

	Ligand Series	Ru-Thioether	Ru-Sulfoxide	Photoisomerize?
Ru - P Bond Lengths	L1	2.292(6)A	2.303(8)	Yes
	L2	2.305(4)	2.297(4)	No
	L3	2.284(1)	2.289(1)	Yes
	L4	2.328(1)	2.324(6)	No
	L7	2.314(8)	2.324(1)	Yes
Ru - N Bond Lengths (*trans* to P)	L1	2.125(2)A	2.122(1)	Yes
	L2	2.117(5)	2.123(5)	No
	L3	2.107(2)	2.095(5)	Yes
	L4	2.118(3)	2.123(2)	No
	L7	2.112(3)	2.120(3)	Yes

Absorption Spectra:

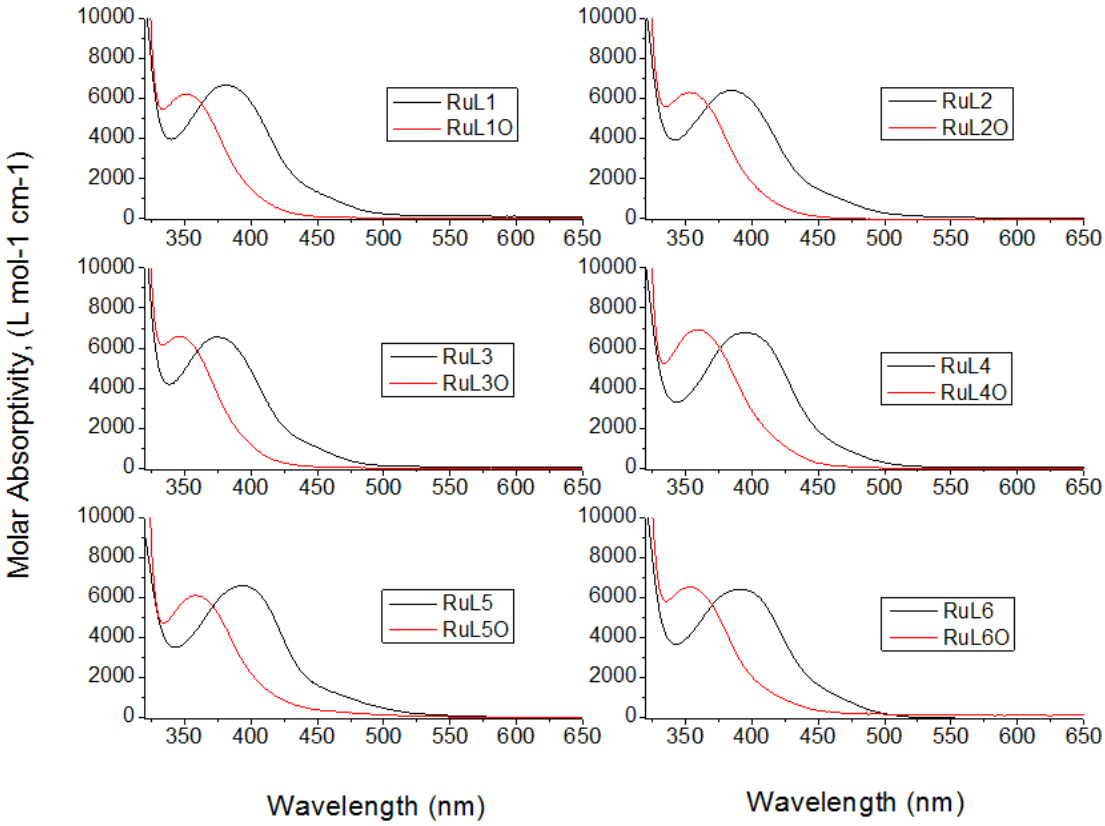

Figure 103: *Absorption spectra of the ruthenium thioether and sulfoxide complexes.*

Table 13: *MLCT absorption properties of the ruthenium phosphine thioether complexes.*

Compound	λ_{max} (nm)	ε (L mol^{-1} cm^{-1})	FWHM (cm^{-1})
RuL1	382	6,680	4716
RuL2	384	6,420	4852
RuL3	375	6,570	4838
RuL4	396	6,790	4894
RuL5	393	6,590	4102
RuL6	391	6,410	4862

Table 14: *MLCT full widths at half max of the ruthenium phosphine sulfoxide complexes.*

Compound	FWHM (cm^{-1})
RuL1O	4811
RuL2O	5122
RuL3O	4808
RuL4O	5353
RuL5O	4797
RuL6O	4960
$Ru(bpy)_3$	3550

Electrochemistry:

Cyclic voltammetry was conducted in a one-compartment electrochemical cell under inert atmosphere using a platinum wire as the counter electrode, glassy carbon as the working electrode, and Ag^{+}/Ag as the standard electrode. The sample solution was prepared in 0.1M tetra butyl ammonium hexafluorophosphate in acetonitrile.

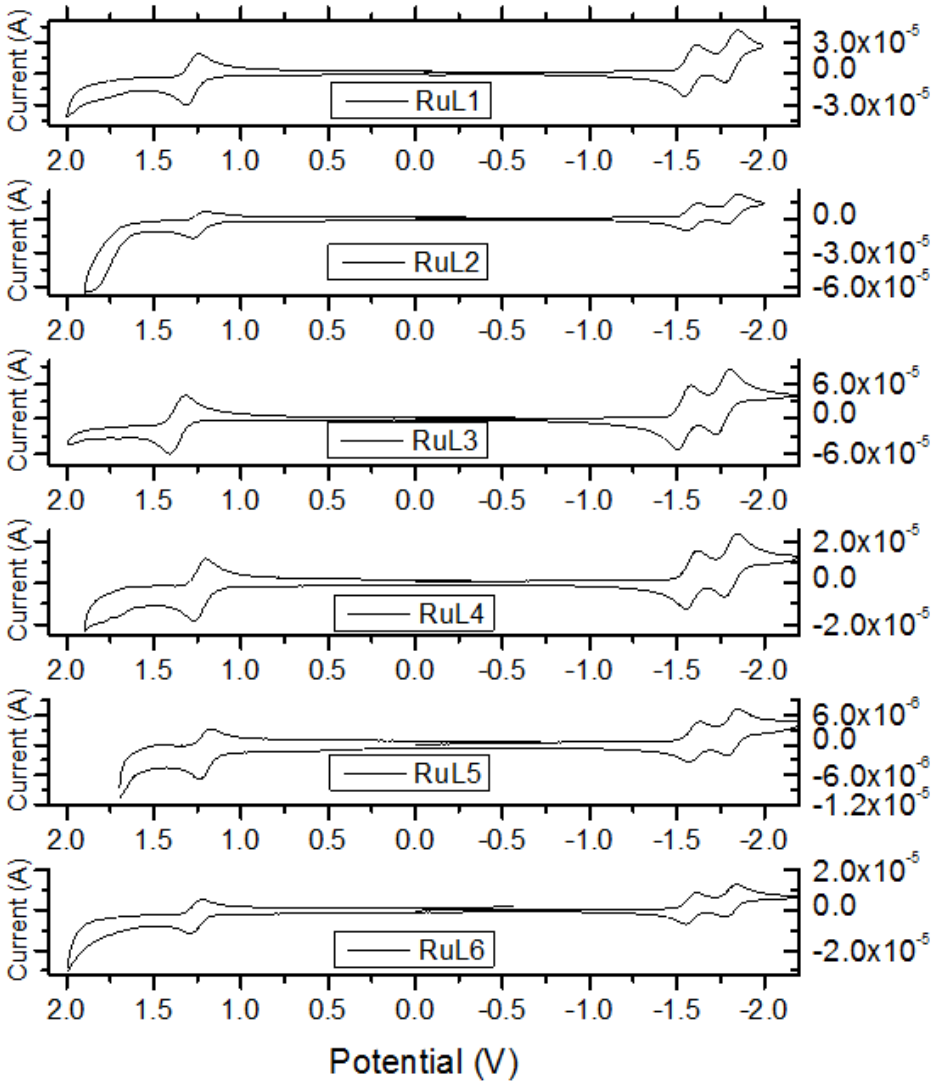

Figure 104: *Cyclic voltammograms of RuL1, RuL2, RuL3, RuL4, RuL5, and RuL6.*

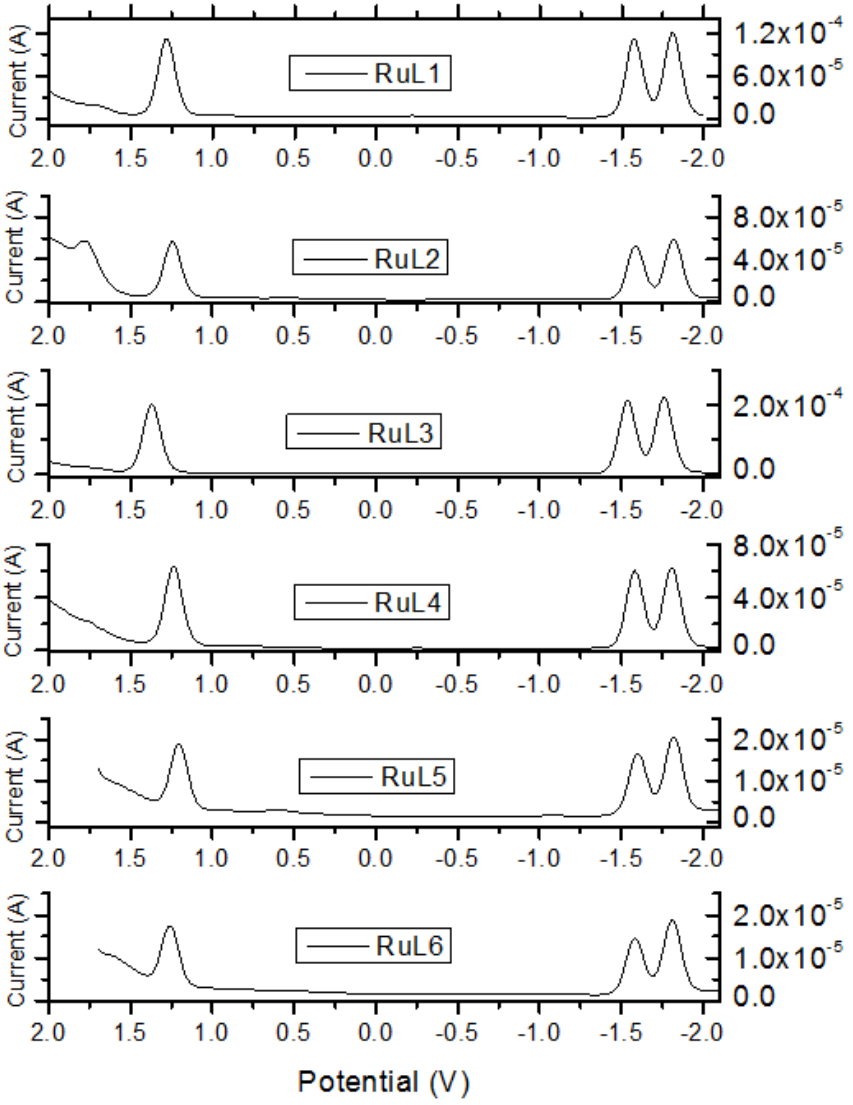

Figure 105: *Square wave voltammograms of RuL1, RuL2, RuL3, RuL4, RuL5, and RuL6.*

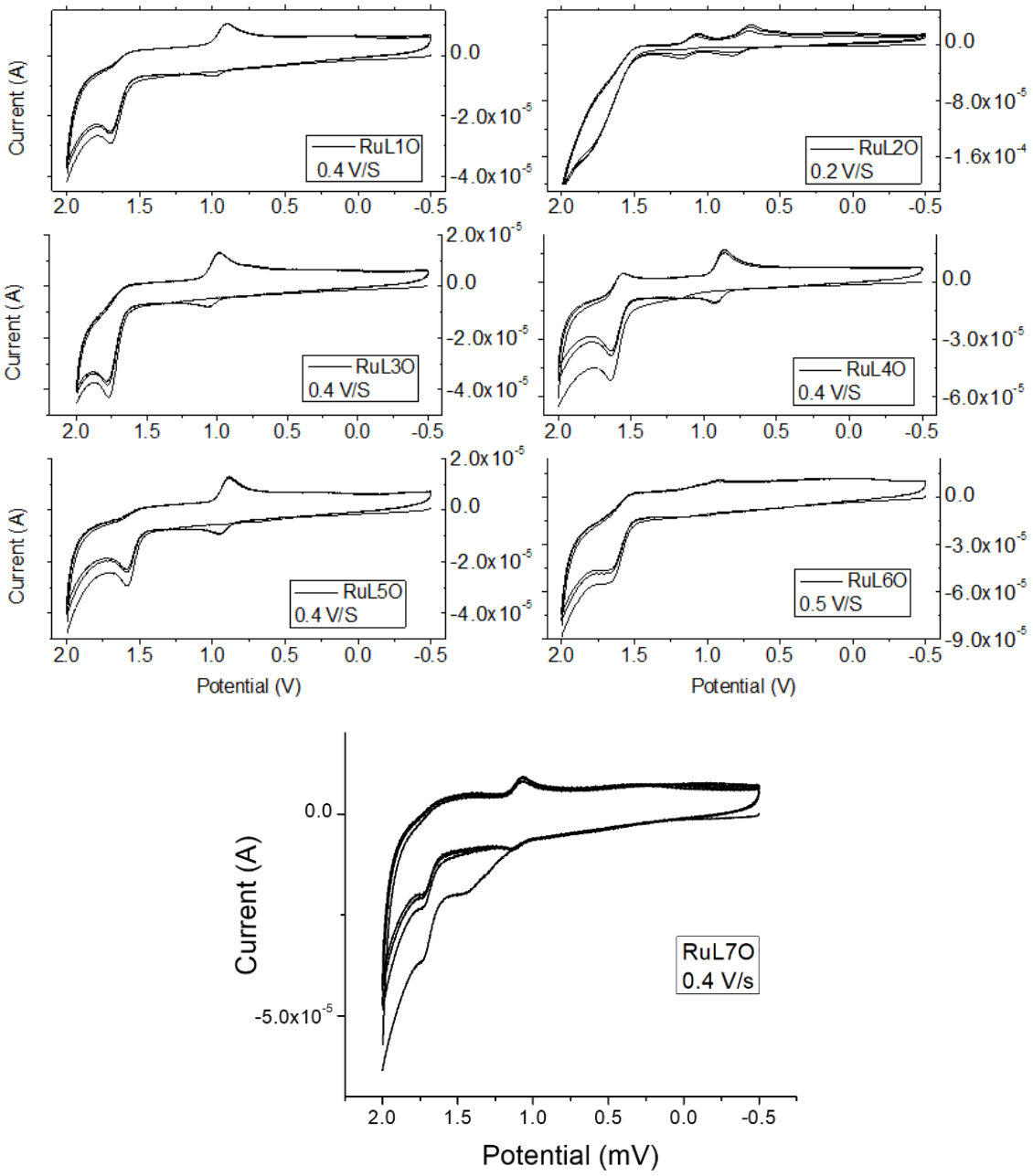

Figure 106: *Cyclic voltammograms of RuL1O, RuL2O, RuL3O, RuL4O, RuL5O, RuL6O, and RuL7O. Scan rates are denoted in the plot.*

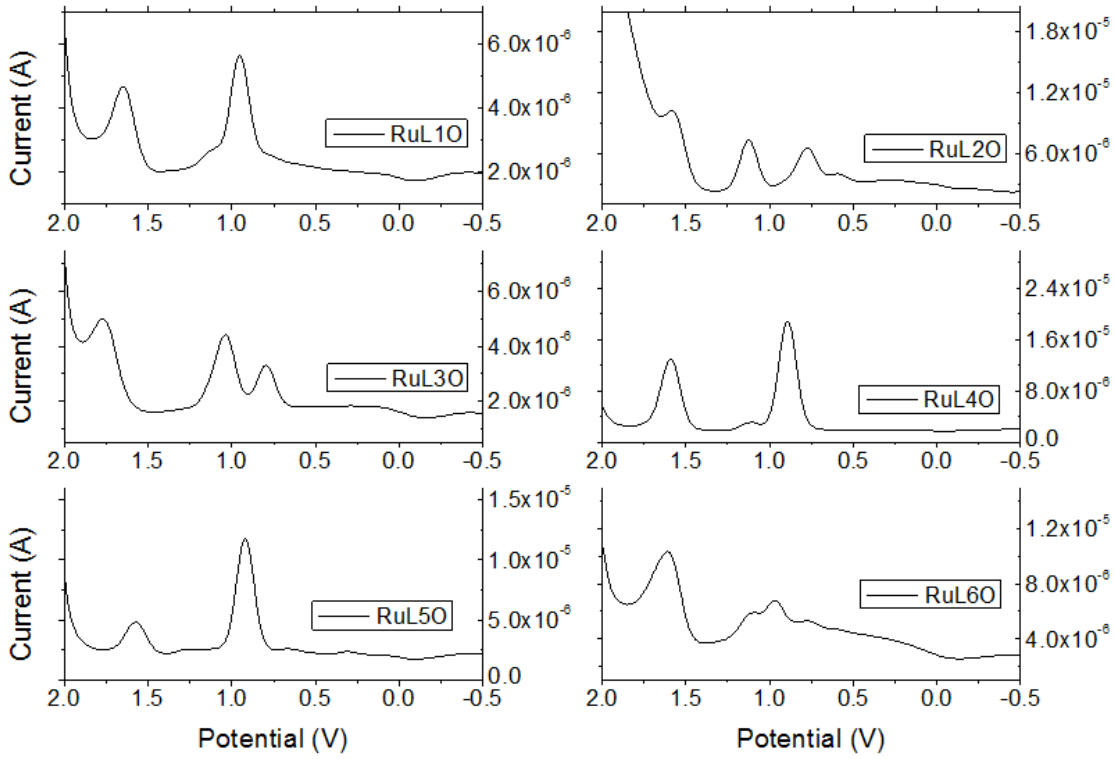

Figure 107: *Square wave voltammograms of RuL1O, RuL2O, RuL3O, RuL4O, RuL5O, and RuL6O.*

Rate of Electrochemical Isomerization:

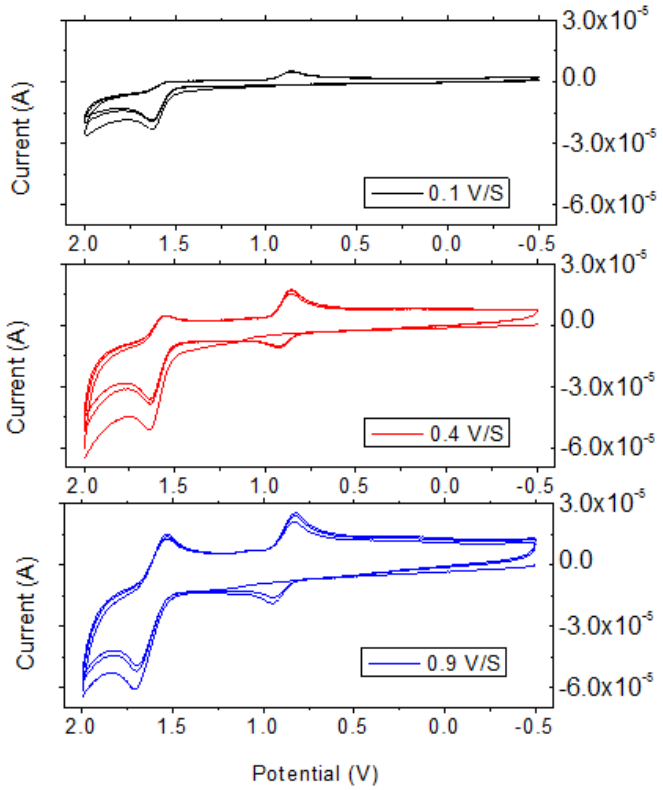

Figure 108: *Cyclic voltammograms of RuL4O at different scan rates in order to determine the rate of electrochemical isomerization.*

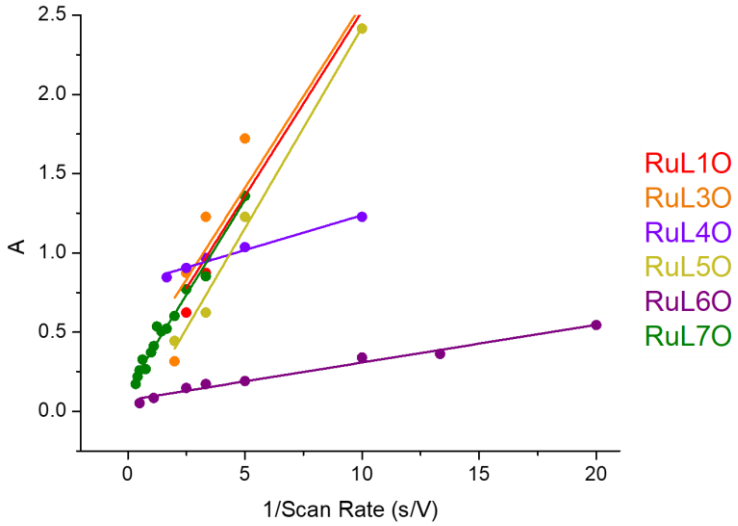

Figure 109: *Plots of A vs. s/V for the electrochemical S → O isomerization of RuL1O, RuL3O, RuL4O, RuL5O, RuL6O, and RuL7O.*

Table 15: *Raw data of V/s for electrochemical S → O isomerization of RuL1O, RuL3O, RuL4O, RuL5O, RuL6O, and RuL7O.*

V/s	RuL1O	RuL2O	RuL3O	RuL4O	RuL5O	RuL6O	RuL7O
0.05	--	--	--	--	--	1.664	--
0.075	--	--	--	--	--	1.676	--
0.1	1.66	--	1.75	1.63	1.57	1.678	1.613
0.2	1.67	--	1.76	1.635	1.59	1.695	1.617
0.3	1.69	--	1.77	1.637	1.61	1.698	1.63075
0.4	1.7	--	1.78	1.639	--	1.7025	1.63375
0.5	--	--	1.81	--	1.62	--	1.641
0.6	--	--	--	1.641	--	--	1.64525
0.7	--	--	--	--	--	--	1.64625
0.8	--	--	--	--	--	--	1.6445
0.9	--	--	--	--	--	1.719	1.65225
1	--	--	--	--	--	--	1.65525
1.3	--	--	--	--	--	--	1.665
1.6	--	--	--	--	--	--	1.659
2	--	--	--	--	--	1.734	1.666
2.4	--	--	--	--	--	--	1.671
3	--	--	--	--	--	--	1.678

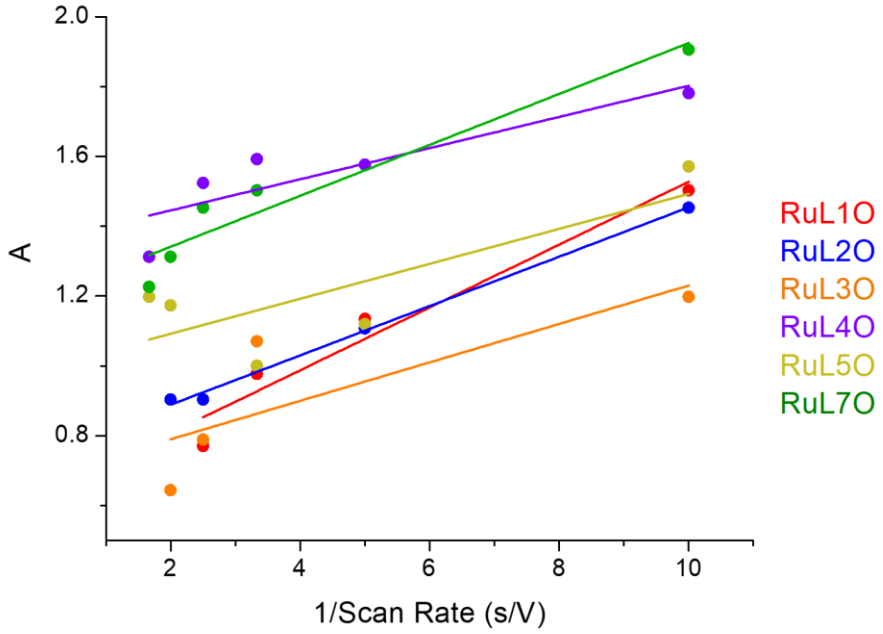

Figure 110: *Plots of A vs. s/V for the electrochemical O → S isomerization of RuL1O, RuL2O, RuL3O, RuL4O, RuL5O, and RuL7O.*

Table 16: *Raw data of V/s for electrochemical O → S isomerization of RuL1O, RuL2O, RuL3O, RuL4O, RuL5O, and RuL7O.*

V/S	RuL1O	RuL2O	RuL3O	RuL4O	RuL5O	RuL6O	RuL7O
0.1	0.918	1.091	0.9953	0.8643	0.8873	--	0.949
0.2	0.9097	1.083	--	0.8607	0.8773	--	0.949
0.3	0.9053	--	0.992	0.861	0.874	--	0.942
0.4	0.8983	1.077	0.983	0.8597	--	--	0.941
0.5	--	1.077	0.977	--	0.8787	--	0.938
0.6	--	--	--	0.8553	0.8793	--	0.936
0.7	--	--	--	--	--	--	0.935
0.8	--	--	--	--	--	--	0.932
0.9	--	--	--	--	--	--	0.93
1	--	--	--	--	--	--	0.93

Table 17: *Rates of electrochemical isomerization (S → O and O → S), and $E_{1/2}$ values for RuL1O, RuL2O, RuL3O, RuL4O, RuL5O, RuL6O, and RuL7O.*

		RuL1O	RuL2O	RuL3O	RuL4O	RuL5O	RuL6O	RuL7O
Ru^{III}	$E_{1/2(SW)}$	1.64	1.58	1.73	1.59	1.55	1.60	1.58
S → O	s^{-1}	0.23 ±0.01	--	0.23 ±0.01	0.04 ±0.01	0.25 ±0.01	0.02 ±0.01	0.24 ±0.01
Ru^{II}	$E_{1/2(SW)}$	0.95	1.13	1.04	0.89	0.92	--	0.97
O → S	s^{-1}	0.09 ±0.01	0.07 ±0.01	0.06 ±0.01	0.05 ±0.01	0.05 ±0.01	--	0.07 ±0.01

Quantum Yield of Isomerization

The reversion rate was calculated by fitting the thermal reversion of the RuL1O and RuL3O in dichloroethane solution.

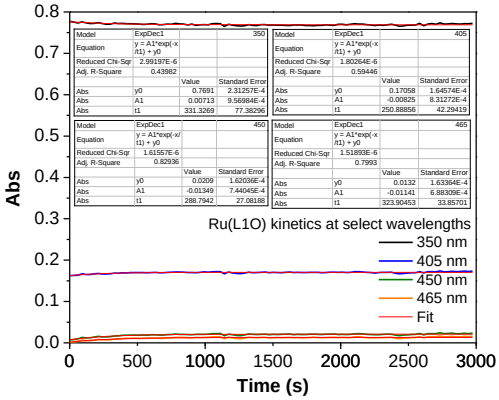

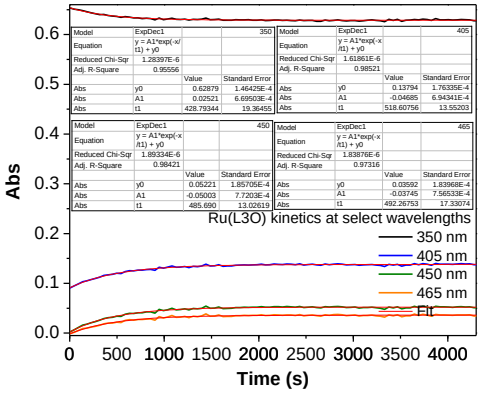

Figure 111: *Plots of absorbance vs. time for the photochemical rise kinetics of RuL1O and RuL3O*

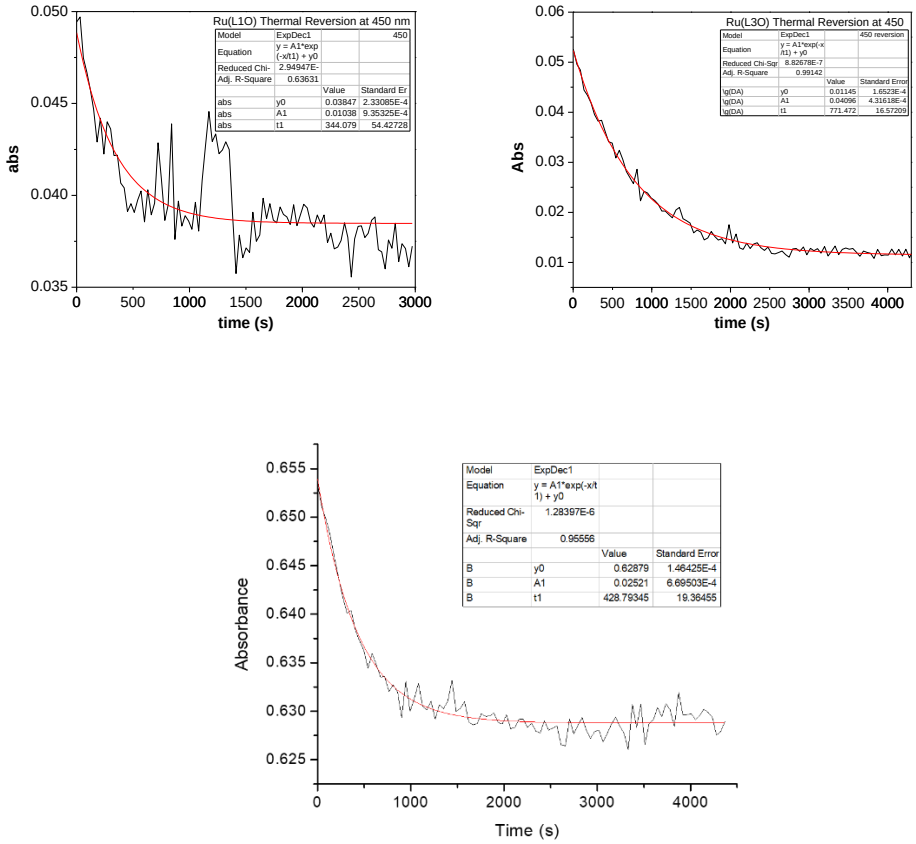

Figure 112: *Plots of absorbance vs. time for the thermal reversion of RuL1O, RuL3O, and RuL5O.*

Transient Absorption

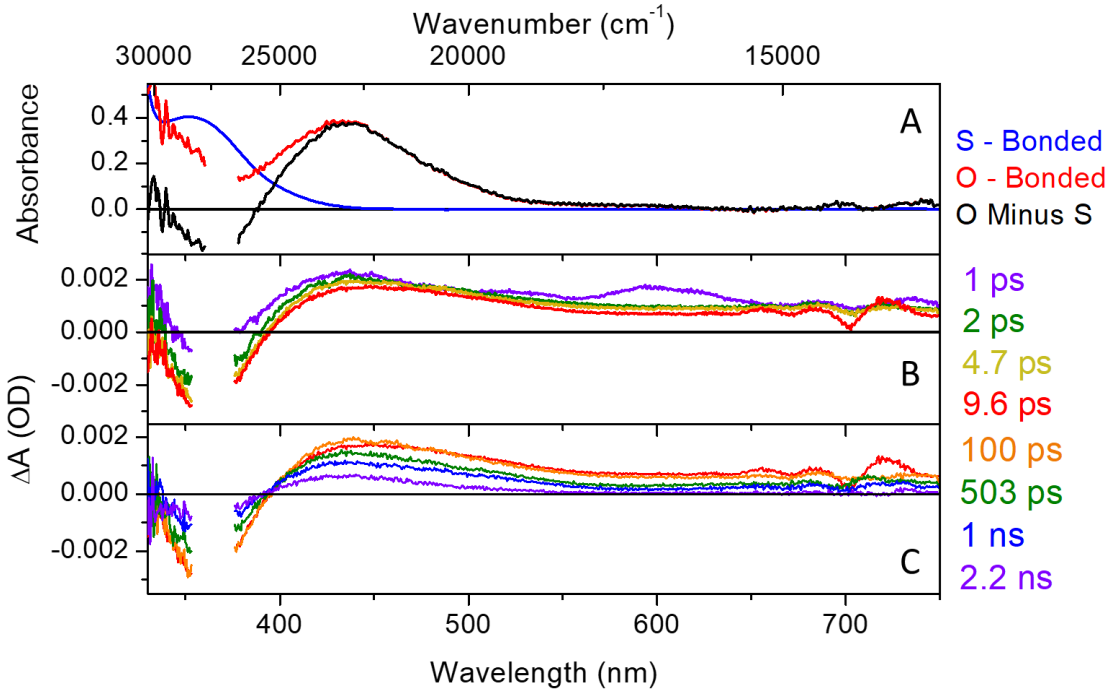

Figure 113: Spectra of RuL1O in Acetonitrile

(A) Spectra obtained from bulk photolysis (λ_{exc} 405 nm) of RuL1O in acetonitrile solution. Blue trace is the S-isomer, red trace is the O-isomer, and black trace is the difference spectrum (O-isomer minus S-isomer) extracted from the data. (B) Time-resolved spectra of RuL1O at short time-delays between 1.0 ps and 9.6 ps. (C) Time-resolved spectra of RuL1O at long time delays between 9.6 ps and 2.2 ns. Excitation wavelength, 365 nm.

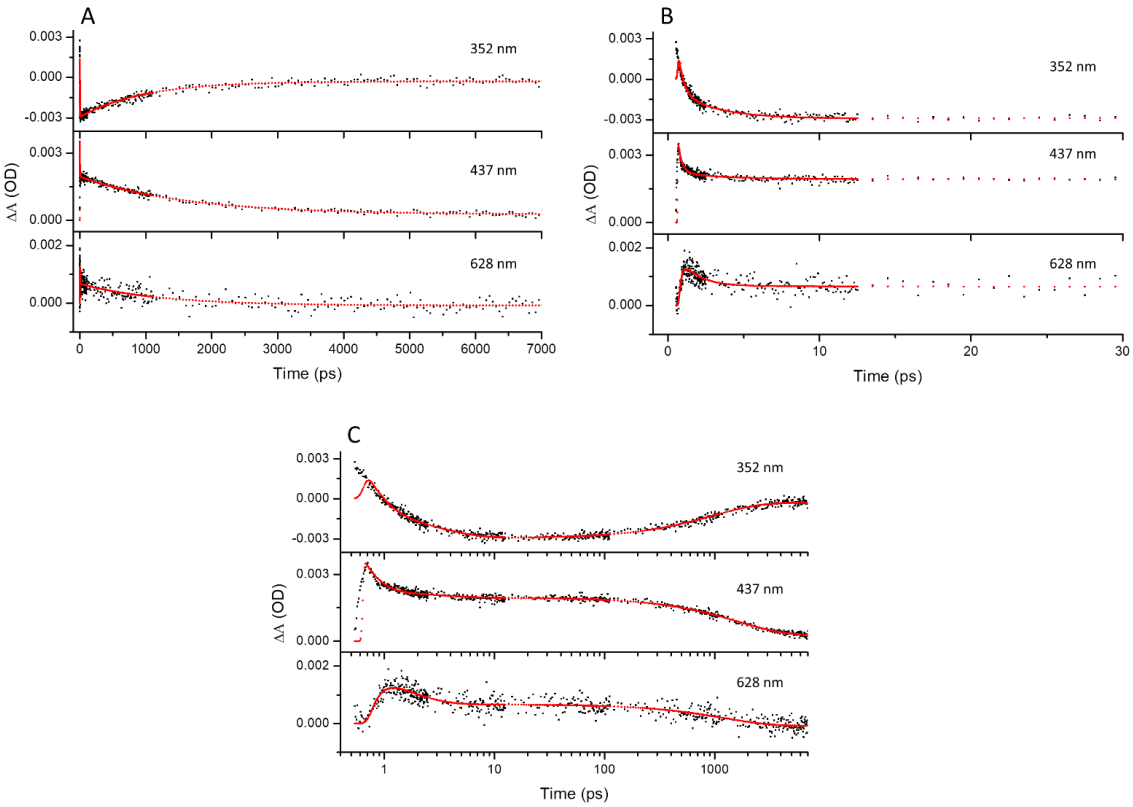

Figure 114: Ultrafast Kinetics of RuL1O in Acetonitrile

(A) Single wavelength kinetics fits out to 7000 ps time delays of RuL1O in acetonitrile solution applied to single-wavelength kinetics at 352 nm, 437 nm, and 628 nm. (B) Single wavelength kinetic fits out to 30 ps time delays. (C) Single wavelength kinetic fits out to 7000 ps time delays with logarithmic scaling on the x-axis. Raw data is black and the kinetic fit is red. A triexponential global fit yields good results with $\tau_1 = 0.27 \pm 0.12$ *ps,* $\tau_2 = 2.12 \pm 1.04$ *ps, and* $\tau_3 = 1156.8 \pm 87.3$ *ps.*

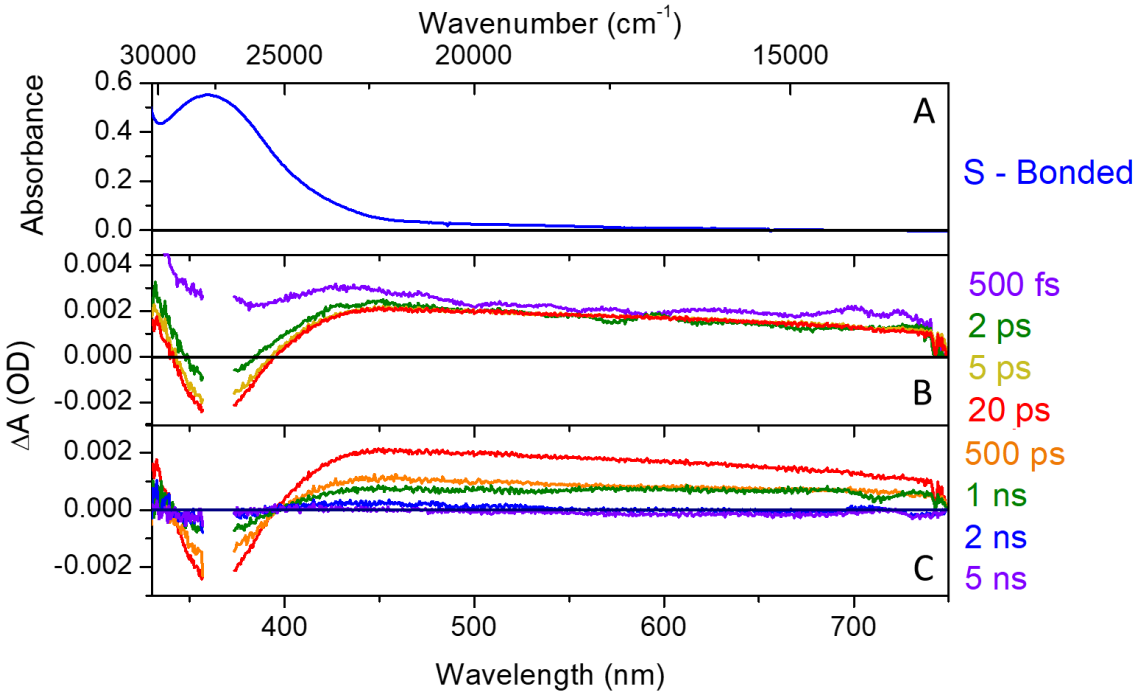

Figure 115: Spectra of RuL2O in Acetonitrile

(A) Spectra obtained from bulk photolysis (λ_{exc} 360 nm) of RuL2O in acetonitrile solution. (B) Time-resolved spectra of RuL2O at short time-delays between 500 fs and 20 ps. (C) Time-resolved spectra of RuL2O at long time delays between 20 ps and 5 ns.

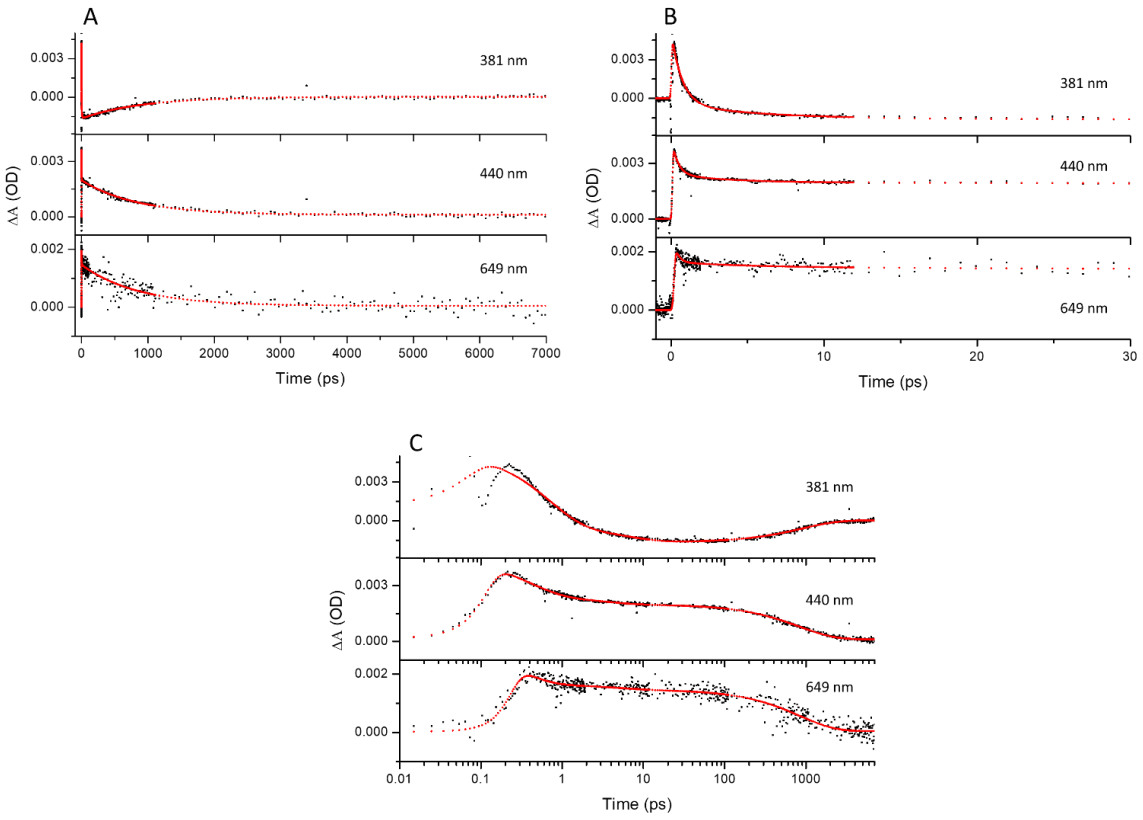

Figure 116: Ultrafast Kinetics of RuL2O in Acetonitrile

(A) Single wavelength kinetics fits out to 7000 ps time delays of RuL2O in acetonitrile solution applied to single-wavelength kinetics at 381 nm, 440 nm, and 649 nm. (B) Single wavelength kinetic fits out to 30 ps time delays. (C) Single wavelength kinetic fits out to 7000 ps time delays with logarithmic scaling on the x-axis. Raw data is black and the kinetic fit is red. A triexponential fit yields good results with $\tau_1 = 0.23 \pm 0.03$ *ps,* $\tau_2 = 4.27 \pm 0.83$ *ps, and* $\tau_3 = 839.2 \pm 92.9$ *ps.*

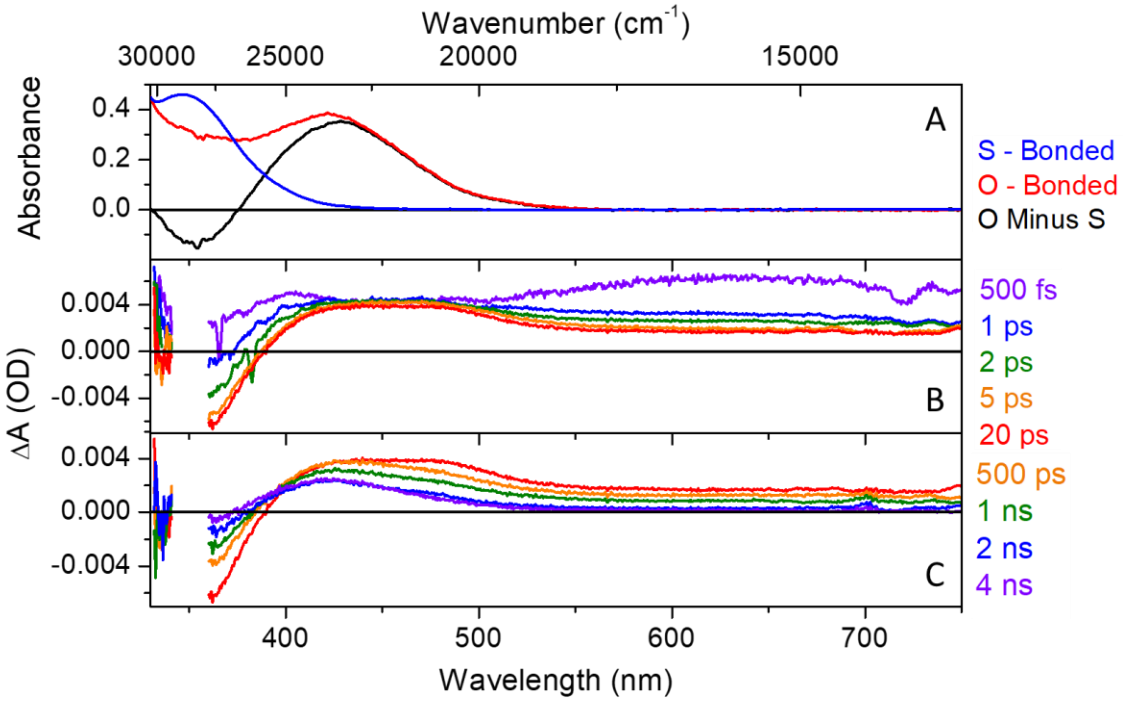

Figure 117: Spectra of RuL3O in Acetonitrile

(A) Spectra obtained from bulk photolysis (λ_{exc} 360 nm) of RuL3O in acetonitrile solution. Blue trace is the S-isomer, red trace is the O-isomer, and black trace is the difference spectrum (O-isomer minus S-isomer) extracted from the data. (B) Time-resolved spectra of RuL3O at short time-delays between 500 fs and 20 ps. (C) Time-resolved spectra of RuL3O at long time delays between 20 ps and 4 ns.

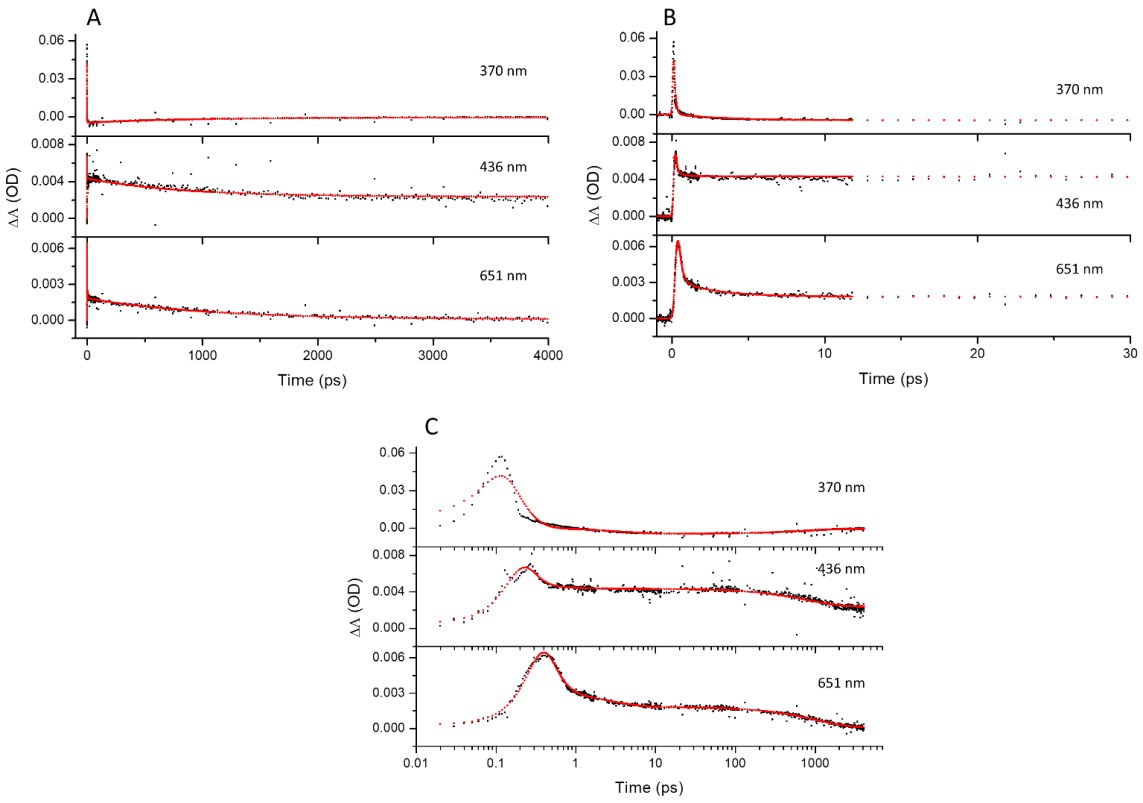

Figure 118: Ultrafast Kinetics of RuL3O in Acetonitrile

(A) Single wavelength kinetics fits out to 4000 ps time delays of RuL3O in acetonitrile solution applied to single-wavelength kinetics at 370 nm, 436 nm, and 651 nm. (B) Single wavelength kinetic fits out to 30 ps time delays. (C) Single wavelength kinetic fits out to 4000 ps time delays with logarithmic scaling on the x-axis. Raw data is black and the kinetic fit is red. A triexponential fit yields good results with $\tau_1 = 0.11 \pm 0.04$ *ps,* $\tau_2 = 1.99 \pm 0.34$ *ps, and* $\tau_3 = 812.4 \pm 120.0$ *ps.*

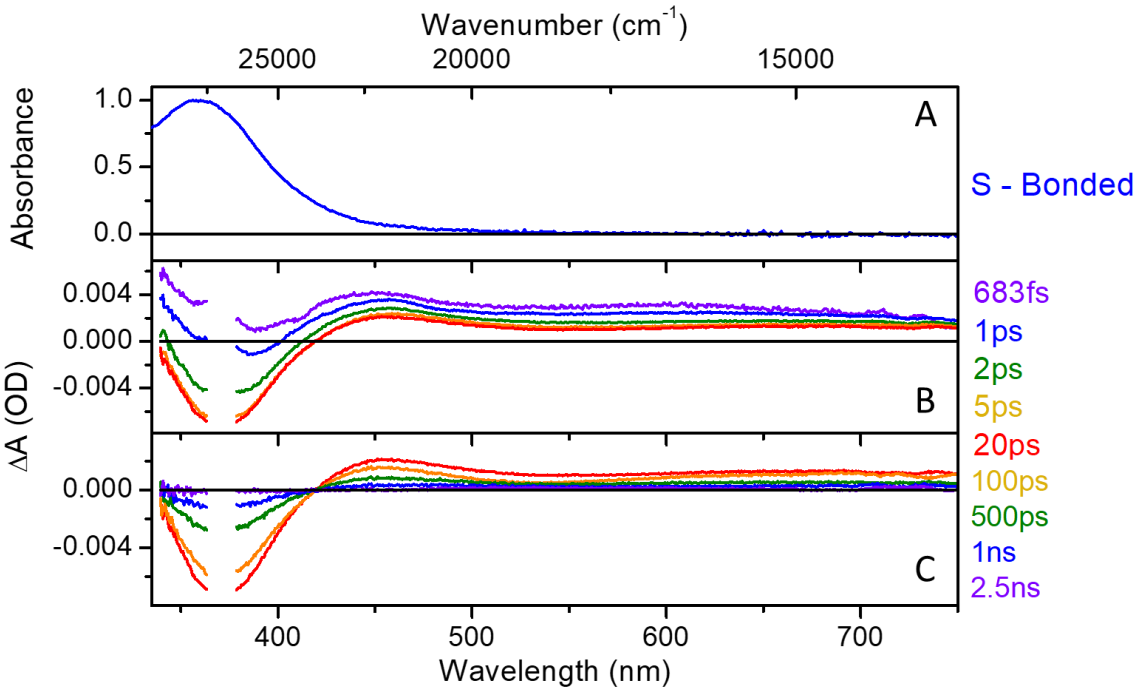

Figure 119: Spectra of RuL4O in Acetonitrile

(A) Spectra obtained from bulk photolysis (λ_{exc} 360 nm) of RuL4O in acetonitrile solution. (B) Time-resolved spectra of RuL4O at short time-delays between 683 fs and 20 ps. (C) Time-resolved spectra of RuL4O at long time delays between 20 ps and 2.5 ns.

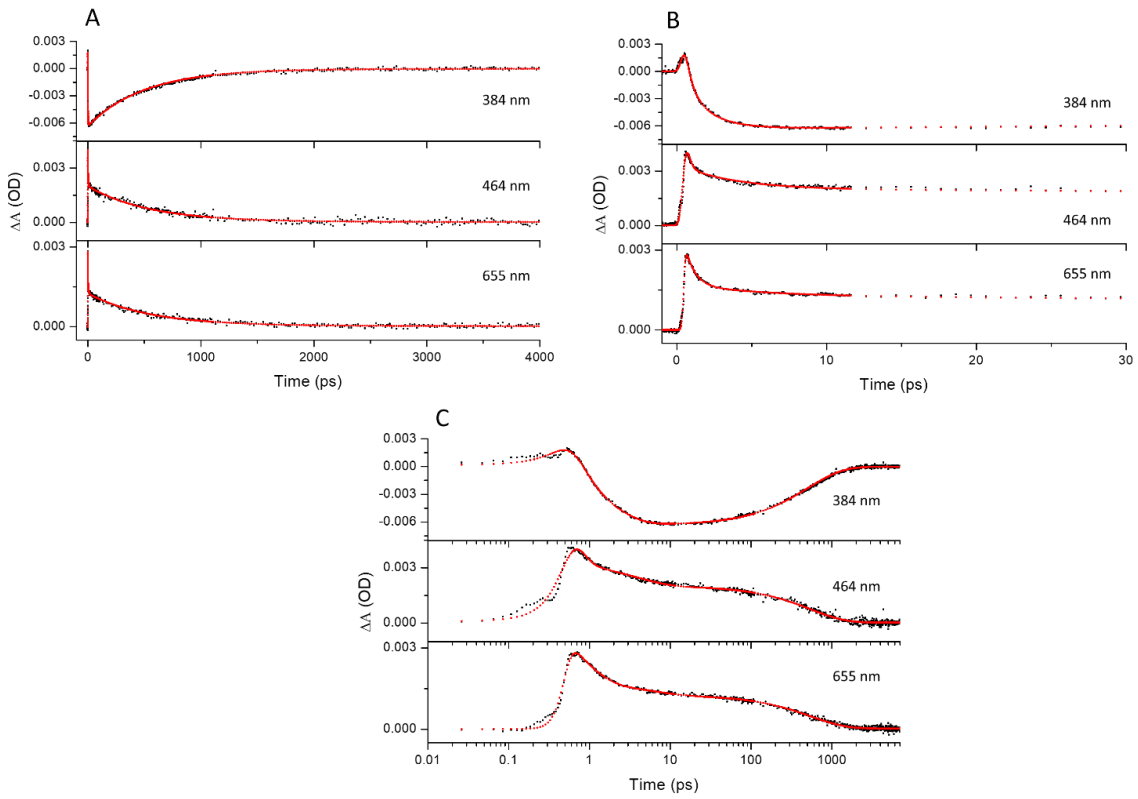

Figure 120: Ultrafast Kinetics of RuL4O in Acetonitrile

(A) Single wavelength kinetics fits out to 4000 ps time delays of RuL4O in acetonitrile solution applied to single-wavelength kinetics at 384 nm, 464 nm, and 655 nm. (B) Single wavelength kinetic fits out to 30 ps time delays. (C) Single wavelength kinetic fits out to 4000 ps time delays with logarithmic scaling on the x-axis. Raw data is black and the kinetic fit is red. A triexponential fit yields good results with $\tau_1 = 0.31 \pm 0.10$ *ps,* $\tau_2 = 3.67 \pm 0.74$ *ps, and* $\tau_3 = 529.2 \pm 31.8$ *ps.*

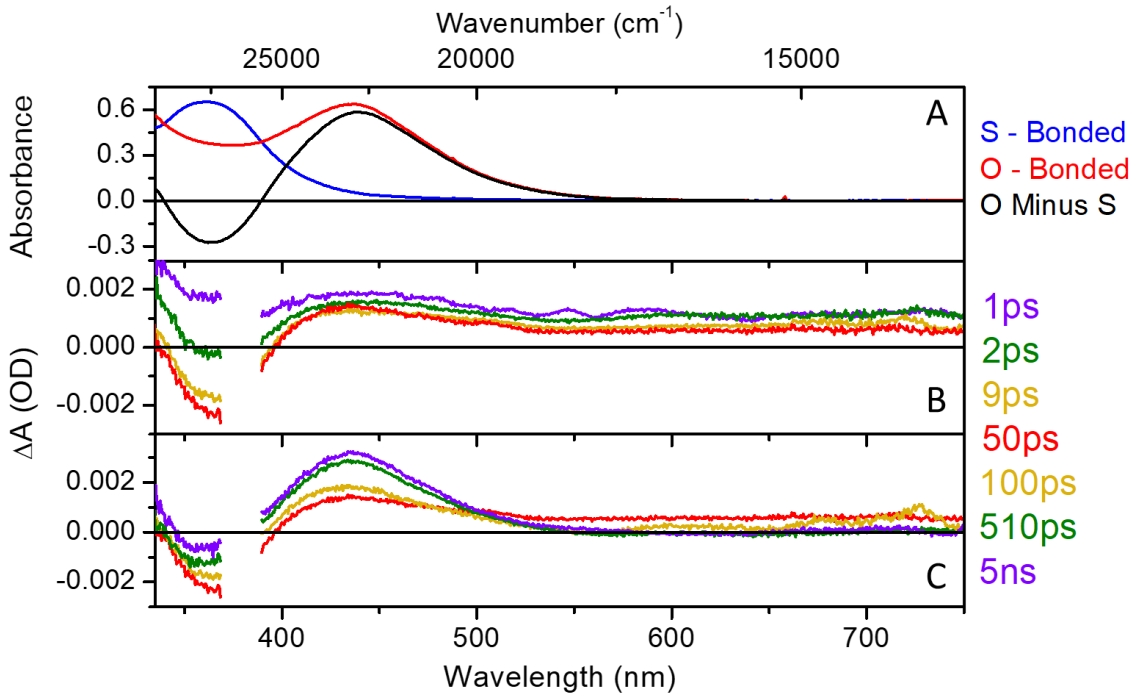

Figure 121: Spectra of RuL5O in Acetonitrile

(A) Spectra obtained from bulk photolysis (λ_{exc} 360 nm) of RuL5O in acetonitrile solution. Blue trace is the S-isomer, red trace is the O-isomer, and black trace is the difference spectrum (O-isomer minus S-isomer) extracted from the data. (B) Time-resolved spectra of RuL5O at short time-delays between 1 ps and 50 ps. (C) Time-resolved spectra of RuL5O at long time delays between 50 ps and 5 ns.

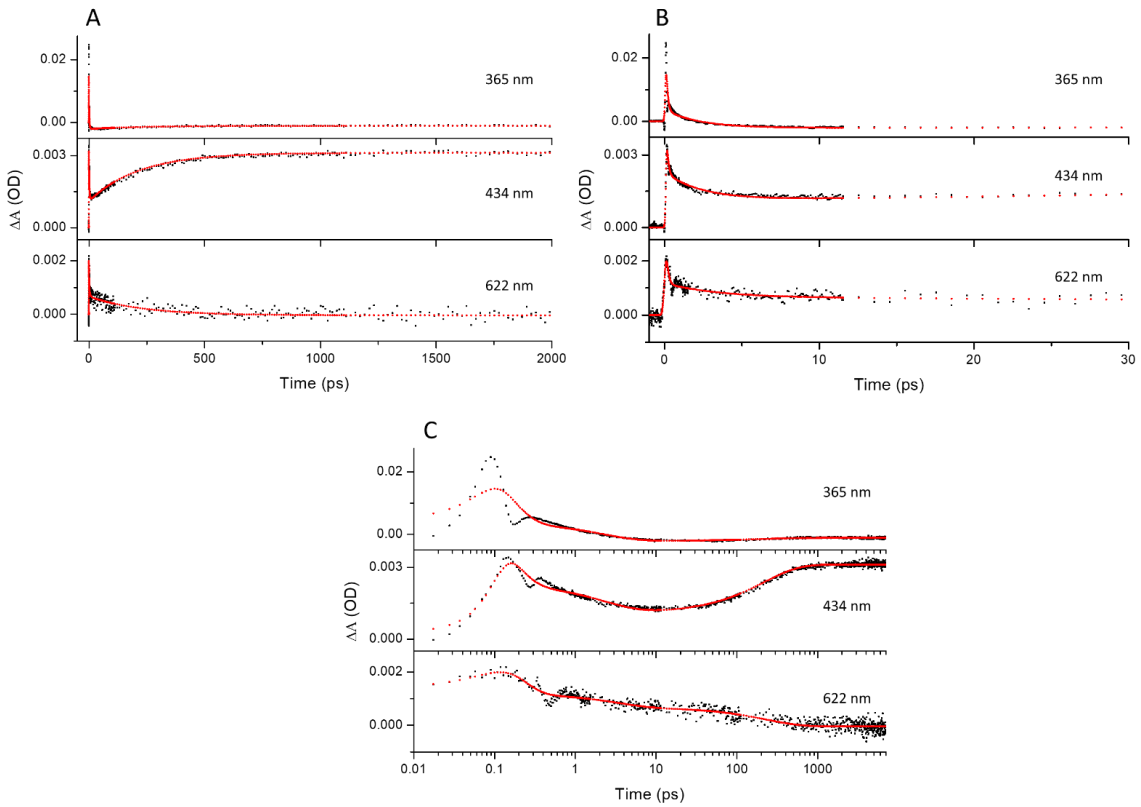

Figure 122: Ultrafast Kinetics of RuL5O in Acetonitrile

(A) Single wavelength kinetics fits out to 2000 ps time delays of RuL5O in acetonitrile solution applied to single-wavelength kinetics at 365 nm, 434 nm, and 622 nm. (B) Single wavelength kinetic fits out to 30 ps time delays. (C) Single wavelength kinetic fits out to 2000 ps time delays with logarithmic scaling on the x-axis. Raw data is black and the kinetic fit is red. A triexponential fit yields good results with $\tau_1 = 0.11 \pm 0.04$ *ps,* $\tau_2 = 2.85 \pm 0.71$ *ps, and* $\tau_3 = 204.9 \pm 19.9$ *ps.*

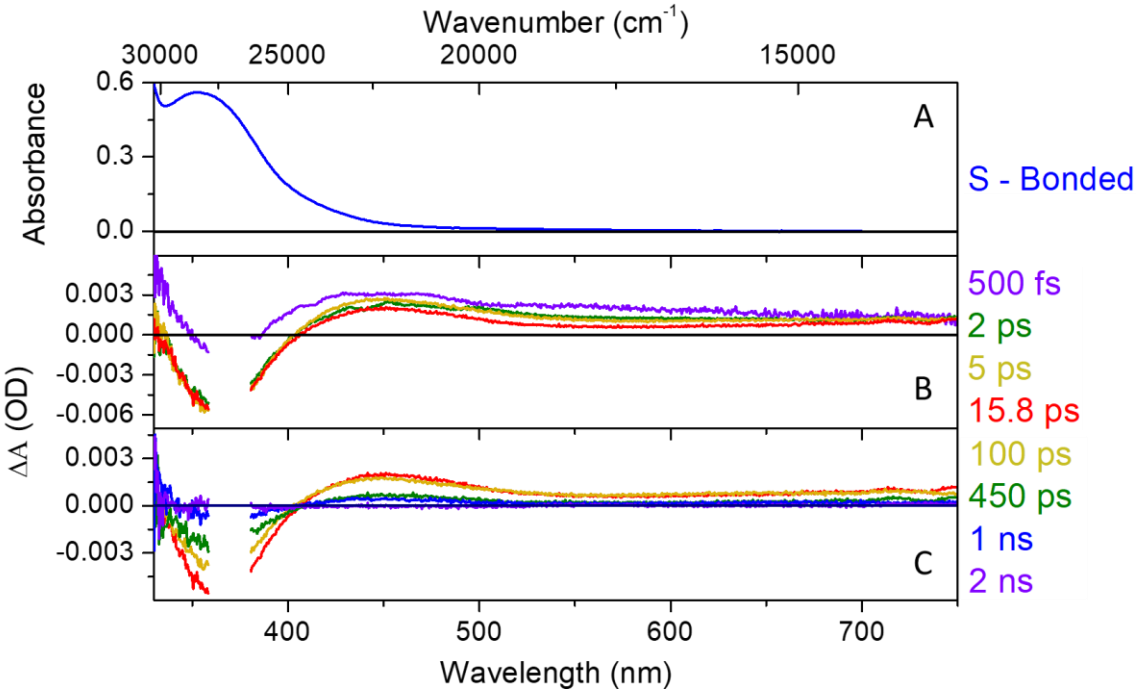

Figure 123: Spectra of RuL6O in Acetonitrile

(A) Spectra obtained from bulk photolysis (λ_{exc} 360 nm) of RuL6O in acetonitrile solution. (B) Time-resolved spectra of RuL6O at short time-delays between 500 fs and 15.8 ps. (C) Time-resolved spectra of RuL6O at long time delays between 15.8 ps and 2 ns.

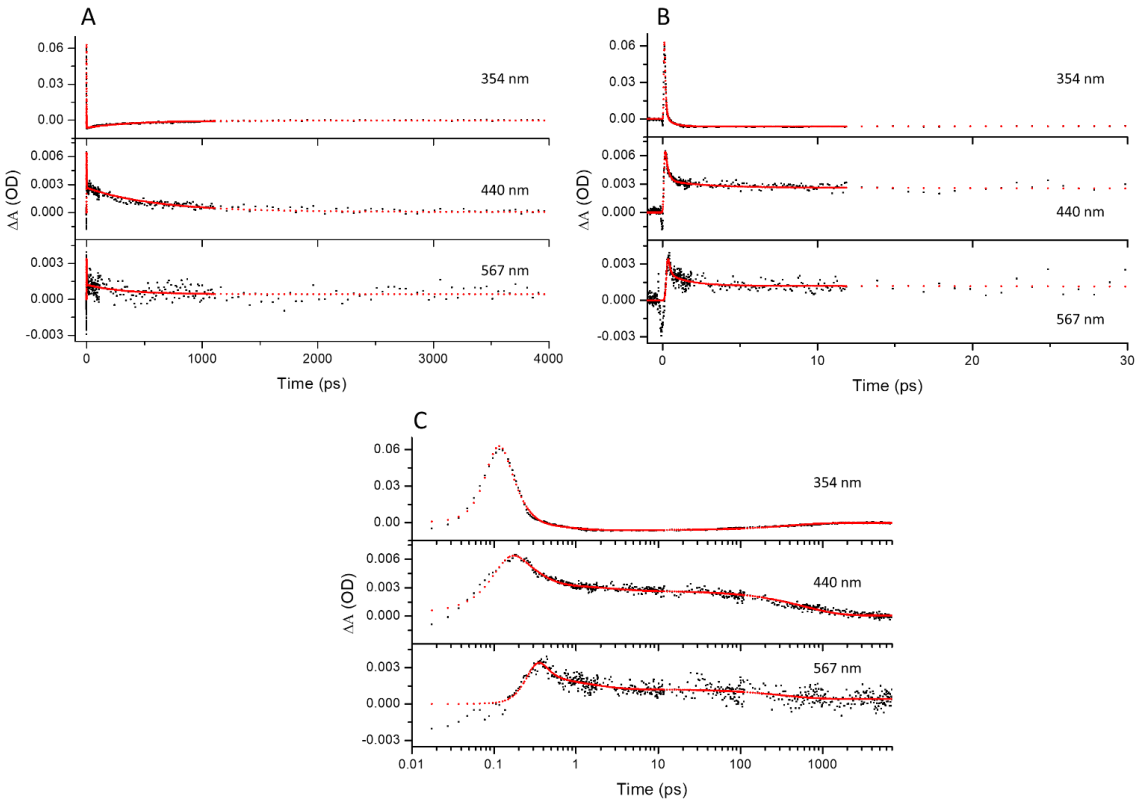

Figure 124: Ultrafast Kinetics of RuL6O in Acetonitrile

(A) Single wavelength kinetics fits out to 4000 ps time delays of RuL6O in acetonitrile solution applied to single-wavelength kinetics at 354 nm, 440 nm, and 567 nm. (B) Single wavelength kinetic fits out to 30 ps time delays. (C) Single wavelength kinetic fits out to 4000 ps time delays with logarithmic scaling on the x-axis. Raw data is black and the kinetic fit is red. A triexponential fit yields good results with $\tau_1 = 0.29 \pm 0.04$ *ps,* $\tau_2 = 2.21 \pm 1.16$ *ps, and* $\tau_3 = 434.2 \pm 65.8$ *ps*

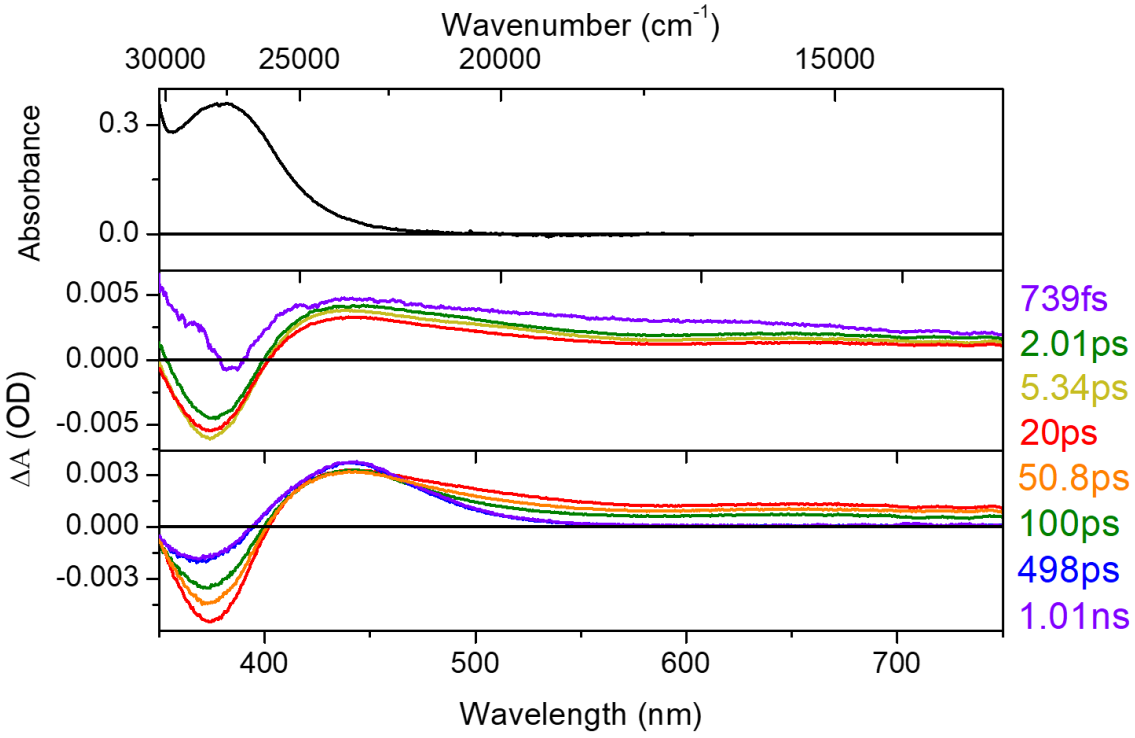

Figure 125: Spectra of RuL7O in Acetonitrile

(A) Spectra obtained from bulk photolysis (λ_{exc} 360 nm) of RuL7O in acetonitrile solution. (B) Time-resolved spectra of RuL7O at short time-delays between 500 fs and 15.8 ps. (C) Time-resolved spectra of RuL7O at long time delays between 15.8 ps and 2 ns.

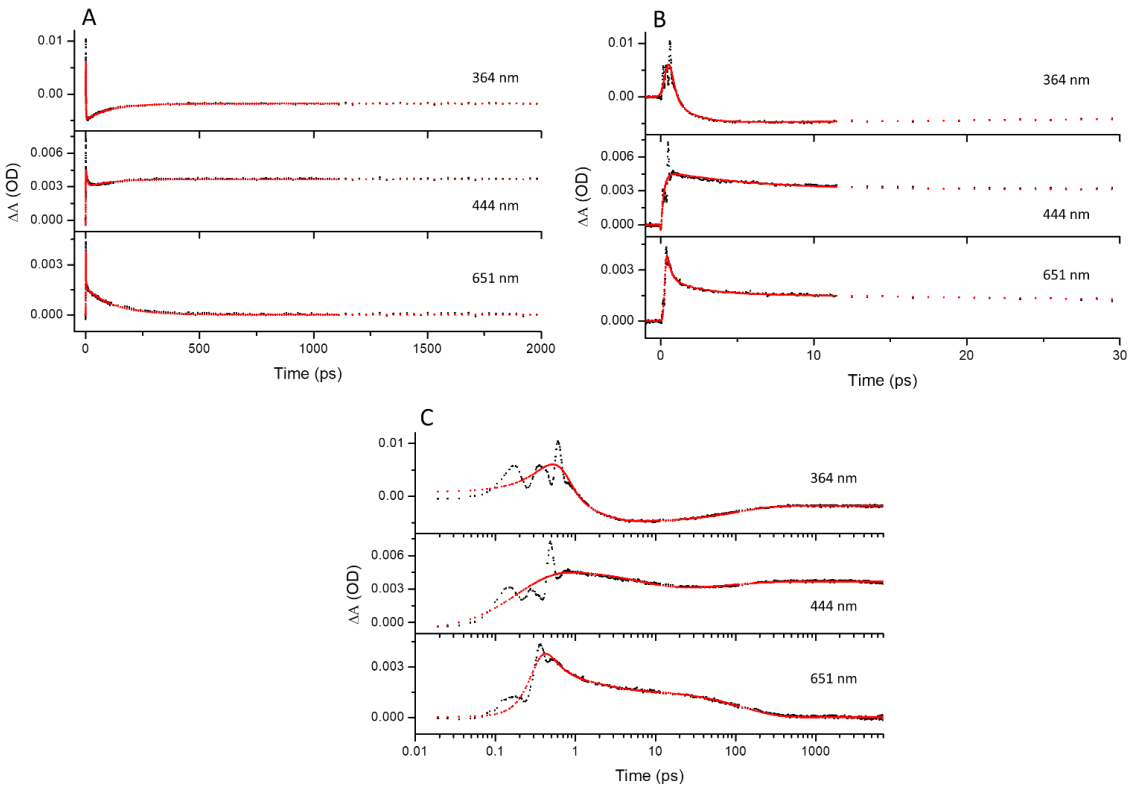

Figure 126: Ultrafast Kinetics of RuL7O in Acetonitrile

(A) Single wavelength kinetics fits out to 2000 ps time delays of RuL7O in acetonitrile solution applied to single-wavelength kinetics at 364 nm, 444 nm, and 651 nm. (B) Single wavelength kinetic fits out to 30 ps time delays. (C) Single wavelength kinetic fits out to 2000 ps time delays with logarithmic scaling on the x-axis. Raw data is black and the kinetic fit is red. A triexponential fit yields good results with $\tau_1 = 0.23 \pm 0.14$ *ps,* $\tau_2 = 1.36 \pm 0.89$ *ps, and* $\tau_3 = 103.7 \pm 21.5$ *ps.*

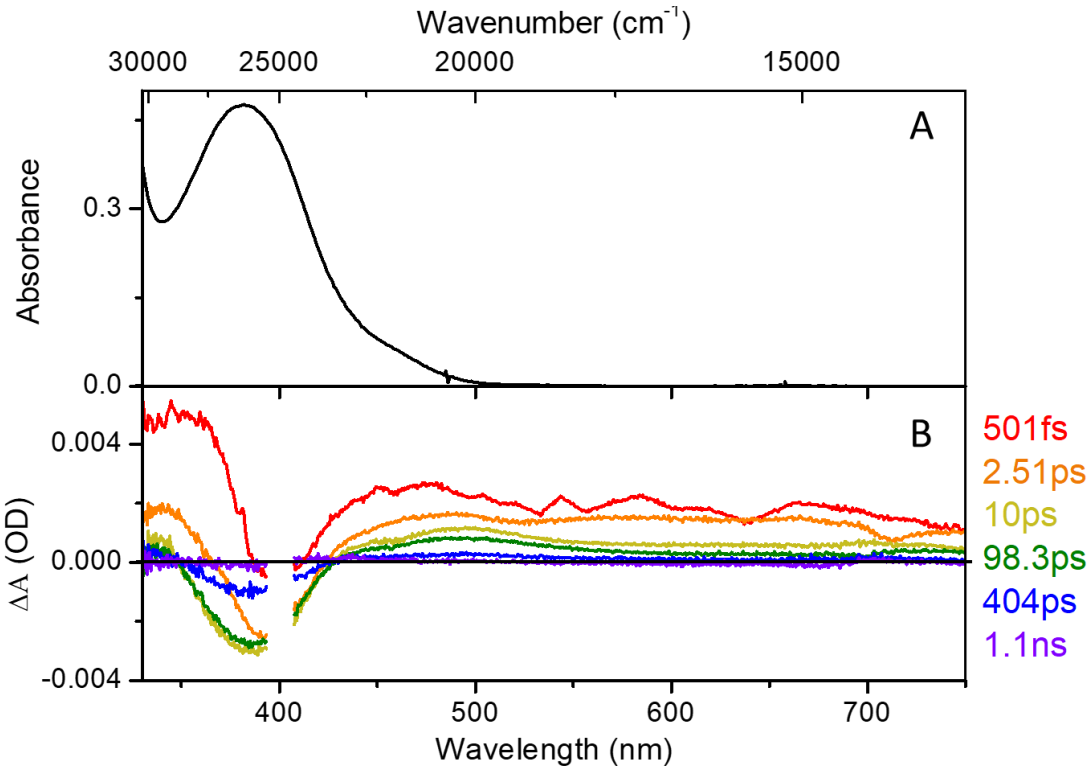

Figure 127: Spectra of RuL1 in Acetonitrile

(A) Steady-state absorption spectrum of RuL1 in acetonitrile solution. (B) Time-resolved spectra of RuL1 at short time-delays between 501 fs and 1.1 ns.

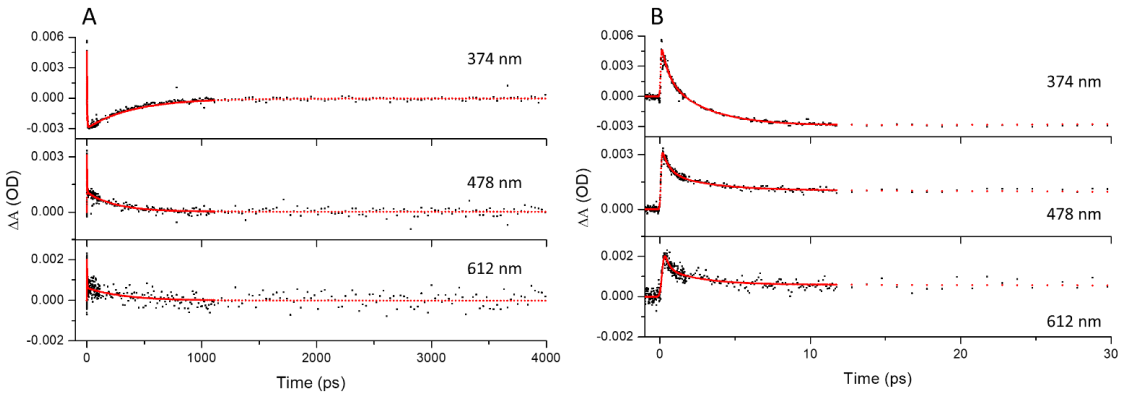

Figure 128: Ultrafast Kinetics of RuL1 in Acetonitrile

(A) Single wavelength kinetics fits out to 4000 ps time delays of RuL1 in acetonitrile solution applied to single-wavelength kinetics at 374 nm, 478 nm, and 612 nm. (B) Single wavelength kinetic fits out to 30 ps time delays. Raw data is black and the kinetic fit is red. A triexponential fit yields good results with $\tau_1 = 0.54 \pm 0.20$ *ps,* $\tau_2 = 2.9 \pm 1.3$ *ps, and* $\tau_3 = 337.2 \pm 52.5$ *ps.*

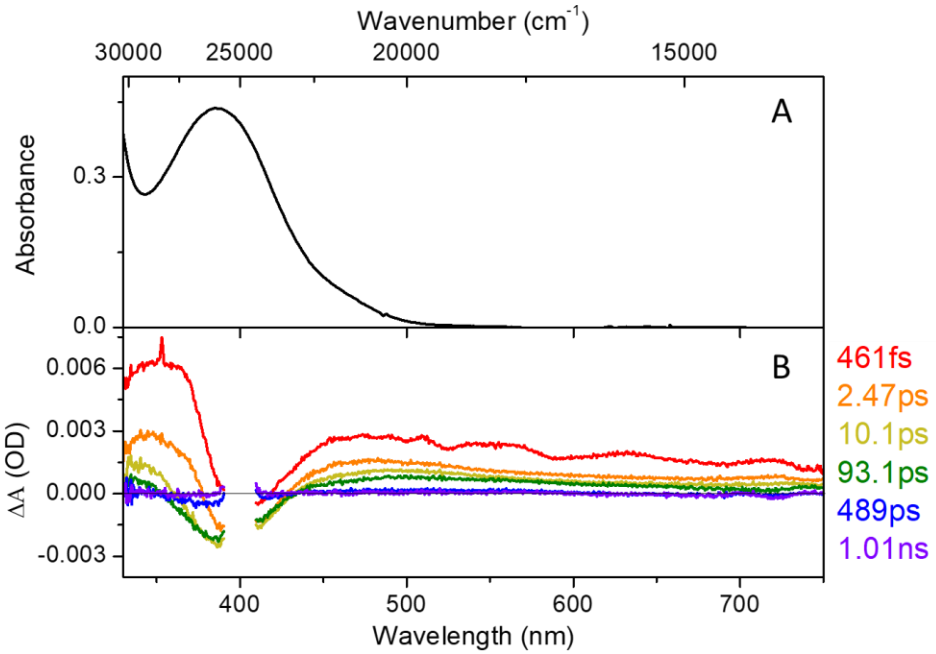

Figure 129: Spectra of RuL2 in Acetonitrile

(A) Steady-state absorption spectrum of RuL2 in acetonitrile solution. (B) Time-resolved spectra of RuL2 at short time-delays between 461 fs and 1.01 ns.

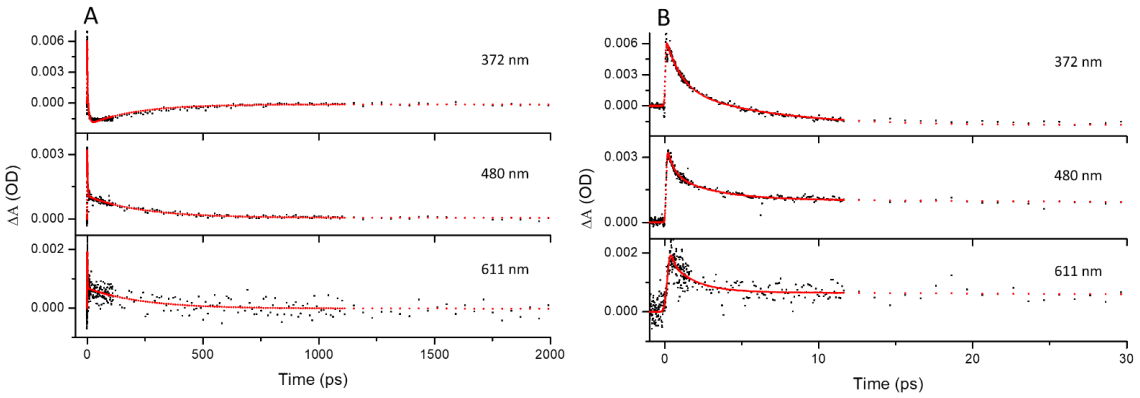

Figure 130: Ultrafast Kinetics of RuL2 in Acetonitrile

(A) Single wavelength kinetics fits out to 2000 ps time delays of RuL2 in acetonitrile solution applied to single-wavelength kinetics at 372 nm, 480 nm, and 611 nm. (B) Single wavelength kinetic fits out to 30 ps time delays. Raw data is black and the kinetic fit is red. A triexponential fit yields good results with $\tau_1 = 0.52 \pm 0.11$ *ps,* $\tau_2 = 2.9 \pm 0.8$ *ps, and* $\tau_3 = 212.4 \pm 22.5$ *ps.*

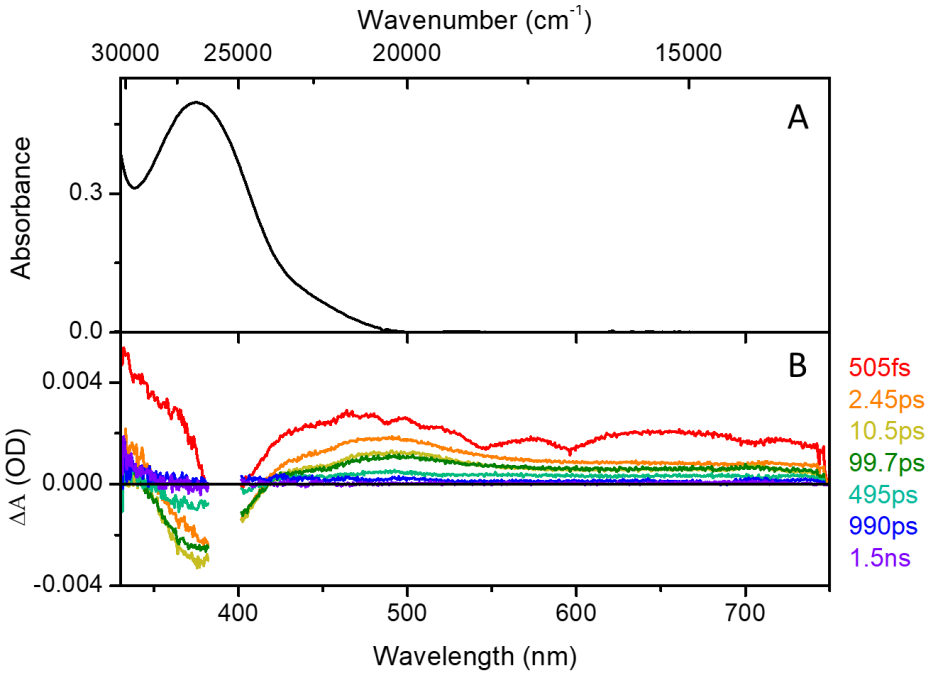

Figure 131: Spectra of RuL3 in Acetonitrile

(A) Steady-state absorption spectrum of RuL3 in acetonitrile solution. (B) Time-resolved spectra of RuL3 at short time-delays between 505 fs and 1.5 ns.

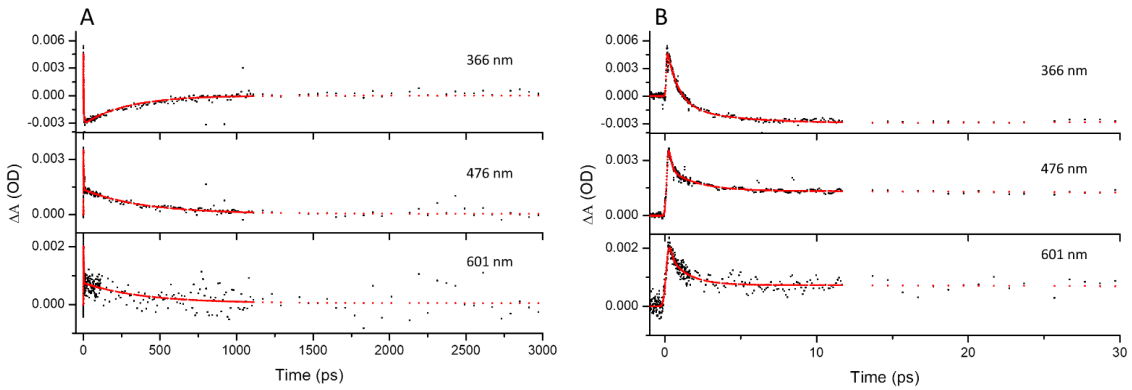

Figure 132: Ultrafast Kinetics of RuL3 in Acetonitrile

(A) Single wavelength kinetics fits out to 3000 ps time delays of RuL3 in acetonitrile solution applied to single-wavelength kinetics at 366 nm, 476 nm, and 601 nm. (B) Single wavelength kinetic fits out to 30 ps time delays. Raw data is black and the kinetic fit is red. A triexponential fit yields good results with $\tau_1 = 0.23 \pm 0.21$ *ps,* $\tau_2 = 1.9 \pm 1.3$ *ps, and* $\tau_3 = 361.8 \pm 42.5$ *ps.*

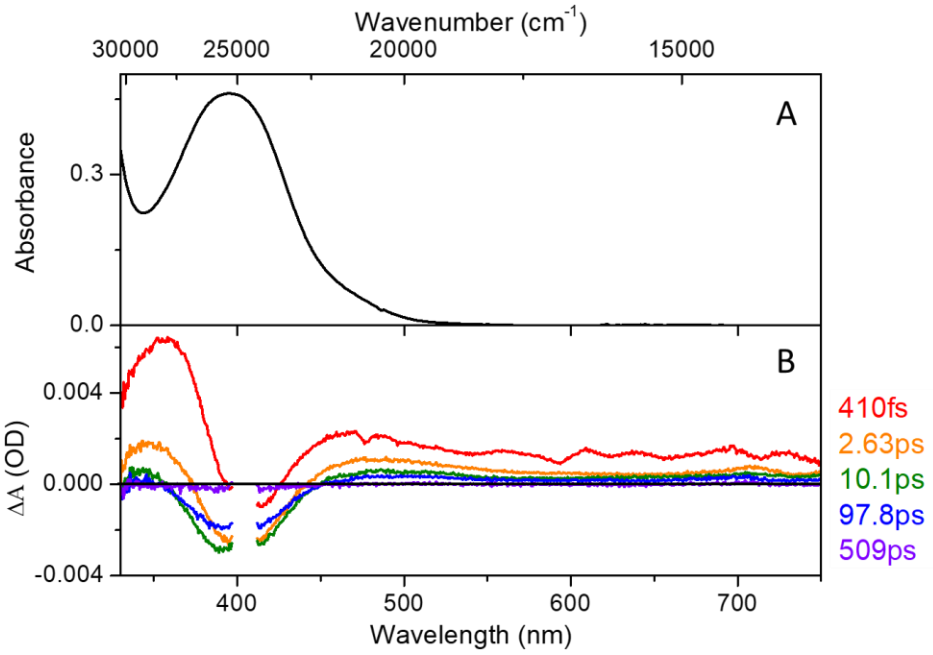

Figure 133: Spectra of RuL4 in Acetonitrile

(A) Steady-state absorption spectrum of RuL4 in acetonitrile solution. (B) Time-resolved spectra of RuL4 at short time-delays between 410 fs and 509 ps.

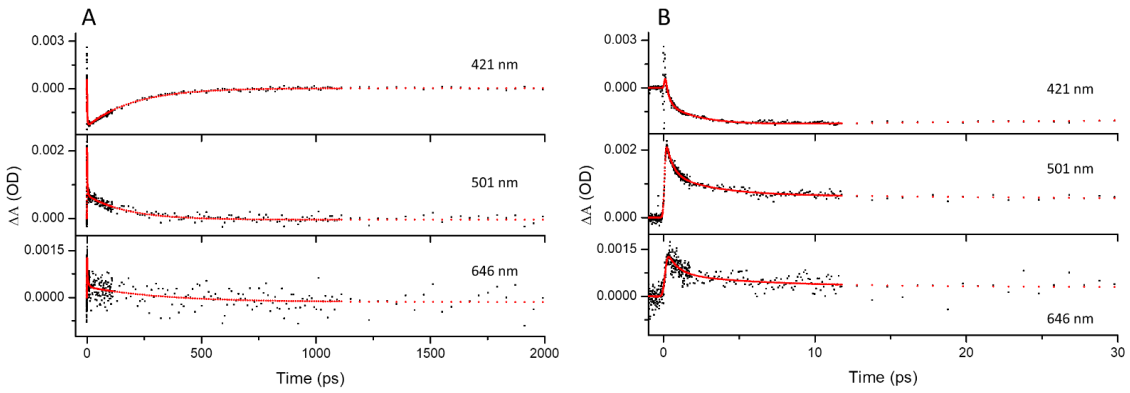

Figure 134: Ultrafast Kinetics of RuL4 in Acetonitrile

(A) Single wavelength kinetics fits out to 2000 ps time delays of RuL4 in acetonitrile solution applied to single-wavelength kinetics at 421 nm, 501 nm, and 646 nm. (B) Single wavelength kinetic fits out to 30 ps time delays. Raw data is black and the kinetic fit is red. A triexponential fit yields good results with $\tau_1 = 0.33 \pm 0.12$ *ps,* $\tau_2 = 2.9 \pm 2.3$ *ps, and* $\tau_3 = 186.5 \pm 28.1$ *ps.*

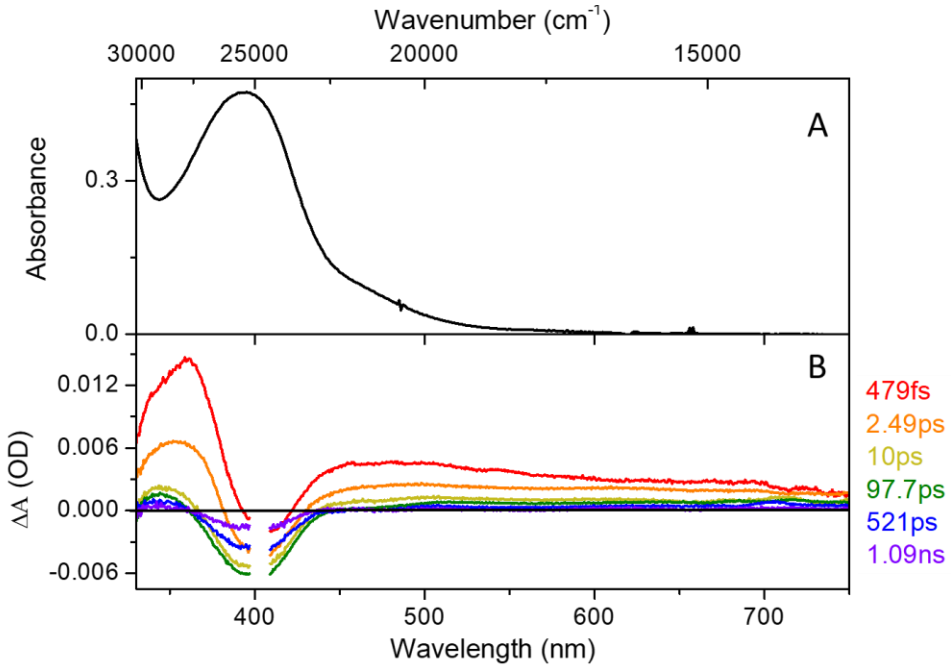

Figure 135: Spectra of RuL5 in Acetonitrile

(A) Steady-state absorption spectrum of RuL5 in acetonitrile solution. (B) Time-resolved spectra of RuL5 at short time-delays between 479 fs and 1.09 ns.

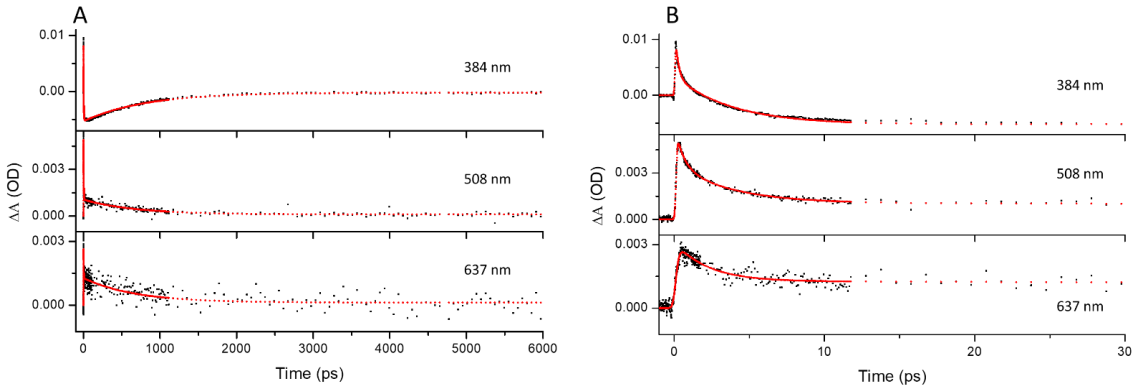

Figure 136: Ultrafast Kinetics of RuL5 in Acetonitrile

(A) Single wavelength kinetics fits out to 6000 ps time delays of RuL5 in acetonitrile solution applied to single-wavelength kinetics at 384 nm, 508 nm, and 637 nm. (B) Single wavelength kinetic fits out to 30 ps time delays. Raw data is black and the kinetic fit is red. A triexponential fit yields good results with $\tau_1 = 0.35 \pm 0.09$ *ps,* $\tau_2 = 3.1 \pm 0.2$ *ps, and* $\tau_3 = 690.8 \pm 84.0$ *ps.*

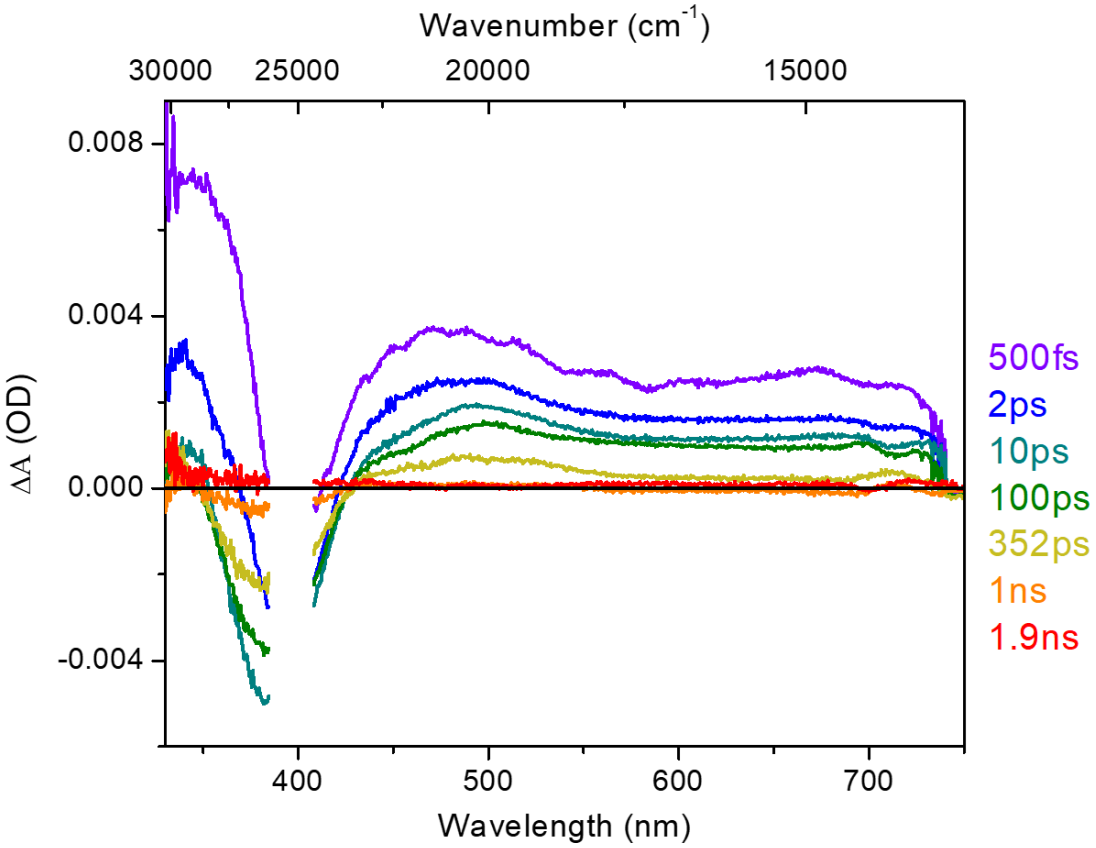

Figure 137: Spectra of RuL6 in Acetonitrile

(A) Steady-state absorption spectrum of Ru7 in acetonitrile solution. (B) Time-resolved spectra of RuL6 at short time-delays between 500 fs and 1.9 ns.

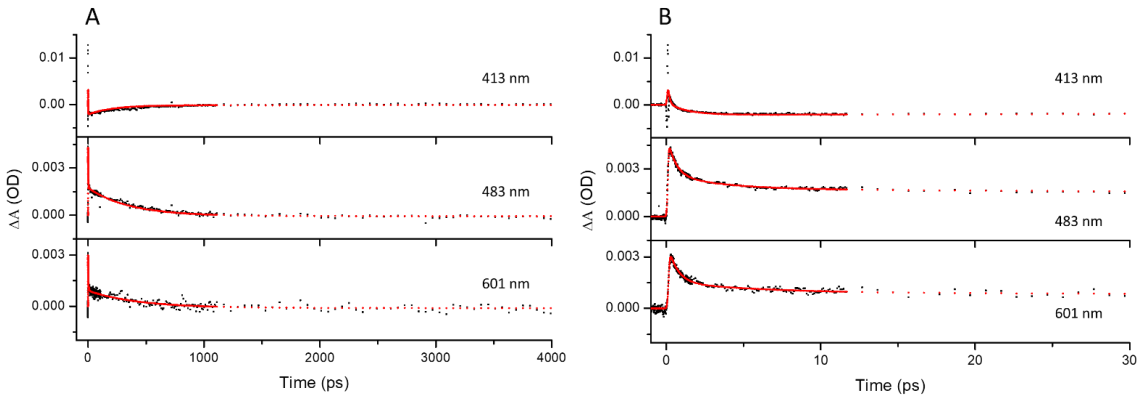

Figure 138: Ultrafast Kinetics of RuL6 in Acetonitrile

(A) Single wavelength kinetics fits out to 4000 ps time delays of RuL6 in acetonitrile solution applied to single-wavelength kinetics at 413 nm, 483 nm, and 601 nm. (B) Single wavelength kinetic fits out to 30 ps time delays. Raw data is black and the kinetic fit is red. A triexponential fit yields good results with $\tau_1 = 0.50 \pm 0.14$ *ps,* $\tau_2 = 4.2 \pm 1.6$ *ps, and* $\tau_3 = 310.9 \pm 103.0$ *ps.*

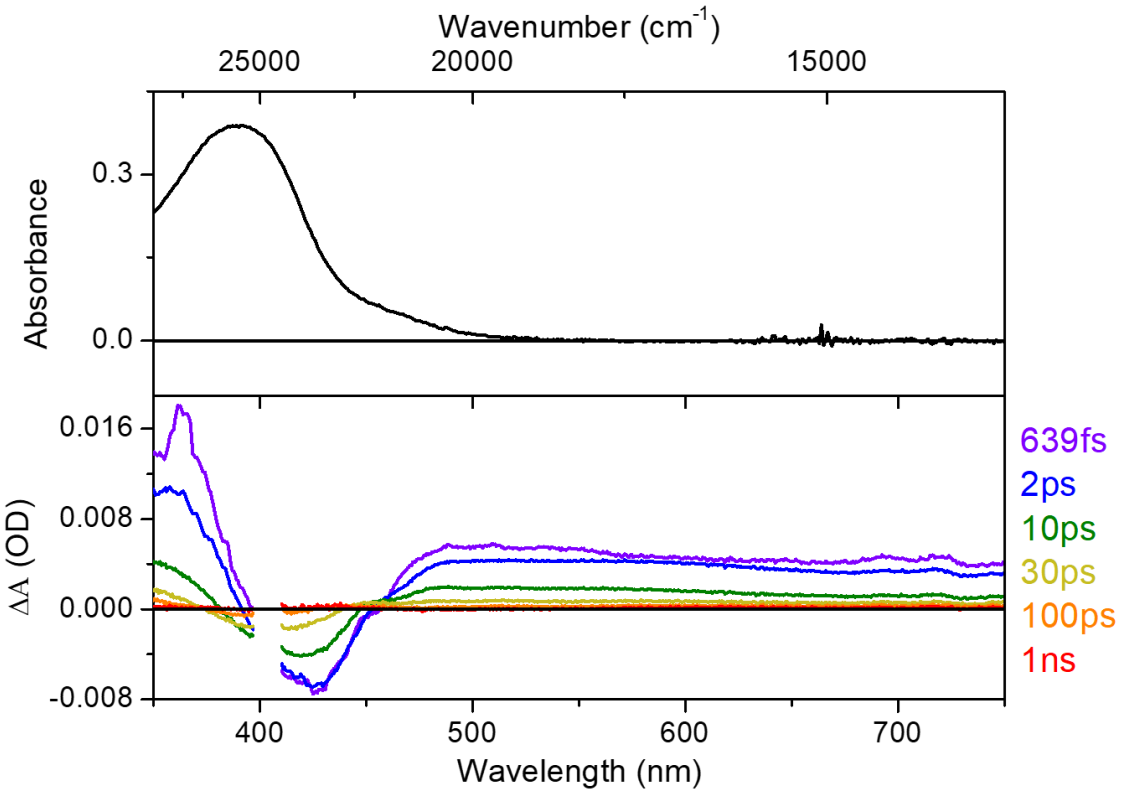

Figure 139: Spectra of RuL7 in Acetonitrile

(A) Steady-state absorption spectrum of Ru7 in acetonitrile solution. (B) Time-resolved spectra of RuL7 at short time-delays between 639 fs and 1 ns.

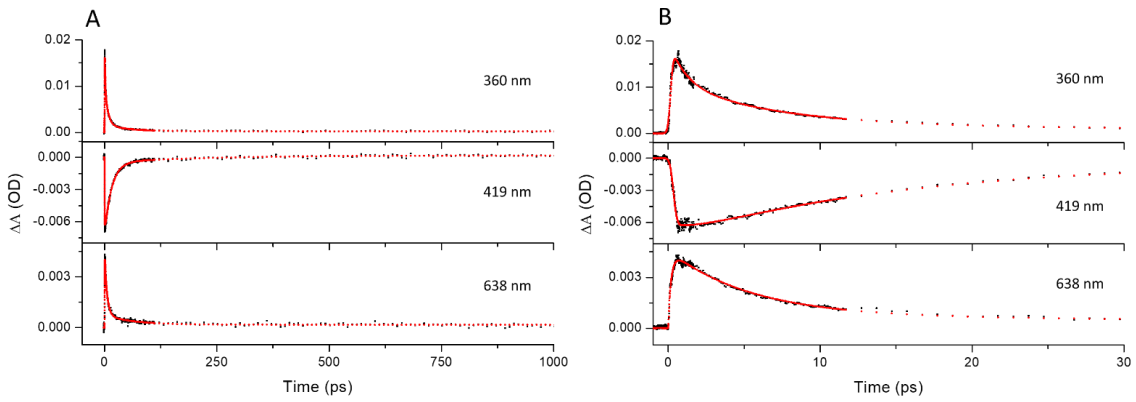

Figure 140: Ultrafast Kinetics of RuL7 in Acetonitrile

(A) Single wavelength kinetics fits out to 1000 ps time delays of RuL7 in acetonitrile solution applied to single-wavelength kinetics at 360 nm, 419 nm, and 638 nm. (B) Single wavelength kinetic fits out to 30 ps time delays. Raw data is black and the kinetic fit is red. A triexponential fit yields good results with $\tau_1 = 1.2 \pm 0.5$ *ps,* $\tau_2 = 5.8 \pm 2.5$ *ps, and* $\tau_3 = 88.2 \pm 23.0$ *ps.*

Table 18: *Time-components and amplitudes returned from single-wavelength fitting analysis for the ruthenium thioether complexes: RuL1, RuL2, and RuL3.*

Complex	λ/nm	A_1	t_1/ps	A_2	t_2/ps	A_3	t_3/ps
RuL1/ CH_3CN	374	0.00145 ± 0.00032	0.48 ± 0.20	0.00099 ± 0.00036	2.81 ± 1.20	0.0011 ± 0.000057	250.8 ± 41.0
	478	0.0018 ± 0.0021	0.26 ± 0.32	0.00085 ± 0.00046	2.33 ± 1.90	0.00063 ± 0.00009	322.5 ± 150
	612	0.0036 ± 0.00058	0.48 ± 0.15	0.0050 ± 0.00066	2.83 ± 0.43	-0.0029 ± 0.0001	399.6 ± 40.0
RuL2/ CH_3CN	372	0.0049 ± 0.00059	0.98 ± 0.17	0.0039 ± 0.00061	6.55 ± 1.30	-0.0020 ± 0.00016	201.4 ± 40.0
	480	0.0014 ± 0.00019	0.42 ± 0.12	0.0013 ± 0.00019	2.75 ± 0.55	0.001 ± 0.00004	234.9 ± 26.0
	611	0.0042 ± 0.003	0.15 ± 0.05	0.0011 ± 0.0005	1.60 ± 1.10	0.0007 ± 0.00009	235.7 ± 98.0
RuL3/ CH_3CN	366	0.0066 ± 0.0009	0.77 ± 0.16	0.0021 ± 0.0010	4.42 ± 2.20	-0.0031 ± 0.0002	285.0 ± 43.0
	476	0.0041 ± 0.0030	0.16 ± 0.07	0.0012 ± 0.0002	1.85 ± 0.54	0.0013 ± 0.00005	387.8 ± 48.0
	601	0.0053 ± 0.037	0.15 ± 0.42	0.0011 ± 0.0007	1.24 ± 0.91	0.0007 ± 0.00008	387.1 ± 140

Table 19: *Time-components and amplitudes returned from single-wavelength fitting analysis for the ruthenium thioether complexes: RuL4, RuL5, RuL6, and RuL7.*

Complex / Solvent	λ/nm	A_1	τ_1/ps	A_2	τ_2/ps	A_3	τ_3/ps
RuL4/ CH_3CN	421	0.0012 ± 0.0002	0.43 ± 0.13	0.0007 ± 0.0002	2.85 ± 1.00	0.0007 ± 0.00004	176.5 ± 25.0
	501	0.0008 ± 0.0004	0.74 ± 0.81	0.0004 ± 0.0004	6.09 ± 8.80	0.0005 ± 0.0001	331.6 ± 200
	646	0.0023 ± 0.0006	0.23 ± 0.11	0.0014 ± 0.0003	2.19 ± 0.88	-0.0024 ± 0.00009	202.4 ± 23.0
RuL5/ CH_3CN	384	0.0021 ± 0.0002	0.53 ± 0.11	0.0025 ± 0.0002	3.66 ± 0.39	0.0010 ± 0.00004	676.3 ± 84.0
	508	-0.0039 ± 0.0016	0.15 ± 0.46	0.0018 ± 0.0003	2.21 ± 0.67	0.0012 ± 0.00009	671.9 ± 150.0
	637	0.0086 ± 0.0008	0.20 ± 0.02	0.0087 ± 0.0002	3.85 ± 0.18	-0.0051 ± 0.0001	801.6 ± 44.0
RuL6/ CH_3CN	413	0.0079 ± 0.013	0.10 ± 0.12	0.0026 ± 0.0011	1.29 ± 0.83	-0.0020 ± 0.00027	213.9 ± 100.0
	483	0.0022 ± 0.0002	0.54 ± 0.11	0.00092 ± 0.00025	3.47 ± 1.10	0.0018 ± 0.00004	356.3 ± 27.0
	601	0.0020 ± 0.0002	0.60 ± 0.17	0.00063 ± 0.00026	5.75 ± 3.20	0.001 ± 0.00007	440.1 ± 85.0
RuL7/ CH_3CN	360	0.0079 ± 0.0008	1.08 ± 1.10	0.0093 ± 0.001	6.80 ± 6.80	0.0014 ± 0.0006	49.6 ± 31.0
	419	0.0011 ± 0.0004	1.92 ± 1.20	-0.0068 ± 0.0003	5.16 ± 1.60	-0.0007 ± 0.0002	218.3 ± 120.0
	638	-0.0036 ± 0.0003	0.20 ± 0.20	0.0038 ± 0.0001	5.40 ± 0.37	0.00056 ± 0.00014	65.54 ± 23.0

Table 20: *Time-components and amplitudes returned from single-wavelength fitting analysis for the ruthenium sulfoxide complexes: RuL1O, RuL2O, and RuL3O.*

Complex / Solvent	λ/nm	A_1	τ_1/ps	A_2	τ_2/ps	A_3	τ_3/ps
RuL1O/ CH_3CN	352	0.0032 ± 0.0005	0.36 ± 0.13	0.0020 ± 0.0005	2.68 ± 1.00	-0.0027 ± 0.0001	953.6 ± 120.0
	437	0.0015 ± 0.0003	0.25 ± 0.12	0.0003 ± 0.0002	2.46 ± 3.70	0.0017 ± 0.00009	1209 ± 270
	628	-0.0018 ± 0.43	0.18 ± 0.12	0.0010 ± 0.0025	1.25 ± 0.72	0.00075 ± 1.9	1216 ± 410
RuL2O/ CH_3CN	381	0.0055 ± 0.0005	0.69 ± 0.15	0.0012 ± 0.0006	6.37 ± 4.30	-0.0017 ± 0.0002	909.0 ± 260.0
	440	0.0017 ± 0.0001	0.38 ± 0.07	0.00050 ± 0.0001	3.20 ± 1.40	0.0019 ± 0.00004	822.2 ± 45.0
	649	0.0007 ± 0.0005	0.27 ± 0.27	0.0002 ± 0.0001	5.00 ± 7.30	0.0014 ± 0.00007	842.9 ± 120.0
RuL3O/ CH_3CN	370	0.11 ± 0.028	0.10 ± 0.01	0.0050 ± 0.001	3.50 ± 1.90	-0.0041 ± 0.0007	801.5 ± 420.0
	436	0.012 ± 0.025	0.10 ± 0.10	0.00039 ± 0.0017	0.63 ± 2.10	0.0020 ± 0.00001	802.2 ± 180.0
	651	0.013 ± 0.0032	0.20 ± 0.03	0.0014 ± 0.00021	2.47 ± 0.62	0.0018 ± 0.00006	877± 120

Table 21: *Time-components and amplitudes returned from single-wavelength fitting analysis for the ruthenium sulfoxide complexes: RuL4O, RuL5O, RuL6O, and RuL7O.*

Complex / Solvent	λ/nm	A_1	τ_1/ps	A_2	τ_2/ps	A_3	τ_3/ps
RuL4O/ CH_3CN	384	0.0083 ± 0.0017	0.40 ± 0.14	0.0055 ± 0.0013	1.65 ± 0.23	-0.0063 ± 0.00003	502.3 ± 9.0
	464	0.010 ± 0.018	0.20 ± 0.11	0.0012 ± 0.00015	3.72 ± 0.65	0.002 ± 0.00004	542.8 ± 29.0
	655	0.0017 ± 0.00012	0.63 ± 0.09	0.00045 ± 0.00010	5.75 ± 1.70	0.0012 ± 0.00002	547.0 ± 25.0
RuL5O/ CH_3CN	365	0.032 ± 0.015	0.10 ± 0.03	0.0056 ± 0.0007	2.30 ± 0.79	-0.001 ± 0.0004	204.5 ± 240.0
	434	0.0032 ± 0.0014	0.10 ± 0.03	0.0011 ± 0.00006	2.44 ± 0.36	-0.002 ± 0.00003	215.7 ± 11.0
	622	0.0096 ± 0.76	0.10 ± 0.08	0.00052 ± 0.00009	3.36 ± 1.80	0.0007 ± 0.00007	228.6 ± 63.0
RuL6O/ CH_3CN	354	0.13 ± 0.0042	0.75 ± 0.04	0.0086 ± 0.0019	0.54 ± 0.11	-0.0060 ± 0.00022	403.4 ± 52.0
	440	0.0058 ± 0.0011	0.18 ± 0.04	0.00073 ± 0.00026	2.61 ± 1.90	0.0026 ± 0.0001	598.2 ± 68.0
	567	0.0053 ± 0.015	0.12 ± 0.20	0.001 ± 0.0009	1.38 ± 1.60	0.00079 ± 0.00017	330.4 ± 240.0
RuL7O/ CH_3CN	364	0.052 ± 0.10	0.23 ± 0.28	0.0068 ± 0.0062	1.22 ± 0.78	-0.0031 ± 0.00026	107.6 ± 24.0
	444	-0.0061 ± 0.0001	0.19 ± 0.19	0.0018 ± 0.0002	6.60 ± 6.60	-0.0007 ± 0.0001	108.0 ± 110.0
	651	0.0032 ± 0.0008	0.24 ± 0.07	0.001 ± 0.0003	1.86 ± 0.72	0.0016 ± 0.00005	121.7 ± 10.0

IR Spectroscopy:

Table 22: *Infrared absorption peak maxima for ruthenium sulfoxide S – O stretching frequencies and their corresponding full widths at half max.*

Compound	ν (S=O) (cm^{-1})	FWHM (cm^{-1})
RuL1O	1100	37
RuL2O	1093	21
RuL3O	1118	58
RuL4O	1083	18
RuL5O	1098	60
RuL6O	1094	31

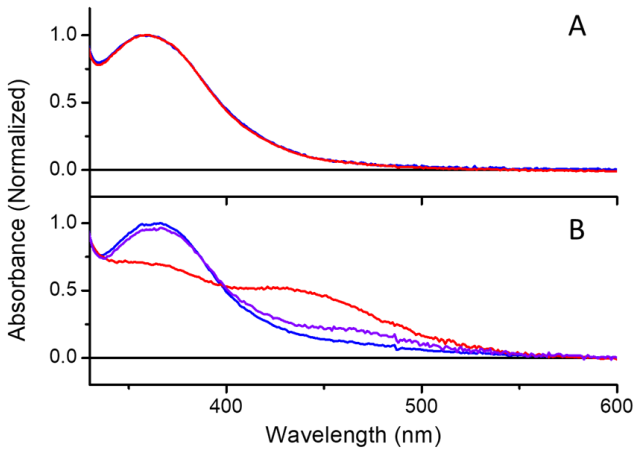

Figure 141: *UV-Vis spectra at various irradiation times from a 355 nm pulsed YAG laser. Irradiation was performed on nujol mulls, but UV-Vis spectra were collected in acetonitrile. (A) RuL4O after 0 minutes (blue) and after 25 minutes. (B) RuL5O after 0 minutes (blue), and after 15 minutes (red). The purple trace is after 1 day of reversion in the dark.*

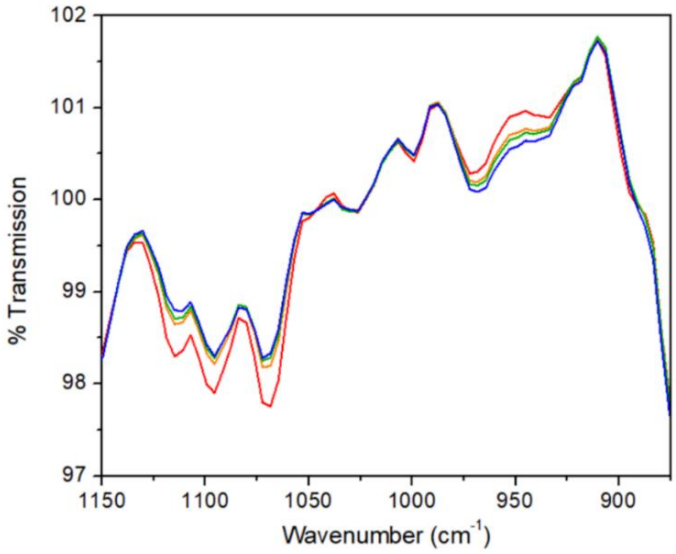

Figure 142: *The change in IR transmission of RuL7O as a sample dissolved in DCE is irradiated with a 405 nm laser diode. The traces are after 0 minutes (red), 10 minutes (orange), 15 minutes (green), and 28 minutes (blue) of irradiation.*

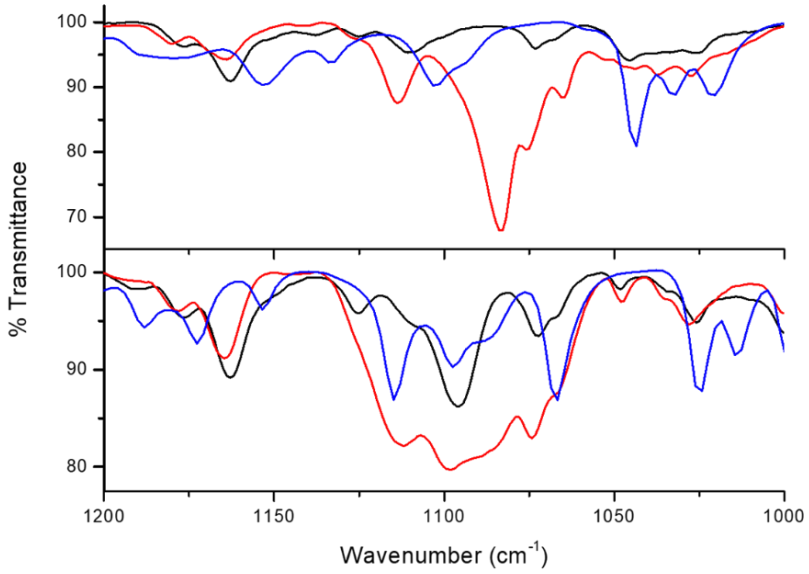

Figure 143: *IR spectra of various P,S compounds from this study. (Top) L4 (blue), RuL4 (black), and RuL4O (red). (Bottom) L5 (blue), RuL5 (black), and RuL5O (red).*

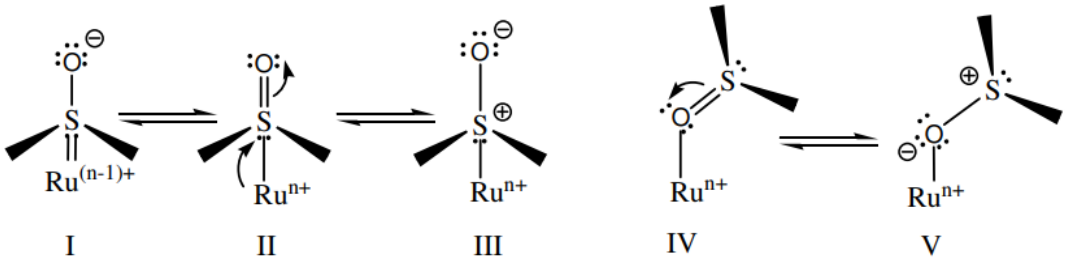

Scheme 8: *Resonance structure for S- and O- bonded ruthenium sulfoxide complexes. This scheme is adopted from Beth Anne McClure's dissertation titled "Spectroscopic and Kinetic Characterization of Photochromic Ruthenium Chelating Sulfoxide Complexes". A Ru-S bond shifts the resonance equilibrium towards structure II, resulting in a shorter S-O bond and a higher-energy sulfoxide stretching mode. A Ru-O bond shifts the resonance equilibrium towards structure V, resulting in a longer S-O bond and a lower-energy sulfoxide stretching mode. Free dmso falls somewhere in the middle in regards to the S-O bond distance and the energy of the sulfoxide stretching mode.*

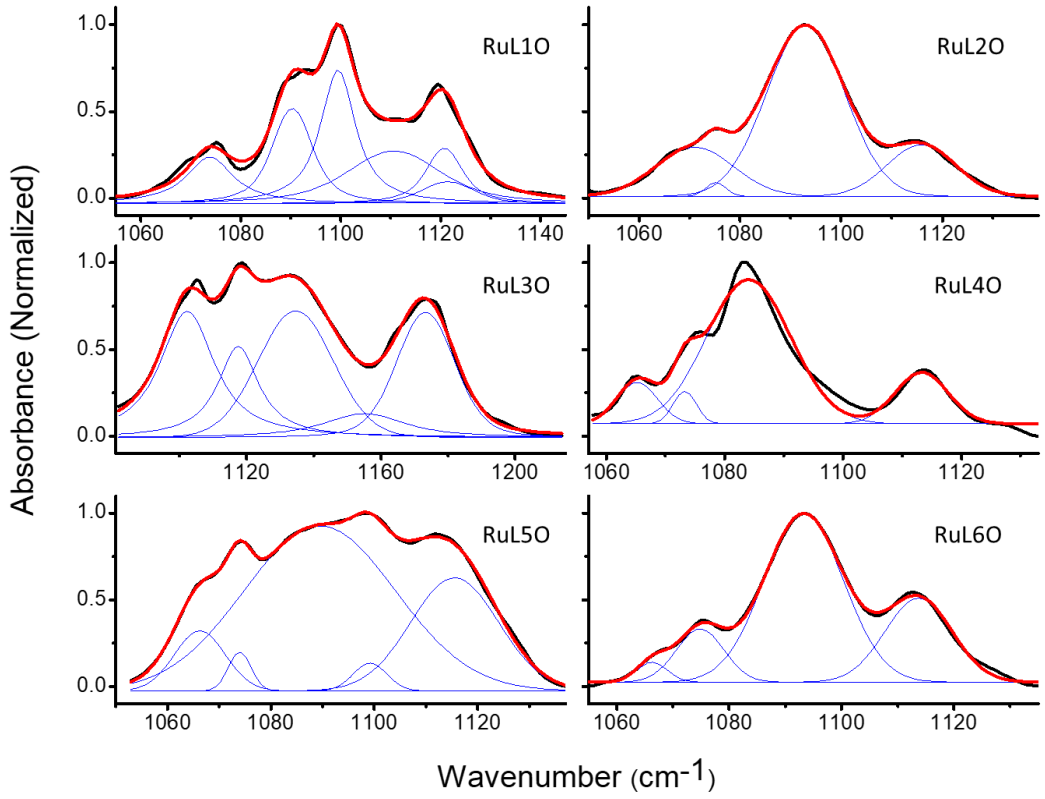

Figure 144: *Crude fits of the S – O vibrational stretching region for S-bonded ruthenium phosphine sulfoxide complexes. Fits are performed using a series of Voigt profiles. We see more vibrational bands in the photoisomerizing complexes (left) than in the non-photoisomerizing complexes (right). We also see more significant overlap of these bands on the left.*

$y = A*\exp(x/t) + y_0$

	937 cm^{-1}	1095 cm^{-1}
y_0	100.035	99.588
A	1.422	-0.936
τ	2.779	3.006
R^2	0.945	0.965

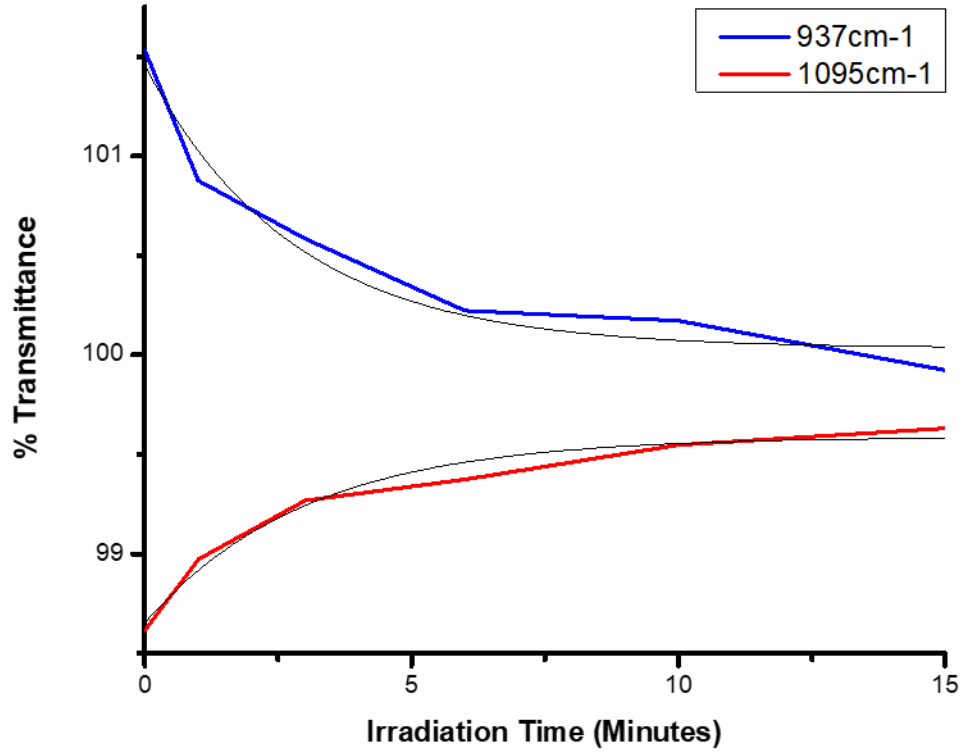

Figure 145: *Infrared transmittance of a RuL5O/Nujol mull as a function of irradiation time from a 355 nm pulsed Nd:YAG laser. The blue line represents decay of the Ru-S υ(S=O) stretching mode and the red line represents growth of the Ru-O υ(S=O) stretching mode. The exponential fit for these two datasets is nearly the same, implying that the loss of one isomer corresponds to the formation of the other.*

Computational Methods

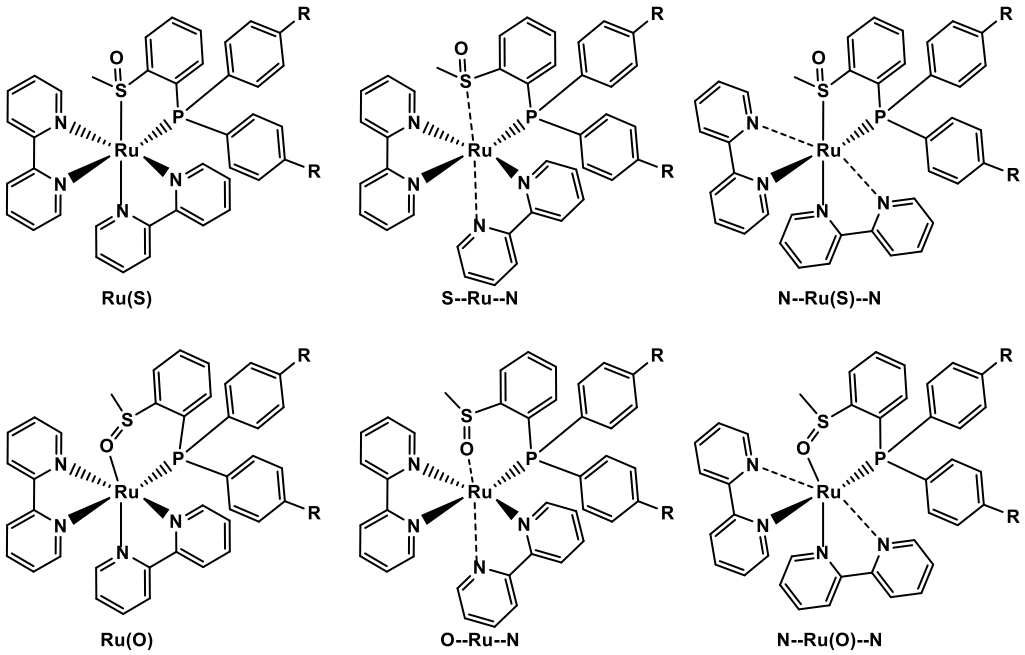

Figure 146: *Representations of the various geometries Ru(E), E--Ru--N, and N--Ru(E)--N, where E = O or S.*

Table 23: *Relative electronic energies (kcal mol^{-1}) from PBE0-D3BJ/BS2//BS1*

	^{1}GS Singlet	^{1}TD-DFT			^{3}TD-DFT//^{1}TD-DFT		
R	**Ru(S)**	**Ru(S)**	**S--Ru--N**	**N--Ru(S)--N**	**Ru(S)**	**S--Ru--N**	**N--Ru(S)--N**
OMe	0.0	58.4	74.8	70.1	57.6	54.8	51.8
H	0.0	64.5	75.0	71.4	61.3	54.9	53.6
CF_3	0.0	66.6	74.5	70.9	60.6	54.9	53.4
R	**Ru(O)**	**Ru(O)**	**O--Ru--N**	**N--Ru(O)--N**	**Ru(O)**	**O--Ru--N**	**N--Ru(O)--N**
OMe	8.0	61.9	71.4	75.1	58.1	50.4	54.0
H	7.9	62.5	71.3	75.0	59.0	50.1	54.0
CF_3	3.8	60.6	69.3	70.8	57.0	48.6	49.9

a) NA: Not Attempted because PBE0-D3BJ/BS1 geometries were not located.

b) NC: Not Computed.

Table 24: *Electronic energies (DFT) and total energies (TD-DFT) (Hartrees) from PBE0-D3BJ/BS2//BS1*

	^{1}GS Singlet	^{1}TD-DFT			^{3}TD-DFT//^{1}TD-DFT		
R	**Ru(S)**	**Ru(S)**	**S--Ru--N**	**N--Ru(S)--N**	**Ru(S)**	**S--Ru--N**	**N--Ru(S)--N**
OMe	–2861.19755	–2861.10443	–2861.07832	–2861.08591	–2861.10569	–2861.11022	–2861.11500
H	–2632.35166	–2632.24881	–2632.23219	–2632.23782	–2632.25393	–2632.26417	–2632.26629
CF_3	–3305.73345	–3305.62727	–3305.61469	–3305.62049	–3305.63695	–3305.64599	–3305.64830
R	**Ru(O)**	**Ru(O)**	**O--Ru--N**	**N--Ru(O)--N**	**Ru(O)**	**O--Ru--N**	**N--Ru(O)--N**
OMe	–2861.18485	–2861.09889	–2861.08384	–2861.07794	–2861.10490	–2861.11716	–2861.11143
H	–2632.33902	–2632.25199	–2632.23808	–2632.23211	–2632.25770	–2632.27175	–2632.26554
CF_3	–3305.72744	–3305.63684	–3305.62294	–3305.62064	–3305.64256	–3305.65598	–3305.65400

a) NA: Not Attempted because PBE0-D3BJ/BS1 geometries were not located.

b) NC: Not Computed.

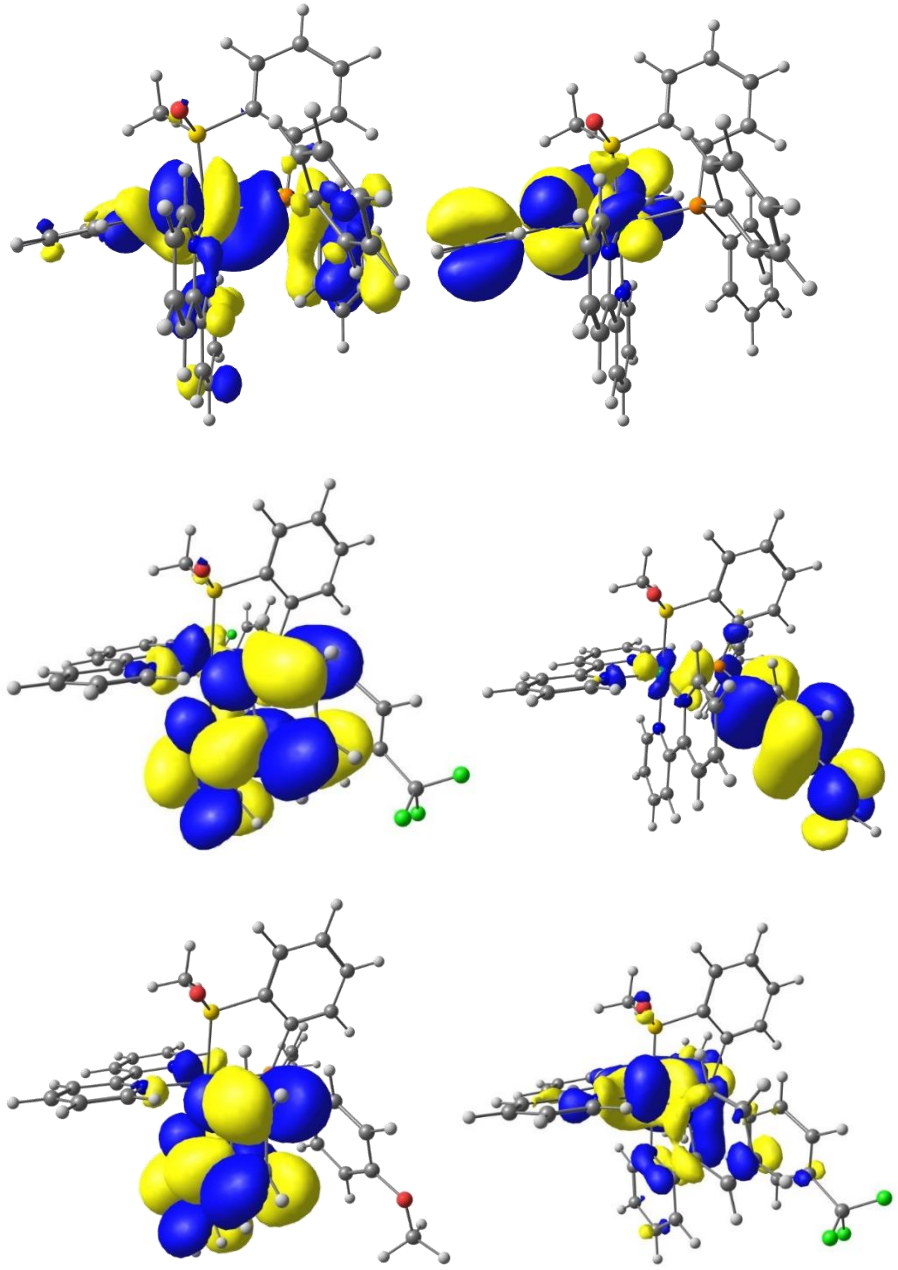

Figure 147: *^{1}TD-PBE0-D3BJ/BS2//^{1}TD-PBE0-D3BJ/BS1 Natural Transition Orbitals (NTOs) for the hole (left) and particle (right) for and S-[(bpy)$_2$Ru(L1O$_H$)]$^{2+}$ (top), S-[(bpy)$_2$Ru(L2O$_{OCH3}$)]$^{2+}$ (middle) and S-[(bpy)$_2$Ru(L3O$_{CF3}$)]$^{2+}$ (bottom). The LUMO for S-[(bpy)$_2$Ru(L1O$_H$)]$^{2+}$ and S-[(bpy)$_2$Ru(L3O$_{CF3}$)]$^{2+}$ are both bpy centered, but on opposite bpy ligands.*

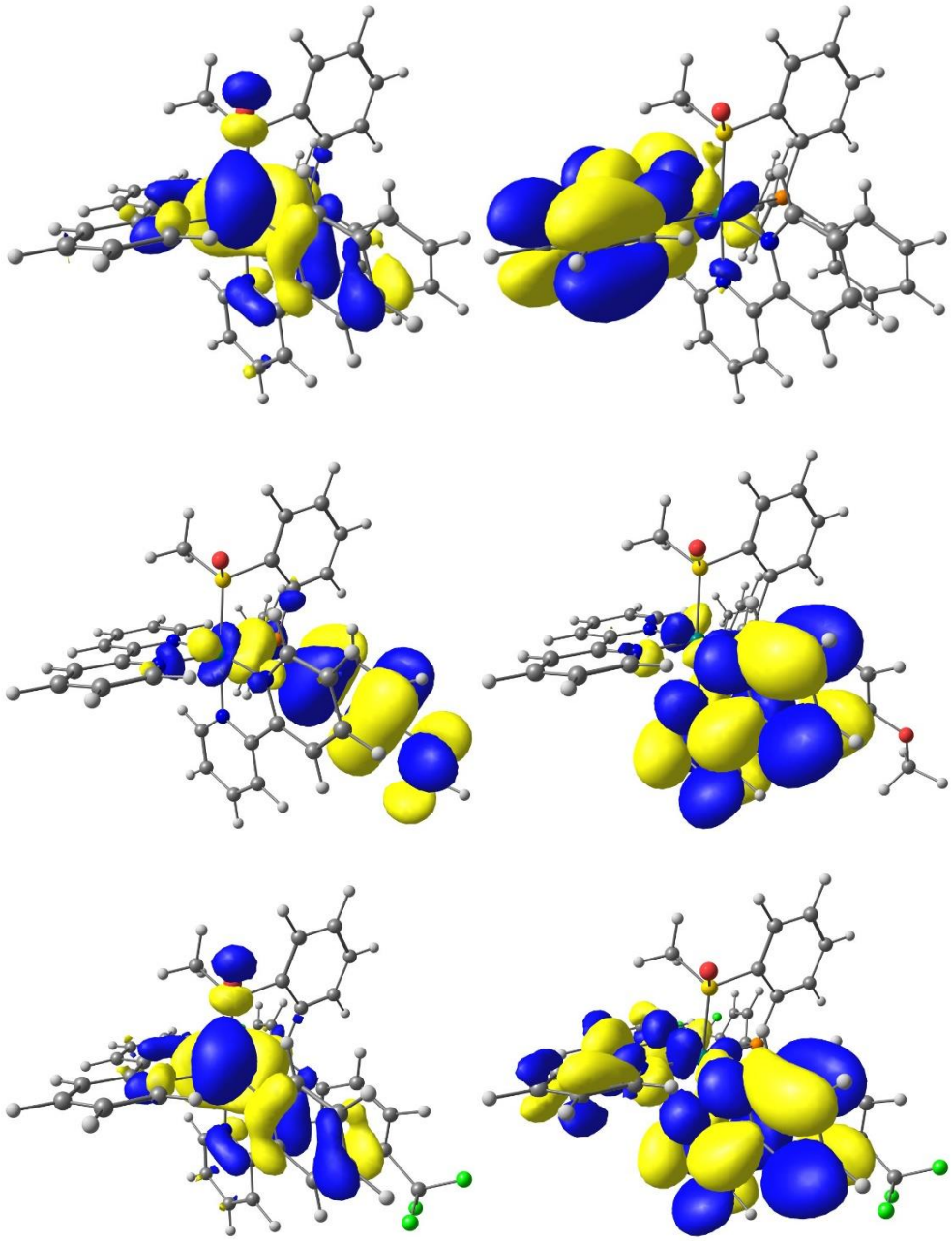

Figure 148: *^{1}TD-PBE0-D3BJ/BS2//PBE0-D3BJ/BS1 Natural Transition Orbitals (NTOs) for the hole (left) and particle (right) for and S-$[(bpy)_2Ru(L1O_H)]^{2+}$ (top), S-$[(bpy)_2Ru(L2O_{OCH3})]^{2+}$ (middle) and S-$[(bpy)_2Ru(L3O_{CF3})]^{2+}$ (bottom). The LUMO for S-$[(bpy)_2Ru(L1O_H)]^{2+}$ and S-$[(bpy)_2Ru(L3O_{CF3})]^{2+}$ are both bpy centered, but on opposite bpy ligands.*

Simulated UV-VIS Spectra

Figure 149: *Simulated Spectra of RuL2O$_{OCH3}$*

^{1}TD-PBE0-D3BJ/BS1//PBE0-D3BJ/BS1 (S_0 geometries) [energies from ^{1}GS PBE0-D3BJ/BS2//BS1]

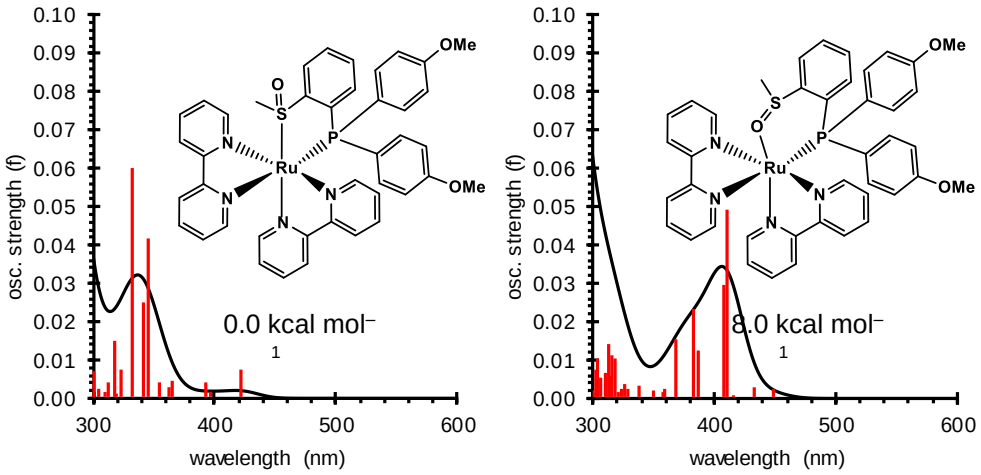

Figure 150: *Simulated Spectra of RuL2O$_{OCH3}$ Part 2*

^{1}TD-PBE0-D3BJ/BS1 (TD-S$_n$ geometries)
[energies from ^{3}TD-PBE0-D3BJ/BS2//^{1}TD-PBE0-D3BJ/BS1]

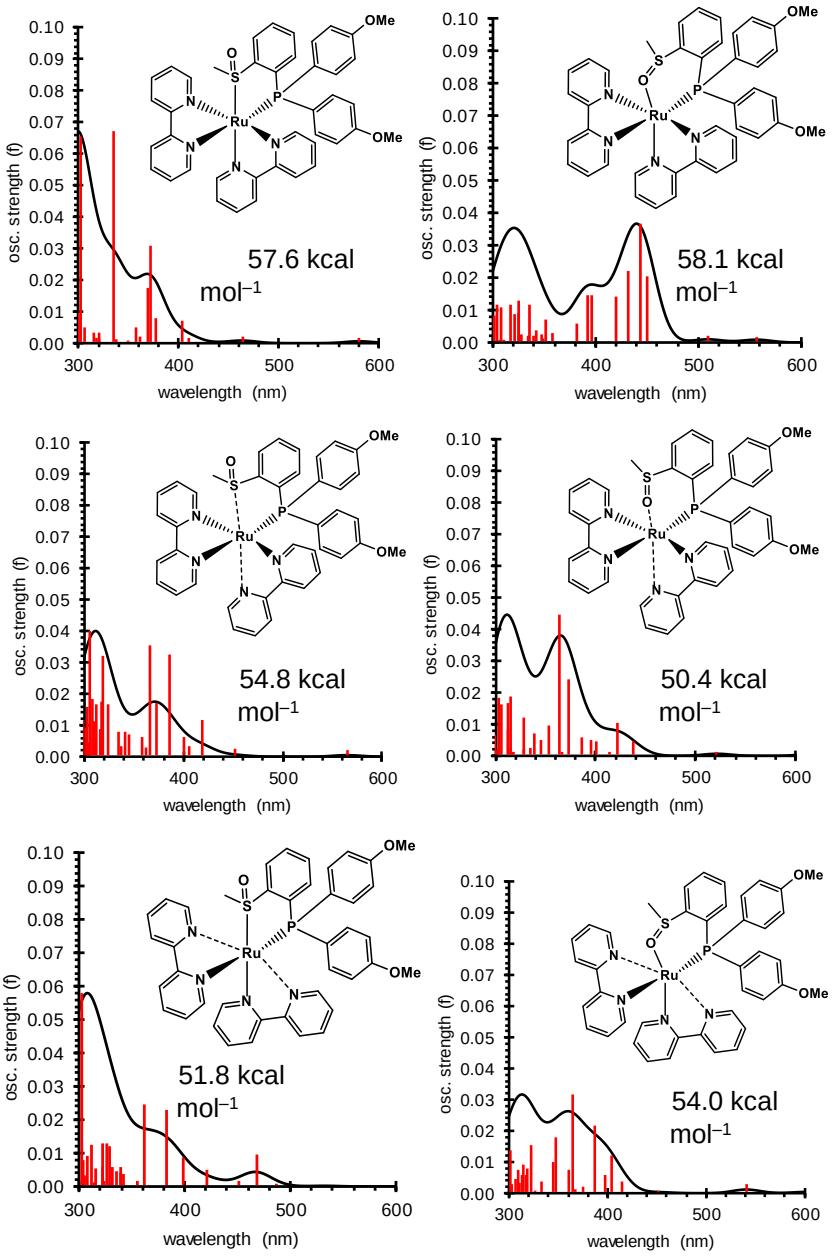

Figure 151: *Simulated Spectra of RuL1O$_H$*

^{1}TD-PBE0-D3BJ/BS1//PBE0-D3BJ/BS1 (S_0 geometries) [energies from ^{1}GS PBE0-D3BJ/BS2//BS1]

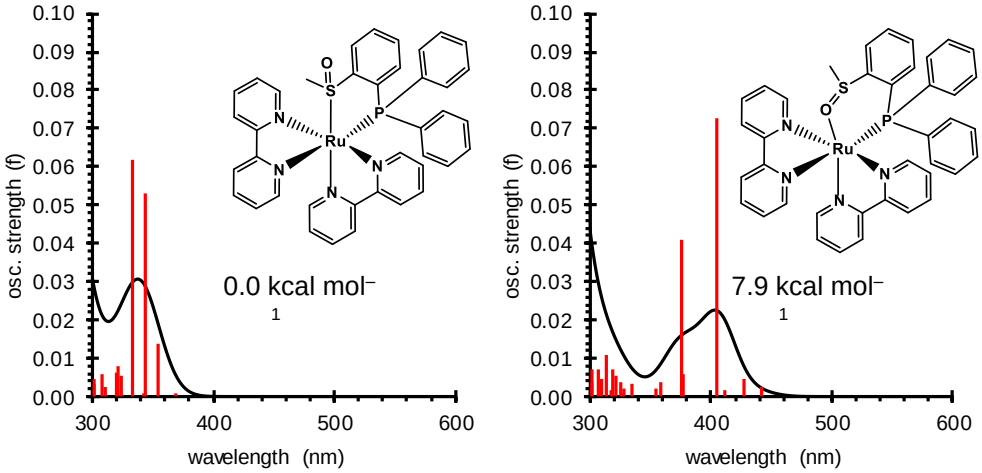

Figure 152: *Simulated Spectra of RuL1O$_H$ Part 2*

^{1}TD-PBE0-D3BJ/BS1 (TD-S$_n$ geometries)
[energies from ^{3}TD-PBE0-D3BJ/BS2//^{1}TD-PBE0-D3BJ/BS1]

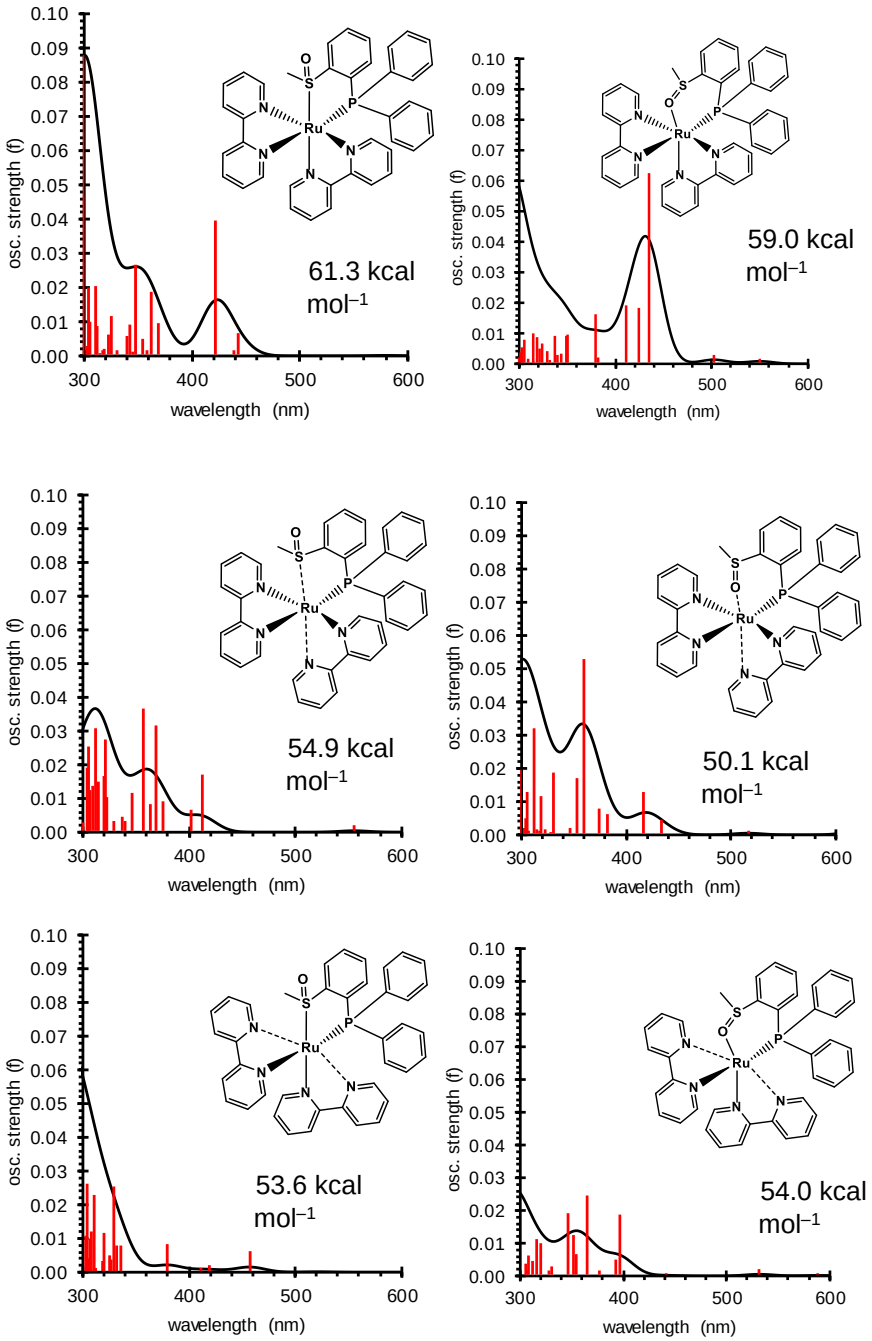

Figure 153: *Simulated Spectra of RuL3O$_{CF3}$*

^{1}TD-PBE0-D3BJ/BS1//PBE0-D3BJ/BS1 (S_0 geometries) [energies from ^{1}GS PBE0-D3BJ/BS2//BS1]

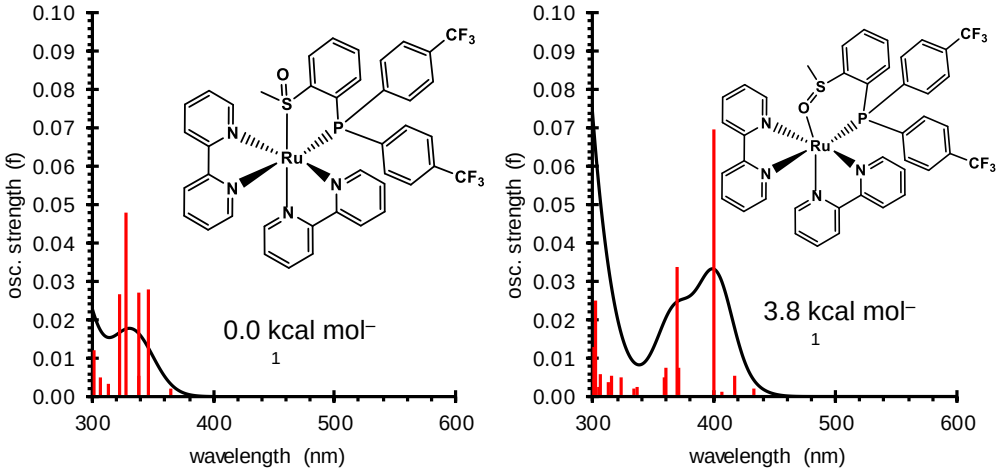

Figure 154: *Simulated Spectra of RuL3O$_{CF3}$ Part 2*

^{1}TD-PBE0-D3BJ/BS1 (TD-S$_n$ geometries)
[energies from ^{3}TD-PBE0-D3BJ/BS2//^{1}TD-PBE0-D3BJ/BS1]

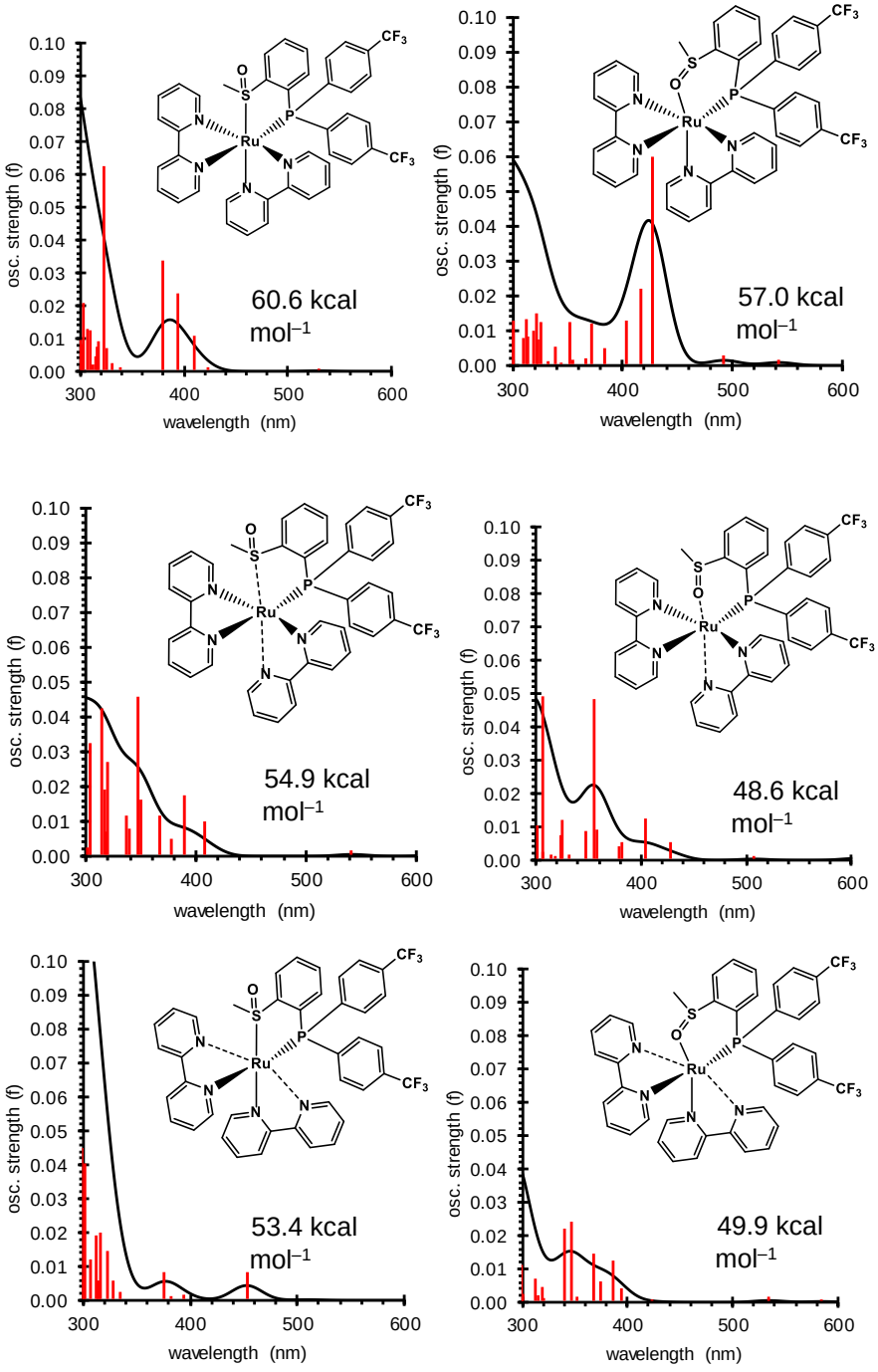

Figure 155: *Simulated Spectra of RuL3O$_{CF3}$ Part 3*

Duplicate of ^{1}TD-PBE0-D3BJ/BS1 (TD-S$_n$ geometries) extended to 650 nm

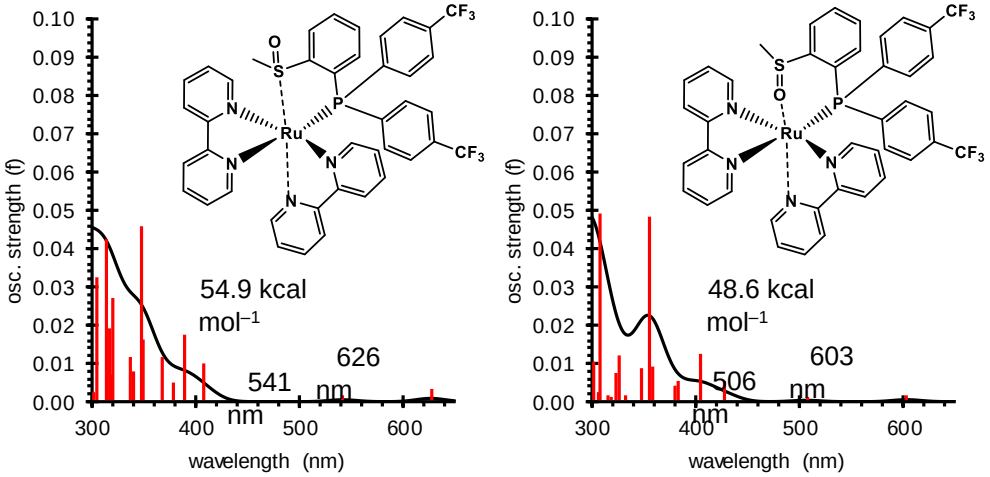

References for this section are numbered 163-180 in Chapter 8.

A3. Slow 3MLCT Formation Prior to Isomerization in Ruthenium Carbene Sulfoxide Complexes

Synthesis

Reagents and Instrumentation:

1-Methyl Imidazole, Benzimidazole, Iodomethane, 2-chloroethyl phenyl sulfide, 2-chloromethyl methyl sulfide and Potassium Ferrioxalate were purchased for Alfa Aesar. 2-chloroethyl methyl sulfide and Tetrabutylammonium hexafluorophosphate were purchased from TCI Chemicals. $RuCl_3.xH_2O$ and 2-chloroethyl ethyl sulfide form Sigma Aldrich. Cesium Carbonate and Silver hexafluorophosphate were purchased from Oakwood chemicals and Strem Chemicals respectively. Acetone-d_6 was purchased from Cambridge Isotopes.

The solvents and the reagents were used as they were received except tetrabutylammonium hexafluorophosphate and Potassium Ferrioxalate, which were recrystallized each time before use. Syntheses were carried out using standard Schleck line technique and solvents used for all experiments were sparged with nitrogen. 1D NMR of the synthesized compounds were recorded at room temperature using Bruker Avance III 300 and Bruker Avance 500 spectrometers in UNM. Accurate Mass was analyzed by Electron Spray Ionization technique in positive mode using Waters Xevo G2 Xs QToF in UNM.

Synthesis of N-heterocyclic (NHC) precursors:

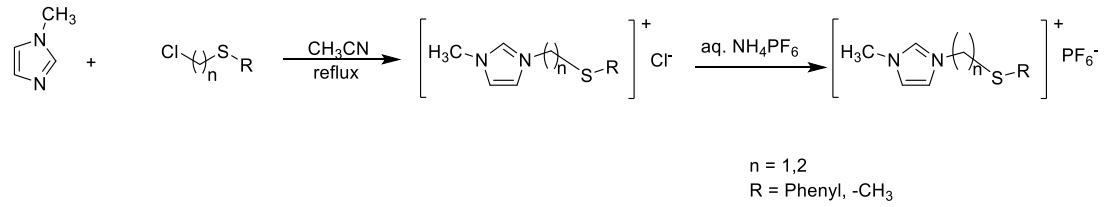

Scheme 9. *General scheme for the synthesis of NHC ligand precursors*

Several synthetic procedures for N-heterocyclic precursors have been reported in literature.[181,182] *The method described here has been slightly modified.*

TE3:

4.1g of N-methyl imidazole was added to dry 50 ml round bottom flask along with 20 mL of acetonitrile. The solution was cooled in ice bath, to this solution 5.97 mL of 1-chloroethyl methyl sulfide was added dropwise with constant stirring and the mixture was refluxed overnight. Using rotary evaporator, the volume was decreased, and 5 to 10 mL of diethyl ether was added dropwise to this mixture while constant stirring. After couple of minutes stirring, two layers separated. The upper diethyl ether was pipetted out and the lower oily layer was mixed in minimum volume of acetonitrile and the process was repeated with diethyl ether. Repetition of this work up procedure yielded pure chloro derivative of the ligand.

For the hexafluorophosphate derivative, the reaction solvent, acetonitrile was evaporated, and the oily product was dissolved in 20 mL of 5% NH_4PF_6 solution. The mixture was extracted twice with additional 20 mL of dichloromethane. The dichloromethane portion was treated with magnesium sulfate, filtered and the solvent

evaporated to obtain yellowish oil which was grown into colorless solid using dichloromethane and ethanol. Yield: 76%. ^{1}H NMR (300 MHz, Acetone) δ (ppm) 9.07 (s, 1H), 7.81 (s, 1H), 7.72 (s, 1H), 4.59 (t, *J* = 6.5 Hz, 2H), 4.08 (s, 3H), 3.06 (t, *J* = 6.5 Hz, 2H), 2.13 (s, 3H). ESI-MS: $[TE3\text{-}PF_6]^+$ calculated *m/z* = 157.079, observed *m/z* = 157.0799

TE4:

1-Bromoethylphenyl sulfide was synthesized from thiophenol, 1-chloroethanol and tribromo phosphine.[183,184] 1-bromoethylphenyl sulfide was then used for the synthesis of ligand by the procedure described as in TE3. Yield: 56% ^{1}H NMR (300 MHz, Acetone) δ (ppm) 9.08 (s, 1H), 7.77 (s, 1H), 7.64 (s, 1H), 7.42 (d, *J* = 7.1 Hz, 2H), 7.30 (m, 3H), 4.62 (t, *J* = 6.3 Hz, 2H), 4.03 (s, 3H), 3.59 (t, *J* = 6.3 Hz, 2H). ESI-MS: $[TE4\text{-}PF_6]^+$ calculated *m/z* = 219.0956, observed *m/z* = 219.0959

TE6:

Synthesized as TE3. Yield: 69.3%. ^{1}H NMR (300 MHz, Acetone) δ (ppm) 9.14 (s, 1H), 7.85 (s, 1H), 7.76 (s, 1H), 5.48 (s, 2H), 4.08 (s, 3H), 2.22 (s, 3H). ESI-MS: $[TE6\text{-}PF_6]^+$ calculated *m/z* = 143.0643, observed *m/z* = 143.0643

TE7:

Benzimidazole was stirred with KOH for half an hour in ethanol and methyl iodide was added dropwise to the solution while stirring.[185] The mixture was refluxed overnight and was subjected to synthesis of TE7 as discussed in TE3. Yield: 62.5%. ^{1}H NMR (300 MHz, Acetone) δ (ppm) 9.63 (s, 1H), 8.15 (m, 1H), 8.08 (m, 1H), 7.83 – 7.73 (m, 2H), 4.92 (t, *J* =

6.5 Hz, 2H), 4.32 (s, 3H), 3.18 (t, *J* = 6.5 Hz, 2H), 2.18 (s, 3H). ESI-MS: $[TE7\text{-}PF_6]^+$ calculated *m/z* = 207.0956, observed *m/z* = 207.0964

TE8:

Synthesized as TE7. Yield: 22%. ^{1}H NMR (300 MHz, Acetone) δ (ppm) 9.76 (s, 1H), 8.30 – 7.98 (m, 2H), 7.90 – 7.71 (m, 2H), 5.86 (s, 2H), 4.33 (s, 3H), 2.25 (s, 3H). ESI-MS: $[TE8\text{-}PF_6]^+$ calculated *m/z* = 193.0799, observed *m/z* = 193.0807.

TE9:

Synthesized as discussed in TE7 and TE4. Yield: 81.5%. ^{1}H NMR (300 MHz, Acetone) δ (ppm) 9.51 (s, 1H), 8.07 – 7.98 (m, 1H), 7.94 – 7.87 (m, 1H), 7.76 – 7.66 (m, 2H), 7.26 (m, 2H), 7.22 – 7.09 (m, 3H), 4.94 (t, *J* = 6.2 Hz, 2H), 4.17 (s, 3H), 3.72 (t, *J* = 6.2 Hz, 2H). ESI-MS: $[TE9\text{-}PF_6]^+$ calculated *m/z* = 269.1112, observed *m/z* = 1269.1123.

TE10:

1-bromomethyl phenyl sulfide was synthesized as reported.[186] The hexafluorophosphate derivative of the ligand was prepared as TE3. Yield: 86.0%. ^{1}H NMR (300 MHz, Acetone) δ (ppm) 8.98 (s, 1H), 7.73 (d, *J* = 4.7 Hz, 2H), 7.44 (m, 5H), 5.82 (s, 2H), 4.03 (s, 3H). ESI-MS: $[TE10\text{-}PF_6]^+$ calculated *m/z* = 205.0799 observed *m/z* = 205.0801.

Ruthenium NHC thioether complexes:

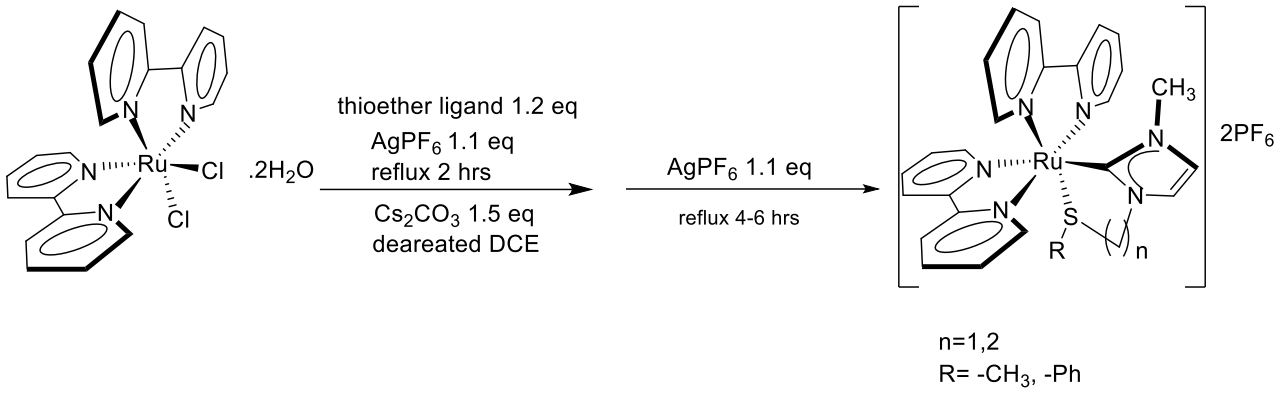

Scheme 10. *General Scheme for the synthesis of ruthenium NHC thioether complexes*

RuTE3:

250 mg (0.48 mmol) of $Ru(bpy)_2Cl_2.2H_2O$ was added to 20 ml of dichloroethane in a three necked flask. 235 mg (0.72 mmol) of Cesium Carbonate, 181 mg (0.6 mmol) of TE3 and 134 mg (0.53 mmol) of $AgPF_6$ was added and the mixture refluxed for 2 to 4 hrs. The mixture was cooled, 134 mg (0.53 mmol) of $AgPF_6$ was then added and refluxed for 6 to 8 hrs. The reaction mixture was then cooled and was filtered through fine frit loaded with Magnesium Sulfate. The reddish-brown filtrate was completely evaporated and the solid was dissolved in minimum volume of acetonitrile and precipitated by adding dropwise into 50 mL of diethyl ether while constant stirring. The orange precipitate was collected in a fine frit and washed with 50 ml of 20% (v/v) Methanol in diethyl ether, air dried and recrystallized through slow diffusion of diethyl ether in acetonitrile solution. Yield: 337.4 mg (81.6 %). ^{1}H NMR (300 MHz, Acetone) δ (ppm) 9.30 (d, *J* = 5.7 Hz, 1H), 8.84 – 8.66 (m, 5H), 8.32 (m, 2H), 8.13 (m, 2H), 7.86 – 7.77 (m, 3H), 7.70 (d, *J* = 4.7 Hz, 1H), 7.57 – 7.50 (m, 1H), 7.48 – 7.39 (m, 2H), 7.18 (d, *J* = 1.9 Hz, 1H), 4.77 (dd, *J* = 15.4,

4.5 Hz, 1H), 4.50 (dd, *J* = 15.3, 8.3 Hz, 1H), 3.23 (dd, *J* = 11.8, 10.0 Hz, 1H), 3.08 (dd, *J* = 14.0, 4.7 Hz, 1H), 2.73 (s, 3H), 1.44 (s, 3H). ESI-MS: $[RuTE3\text{-}PF_6]^+$ calculated *m/z* = 715.0781, observed *m/z* = 715.0801

Alternatively,

250mg (0.48 mmol) of $Ru(bpy)_2Cl_2.2H_2O$ was added to 20 ml dichloroethane in a three necked flask. 235 mg (0.72 mmol) of Cesium Carbonate, 181 mg (0.6 mmol) of TE3 and 268 mg (1.2 mmol) of $AgPF_6$ was added and refluxed for 8 hrs.

RuTE4:

It was prepared by replacing TE3 with TE4 in the procedure described for RuTE3. The orange solid was recrystallized using acetonitrile and diethyl ether in slow diffusion method. Yield 79.2% ^{1}H NMR (500 MHz, Acetone) δ (ppm) 9.81 (d, *J* = 5.5 Hz, 1H), 8.76 – 8.70 (m, 2H), 8.65 (d, *J* = 8.1 Hz, 1H), 8.31 (t, *J* = 7.9 Hz, 1H), 8.20 (d, *J* = 8.1 Hz, 1H), 8.15 – 8.05 (m, 3H), 7.95 (t, *J* = 7.9 Hz, 1H), 7.90 (d, *J* = 5.0 Hz, 2H), 7.86 (d, *J* = 5.3 Hz, 1H), 7.70 (t, *J* = 6.5 Hz, 1H), 7.48 – 7.42 (m, 2H), 7.37 (t, *J* = 6.6 Hz, 1H), 7.21 (m, 2H), 6.85 (t, *J* = 7.8 Hz, 2H), 6.60 (d, *J* = 7.8 Hz, 2H), 4.91 – 4.76 (m, 2H), 3.67 (t, *J* = 5.0 Hz, 2H), 2.87 (s, 3H). ESI-MS: $[RuTE4\text{-}PF_6]^+$ calculated *m/z* = 777.0938, observed *m/z* = 777.0930.

RuTE6:

Synthesized as RuTE3. Yield: 72.1%. ^{1}H NMR (300 MHz, Acetone) δ (ppm) 9.27 (d, *J* = 5.7 Hz, 1H), 8.83 (d, *J* = 8.1 Hz, 1H), 8.75 (t, *J* = 8.6 Hz, 3H), 8.55 (d, *J* = 5.7 Hz, 1H), 8.31

(m, 2H), 8.16 (t, *J* = 7.8 Hz, 2H), 7.99 (d, *J* = 5.2 Hz, 1H), 7.90 (d, *J* = 4.9 Hz, 1H), 7.83 – 7.72 (m, 2H), 7.67 (s, 1H), 7.51 (m, 2H), 7.27 (s, 1H), 5.70 (d, *J* = 12.5 Hz, 1H), 5.13 (d, *J* = 12.5 Hz, 1H), 3.00 (s, 3H), 1.73 (s, 3H). ESI-MS: $[RuTE6]^{2+}$ calculated *m/z* = 278.0495, observed *m/z* = 278.0503.

RuTE7:

Synthesized as RuTE3. Yield: 68.2%. ^{1}H NMR (300 MHz, Acetone) δ (ppm) 9.35 (d, *J* = 5.5 Hz, 1H), 8.98 (d, *J* = 5.1 Hz, 1H), 8.89 – 8.68 (m, 4H), 8.36 (t, *J* = 7.8 Hz, 2H), 8.28 – 8.08 (m, 2H), 7.96 – 7.66 (m, 5H), 7.65 – 7.56 (m, 1H), 7.42 (m, 4H), 5.20 (d, *J* = 10.5 Hz, 1H), 4.81 – 4.63 (m, 1H), 3.24 (d, *J* = 6.1 Hz, 1H), 2.99 (s, 3H), 1.54 (s, 3H). ESI-MS: $[RuTE7]^{2+}$ calculated *m/z* = 310.0652, observed *m/z* = 310.0655.

RuTE8:

Synthesized as RuTE3. Yield:75%. ^{1}H NMR (300 MHz, Acetone) δ (ppm) 9.28 (d, *J* = 5.6 Hz, 1H), 8.86 (d, *J* = 8.4 Hz, 1H), 8.77 (d, *J* = 8.7 Hz, 4H), 8.35 (t, *J* = 8.1 Hz, 1H), 8.30 – 8.16 (m, 3H), 8.06 (d, *J* = 5.2 Hz, 1H), 7.95 (d, *J* = 5.4 Hz, 1H), 7.76 (t, *J* = 6.6 Hz, 1H), 7.70 – 7.64 (m, 1H), 7.58 (d, *J* = 7.1 Hz, 3H), 7.49 (d, *J* = 8.4 Hz, 1H), 7.37 (m, 2H), 5.94 (d, *J* = 12.2 Hz, 1H), 5.38 (d, *J* = 12.3 Hz, 1H), 3.25 (s, 3H), 1.84 (s, 3H). $[RuTE8\text{-}PF_6]^{+}$ calculated *m/z* = 303.0573 , observed *m/z* = 303.0580.

RuTE9:

Synthesized as RuTE3. Yield: 83.9%. ^{1}H NMR (300 MHz, Acetone) δ (ppm) 9.85 (d, *J* = 5.7 Hz, 1H), 9.00 (d, *J* = 5.6 Hz, 1H), 8.71 (m, 2H), 8.36 – 8.22 (m, 2H), 8.22 – 8.06 (m, 3H), 8.06 – 7.96 (m, 2H), 7.92 (m, 2H), 7.78 – 7.70 (m, 1H), 7.70 – 7.60 (m, 1H), 7.56 – 7.29 (m, 5H), 7.24 (t, *J* = 7.5 Hz, 1H), 6.89 (t, *J* = 7.9 Hz, 2H), 6.72 – 6.59 (m, 2H), 5.28 – 5.01 (m, 2H), 3.88 – 3.71 (m, 2H), 3.13 (s, 3H). ESI-MS: $[RuTE9\text{-}PF_6]^+$ calculated *m/z* = 824.1110 , observed *m/z* = 824.1124.

RuTE10:

Synthesized as RuTE3. Yield: 73.3%. ^{1}H NMR (300 MHz, Acetone) δ (ppm) 9.44 (s, 1H), 8.84 – 8.67 (m, 2H), 8.46 – 8.23 (m, 4H), 8.21 – 7.92 (m, 5H), 7.84 (d, *J* = 9.4 Hz, 2H), 7.61 – 7.42 (m, 3H), 7.36 (s, 1H), 7.20 (t, *J* = 7.3 Hz, 1H), 7.01 (d, *J* = 7.8 Hz, 2H), 6.69 (d, *J* = 7.4 Hz, 2H), 5.96 (dd, *J* = 33.9, 13.5 Hz, 2H), 3.06 (s, 3H). ESI-MS: $[RuTE10\text{-}PF_6]^+$ calculated *m/z* = 763.0781, observed *m/z* = 763.0776.

Ruthenium NHC Sulfoxide Complexes:

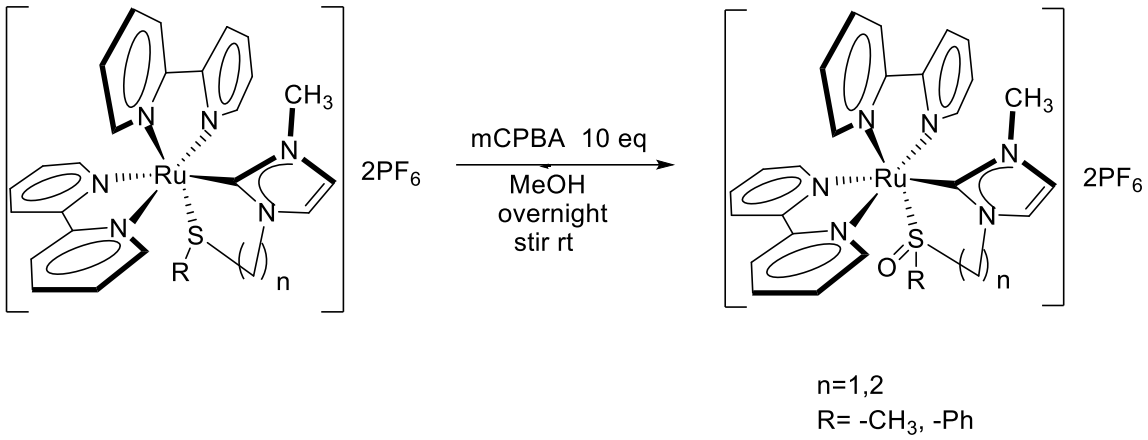

Scheme 11. *General Scheme for the synthesis of Ruthenium NHC sulfoxide complexes*

All metal sulfoxide complexes were synthesized by stirring methanolic solution of metal thioethers in excess of mCPBA (meta chloroperbenzoic acid) at room temperature. The progress of reaction was monitored by using UV-Vis spectrometer. After the completion of reaction, the volume of the solution was evaporated to minimum and was added dropwise to diethyl ether. The yellow precipitate was collected in fine frit and was then washed with 50 mL of 20% (v/v) methanol/ether. The sulfoxide complexes isolated had 90-95% yield. Crystals were grown by diffusing diethyl ether slowly to the solution of the sulfoxide complexes in acetonitrile.

RuOTE3:

^{1}H NMR (300 MHz, Acetone) δ (ppm) 10.06 (d, *J* = 5.0 Hz, 1H), 8.97 (d, *J* = 7.9 Hz, 1H), 8.84 (d, *J* = 8.1 Hz, 1H), 8.71 (d, *J* = 8.1 Hz, 2H), 8.58 (d, *J* = 4.9 Hz, 1H), 8.52 – 8.42 (m, 1H), 8.37 – 8.17 (m, 3H), 7.96 (d, *J* = 5.5 Hz, 1H), 7.91 – 7.77 (m, 3H), 7.66 – 7.49 (m, 2H), 7.47 (d, *J* = 1.9 Hz, 1H), 7.22 (d, *J* = 1.9 Hz, 1H), 5.09 – 4.92 (m, 1H), 4.80 – 4.67 (m, 1H), 3.92 (dd, *J* = 7.9, 3.5 Hz, 2H), 2.93 (s, 3H), 2.34 (s, 3H). ESI-MS: $[RuOTE3]^{2+}$ calculated *m/z* = 293.0547, observed *m/z* = 293.0553.

RuOTE4:

^{1}H NMR (500 MHz, Acetone) δ (ppm) 10.54 (d, *J* = 5.4 Hz, 1H), 8.67 (m, 3H), 8.29 (m, 3H), 8.23 – 8.08 (m, 4H), 7.95 (t, *J* = 6.6 Hz, 1H), 7.75 – 7.69 (m, 2H), 7.61 – 7.55 (m, 1H), 7.50 (s, 1H), 7.46 (t, *J* = 6.6 Hz, 1H), 7.35 (t, *J* = 7.4 Hz, 1H), 7.25 (s, 1H), 7.05 (t, *J* = 7.8 Hz, 2H), 6.81 (d, *J* = 7.7 Hz, 2H), 5.28 – 5.19 (m, 1H), 5.09 (d, *J* = 14.3 Hz, 1H), 4.41 (t, *J* = 12.1 Hz, 1H), 3.95 – 3.87 (m, 1H), 3.04 (s, 3H). ESI-MS: $[RuOTE4]^{2+}$ calculated *m/z* = 324.0627, observed *m/z* = 324.0626.

RuOTE5:

^{1}H NMR (300 MHz, Acetone) δ (ppm) 10.21 (d, *J* = 5.5 Hz, 1H), 8.93 (d, *J* = 8.1 Hz, 1H), 8.80 (d, *J* = 8.1 Hz, 1H), 8.65 (d, *J* = 8.0 Hz, 2H), 8.57 (d, *J* = 5.3 Hz, 1H), 8.43 (t, *J* = 7.8 Hz, 1H), 8.23 (m, 3H), 7.99 (d, *J* = 5.0 Hz, 1H), 7.91 – 7.73 (m, 3H), 7.61 – 7.47 (m, 2H), 7.43 (s, 1H), 7.18 (s, 1H), 5.02 – 4.84 (m, 1H), 4.75 (m, 1H), 3.84 (m, 1H), 3.78 – 3.62 (m, 1H), 2.91 (s, 3H), 2.26 (m, 2H), 1.09 (q, *J* = 6.9 Hz, 3H).

RuOTE9:

^{1}H NMR (300 MHz, Acetone) δ (ppm) 10.62 (d, *J* = 4.9 Hz, 1H), 8.86 (d, *J* = 5.0 Hz, 1H), 8.63 (m, 2H), 8.40 – 8.11 (m, 7H), 8.00 – 7.90 (m, 1H), 7.87 (d, *J* = 5.0 Hz, 1H), 7.78 (d, *J* = 7.3 Hz, 1H), 7.72 – 7.59 (m, 2H), 7.57 – 7.48 (m, 2H), 7.39 (m, 3H), 7.08 (t, *J* = 7.9 Hz, 2H), 6.90 – 6.80 (m, 2H), 5.58 (m, 1H), 5.32 (m, 1H), 4.60 – 4.42 (m, 1H), 4.06 (m, 1H), 3.34 (s, 3H). ESI-MS: $[RuOTE9\text{-}PF_6]^+$ calculated *m/z* = 840.1060, observed *m/z* = 840.1052.

N-heterocyclic Carbene precursors:

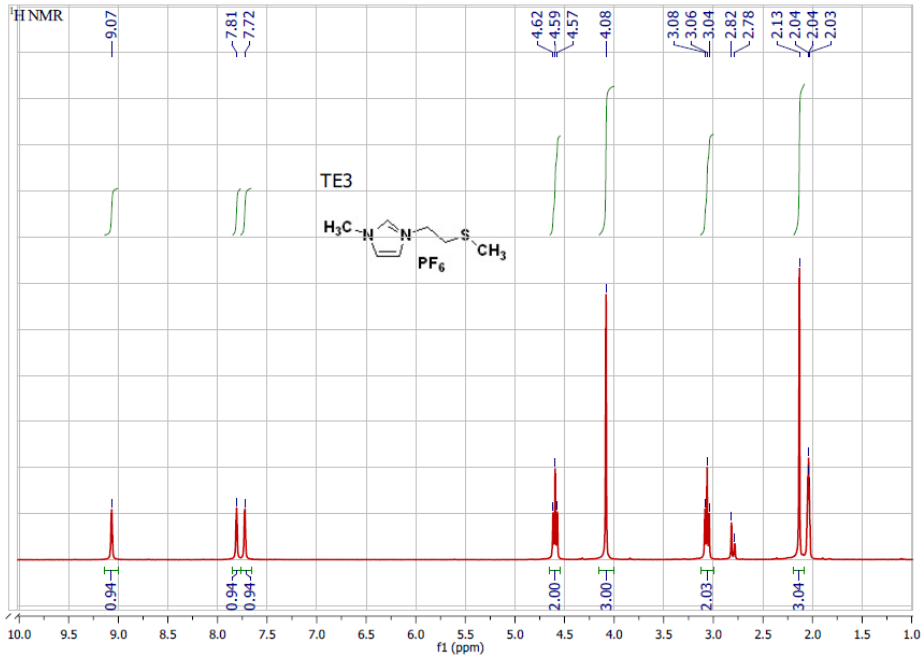

Figure 156: *[1]HNMR of TE*

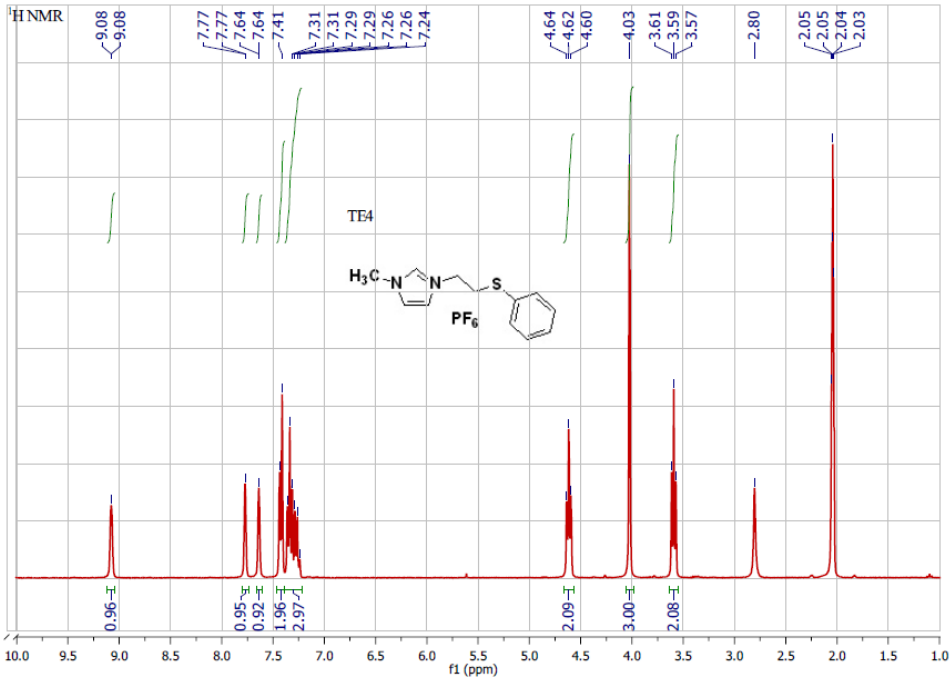

Figure 157: *[1]HNMR of TE4*

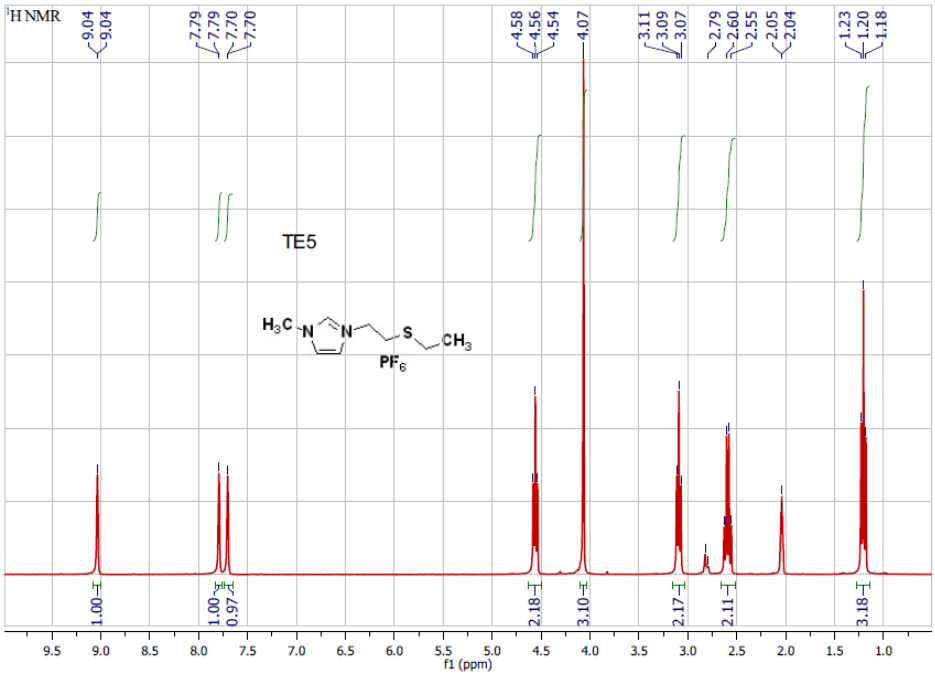

Figure 158: *[1]HNMR of TE5*

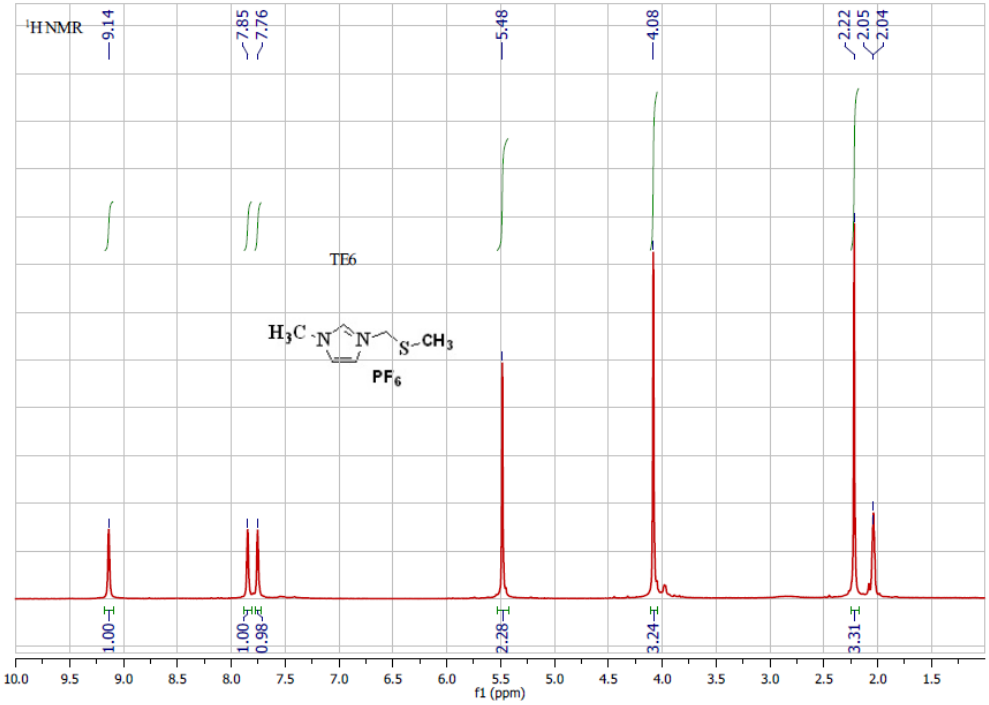

Figure 159: *[1]HNMR of TE6*

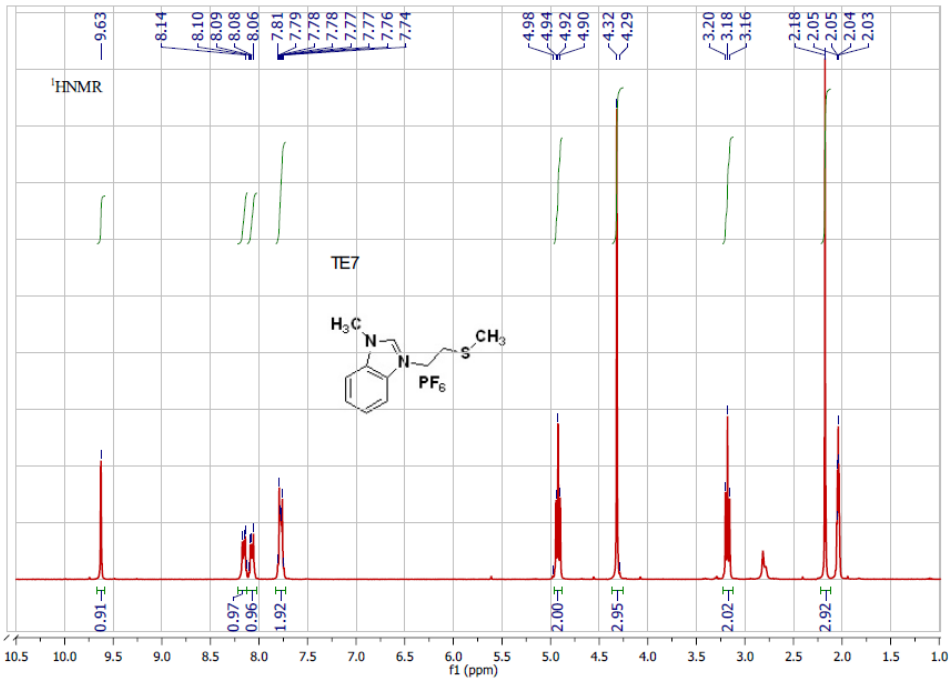

Figure 160: *[1]HNMR of TE7*

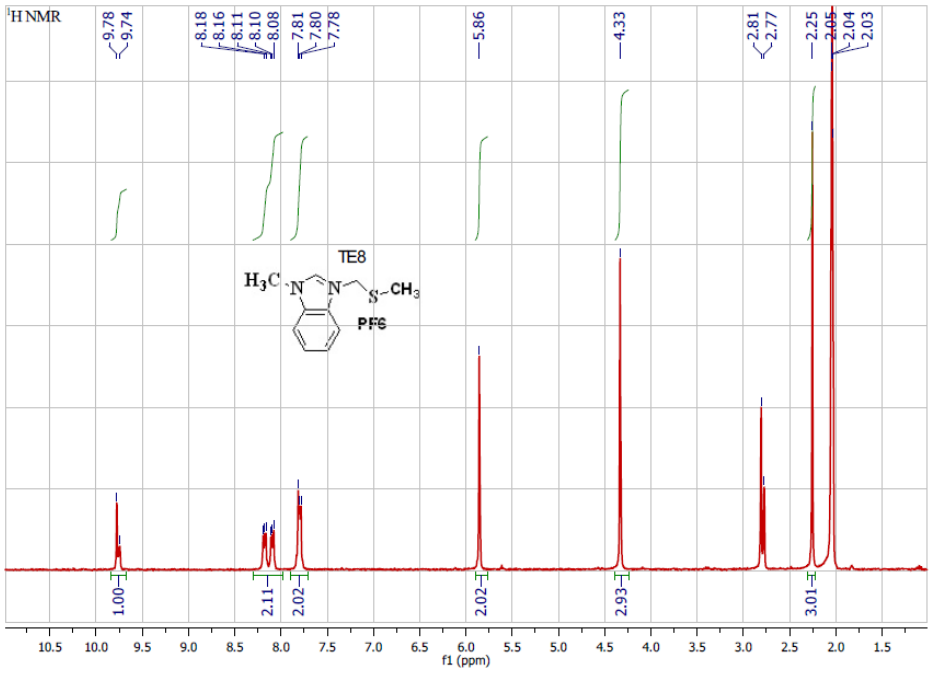

Figure 161: *[1]HNMR of TE8*

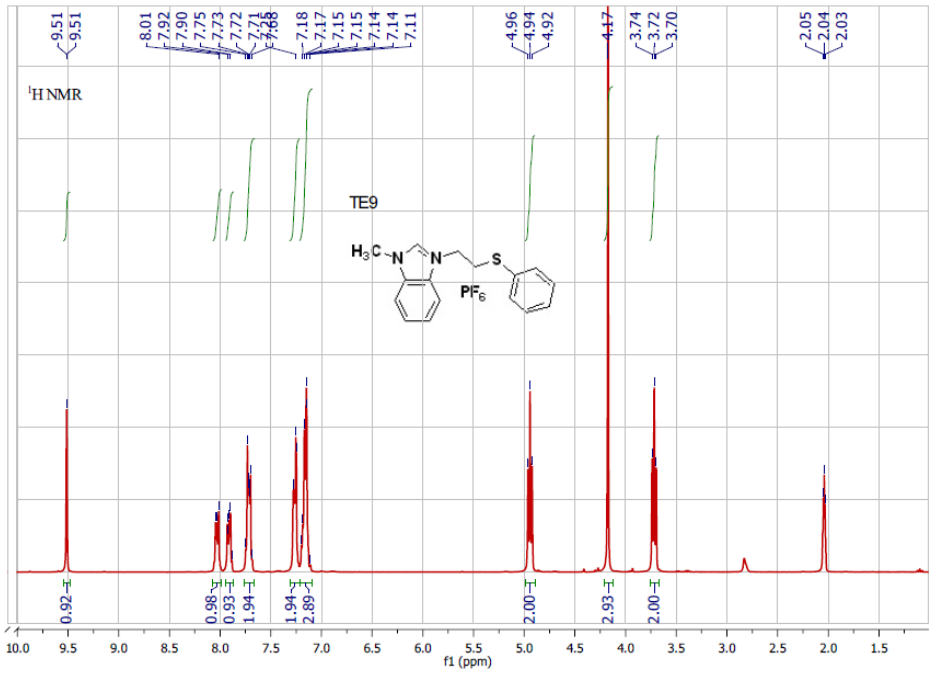

Figure 162: *[1]HNMR of TE9*

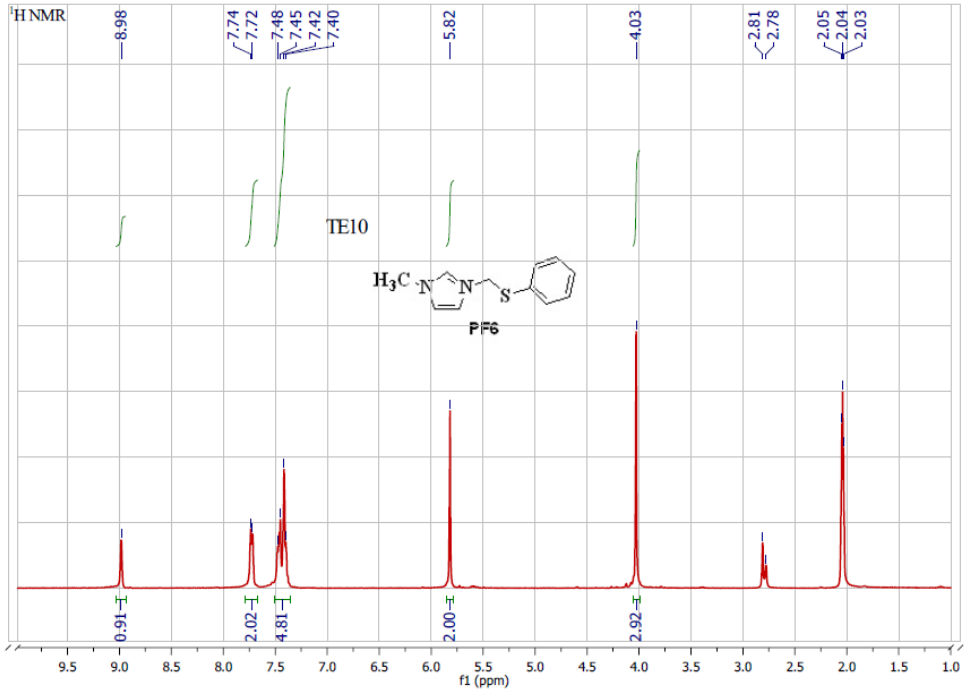

Figure 163: *[1]HNMR of TE10*

Ruthenium NHC Complexes:

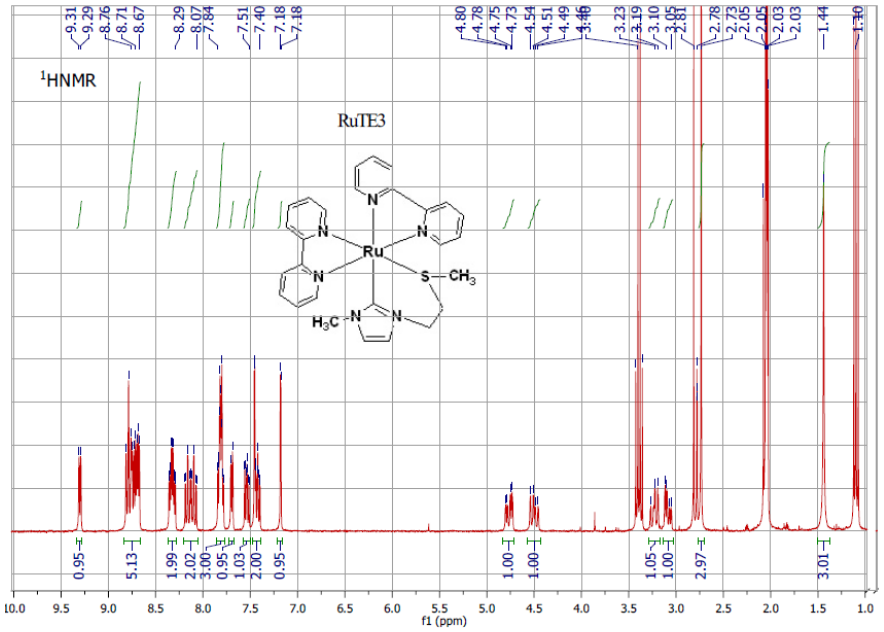

Figure 164: *^{1}HNMR of RuTE3*

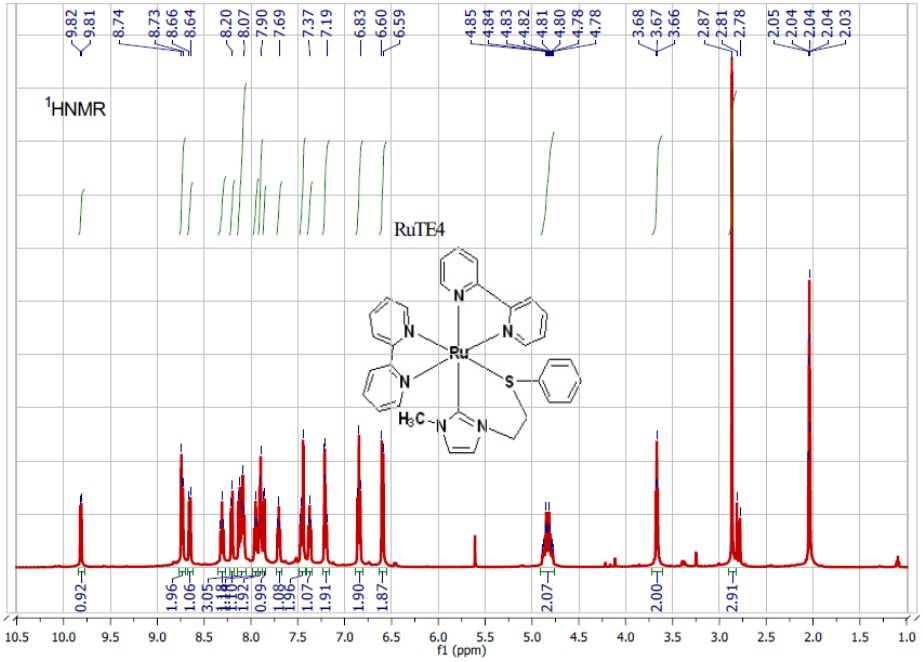

Figure 165: *^{1}HNMR of RuTE4*

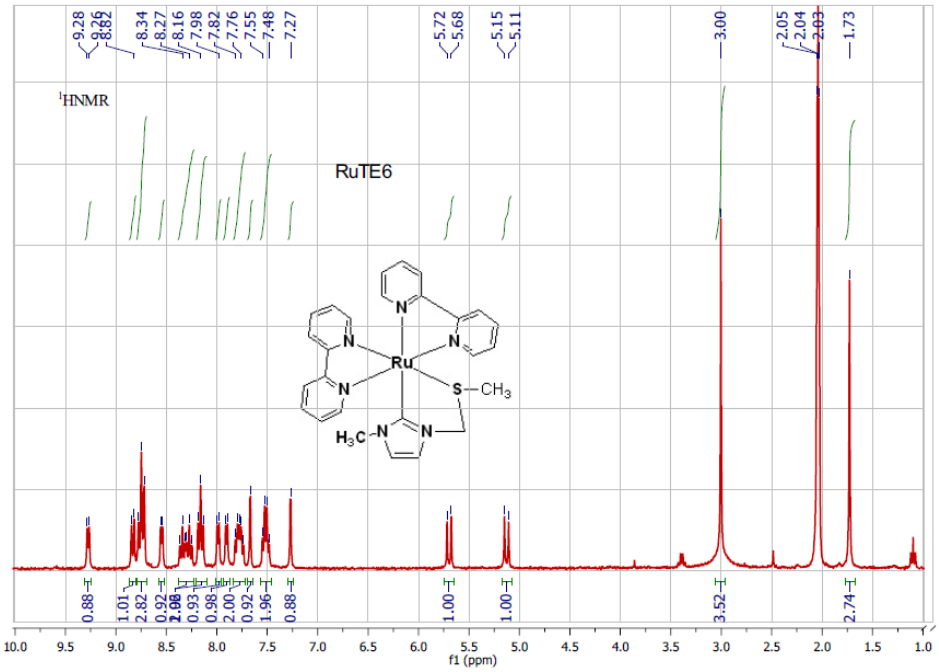

Figure 166: *^{1}HNMR of RuTE6*

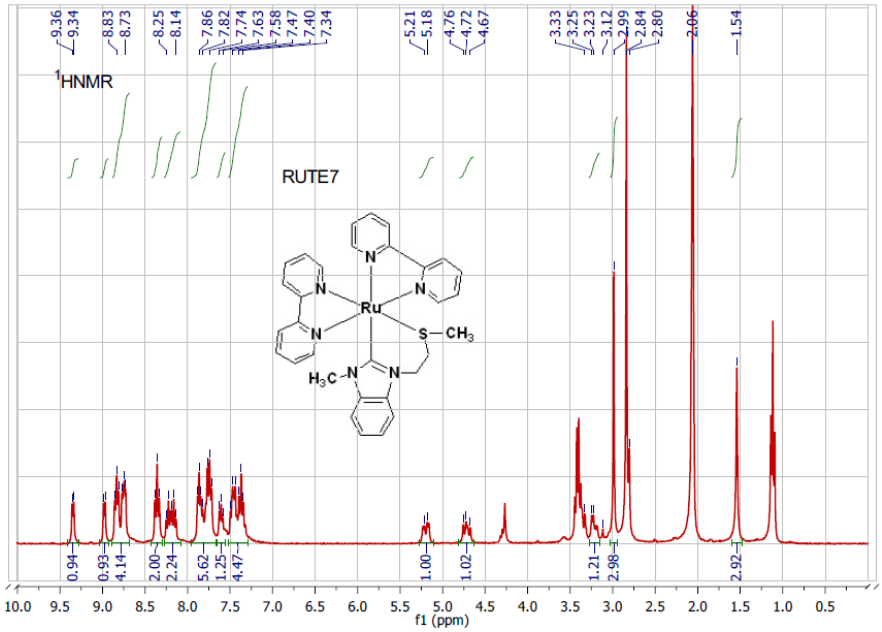

Figure 167: *^{1}HNMR of RuTE7*

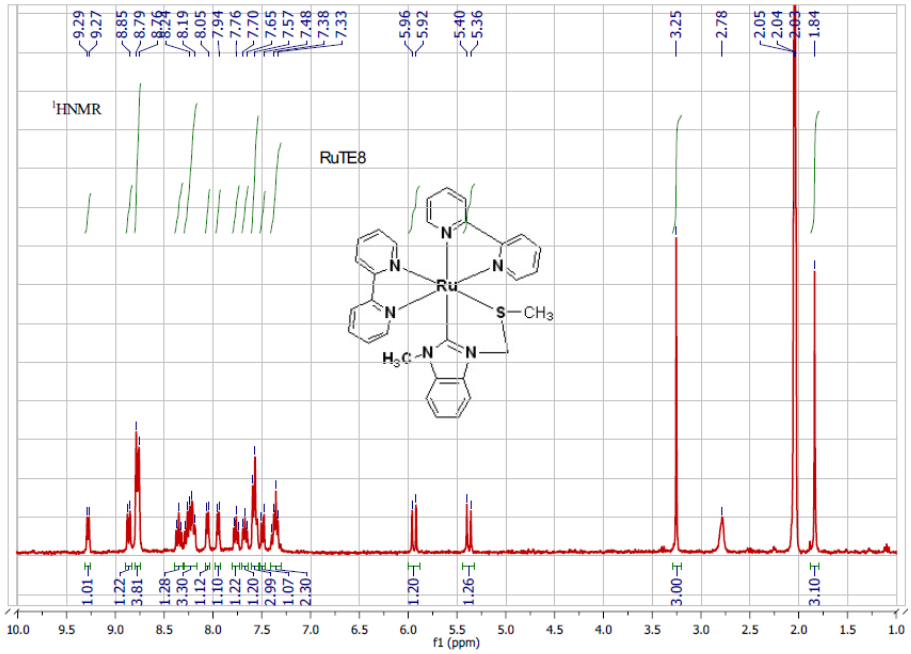

Figure 168: *[1]HNMR of RuTE8*

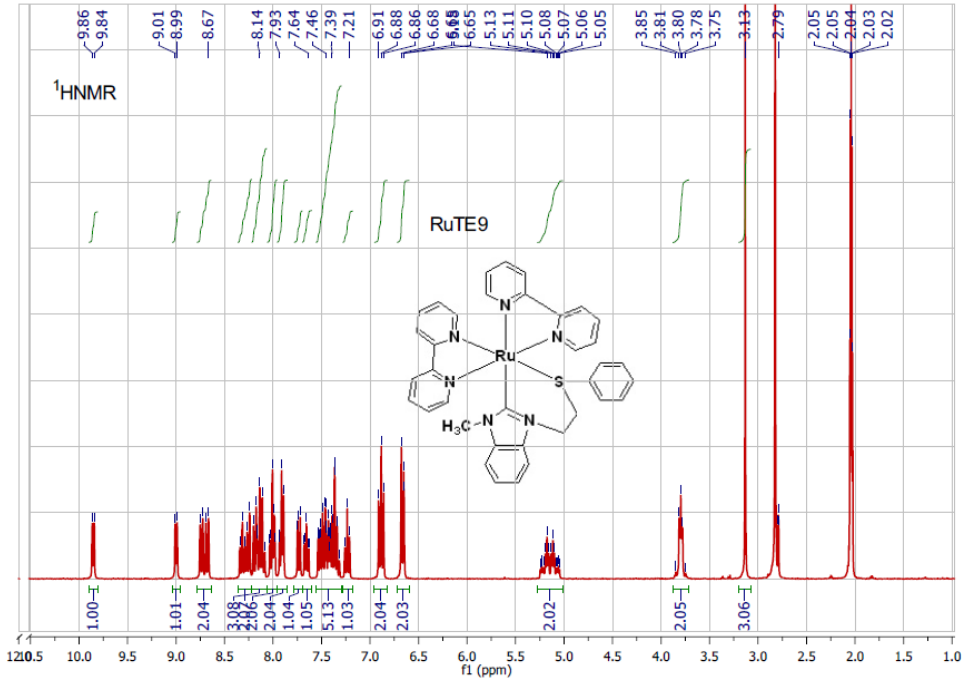

Figure 169: *[1]HNMR of RuTE9*

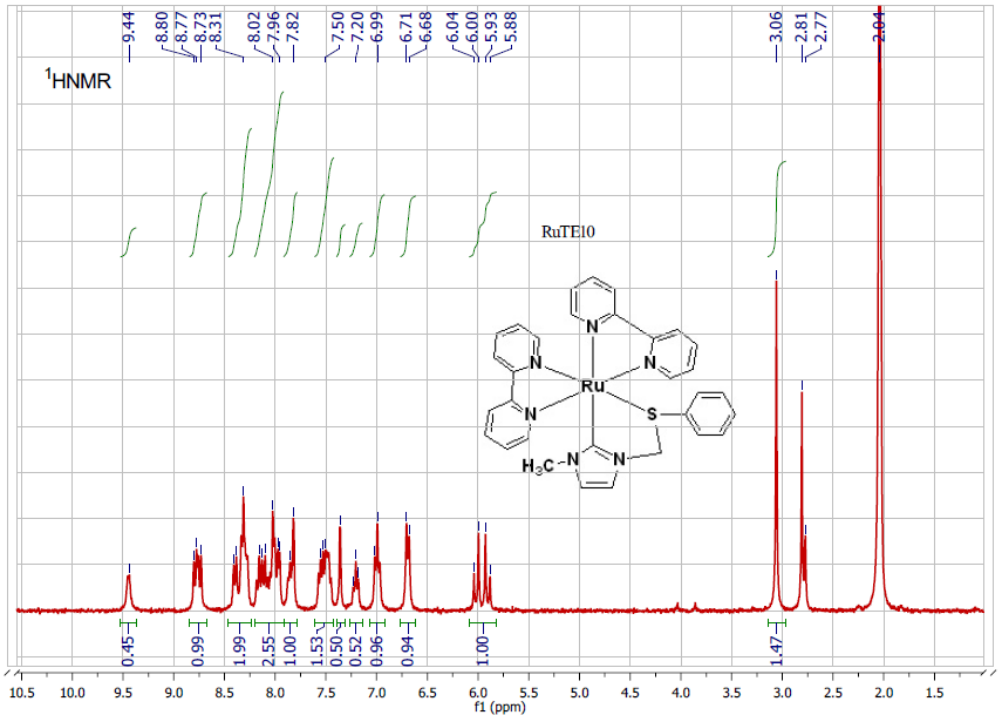

Figure 170: *[1]HNMR of RuTE10*

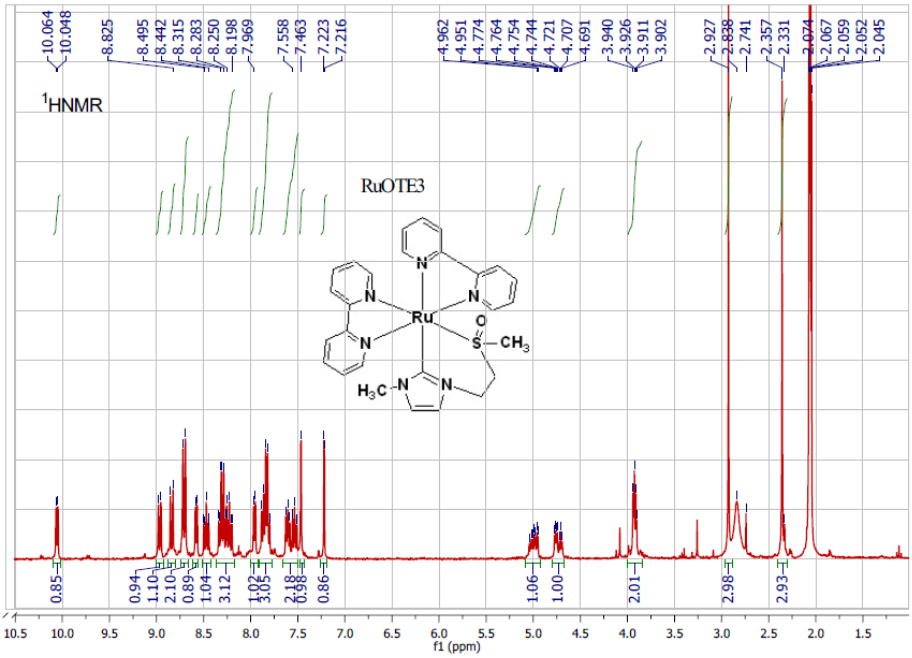

Figure 171: *[1]HNMR of RuOTE3*

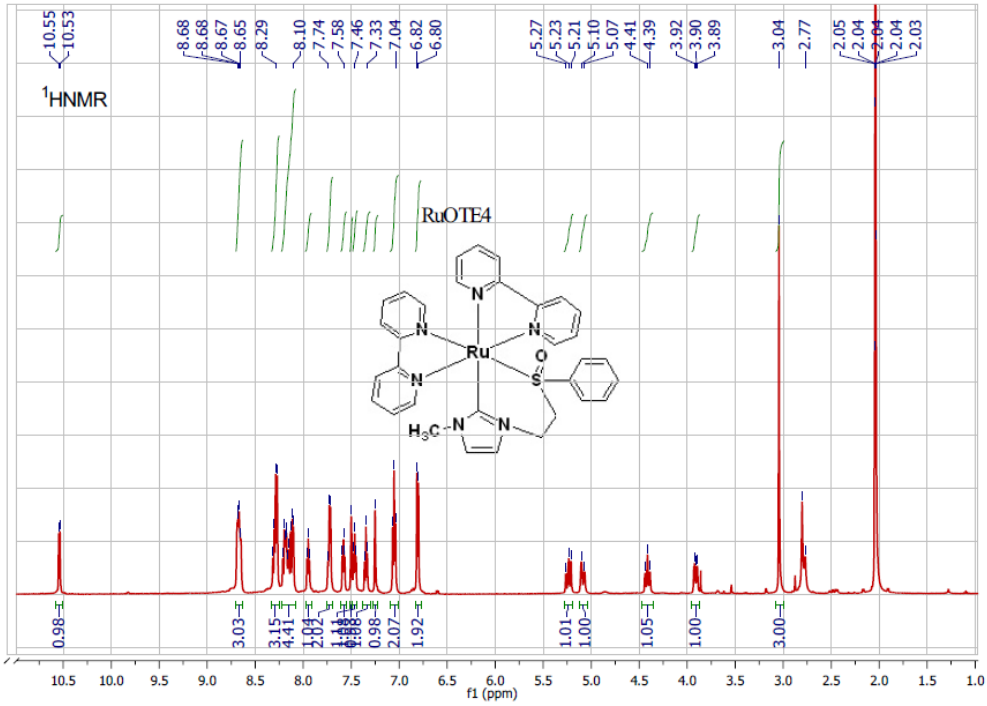

Figure 172: *[1]HNMR of RuOTE4*

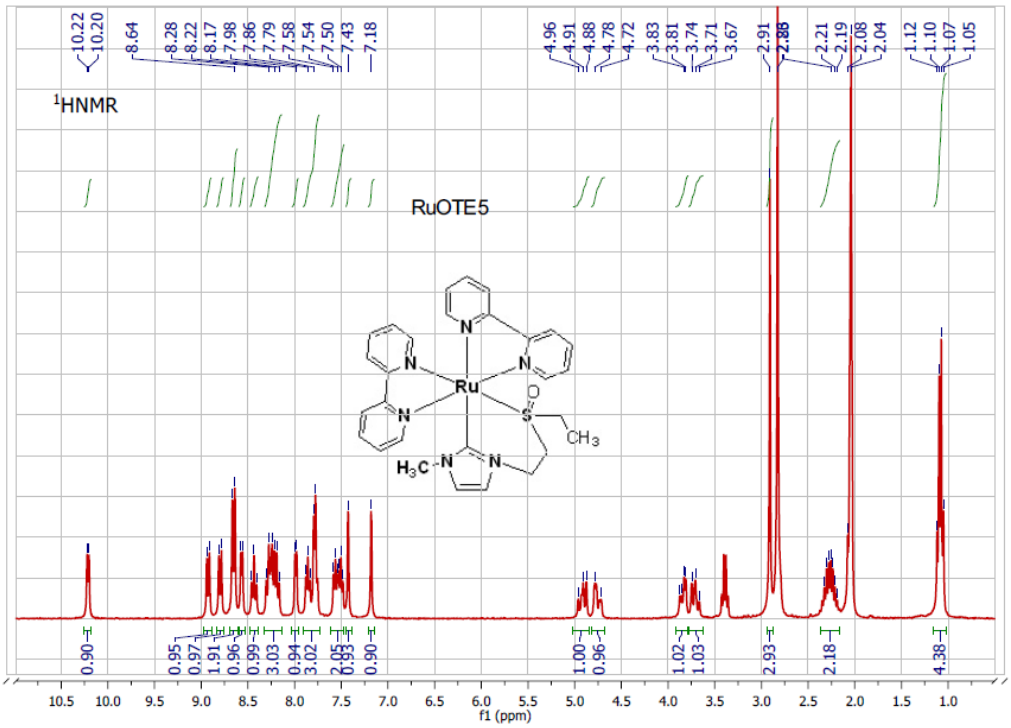

Figure 173. *[1]HNMR of RuOTE5*

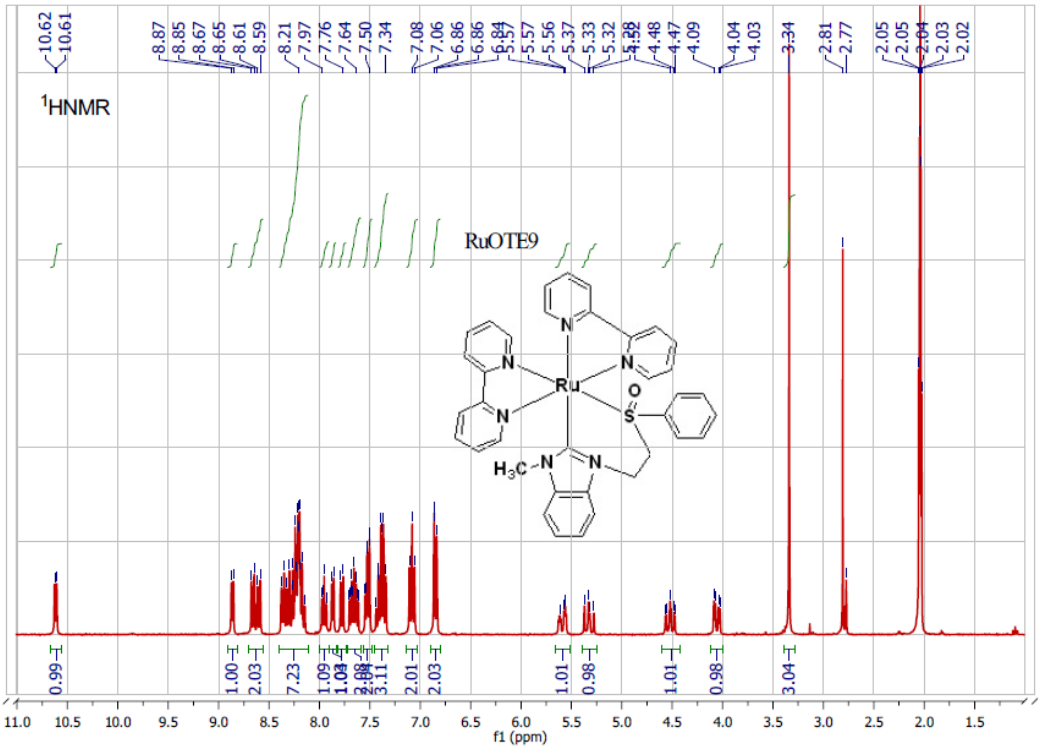

Figure 174. *[1]HNMR of RuOTE9*

Electrochemistry:

Table 25: *Electrochemical properties*

	$E^{o'}_{Ru3+/2+}$ (V ± 0.01)			E^{o} (V ± 0.01)		Rate constant(s^{-1})	
Complexes	$E_S^{o'}$	$E_O^{o'}$	$E^{o'}$	$bpy^{0/-1}$	$bpy^{-1/-2}$	$k_{S\rightarrow O}$	$k_{O\rightarrow S}$
RuTE3			+0.84	-1.68	-1.85		
RuOTE3	+1.09	+0.61		-1.60	-1.84	0.18 ± 0.002	1.57 ± 0.02
RuTE4			+0.87	-1.69	-1.94		
RuOTE4	+1.12	+0.65		-1.63	-1.85	0.89 ± 0.01	1.01 ± 0.04
RuTE9			+0.97	-1.65	-1.91		
RuOTE9	+1.24	+0.71		-1.63	-1.85	0.86 ± 0.01	2.97 ± 0.03

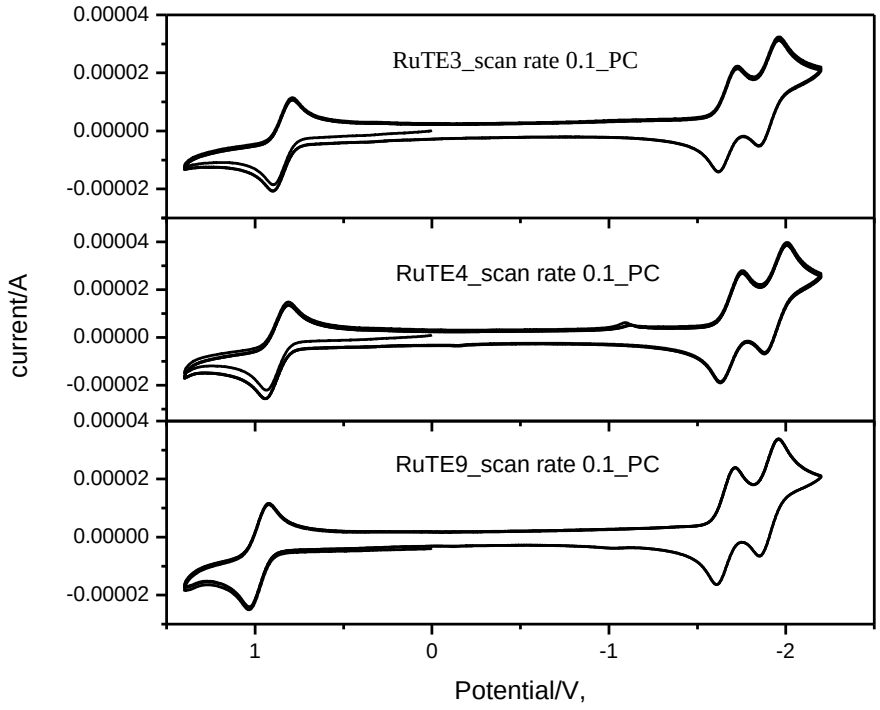

Figure 175: *Cyclic Voltammetry of RuTE3, RuTE4 and RuTE9*

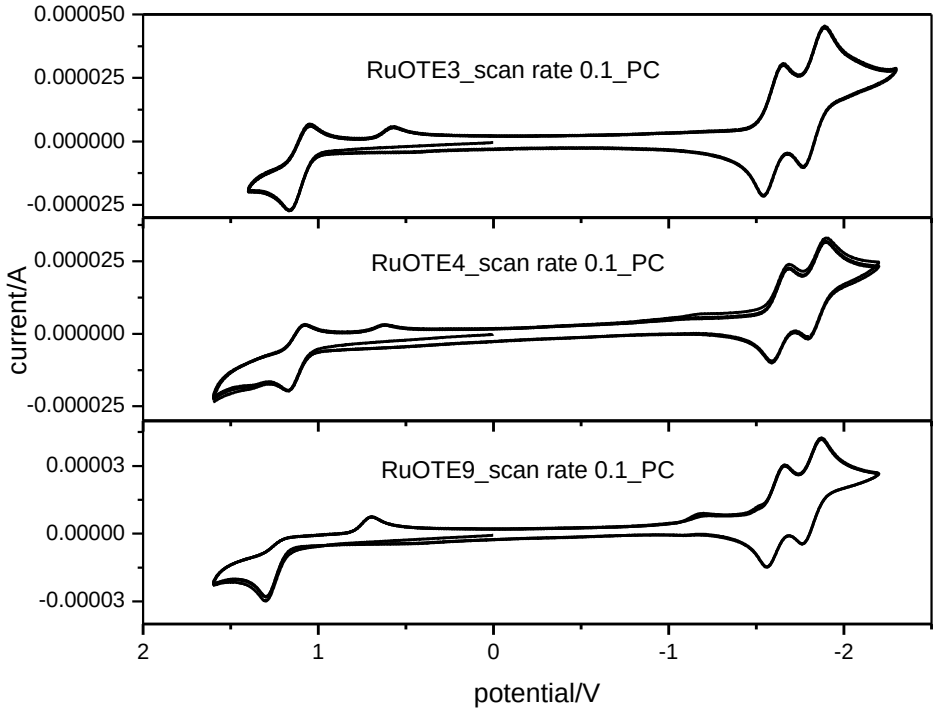

Figure 176: *Cyclic Voltammetry of RuOTE3, RuOTE4 and RuOTE9*

Rate of Electrochemical Isomerization

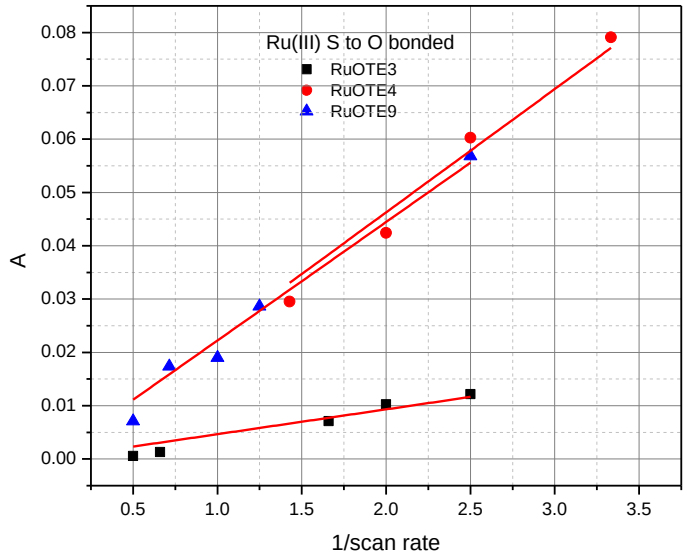

Figure 177. *Rate of Electrochemical Isomerization* $Ru^{III}{}_{S \rightarrow O}$

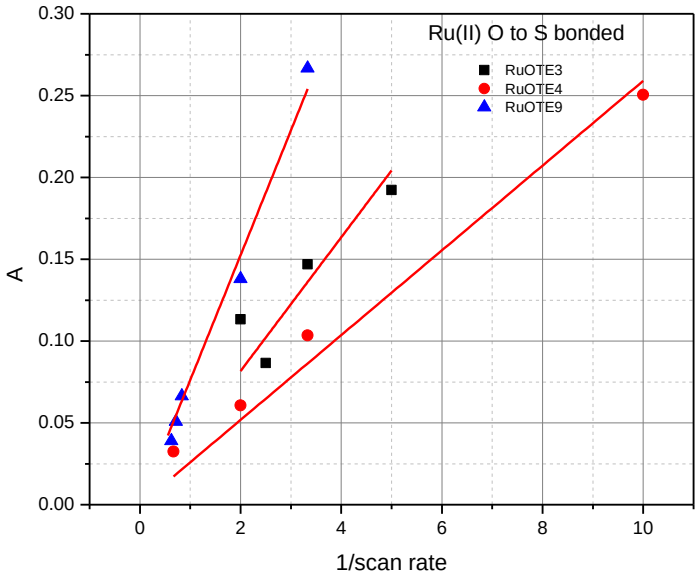

Figure 178: *Rate of Electrochemical Isomerization* $Ru^{II}{}_{O \rightarrow S}$

Quantum Yield of Isomerization:

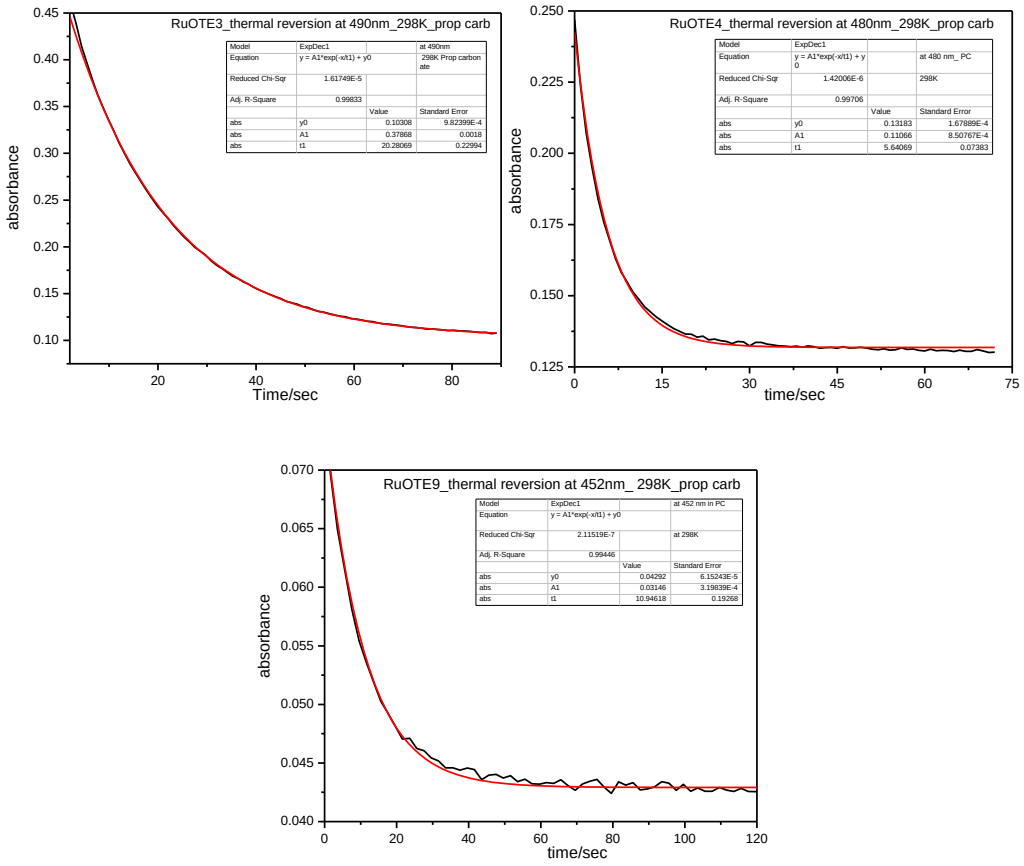

Figure 179. *Thermal Reversion: absorbance vs. Time plot at 298K in Propylene Carbonate*

Table 26: *Time constant at different temperatures*

	Time constant for thermal reversion in Propylene Carbonate			
Complexes	**298K**	**285K**	**273K**	**263K**
RuOTE3	20 ± 0.2	49 ± 0.4	223 ± 5	796 ± 66
RuOTE4	6 ± 0.07	15 ± 0.2	66 ± 0.7	175 ± 4
RuOTE9	11± 0.2	22 ± 0.15	109 ± 0.9	212 ± 5

Table 27: *Activation Parameters calculated for system in Propylene Carbonate*

Complexes	**E_a/KJ $K^{-1}mol^{-1}$**	**A**	**ΔH/KJ $K^{-1}mol^{-1}$**	**ΔS/J $K^{-1}mol^{-1}$**
RuOTE3	68.0	4.77E+10	66.0	-48.3
RuOTE4	63.0	1.82E+10	61.0	-56.3
RuOTE9	60.0	0.29E+10	57.4	-71.3

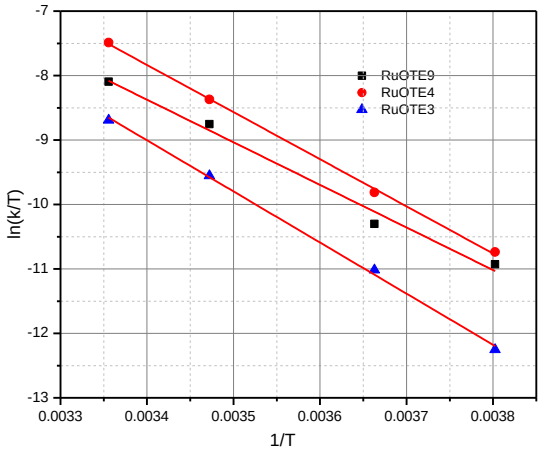

Figure 180: Eyring *Plot*

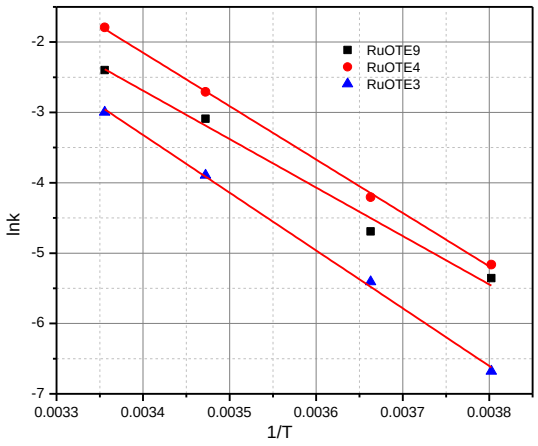

Figure 181: *Arrhenius Plot*

Transient Absorption:

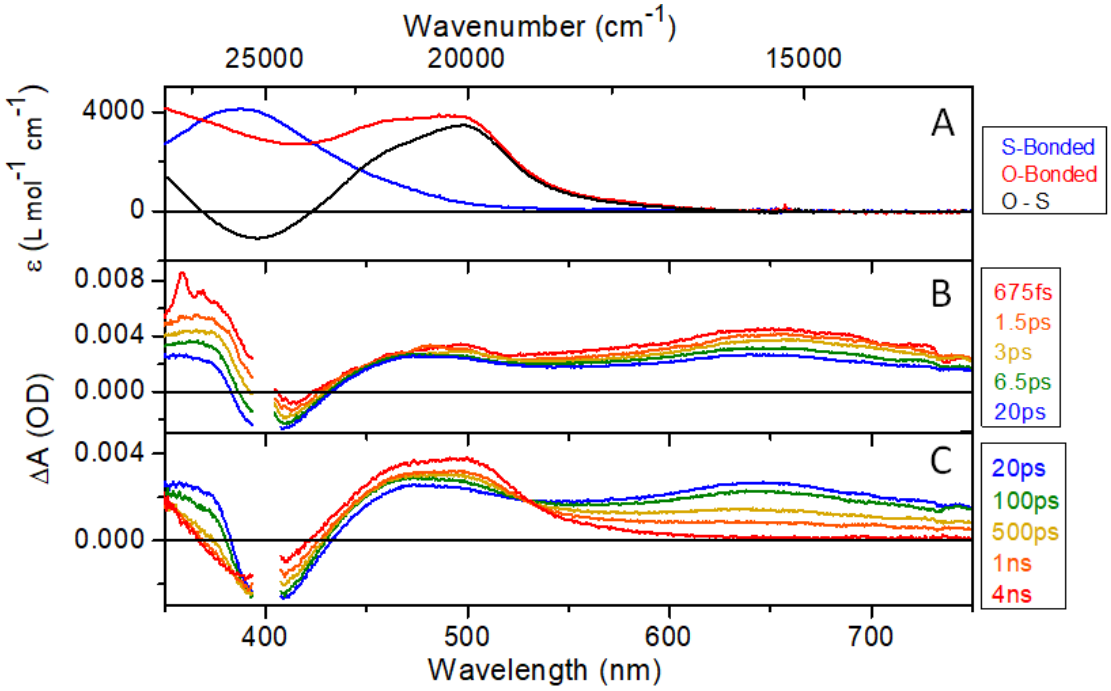

Figure 182: *Spectra of RuOTE3 in Acetonitrile*

(A) Spectra obtained from bulk photolysis (λ_{exc} 405 nm) of RuOTE3 in acetonitrile solution. Blue trace is the S-isomer, red trace is the O-isomer, and black trace is the difference spectrum (O-isomer minus S-isomer) extracted from the data. (B) Time-resolved spectra of RuOTE3 at short time-delays between 675 fs and 20 ps. (C) Time-resolved spectra of RuOTE3 at long time-delays between 20ps and 4ns.

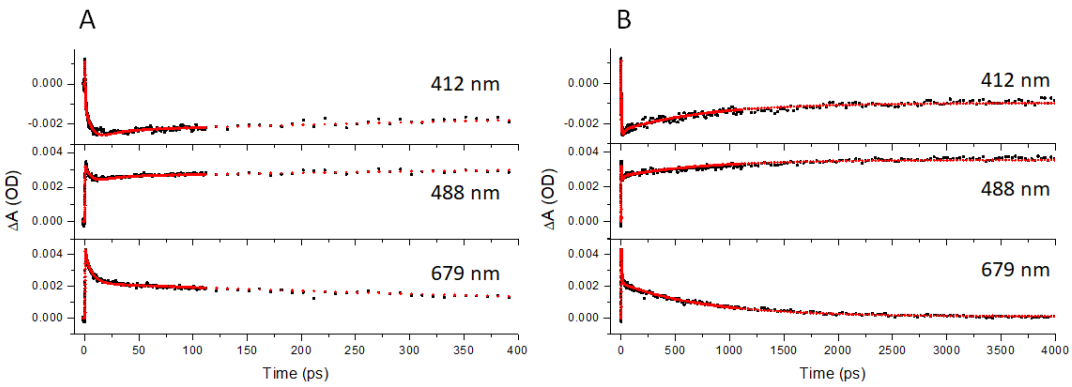

Figure 183: *Transient Absorption Kinetics of RuOTE3 in Acetonitrile*

(A) Single wavelength kinetics fits out to 400 ps time delay of RuOTE3 in acetonitrile solution applied to single-wavelength kinetics at 412 nm, 488 nm, and 679 nm. (B) Single wavelength kinetic fits out to 4000 ps time delays. Raw data is black and the kinetic fit is red. A triexponential fit yields good results with $\tau 1 = 0.4 \pm 0.1$ *ps,* $\tau 2 = 6.6 \pm 0.4$ *ps, and* $\tau 3 = 779.3 \pm 25.0$ *ps. A fourth kinetic component,* $\tau 4 = 13.3 \pm 4.4$ *ps, was required to optimally fit around the ground state bleach near 400 nm and the O-bonded absorption around 500 nm.*

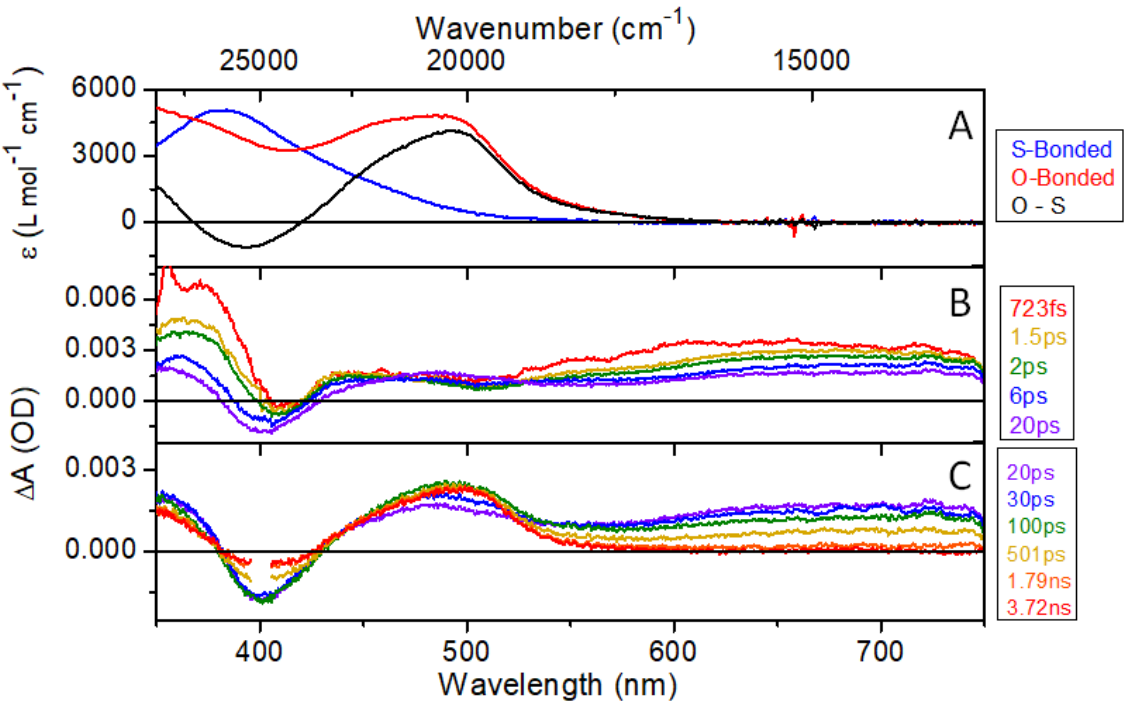

Figure 184: *RuOTE4 in Propylene Carbonate*

(A) Spectra obtained from bulk photolysis (λ_{exc} 405 nm) of RuOTE4 in propylene carbonate solution. Blue trace is the S-isomer, red trace is the O-isomer, and black trace is the difference spectrum (O-isomer minus S-isomer) extracted from the data. (B) Time-resolved spectra of RuOTE4 at short time-delays between 723 fs and 20 ps. (C) Time-resolved spectra of RuOTE4 at long time-delays between 20ps and 3.72ns.

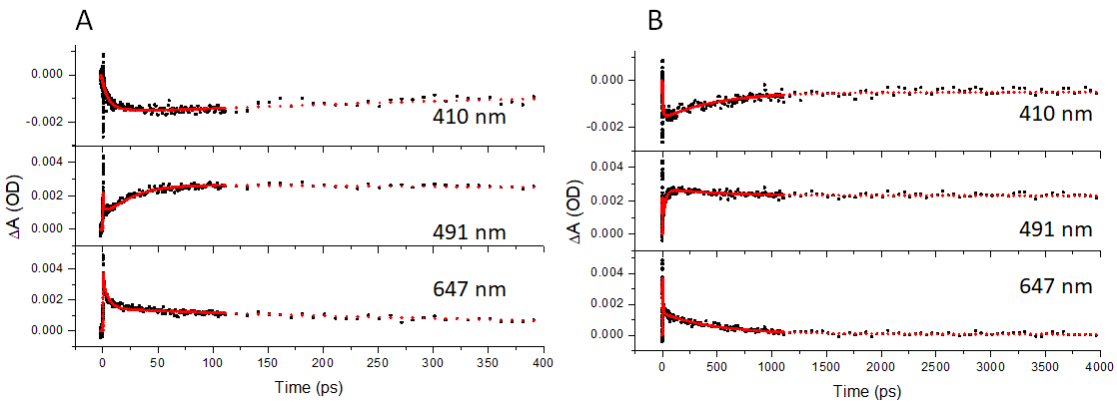

Figure 185: *Transient Absorption Kinetics of RuOTE4 in Propylene Carbonate*

(A) Single wavelength kinetics fits out to 400 ps time delays of RuOTE4 in propylene carbonate applied to single-wavelength kinetics at 410 nm, 491 nm, and 647 nm. (B) Single wavelength kinetic fits out to 4000 ps time delays. Raw data is black and the kinetic fit is red. A triexponential fit yields good results with $\tau 1 = 0.2 \pm 0.1$ *ps,* $\tau 2 = 5.4 \pm 1.2$ *ps, and* $\tau 3 = 490.3 \pm 78.2$ *ps. A fourth kinetic component,* $\tau 4 = 25.2 \pm 8.8$ *ps, was required to optimally fit around the ground state bleach near 400 nm and the O-bonded absorption around 500 nm.*

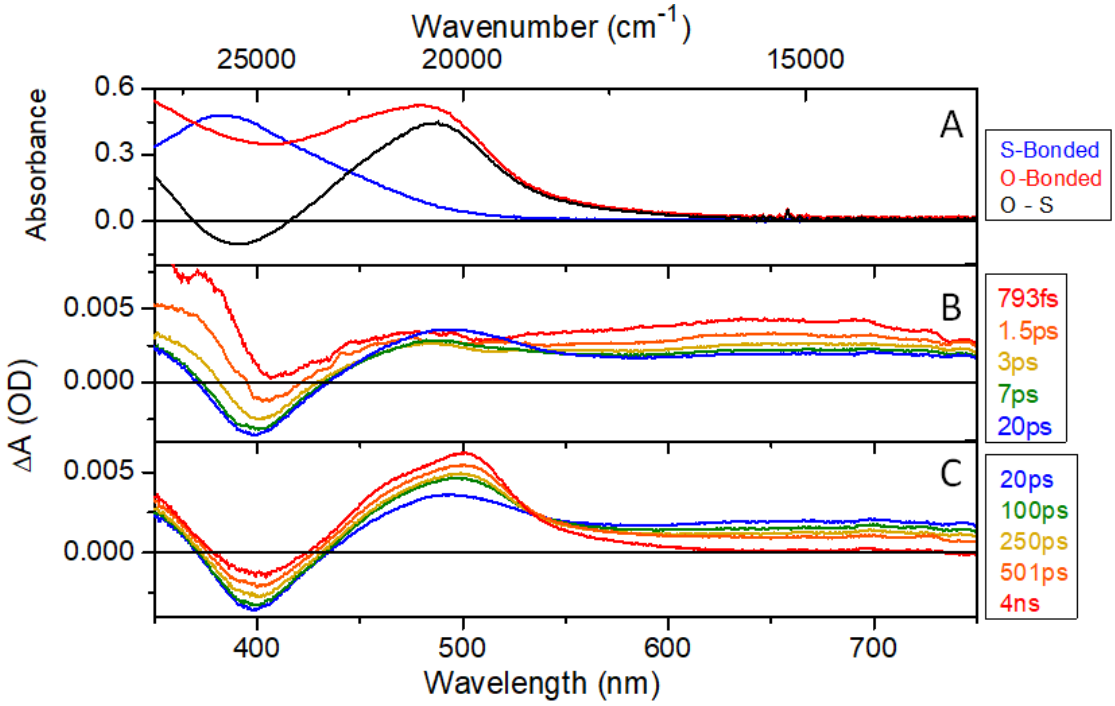

Figure 186: *RuOTE4 in DCE*

(A) Spectra obtained from bulk photolysis (λ_{exc} 405 nm) of RuOTE4 in dichloroethane solution. Blue trace is the S-isomer, red trace is the O-isomer, and black trace is the difference spectrum (O-isomer minus S-isomer) extracted from the data. (B) Time-resolved spectra of RuOTE4 at short time-delays between 793 fs and 20 ps. (C) Time-resolved spectra of RuOTE4 at long time-delays between 20ps and 4ns.

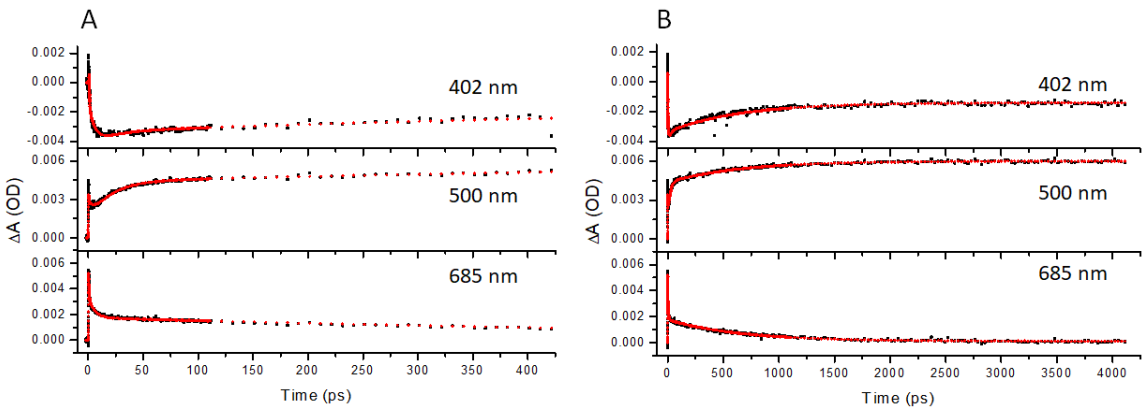

Figure 187: *Transient Absorption Kinetics of RuOTE4 in DCE*

(A) Single wavelength kinetics fits out to 425 ps time delays of RuOTE4 in dichloroethane solution applied to single-wavelength kinetics at 402 nm, 500 nm, and 685 nm. (B) Single wavelength kinetic fits out to 4250 ps time delays. Raw data is black and the kinetic fit is red. A triexponential fit yields good results with $\tau 1 = 0.3 \pm 0.1$ *ps,* $\tau 2 = 5.6 \pm 1.0$ *ps, and* $\tau 3 = 648.9 \pm 67.8$ *ps. A fourth kinetic component,* $\tau 4 = 18.1 \pm 3.9$ *ps, was required to optimally fit around the ground state bleach near 400 nm and the O-bonded absorption around 500 nm.*

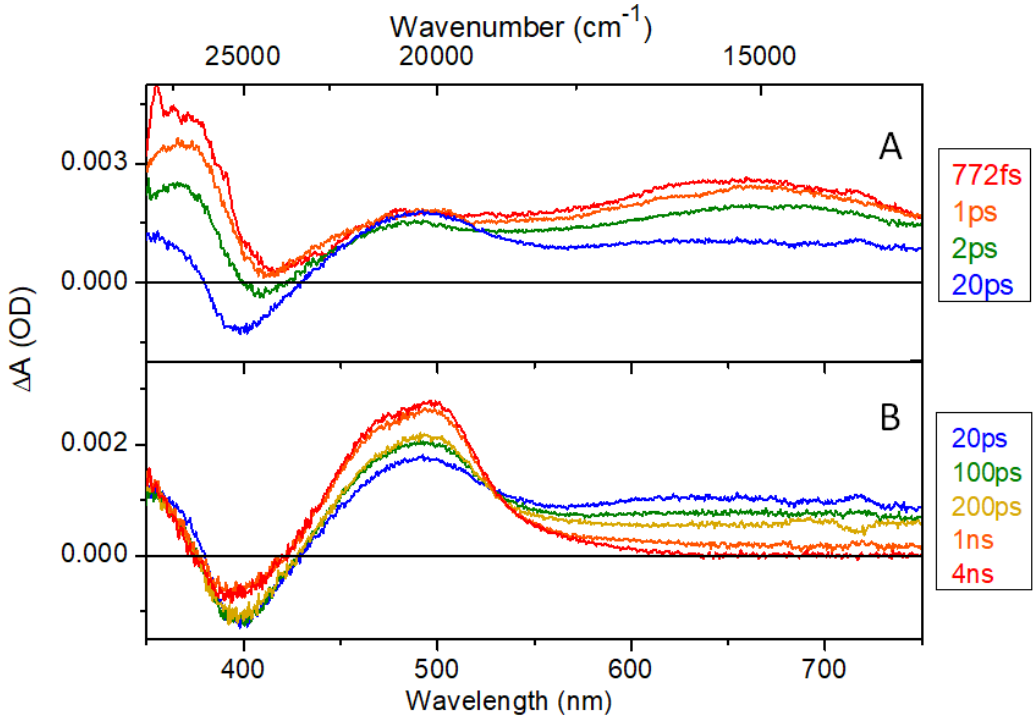

Figure 188: *RuOTE4 in Acetonitrile*

(A) Time-resolved spectra of RuOTE4 in acetonitrile solution at short time-delays between 772 fs and 20 ps. (B) Time-resolved spectra of RuOTE4 at long time-delays between 20ps and 4ns.

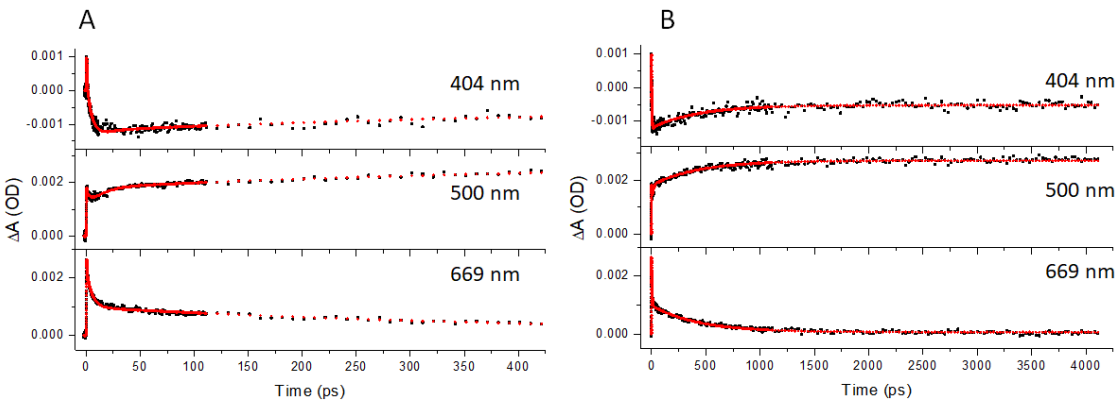

Figure 189: *Transient Absorption Kinetics of RuOTE4 in Acetonitrile*

(A) Single wavelength kinetics fits out to 425 ps time delays of RuOTE4 in acetonitrile solution applied to single-wavelength kinetics at 404 nm, 500 nm, and 669 nm. (B) Single wavelength kinetic fits out to 4250 ps time delays. Raw data is black and the kinetic fit is red. A triexponential fit yields good results with $\tau 1 = 0.4 \pm 0.1$ *ps,* $\tau 2 = 5.2 \pm 0.5$ *ps, and* $\tau 3 = 431.7 \pm 33.0$ *ps. A fourth kinetic component,* $\tau 4 = 10.8 \pm 3.3$ *ps, was required to optimally fit around the ground state bleach near 400 nm and the O-bonded absorption around 500 nm.*

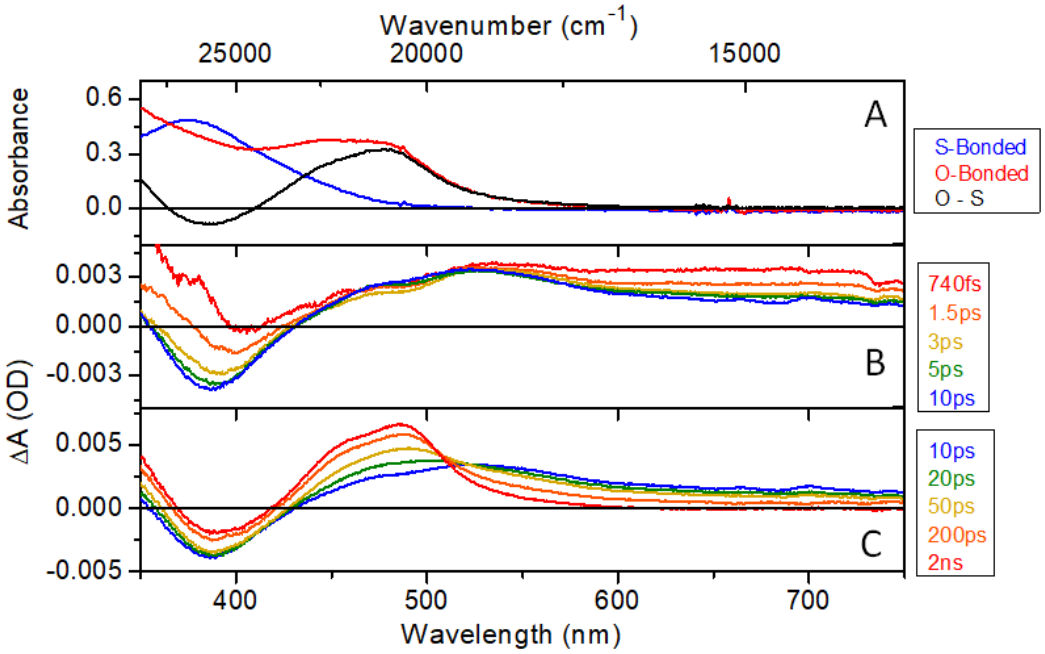

Figure 190: *RuOTE9 in DCE*

(A) Spectra obtained from bulk photolysis (λ_{exc} 405 nm) of RuOTE9 in dichloroethane solution. Blue trace is the S-isomer, red trace is the O-isomer, and black trace is the difference spectrum (O-isomer minus S-isomer) extracted from the data. (B) Time-resolved spectra of RuOTE9 at short time-delays between 740 fs and 10 ps. (C) Time-resolved spectra of RuOTE9 at long time-delays between 10ps and 2ns.

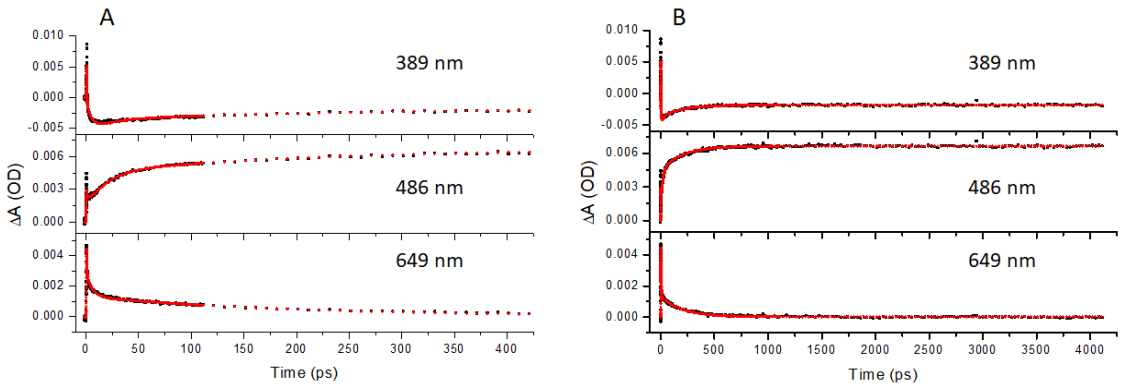

Figure 191: *Transient Absorption Kinetics of RuOTE9 in DCE*

(A) Single wavelength kinetics fits out to 425 ps time delays of RuOTE9 in dichloroethane solution applied to single-wavelength kinetics at 380 nm, 483 nm, and 649 nm. (B) Single wavelength kinetic fits out to 4250 ps time delays. Raw data is black and the kinetic fit is red. A triexponential fit yields good results with $\tau 1 = 0.2 \pm 0.1$ *ps,* $\tau 2 = 5.5 \pm 1.2$ *ps, and* $\tau 3 = 197.6 \pm 26.0$ *ps. A fourth kinetic component,* $\tau 4 = 16.5 \pm 4.0$ *ps, was required to optimally fit around the ground state bleach near 400 nm and the O-bonded absorption around 500 nm.*

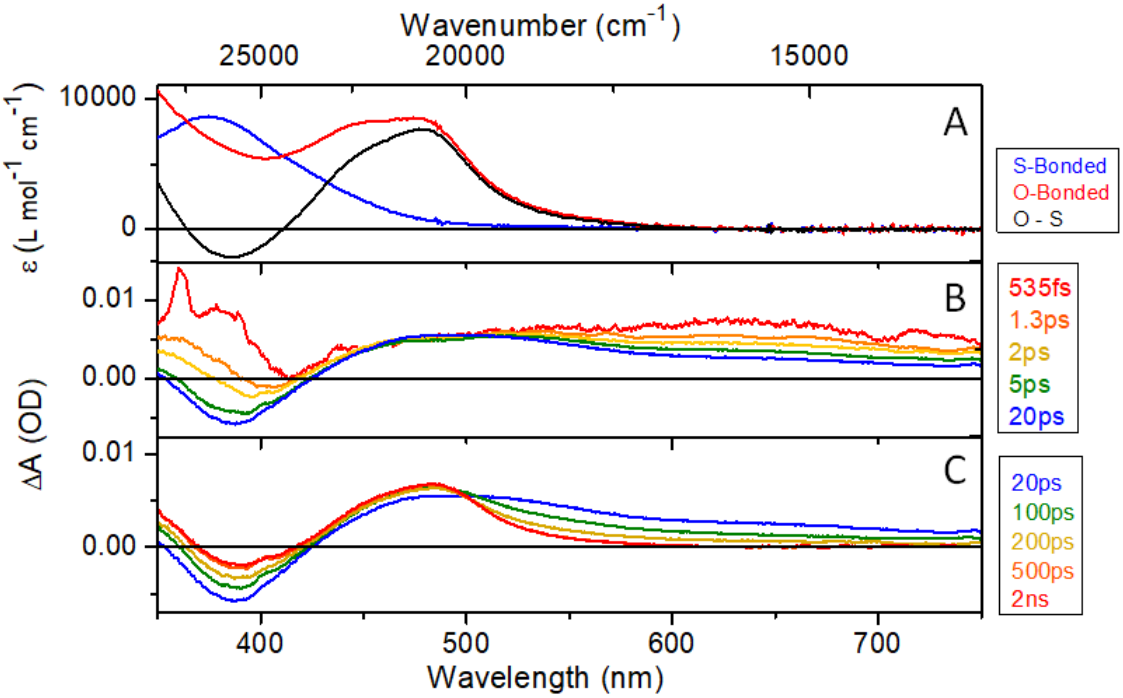

Figure 192: *RuOTE9 in Propylene Carbonate*

(A) Spectra obtained from bulk photolysis (λ_{exc} 405 nm) of RuOTE9 in propylene carbonate solution. Blue trace is the S-isomer, red trace is the O-isomer, and black trace is the difference spectrum (O-isomer minus S-isomer) extracted from the data. (B) Time-resolved spectra of RuOTE9 at short time-delays between 535 fs and 20 ps. (C) Time-resolved spectra of RuOTE9 at long time-delays between 20ps and 2ns.

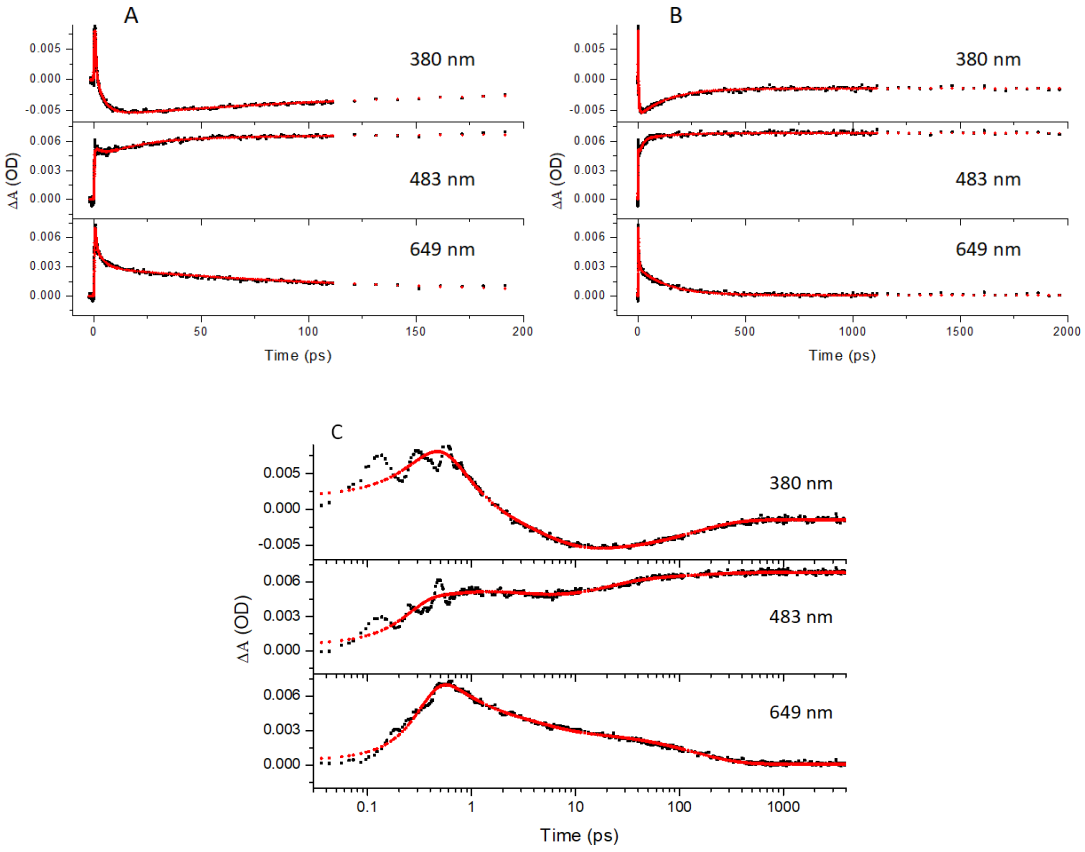

Figure 193: *Transient Absorption Kinetics of RuOTE9 in Propylene Carbonate*

(A) Single wavelength kinetics fits out to 200 ps time delays of RuOTE9 in propylene carbonate solution applied to single-wavelength kinetics at 380 nm, 483 nm, and 649 nm. (B) Single wavelength kinetic fits out to 2000 ps time delays. (C) Single wavelength kinetic fits out to 4000 ps time delays with logarithmic scaling on the x-axis. Raw data is black and the kinetic fit is red. A triexponential fit yields good results with $\tau 1 = 0.6 \pm 0.1$ *ps,* $\tau 2 = 3.9 \pm 1.3$ *ps, and* $\tau 3 = 137.2 \pm 12.5$ *ps. A fourth kinetic component,* $\tau 4 = 16.43 \pm 4.3$ *ps, was required to optimally fit around the ground state bleach near 400 nm and the O-bonded absorption around 500 nm.*

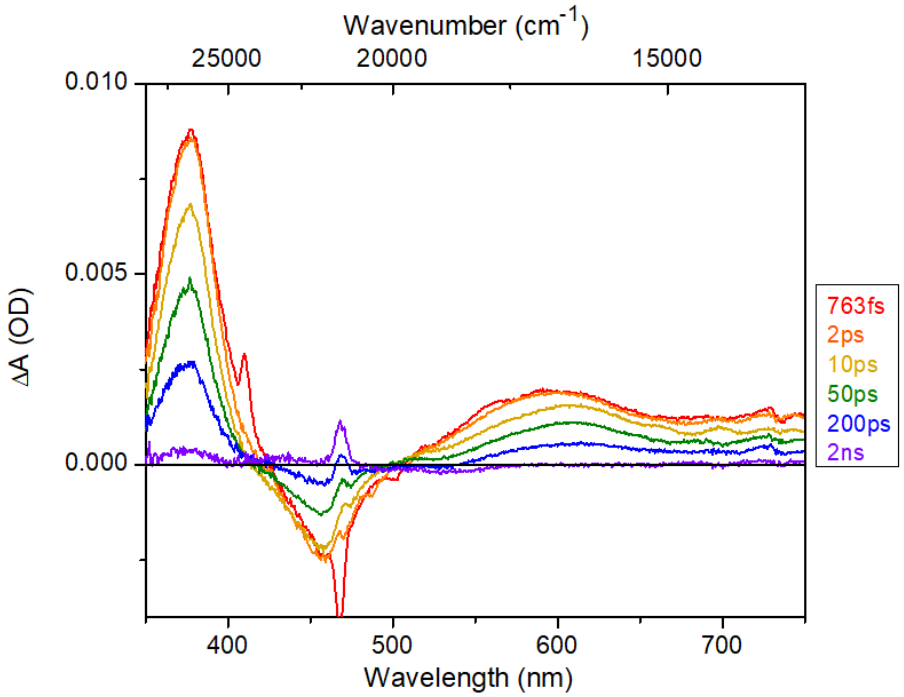

Figure 194: *RuTE3 in DCE*

Time-resolved spectra (λ_{exc} 465 nm) of RuTE3 in dichloroethane solution at time-delays between 763 fs and 2 ns.

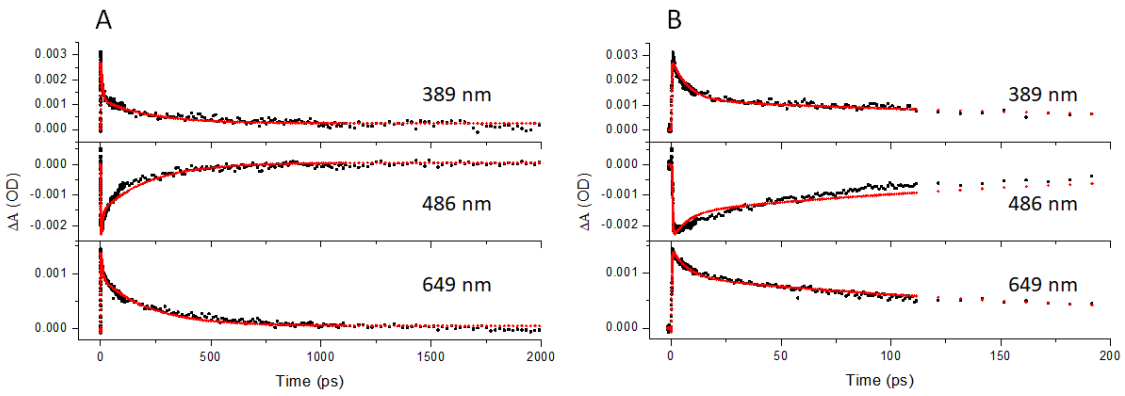

Figure 195: *Transient Absorption Kinetics of RuTE3 in DCE*

(A) Single wavelength kinetics fits of RuTE3 in dichloroethane solution applied to single-wavelength kinetics at 389 nm, 486 nm, and 649 nm out to 2000 ps time delays. (B) Single wavelength kinetic fits out to 200 ps time delays. Raw data is black and the kinetic fit is red. A triexponential fit yields good results with $\tau 1 = 0.2 \pm 0.1$ *ps,* $\tau 2 = 7.2 \pm 2.9$ *ps, and* $\tau 3 = 219.3 \pm 46.9$ *ps.*

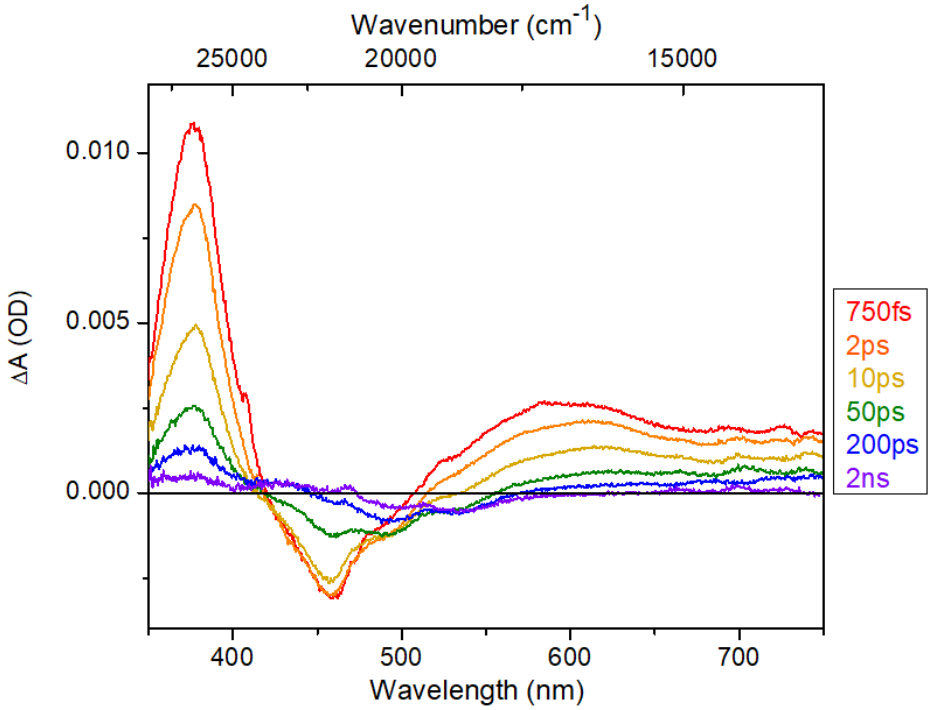

Figure 196: *RuTE4 in DCE*

Time-resolved spectra (λ_{exc} 460 nm) of RuTE4 in dichloroethane solution at time-delays between 750 fs and 2 ns.

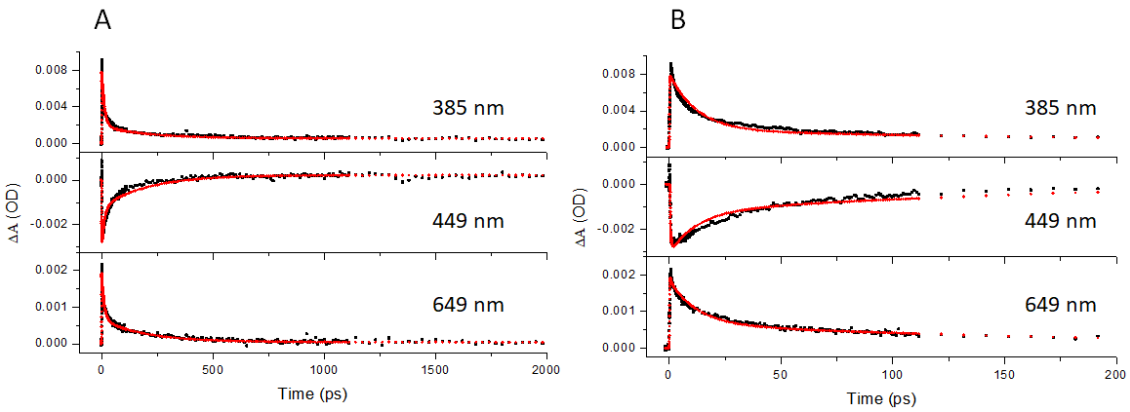

Figure 197: *Transient Absorption Kinetics of RuTE4 in DCE*

(A) Single wavelength kinetics fits of RuTE4 in dichloroethane solution applied to single-wavelength kinetics at 385 nm, 449 nm, and 649 nm out to 2000 ps time delays. (B) Single wavelength kinetic fits out to 200 ps time delay. Raw data is black and the kinetic fit is red. A triexponential fit yields good results with $\tau 1 = 0.5 \pm 0.1$ *ps,* $\tau 2 = 12.3 \pm 1.2$ *ps, and* $\tau 3 = 203.4 \pm 27.5$ *ps.*

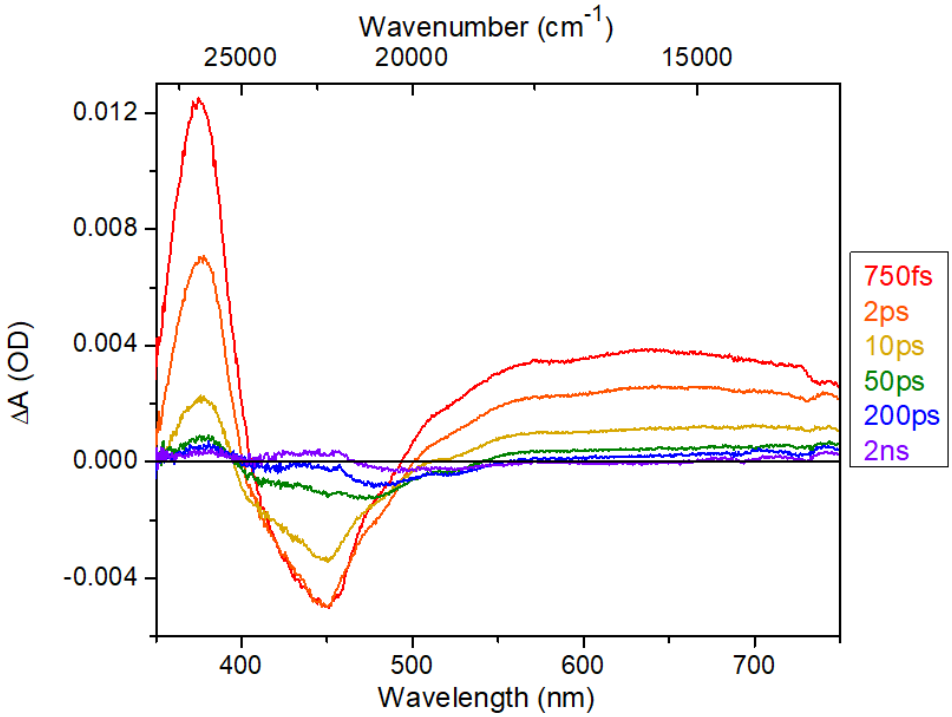

Figure 198: *RuTE9 in DCE*

Time-resolved spectra (λ_{exc} 455 nm) of RuTE9 in dichloroethane solution at time-delays between 750 fs and 2 ns.

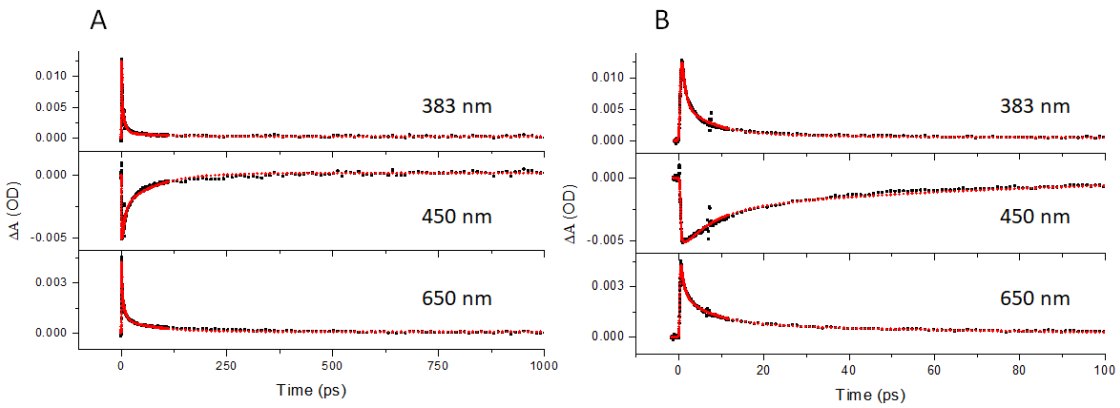

Figure 199: *Transient Absorption Kinetics of RuTE9 in DCE*

(A) Single wavelength kinetics fits of RuTE9 in dichloroethane solution applied to single-wavelength kinetics at 383 nm, 450 nm, and 650 nm out to 1000 ps time delay. (B) Single wavelength kinetic fits out to 100 ps time delays. Raw data is black and the kinetic fit is red. A triexponential fit yields good results with $\tau 1 = 0.8 \pm 0.1$ *ps,* $\tau 2 = 7.2 \pm 1.6$ *ps, and* $\tau 3 = 78.7 \pm 20.9$ *ps.*

***Table 28**: Transient Absorption Lifetimes of RuTE and RuOTE Complexes (Global Fitting Analysis).*

Complex	Solvent	τ1 (ps)	τ2 (ps)	τ3 (ps)	τ4 (ps)
RuTE3	DCE	0.21 ± 0.08	7.18 ± 2.95	219.3 ± 46.9	-
RuTE4	DCE	0.46 ± 0.10	12.31 ± 1.23	203.4 ± 27.5	-
RuTE9	DCE	0.82 ± 0.14	7.23 ± 1.57	78.7 ± 20.9	-
RuOTE3	MeCN	0.37 ± 0.10	6.55 ± 0.39	779.3 ± 25.0	13.27 ± 4.36
RuOTE4	MeCN	0.35 ± 0.07	5.15 ± 0.48	431.7 ± 33.0	10.83 ± 3.32
	DCE	0.31 ± 0.07	5.55 ± 0.97	648.9 ± 67.8	18.05 ± 3.87
	PC	0.20 ± 0.13	5.36 ± 1.21	490.3 ± 78.2	25.18 ± 8.84
RuOTE9	DCE	0.20 ± 0.05	5.54 ± 1.15	197.6 ± 26.0	16.48 ± 3.98
	PC	0.55 ± 0.12	3.85 ± 1.26	137.2 ± 12.5	16.43 ± 4.25

Table 29: *Transient Absorption Lifetimes of RuOTE Complexes (Single Wavelength Kinetics).*

Complex/ Solvent	λ/nm	A1	t1/ps	A2	t2/ps	A3	t3/ps	A4	t4/ps
RuOTE3/ CH3CN	412	0.0023 ± 0.00024	0.46 ± 0.11	0.0021 ± 0.00023	5.5 ± 4.2	-0.00080 ± 0.0024	14.79 ± 23.1	-0.00080 ± 0.0024	779.0 ± 92.7
	488	-0.016 ± 0.0320	0.14 ± 0.05	0.0014 ± 0.00010	4.98 ± 2.70	-0.00062 ± 0.00099	16.00 ± 17.10	-0.00094 ± 0.000049	796.2 ± 111.0
	679	-0.0099 ± 0.0083	0.17 ± 0.04	0.0012 ± 0.00026	2.83 ± 1.09	-	-	-0.00097 ± 0.00005	800.8 ± 104
RuOTE4/ CH3CN	404	-0.00057 ± 0.0023	0.12 ± 0.27	0.0021 ± 0.00023	2.00 ± 0.39	0.0004 ± 0.00025	12.21 ± 11.40	-0.0007 ± 0.00004	433 ± 65.1
	500	-0.0057 ± 1.8	0.15 ± 0.13	0.00080 ± 0.025	1.55 ± 0.60	-0.00054 ± 0.0015	17.26 ± 5.78	-0.00091 ± 0.0001	430.9 ± 40.1
	669	0.00093 ± 0.00017	0.55 ± 0.17	0.0013 ± 0.00009	5.11 ± 0.44	-	-	0.00093 ± 0.000018	430.2 ± 25.8
RuOTE4/ DCE	402	0.0028 ± 0.00051	0.40 ± 0.15	0.0026 ± 0.0013	4.50 ± 3.05	-0.0007 ± 0.0015	18.22 ± 32.20	-0.0020 ± 0.00002	652.4 ± 92.9
	500	0.0017 ± 0.00094	0.38 ± 0.33	0.0013 ± 0.0005	3.50 ± 3.05	-0.0028 ± 0.00063	19.66 ± 4.98	-0.0017 ± 0.00094	652.7 ± 88.5
	685	0.0035 ± 0.0002	0.51 ± 0.05	0.0012 ± 0.00011	7.13 ± 0.92	-	-	0.0017 ± 0.000033	655.3 ± 38.8
RuOTE4/ PC	410	-0.00056 ± 0.00064	0.28 ± 0.08	0.0010 ± 0.00085	2.74± 3.96	0.00079 ± 0.00099	15.12 ± 23.11	-0.0011 ± 0.00015	519.3 ± 17.0
	491	0.011± 0.016	0.10 ± 0.05	0.00063 ± 0.00046	3.35 ± 4.30	-0.0021 ± 0.00047	23.46 ± 8.63	0.00034 ± 0.00016	514.4 ± 43.3
	647	0.00073 ± 0.00032	0.5 ± 0.49	0.0017 ± 0.00035	3.68 ± 0.82	-	-	0.0015 ± 0.000054	384.8 ± 42.3
RuOTE9/ DCE	389	0.013 ± 0.0027	0.39 ± 0.15	0.0036 ± 0.0016	3.18 ± 2.85	-0.00047 ± 0.00018	15.85 ± 7.61	-0.0021 ± 0.00046	202.8 ± 80.4
	486	-0.0018 ± 0.0018	0.13 ± 0.10	0.0015 ± 0.00064	3.00 ± 1.84	-0.0033 ± 0.00062	17.40 ± 5.38	-0.0028 ± 0.00026	203.9 ± 41.1
	649	0.0038 ± 0.0011	0.30 ± 0.08	0.0015 ± 0.00014	4.77 ± 0.76	-	-	0.0014 ± 0.000059	200.1 ± 23.3
RuOTE9/ PC	380	0.013 ± 0.0028	0.88 ± 0.27	0.0060 ± 0.0027	4.69 ± 5.04	-0.00014 ± 0.0003	22.89 ± 76.2	-0.0044 ± 0.0014	165.4 ± 56.7
	483	-0.0080 ± 0.0024	0.30 ± 0.07	0.0027 ± 0.0024	2.00 ± 2.02	-0.0018 ± 0.00053	21.9 ± 11.10	-0.00095 ± 0.00011	134.2 ± 16.0
	649	0.0037 ± 0.00039	0.80 ± 0.18	0.0018 ± 0.00039	5.83 ± 1.76	-	-	0.0028 ± 0.00014	134.2 ± 134.

X-ray Crystallography:

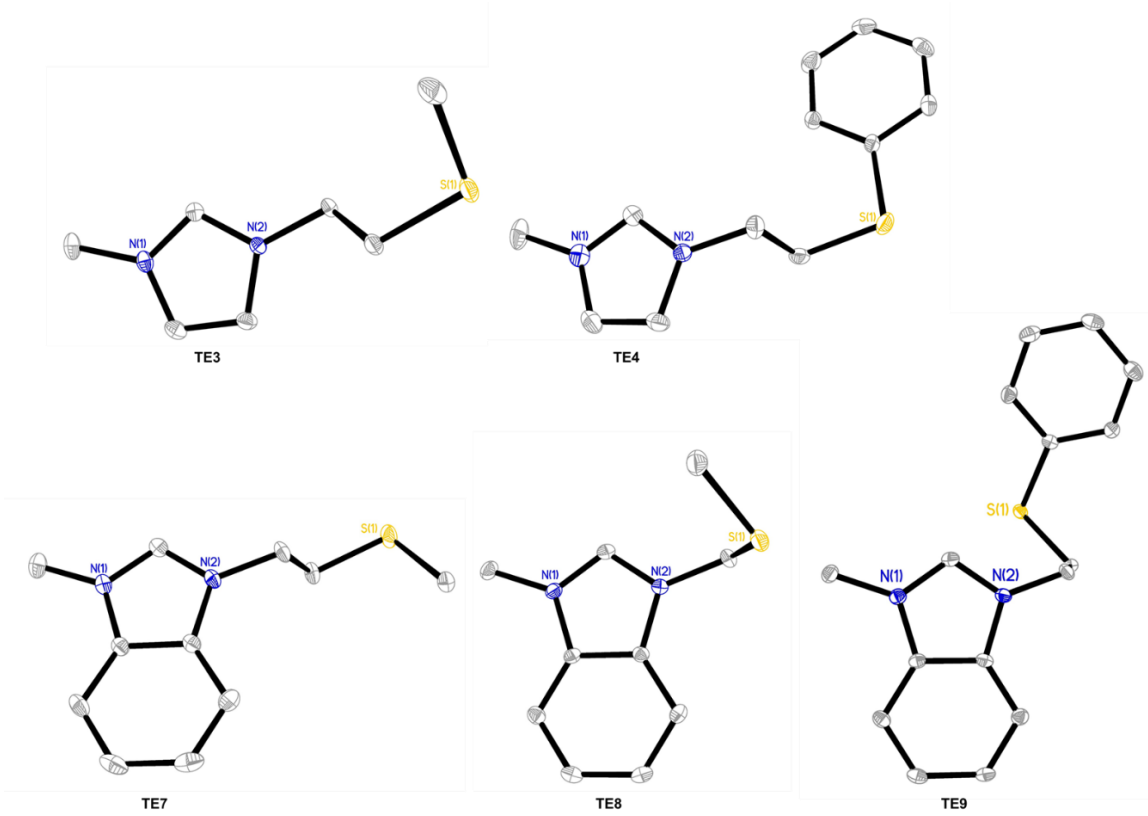

Figure 200. *X-ray structures of TE3, TE4, and TE7-TE9 with 35% thermal ellipsoids. Hydrogen atoms and anions have been omitted for clarity.*

Table 30: *X-ray crystal data and structure parameters for compounds RuOTE3, RuOTE4, RuOTE9, and RuOTE10.*

Compound	RuOTE3	RuOTE4	RuOTE9	RuOTE10
Empirical formula	$C_{75}H_{68}B_2N_6ORuS$	$C_{32}H_{30}F_{12}N_6OP_2RuS$	$C_{38}H_{35}F_{12}N_7OP_2RuS$	$C_{31}H_{28}F_{12}N_6OP_2RuS$
Formula weight	1224.10	937.69	1028.80	923.66
Crystal system	Triclinic	Monoclinic	Triclinic	Monoclinic
Space group	P-1	$P2_1/c$	P-1	$P2_1/c$
a/ Å	13.9048(5)	20.9909(14)	8.2877(3)	21.2650(12)
b/ Å	14.1940(6)	10.1463(7)	12.3028(4)	9.9691(6)
c/ Å	17.8329(7)	16.8080(12)	20.6751(7)	16.4028(10)
α(°)	95.003(2)	90	84.676(2)	90
β(°)	94.289(2)	103.000(2)	82.568(2)	102.0340(10)
γ(°)	118.912(2)	90	72.563(2)	90
Volume ($Å^3$)	3041.4(2)	3488.0(4)	1991.05(12)	3400.9(3)
Z	2	4	2	4
Dc (Mg/m^3)	1.337	1.789	1.716	1.804
μ (mm^{-1})	0.345	0.705	0.627	0.721
F(000)	1276	1880	1036	1848
reflns collected	43993	27060	33915	25345
indep. reflns	10952	6280	10036	6006
GOF on F^2	1.037	1.051	1.063	1.020
R1 (on F_o^2, I > 2σ(I))	0.0499	0.0471	0.0351	0.0438
wR2 (on F_o^2, I > 2σ(I))	0.1219	0.0928	0.0702	0.1079
R1 (all data)	0.0619	0.0727	0.0476	0.0553
wR2 (all data)	0.1290	0.1049	0.0746	0.1168

Table 31: *X-ray crystal data and structure parameters for compounds RuTE4, RuTE7, RuTE9, and RuTE10.*

Compound	RuTE4	RuTE7	RuTE9	RuTE10
Empirical formula	$C_{32}H_{30}F_{12}N_6P_2RuS$	$C_{31}H_{30}F_{12}N_6P_2RuS$	$C_{39}H_{39}F_{12}N_7OP_2RuS$	$C_{31}H28F_{12}N_6P_2RuS$
Formula weight	921.69	909.68	1044.84	907.66
Crystal system	Monoclinic	Triclinic	Monoclinic	Monoclinic
Space group	$P2_1/c$	P-1	$P2_1/c$	$P2_1/c$
a/ Å	21.3764(18)	10.9439(8)	20.2475(19)	21.6137(5)
b/ Å	11.6246(10)	11.6391(9)	14.5098(13)	11.6808(3)
c/ Å	14.8063(12)	15.9753(12)	14.7327(14)	14.0949(3)
α(°)	90	74.462(3)	90	90
β(°)	107.194(3)	72.181(3)	110.843(5)	105.2490(10)
γ(°)	90	84.659(3)	90	90
Volume ($Å^3$)	3514.8(5)	1866.3(2)	4045.0(7)	3433.19(14)
Z	4	2	4	4
Dc (Mg/m^3)	1.742	1.619	1.716	1.756
μ (mm^{-1})	0.696	0.654	0.618	0.711
F(000)	1848	912	2112	1816
reflns collected	64779	23841	71679	32957
indep. reflns	8826	9518	10119	8675
GOF on F^2	1.053	1.022	1.021	1.081
R1 (on F_o^2, $I > 2\sigma(I)$)	0.0348	0.0749	0.0293	0.0456
wR2 (on F_o^2, $I > 2\sigma(I)$)	0.0779	0.2019	0.0709	0.1063
R1 (all data)	0.0477	0.0961	0.0369	0.0613
wR2 (all data)	0.0836	0.2187	0.0754	0.1143

Table 32: *X-ray crystal data and structure parameters for compounds TE3, TE4, and TE7-TE9.*

Compound	TE3	TE4	TE7	TE8	TE9
Empirical formula	$C_7H_{13}F_6N_2PS$	$C_{12}H_{15}F_6N_2PS$	$C_{11}H_{15}F_6N_2PS$	$C_{10}H_{13}F_6N_2PS$	$C_{16}H_{17}F_6N_2PS$
Formula weight	302.22	364.29	352.28	338.25	414.34
Crystal system	Monoclinic	Monoclinic	Monoclinic	Monoclinic	Triclinic
Space group	$P2_1/c$	$P2_1$	$P2_1/n$	$P2_1/n$	P-1
a/ Å	6.6717(3)	7.6189(10)	9.560(5)	7.599(5)	8.2545(4)
b/ Å	10.8505(5)	11.2617(15)	9.163(6)	19.463(15)	10.1527(5)
c/ Å	16.9455(7)	9.0685(13)	16.878(11)	9.584(7)	20.9013(11)
α(°)	90	90	90	90	88.728(3)
β(°)	97.874(2)	102.954(5)	95.21(2)	104.685(14)	83.354(3)
γ(°)	90	90	90	90	82.657(3)
Volume ($Å^3$)	1215.14(9)	758.29(18)	1472.3(15)	1371.3(17)	1725.55(15)
Z	4	2	4	4	4
Dc (Mg/m^3)	1.652	1.595	1.589	1.638	1.595
μ (mm^{-1})	0.454	0.379	0.387	0.412	0.344
F(000)	616	372	720	688	848
reflns collected	11870	6954	33414	29643	30252
indep. reflns	3050	3328	3666	3396	8452
GOF on F^2	1.067	1.007	1.003	1.047	1.083
R1 (on F_o^2, $I > 2\sigma(I)$)	0.0265	0.0507	0.0304	0.0340	0.0578
wR2 (on F_o^2, $I > 2\sigma(I)$)	0.0699	0.0828	0.0716	0.0822	0.1547
R1 (all data)	0.0300	0.0769	0.0406	0.0442	0.0705
wR2 (all data)	0.0717	0.0939	0.0744	0.0858	0.1653

Appendix B. Chapter 4 Supporting Information

Materials and Reagents

The reagents 1-bromopyrene, bis(4-methoxyphenyl)disulfide, and 4-(trifluoromethyl)thiophenol were obtained from Alfa Aesar. Diphenyl disulfide, 2.5 M *n*-Butyllithium solution in hexanes, and 3-chloroperoxybenzoic acid (mCPBA) 70%, were obtained from Sigma-Aldrich. The solvents used were reagent grade and used as received.

Synthesis

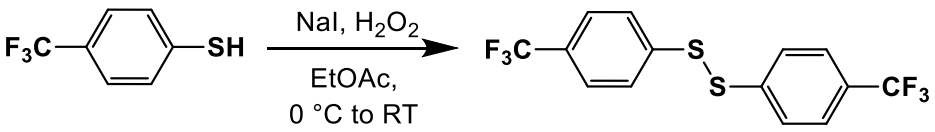

Scheme 12. *Synthetic scheme for bis(4-trifluoromethylphenyl)disulfide.*[187]

Bis(4-trifluoromethylphenyl)disulfide **(F_3CpS-$SpCF_3$)**

4-(trifluoromethyl)thiophenol (1.0 g, 5.6 mmol, 1.0 equiv.) dissolved in EtOAc (20 mL) at 0 °C was added sodium iodide (84 mg, 0.56 mmol, 0.1 equiv.) and hydrogen peroxide (0.6 mL, 30%, 5.6 mmol, 1.0 equiv.). The mixture was stirred at room temperature for 1 hour. Saturated aqueous sodium thiosulfate (20 mL) was added and extracted with EtOAc (20 mL x 3). The combined organic phases were washed with brine (20 mL) and dried with $MgSO_4$. The product was obtained in quantitative yield after concentration and drying. ^{1}H NMR (300MHz, RT, $CDCl_3$): δ (ppm) 7.55 – 7.61 (m, 8H).

Synthesis of Thioethers

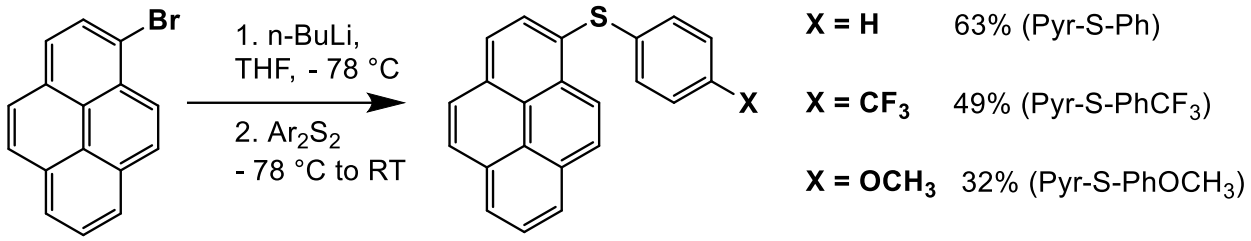

Scheme 13. *General synthetic scheme for the pyrene thioether compounds.*[188]

Phenyl 1-Pyrenyl Thioether **(PySPh)**

1-Bromopyrene (1.0 g, 3.55 mmol, 1.0 equiv.) in N_2(g) degassed anhydrous THF (40 mL) was lithiated slowly at – 78 °C with *n*-butyllithium (1.6 mL, 3.91 mmol, 1.1 equiv. of 2.5 M solution in hexanes). It was stirred for 30 min before slowly adding diphenyl disulfide (0.93 g, 4.27 mmol, 1.2 equiv.) dissolved in THF (10 mL). It was warmed gradually to RT for 1 h. Aqueous solution of NaCl (50 mL) was added and extracted with dichloromethane (50 mL x 3). It was dried using anhydrous $MgSO_4$, filtered and concentrated. The crude product was purified by precipitating and triturating using cold (– 78 °C) methanol. Yield 0.70 g, 63%. ^{1}H NMR (300MHz, RT, $CDCl_3$): δ (ppm) 8.65 (d, *J*=9.3 Hz, 1H), 8.01-8.23 (m, 8H), 7.14-7.25 (m, 5H). Mass Spec. for $[C_{22}H_{14}S]^+$ calculated *m/z* = 310.0816, observed *m/z* = 310.0820, 1.2 ppm difference.

(4-(Trifluoromethyl) Phenyl) 1-Pyrenyl Thioether (PySPhCF_3)

The compound was synthesized by following a similar procedure as **PySPh**. 1-Bromopyrene (0.5 g, 1.78 mmol, 1.0 equiv.), *n*-butyllithium (0.8 mL, 1.96 mmol, 1.1 equiv. of 2.5 M solution in hexanes). bis(4-trifluoromethylphenyl)disulfide (0.76 g, 2.14

mmol, 1.2 equiv.). Yield 0.184 g, 49%. ^{1}H NMR (300MHz, RT, $CDCl_3$): δ (ppm) 8.58 (d, *J*=9.0 Hz, 1H), 8.04-8.28 (m, 8H), 7.37 (d, *J* = 8.4 Hz, 2H), 7.08 (d, *J* = 8.1 Hz, 2H). Mass Spec. for $[C_{23}H_{13}F_3S]^+$ calculated *m/z* = 378.0690, observed *m/z* = 378.0685, 1.3 ppm difference.

(4-Methoxyphenyl) 1-Pyrenyl Thioether (PySPhOCH$_3$)

The compound was synthesized by following a similar procedure as **PySPh**. 1-Bromopyrene (1.0 g, 3.55 mmol, 1.0 equiv.), *n*-butyllithium (1.6 mL, 3.91 mmol, 1.1 equiv. of 2.5 M solution in hexanes). bis(4-methoxyphenyl)disulfide (1.19 g, 4.27 mmol, 1.2 equiv.). Yield 0.38 g, 32%. ^{1}H NMR (300MHz, RT, CDCl3): δ (ppm) 8.64 (d, *J* = 9.3 Hz, 1H), 8.17-8.21 (m, 2H), 8.13 (d, *J* = 9.3 Hz, 1H), 7.99-8.06 (m, 4H), 7.89 (d, *J* = 8.1 Hz, 1H), 7.34 (d, *J* = 8.7 Hz, 2H), 7.85 (d, *J* = 8.7 Hz, 2H), 3.79 (s, 3H). ^{19}F NMR (δ = -61.00 ppm), relative to (hexafluorobenzene, C_6F_6) (δ = -164.9 ppm) as an external standard. Mass Spec. for $[C_{23}H_{16}OS]^+$ calculated *m/z* = 340.0922, observed *m/z* = 340.0922, 0.0 ppm difference.

Synthesis of Sulfoxides [2]

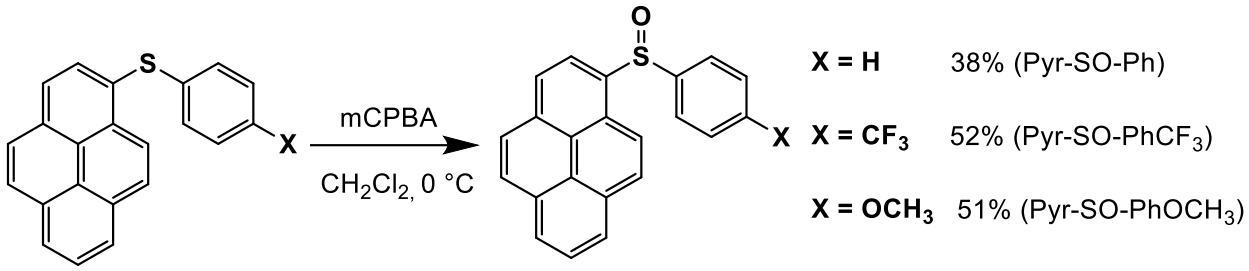

Scheme 14. *General synthetic scheme for the pyrene sulfoxide compounds.*

Phenyl 1-Pyrenyl Sulfoxide **(PySOPh)**

The compound **PySPh** (100 mg, 0.322 mmol) was dissolved in 20 mL of dichloromethane. In a separate 10 mL of dichloromethane, mCPBA 73 mg 70% peroxo reagent, 0.419 mmol) was dissolved and added slowly to the **PySPh** solution. The combined solutions were stirred at 0 °C for 1 hour. The solvent was removed by rotary evaporation. The crude product was purified by precipitating and triturating using cold (– 78 °C) DEE. Yield 40 mg, 38%. ^{1}H NMR (300MHz, RT, $CDCl_3$): δ (ppm) 8.58-8.63 (m, 2H), 8.07-8.32 (m, 7H), 7.70-7.72 (m, 2H), 7.36 (m, 3H). Mass Spec. for $[C_{22}H_{14}SO+H]^+$ calculated *m/z* = 327.0844, observed *m/z* = 327.0843, 0.2 ppm difference.

(4-(Trifluoromethyl) Phenyl) 1-Pyrenyl Sulfoxide (PySOPhCF_3)

The compound was synthesized by following a similar procedure as **PySOPh.** **PySPhCF_3** (100 mg, 0.264 mmol), mCPBA (59 mg 70% peroxo reagent, 0.382 mmol). The crude product was purified by precipitating and triturating using cold (– 78 °C) methanol. Yield 55 mg, 52%. ^{1}H NMR (300MHz, RT, $CDCl_3$): δ (ppm) 8.66 (d, *J* = 9.3 Hz, 1H), 8.49 (d, *J* = 8.1 Hz, 1H), 8.18-8.31 (m, 5H), 8.07-8.012 (m, 2H), 7.82 (d, *J* = 7.8 Hz,

2H), 7.62 (d, *J* = 8.1 Hz, 2H). ^{19}F NMR (δ = -61.56 ppm), relative to C_6F_6 (δ = -164.9 ppm) as an external standard. Mass Spec. for $[C_{22}H_{13}F_3SO+H]^+$ calculated *m/z* = 395.0717, observed *m/z* = 395.0713, 1.1 ppm difference.

(4-Methoxyphenyl) 1-Pyrenyl Sulfoxide (PySOPhOCH$_3$)

The compound was synthesized by following a similar procedure as **PySOPh.** **PySPhOCH$_3$** (100 mg, 0.294 mmol), mCPBA (66 mg 70% peroxo reagent, 0.382 mmol). The crude product was purified by precipitating and triturating using cold (– 78 °C) methanol. Yield 53 mg, 51%. ^1H NMR (300MHz, RT, $CDCl_3$): δ (ppm) 8.66 (d, *J* = 8.1 Hz, 1H), 8.45 (d, *J* = 9.3 Hz, 1H), 8.32 (d, *J* = 8.1 Hz, 1H), 8.21-8.25 (m, 2H), 8.13 (d, *J* = 9.3 Hz, 2H), 8.02-8.09 (m, 2H), 7.61 (d, *J* = 8.7 Hz, 2H), 6.85 (d, *J* = 8.4 Hz, 2H), 3.74 (s, 3H). Mass Spec. for $[C_{23}H_{16}OSO+H]^+$ calculated *m/z* = 357.0949, observed *m/z* = 357.0949, 0.1 ppm difference.

NMR Spectra.

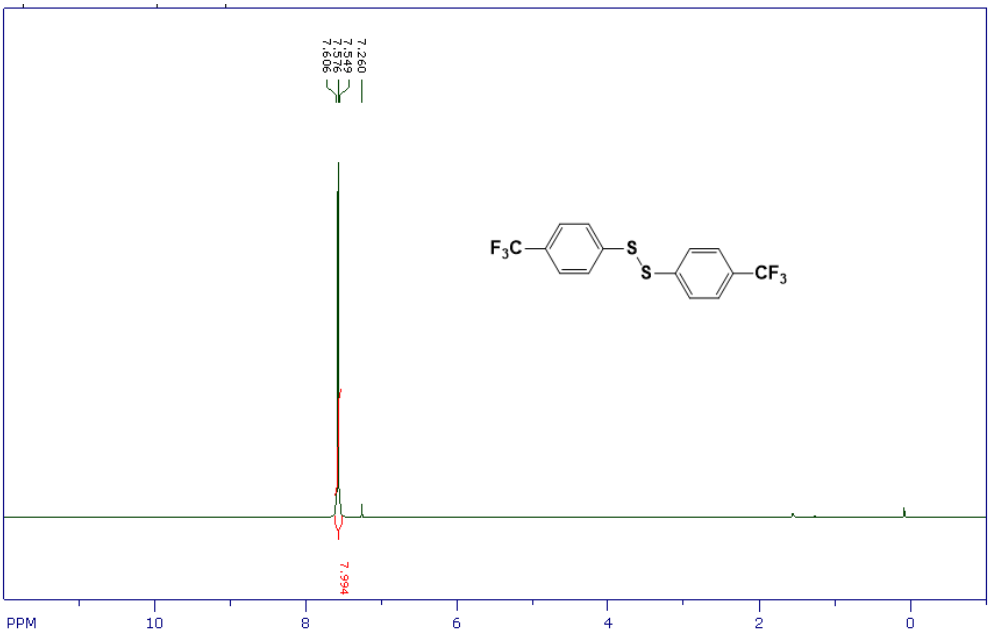

Figure 201. *^{1}H NMR of bis(4-trifluoromethylphenyl)disulfide.*

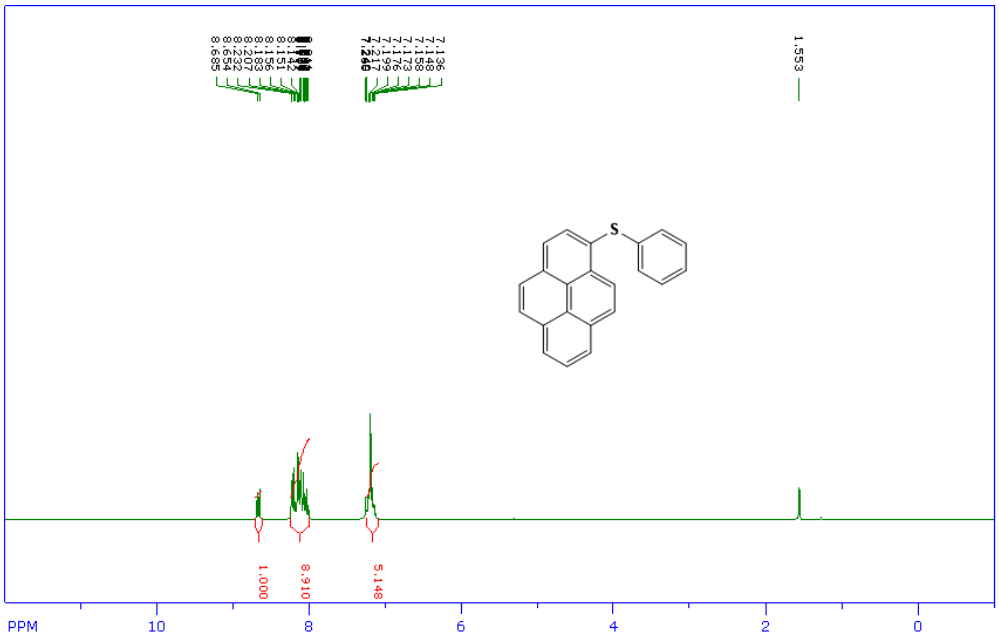

Figure 202. *^{1}H NMR of PySPhH*

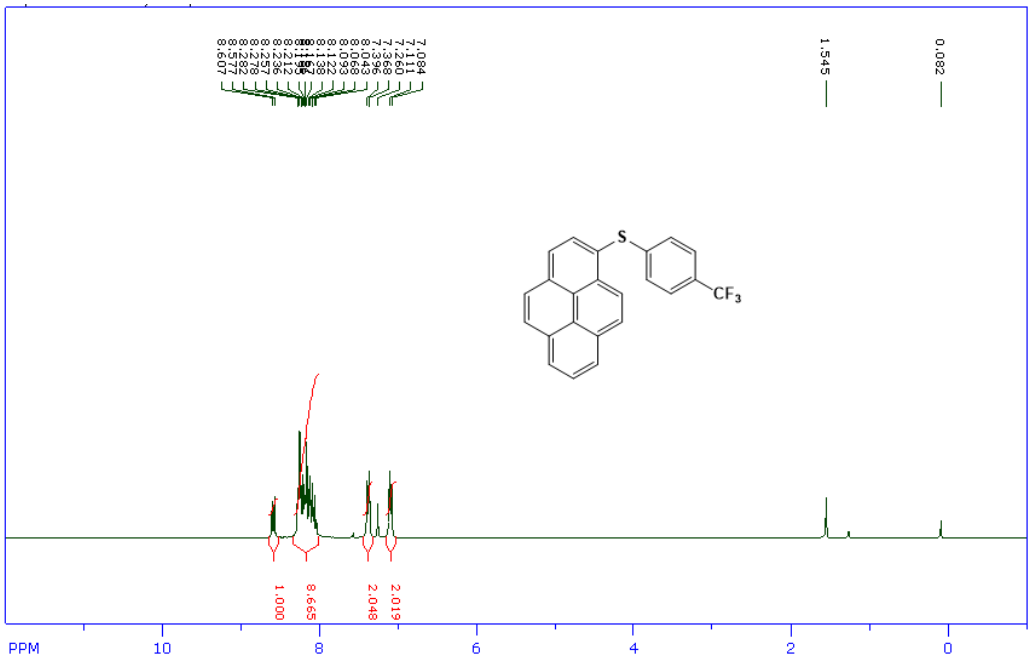

Figure 203. *^{1}H NMR of $PySPhCF_3$*

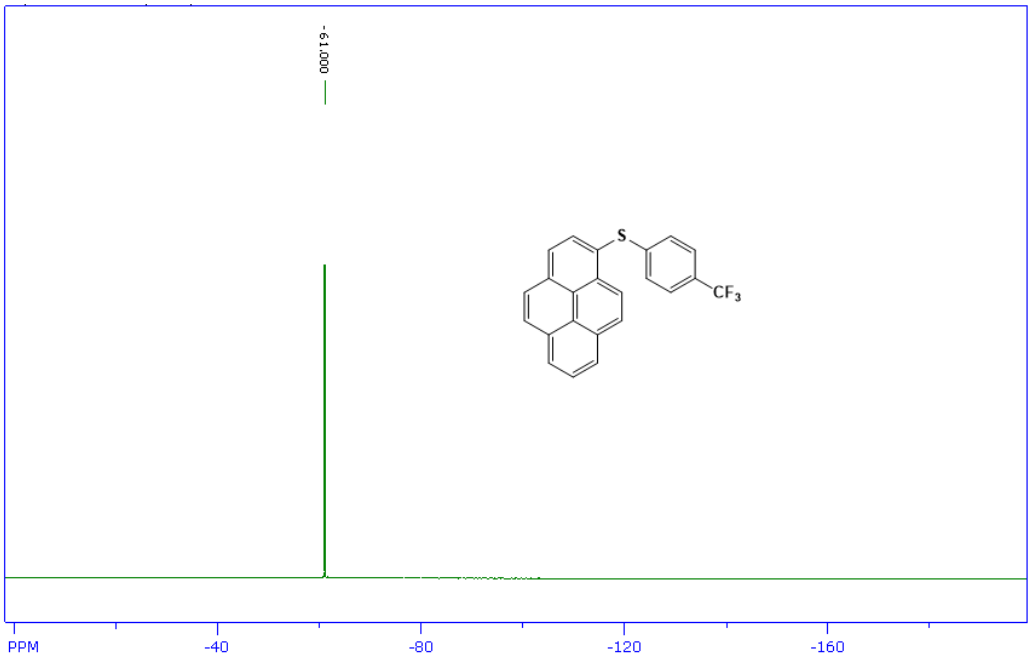

Figure 204. *^{19}F NMR of $PySPhCF_3$*

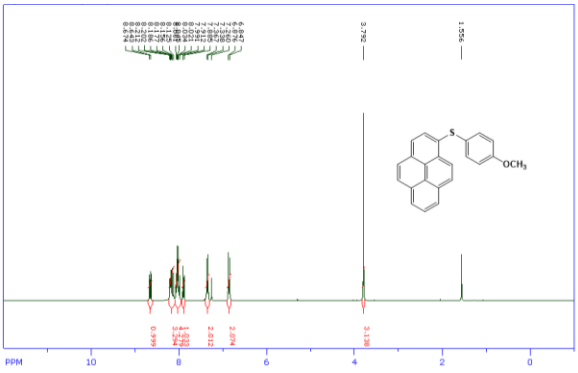

Figure 205. *^{1}H NMR of $PySPhOCH_3$*

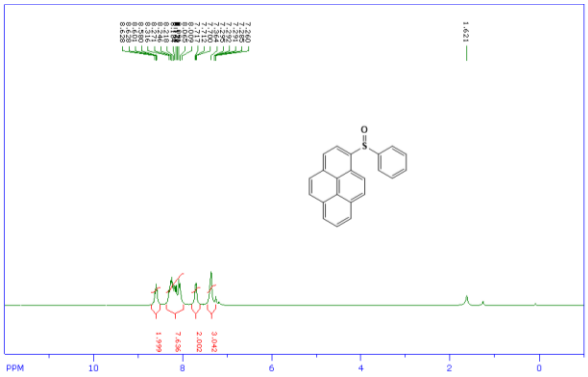

Figure 206. *^{1}H NMR of PySOPhH*

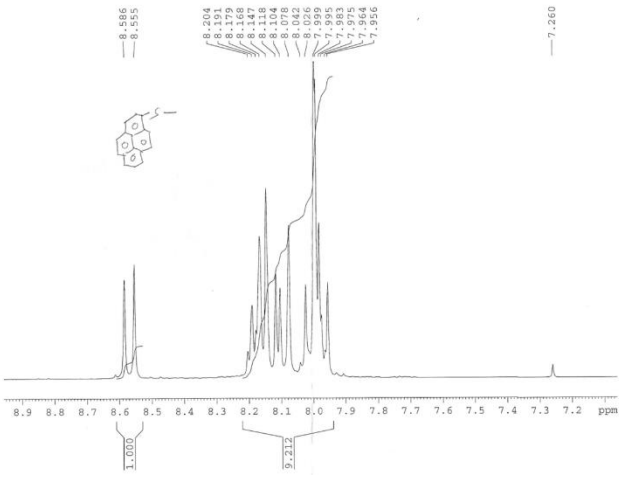

Figure 7. *^{1}H NMR of PySMe*

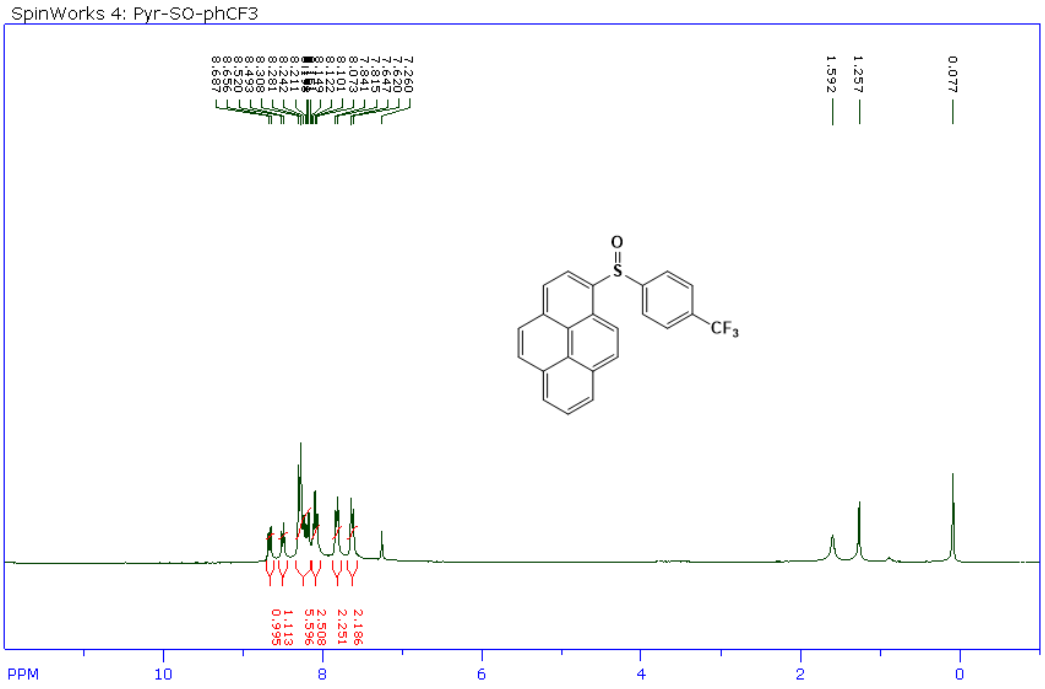

Figure 207. *^{1}H NMR of PySOPhCF$_3$*

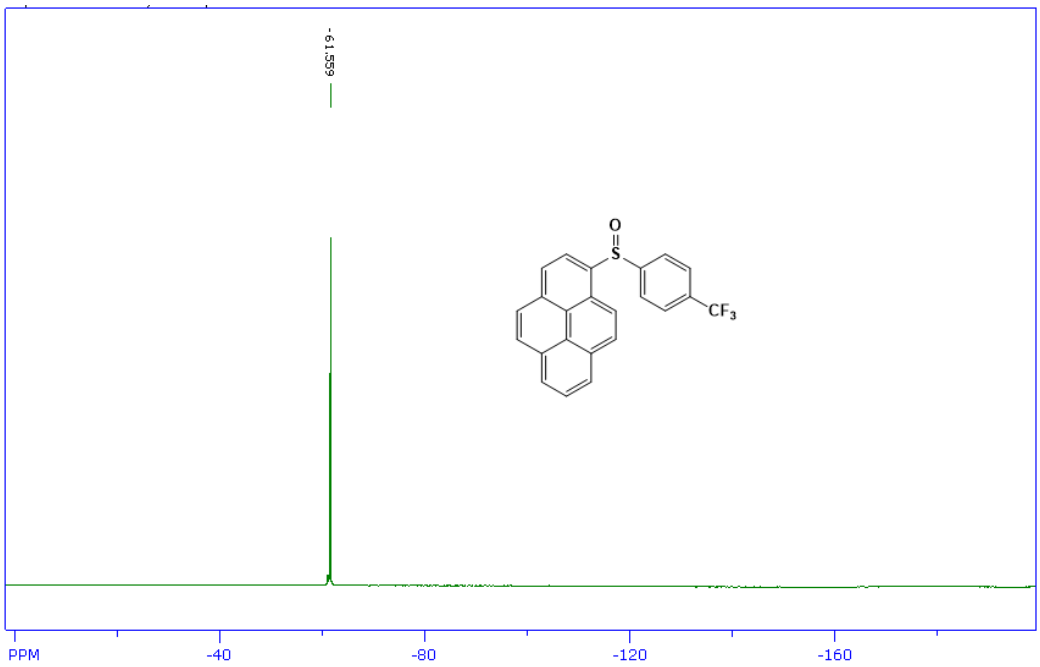

Figure 208. *^{19}F NMR of PySOPhCF$_3$*

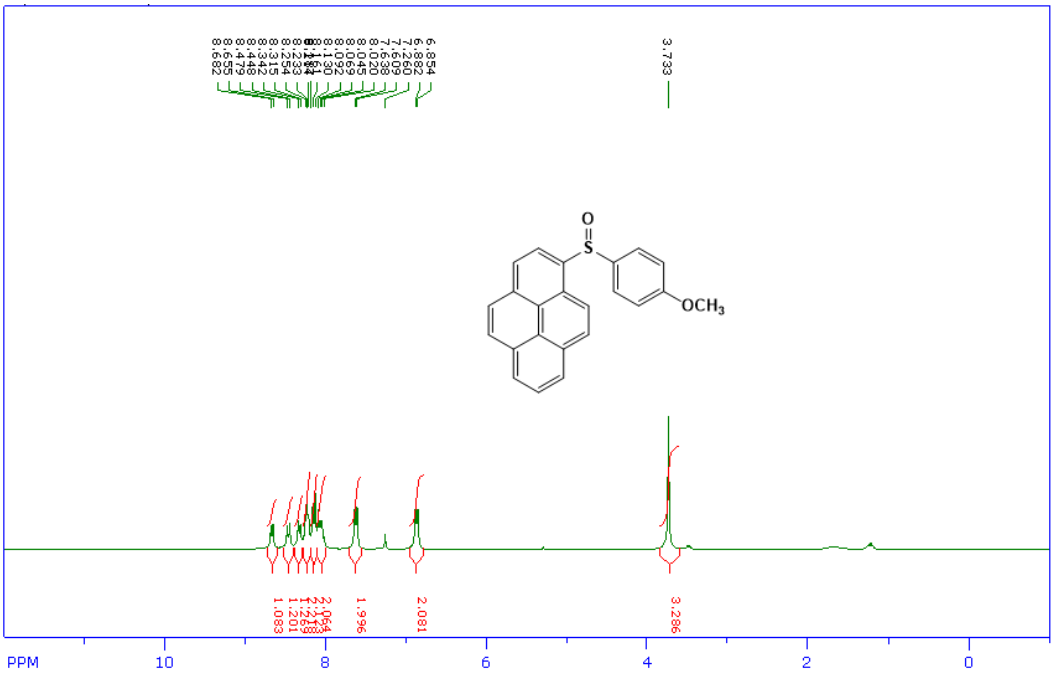

Figure 209. *^{1}H NMR of PySOPhOCH$_3$*

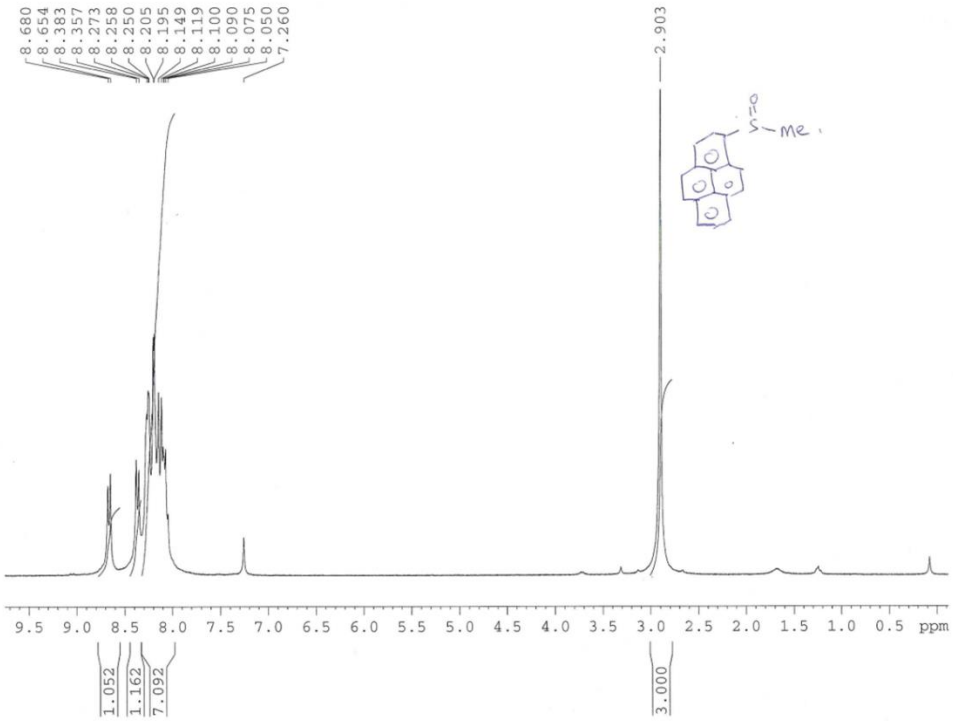

Figure 210. *^{1}H NMR of PySOMe*

Steady State Spectra

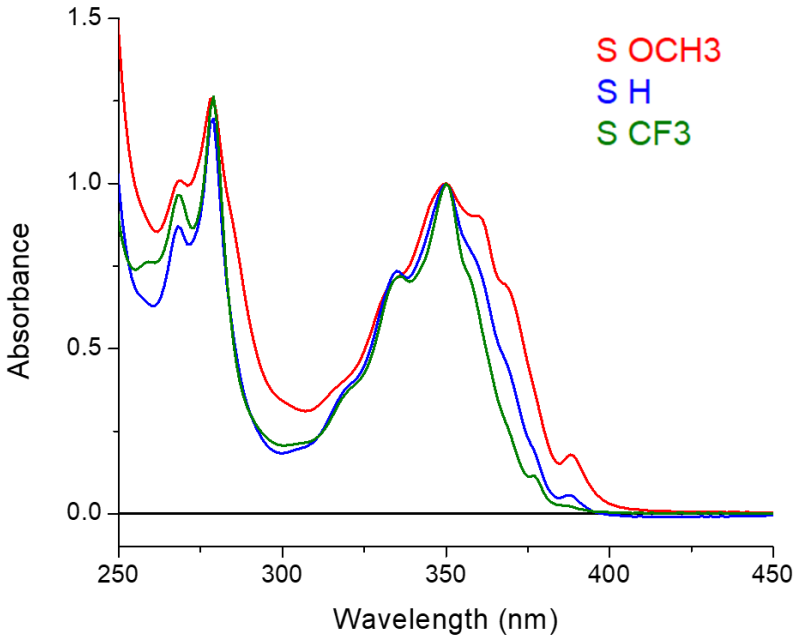

Figure 211. *UV-Vis spectra of $PySOPhOCH_3$ (red), PySOPhH (blue), and $PySOPhCF_3$ (green) in acetonitrile.*

Table 33. *Emission quantum yields of $PySOPhOCH_3$ in various solvents*

Compound	Solvent	Φ_{Em}	λ_{Em} (nm)
$PySOPhOCH_3$	DCE	1.04	381
	EG	3.94	382
	MeCN	0.68	380
	Hexane	0.4	379
	Toluene	0.84	383
	EtOH	2.5	381

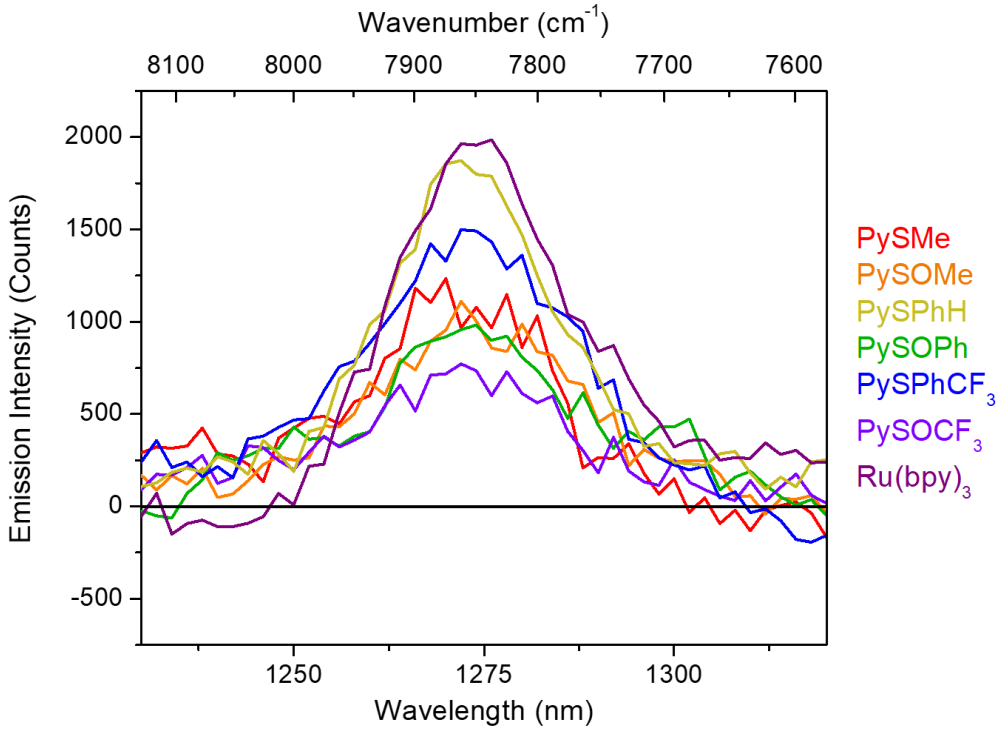

Figure 212. *$^1O_2$ emission measured from unsparged pyrene sulfoxide compounds and $Ru(bpy)_3$ in acetonitrile. A 1000 nm long pass filter was used to remove 2nd order emission.*

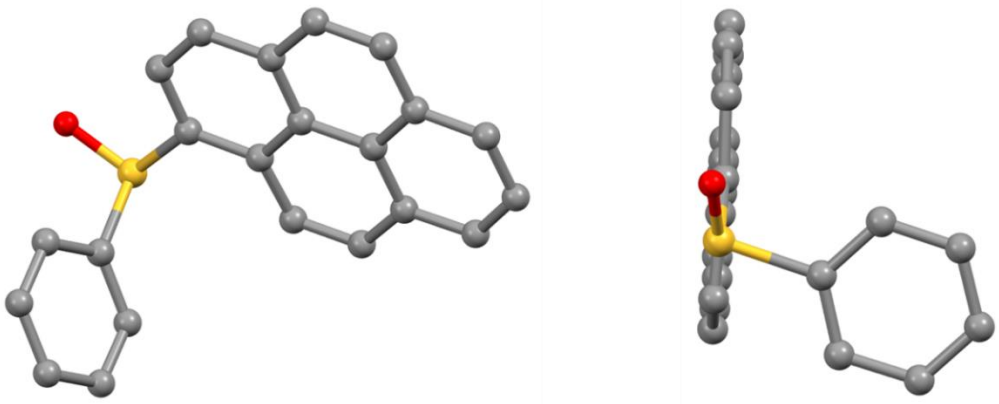

Figure 213. *X-ray crystallographic data of PySOPhH. (Left) Front-on view of the molecule. (Right) Side view of the molecule, illustrating the small dihedral angle between pyrene and the sulfoxide moiety.*

Transient Absorption Spectroscopy

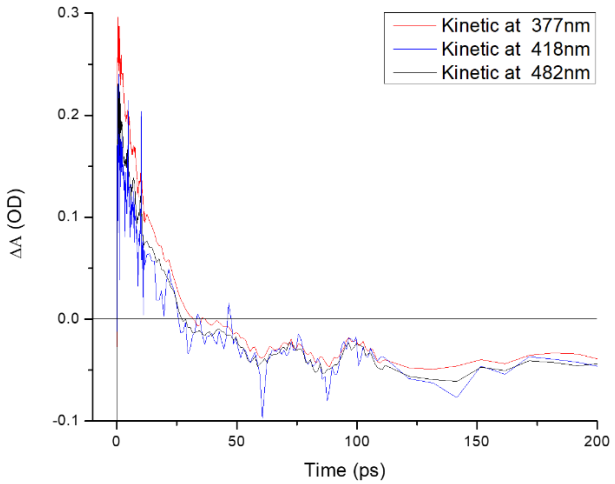

Figure 214. *Transient absorption polarization anisotropy measurements for PySOMe in acetonitrile at various probe wavelengths. At 377 nm, τ = 24.64 ± 3.64 ps. At 418 nm, τ = 23.26 ± 3.97 ps. At 480 nm, τ = 28.81 ± 4.13 ps.*

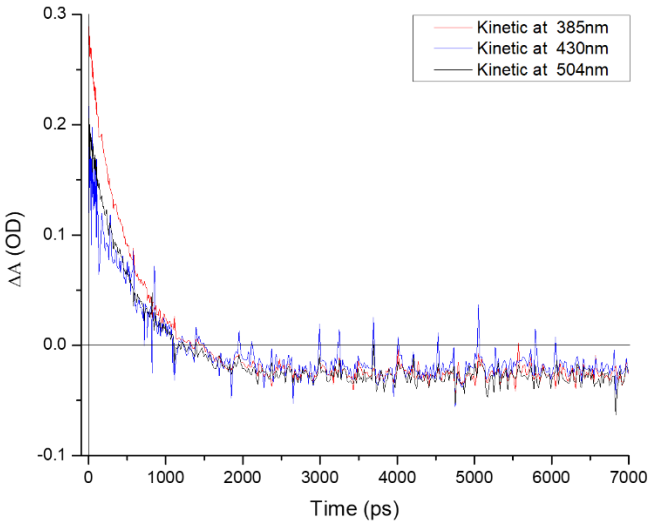

Figure 215. *Transient absorption polarization anisotropy measurements for PySOMe in ethylene glycol at various probe wavelengths. At 385 nm, τ = 444.31 ± 47.54 ps. At 430 nm, τ = 498.79 ± 28.39 ps. At 504 nm, τ = 572.52 ± 13.84 ps.*

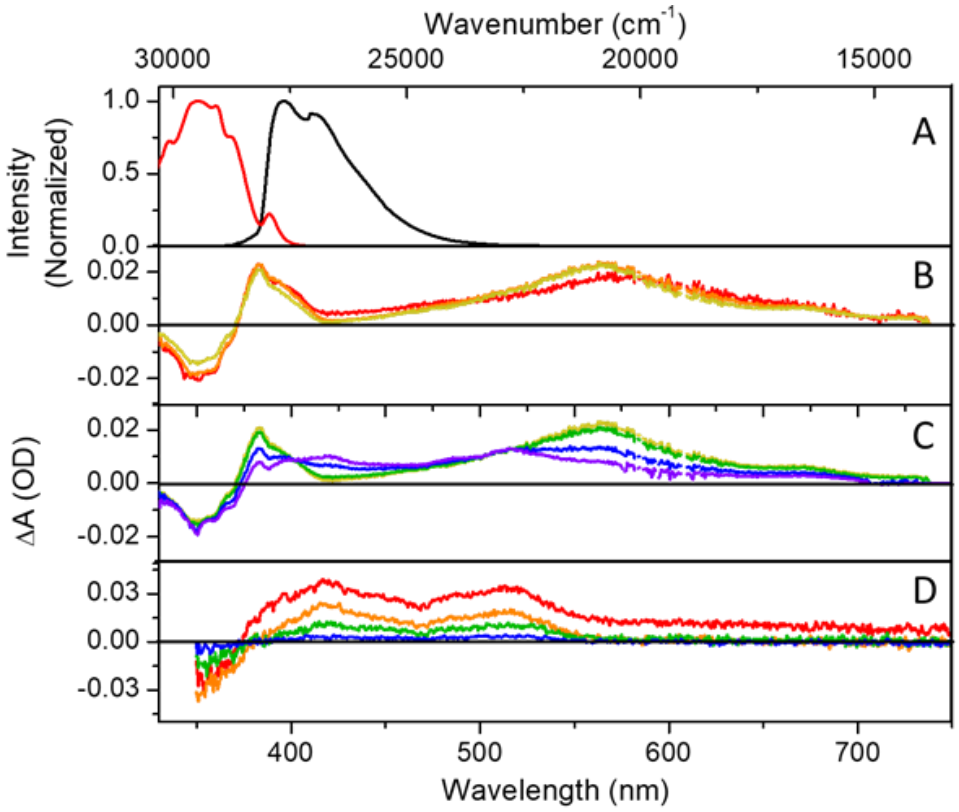

Figure 216*. (A) Steady-state absorbance and emission spectra of PySMe in acetonitrile. (B) Pump-probe transients collected at 0.3 ps (red), 2 ps (orange), and 50 ps (yellow) time delays. (C) Pump-probe transients collected at 50 ps (yellow), 500 ps (green), 2.5 ns (blue), and 5 ns (violet) time delays. (D) Flash photolysis transients collected at 30 ns (red), 5 ms (orange), 10 ms (green), and 20 ms (blue) time delays. Global fitting analysis reveals three time-components:* $\tau_1 = 230 \pm 85$ *fs,* $\tau_2 = 7.56 \pm 1.58$ *ps,* $\tau_3 = 4805.0 \pm 87.0$ *ps, and* $\tau_4 = 1.8 \pm 0.1$ μ*s.*

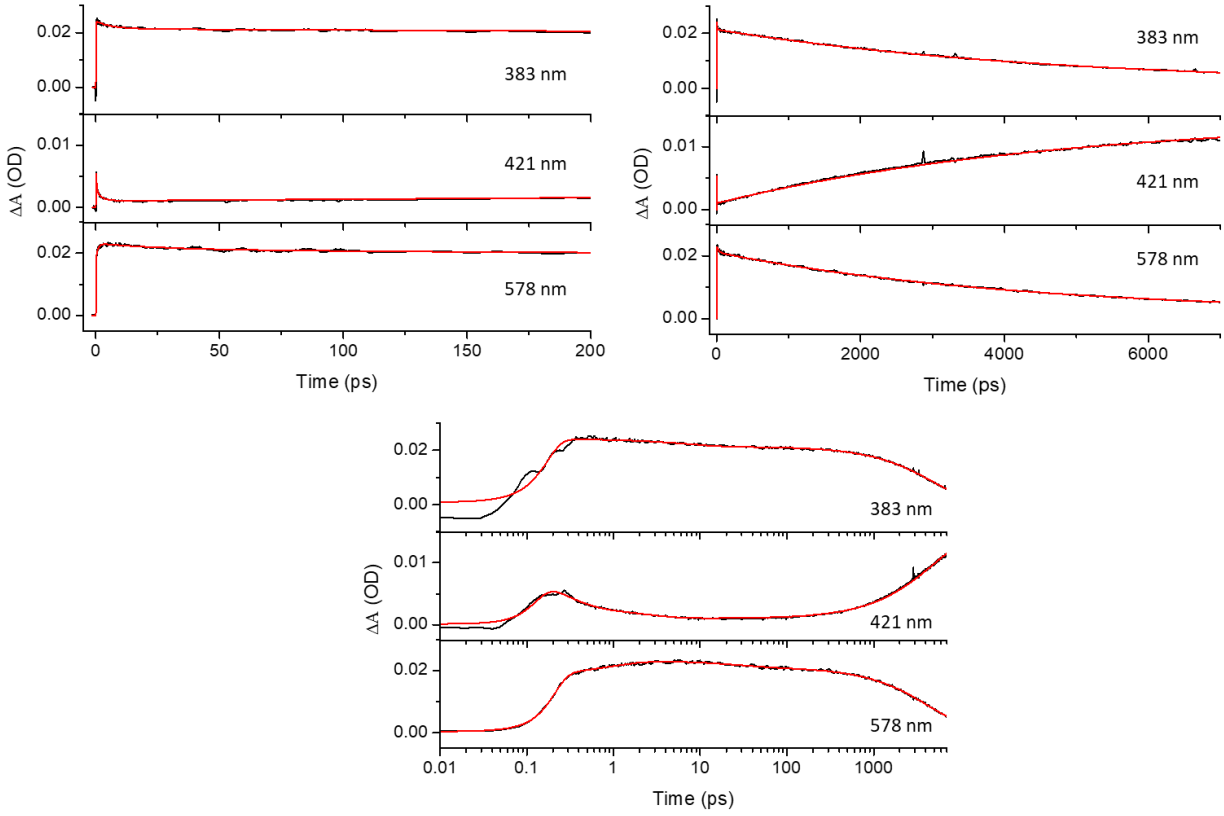

Compound	Wavelength (nm)	A_1	τ_1 (ps)	A_2	τ_2 (ps)	A_3	τ_3 (ps)
PySMe	383	0.0044 ± 0.00045	0.226 ± 0.04	0.0018 ± 0.00034	2.21 ± 0.44	-0.014 ± 0.00023	4868 ± 160
	421	--	--	0.00276 ± 0.00022	6.83 ± 1.6	0.020 ± 0.00087	4813 ± 400
	578	-0.0044 ± 0.00021	0.86 ± 0.08	0.0021 ± 0.00012	28.61 ± 4.9	0.020 ± 0.00025	4334 ± 130

Figure 217: *Ultrafast TA kinetic fits of PySMe in acetonitrile. (Top) Single wavelength kinetic fits out to pump-probe delays of 200 ps and 7000 ps. (Middle) Single wavelength kinetic fits with a logarithmic x-axis. (Bottom) Time-components and amplitudes returned from single-wavelength fitting analysis.*

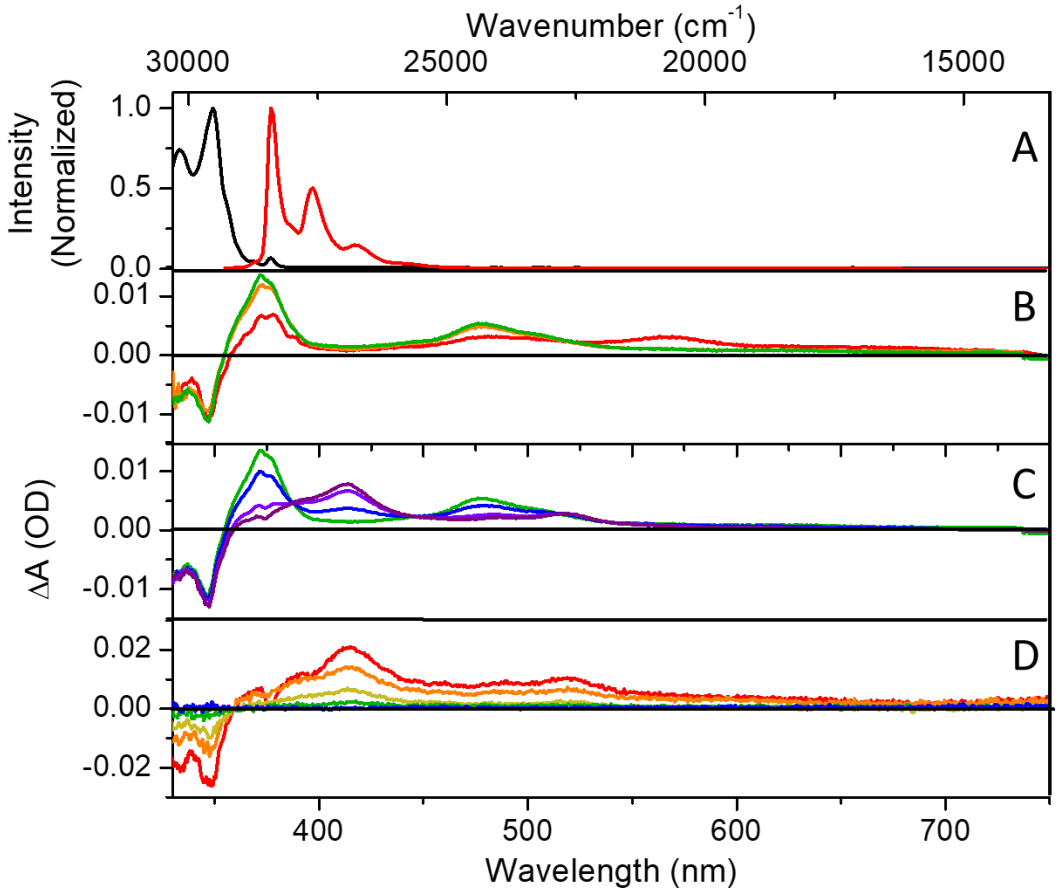

Figure 218. *(A) Steady-state absorbance and emission spectra of PySOMe in acetonitrile. (B) Pump-probe transients collected at 0.3 ps (red), 2 ps (orange), 10 ps (yellow), and 50 ps (green) time delays. (C) Pump-probe transients collected at 50 ps (green), 100 ps (blue), 500 ps (violet), and 5 ns (purple) time delays. (D) Flash photolysis transients collected at 30 ns (red), 10 μs (orange), 20 μs (yellow), 50 μs (green), and 200 μs (blue) time delays. Global fitting analysis reveals three time-components:* τ_1 *= 110 ± 60 fs,* τ_2 *= 4.82 ± 0.64 ps,* τ_3 *= 1024.0 ± 9.0 ps, and* τ_4 *= 18.3 ± 0.36 μs.*

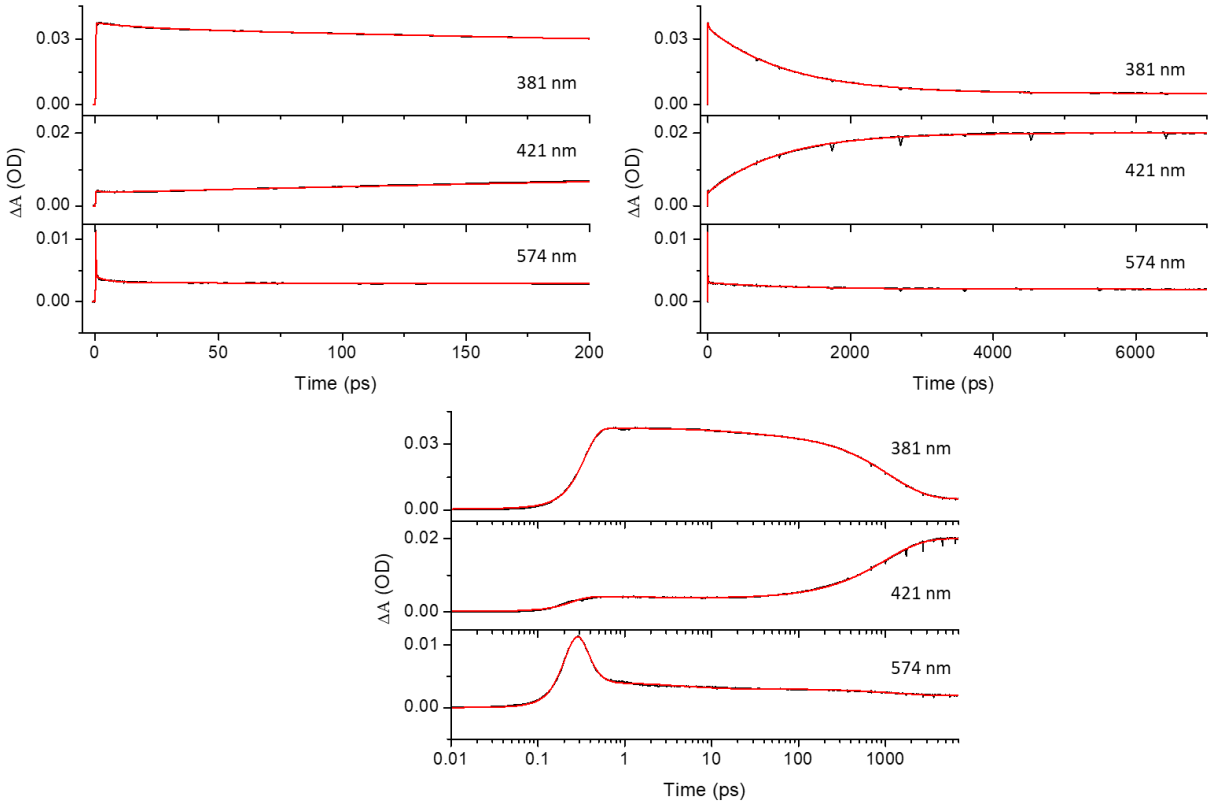

Compound	Wavelength (nm)	A_1	τ_1 (ps)	A_2	τ_2 (ps)	A_3	τ_3 (ps)
PyrSOMe	381	--	--	0.0023 ± 0.00001	21.99 ± 2.8	0.030 ± 0.00001	1109 ± 10
	421	--	--	--	--	-0.016 ± 0.00010	991 ±19
	574	0.030 ± 0.0039	0.11 ± 0.06	0.0010 ± 0.00001	4.92 ± 0.84	0.0011 ± 0.00001	1209 ± 160

Figure 219: *Ultrafast TA kinetic fits of PySOMe in acetonitrile. (Top) Single wavelength kinetic fits out to pump-probe delays of 200 ps and 7000 ps. (Middle) Single wavelength kinetic fits with a logarithmic x-axis. (Bottom) Time-components and amplitudes returned from single-wavelength fitting analysis.*

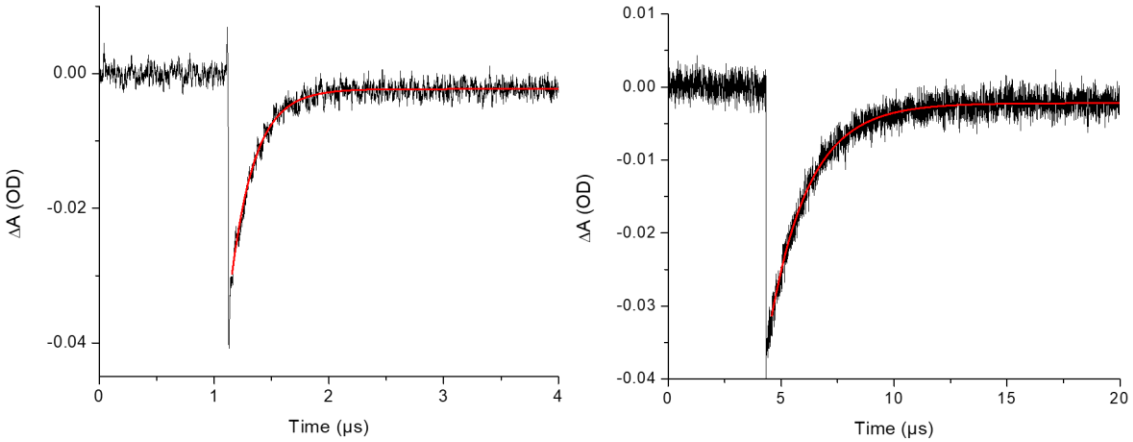

PySMe	Wavelength (nm)	Non-Degassed	Degassed w/N_2
τ	335	207.20 ns	1.75 μs

Figure 220. *Flash photolysis kinetics of PySMe in acetonitrile under non-degassed and degassed conditions.*

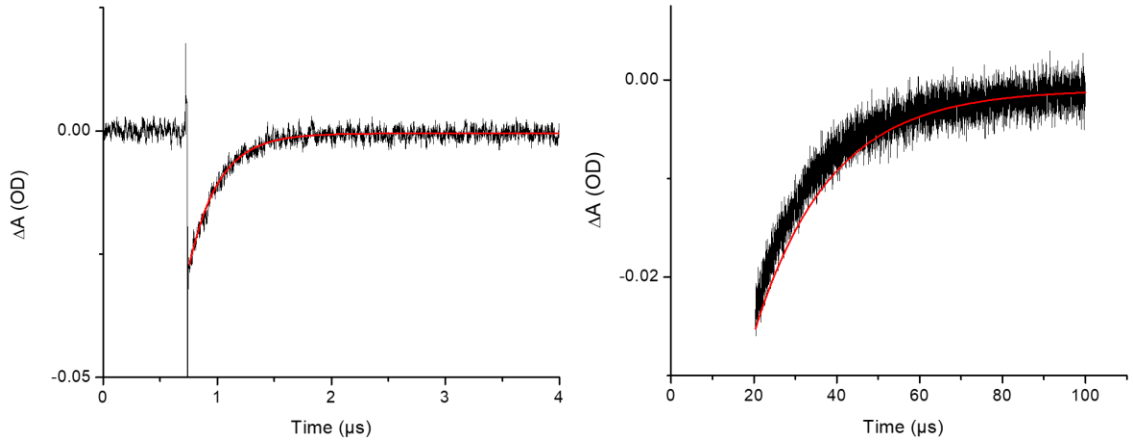

PySOMe	Wavelength (nm)	Non-Degassed	Degassed w/N_2
τ	335	258.41 ns	18.25 μs

Figure 221. *Flash photolysis kinetics of PySOMe in acetonitrile under non-degassed and degassed conditions.*

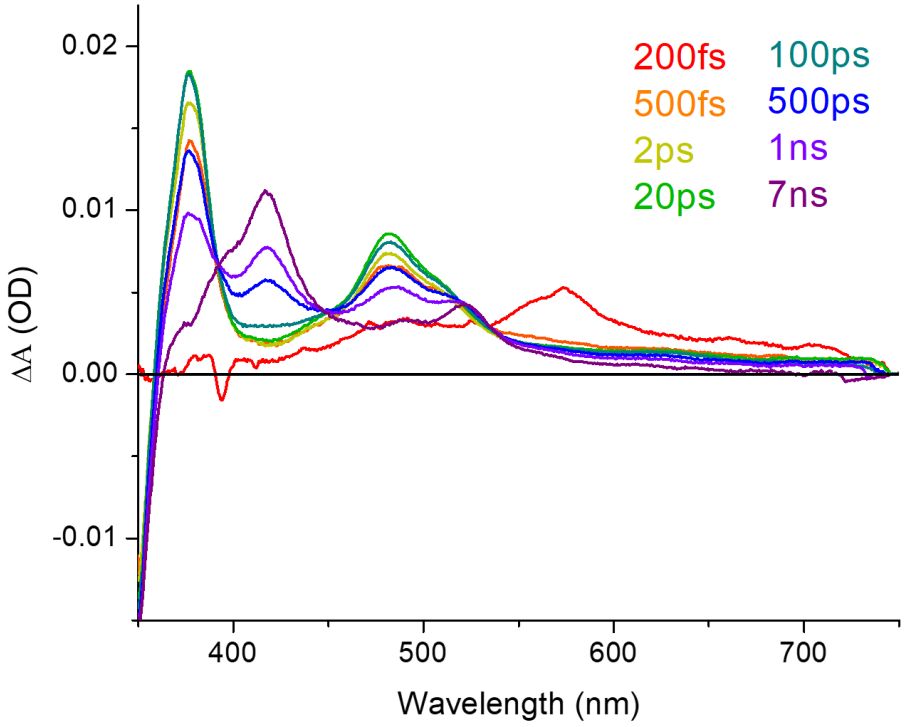

Figure 222. *Ultrafast pump-probe spectra of PySOMe in acetonitrile.*

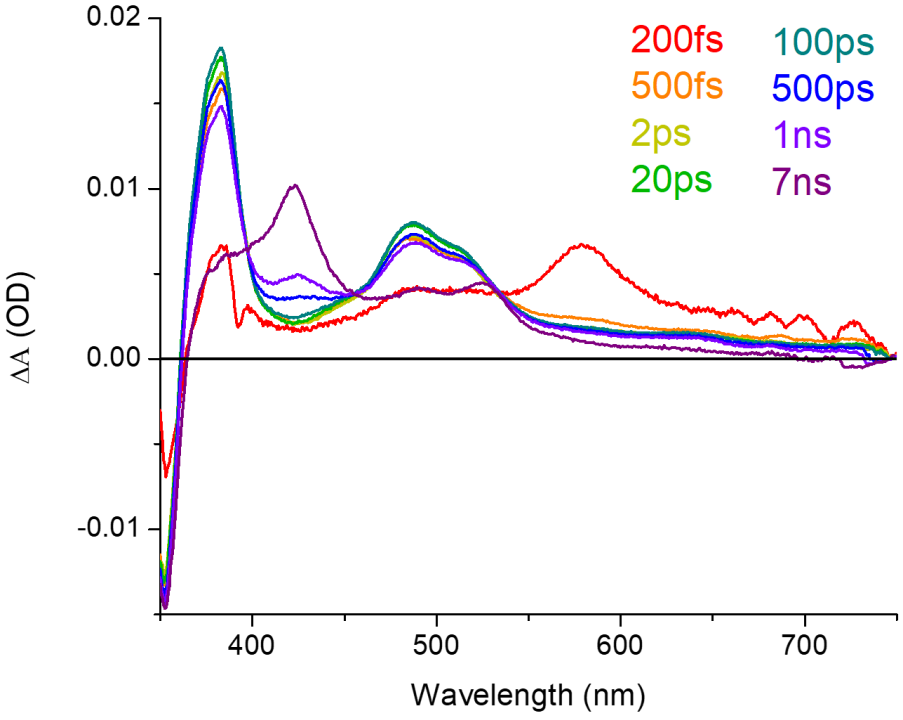

Figure 223. *Ultrafast pump-probe spectra of PySOMe in DCE.*

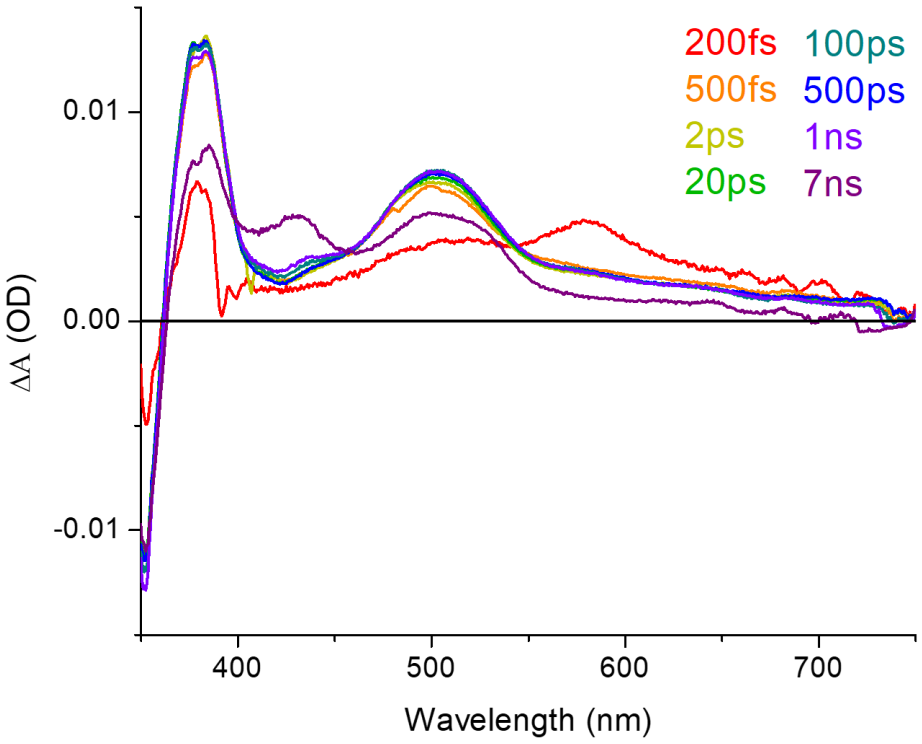

Figure 224. *Ultrafast pump-probe spectra of PySOMe in Ethylene Glycol.*

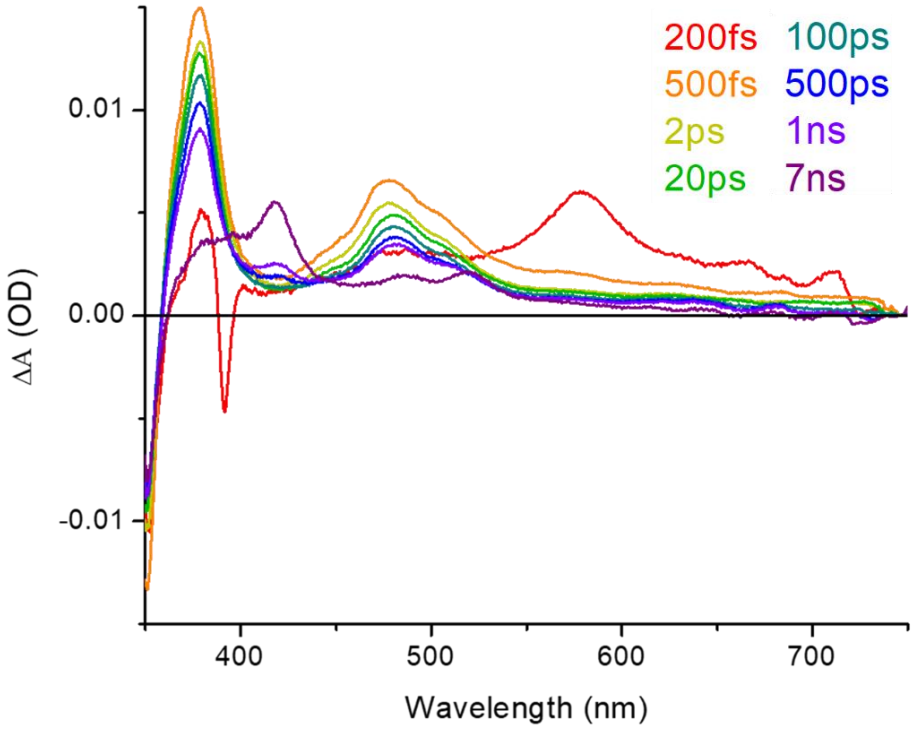

Figure 225. *Ultrafast pump-probe spectra of PySOMe in Hexanes.*

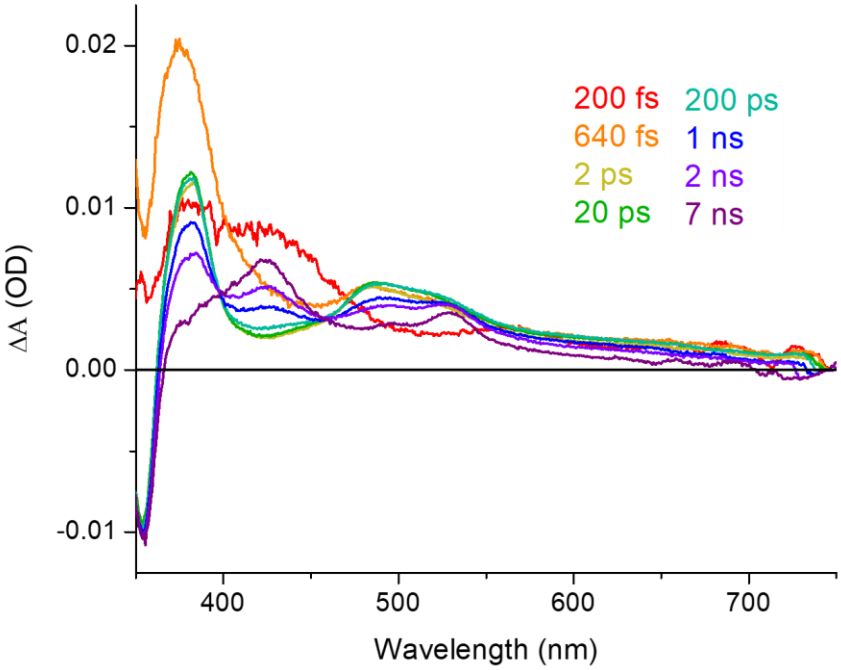

Figure 226. *Ultrafast pump-probe spectra of PySOMe in Toluene.*

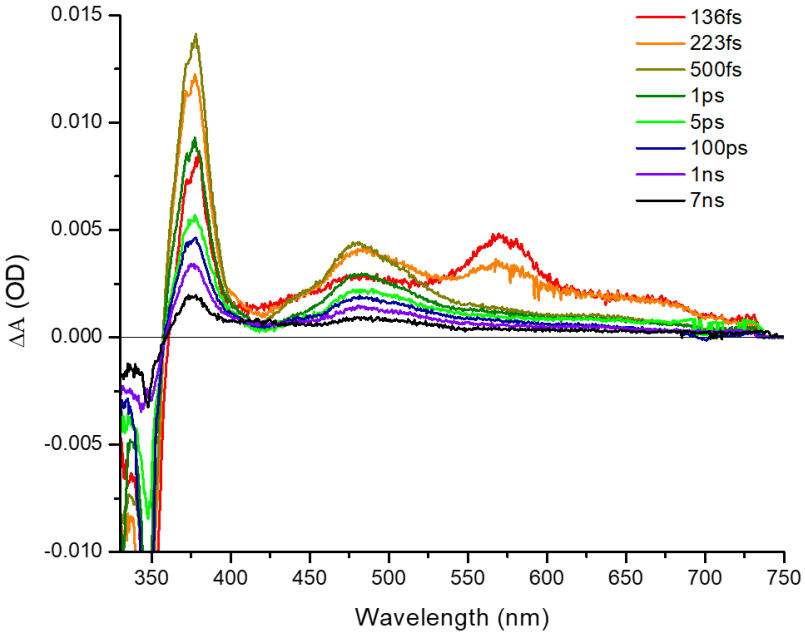

Figure 227. *Ultrafast pump-probe spectra of PySOMe in PMMA.*

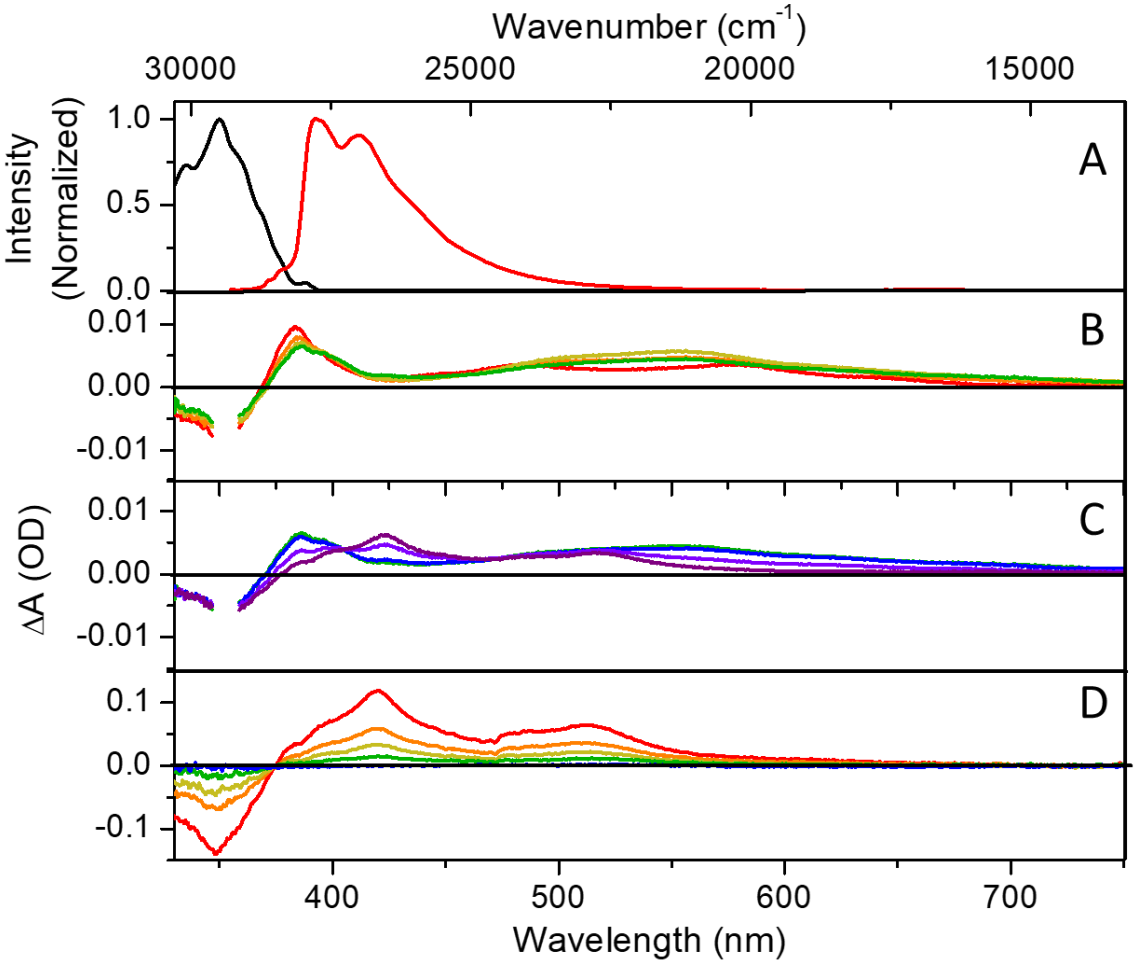

Figure 228. *(A) Steady-state absorbance and emission spectra of PySPhH in acetonitrile. (B) Pump-probe transients collected at 0.3 ps (red), 2 ps (orange), 10 ps (yellow), and 50 ps (green) time delays. (C) Pump-probe transients collected at 50 ps (green), 100 ps (blue), 500 ps (violet), and 5 ns (purple) time delays. (D) Flash photolysis transients collected at 30 ns (red), 5 ms (orange), 10 ms (yellow), 20 ms (green), and 50 ms (blue) time delays. Global fitting analysis reveals three time-components:* $\tau_1 = 180 \pm 20$ *fs,* $\tau_2 = 23.8 \pm 2.8$ *ps,* $\tau_3 = 512.9 \pm 32.5$ *ps, and* $\tau_4 = 18.64 \pm 0.33$ μ*s.*

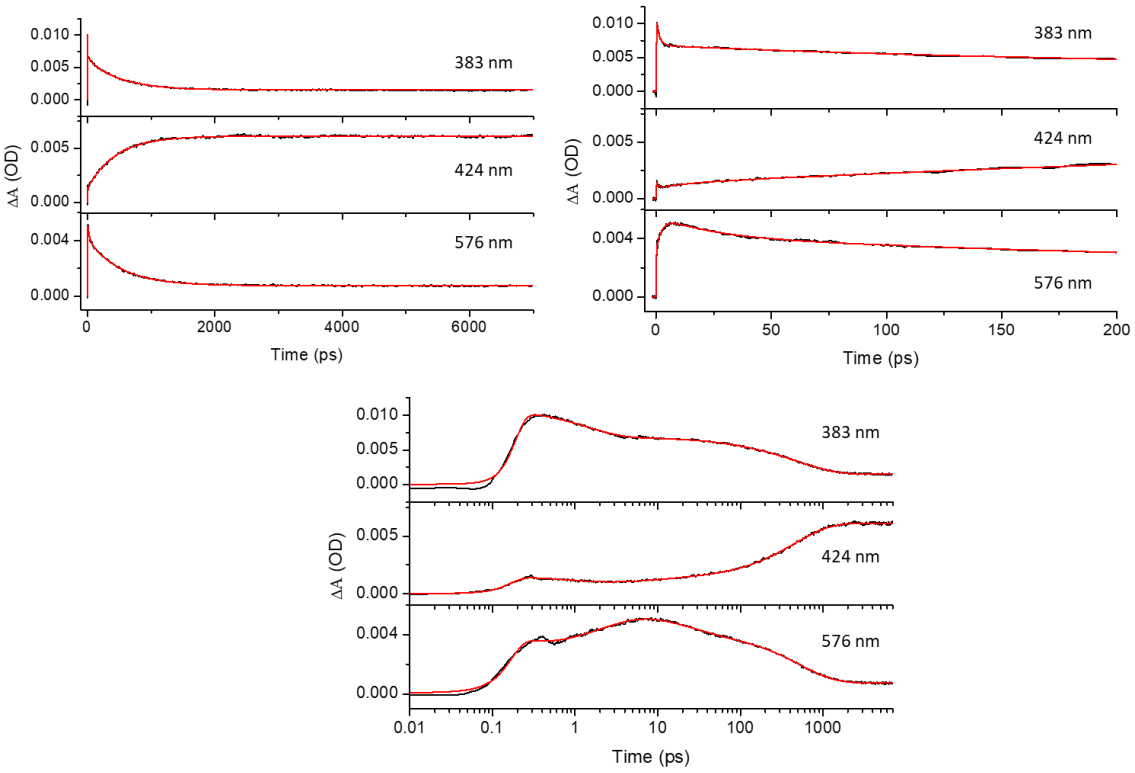

Compound	Wavelength (nm)	A_1	τ_1 (ps)	A_2	τ_2 (ps)	A_3	τ_3 (ps)
PyrSPh	383	0.0037 ± 0.00008	1.39 ± 0.07	0.00063 ± 0 00028	82.12 ± 46.0	0.0047 ± 0.00039	528.1 ± 32.0
	424	0.00058 ± 0.00007	0.89 ± 0.22	-0.00038 ± 0.00007	10.95 ± 3.7	-0.0048 ± 0.00002	448.5 ± 5.9
	576	-0.0024 ± 0.00008	2.38 ± 0.19	0.0015 ± 0.00007	23.8 ± 2.8	0.0034 ± 0.00004	517.2 ± 11.0

Figure 229. *Ultrafast TA kinetic fits of PySPhH in acetonitrile. (Top) Single wavelength kinetic fits out to pump-probe delays of 7000 ps and 200 ps. (Middle) Single wavelength kinetic fits with a logarithmic x-axis. (Bottom) Time-components and amplitudes returned from single-wavelength fitting analysis.*

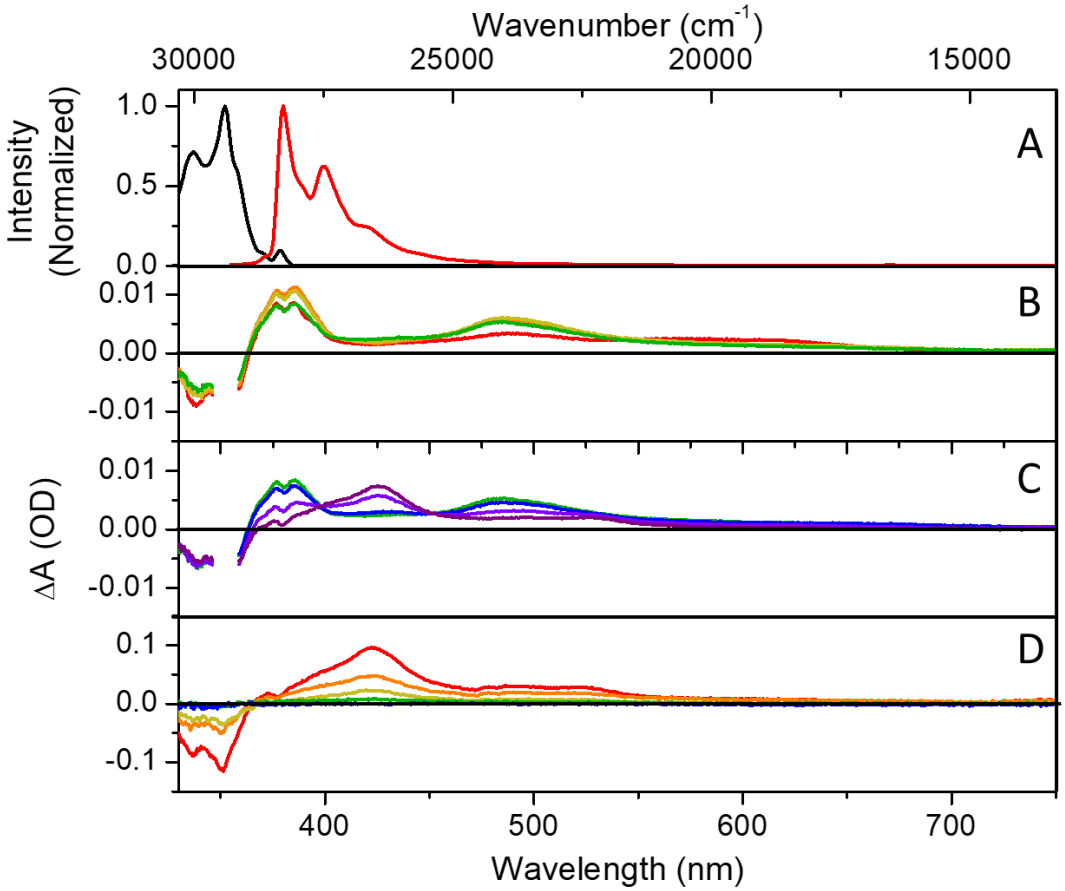

Figure 230. *(A) Steady-state absorbance and emission spectra of PySOPhH in acetonitrile. (B) Pump-probe transients collected at 0.2 ps (red), 2 ps (orange), 10 ps (yellow), and 50 ps (green) time delays. (C) Pump-probe transients collected at 50 ps (green), 100 ps (blue), 500 ps (violet), and 5 ns (purple) time delays. (D) Flash photolysis transients collected at 30 ns (red), 10 μs (orange), 20 μs (yellow), 50 μs (green), and 100 μs (blue) time delays. Global fitting analysis three time-components:* τ_1 *= 250 ± 50 fs,* τ_2 *= 28.7 ± 2.6 ps,* τ_3 *= 485.3 ± 27.5 ps, and* τ_4 *= 18.29 ± 0.25 μs.*

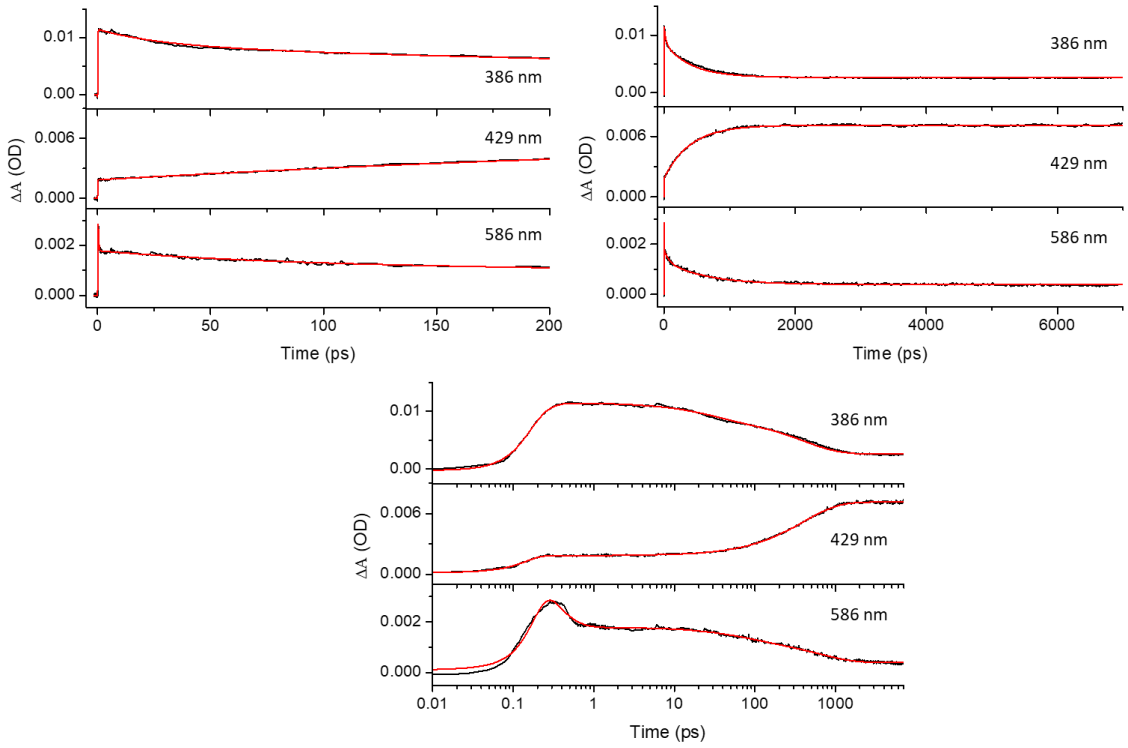

Compound	Wavelength (nm)	A_1	τ_1 (ps)	A_2	τ_2 (ps)	A_3	τ_3 (ps)
PyrSOPh	386	-0.061 ± 5.56	0.07 ± 0.01	0.0028 ± 0.00012	28.09 ± 2.6	0.0061 ± 0.00012	401.7 ± 14.0
	429	0.000005 ± 0.00012	0.42 ± 11	-0.000017 ± 0.00029	94.25 ± 1400	-0.0053 ± 0.00029	401 ± 17
	586	0.0027 ± 0.00032	0.20 ± 0.02	0.00046 ± 0.00007	67.05 ± 15.0	0.00094 ± 0.00007	632.8 ± 59.0

Figure 231. *Ultrafast TA kinetic fits of PySOPhH in acetonitrile. (Top) Single wavelength kinetic fits out to pump-probe delays of 200 ps and 7000 ps. (Middle) Single wavelength kinetic fits with a logarithmic x-axis. (Bottom) Time-components and amplitudes returned from single-wavelength fitting analysis.*

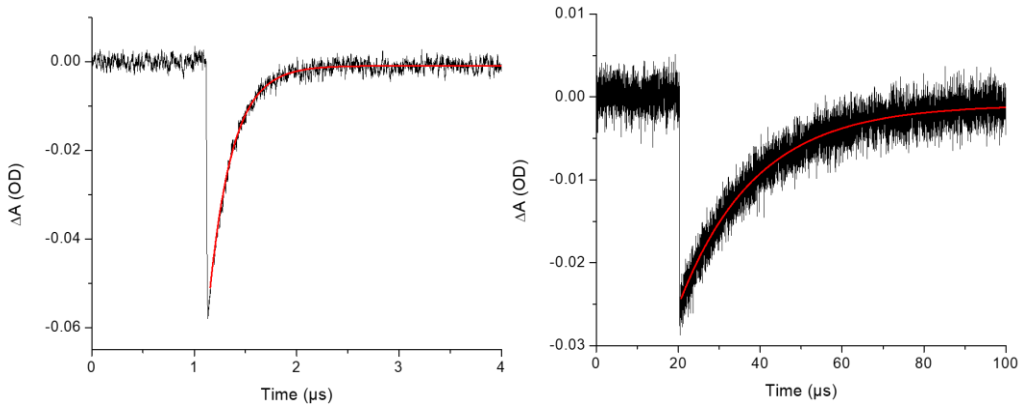

PySOMe	Wavelength (nm)	Non-Degassed	Degassed w/N_2
τ	335	227.76 ns	18.64 μs

Figure 232. *Flash photolysis kinetics of PySPhH in acetonitrile under non-degassed and degassed conditions.*

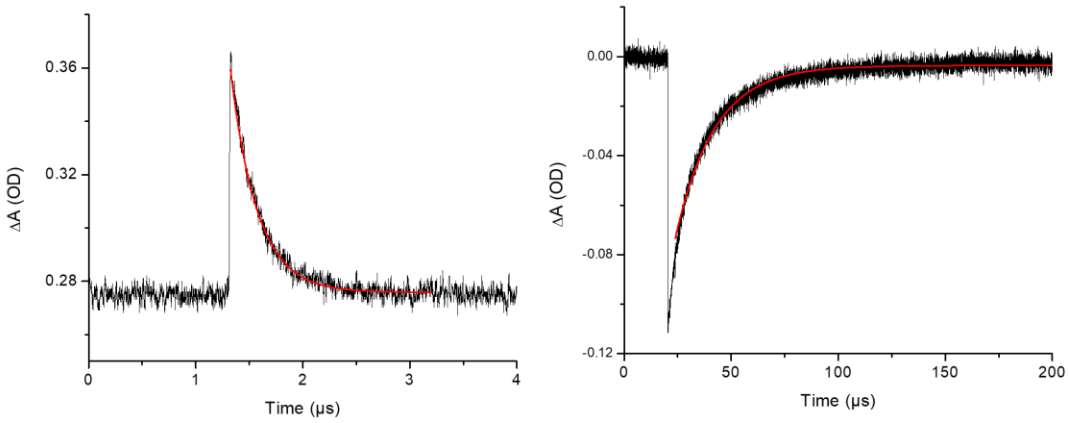

PySOMe	Wavelength (nm)	Non-Degassed	Degassed w/N_2
τ	425, 335	250.61 ns	18.29 μs

Figure 233. *Flash photolysis kinetics of PySOPhH in acetonitrile under non-degassed and degassed conditions.*

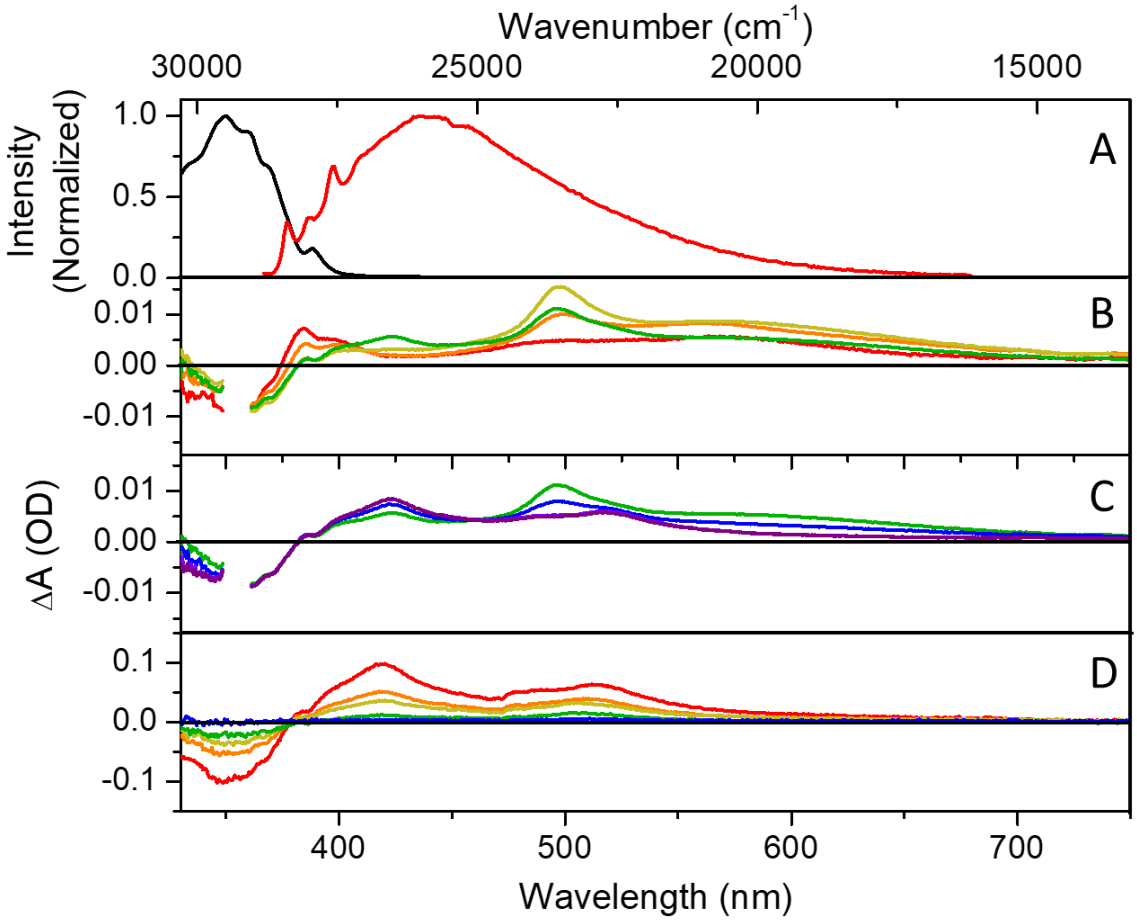

Figure 234. *(A) Steady-state absorbance and emission spectra of $PySPhOCH_3$ in acetonitrile. (B) Pump-probe transients collected at 0.3 ps (red), 2 ps (orange), 10 ps (yellow), and 50 ps (green) time delays. (C) Pump-probe transients collected at 50 ps (green), 100 ps (blue), 500 ps (violet), and 5 ns (purple) time delays. (D) Flash photolysis transients collected at 30 ns (red), 10 μs (orange), 20 μs (yellow), 50 μs (green), and 200 μs (blue) time delays. Global fitting analysis reveals three time-components: τ_1 = 110 ± 40 fs, τ_2 = 12.50 ± 6.8 ps, τ_3 = 65.1 ± 1.3 ps, and τ_4 = 24.55 ± 0.42 μs.*

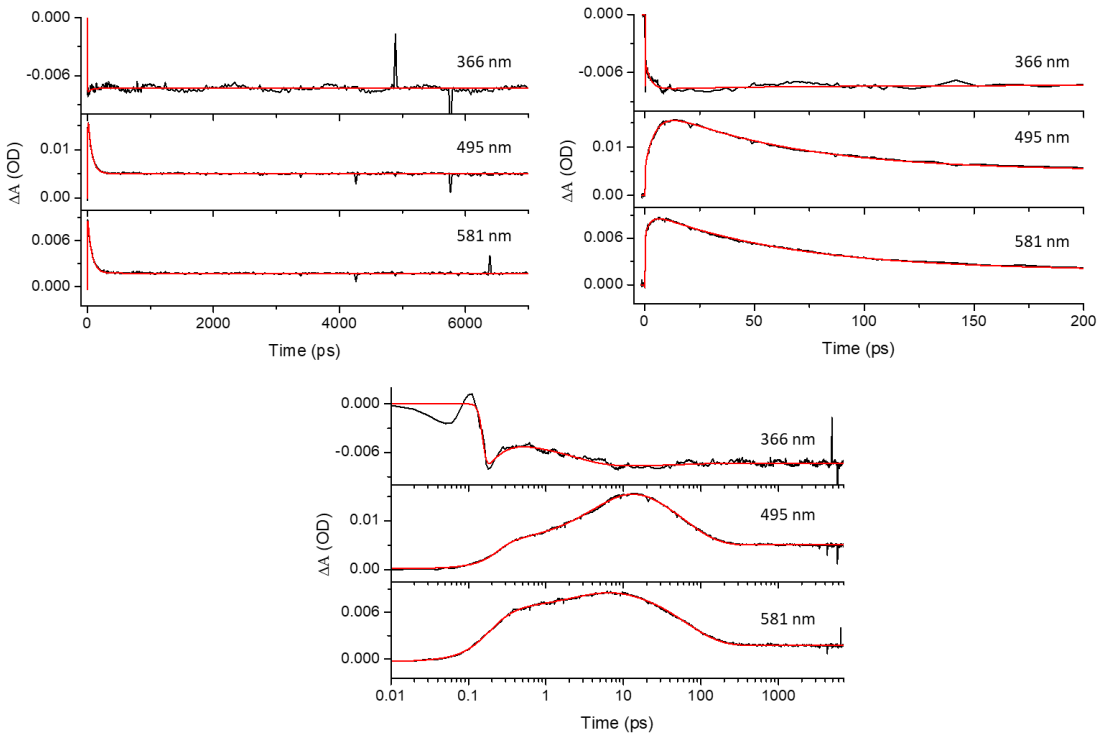

Compound	Wavelength (nm)	A_1	τ_1 (ps)	A_2	τ_2 (ps)	A_3	τ_3 (ps)
PyrSOCH3	366	-0.0038 ± 0.0014	0.10 ± 0.05	0.0030 ± 0.00033	2.36 ± 0.75	-0.0004 ± 0.0002	65.28 ± 80.0
	495	-0.0016 ± 0.0022	0.21 ± 0.19	-0.013 ± 0.00023	4.87 ± 0.20	0.014 ± 0.00025	61.53 ± 1.4
	581	-0.015 ± 0.0032	0.13 ± 0.01	-0.0032 ± 0.00009	2.67 ± 0.23	0.0078 ± 0.00008	65.43 ± 1.2

Figure 235. *Ultrafast TA kinetic fits of $PySPhOCH_3$ in acetonitrile. (Top) Single wavelength kinetic fits out to pump-probe delays of 7000 ps and 200 ps. (Middle) Single wavelength kinetic fits with a logarithmic x-axis. (Bottom) Time-components and amplitudes returned from single-wavelength fitting analysis.*

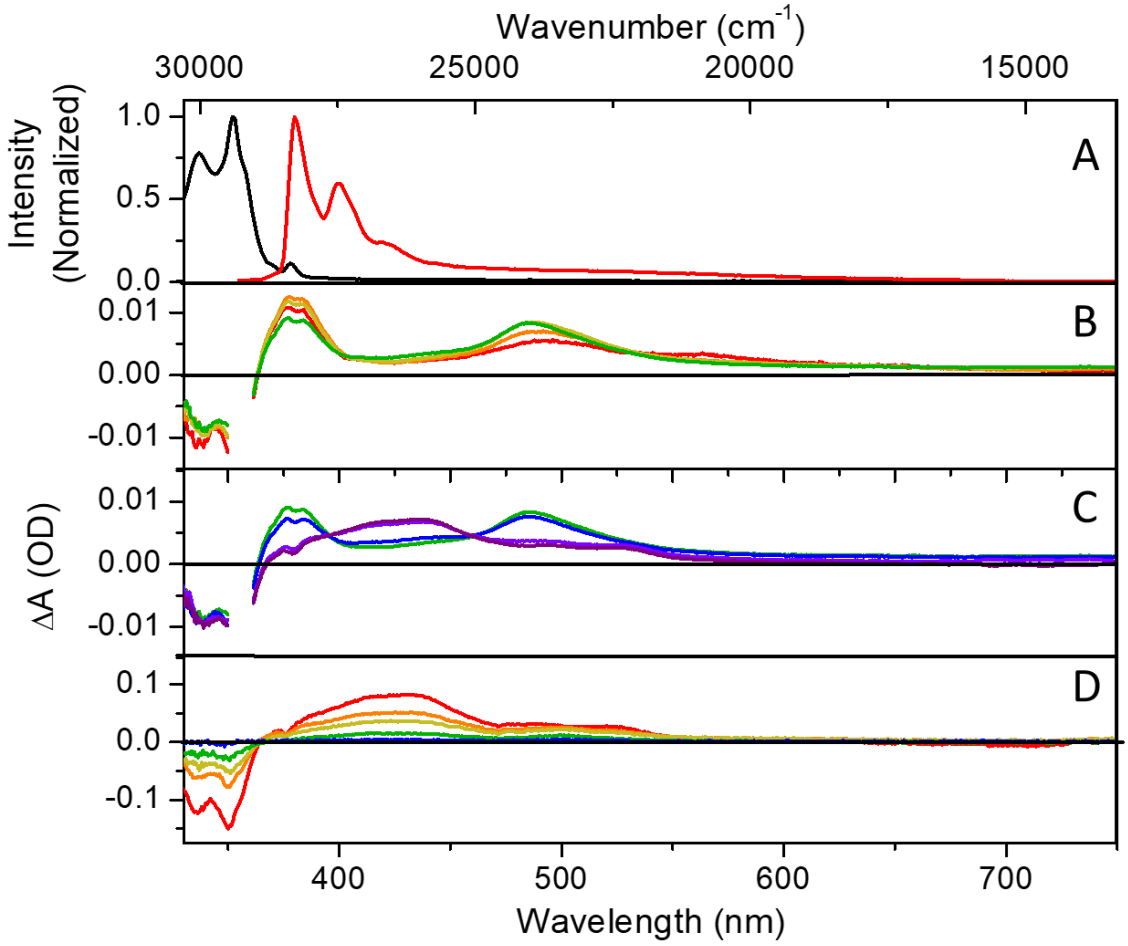

Figure 236. *(A) Steady-state absorbance and emission spectra of PySOPhOCH₃ in acetonitrile. (B) Pump-probe transients collected at 0.3 ps (red), 2 ps (orange), 10 ps (yellow), and 50 ps (green) time delays. (C) Pump-probe transients collected at 50 ps (green), 100 ps (blue), 500 ps (violet), and 5 ns (purple) time delays. (D) Flash photolysis transients collected at 30 ns (red), 10 ms (orange), 20 ms (yellow), 50 ms (green), and 200 ms (blue) time delays. Global fitting analysis reveals three time-components:* τ_1 *= 160 ± 80 fs,* τ_2 *= 21.9 ± 3.5 ps,* τ_3 *= 182.9 ± 25.6 ps, and* τ_4 *= 37.44 ± 0.54* μ*s.*

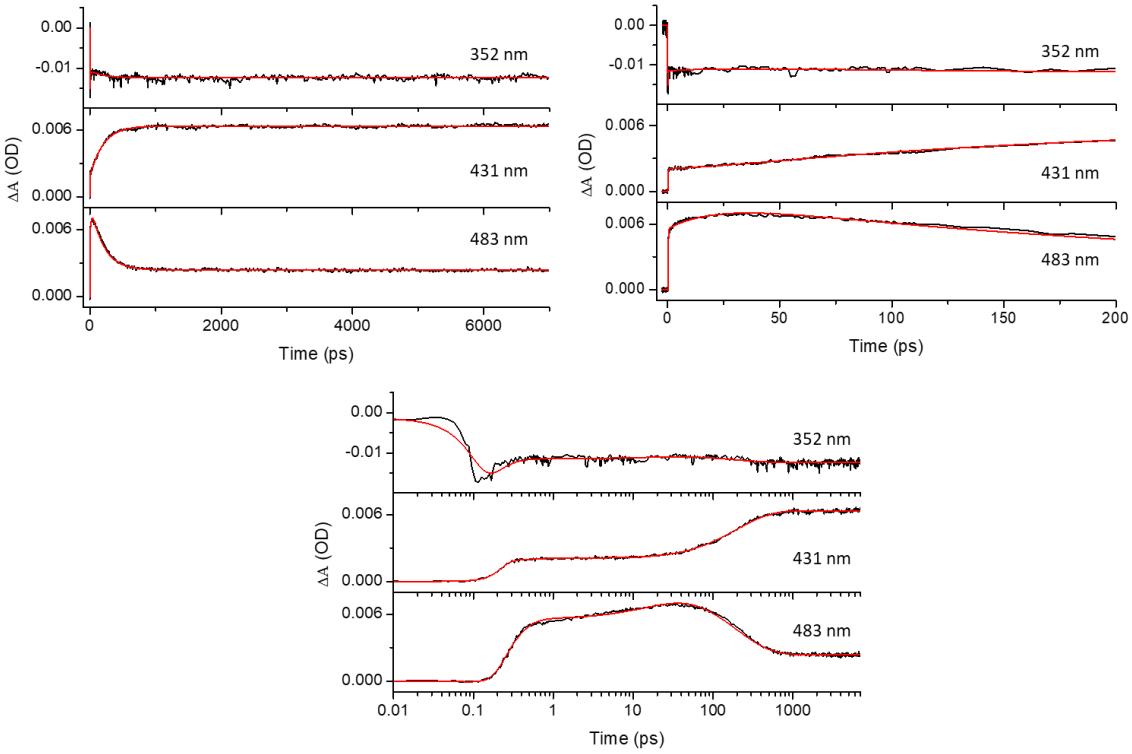

Compound	Wavelength (nm)	A_1	τ_1 (ps)	A_2	τ_2 (ps)	A_3	τ_3 (ps)
PyrSOOCH3	352	-0.012 ± 0.0099	0.10 ± 0.05	-0.00097 ± 0.00076	18.98 ± 26.0	0.0019 ± 0.00078	194.5 ± 130.0
	431	-0.00029 ± 0.00023	0.30 ± 0.29	0.00034 ± 0.0001	20.39 ± 13.0	-0.0046 ± 0.00011	195.0 ± 7.3
	483	-0.0077 ± 0.0017	0.15 ± 0.01	-0.0031 ± 0.00013	21.40 ± 1.7	0.0062 ± 0.00014	195.1 ± 6.8

Figure 237. *Ultrafast TA kinetic fits of $PySOPhOCH_3$ in acetonitrile. (Top) Single wavelength kinetic fits out to pump-probe delays of 7000 ps and 200 ps. (Middle) Single wavelength kinetic fits with a logarithmic x-axis. (Bottom) Time-components and amplitudes returned from single-wavelength fitting analysis.*

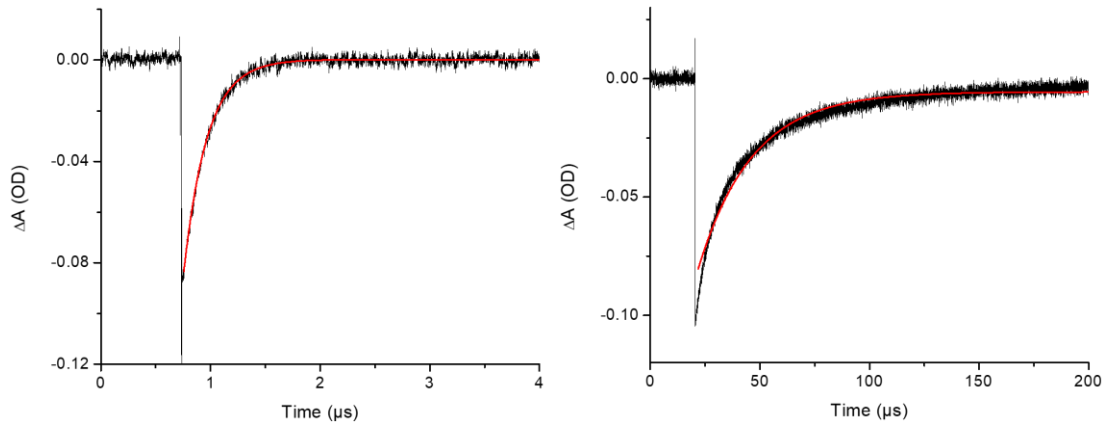

PySOMe	Wavelength (nm)	Non-Degassed	Degassed w/N_2
τ	335	213.41 ns	24.55 μs

Figure 238. *Flash photolysis kinetics of $PySPhOCH_3$ in acetonitrile under non-degassed and degassed conditions.*

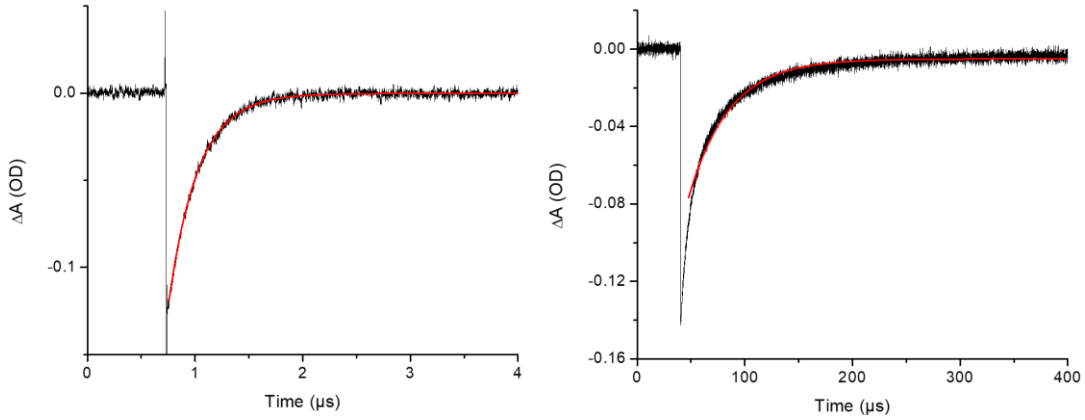

PySOMe	Wavelength (nm)	Non-Degassed	Degassed w/N_2
τ	335	272.58 ns	37.44 μs

Figure 239. *Flash photolysis kinetics of $PySOPhOCH_3$ in acetonitrile under non-degassed and degassed conditions.*

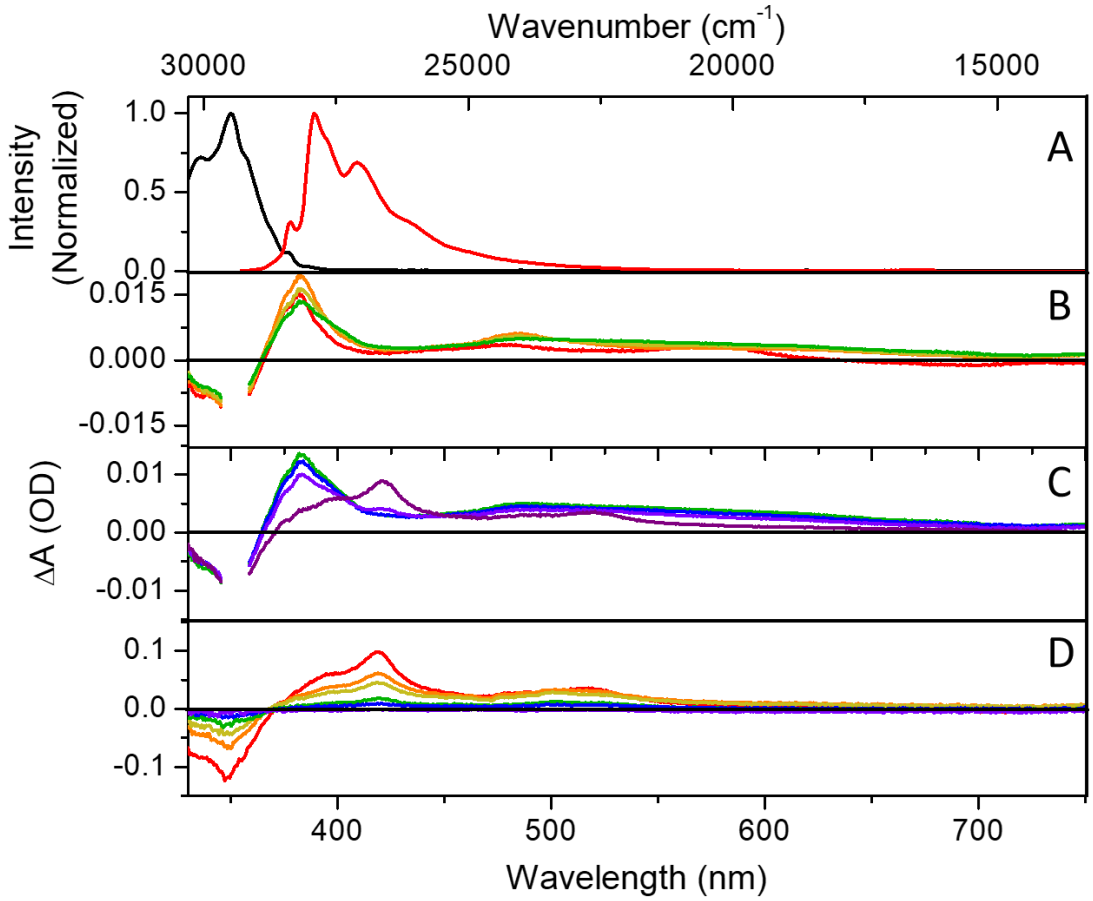

***Figure 240**. (A) Steady-state absorbance and emission spectra of $PySPhCF_3$ in acetonitrile (B) Pump-probe transients collected at 0.4 ps (red), 2 ps (orange), 10 ps (yellow), and 50 ps (green) time delays. (C) Pump-probe transients collected at 50 ps (green), 100 ps (blue), 500 ps (violet), and 5 ns (purple) time delays. (D) Flash photolysis transients collected at 30 ns (red), 10 ms (orange), 20 ms (yellow), 50 ms (green) 100 ms (blue), and 200 ms (violet) time delays. Global fitting analysis reveals three time-components: τ_1 = 170 ± 10 fs, τ_2 = 14.9 ± 9.6 ps, τ_3 = 1485.0 ± 94.2 ps, and τ_4 = 31.80 ± 0.38 μs.*

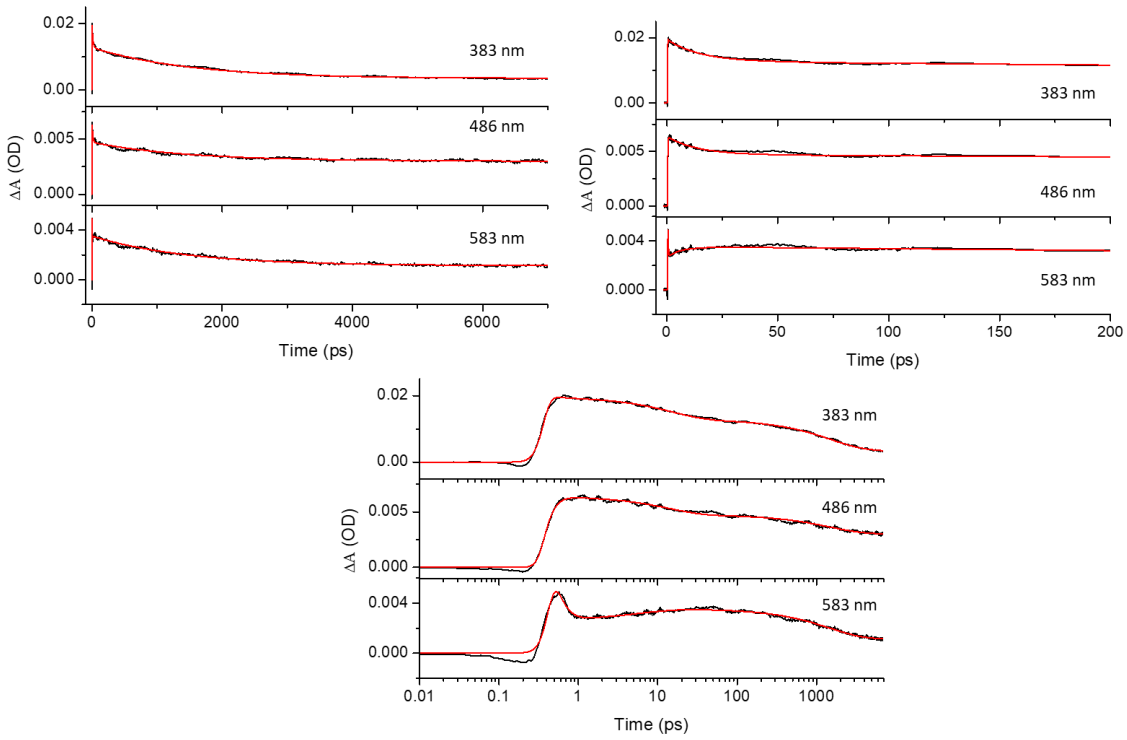

Compound	Wavelength (nm)	A_1	τ_1 (ps)	A_2	τ_2 (ps)	A_3	τ_3 (ps)
PyrSCF3	383	0.00037 ± 0.00004	0.50 ± 0.82	0.0065 ± 0.00015	15.06 ± 0.87	0.0093 ± 0.00009	1502 ± 44
	486	-0.0066 ± 0.0060	0.10 ± 0.01	0.0016 ± 0.00004	13.80 ± 0.93	0.0017 ± 0.00004	1471 ± 96
	583	0.0065 ± 0.0013	0.17 ± 0.02	-0.00082 ± 0.00006	6.07 ± 0.96	0.0024 ± 0.0004	1466 ± 77

Figure 241: *Ultrafast TA kinetic fits of PySPhCF$_3$ in acetonitrile. (Top) Single wavelength kinetic fits out to pump-probe delays of 7000 ps and 200 ps. (Middle) Single wavelength kinetic fits with a logarithmic x-axis. (Bottom) Time-components and amplitudes returned from single-wavelength fitting analysis.*

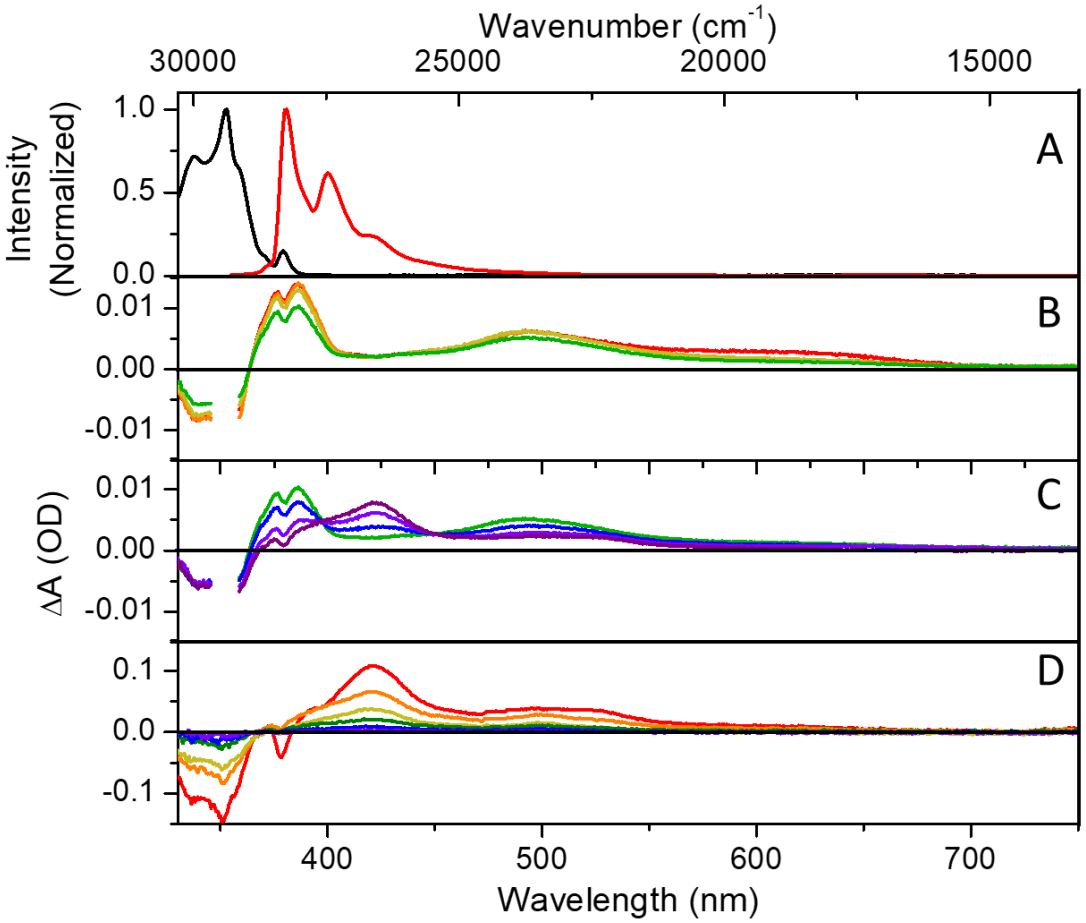

Figure 242. *(A) Steady-state absorbance and emission spectra of PySOPhCF$_3$ in acetonitrile. (B) Pump-probe transients collected at 0.6 ps (red), 2 ps (orange), 10 ps (yellow), and 50 ps (green) time delays. (C) Pump-probe transients collected at 50 ps (green), 500 ps (blue), 2 ns (violet), and 5 ns (purple) time delays. (D) Flash photolysis transients collected at 30 ns (red), 10 μs (orange), 20 μs (yellow), 50 μs (green), 100 μs (blue), and 200 μs (violet) time delays. Global fitting analysis reveals three time-components: τ_1 = 200 ± 20 fs, τ_2 = 25.9 ± 2.9 ps, τ_3 = 1590.0 ± 54.7 ps, and τ_4 = 26.48± 0.21 μs.*

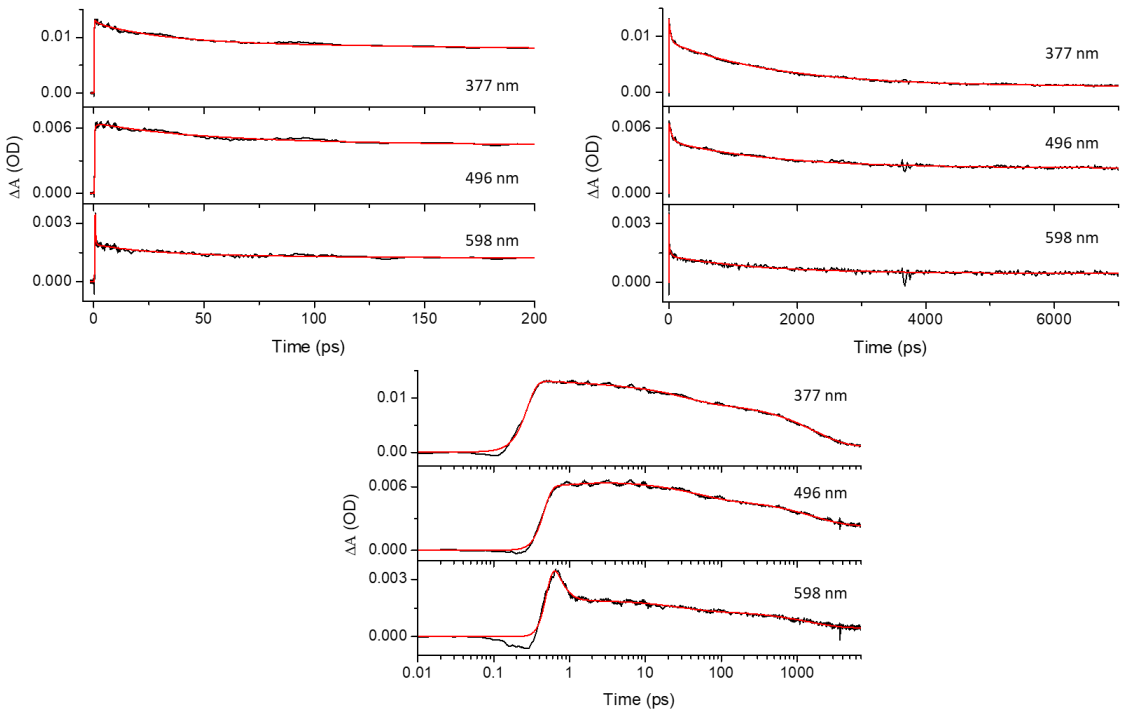

Compound	Wavelength (nm)	A_1	τ_1 (ps)	A_2	τ_2 (ps)	A_3	τ_3 (ps)
PyrSOCF3	377	0.00054 ± 0.00013	1.50 ± 0.76	0.0036 ± 0.00009	31.25 ± 2.8	0.0079 ± 0.00008	1680 ± 47
	496	-0.00046 ± 0.00011	1.04 ± 0.41	0.0017 ± 0.00007	46.99 ± 5.1	0.0025 ± 0.00006	1638 ± 110
	598	0.0039 ± 0.0006	0.24 ± 0.03	0.00057 ± 0.00005	28.13 ± 7.3	0.00089 ± 0.00004	1396 ± 180

Figure 243. *Ultrafast TA kinetic fits of PySOPhCF$_3$ in acetonitrile. (Top) Single wavelength kinetic fits out to pump-probe delays of 200 ps and 7000 ps. (Middle) Single wavelength kinetic fits with a logarithmic x-axis. (Bottom) Time-components and amplitudes returned from single-wavelength fitting analysis.*

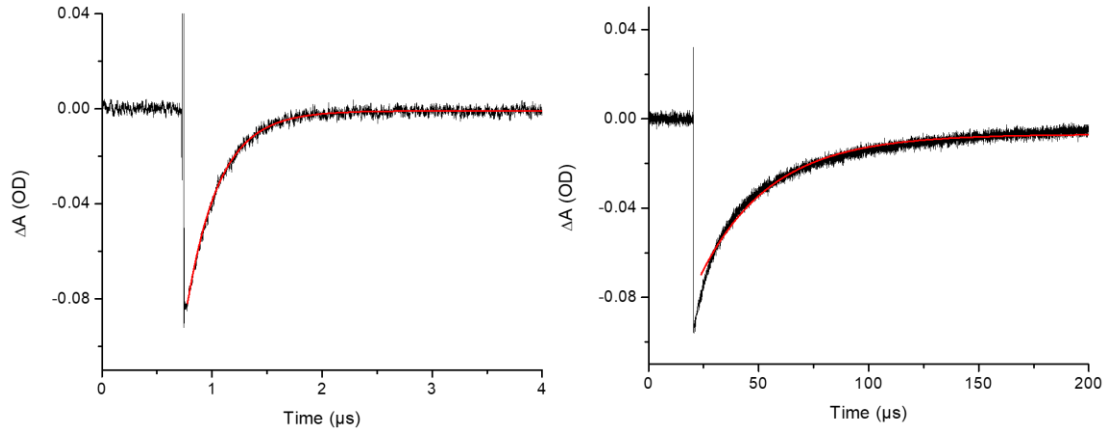

PySOMe	Wavelength (nm)	Non-Degassed	Degassed w/N_2
τ	335	294.18 ns	31.80μs

Figure 244. *Flash photolysis kinetics of $PySPhCF_3$ in acetonitrile under non-degassed and degassed conditions.*

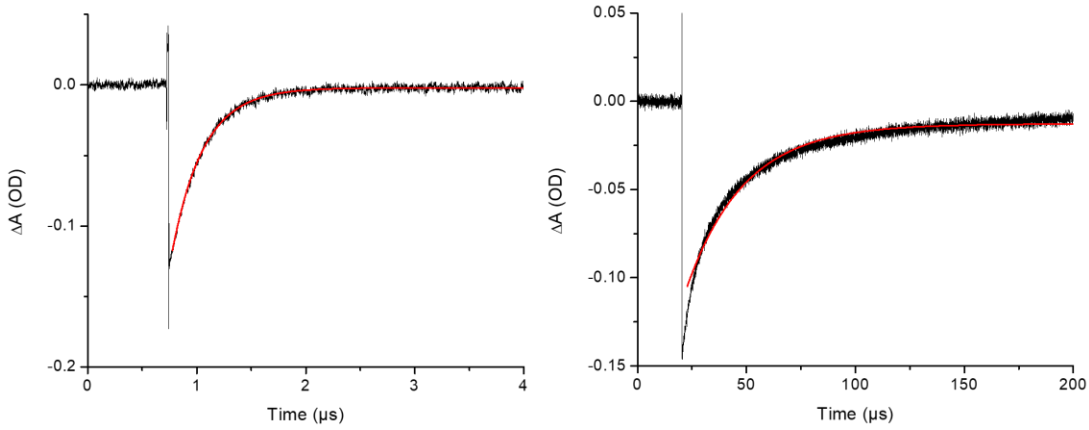

PySOMe	Wavelength (nm)	Non-Degassed	Degassed w/N_2
τ	335	288.78 ns	26.48μs

Figure 245. *Flash photolysis kinetics of $PySOPhCF_3$ in acetonitrile under non-degassed and degassed conditions.*

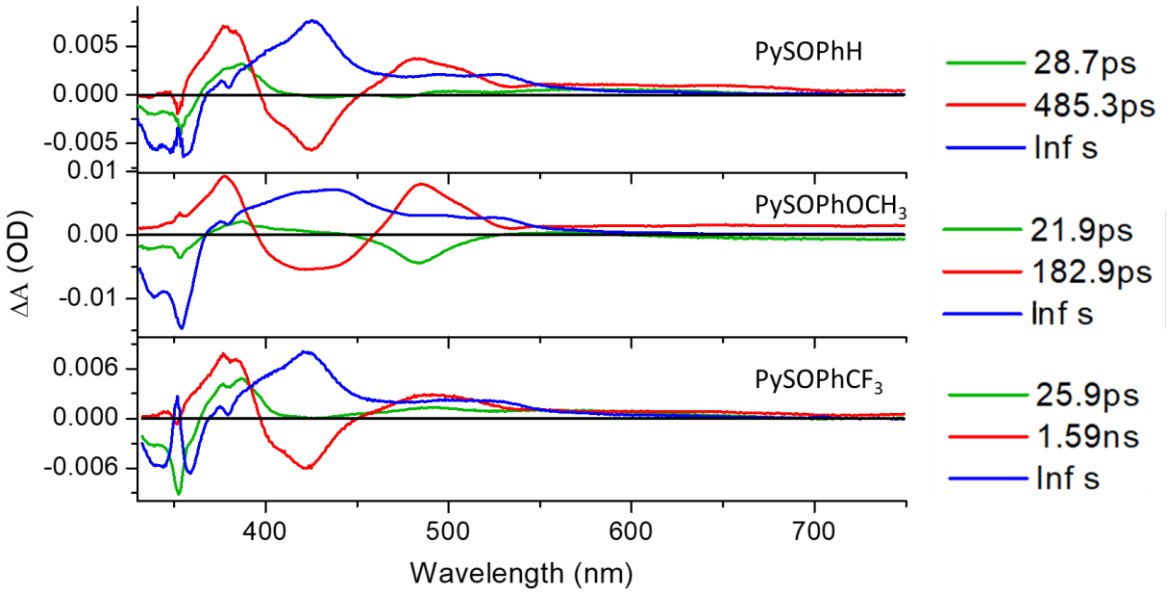

Figure 246. *Spectra returned from global fitting analysis of diaryl sulfoxides and the lifetimes corresponding to the spectra.*

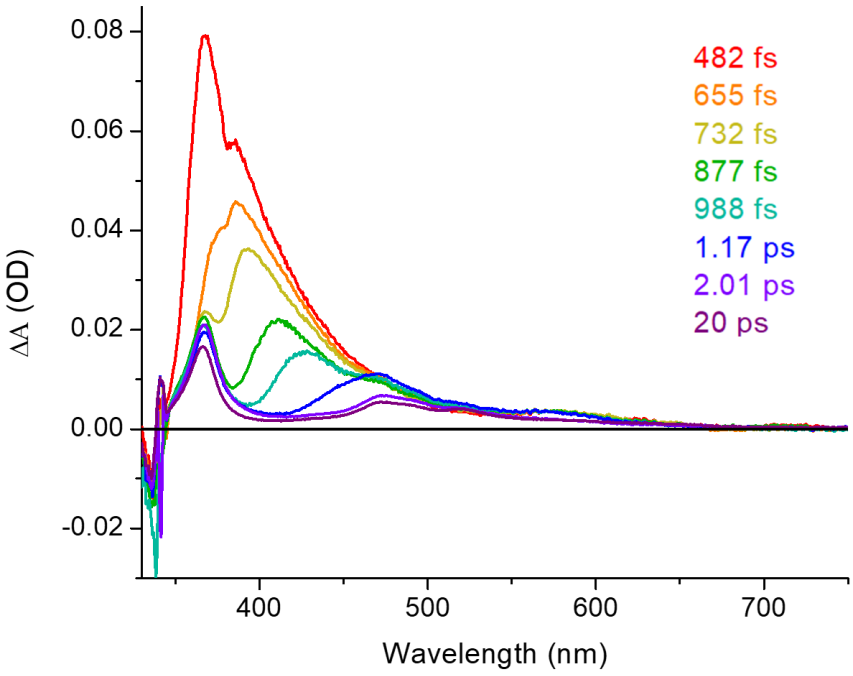

Figure 247. *Ultrafast pump-probe spectra of Pyrene in Toluene.*

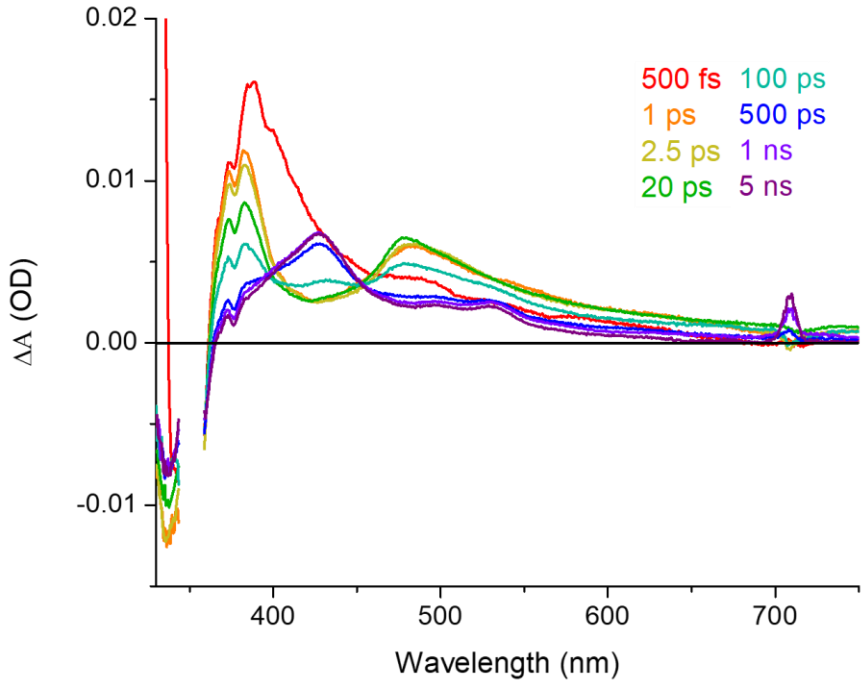

Figure 248. *Ultrafast pump-probe spectra of PySOPhH in Toluene.*

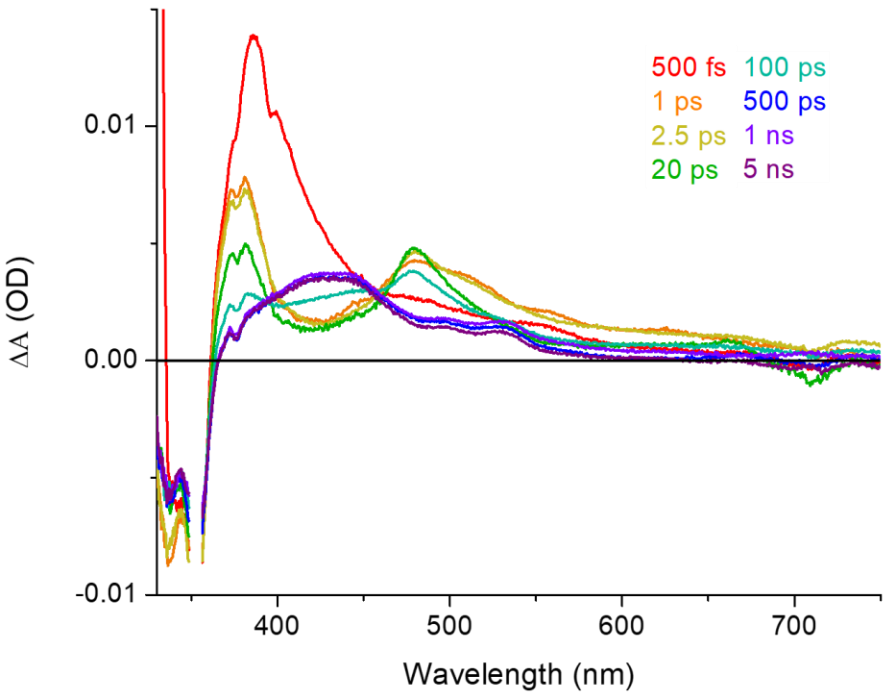

Figure 249. *Ultrafast pump-probe spectra of PySOPhOCH$_3$ in Toluene.*

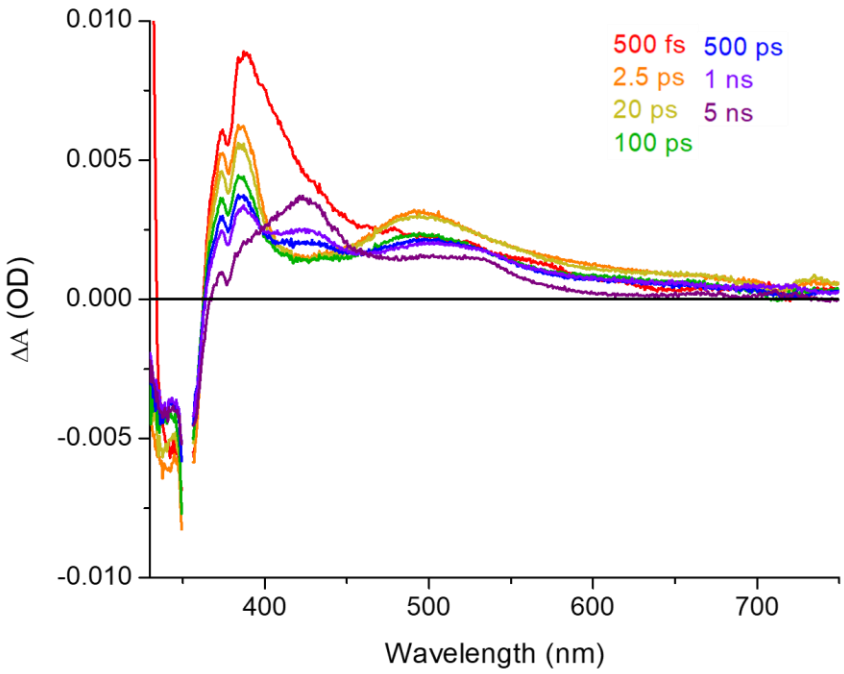

Figure 250. *Ultrafast pump-probe spectra of $PySOPhCF_3$ in Toluene.*

***Table 34**. Pump-probe single-wavelength kinetics of pyrene compounds in acetonitrile.*

Solvent	Compound	Wavelength (nm)	A_1	τ_1 (ps)	A_2	τ_2 (ps)	A_3	τ_3 (ps)
Acetonitrile	PyrSOMe	381	--	--	0.0023 ± 0.00001	21.99 ± 2.8	0.030 ± 0.00001	1109 ± 10
		421	--	--	--	--	-0.016 ± 0.00010	991 ±19
		574	0.030 ± 0.0039	0.11 ± 0.06	0.0010 ± 0.00001	4.92 ± 0.84	0.0011 ± 0.00001	1209 ± 160
	PyrSMe	383	0.0044 ± 0.00045	0.226 ± 0.04	0.0018 ± 0.00034	2.21 ± 0.44	-0.014 ± 0.00023	4868 ± 160
		421	--	--	0.00276 ± 0.00022	6.83 ± 1.6	0.020 ± 0.00087	4813 ± 400
		578	-0.0044 ± 0.00021	0.86 ± 0.08	0.0021 ± 0.00012	28.61 ± 4.9	0.020 ± 0.00025	4334 ± 130
	PyrSOPh	386	-0.061 ± 5.56	0.07 ± 0.01	0.0028 ± 0.00012	28.09 ± 2.6	0.0061 ± 0.00012	401.7 ± 14.0
		429	0.000005 ± 0.00012	0.42 ± 11	-0.000017 ± 0.00029	94.25 ± 1400	-0.0053 ± 0.00029	401 ± 17
		586	0.0027 ± 0.00032	0.20 ± 0.02	0.00046 ± 0.00007	67.05 ± 15.0	0.00094 ± 0.00007	632.8 ± 59.0
	PyrSPh	383	0.0037 ± 0.00008	1.39 ± 0.07	0.0006 ± 0.0003	82.12 ± 46.0	0.0047 ± 0.00039	528.1 ± 32.0
		424	0.00058 ± 0.00007	0.89 ± 0.22	-0.00038 ± 0.00007	10.95 ± 3.7	-0.0048 ± 0.00002	448.5 ± 5.9
		576	-0.0024 ± 0.00008	2.38 ± 0.19	0.0015 ± 0.00007	23.8 ± 2.8	0.0034 ± 0.00004	517.2 ± 11.0

Table 35. *Pump-probe single-wavelength kinetics of pyrene compounds in acetonitrile.*

Solvent	Compound	Wavelength (nm)	A_1	τ_1 (ps)	A_2	τ_2 (ps)	A_3	τ_3 (ps)
Acetonitrile	PyrSOOCH3	352	-0.012 ± 0.0099	0.10 ± 0.05	-0.00097 ± 0.00076	18.98 ± 26.0	0.0019 ± 0.00078	194.5 ± 130.0
		431	-0.00029 ± 0.00023	0.30 ± 0.29	0.00034 ± 0.0001	20.39 ± 13.0	-0.0046 ± 0.00011	195.0 ± 7.3
		483	-0.0077 ± 0.0017	0.15 ± 0.01	-0.0031 ± 0.00013	21.40 ± 1.7	0.0062 ± 0.00014	195.1 ± 6.8
	PyrSOCH3	366	-0.0038 ± 0.0014	0.10 ± 0.05	0.0030 ± 0.00033	2.36 ± 0.75	-0.0004 ± 0.0002	65.28 ± 80.0
		495	-0.0016 ± 0.0022	0.21 ± 0.19	-0.013 ± 0.00023	4.87 ± 0.20	0.014 ± 0.00025	61.53 ± 1.4
		581	-0.015 ± 0.0032	0.13 ± 0.01	-0.0032 ± 0.00009	2.67 ± 0.23	0.0078 ± 0.00008	65.43 ± 1.2
	PyrSOCF3	377	0.00054 ± 0.00013	1.50 ± 0.76	0.0036 ± 0.00009	31.25 ± 2.8	0.0079 ± 0.00008	1680 ± 47
		496	-0.00046 ± 0.00011	1.04 ± 0.41	0.0017 ± 0.00007	46.99 ± 5.1	0.0025 ± 0.00006	1638 ± 110
		598	0.0039 ± 0.0006	0.24 ± 0.03	0.00057 ± 0.00005	28.13 ± 7.3	0.00089 ± 0.00004	1396 ± 180
	PyrSCF3	383	0.00037 ± 0.00004	0.50 ± 0.82	0.0065 ± 0.00015	15.06 ± 0.87	0.0093 ± 0.00009	1502 ± 44
		486	-0.0066 ± 0.0060	0.10 ± 0.01	0.0016 ± 0.00004	13.80 ± 0.93	0.0017 ± 0.00004	1471 ± 96
		583	0.0065 ± 0.0013	0.17 ± 0.02	-0.00082 ± 0.00006	6.07 ± 0.96	0.0024 ± 0.0004	1466 ± 77

***Table 36**. Pump-probe single-wavelength kinetics of pyrene compounds in toluene.*

Solvent	Compound	Wavelength (nm)	A_1	τ_1 (ps)	A_2	τ_2 (ps)	A_3	τ_3 (ps)
Toluene	PyrSOMe	375	0.350 ± 0.074	0.10 ± 0.07	-0.0027 ± 0.0008	1.76 ± 0.67	0.008 ± 0.0002	1804 ± 160
		424	0.175 ± 0.033	0.10 ± 0.06	-0.0004 ± 0.0005	1.51 ± 2.60	-0.0046 ± 0.0001	1498 ± 120
		492	0.0087 ± 0.013	0.10 ± 0.04	-0.0007 ± 0.00006	26.83 ± 7.4	-0.0028 ± 0.00007	1886 ± 150
	PyrSOPh	383	0.062 ± 0.0021	0.18 ± 0.06	0.0038 ± 0.0005	27.43 ± 6.9	0.0045 ± 0.0005	300 ±54
		418	0.016 ± 0.0005	0.35 ±0.02	0.0003 ± 0.002	66.72 ± 280	-0.0038 ± 0.0018	247 ±76
		611	-0.0033 ± 0.0004	0.34 ± 0.03	0.0006 ± 0.00008	17.09 ± 5.50	0.0012 ± 0.00007	299 ± 39
	PyrSOOCH3	381	0.048 ± 0.002	0.18 ± 0.01	--	--	0.0055 ± 0.0001	51 ± 4
		430	0.0072 ± 0.0003	0.43 ± 0.01	--	--	-0.0020 ± 0.00006	95 ± 10
		580	-0.004 ± 0.002	0.31 ± 0.08	0.0003 ±0.0002	7.53 ± 9.90	0.0012 ± 0.0002	114 ± 28
	PyrSOCF3	385	0.035 ± 0.001	0.19 ± 0.01	0.0019 ± 0.0002	46.03 ± 10.00	0.0028 ± 0.0002	1637 ± 240
		424	0.0086 ± 0.0003	0.42 ± 0.03	-0.0005 ± 0.0003	3.00 ± 2.30	-0.0022 ± 0.00005	1499 ± 120
		603	-0.0031 ± 0.0011	0.29 ± 0.05	0.0003 ± 0.00005	36.80 ± 17.00	0.0007 ± 0.00005	1726 ± 320

Table 37. *Pump-probe single-wavelength kinetics of PySOMe in various solvents.*

Solvent	Compound	Wavelength (nm)	A_1	τ_1 (ps)	A_2	τ_2 (ps)	A_3	τ_3 (ps)
DCE	PyrSOMe	383			-0.0024 ± 0.00009	21.29 ± 2.0	0.015 ± 0.00015	3090 ± 94
		422					-0.0085 ± 0.00010	2667 ± 71
		576	0.011 ± 0.00087	0.11 ± 0.01	0.00009 ± 0.00006	22.96 ± 38.0	0.00079 ± 0.00009	2986 ± 990
EG	PyrSOMe	385			-0.00078 ± 0.00022	196.0 ± 98	0.011 ± 0.0035	10550 ± 5100
		427					-0.0047 ± 0.00053	6125 ± 1100
		585	0.0053 ± 0.00063	0.13 ± 0.01	-0.00028 ± 0.00011	249.7 ± 170.0	0.0027 ± 0.0014	10000 ± 8100
Hexane	PyrSOMe	379			0.0038 ± 0.00026	1.40 ± 0.18	0.0094 ± 0.00019	2146 ± 120
		421			0.00067 ± 0.00008	2.06 ± 0.59	-0.0044 ± 0.00013	3018 ± 210
		581	0.011 ± 0.00081	0.12 ± 0.01	0.00072 ± 0.00007	1.51 ± 0.30	0.00055 ± 0.00007	2996 ± 870

Appendix C. Chapter 5 Supporting Information

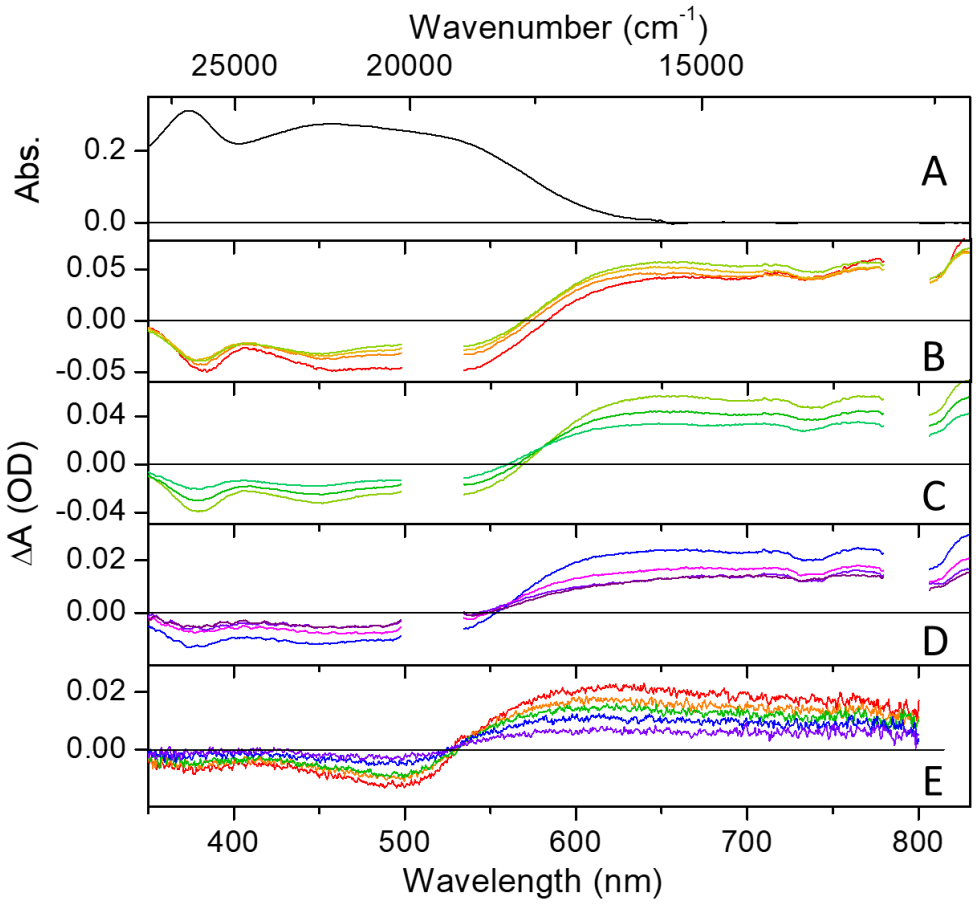

Figure 251. *(A) Absorbance spectrum of RWPt-4 (B) Pump-probe transients collected at 0.5 ps (red), 1 ps (orange), 2 ps (amber), and 5.3 ps (yellow) time delays. (C) Pump-probe transients collected at 5.3 ps (yellow-green), 20 ps (green), and 50 ps (cyan). (D) Pump-probe transients collected at 100 ps (blue), 300 ps (pink) 1 ns (violet), and 6 ns (purple). (E) Flash photolysis transients collected at 30 ns (red), 1 μs (orange), 2 μs (green), 3 μs (blue), and 5 μs (violet). Global fitting analysis reveals four time components:* $\tau_1 = 220 \pm 30$ *fs,* $\tau_2 = 1.6 \pm 0.3$ *ps,* $\tau_3 = 41 \pm 6$ *ps, and* $\tau_4 = 694 \pm 198$ *ps.*

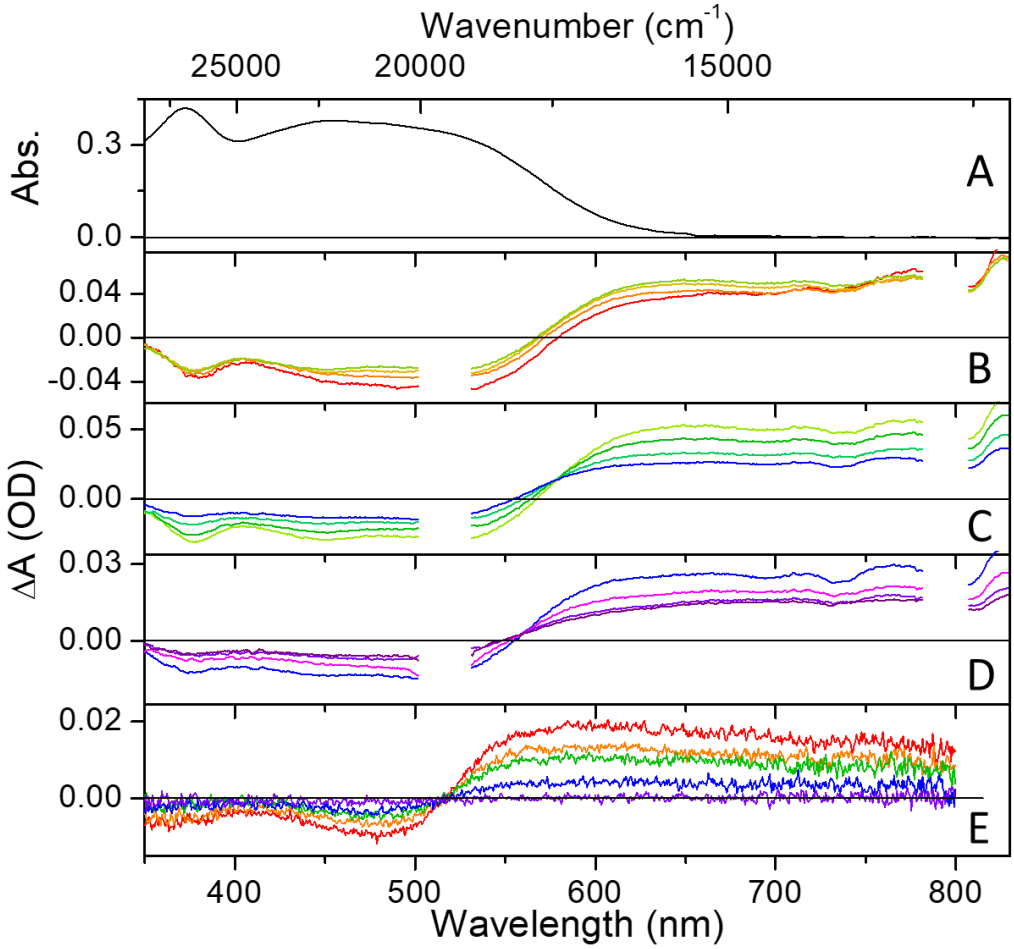

Figure 252. *(A) Absorbance spectrum of RWPt-5 (B) Pump-probe transients collected at 0.5 ps (red), 1 ps (orange), 2 ps (amber), and 5.5 ps (yellow) time delays. (C) Pump-probe transients collected at 5.5 ps (yellow-green), 20 ps (green), and 50 ps (cyan) and 100 ps (blue). (D) Pump-probe transients collected at 100 ps (blue), 300 ps (pink) 1 ns (violet), and 6 ns (purple). (E) Flash photolysis transients collected at 30 ns (red), 1 μs (orange), 2 μs (green), 5 μs (blue), and 15 μs (violet). Global fitting analysis reveals four time components:* $\tau_1 = 140 \pm 40$ *fs,* $\tau_2 = 1.2 \pm 0.2$ *ps,* $\tau_3 = 36.7$ *ps* ± 5.6 *ps, and* $\tau_4 = 702 \pm 186$ *ps.*

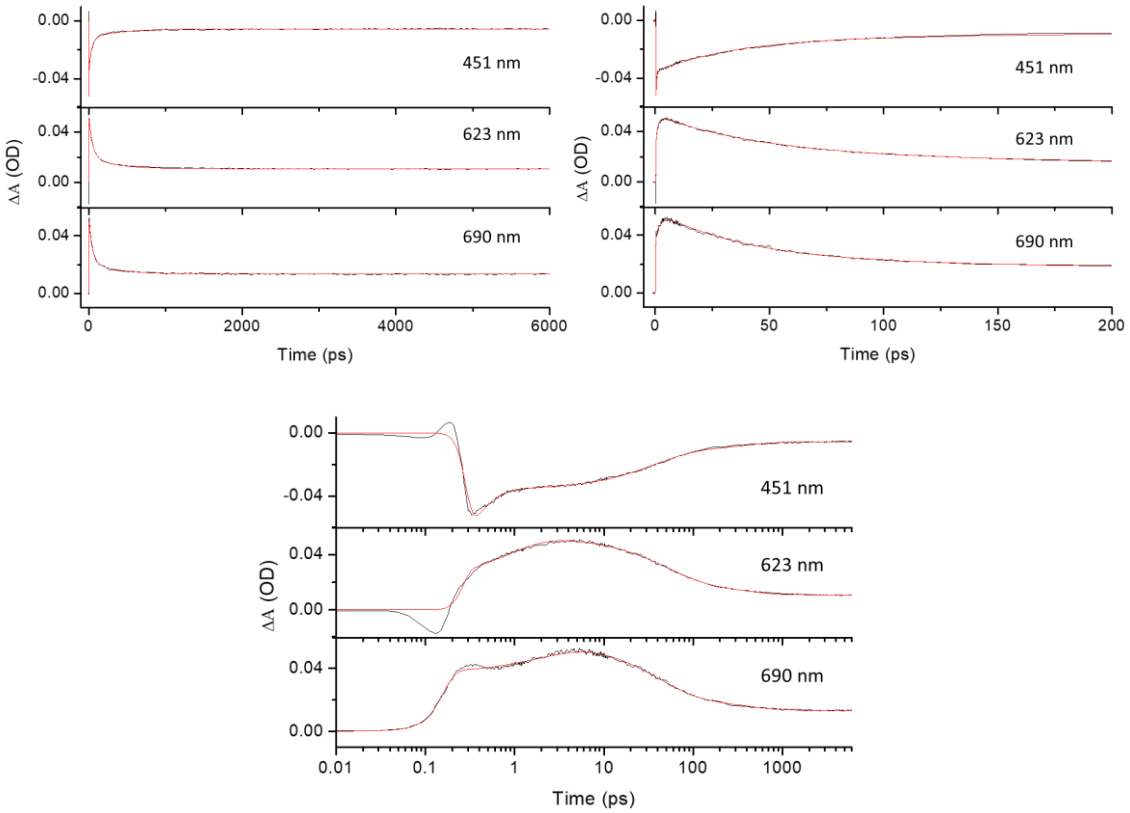

Compound	Wavelength (nm)	A_1	τ_1 (ps)	A_2	τ_2 (ps)	A_3	τ_3 (ps)	A_4	τ_4 (ps)
RWPt-4	451	-0.03 ± 0.0027	0.22 ± 0.03	--	--	-0.023 ± 0.0019	35.12 ± 5.0	-0.0071 ± 0.0020	693.4 ± 303
	623	--	--	-0.025 ± 0.0017	0.85 ± 0.10	0.032 ± 0.0051	48.16 ± 10.0	0.010 ± 0.0054	693.8 ± 180
	690	--	--	-0.018 ± 0.0007	2.35 ± 0.20	0.034 ± 0.0014	40.03 ± 3.5	0.0088 ± 0.0017	696.9 ± 192

Figure 253: *Ultrafast TA kinetic fits of RWPt-4 in DCE. (Top) Single wavelength kinetic fits out to pump-probe delays of 6000 ps and 200 ps. (Middle) Single wavelength kinetic fits with a logarithmic x-axis. (Bottom) Time-components and amplitudes returned from single-wavelength fitting analysis.*

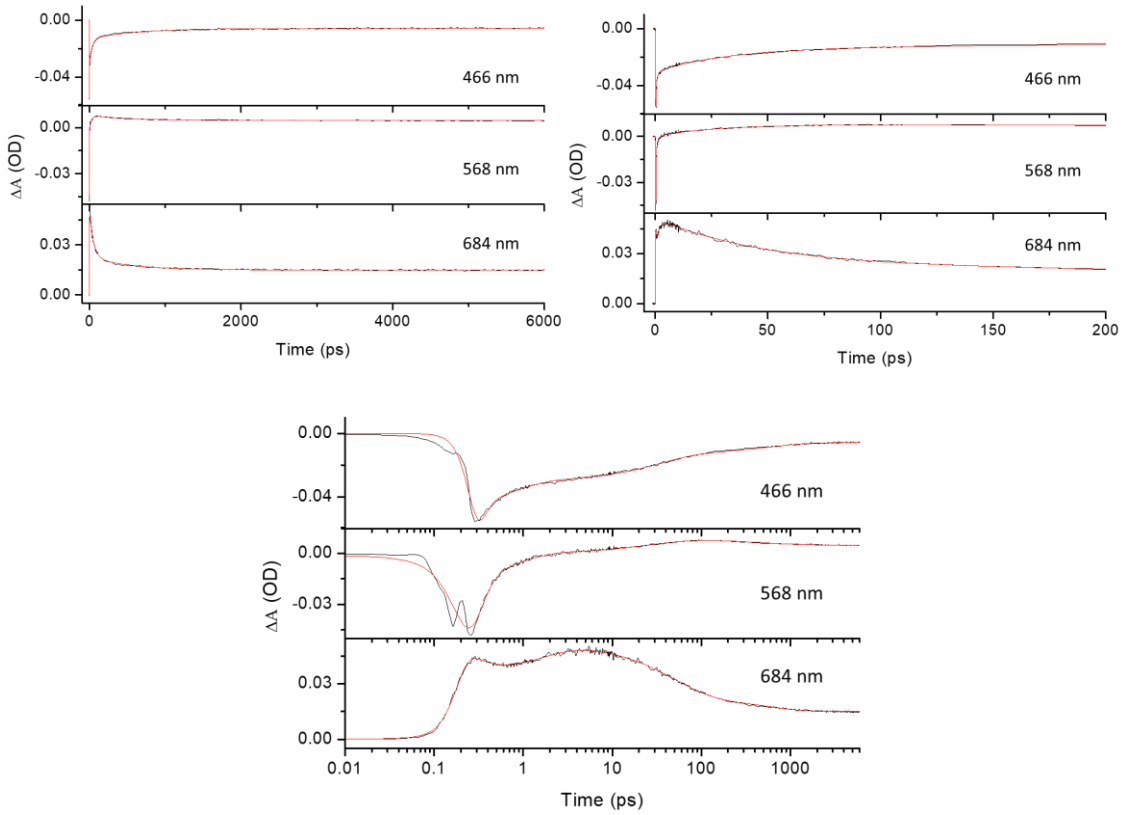

Compound	Wavelength (nm)	A_1	τ_1 (ps)	A_2	τ_2 (ps)	A_3	τ_3 (ps)	A_4	τ_4 (ps)
RWPt-5	466	-0.16 ± 2.8	0.06 ± 0.03	-0.015 ± 0.0028	0.68 ± 0.14	-0.017 ± 0.00084	33.80 ± 4.80	-0.0076 ± 0.0010	`709.8 ± 181.0
	568	-0.15 ± 0.076	0.10 ± 0.03	-0.016 ± 0.0054	0.71 ± 0.24	-0.0081 ± 0.0009	27.18 ± 9.20	0.0034 ± 0.0009	736.7 ± 385.0
	684	0.016 ± 0.0018	0.21 ± 0.05	-0.018 ± 0.0015	1.47 ± 0.18	0.029 ± 0.0008	49.09 ± 2.90	0.0079 ± 0.00095	536.1 ± 84.0

Figure 254: *Ultrafast TA kinetic fits of RWPt-5 in DCE. (Top) Single wavelength kinetic fits out to pump-probe delays of 6000 ps and 200 ps. (Middle) Single wavelength kinetic fits with a logarithmic x-axis. (Bottom) Time-components and amplitudes returned from single-wavelength fitting analysis.*

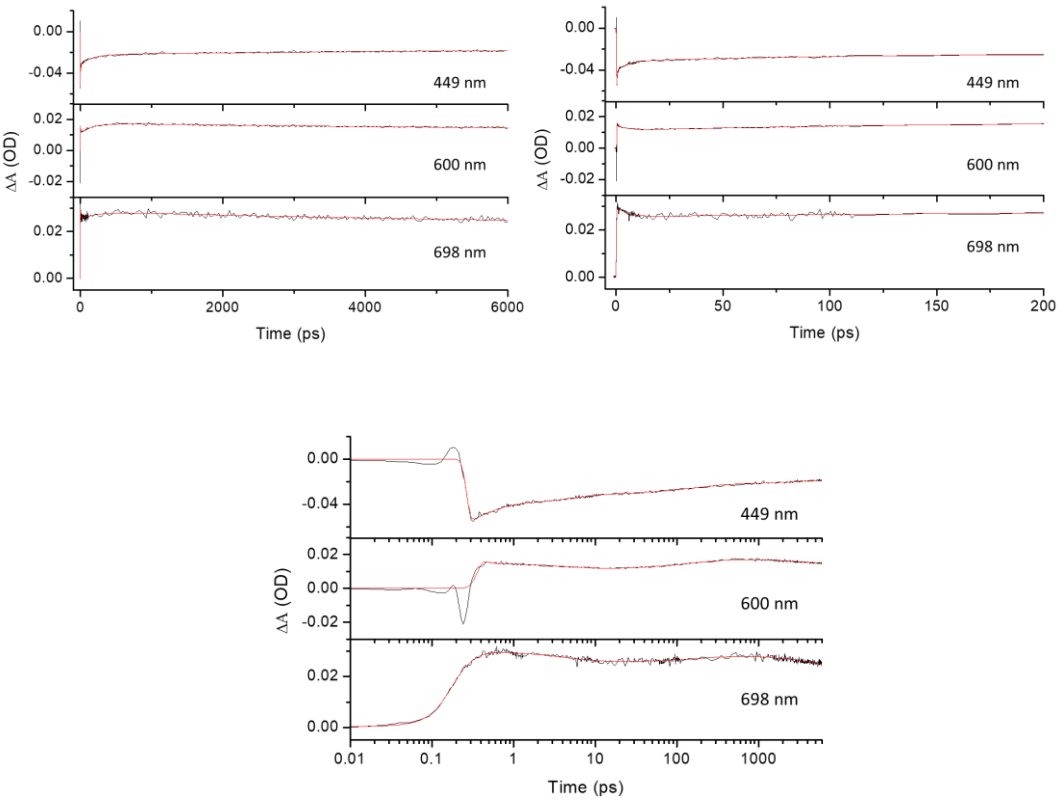

Compound	Wavelength (nm)	A_1	τ_1 (ps)	A_2	τ_2 (ps)	A_3	τ_3 (ps)	A_4	τ_4 (ps)
RWPt-7	449	-0.117 ± 0.17	0.09 ± 0.03	-0.013 ± 0.0009	4.35 ± 0.80	-0.009 ± 0.001	285.8 ± 104	-0.021 ± 0.0008	35000 ± 16800
	600	-0.21 ± 0.99	0.08 ± 0.01	0.0035 ± 0.0005	3.42 ± 1.38	-0.0051 ± 0.0005	286.0 ± 98.9	0.017 ± 0.0005	35000 ± 11700
	698	-0.0069 ± 0.028	0.19 ± 0.01	0.00366 ± 0.0006	3.38 ± 1.14	-0.0029 ± 0.0004	397.2 ± 195	0.029 ± 0.006	35000 ± 6190

Figure 255: *Ultrafast TA kinetic fits of RWPt-7 in DCE. (Top) Single wavelength kinetic fits out to pump-probe delays of 6000 ps and 200 ps. (Middle) Single wavelength kinetic fits with a logarithmic x-axis. (Bottom) Time-components and amplitudes returned from single-wavelength fitting analysis.*

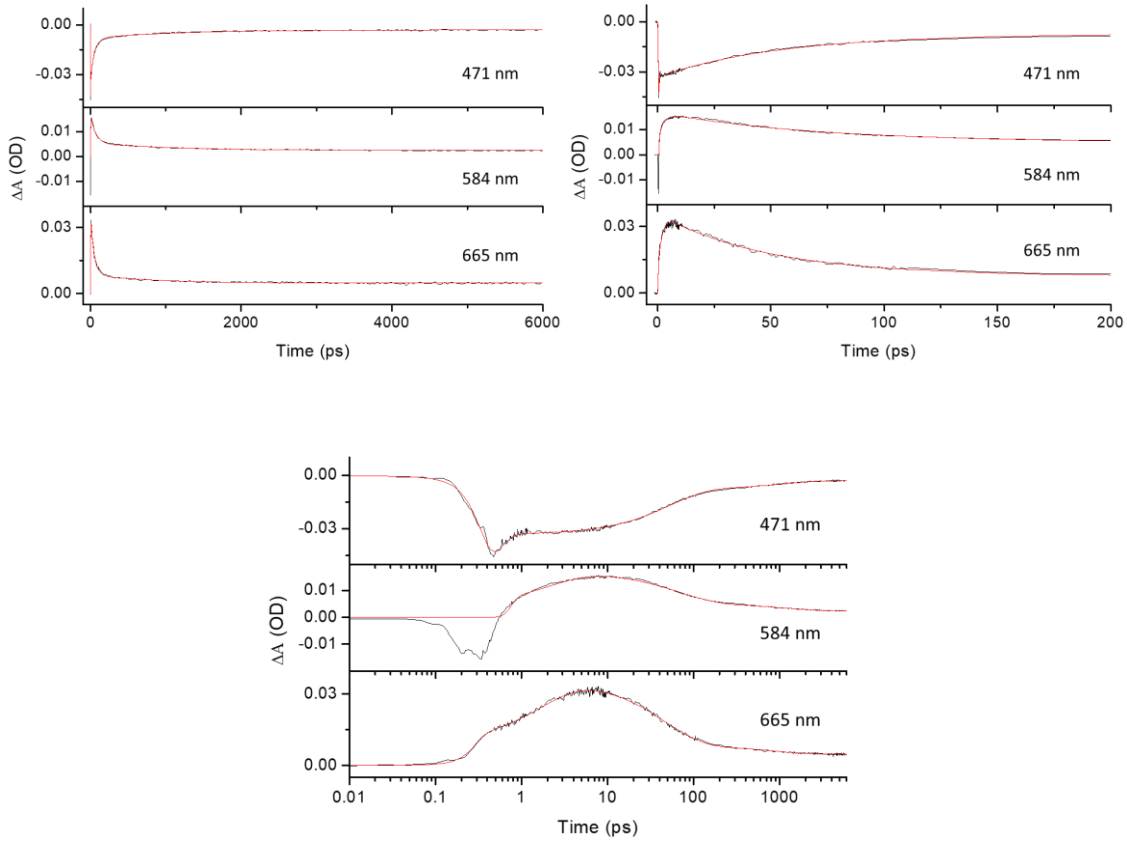

Compound	Wavelength (nm)	A_1	τ_1 (ps)	A_2	τ_2 (ps)	A_3	τ_3 (ps)	A_4	τ_4 (ps)
RWPt-6	471	-0.14 ± 1.6	0.12 ± 0.02	--	--	-0.025 ± 0.0007	52.30 ± 3.20	-0.005 ± 0.0007	1166 ± 310
	584	--	--	-0.0092 ± 0.0019	2.19 ± 1.30	0.011 ± 0.0033	67.90 ± 39.0	0.0029 ± 0.0032	1167 ± 2200
	665	--	--	-0.023 ± 0.0004	1.82 ± 0.09	0.027 ± 0.0005	47.17 ± 2.40	0.0037 ± 0.0006	837.1 ± 220.0

Figure 256: *Ultrafast TA kinetic fits of RWPt-6 in DCE. (Top) Single wavelength kinetic fits out to pump-probe delays of 6000 ps and 200 ps. (Middle) Single wavelength kinetic fits with a logarithmic x-axis. (Bottom) Time-components and amplitudes returned from single-wavelength fitting analysis.*

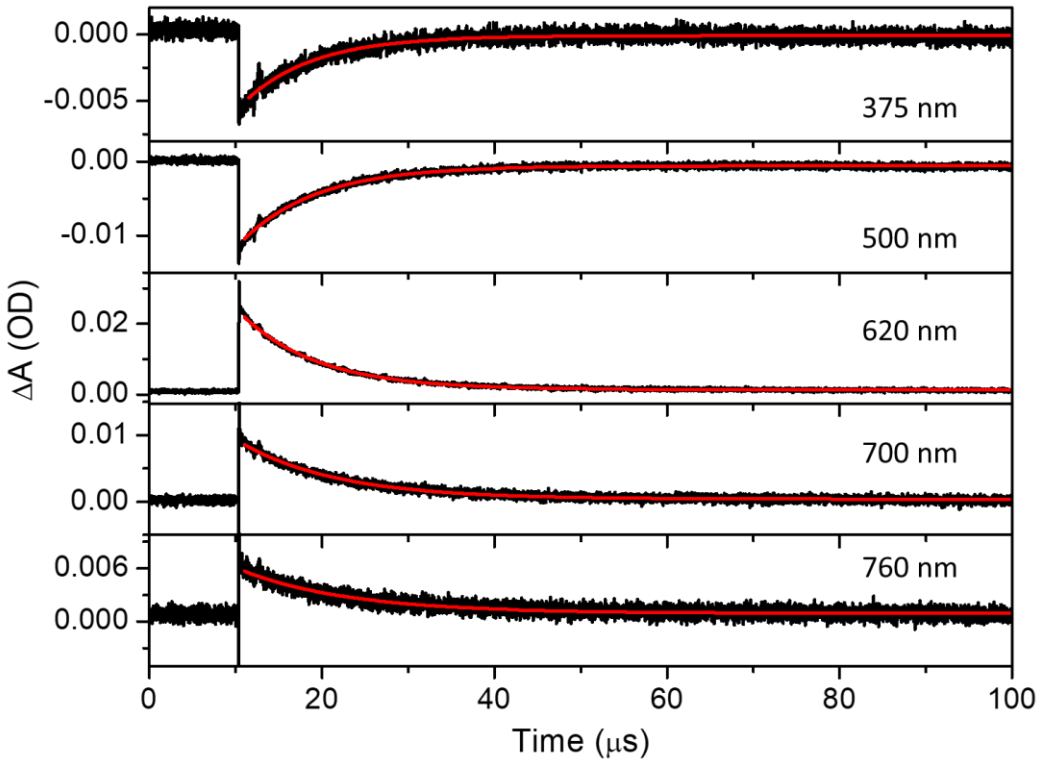

Compound	Wavelength (nm)	A_5	τ_5 (μs)
RWPt-4	375	-0.0047 ± 0.000024	8.09 ± 0.07
	500	-0.0099 ± 0.000017	8.70 ± 0.02
	620	0.021 ± 0.000017	8.91 ± 0.01
	700	0.0082 ± 0.000022	11.32 ± 0.05
	760	0.0047 ± 0.000030	12.67 ± 0.15

Figure 257: *Nanosecond flash photolysis kinetic fits of RWPt-4 in DCE. (Top) Single wavelength kinetic fits out to 100 microseconds. (Bottom) Time-components and amplitudes returned from single-wavelength fitting analysis.*

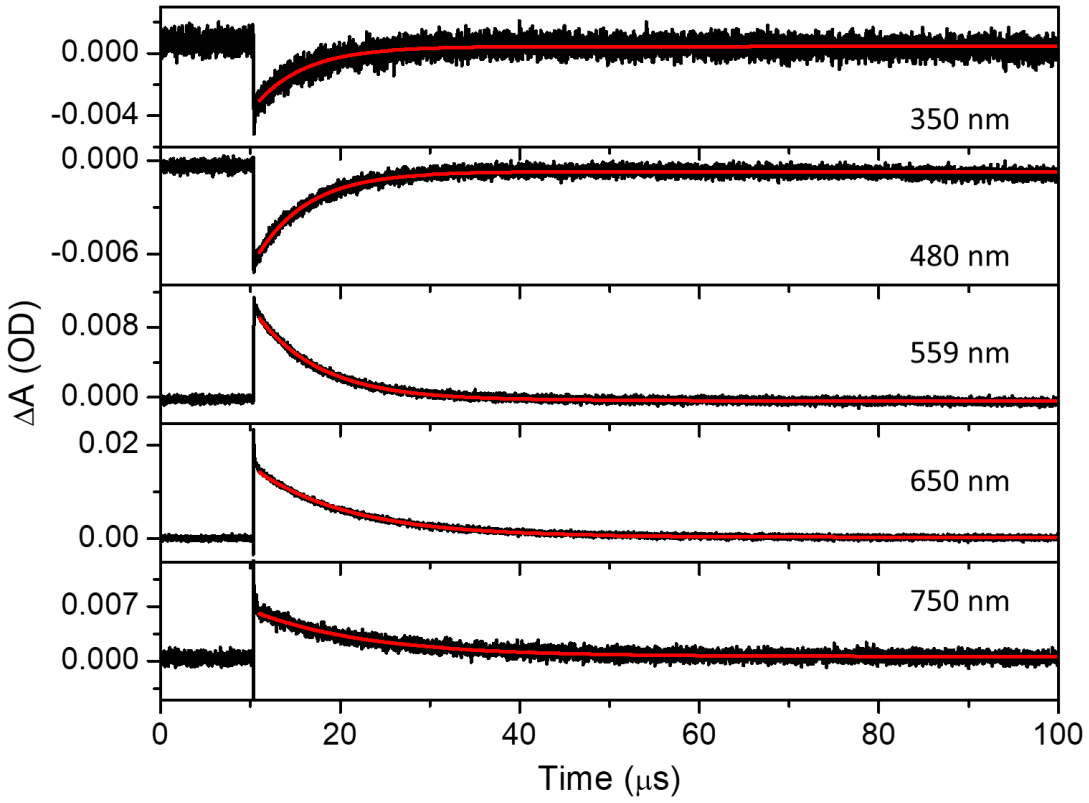

Compound	Wavelength (nm)	A_5	τ_5 (μs)
RWPt-5	350	-0.00348 ± 0.000040	5.56 ± 0.10
	480	-0.0052 ± 0.000020	5.74 ± 0.03
	595	0.0094 ± 0.000017	7.20 ± 0.02
	650	0.014 ± 0.000018	10.76 ± 0.02
	750	0.0055 ± 0.000027	12.90 ± 0.12

Figure 258: *Nanosecond flash photolysis kinetic fits of RWPt-5 in DCE. (Top) Single wavelength kinetic fits out to 100 microseconds. (Bottom) Time-components and amplitudes returned from single-wavelength fitting analysis.*

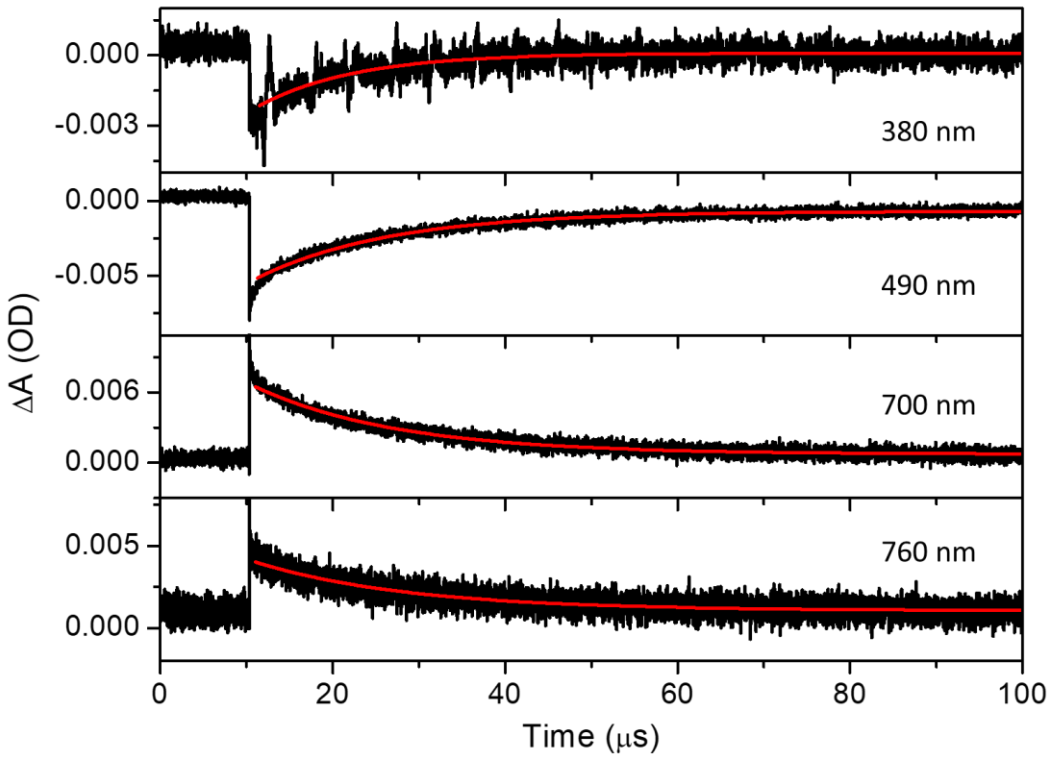

Compound	Wavelength (nm)	A_5	τ_5 (μs)
RWPt-7	380	-0.00223 ± 0.000020	11.35 ± 0.18
	490	-0.00446 ± 0.000011	15.72 ±0.08
	700	0.00576 ± 0.000018	16.75 ± 0.11
	760	0.00296 ± 0.000026	18.06 ± 0.35

Figure 259: *Nanosecond flash photolysis kinetic fits of RWPt-7 in DCE. (Top) Single wavelength kinetic fits out to 100 microseconds. (Bottom) Time-components and amplitudes returned from single-wavelength fitting analysis.*

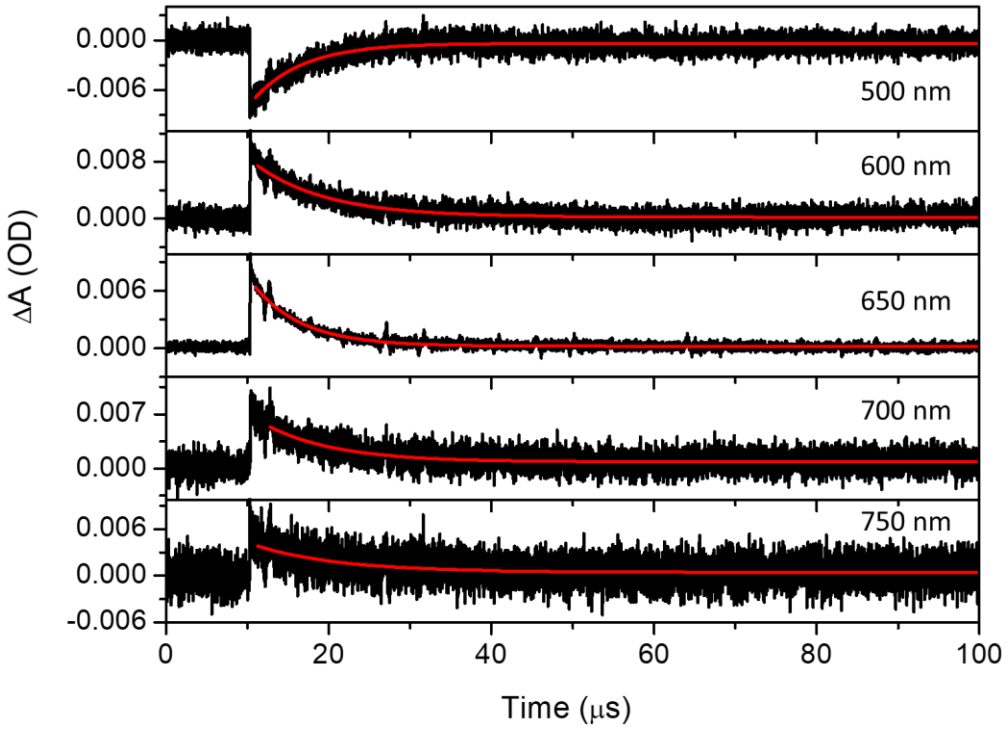

Compound	Wavelength (nm)	A_5	τ_5 (μs)
RWPt-6	500	-0.0065 ± 0.000071	6.14 ± 0.10
	600	0.0072 ± 0.000062	8.79 ± 0.12
	650	0.0062 ±0.000022	6.02 ± 0.03
	700	0.0045 ± 0.000081	8.58 ± 0.25
	750	0.0034 ± 0.00011	10.45 ± 0.57

Figure 260: *Nanosecond flash photolysis kinetic fits of RWPt-6 in DCE. (Top) Single wavelength kinetic fits out to 100 microseconds. (Bottom) Time-components and amplitudes returned from single-wavelength fitting analysis.*

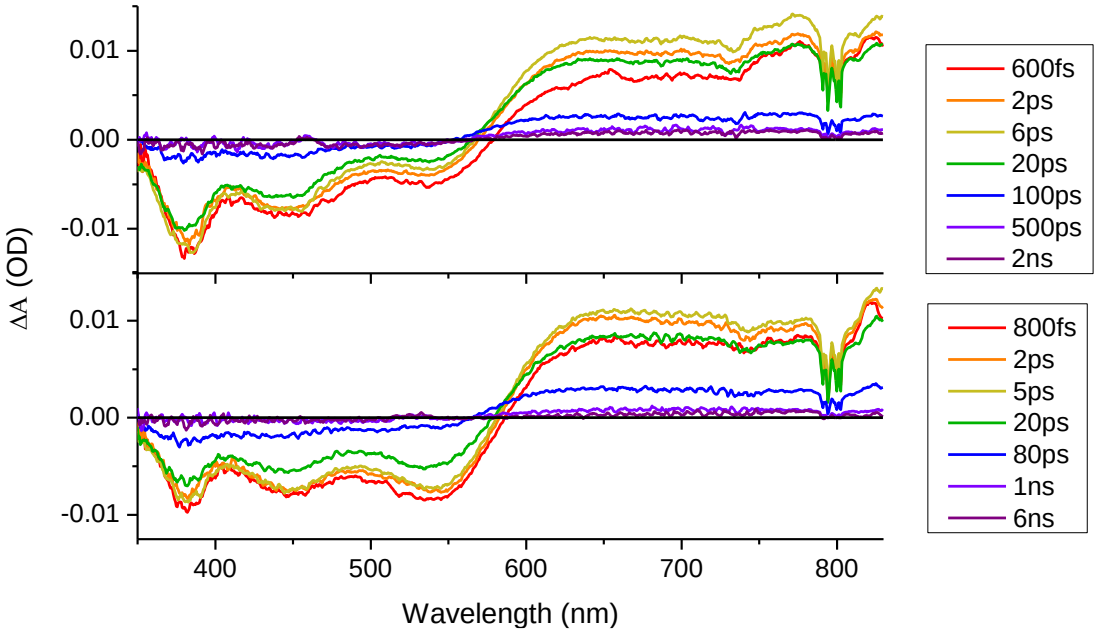

Figure 261: *Ultrafast TA Spectra of RWPt-4 excited at 450 nm (top) and 520 nm (bottom).*

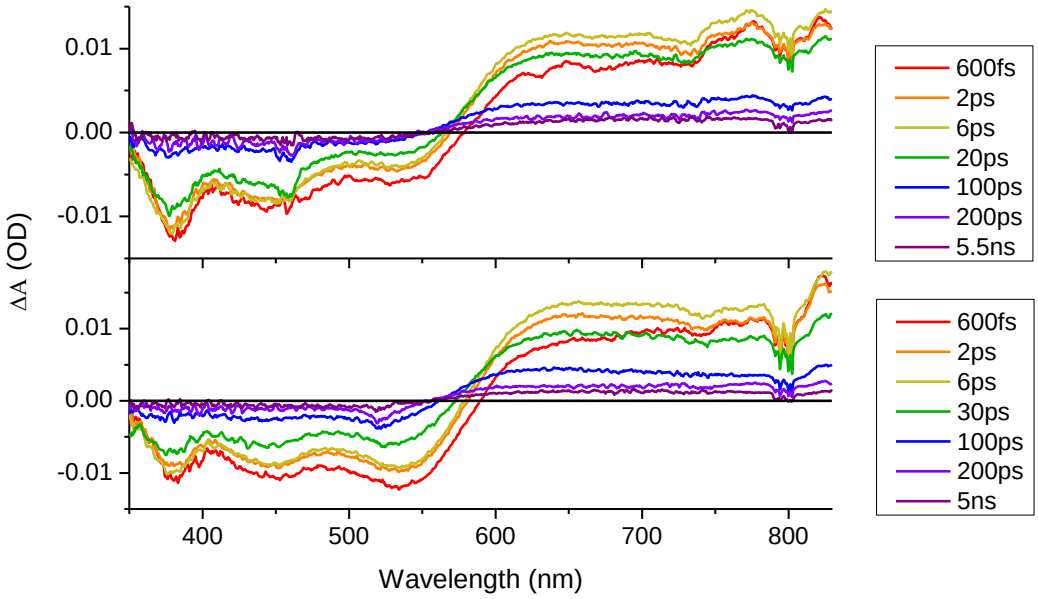

Figure 262: *Ultrafast TA Spectra of RWPt-5 excited at 450 nm (top) and 520 nm (bottom).*

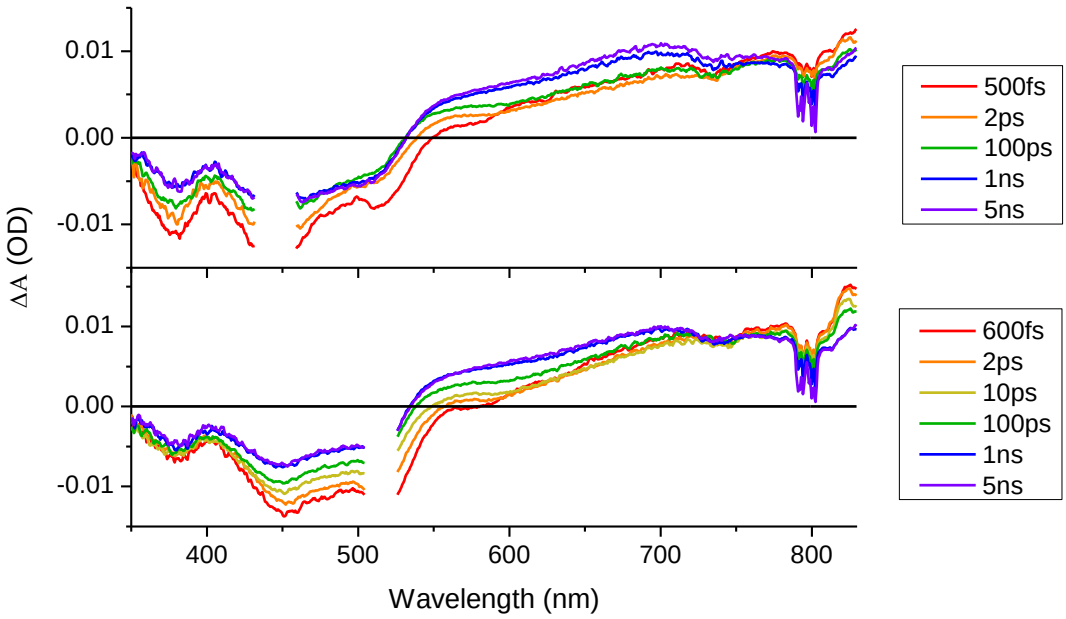

Figure 263: *Ultrafast TA Spectra of RWPt-7 excited at 440 nm (top) and 510 nm (bottom).*

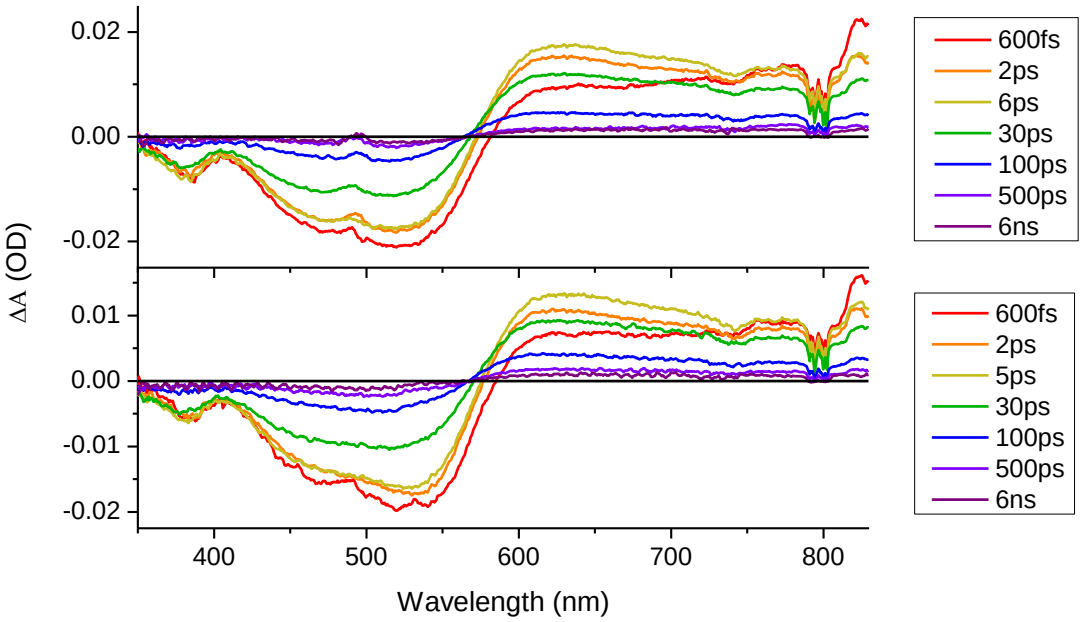

Figure 264: *Ultrafast TA Spectra of RWPt-6 excited at 480 nm (top) and 520 nm (bottom).*

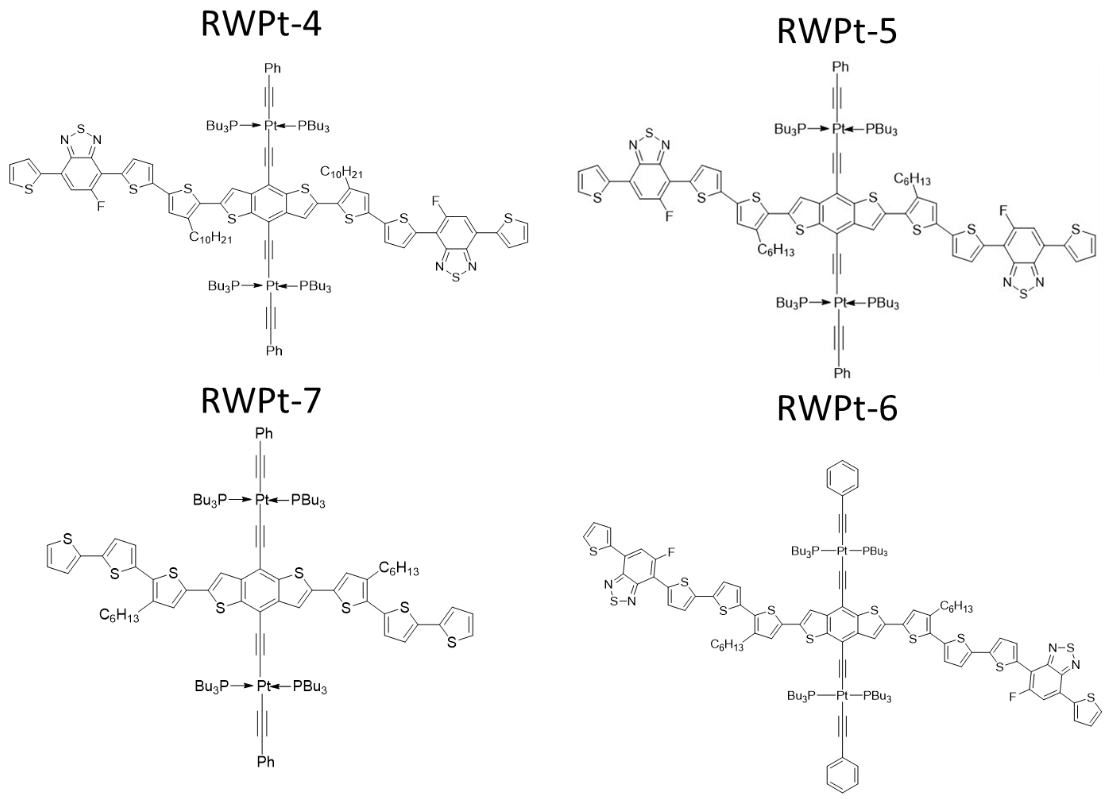

Figure 266*. Bond-line drawings for the platinum roller wheel complexes investigated in this study.*

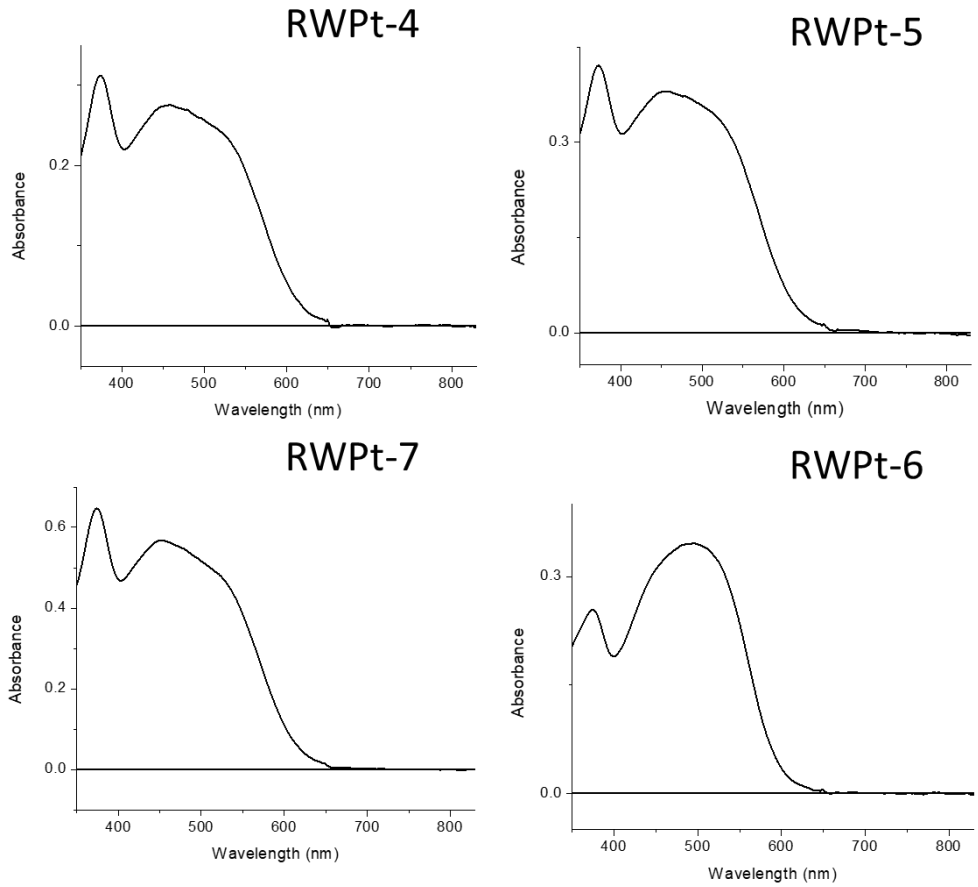

Figure 267. *UV-Vis Spectra for the platinum roller wheel complexes.*

Table 38. *Emission lifetimes of the platinum roller wheel complexes.*

Lifetime	RWPt-4	RWPt-5	RWPt-6	RWPt-7
τ_4 (ps)	694	702	1056	310

CHAPTER 8

References

1. Johnson, P. J. M.; Halpin, A.; Morizumi, T.; Prokhorenko, V. I.; Ernst, O. P.; Miller, R. J. D.; Local Vibrational Coherences Drive the Primary Photochemistry of Vision. *Nature Chem.* **2015** *7*, 980-986.

2. Yeh, A.; Scott, N.; & Taube, H., S to O and O to S Linkage Isomerization in Sulfoxide Complexes of Pentaammineruthenium. *Inorg. Chem.* **1982**, *21*, 2542–2545.

3. He, W.; Livshits, M. Y.; Dickie, D. A.; Yang, J.; Quinnett, R.; Rack, J. J.; Wu, Q.; Qin, Y., A "Roller Wheel" Pt-Containing Small Molecule that Outperforms its Polymer Analogs in Organic Solar Cells. *Chem. Sci.* **2016**, *7*, 5798-5804.

4. Livshits, M. Y.; He, W.; Zhang, Z.; Qin, Y.; Rack, J. J., Triplet Excitet-State Energetics and Dynamics in Molecular "Roller Wheels". *J. Phys. Chem. C.* **2019**, *123*, 16556-16564.

5. Espenson, J. H. Chemical Kinetics and Reaction Mechanisms. **2002**, New York, McGraw Hill.

6. Rack, J. J.; Electron Transfer Triggered Isomerization in Ruthenium and Osmium Sulfoxide Complexes. *Coord. Chem. Rev.* **2009**, *253* (1−2), 78−85.

7. King, A. W.; Wang, L.; Rack, J. J., Excited State Dynamics and Isomerization in Ruthenium Sulfoxide Complexes. *Acc. Chem. Res.* **2015**, *48* (4), 1115−1122.

8. Garg, K.; King, A. W.; Rack, J. J., One Photon Yields Two Isomerizations: Large Atomic Displacements during Electronic Excited-State Dynamics in Ruthenium Sulfoxide Complexes. *J. Am. Chem. Soc*. **2014**, *136* (5), 1856−1863.

9. Garg, K.; Engle, J. T.; Ziegler, C. J.; Rack, J. J., Tuning excited state isomerization dynamics through ground state structural changes in analogous ruthenium and osmium sulfoxide complexes. *Chem. Eur. J.* **2013**, *19* (35), 11686−11695.

10. Angell, S. E.; Rogers, C. W.; Zhang, Y.; Wolf, M. O.; Jones, W. E., Hemilabile coordination complexes for sensing applications. *Coord. Chem*. *Rev*. **2006**, *250* (13−14), 1829−1841.

11. Dixon, I. M.; Lebon, E.; Sutra, P.; Igau, A., Luminescent ruthenium-polypyridine complexes & phosphorus ligands: anything but a simple story. *Chem. Soc. Rev.* **2009**, *38* (6), 1621−1634.

12. Gutmann, R.; Czermak, G.; Dumfort, A.; Van der Veer, W. E.; Hong, B.; Kopacka, H.; Ongania, K. H.; Bechtold, T.; Bruggeller, P., Title *Inorg. Chem. Commun*. **2005**, *8* (3), 319−322.

13. Lebon, E.; Bastin, S.; Sutra, P.; Vendier, L.; Piau, R. E.; Dixon, I. M.; Boggio-Pasqua, M.; Alary, F.; Heully, J. L.; Igau, A.; Juris, A., Can a functionalized phosphine ligand promote room temperature luminescence of the $[Ru(bpy)(tpy)]^{2+}$ core? *Chem. Commun*. **2012**, *48* (5), 741−743.

14. Lebon, E.; Sylvain, R.; Piau, R. E.; Lanthony, C.; Pilme, J.; Sutra, P.; Boggio-Pasqua, M.; Heully, J. L.; Alary, F.; Juris, A.; Igau, A., Phosphoryl Group as a Strong σ-Donor Anionic Phosphine-Type Ligand: A Combined Experimental and Theoretical Study on Long-Lived Room Temperature Luminescence of the $[Ru(tpy)(bpy)(Ph2PO)]^{+}$ Complex. *Inorg. Chem*. **2014**, *53* (4), 1946−1948.

15. Litke, S. V.; Ershov, A. Y.; Meyer, T. J., Deactivation Pathways for Metal-to-Ligand Charge-Transfer Excited States of Ruthenium Polypyridyl Complexes with Triphenylphosphine as a Ligand. *J. Phys. Chem. A* **2011**, *115* (50), 14235−14242.

16. Rogers, C. W.; Patrick, B. O.; Rettig, S. J.; Wolf, M. O., Ligand assisted O-dealkylation of bis(bipyridyl) ruthenium(II) phosphineether complexes. *J. Chem. Soc. Dalton Trans*. **2001**, *8*, 1278−1283.

17. Sutra, P.; Igau, A., Anionic phosph(in)ito ("phosphoryl") ligands: Non-classical "actor" phosphane-type ligands in coordination chemistry. *Coord. Chem. Rev.* **2016**, *308*, 97−116.

18. Dixon, I. M.; Lebon, E.; Loustau, G.; Sutra, P.; Vendier, L.; Igau, A.; Juris, A., Broad HOMO–LUMO gap tuning through the coordination of a single phosphine, aminophosphine or phosphite onto a Ru(tpy)(bpy)2+ core. *Dalton Trans.* **2008**, *41*, 5627−5635.

19. Suzuki, T.; Kuchiyama, T.; Kishi, S.; Kaizaki, S.; Takagi, H. D.; Kato, M., Ruthenium(II) Complexes Containing 8-(Dimethylphosphino)quinoline (Me2Pqn): Preparation, Crystal Structures, and Electrochemical and Spectroscopic Properties of [Ru(bpy or phen)3-n(Me2Pqn)n](PF6)2 (bpy = 2,2′-Bipyridine; phen = 1,10-Phenanthroline; n = 1, 2, or 3). *Inorg. Chem*. **2003**, *42* (3), 785−795.

20. Carlson, B.; Phelan, G. D.; Kaminsky, W.; Dalton, L.; Jiang, X. Z.; Liu, S.; Jen, A. K. Y., Divalent Osmium Complexes: Synthesis, Characterization, Strong Red Phosphorescence, and Electrophosphorescence. *J. Am. Chem*. *Soc*. **2002**, *124* (47), 14162− 14172.

21. Klassen, D. M.; DelPup, R. V., Excited State Properties of Mixed Phosphine 2-(2'-Pyridyl)quinoline Complexes of Ruthenium(II) *Inorg. Chem*. **2002**, *41* (12), 3155−3160.

22. La Pensee, A. A.; Bickley, J.; Higgins, S. J.; Marcaccio, M.; Paolucci, F.; Roffia, S.; Charnock, J. M., Syntheses, characterization and redox properties of homoleptic ruthenium(ii)–diphosphine and diarsine complexes: deviations from ligand additivity. *J. Chem. Soc. Dalton Trans*. **2002**, *22*, 4095−4104.

23. Angell, S. E.; Zhang, Y.; Rogers, C. W.; Wolf, M. O.; Jones, W. E., Photophysical properties of Ru(II) bipyridyl complexes containing hemilabile phosphine-ether ligands. *Inorg. Chem*. **2005**, *44* (21), 7377−7384.

24. Rogers, C. W.; Wolf, M. O., Towards multianalyte molecule-based sensors: Reactivity and photophysical behaviour of hemilabile ligand-containing Ru(II) bipyridyl complexes. *Chem. Commun*. **1999**, *22*, 2297− 2298.

25. Juris, A.; Balzani, V.; Barigelletti, F.; Campagna, S.; Belser, P.; von Zelewsky, A., Ru(II) polypyridine complexes: photophysics, photochemistry, eletrochemistry, and chemiluminescence. *Coord. Chem. Rev.* **1988**, *84*, 85−277.

26. Feringa, B. L.; Browne, W. R., *Molecular Switches*, second completely revised and enlarged edition; Wiley-VCH: Weinheim, Germany, 2011.

27. Goulet-hanssens, A.; Eisenreich, F.; & Hecht, S., Enlightening Materials with Photoswitches. *Adv. Mater*. **2020**, *32* (20), 23.

28. Taniguchi, T.; Asahi, T.; Koshima, H., Photomechanical Azobenzene Crystals. *Crystals* **2019**, *9* (9), 14.

29. Crespi, S.; Simeth, N. A.; Koinig, B., Heteroaryl Azo Dyes as Molecular Photoswitches. *Nat. Rev. Chem*. **2019**, *3* (3), 133-146.

30. Lerch, M. M.; Szymanski, W.; Feringa, B., The (photo)chemistry of Stenhouse photoswitches: guiding principles and system design. *Chem. Soc. Rev*. **2018**, *47* (6), 1910-1937.

31. Seshadri, S.; Gockowski, L. F.; Lee, J.; Sroda, M.; Helgeson, M. E.; de Alaniz, J. R.; Valentine, M. T., Self-regulating photochemical Rayleigh-Benard convection using a highly-absorbing organic photoswitch. *Nat. Commun*. **2020**, *11* (1), 8.

32. Castellano, M.; Ruiz-Garcia, R.; Cano, J.; Ferrando-Soria, J.; Pardo, E.; Fortea-Perez, F. R.; Stiriba, S. E.; Barros, W. P.; Stumpf, H. O.; Canadillas-Delgado, L.; Pasan, J.; Ruiz-Perez, C.; de Munno, G.; Armentano, D.; Journaux, Y.; Lloret, F.; Julve, M., Metallosupramolecular approach toward multifunctional magnetic devices for molecular spintronics. *Coord. Chem. Rev*. **2015**, *303*, 110-138.

33. Fihey, A.; Perrier, A.; Browne, W. R.; Jacquemin, D., Multiphotochromic molecular systems. *Chem. Soc. Rev*. **2015**, *44* (11), 3719-3759.

34. Harvey, E. C.; Feringa, B. L.; Vos, J. G.; Browne, W. R.; Pryce, M. T., Transition metal functionalized photo- and redox-switchable diarylethene based molecular switches. *Coord. Chem. Rev*. **2015**, *282*, 77-86.

35. Ko, C. C.; Yam, V. W. W., Coordination Compounds with Photochromic Ligands: Ready Tunability and Visible Light-Sensitized Photochromism. *Accounts Chem. Res*. **2018**, *51* (1), 149-159.

36. Matsuda, K.; Irie, M., Diarylethene as a photo switching unit. J. *Photochem. Photobiol. C-Photochem. Rev*. **2004**, *5* (2), 169-182.

37. McClure, B. A.; Abrams, E. R.; & Rack, J. J., Excited state distortion in photochromic ruthenium sulfoxide complexes. *J. Am. Chem. Soc.* **2010**, *132*, 5428-5436.

38. Porter, B. L.; McClure, B. A.; Abrams, E. R.; Engle, J. T.; Ziegler, C. J.; Rack, J. J., Photoisomerization in an analogous set of ruthenium sulfoxide complexes. *J. Photochem. Photobiol. A-Chem*. **2011**, *217* (2-3), 341-346.

39. Vittardi, S. B.; Thapa Magar, R.; Breen, D. J.; Rack, J. J. A Future Perspective on Phototriggered Isomerizations of Transition Metal Sulfoxides and Related Complexes. *J. Am. Chem. Soc.* **2021**, *143* (2), 526–537.

40. Litke, S. V.; Mezentseva, T. V.; Litke, A. S.; Lyalin, G. N.; & Ershov, A. Y., Photophysics of Mixed Ligand Complexes of Ruthenium(II) with 2,2'-bipyridyl and Phosphines. *Optics and* Spectroscopy, **2000**, *89*, 924–930.

41. Litke, S. V. & Ershov, A. Y., Photophysics of Bis-Bipyridyl Complexes of Ruthenium (II) with Triphenylphosphine. *Optics and Spectroscopy*, **2011**, *110*, 561–567.

42. Spokoyny, A. M.; Machan, C. W.; Clingerman, D. J.; Rosen, M. S.; Wiester, M. J.; Kennedy, R. D.; Stern, C. L.; Sarjeant, A. A.; Mirking, C. A., A coordination chemistry dichotomy for icosahedral carborane-based ligands. *Nat. Chem.* **2011**, *3*, 590–596.

43. Grapperhaus, C. A.; & Darensbourg, M. Y., Oxygen Capture by Sulfur in Nickel Thiolates. *Acc. Chem. Res.* **1998**, *31*, 451–459.

44. Ouch, K.; Mashuta, M. S.; & Grapperhaus, C. A., Metal-Stabilized Thiyl Radicals as Scaffolds for Reversible Alkene Addition via C-S Bond Formation/Cleavage. *Inorg. Chem.* **2011**, *50*, 9904-9914.

45. Sampson, K. O.; Kumar, D.; Mashuta, M. S.; & Grapperhaus, C. A., Addition of

polysubstituted alkenes, aromatic alkynes, and dienes to a metal-stabilized thiyl radical via carbon-sulfur bond formation: Electrochemical, chemical, and computational investigations. *Inorganica Chim. Acta.* **2013**, *408*, 1-8.

46. Masitas, C. A.; Mashuta, M. S.; & Grapperhaus, C. A., Asymmetric oxygenation of a ruthenium dithiolate mimics the mixed sulfenato/sulfinato donor sets of nitrile hydratase and thiocyanate hydrolase. *Inorg. Chem.* **2010**, *49*, 5344–5346.

47. Masitas, C. A.; Kumar, M.; Mashuta, M. S.; Kozlowski, P. M.; & Grapperhaus, C. A., Controlled sulfur oxygenation of the ruthenium dithiolate (4,7-Bis-(2'-methyl-2'-mercaptopropyl)-1-thia-4,7-diazacyclononane) RuPPh3 under limiting O2 conditions yields thiolato/sulfinato, sulfenato/sulfinato, and bis-sulfinato derivatives. *Inorg. Chem.* **2010**, *49*, 10875-10881.

48. Grapperhaus, C. A.; Poturovic, S; & Mashuta, M. S., Dichloromethane alkylates a trithiolato-ruthenium complex to yield a methylene-bridged thioether core. Synthesis and structural comparison to the thiolato-ruthenium precursor. *Inorg. Chem.* **2002**, *41*, 4309-4311.

49. Ouch, K.; Mashuta, M. S.; & Grapperhaus, C. A., Alkyne addition to a metal-stabilized thiyl radical: Carbon-sulfur bond formation between 1-octyne and [Ru(SP)3]+. *Eur. J. Inorg. Chem.* **2012**, 475–478.

50. Kosgei, G. K.; Breen, D. J.; Lamb, R. W.; Livshits, M. Y.; Crandall, L. A.; Ziegler, C. J. ; Webster, C. E.; Rack, J. J.; Controlling Photoisomerization Reactivity Through Single Functional Group Substitutions in Ruthenium Phosphine Sulfoxide Complexes. *J. Am. Chem. Soc.* **2018**, *140*, 9819–9822.

51. Rack, J. J.; Rachford, A. A.; & Shelker, A. M., Turning off Phototriggered Linkage Isomerizations in Ruthenium Dimethyl Sulfoxide Complexes. *Inorg. Chem.* **2003**, *42*, 7357–7359.

52. McClure, B. A.; & Rack, J. J., Two-Color Reversible Switching in a Photochromic Ruthenium Sulfoxide Complex. *Angew. Chemie.* **2009**, *121*, 8708–8710.

53. McClure, B. A.; Mockus, N. V.; Butcher, D. P.; Lutterman, D. A.; Turro, C.; Peterson, J. L.; & Rack, J. J.; Photochromic ruthenium sulfoxide complexes: Evidence for isomerization through a conical intersection. *Inorg. Chem.* **2009**, *48*, 8084–8091.

54. Rachford, A. A.; Petersen, J. L.; & Rack, J. J., Efficient energy conversion in photochromic ruthenium DMSO complexes. *Inorg. Chem.* **2006**, *45*, 5953–5960.

55. Butcher, D. P.; Rachford, A. A.; Petersen, J. L.; & Rack, J. J., Phototriggered S → O isomerization of a ruthenium-bound chelating sulfoxide. *Inorg. Chem.* **2006**, *45*, 9178–9180.

56. Moorlag, C.; Clot, O.; Wolf, M. O.; & Patrick, B. O., Switchable thiophene coordination in Ru(II) bipyridyl phosphinoterthiophene complexes. *Chem. Commun.* **2002**, 3028–3029.

57. Orpen, A. G.; & Connelly, N. G., Structural Systematics: Role of P-A σ* Orbitals in Metal-Phosphorus π-Bonding in Redox-Related Pairs of M-PA3 Complexes (A = R, Ar, OR; R = Alkyl). *Organometallics* **1990**, *9*, 1206–1210.

58. Anderson, K. M.; & Orpen, A. G., On the relative magnitudes of *cis* and *trans* influences in metal complexes. *Chem. Commun.* **2001**, *1*, 2682–2683.

59. Dunne, B. J.; Morris, R. B.; & Orpen, A. G., Structural systematics. Part 3. Geometry deformations in triphenylphosphine fragments: A test of bonding theories in phosphine complexes. *J. Chem. Soc. Dalt. Trans.* **1991**, 653–661.

60. Leyssens, T.; Peeters, D.; Orpen, A. G.; & Harvey, J. N., Insight into metal-phosphorus bonding from analysis of the electronic structure of redox pairs of metal-phosphine complexes. *New J. Chem.* **2005**, *29*, 1424–1430.

61. Arias-Rotondo, D. M.; & Mccusker, J. K., An Overview of the Physical and Photophysical Properties of [Ru(bpy)3]2+. *Visible Light Photocatalysis in Organic Chemistry.* **2018**, 5803–5820.

62. McClure, B. A.; & Rack, J. J., Isomerization in photochromic ruthenium sulfoxide complexes. *Eur. J. Inorg. Chem.* **2010**, 3895–3904.

63. Magar, R. T.; Breen, D. J.; Schrage, B. R.; Ziegler, C. J.; & Rack, J., Slow 3MLCT Formation Prior to Isomerization in Ruthenium Carbene Sulfoxide Complexes. *Inorg. Chem.* **2021**, *60*, 16120-16127.

64. Roecker, L.; Dobson, J. C.; Vining, W. J.; & Meyer, T. J., Oxygen Atom Transfer in the Oxidations of Dimethyl Sulfide and Dimethyl Sulfoxide by [(bpy)2(py)Ru(O)]2+. *Inorg. Chem.* **1987**, *26*, 779-781.

65. Grusenmeyer, T. A.; Mcclure, B. A.; Ziegler, C. J.; & Rack, J. J., Solvent Effects on Isomerization in a Ruthenium Sulfoxide Complex. *Inorg. Chem.* **2010**, *49*, 4466-4470.

66. Alessio, E., Synthesis and reactivity of Ru-, Os-, Rh-, Ir-Halide-Sulfoxide Complexes. *Chem. Rev.* **2004**, *104* (9), 4203–4242.

67. Geremia, S.; Mestroni, S.; Calligaris, M; & Alessio, E., The first example of a double bridged diruthenium(II) complex containing the rare bridging S,O bidentate dimethyl sulfoxide ligand which defines a stable Ru-Cl-Ru-S-O five-membered ring. *J. Chem. Soc., Dalt. Trans.* **1998**, 2447–2448.

68. Calligaris, M., Structure and bonding in metal sulfoxide complexes: An update. *Coordination Chemistry Reviews* **2004**, *248*, 351–375.

69. Calligaris, M.; & Carugo, O., Structure and bonding in metal sulfoxide complexes. *Coordination Chemistry Reviews* **1996**, *153*, 83–154.

70. Keating, C. S.; McClure, B. A.; Rack, J. J.; & Rubtsov, I. V., Sulfoxide Stretching Modeas a Structural Reporter via Dual-Frequency Two-Dimensional Infrared Spectroscopy. *J. Chem. Phys.* **2010**, *133*, 144513.

71. Porter, T. M.; Wang, J.; Li, Y.; Xiang, B.; Salsman, C.; Miller, J.; Xiong, W.; & Kubiak, C. P., Direct Observation of the Intermediate in an Ultrafast Isomerization. *Chem. Sci.* **2019**, *10*, 113-117.

72. Zhu, S. Q.; Li, W. L.; Zhu, W. H. Photochromic Diarylethenes Based on Novel Ethene Bridges. *Prog. Chem*. **2016**, *28* (7), 975−992.

73. Fuchter, M. J. On the Promise of Photopharmacology Using Photoswitches: A Medicinal Chemist's Perspective. *J. Med. Chem*. **2020**, *63* (20), 11436−11447.

74. Gerkman, M. A.; Gibson, R. S. L.; Calbo, J.; Shi, Y. R.; Fuchter, M. J.; Han, G. G. D. Arylazopyrazoles for Long-Term Thermal Energy Storage and Optically Triggered Heat Release below 0 degrees C. *J. Am. Chem. Soc*. **2020**, *142* (19), 8688−8695.

75. Cole, J. M.; Gosztola, D. J.; Velazquez-Garcia, J. D.; Grass Wang, S.; Chen, Y. S. Rapid build up of nanooptomechanical transduction in single crystals of a ruthenium-based SO2 linkage photoisomer. *Chem. Commun*. **2021**, *57* (11), 1320−1323.

76. Coppens, P.; Novozhilova, I.; Kovalevsky, A. Photoinduced linkage isomers of transition-metal nitrosyl compounds and related complexes. Chem. Rev. **2002**, 102 (4), 861−883.

77. Hatcher, L. E.; Skelton, J. M.; Warren, M. R.; Raithby, P. R. Photocrystallographic Studies on Transition Metal Nitrito Metastable Linkage Isomers: Manipulating the Metastable State. *Acc. Chem. Res*. **2019**, *52* (4), 1079−1088.

78. Mukaddem, K. T.; Cole, J. M.; Beyer, K. A.; Sylvester, S. O. Local Atomic Structure in Photoisomerized Ruthenium Sulfur Dioxide Complexes Revealed by Pair Distribution Function Analysis. *J. Phys. Chem. C* **2020**, *124* (18), 10094−10104.

79. Sylvester, S. O.; Cole, J. M.; Waddell, P. G. Photoconversion Bonding Mechanism in Ruthenium Sulfur Dioxide Linkage Photoisomers Revealed by in Situ Diffraction. *J. Am. Chem. Soc*. **2012**, *134* (29), 11860−11863.

80. Bokareva, O. S.; Baig, O.; Al-Marri, M. J.; Kuhn, O.; Gonzalez, L. The effect of N-heterocyclic carbene units on the absorption spectra of Fe(ii) complexes: a challenge for theory. *Phys. Chem. Chem*. *Phys.* **2020**, *22* (47), 27605−27616.

81. Fliedel, C.; Labande, A.; Manoury, E.; Poli, R. Chiral N-heterocyclic carbene ligands with additional chelating group(s) applied to homogeneous metal-mediated asymmetric catalysis. *Coord. Chem. Rev*. **2019**, *394*, 65−103.

82. Peris, E. Smart N-Heterocyclic Carbene Ligands in Catalysis. *Chem. Rev*. **2018**, *118* (19), 9988−10031.

83. Romain, C.; Bellemin-Laponnaz, S.; Dagorne, S. Recent progress on NHC-stabilized early transition metal (group 3−7) complexes: Synthesis and applications. *Coord. Chem. Rev.* **2020**, *422*, 213411.

84. Das, S.; Rodrigues, R. R.; Lamb, R. W.; Qu, F. R.; Reinheimer, E.; Boudreaux, C. M.; Webster, C. E.; Delcamp, J. H.; Papish, E. T. Highly Active Ruthenium CNC Pincer Photocatalysts for VisibleLight-Driven Carbon Dioxide Reduction. *Inorg. Chem*. **2019**, *58* (12), 8012−8020.

85. Eivgi, O.; Phatake, R. S.; Nechmad, N. B.; Lemcoff, N. G. Light-Activated Olefin Metathesis: Catalyst Development, Synthesis, and Applications. *Acc. Chem. Res*. **2020**, *53* (10), 2456−2471.

86. Kender, W. T.; Turro, C. Unusually Slow Internal Conversion in N-Heterocyclic Carbene/Carbanion Cyclometallated Ru(II) Complexes: A Hammett Relationship. *J. Phys. Chem. A* **2019**, *123* (13), 2650−2660.

87. Ryan, R. T.; Stevens, K. C.; Calabro, R.; Parkin, S.; Mahmoud, J.; Kim, D. Y.; Heidary, D. K.; Glazer, E. C.; Selegue, J. P. Bis-tridentate N-Heterocyclic Carbene Ru(II) Complexes are Promising New Agents for Photodynamic Therapy. *Inorg. Chem*. **2020**, *59* (13), 8882−8892.

88. Tang, Z.; Chang, X. Y.; Wan, Q. Y.; Wang, J.; Ma, C. S.; Law, K. C.; Liu, Y. G.; Che, C. M. Bis(tridentate) Iron(II) Complexes with a Cyclometalating Unit: Photophysical Property Enhancement with Combinatorial Strong Ligand Field Effect. *Organometallics* **2020**, *39* (15), 2791−2802.

89. Torres, J.; Carrion, M. C.; Leal, J.; Castaneda, G.; Manzano, B. R.; Jalon, F. A. Homoleptic ruthenium complexes with N-heterocyclic carbene ligands as photosensitizers in the photocatalytic generation of H-2 from water. *J. Organomet. Chem*. **2019**, *898*, 120880.

90. Aghazada, S.; Zimmermann, I.; Scutelnic, V.; Nazeeruddin, M. K. Synthesis and Photophysical Characterization of Cyclometalated Ruthenium Complexes with N-Heterocyclic Carbene Ligands. *Organometallics* **2017**, *36* (13), 2397−2403.

91. Schleicher, D.; Leopold, H.; Borrmann, H.; Strassner, T. Ruthenium(II) Bipyridyl Complexes with Cyclometalated NHC Ligands. Inorg. Chem. **2017**, 56 (12), 7217−7229.

92. Kroener, R.; Heeg, M. J.; Deutsch, E. Synthesis and characterization of polypyridine ruthenium(II) complexes containing s-bonded thioether ligands: X-ray crystal-structures of cis-bis(2,2'- bipyridine)bis(phenothiazine-s)ruthenium(II) and trans-bis(2,2'- bipyridine)bis(phenothiazine-s)ruthenium(II) hexafluorophosphates. *Inorg. Chem*. **1988**, *27* (3), 558−566.

93. Root, M. J.; Deutsch, E. Synthesis and characterization of (bipyridine)(terpyridine)(chalcogenoether)ruthenium(II) complexes: kinetics and mechanism of the hydrogen-peroxide oxidation of (BPY)(TPY)RUS(CH3)2 2+ to (BPY)(TPY)RUS(O)(CH3)2 2+: Kinetics of the aquation of (BPY)(TPY)RUS(O)(CH3)2 2+. *Inorg. Chem.* **1985**, *24* (10), 1464−1471.

94. Root, M. J.; Sullivan, B. P.; Meyer, T. J.; Deutsch, E. Thioether, thiolato, and 1,1-dithioato complexes of bis(2,2'-bipyridine)- ruthenium(II) and bis(2,2'-bipyridine)osmium(II). *Inorg. Chem*. **1985**, *24* (18), 2731−2739.

95. Anderson, P. A.; Keene, F. R.; Meyer, T. J.; Moss, J. A.; Strouse, G. F.; Treadway, J. A. Manipulating the properties of MLCT excited states. *J. Chem. Soc. Dalton Trans*. **2002**, *20*, 3820−3831.

96. Mangalum, A.; Htet, Y.; Roe, D. A.; McMillen, C. D.; Tennyson, A. G. Net charge effects in N-heterocyclic carbene ruthenium complexes with similar oxidation states and coordination geometries. *Inorg. Chim. Acta* **2015**, *435*, 320−326.

97. Rachford, A. A.; Petersen, J. L.; Rack, J. J. Designing molecular bistability in ruthenium dimethyl sulfoxide complexes. *Inorg. Chem*. **2005**, *44* (22), 8065−8075.

98. Powell, D. W.; Lay, P. A. Linkage isomerization-reactions of (acetone)pentaammineruthenium(III) and (acetone)- pentaammineruthenium(II) complexes. *Inorg. Chem*. **1992**, *31* (17), 3542−3550.

99. Krishnan, R.; Schultz, R. H. Electronic and steric effects in ligand substitution at a transient organometallic species: The reaction of W(CO)(5)(cyclohexane) with (CH3)(n)THF and (CH3)(n)- furan (n = 1, 2). *Organometallics* **2001**, *20* (15), 3314−3322.

100. Shagal, A.; Schultz, R. H. Linkage isomerization in M(CO) (5)(DHF) complexes (M = Cr, Mo, W; DHF = 2,3-dihydrofuran, 2,5- dihydrofuran) studied by time-resolved infrared absorption spectroscopy. *Organometallics* **2002**, *21* (25), 5657−5665.

101. Shagal, A.; Schultz, R. H. Steric and electronic effects in linkage isomerization reactions of M(CO)(5)(L) (M = Cr, Mo, W; L = 2- methyl-2,3-dihydrofuran, 2,3-dihydropyran). *Organometallics* **2007**, *26* (20), 4896−4903.

102. To, T. T.; Duke, C. B.; Junker, C. S.; O'Brien, C. M.; Ross, C. R.; Barnes, C. E.; Webster, C. E.; Burkey, T. J. Linkage isomerization as a mechanism for photochromic materials: Cyclopentadienylmanganese tricarbonyl derivatives with chelatable functional groups. *Organometallics* **2008**, *27* (2), 289−296.

103. Yoon, S.; Kukura, P.; Stuart, C. M.; Mathies, R. A. Direct observation of the ultrafast intersystem crossing in tris(2,2 '-bipyridine) ruthenium(II) using femtosecond stimulated Raman spectroscopy. *Mol. Phys*. **2006**, *104* (8), 1275−1282.

104. Bhasikuttan, A. C.; Suzuki, M.; Nakashima, S.; Okada, T. Ultrafast fluorescence detection in tris(2,2 '-bipyridine)ruthenium(II) complex in solution: Relaxation dynamics involving higher excited states. *J. Am. Chem. Soc*. **2002**, *124* (28), 8398−8405.

105. Shimizu, T.; Takaya, N.; Nakamura, A., An L-Glucose Catabolic Pathway in *Paracoccus* Species 43P*, *J. Biol. Chem.*, **2012**, *287* (48), 40448-40456.

106. Burton, A. S.; Berger, E. L., Insights into Abiotically-Generated Amino Acid Enantiomeric Excesses Found in Meteroites, *Life*, **2018**, *8* (14).

107. Montgomery, C. D., Factors Affecting Energy Barriers for Pyramidal Inversion in Amines and Phosphines: A Computational Chemistry Lab Exercise, *J. Chem. Educ.* **2013**, *90*, 661–664.

108. Lee, W.; & Jenks, W. S., Photophysics and Photostereomutation of Aryl Methyl Sulfoxides. *J. Org. Chem*. **2001**, *66,* 474–480.

109. Carreño, M., Applications of Sulfoxides to Asymmetric Synthesis of Biologically Active Compounds, *Chem. Rev.* **1995**, *95*, 1717-1760.

110. Spry, D. O., Conversion of Penicillin to Cephalosporin *via* a Double Sulfoxide Rearrangement, *J. Am. Chem. Soc.* **1970**, *92* (16), 5006-5008.

111. Hammond, G. S.; Gotthardt, H.; Coyne, L. M.; Axelrod, M.; Rayner, D. R.; Mislow, K., Energy Transfer in the Racemization of Aryl Sulfoxides. *J. Am. Chem. Soc.* **1965**, *87* (21), 4959-4960.

112. Mislow, K.; Axelrod, M.; Rayner, D. R.; Gottardt, H.; Coyne, L. M.; Hammond, G. S. Energy Transfer in the Racemization of Aryl Sulfoxides, *J. Am. Chem. Soc*. **1965**, *87*, 4958-4959.

113. Rayner, D. R.; Miller, E. G.; Bickart, P.; Gordon, A. J.; Mislow, K., Mechanisms of Thermal Racemization of Sulfoxides, *J. Am. Chem. Soc.* **1966**, *88* (13), 3138-3139.

114. Rayner, D. R.; Gordon, A. J.; Mislow, K., Thermal Racemization of Diaryl, Alkyl Aryl, and Dialkyl Sulfoxides by Pyramidal Inversion, *J. Am. Chem. Soc.* **1968**, *90* (18), 4854-4860.

115. Cubbage, J. W.; Tetzlaff, T. A.; Groundwater, H.; McCulla, R. D.; Nag, M.; Jenks, W. S., Bimolecular Photoreduction of Aromatic Sulfoxides. *J. Org. Chem*. **2001**, *66*, 8621–8628.

116. Darmanyan, A. P.; Gregory, D. D.; Guo, Y; & Jenks, W. S., Generation and Decay of Aryl Sulfinyl and Sulfenyl Radicals: A Transient Absorption and Computational Study, *J. Phys. Chem. A.* **1977**, *101*, 6855–6863.

117. Guo, Y.; & Jenks, W. S., Photolysis of Alkyl Aryl Sulfoxides: a-Cleavage, Hydrogen Abstraction, and Racemization. *J. Org. Chem*. **1997**, *62*, 857–864.

118. Johnson, C., The Inversion of the Sulfoxide Configuration, *J. Am. Chem. Soc.* **1963**, *85* (7), 1020-1021.

119. Gurria, G. M.; Posner, G. H., Photochemical Deoxygenation of Aryl Sulfoxides, *J. Org. Chem.* **1973**, *38* (13) 2419-2420.

120. Vos, B. W.; & Jenks, W. S., Evidence for a Nonradical Pathway in the Photoracemization of Aryl Sulfoxides. *J. Am. Chem. Soc*. **2002**, *124* (11), 2544–2547.

121. Tsurutani, Y.; Machida, S.; Horie, K.; Kawashima, Y.; Nakano, H.; Hirao, K., Fluorescence and Photoinversion Reactions in Solutions of Chiral Diaryl Sulfoxides with Various Sizes of Aromatic Rings. *J. Photochem. Photobiol. A Chem.* **1999**, *122*, 161-168.

122. Tsurutani, Y.; Yamashita, T.; Horie, K., Photoinversion Reaction of a Pyrenyl Sulfoxide in Solution and in Polymer Matrices, *Polym. J.*, **1998**, *30* (1), 11-16.

123. Kathayat, R. S.; Finney, N. S., Sulfoxides as Response Elements for Fluorescent Chemosensors, *J. Am. Chem. Soc.* **2013**, *135* (34) 12612-12614.

124. Kathayat, R. S.; Yang, L.; Sattasathuchana, T.; Zoppi, L.; Baldridge, K.; Linden, A.; Finney, N. S., On the Origins of Nonradiative Excited State Relaxation in Sulfoxides Relevant to Fluorescent Chemosensing, *J. Am. Chem. Soc.* **2016**, *138*, 15889-15895.

125. Raytchev, M.; Pandurski, E.; Buchvarov, I.; Modrakowski, C.; Fiebig, T., Bichromophoric Interactions and Time-Dependent Excited State Mixing in Pyrene

Derivatives. A Femtosecond Broad-Band Pump-Probe Study, *J. Phys. Chem. A.* **2003**, *107*, 4592-4600.

126. Pandurski, E.; Fiebig, T., Femtosecond Dynamics in Directly Linked Pyrenyl Donor-Acceptor Systems: Orbital Control of Optical Charge Transfer in the Excited State, *Chem. Phys. Lett.* **2002**, *357*, 272-278.

127. Neuwahl, F. V. R.; Foggi, P., Direct Observation of S_2-S_1 Internal Conversion in Pyrene by Femtosecond Transient Absorption, *Laser Chem.* **1999**, *19*, 375-379.

128. Foggi, P.; Pettini, L.; Santa, I.; Righini, R.; Califano, S., Transient Absorption and Vibrational Relaxation Dynamics of the Lowest Excited Singlet State of Pyrene in Solution, *J. Phys. Chem.* **1995**, *99*, 7439-7455.

129. Heinzelmann, W.; & Labhart, H., Triplet-Triplet Spectra and Triplet Quantum Yields of Some Aromatic Hydrocarbons in Liquid Solution, *Chem. Phys. Lett.* **1969**, *4*, 20–24.

130. Masetto, M., New insights into the femtosecond to microsecond photoinduced dynamics of Pyrene and Indole. **2014**.

131. Ohta, N.; Baba, H.; & Marconi, G., Vibronic Coupling and Intramolecular Dynamics of Pyrene as Revealed by the $S_0 \rightarrow S_2$ Excitation Spectrum in a Supersonic Jet. *Chem. Phys. Lett.* **1987**, *133,* 222–229.

132. Mangle, E. A.; & Topp, M. R., Excited-State Dynamics of Jet-Cooled Pyrene and Some Molecular Complexes. J. *Phys. Chem.* **1986**, *90*, 802–807.

133. Birks, J. B.; Dyson, D. J.; Munro, I. H., 'Excimer' Fluorescence II. Lifetime Studies of Pyrene Solutions, *Proc. R. Soc. Lond. A.* **1963**, *275*, 575-588.

134. Krebs, N.; Pugliesi, I.; Hauer, J; & Riedle, E., Two-Dimensional Fourier Transform Spectroscopy in the Ultraviolet with Sub-20 fs Pump Pulses and 250-720 nm Supercontinuum Probe. *New J. Phys.* **2013**, *15*, 1–18.

135. Amann, N.; Pandurski, E.; Fiebig, T.; Wagenknecht, H., Electron Injection into DNA: Synthesis and Spectroscopic Properties of Pyrenyl-Modified Oligonucleotides, *Chem. Eur. J.* **2002**, *8* (21), 4877-4883.

136. Masuko, M.; Ohtani, H.; Ebata, K.; & Shimadzu, A., Optimization of Excimer-Forming Two-Probe Nucleic Acid Hybridization Method with Pyrene as a Fluorophore. *Nucleic Acids Res.* **1998**, *26*, 5409–5416.

137. Vishe, M.; Lathion, T.; Pascal, S.; Yushchenko, O.; Homberg, A.; Brun, E.; Vauthey, E.; Piguet, C.; Lacour, J., Excimer-Based On-Off Bis(pyreneamide) Macrocyclic Chemosensors. *Helv. Chim. Acta, **2018**, 101*.

138. Grusenmeyer, T. A.; King, A. W.; Mague, J. T.; Rack, J. J.; & Schmehl, R. H., Sn(iv) Schiff Base Complexes: Triplet Photosensitizers for Photoredox Reactions. *Dalt. Trans.* 2014, *43*, 17754–17765.

139. Hurst, J. R.; McDonald, J. D.; & Schuster, G. B., Lifetime of Singlet Oxygen in Solution Directly Determined by Laser Spectroscopy. *J. Am. Chem. Soc*. ***1982****, 104*, 2065–2067.

140. Abdel-Shafi, A. A.; Worrall, D. R.; Ershov, A. Y., Photosensitized Generation of Singlet Oxygen from Ruthenium(II) and Osmium(II) Bipyridyl Complexes, *Dalton Trans.* **2004**, 30-36.

141. Nag, A.; Kundu, T.; Bhattacharyya, K, Effect of Solvent Polarity on the Yield of Twisted Intramolecular Charge Transfer (TICT) Emission. Competition Between Formation and Nonradiative Decay of the TICT State, *Chem. Phys. Lett.* **1989**, *160* (3), 257-260.

142. Sasaki, S.; Drummen, G. P. C.; & Konishi, G. I.; Recent Advances in Twisted Intramolecular Charge Transfer (TICT) Fluorescence and Related Phenomena in Materials Chemistry. *J. Mater. Chem*. *C*. **2016**, *4*, 2731–2743.

143. LaFemina, J. P.; Duke, C. B.; & Paton, A., Electronic Structure and Twisted Intramolecular Charge Transfer in Dimethylanilines. *J. Chem. Phys.* **1987**, *87*, 2151-2157.

144. Grabowski, Z. R; Rotkiewicz, K., Siemiarczuk, A., Dual Fluorescence of Donor-Acceptor Molecules and the Twisted Intramolecular Charge Transfer (TICT) States, *Journal of Luminescence*, **1979**, *18-19*, 420-424.

145. Grabowski, Z. R.; Rotkiewicz, K.; Rettig, W., Structural Changes Accompanying Intramolecular Electron Charge Transfer: Focus on Twisted Intramolecular Charge-Transfer States and Structures, *Chem. Rev.* **2003**, *103*, 3899-4031.

146. Lu, L.; Zheng, T. Y.; Wu, Q. H.; Schneider, A. M.; Zhao, D. L.; Yu, L. P., Recent Advances in Bulk Heterojunction Polymer Solar Cells. *Chem. Rev*. **2015**, *115,* 12666−12731.

147. Chen, Y.; Wan, X.; Long, G. High Performance Photovoltaic Applications Using Solution-Processed Small Molecules. *Acc. Chem. Res*. **2013**, *46*, 2645−2655.

148. Roncali, J.; Leriche, P.; Blanchard, P. Molecular Materials for Organic Photovoltaics: Small is Beautiful. *Adv. Mater*. **2014**, *26*, 3821−3838.

149. Mikhnenko, O. V.; Blom, P. W. M.; Nguyen, T.-Q. Exciton Diffusion in Organic Semiconductors. *Energy Environ*. Sci. **2015***, 8*, 1867−1888.

150. Mikhnenko, O. V.; Azimi, H.; Scharber, M.; Morana, M.; Blom, P. W. M.; Loi, M. A. Exciton Diffusion Length in Narrow Bandgap Polymers. *Energy Environ*. *Sci.* **2012**, *5*, 6960−6965.

151. Castrucci, J. S.; Josey, D. S.; Thibau, E.; Lu, Z.-H.; Bender, T. P. Boron Subphthalocyanines as Triplet Harvesting Materials within Organic Photovoltaics. *J. Phys. Chem. Lett*. **2015***, 6*, 3121−3125.

152. Luppi, B. T.; Majak, D.; Gupta, M.; Rivard, E.; Shankar, K. Triplet Excitons: Improving Exciton Diffusion Length for Enhanced Organic Photovoltaics. *J. Mater. Chem. A* **2019**, *7*, 2445−2463.

153. Guo, F.; Ogawa, K.; Kim, Y.-G.; Danilov, E. O.; Castellano, F. N.; Reynolds, J. R.; Schanze, K. S. A Fulleropyrrolidine End-Capped Platinum-Acetylide Triad: the Mechanism of Photoinduced Charge Transfer in Organometallic Photovoltaic Cells*. Phys. Chem. Chem. Phys.* **2007**, *9*, 2724−2734.

154. Köhler, A.; Wittmann, H. F.; Friend, R. H.; Khan, M. S.; Lewis, J. The Photovoltic Effect in a Platinum Poly-yne. *Synth. Met*. **1994**, *67*, 245−249.

155. Harvey, P. D.; Gray, H. B. Low-lying Singlet and Triplet Electronic Excited States of Binuclear (D10-D10) Palladium and Platinum Complexes. *J. Am. Chem. Soc*. **1988**, *110*, 2145−2147.

156. Juvenal, F.; Lei, H.; Schlachter, A.; Karsenti, P.-L.; Harvey, P. D. Ultrafast Photoinduced Electron Transfers in Platinum(II)- Anthraquinone Diimine Polymer/PCBM Films*. J. Phys. Chem. C* **2019**, *123*, 5289−5302

157. Wong, W.-Y.; Ho, C.-L. Di-, Oligo- and Polymetallaynes: Syntheses, Photophysics, Structures and Applications. *Coord. Chem. Rev*. **2006**, *250*, 2627−2690s.

158. Mei, J.; Ogawa, K.; Kim, Y.-G.; Heston, N. C.; Arenas, D. J.; Nasrollahi, Z.; McCarley, T. D.; Tanner, D. B.; Reynolds, J. R.; Schanze, K. S. Low-Band-Gap Platinum Acetylide Polymers as Active Materials for Organic Solar Cells. *ACS Appl. Mater. Interfaces* **2009**, *1*, 150−161.

159. Hsu, H.-Y.; Vella, J. H.; Myers, J. D.; Xue, J.; Schanze, K. S. Triplet Exciton Diffusion in Platinum Polyyne Films. *J. Phys. Chem. C* **2014**, *118*, 24282−24289.

160. He, W.; Livshits, M. Y.; Dickie, D. A.; Zhang, Z.; Mejiaortega, L. E.; Rack, J. J.; Wu, Q.; Qin, Y. “Roller-Wheel”-Type Pt-Containing Small Molecules and the Impact of “Rollers” on Material Crystallinity, Electronic Properties, and Solar Cell Performance. *J. Am. Chem. Soc.* **2017**, *139*, 14109−14119. (26) Cataldo, F.; Iglesias-G

161. Sullivan, B. P.; D. J. Salmon; and T. J. Meyer, Mixed phosphine 2, 2'-bipyridine complexes of ruthenium. *Inorganic Chemistry* **1978**, *17* (12), 3334-3341.

162. Hunter, C.; Sanders, J., The Nature of $\pi - \pi$ Interactions. *J. Am. Chem. Soc*. **1990**, *112* (14), 5525-5534.

163. Parr, R. G., Density Functional Theory of Atoms and Molecules, *Springer* Netherlands, Dordrecht. **1980**, 5-15.

164. Runge, E., and Gross, E. K. U., Density-Functional Theory for Time-Dependent Systems, *Phys. Rev. Lett.* **1984**, *52*, 997-1000.

165. Frisch, M. J., Trucks, G. W., Schlegel, H. B., Scuseria, G. E., Robb, M. A., Cheeseman, J. R., Scalmani, G., Barone, V., Mennucci, B., Petersson, G. A., Nakatsuji, H., Caricato, M., Li, X., Hratchian, H. P., Izmaylov, A. F., Bloino, J., Zheng, G., Sonnenberg, J. L., Hada, M., Ehara, M., Toyota, K., Fukuda, R., Hasegawa, J., Ishida, M., Nakajima, T., Honda, Y., Kitao, O., Nakai, H., Vreven, T., Jr., J. A. M., Peralta, J. E., Ogliaro, F., Bearpark, M. J., Heyd, J., Brothers, E. N., Kudin, K. N., Staroverov, V. N., Kobayashi, R., Normand, J., Raghavachari, K., Rendell, A. P., Burant, J. C., Iyengar, S. S., Tomasi, J., Cossi, M., Rega, N., Millam, N. J., Klene, M., Knox, J. E., Cross, J. B., Bakken, V., Adamo, C., Jaramillo, J., Gomperts, R., Stratmann, R. E., Yazyev, O., Austin, A. J., Cammi, R., Pomelli, C., Ochterski, J. W., Martin, R. L., Morokuma, K., Zakrzewski, V. G., Voth, G. A., Salvador, P., Dannenberg, J. J., Dapprich, S., Daniels, A. D., Farkas, Ö., Foresman, J. B., Ortiz, J. V., Cioslowski, J., and Fox, D. J. **2013**, Gaussian 09, Revision D.01, Gaussian, Inc., Wallingford, CT, USA.

166. Frisch, M. J., Trucks, G. W., Schlegel, H. B., Scuseria, G. E., Robb, M. A., Cheeseman, J. R., Scalmani, G., Barone, V., Petersson, G. A., Nakatsuji, H., Li, X., Caricato, M., Marenich, A. V., Bloino, J., Janesko, B. G., Gomperts, R., Mennucci, B., Hratchian, H. P., Ortiz, J. V., Izmaylov, A. F., Sonnenberg, J. L., Williams, Ding, F., Lipparini, F., Egidi, F., Goings, J., Peng, B., Petrone, A., Henderson, T., Ranasinghe, D., Zakrzewski, V. G., Gao, J., Rega, N., Zheng, G., Liang, W., Hada, M., Ehara, M., Toyota, K., Fukuda, R., Hasegawa, J., Ishida, M., Nakajima, T., Honda, Y., Kitao, O., Nakai, H., Vreven, T., Throssell, K., Montgomery Jr., J. A., Peralta, J. E., Ogliaro, F., Bearpark, M. J., Heyd, J. J., Brothers, E. N., Kudin, K. N., Staroverov, V. N., Keith, T. A., Kobayashi, R., Normand, J., Raghavachari, K., Rendell, A. P., Burant, J. C., Iyengar, S. S., Tomasi, J., Cossi, M., Millam, J. M., Klene, M., Adamo, C., Cammi, R., Ochterski, J. W., Martin, R. L., Morokuma, K., Farkas, O., Foresman, J. B., and Fox, D. J. **2016**, Gaussian 16, Revision A.03, Wallingford, CT.

167. Adamo, C., and Barone, V. Toward reliable density functional methods without adjustable parameters: The PBE0 model, *J. Chem. Phys.* **1999**, *110*, 6158-6170.

168. Grimme, S., Ehrlich, S., and Goerigk, L., Effect of the damping function in dispersion corrected density functional theory, *J. Comput. Chem.* **2011**, *32*, 1456-1465.

169. Couty, M., and Hall, M. B., Basis sets for transition metals: Optimized outer p functions, *J. Comput. Chem.* **1996**, *17*, 1359-1370.

170. Check, C. E., Faust, T. O., Bailey, J. M., Wright, B. J., Gilbert, T. M., and Sunderlin, L. S., Addition of Polarization and Diffuse Functions to the LANL2DZ Basis Set for P-Block Elements, *The Journal of Physical Chemistry A,* **2001**, *105*, 8111-8116.

171. Wadt, W. R., and Hay, P. J., Ab initio effective core potentials for molecular calculations. Potentials for main group elements Na to Bi, *J. Chem. Phys.* **1985**, *82*, 284-298.

172. Hehre, W. J., Ditchfield, R., and Pople, J. A., Self-Consistent Molecular Orbital Methods. XII. Further Extensions of Gaussian—Type Basis Sets for Use in Molecular Orbital Studies of Organic Molecules, *J. Chem. Phys.* **1972**, *56*, 2257-2261.

173. Hariharan, P. C., and Pople, J. A., The influence of polarization functions on molecular orbital hydrogenation energies, *Theor. Chim. Acta* **1973**, *28*, 213-222.

174. Petersson, G. A., and Al-Laham, M. A., A complete basis set model chemistry. II. Open-shell systems and the total energies of the first-row atoms, *J. Chem. Phys.* **1991**, *94*, 6081-6090.

175. McLean, A. D., and Chandler, G. S., Contracted Gaussian basis sets for molecular calculations. I. Second row atoms, Z=11–18, *J. Chem. Phys.* **1980**, *72*, 5639-5648.

176. Petersson, G. A., and Al-Laham, M. A., A complete basis set model chemistry. II. Open-shell systems and the total energies of the first-row atoms, *J. Chem. Phys.* **1991**, *94*, 6081-6090.

177. Andrae, D., Häußermann, U., Dolg, M., Stoll, H., and Preuß, H., Energy-adjustedab initio pseudopotentials for the second and third row transition elements, *Theor. Chim. Acta* **1990**, *77*, 123-141.

178. Martin, J. M. L., and Sundermann, A., Correlation consistent valence basis sets for use with the Stuttgart–Dresden–Bonn relativistic effective core potentials: The atoms Ga–Kr and In–Xe, *J. Chem. Phys.* **2001**, *114*, 3408-3420.

179. Papajak, E., Zheng, J., Xu, X., Leverentz, H. R., and Truhlar, D. G., Perspectives on Basis Sets Beautiful: Seasonal Plantings of Diffuse Basis Functions, *J. Chem. Theory Comput.* **2011**, *7*, 3027-3034.

180. Press, W. H., Teukolsky, S. A., Vetterling, W. T., and Flannery, B. P., **1992**, *Numerical recipes in C (2nd ed.): the art of scientific computing*, Cambridge University Press.

181. Canovese, L.; Visentin, F.; Levi, C.; Santo, C.; Bertolasi, V. The Interaction between Heteroditopic Pyridine-Nitrogen NHC with Novel Sulfur NHC Ligands in Palladium(0) Derivatives: Synthesis and Structural Characterization of a Bis-Carbene Palladium(0) Olefin Complex and Formation in Solution of an Alkene-Alkyne Mixed Intermediate as a Consequence of the Ligands Hemilability. *Inorganica Chimica Acta* **2012**, *390*, 105–118.

182. Fliedel, C.; Schnee, G.; Braunstein, P. Versatile Coordination Modes of Novel Hemilabile S -NHC Ligands. **2009**, *0* (1), 2474–2476.

183. Kirner, W. R.; Holmes Richter, G. *THE EFFECT OF STRUCTURE OF ORGANIC HALIDES ON THEIR RATE OF REACTION WITH INORGANIC HALIDES. III. THE EFFECT OF THE PHENYLTHIO, ALPHA-NAPHTHOXYL AND BETA-NAPHTHOXYL GROUPS*; **1926**; Vol. 48.

184. Dub, P. A.; Scott, B. L.; Gordon, J. C. Air-Stable NNS (ENENES) Ligands and Their Well-Defined Ruthenium and Iridium Complexes for Molecular Catalysis. *Organometallics* **2015**, *34* (18), 4464–4479.

185. Özdemir, I.; Şahin, N.; Gök, Y.; Demir, S.; Çetinkaya, B. In Situ Generated 1-Alkylbenzimidazole-Palladium Catalyst for the Suzuki Coupling of Aryl Chlorides. *Journal of Molecular Catalysis A: Chemical* **2005**, *234* (1–2), 181–185.

186. Silva-Cuevas, C.; Paleo, E.; León-Rayo, D. F.; Lujan-Montelongo, J. A. An Expeditious and Efficient Bromomethylation of Thiols: Enabling Bromomethyl Sulfides as Useful Building Blocks. *RSC Advances* **2018**, *8* (43), 24654–24659.

187. Mampuys, Pieter, et al. "Iodide-Catalyzed Synthesis of Secondary Thiocarbamates from Isocyanides and Thiosulfonates." *Org. Lett*., **2016**, 18 (12), pp 2808–2811

188. Kathayat, Rahul S., and Nathaniel S. Finney. "Sulfoxides as Response Elements for Fluorescent Chemosensors." *J. Am. Chem. Soc*., **2013**, 135 (34), pp 12612–12614